STUDIES OF NOBLE GASES IN METEORITES AND IN THE EARTH

Thesis by

Stephen Pritchard Smith

In Partial Fulfillment of the Requirements

for the Degree of

Doctor of Philosophy

California Institute of Technology

Pasadena, California

1979

(Submitted May 16, 1979)

ACKNOWLEDGMENT

This thesis is the outgrowth of a lifelong love of natural history and science nurtured in me by my family and many teachers during my formal and informal education. I thank particularly Professor Fred Whipple at Harvard for reawakening my interest in stones from the sky, and the faculty and students of Caltech for opening my eyes to the stones beneath my feet. I am grateful to Dr. Edward Fireman of the Smithsonian Observatory for introducing me to the noblest of gases. I owe immeasurable thanks to Jack Huneke for instruction and companionship, both in and out of the Gas Lab at Caltech. His painstaking instruction in the art of noble-gas mass-spectrometry is deeply appreciated. Our many trips to out-of-the-way salt pans and holes in the ground in search of mineralogical esoterica will live long in my memory. Finally, I thank my thesis advisor at Caltech, Professor Gerald Wasserburg, not least of all for his patience with my all-too-often uninspired prose. Gerry Wasserburg, the chief lunatic, provides a continual source of inspiration, ideas, and guidance without which too many of us would soon find ourselves in deepest yoghurt!

I thank the National Science Foundation for the financial support of an Energy Related Graduate Traineeship during my tenure at Caltech. Financial support for the research embodied in this thesis was received from the National Science Foundation, Department of Energy, and Ford Motor Company.

The kind permissions of the American Geophysical Union, Pergamon Press, and Elsevier Scientific Publishing Company to reproduce the papers in Appendix A are acknowledged.

Last, and certainly not least, thanks to Evelyn Brown for her seemingly inexhaustible supply of good cheer, and to Joanne Clark for indispensible help in preparing this manuscript.

ABSTRACT

The isotopic and elemental abundances of noble gases in the solar system are investigated, using simple mixing models and mass-spectrometric measurements of the noble gases in meteorites and terrestrial rocks and minerals.

Primordial neon is modeled by two isotopically distinct components from the interstellar gas and dust. Neon from the gas dominates solar neon, which contains about ten times more ^{20}Ne than ^{22}Ne. Neon from the dust is represented in meteorites by neon-E, with $^{20}Ne/^{22}Ne$ less than 0.6. Isotopic variations in meteorites require neon from both dust and gas to be present. Mixing dust and gas without neon loss generates linear correlation lines on three-isotope and composition-concentration diagrams. A model for solar wind implantation predicts small deviations from linear mixing, due to preferential sputtering of the lighter neon isotopes.

Neon in meteorites consists of galactic cosmic ray spallation neon and at least two primordial components, neon-E and neon-S. Neon was measured in several meteorites to investigate these end-members. Cosmogenic neon produced from sodium is found to be strongly enriched in ^{22}Ne. Neon measurements on sodium-rich samples must be interpreted with care so not to confuse this source of ^{22}Ne with neon-E, which is also rich in ^{22}Ne.

Neon data for the carbonaceous chondrite Mokoia show that the end-member composition of neon-S in meteorites is $^{20}Ne/^{22}Ne = 13.7$, the same as the present solar wind. The solar wind composition evidently has remained constant since before the compaction of Mokoia.

Ca, Al-rich inclusions from the Allende meteorite were examined for correlation between neon-E and oxygen or magnesium isotopic anomalies. ^{22}Ne and ^{36}Ar enrichments found in some inclusions are attributed to cosmic-

ray-induced reactions on Na and Cl, not to a primordial component. Neon-E is not detectably enriched in Allende.

Measurements were made to determine the noble gas contents of various terrestrial rocks and minerals, and to investigate the cycling of noble gases between different terrestrial reservoirs. Beryl crystals contain a characteristic suite of magmatic gases including nucleogenic ^{21}Ne and ^{22}Ne from (α,n) reactions, radiogenic ^{40}Ar, and fissiogenic $^{131-136}Xe$ from the decay of K and U in the continental crust. Significant concentrations of atmospheric noble gases are also present in beryl.

Both juvenile and atmospheric noble gases are found in rocks from the Skaergaard intrusion. The ratio $^{40}Ar/^{36}Ar$ (corrected for in situ decay of ^{40}K) correlates with $\delta^{18}O$ in plagioclase. Atmospheric argon has been introduced into samples that have experienced oxygen-isotope exchange with circulating meteoric hydrothermal fluids. Unexchanged samples contain juvenile argon with $^{40}Ar/^{36}Ar$ greater than 6000 that was trapped from the Skaergaard magma.

Juvenile and atmospheric gases have been measured in the glassy rims of mid-ocean ridge (MOR) pillow basalts. Evidence is presented that three samples contain excess radiogenic ^{129}Xe and fission xenon, in addition to the excess radiogenic ^{40}Ar found in all samples. These juvenile gases are being outgassed from the upper-mantle source region of the MOR magma. No isotopic evidence has been found here for juvenile primordial noble gases accompanying the juvenile radiogenic gases in the MOR glasses. Large argon isotopic variations in a single specimen provide a clear indication of the late-stage addition of atmospheric argon, probably from seawater.

The Skaergaard data demonstrate that atmospheric noble gases dissolved in ground water can be transferred into crustal rocks. Subduction

of oceanic crust altered by seawater can transport atmospheric noble gases into the upper mantle. A substantial portion of the noble gases in mantle-derived rocks may represent subducted gases, not a primordial component as is often assumed.

TABLE OF CONTENTS

LIST OF FIGURES

LIST OF TABLES

CHAPTER 1. INTRODUCTION

In this thesis several aspects of the problem of the origin and distribution of noble gases in the solar system will be examined. The volatility and chemical inertness of the noble gases determine the nature of their occurrence. In the sun and giant planets, predominantly gaseous objects, the combined abundance of all the noble gases is high, at least several percent by number. In dominantly solid objects such as the terrestrial planets and meteorites, the noble gases are very rare, constituting roughly one part per billion. As a result of their very low abundance in solids, the noble gases can be uniquely used to study the products of a variety of nuclear reactions that cannot be probed with other elements because of the extremely low concentrations of the reaction products. A good example is cosmic ray spallation reactions in meteorites and lunar samples. The study of the noble gases is at times simplified by their chemical inertness. For example, in natural fluid circulation systems, noble gases, unlike other elements, cannot be removed from the system by chemical reaction. Thus the gases will be more nearly conserved quantities when outflux is compared with influx.

The thesis text is divided into four main parts; Chapter 1, an introduction, Chapter 2, a compilation of solar system noble gas abundances, Chapter 3, a study of noble gases in extra-terrestrial materials, Chapter 4, an investigation of terrestrial noble gases. In this introductory chapter, we review sources and reservoirs of noble gases in the solar system, and some of the terminology used to describe different noble gas components. A brief history of the discovery and identification of the noble gases on the Earth and in astronomical objects is given at the end of this section. Chapter 2 is a compilation

of known elemental and isotopic abundances of the noble gases in various objects in the solar system. Striking differences are evident among the various reservoirs, and will be briefly described. Chapter 3 is devoted primarily to an investigation of the origin and distribution of neon in the solar system. Included in this chapter is a summary of measurements of the neon and argon contents of several meteorites carried out in the course of research of this thesis. In Chapter 4, we examine the occurrence and transport of noble gases on the Earth. This discussion is based on new measurements made of the noble gases in rocks and minerals from the crust and upper mantle. Appendices A and B contain copies of published papers and manuscripts submitted for publication that describe in detail the new meteorite and terrestrial noble gas data.

The five stable noble gases helium, neon, argon, krypton, and xenon comprise a total of twenty-three stable isotopes (Table 1-1). All naturally occurring isotopes of radon are radioactive. Within the solar system, noble gases have been detected in the objects listed in Table 1-2. Noble gases have been identified in the solar atmosphere by both ground-based spectroscopy and rocket or satellite-based measurements. Except for the Earth, all observations of noble gases in planetary atmospheres have been obtained with the aid of spacecraft. Noble gas contents of the Earth's atmosphere, surface samples from the moon and the Earth, and of in-falling meteorites and interplanetary dust have been measured by laboratory mass-spectrometry or residual gas analysis. Noble gases have also been detected in a variety of objects outside the solar system, including O and B stars, novae, planetary nebulae, and HII regions (ionized interstellar gas) both in our galaxy

Table 1-1. The noble gases in nature.

Noble Gas	Atomic Number	Stable Isotopes
He	Z=2	^{3}He, ^{4}He
Ne	Z=10	^{20}Ne, ^{21}Ne, ^{22}Ne
Ar	Z=18	^{36}Ar, ^{38}Ar, ^{40}Ar
Kr	Z=36	^{78}Kr, ^{80}Kr, ^{82}Kr, ^{83}Kr, ^{84}Kr, ^{86}Kr
Xe	Z=54	^{124}Xe, ^{126}Xe, ^{128}Xe, ^{129}Xe, ^{130}Xe, ^{131}Xe, ^{132}Xe, ^{134}Xe, ^{136}Xe
		Radioactive Isotopes[1]
Kr	Z=36	$^{81}Kr(2x10^{5}y)$[2]
Rn	Z=86	$^{219}Rn(3.9s)$[3] $^{220}Rn(55s)$[4] $^{222}Rn(3.8d)$[5]

[1]Half-life in parentheses.

[2]Found in meteorites and lunar samples; product of cosmic-ray irradiation.

[3]Also known as actinon. Produced during ^{235}U decay chain.

[4]Also known as thoron. Produced during ^{232}Th decay chain.

[5]Produced during ^{238}U decay chain.

Table 1-2. Stable noble gases detected in the solar system.

Sun	He (chromosphere)
	He,Ne,Ar (corona)
Planets	
Mercury	He (atmosphere - Mariner 10)
Venus	He,Ne,Ar (atmosphere - Venera 9-12; Pioneer-Venus)
Earth	He,Ne,Ar,Kr,Xe (atmosphere)
	He,Ne,Ar,Kr,Xe (surface samples)
Moon	He,Ne,Ar (atmosphere - Apollo)
	He,Ne,Ar,Kr,Xe (surface samples - Apollo)
Mars	Ne,Ar,Kr,Xe (atmosphere - Viking)
Jupiter	He (atmosphere - Pioneer 10)
Meteorites	He,Ne,Ar,Kr,Xe
Interplanetary Medium	
Dust	He,Ne,Ar
Solar Wind	He,Ne,Ar (Apollo; spacecraft)
Solar Cosmic Rays	He,Ne (spacecraft)
Galactic Cosmic Rays	He,Ne,Ar (spacecraft)

and in other galaxies. Average, or so-called "cosmic," abundances of He, Ne, and Ar determined from these astronomical objects are listed in Table 1-3. The light noble gases are comparatively abundant in the cosmos. He is the second most common element, while Ne is the sixth, following H, He, C, N, and O. Although the cosmic abundance pattern of Table 1-3 is not typical of all astronomical bodies (cf. Trimble, 1975), it does present a surprisingly good picture of the noble gas abundances in many objects, and is a useful reference composition.

To avoid any possible confusion, it is useful to define explicitly several terms dealing with isotopic compositions. A preferred isotopic composition is an empirically defined composition found to recur frequently in various samples. A preferred composition may be an experimental artifact, and need not correspond to any actual reservoir of gas in a sample. An isotopic component does correspond to an actual or potential reservoir of gas within a geological or astronomical object. A component is characterized either by a single isotopic composition or possibly by a limited range of compositions. A component is often the product of a single, well-defined process or source. An end-member is an extreme composition of a series of mixtures. An end-member composition may be observed, but not surpassed, in nature. The term endpoint is used to refer to the graphed point corresponding to an end-member composition.

Noble gases in the solar system arise from a number of sources. A large fraction of the solar system noble gases undoubtedly accompanied the interstellar dust and gas from which the solar system formed some 4.5 billion years ago. The term primordial is used to designate these initial gases. Other noble gases may be generated by nuclear reactions

Table 1-3. Cosmic abundances of noble gases; by number.

He/H[1]	0.1	
Ne/H[2]	1.2×10^{-4}	
Ar/H[3]	3.6×10^{-6}	
Kr/H[4]	(2×10^{-9})[5]	(1.5×10^{-9})[6]
Xe/H[4]	(3×10^{-10})[5]	(1.7×10^{-10})[6]
He/Ne	800	
Ne/Ar	32[3]	
Ar/Kr	(1800)[5]	(2400)[6]
Kr/Xe	(7)[5]	(9)[6]

[1] Trimble, 1975.

[2] Ne/H is calculated from Ne/O = 0.23 (Aller and Czyzak, 1973; Kaler, 1978) together with O/H = 5×10^{-4} (Aller and Czyzak, 1973; Trimble, 1975).

[3] Ar/H is calculated from Ne/H and Ne/Ar = 32±3 (Kaler, 1978).

[4] These values are derived by interpolation from neighboring element abundances based on meteorites. Strictly speaking, therefore, these are solar system abundances, but the general agreement of cosmic and solar abundances (Trimble, 1975) suggests the interpolated values should be representative of cosmic Kr and Xe abundances.

[5] Marti et al., 1972.

[6] Cameron, 1973.

within the solar system as it forms or during its subsequent evolution. Isotopes arising from the spontaneous decay of radioactive parent nuclei are called radiogenic. Important radiogenic noble gases are ^{4}He from decay of U and Th, ^{40}Ar from decay of K, ^{129}Xe from decay of short-lived ^{129}I ($t_{1/2}$ = 17 m.y.), and $^{131-136}Xe$ from spontaneous fission of ^{238}U or short-lived ^{244}Pu ($t_{1/2}$ = 82 m.y.). In some instances, radiogenic gases may become separated from their parent nuclides during thermal metamorphism, phase changes, etc. If these gases are then incorporated in a new host where they are not supported by in situ decay, they are termed excess radiogenic gases. Isotopes produced in other nuclear reactions may be grouped under the general label of nucleogenic noble gases. An important example in extraterrestrial samples are the spallogenic noble gases. These are the products of spallation reactions (cf. Friedlander et al., 1964, Chap. 10) caused by the exposure of the samples to high energy (~ 1-10 MeV) galactic cosmic-ray protons. The contributions of spallogenic noble gases are most visible at the rarer isotopes ^{3}He, ^{21}Ne, ^{38}Ar, and the lighter isotopes of Kr and Xe. Additional noble gas isotopes including ^{36}Ar, ^{80}Kr, ^{82}Kr, and ^{128}Xe may be produced by neutron capture from the substantial flux of secondary neutrons generated by the cosmic ray bombardment. Since spallation reactions are properly only a subset of the reactions induced by the cosmic rays, the term cosmogenic is used to refer to the total spectrum of noble gases generated by the bombardment.

A different source of nucleogenic noble gases are reactions of the α-particles and neutrons emitted during the radioactive decay of U and Th with the elements surrounding the active nuclei. For example,

^{3}He may be generated by $^{6}Li(n,\alpha)^{3}H \xrightarrow{\beta} {}^{3}He$, neon isotopes by $^{17}O(\alpha,n)^{20}Ne$, $^{18}O(\alpha,n)^{21}Ne$, $^{19}F(\alpha,n)^{22}Na \xrightarrow{\beta} {}^{22}Ne$, ^{38}Ar by $^{35}Cl(\alpha,p)^{38}Ar$, and ^{129}Xe and ^{131}Xe by neutron capture on Te isotopes (Wetherill, 1954; Cherdyntsev, 1961).

Noble gases may be subjected to a variety of transport processes that can result in systematic abundance changes among the different gases or isotopes. Such changes are identified under the general heading of fractionation effects, and are to be distinguished from chemical or isotopic changes due to nuclear reactions or mixing of components of different composition. Fractionation may be either elemental, affecting the elemental abundances of the noble gases, or isotopic. Examples of elemental fractionation processes include adsorption, solution, and other processes depending on elemental properties such as ionization potential, strength of Van de Waals interactions, atomic radius, etc. Isotopic fractionation effects arise predominantly through the differences in mass between isotopes. Thermally-activated diffusion is an important process leading to isotopic mass-fractionation of noble gases.

In meteorites, the expected isotopic compositions of both the radiogenic and cosmogenic components of the noble gases can be fairly accurately calculated given the chemical composition of the sample. Thus it is often possible to subtract from the total noble gas content the contributions made by these components--or to ignore the few isotopes where a correction cannot be safely made. In this way we obtain information about the remaining noble gases in meteorites. The isotopes of those noble gases which are not due to radiogenic or cosmogenic processes are conventionally referred to by the neutral

term "trapped" to avoid genetic implications of terms such as primordial or fractionated. The term trapped can be extended to describe the noble gases in any sample that have not arisen through in situ processes.

In the terrestrial environment, noble gases may be classified as either atmospheric or juvenile. The term juvenile is reserved for gases that have never been cycled through the atmosphere. Juvenile gases are further subdivided into primary juvenile and secondary juvenile gases. Primary juvenile gases include those not now being generated in the Earth, for example primordial gases, ^{129}Xe from the decay of short-lived ^{129}I, and fission xenon from ^{244}Pu. Secondary juvenile gases include nucleogenic and radiogenic species formed by the ongoing decay of U, Th, and K and other nuclear reactions.

The discovery of the noble gases was foreshadowed by experiments performed in about 1785 by Henry Cavendish, in which he removed the chemically active species from air and obtained a gaseous residue of about 0.83% of the whole (Holloway, 1968, and references therein). We know now that this residue corresponds closely to the fraction of argon in the atmosphere (0.93%), but Cavendish made no attempt to characterize it further. Spectroscopic evidence for the existence of a new element, helium, in the solar chromosphere was obtained during the solar eclipse of August 18, 1868. The chemical and physical characteristics of helium were, however, to remain unknown for about thirty years, until its discovery on the Earth. Not helium, but argon was the first of the noble gases to be identified on the Earth (Holloway, 1968; Rayleigh, 1968; Hiebert, 1963). Its chemical and

physical characterization by Lord Rayleigh and Sir William Ramsay (1895) led to the addition of Group 0 to the periodic table. The work leading to the discovery of argon was initiated when Lord Rayleigh found that nitrogen prepared from ammonia and other chemicals was consistently about 0.5% less dense than nitrogen prepared from samples of air by removal of oxygen, carbon dioxide, and water. Subsequent removal of the nitrogen from the air samples left a dense residue which Rayleigh and Ramsay showed to be a previously unrecognized constituent of the atmosphere, and which they named argon. Shortly after this discovery, Ramsay (1895) found helium in the mineral cleveite (hydrated oxide of U, Fe, and REE). Experiments soon showed that helium too was a chemically inert gas (Ramsay and Collie, 1896). The remaining stable noble gases neon, krypton, and xenon were discovered in rapid succession in 1898 by Ramsay and Travers, using a technique of fractional distillation of liquid air (Holloway, 1968). In 1904, Rayleigh was awarded the Nobel prize in physics and Ramsay the prize in chemistry largely for their work leading to the discovery of argon and the other stable noble gases (Rayleigh, 1968, p. 313). Isotopes of the radioactive noble gas radon were discovered in 1900, during investigation of the radioactive decay of thorium and radium (Holloway, 1968).

An important theme underlying this thesis is the information obtained from the isotopic abundances of the noble gases in different samples. The theory of isotopes originated in the early part of this century during the study of the radioactive elements. It was developed in response to the findings that several elements from different radioactive series which differed in atomic weight were nevertheless chemically and spectroscopically indistinguishable (Aston 1924, 1933,

and references therein). The existence of isotopes among the stable elements was first indicated during J. J. Thomson's positive ray analysis of air in 1912. Thomson detected a weak signal at mass 22, that varied in intensity in parallel with the neon line at mass 20 (Aston, 1924, Chap. III). In 1919, under the impetus of the question of the complexity of neon, Aston devised a new method of positive ray analysis, the mass-spectrograph, capable of much higher resolution and accurate mass determination, with which he confirmed the existence of ^{20}Ne and ^{22}Ne. Measurement of the isotopes of the remaining noble gases and other stable elements proceeded rapidly. By the end of 1922, all the major isotopes of the noble gases were known (Aston, 1933, Chap. 1). The most important exception was ^{3}He, which because of its very low abundance in air, about 10^{-6} that of ^{4}He, was not discovered until 1939 (Alvarez and Cornog, 1939).

Little studied by chemists after the initial period following their discovery, the noble gases have provided physicists many avenues of fruitful research (Smith, 1971). A particularly important example is the phenomenon of superfluidity exhibited by ^{4}He. To the delight of chemists, it has been discovered relatively recently that the noble gases do form chemical compounds, typically involving fluorine (Holloway, 1968; Hyman, 1963). Geologists have for many years taken a rather proprietary interest in two selected isotopes of the noble gases, ^{4}He and ^{40}Ar, ever since the recognition that these products of the radioactive decay of uranium, thorium, and potassium could be used to date geological samples. Perhaps one of the first practical uses found for helium, other than for inflating balloons, was as ammunition in the dispute between geologists and physicists over the age of the

Earth (Holmes, 1913).

Following their discovery on the Earth, the noble gases were sought in extraterrestrial objects. As indicated, helium had previously been found in the flash spectrum of the solar chromosphere seen during eclipse. The presence of helium outside the solar system was shown by an observation of its yellow D_3 spectral line (5876 Å) in the visible spectrum of the Great Nebula in Orion (Copeland, 1886). Neon was first identified in astrophysical objects in 1933, in the forbidden line spectra of gaseous nebulae and novae (Boyce et al., 1933) and in hot young O and B stars (Menzel and Marshall, 1933). Spectral lines of argon were identified in nebular spectra by Swings and Edlén and Boyce et al. in 1934, and in the spectrum of the star γ Pegasi by Underhill (1948). The presence of argon and neon in our own sun was confirmed comparatively recently. Lines of highly ionized argon were identified in the optical spectrum of the corona by Edlén in 1942. The first lines of neon identified from the sun were coronal ultraviolet resonance lines photographed by a rocket-born spectrograph (Detwiler et al., 1961). Because of their comparatively low abundances and high excitation potentials, krypton and xenon have yet to be measured reliably in the spectra of astronomical objects (Trimble, 1975).

REFERENCES, CHAPTER 1

Aller L. H. and Czyzak S. J. (1973) Introductory report: chemical composition of planetary nebulae. Mém. Soc. Roy. Sci. Liège 6th series, 285-299.

Alvarez L. W. and Cornog R. (1939) He^3 in helium. Phys. Rev. 56, 379.

Aston F. W. (1924) Isotopes, 2nd ed. Edward Arnold.

Aston F. W. (1933) Mass-Spectra and Isotopes. Longmans, Green.

Boyce J. C., Menzel D. H., and Payne C. H. (1933) Forbidden lines in astrophysical sources. Proc. Nat. Acad. Sci. 19, 581-591.

Boyce J. C., Payne-Gaposchkin C., and Menzel D. H. (1934) Further identification of nebular lines. Publ. Astr. Soc. Pacific 46, 213-215.

Cameron A.G.W. (1973) Abundances of the elements in the solar system. Space Sci. Rev. 15, 121-146.

Cherdyntsev V. V. (1961) Abundance of Chemical Elements, pp. 58-60. U. of Chicago.

Copeland R. (1886) Note on the visible spectrum of the Great Nebula in Orion. Month. Not. Roy. Ast. Soc. 48, 360-362.

Detwiler C. R., Purcell J. D., and Tousey R. (1961) The extreme ultraviolet spectrum of the sun. Mém. Soc. Roy. Sci. Liège 5th series, 253-264.

Edlén B. (1942) Die Deutung der Emissionslinien im Spektrum der Sonnenkorona. Z. Astrophys. 22, 30-64.

Friedlander G., Kennedy J. W., and Miller J. M. (1964) Nuclear and Radiochemistry, 2nd ed. Wiley.

Hiebert E. N. (1963) Historical remarks on the discovery of argon: the first noble gas. In Noble-Gas Compounds (ed. H. H. Hyman), pp.3-20. U. of Chicago.

Holloway J. H. (1968) Noble-Gas Chemistry, pp. 1-36. Methuen.

Holmes A. (1913) The Age of the Earth. Harpers.

Hyman H. H. (1963) Noble-Gas Compounds. U. of Chicago.

Kaler J. B. (1978) Galactic abundances of neon, argon, and chlorine derived from planetary nebulae. Astrophys. J. 225, 527-541.

Marti K., Wilkening L. L., and Suess H. E. (1972) Solar rare gases and the abundances of the elements. Astrophys. J. 173, 445-450.

Menzel D. H. and Marshall R. K. (1933) Neon absorption lines in stellar spectra. Proc. Nat. Acad. Sci. 19, 879-881.

Ramsay W. (1895) On a gas showing the spectrum of helium, the reputed cause of D_3, one of the lines in the coronal spectrum. Preliminary note. Proc. Roy. Soc. (London) 58, 65-67.

Ramsay W. and Collie J. N. (1896) Helium and argon. Part III. Experiments which show the inactivity of these elements. Proc. Roy. Soc. (London) 60, 53-56.

Lord Rayleigh (J. W. Strutt) and Ramsay W. (1895) Argon, a new constituent of the atmosphere. Phil. Trans. A, 187-241.

Lord Rayleigh (R. J. Strutt)(1968) Life of John William Strutt, Third Baron Rayleigh, 2nd ed., pp. 187-225. U. of Wisconsin.

Smith B. L. (1971) The Inert Gases, Model Systems for Science. Wykeham.

Swings P. and Edlén B. (1934) Sur la présence des raies interdite d'argon IV dans le spectre des nébuleuses. Comptes Rendus, Acad. Sci. (Paris) 198, 2071-2073.

Trimble V. (1975) The origin and abundances of the chemical elements. Rev. Mod. Phys. 47, 877-976.

Underhill A. B. (1948) The spectrum of γ Pegasi. Astrophys. J.107, 337-348.

Wetherill G. W. (1954) Variations in the isotopic abundances of neon and argon extracted from radioactive minerals. Phys. Rev. 96, 679-683.

CHAPTER 2. COMPILATION OF SOLAR SYSTEM NOBLE GAS ABUNDANCES

Data on the abundances and isotopic compositions of noble gases in solar system materials have been collected from the literature, and are summarized in this chapter. For convenience, all tables are placed together at the end of the chapter.

Solar abundance determinations are listed in Table 2-1. Data are available for the chromosphere, corona, solar wind, and solar cosmic rays. The photospheric abundances cannot be measured spectroscopically. The high first excitation potentials of the noble gas atoms preclude them from radiating below chromospheric or coronal temperatures. Present uncertainties in the solar noble gas abundances are about a factor of two. The cosmic abundances for He, Ne, and Ar (Table 1-3) are listed in the last column. The solar noble gas abundances are not significantly different from the cosmic values.

In Table 2-2, noble gas abundances are given for the atmospheres of terrestrial planets, lunar samples, meteorites, and interplanetary dust collected in the Earth's atmosphere. For the planets, the values represent the abundances of each gas in the atmosphere divided by the mass of the planet. Small concentrations of He, and of He, Ne, and Ar have also been detected in the exospheric atmospheres of Mercury (Broadfoot et al., 1974) and the moon (Hoffman et al., 1973) respectively. Helium in roughly solar proportion to hydrogen has been found in the atmosphere of Jupiter (Carlson and Judge, 1976; Larson, 1977). Cosmic abundances are given at the bottom of the table for comparison. In the first entry, "Total," the cosmic noble gas abundances are normalized to the total mass of all elements including hydrogen. For the second entry, "Ice and Rock," only elements heavier than helium were used for normalization. These

comprise about 2% of the total cosmic mass abundance. This second normalization provides a more accurate comparison for the meteorite and planet data, since these objects contain almost none of their cosmic complement of hydrogen.

The tabulated noble gas data are most easily compared using Fig. 2-1. The logarithm of the total elemental abundance is plotted versus atomic charge Z. The observed abundances range over many orders of magnitude. It can be seen that a dichotomy exists between the low abundances of the noble gases on the Earth, the other terrestrial planets, and meteorites, and the high cosmic abundances of these elements in the sun, stars, and nebulae. Depletion factors for the planets and meteorites range from roughly 10^3 to 10^{13} for individual noble gases, compared to the cosmic abundances normalized to the ice and rock-forming elements.

The scarcity of the noble gases in the smaller planetary objects is one of the main features of the distribution of noble gases in the solar system. Even without reference to astronomical observations, Aston (1924) realized that the terrestrial abundances of the noble gases were unusually low. When compared to the average level of abundances of the elements on the Earth, the noble gases appeared to be deficient by at least six orders of magnitude. Aston attributed this to their inability to form chemical compounds, rather than an inherently low abundance in the cosmos. The first quantitative analysis of neon and argon abundances in a planetary nebula (Page, 1936) confirmed that the noble gases in the nebula were much more abundant relative to oxygen than on the Earth.

A second important feature of solar system noble gases is that

Figure 2-1. Noble gas abundances in solar system materials. Cosmic abundance curve labeled "TOTAL" represents noble gas abundances normalized to the sum of all elements including hydrogen. Curve labeled "ICE + ROCK" reflects normalization to the sum of all elements more massive than helium. Abundances for the planets are obtained by dividing the atmospheric abundance of each gas by the total mass of the planet. Noble gas abundances in the planets, lunar samples, and meteorites are at least three orders of magnitude lower than the cosmic "ICE + ROCK" abundances. Detailed comparison of the curves shows that, compared to the cosmic abundance pattern, the light noble gases are systematically more depleted than the heavy noble gases in the gas-poor objects of the solar system.

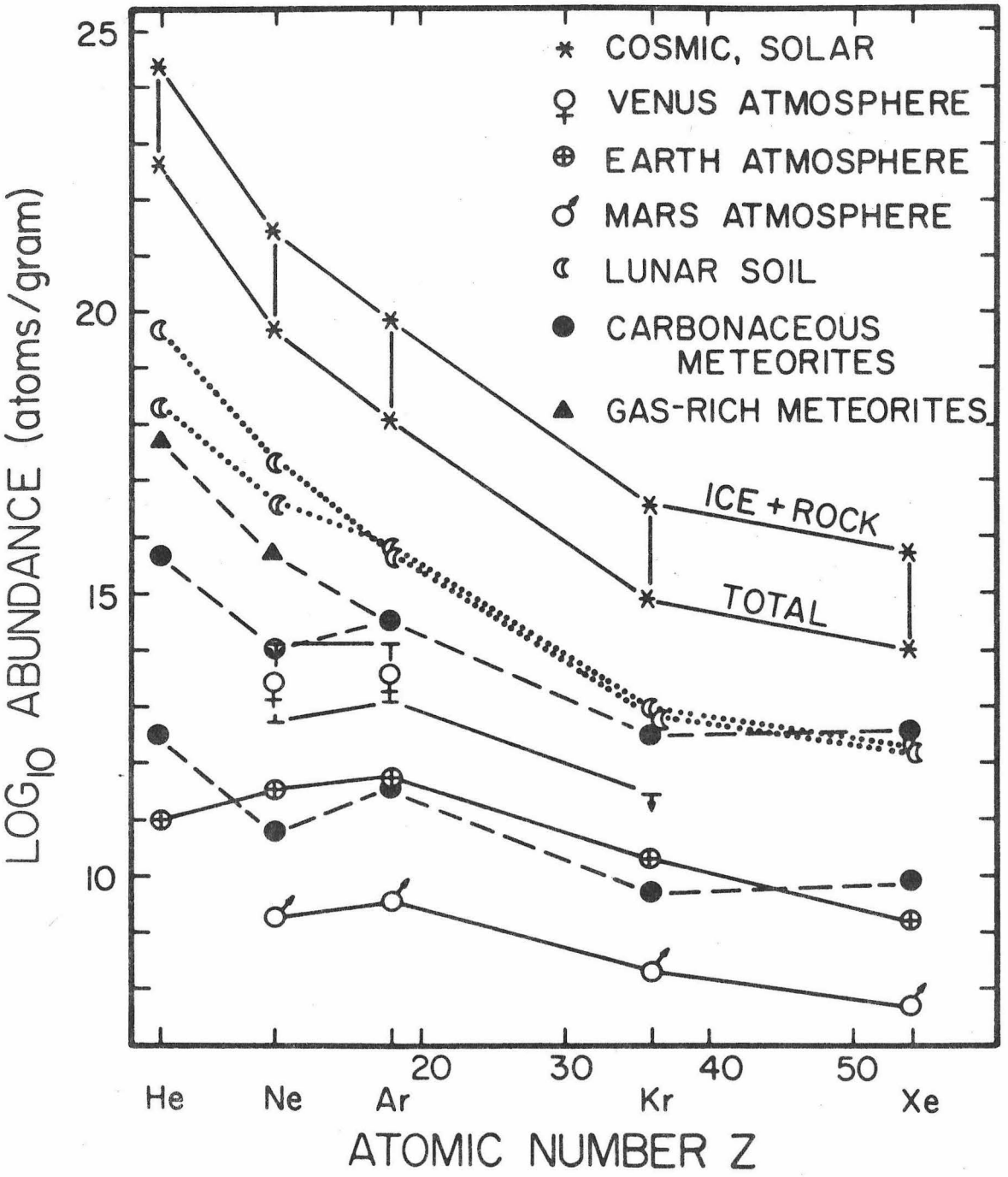
COSMIC, SOLAR
VENUS ATMOSPHERE
EARTH ATMOSPHERE
MARS ATMOSPHERE
LUNAR SOIL
CARBONACEOUS METEORITES
GAS-RICH METEORITES
ICE + ROCK
TOTAL
LOG10 ABUNDANCE (atoms/gram)
25
20
15
10
He
Ne
Ar
Kr
Xe
20
30
40
50
ATOMIC NUMBER Z

Figure 2-1

a dichotomy exists in the relative abundances of the gases as well as in the absolute abundances. Ratios of the noble gas abundances are tabulated in Table 2-3, using ^{4}He, ^{20}Ne, ^{36}Ar, ^{84}Kr, and ^{132}Xe as representative isotopes. It can be seen for example that the relative abundances among the gases in the Earth's atmosphere differ greatly from the cosmic abundance pattern. The most diagnostic ratios are $^{20}Ne/^{36}Ar$ and $^{36}Ar/^{84}Kr$. Both ratios in the atmosphere are 60 to 70 times lower than the cosmic values. The lighter noble gases are systematically depleted relative to the heavier. The comparatively low helium abundance in the atmosphere is not significant, since helium is not gravitationally bound to the Earth. Fractionated noble gas abundance patterns similar to the terrestrial one are also found for the atmosphere of Mars, possibly for the atmosphere of Venus, and for a component of the noble gases trapped in meteorites. Lunar soils and some gas-rich meteorites show abundances intermediate between the fractionated and cosmic values. As previously indicated, noble gases in the solar wind and solar corona resemble the cosmic abundances derived from other stars and nebulae. Signer and Suess (1963) distinguished the two general abundance patterns, and proposed the terms "solar" and "planetary" for the unfractionated and fractionated components respectively. Typical examples of each pattern are given in Table 2-4. Here the abundances are normalized to $^{36}Ar = 1$. The atmospheric composition in the last row is seen to be close to the planetary pattern as defined from meteorite samples.

The third important characteristic of noble gases in the solar system is their wide range of isotopic composition. Isotopic data are

summarized in Table 2-5. We have included primarily compositions for trapped noble gases. The presence of cosmogenic and radiogenic components causes very large additional isotopic variations in some samples. The isotopic composition of trapped helium varies by a factor of about four. The low $^{3}He/^{4}He$ ratio in the Earth's atmosphere reflects the addition of radiogenic ^{4}He. Trapped neon compositions are highly variable, especially in meteorites, where $^{20}Ne/^{22}Ne$ varies by a factor of about 30. In contrast, trapped $^{36}Ar/^{38}Ar$ ratios differ only by about 10%. The variations in $^{40}Ar/^{36}Ar$ are caused by the presence of radiogenic ^{40}Ar. The primordial $^{40}Ar/^{36}Ar$ ratio is very low, $< 5 \times 10^{-4}$, as determined from ureilite meteorites. Krypton isotopic variations are relatively minor and have not been studied in detail. Trapped xenon is more complex. Particularly notable is the difference between xenon in the Earth's atmosphere and the average trapped xenon composition in meteorites. The difference is approximately that of a 3% to 4% per mass unit fractionation, but its origin is not understood.

Trapped noble gases of both the planetary and solar types discussed above are present in meteorites. It has been found that each is characterized by a distinct isotopic signature (Signer and Suess, 1963). The differences are most striking for helium and neon (Table 2-6). $^{3}He/^{4}He$ varies by a factor of about three or four from planetary to solar gases, and neon by about 70%. In contrast, the isotopic compositions of planetary and solar argon are indistinguishable. More recently it has been discovered that the planetary trapped gases are themselves isotopically complex (cf. Black and Pepin, 1969; Black, 1972b). The complexity is most marked for neon and xenon. The trapped gases in meteorites are interpreted as comprising a suite of

isotopically distinct components. The number and possible origins of these components will be discussed in Chapter 3.

REFERENCES, CHAPTER 2

Aston F. W. (1924) The rarity of the inert gases on the Earth. Nature 114, 786.

Black D. C. and Pepin R. O. (1969) Trapped neon in meteorites - II. Earth Planet. Sci. Lett. 6, 395-405.

Black D. C. (1972a) On the origins of trapped helium, neon and argon isotopic variations in meteorites - I. Gas-rich meteorites, lunar soil and breccia. Geochim. Cosmochim. Acta 36, 347-375.

Black D. C. (1972b) On the origins of trapped helium, neon, and argon isotopic variations in meteorites - II. Carbonaceous meteorites. Geochim. Cosmochim. Acta 36, 377-394.

Broadfoot A. L., Kumar S., Belton M. J. S., and McElroy M. B. (1974) Mercury's atmosphere from Mariner 10: preliminary results. Science 185, 166-169.

Cameron A. G. W. (1973) Abundances of the elements in the solar system. Space Sci. Rev. 15, 121-146.

Carlson R. W. and Judge D. L. (1976) Pioneer 10 ultraviolet photometer observations of Jupiter: the helium to hydrogen ratio. In Jupiter (ed. T. Gehrels), pp. 418-440. U. of Arizona.

Eberhardt P., Eugster O., and Marti K. (1965) A redetermination of the isotopic composition of atmospheric neon. Z. Naturforsch.20a, 623-624.

Eberhardt P., Geiss J., Graf H., Grögler N., Mendia M. D., Mörgeli M., Schwaller H., Stettler A., Krähenbühl U., and von Gunten H. R. (1972) Trapped solar wind noble gases in Apollo 12 lunar fines

12001 and Apollo 11 breccia 10046. Proc. Lunar Sci. Conf. 3rd, 1821-1856.

Eberhardt P., Jungck M. H. A., Meier F. O., and Niederer F. (1979) Neon-E: New limits for isotopic composition. Two host phases? In Lunar and Planetary Science X, pp. 341-343. Lunar and Planetary Institute.

Eugster O., Eberhardt P., and Geiss J. (1967) Krypton and xenon isotopic composition in 3 carbonaceous chondrites. Earth Planet. Sci. Lett. 2, 249-257.

Frick U. and Moniot R. K. (1977) Planetary noble gas components in Orgueil. Proc. Lunar Sci. Conf. 8th, 229-261.

Geiss J. (1973) Solar wind composition and implications about the history of the solar system. Invited paper, 13th Int. Cosmic Ray Conf., Denver.

Göbel R., Ott U., and Begemann F. (1978) On trapped noble gases in Ureilites, J. Geophys. Res. 83, 855-867.

Heymann D. (1971) The inert gases. In Handbook of Elemental Abundances in Meteorites (ed. B. Mason), pp. 29-66. Gordon and Breach.

Hoffman J. H., Hodges R. R. Jr., Johnson F. S., and Evans D. E. (1973) Lunar atmospheric composition results from Apollo 17. Proc. Lunar Sci. Conf. 4th, 2865-2875.

Hoffman J. H., Hodges R. R. Jr., McElroy M. B., Donahue T. M., and Kolpin M. (1979) Venus lower atmospheric composition: preliminary results from Pioneer Venus. Science 203, 800-802.

Krummenacher D., Merrihue C. M., Pepin R. O., and Reynolds J. H. (1961) Meteoritic krypton and barium versus the general isotopic anomalies in meteoritic xenon. Geochim. Cosmochim. Acta 26, 231-249.

Larson H. P. (1977) Abundances of molecules in planetary atmospheres from middle infrared spectroscopic observations. In Proceedings Symposium on Planetary Atmospheres (ed. A. Vallance Jones), pp. 19-24. Royal Society of Canada.

Mamyrin B. Z., Anufriyev G. S., Kamenskiy I. L., and Tolstikhin I. N. (1970) Determination of the isotopic composition of atmospheric helium. Geochemistry Int. 7, 498-505.

Marti K., Wilkening L. L., and Suess H. E. (1972) Solar rare gases and the abundances of the elements. Astrophys. J. 173, 445-450.

Mazor E., Heymann D., and Anders E. (1970) Noble gases in carbonaceous chondrites. Geochim. Cosmochim. Acta 34, 781-824.

McElroy M. B. (1979) private communication. Present address; Center for Earth and Planetary Physics, Harvard University.

Merrihue C. (1964) Rare gas evidence for cosmic dust in modern Pacific red clay. Ann. N. Y. Acad. Sci. 119, 351-367.

Niederer F. and Eberhardt P. (1977) A neon-E-rich phase in Dimmitt. Meteoritics 12, 327-331.

Nier A. O. (1950a) A redetermination of the relative abundances of the isotopes of carbon, nitrogen, oxygen, argon, and potassium. Phys. Rev. 77, 789-793.

Nier A. O. (1950b) A redetermination of the relative abundances of the isotopes of neon, krypton, rubidium, xenon, and mercury. Phys. Rev. 79, 450-454.

Owen T., Biemann K., Rushneck D. R., Biller J. E., Howarth D. W., and Lafleur A. L. (1977) The composition of the atmosphere at the surface of Mars. J. Geophys. Res. 82, 4635-4639.

Oyama V. I., Carle G. C., Woeller F., and Pollack J. B. (1979) Venus

lower atmospheric composition: analysis by gas chromatography. Science 203, 802-805.

Page T. L. (1936) Chemical composition of planetary nebulae. Nature 138, 503-504.

Pepin R. O. and Signer P. (1965) Primordial rare gases in meteorites. Science 149, 253-265.

Pepin R. O. and Phinney D. (1979) Components of xenon in the solar system. Geochim. Cosmochim. Acta, submitted for publication.

Phinney D., Frick U., and Reynolds J. H. (1976) Rare-gas-rich separates from carbonaceous chondrites. In Lunar Science VII, pp. 691-693. Lunar Science Institute.

Podosek F. A., Huneke J. C., Burnett D. S., and Wasserburg G. J. (1971) Isotopic composition of xenon and krypton in the lunar soil and in the solar wind. Earth Planet. Sci. Lett. 10, 199-216.

Rajan R. S., Brownlee D. E., Tomandl D., Hodge P. W., Farrar H. IV, and Britten R. A. (1977) Detection of ^{4}He in stratospheric particles gives evidence of extraterrestrial origin. Nature 267, 133-134.

Reynolds J. H., Frick U., Neil J. M., and Phinney D. L. (1978) Rare-gas-rich separates from carbonaceous chondrites. Geochim. Cosmochim. Acta 42, 1775-1797.

Ross J. E. and Aller L. H. (1976) The chemical composition of the sun. Science 191, 1223-1229.

Signer P. and Suess H. E. (1963) Rare gases in the sun, in the atmosphere and in meteorites. In Earth Science and Meteoritics (eds. J. Geiss and E. D. Goldberg), pp. 241-272. North-Holland.

Smith S. P., Huneke J. C., and G. J. Wasserburg (1978) Neon in

gas-rich samples of the carbonaceous chondrites Mokoia, Murchison and Cold Bokkeveld. Earth Planet. Sci. Lett. 39, 1-13.

Srinivasan B., Gros J., and Anders E. (1977) Noble gases in separated meteoritic minerals: Murchison (C2), Ornans (C3), Karoonda (C5), and Abee (E4). J. Geophys. Res. 82, 762-778.

Tilles D. (1966) Implantation in interplanetary dust of rare-gas ions from solar flares. Science 153, 981-984.

Trimble V. (1975) The origin and abundances of the chemical elements. Rev. Mod. Phys. 47, 877-976.

Table 2-1. Noble gases in the sun.[1]

	Ross & Aller (1976)	Trimble (1975) (Corona)	Cameron (1973)	Solar Wind[2]	Cosmic (Table 1-3)
He/H	0.063 (CH,W)	0.080	0.070 (SCR)	~ 0.05	0.1
Ne/H	3.7×10^{-5} (C,W)	6.8×10^{-5}	1.1×10^{-4} (SCR)	9.4×10^{-5}	1.2×10^{-4}
Ar/H	1×10^{-6} (C,W)	3×10^{-6}	3.7×10^{-6} (INT)	3.8×10^{-6}	3.6×10^{-6}
Kr/H	-	-	1.5×10^{-9} (INT)	2.5×10^{-9}	-
Xe/H	-	-	1.7×10^{-10} (INT)	6.3×10^{-10}	-

[1] Ratios by number of atoms. Uncertainty is about a factor of two at best. CH = chromosphere W = solar wind C = corona SCR = solar cosmic rays INT = interpolated.

[2] He, Ne, Ar from Geiss (1973). He/H can be quite variable. Kr,Xe estimated from lunar soil and gas-rich meteorites (Marti et al., 1972).

Table 2-2. Abundances of noble gases in solar system materials (atoms/gram).

	He	Ne	^{36}Ar	^{40}Ar	Kr	Xe
TERRESTRIAL ATMOSPHERE[1]						
a) normalized to total Earth	9.64×10^{10}	3.34×10^{11}	5.79×10^{11}	1.71×10^{14}	2.10×10^{10}	1.60×10^{9}
b) normalized to Earth, less core	14.1×10^{10}	4.89×10^{11}	8.48×10^{11}	2.50×10^{14}	3.08×10^{10}	2.34×10^{9}
MARS ATMOSPHERE[2]	n.d.	1.8×10^{9}	3.5×10^{9}	1.04×10^{13}	2.0×10^{8}	5.2×10^{7}
VENUS ATMOSPHERE[3]						
a) mass spectrometer	($\sim 2\times10^{14}$)	(1.1×10^{14})	(1.0×10^{14})	(1.0×10^{14})	n.d.	n.d.
b) gas chromatograph	n.d.	(5.7×10^{12})	(1.2×10^{13})	(1.2×10^{13})	$<2.7\times10^{11}$	n.d.
LUNAR SAMPLES[4]						
12001 (soil)	$\sim 2\times10^{18}$	3.7×10^{16}	6.6×10^{15}	-	9.3×10^{12}	2.7×10^{12}
12001 (Ilmenite)	4.9×10^{19}	2.1×10^{17}	5.9×10^{15}	-	7.1×10^{12}	2.0×10^{12}
METEORITES						
carbonaceous chondrites (bulk)[5]	3×10^{14} to 5×10^{16}	3×10^{11} to 1×10^{14}	8×10^{11} to 8×10^{13}	-	5×10^{10} to 7×10^{11}	8×10^{10} to 1×10^{12}
ureilites[6]	$\leq 3\times10^{12}$ to 5×10^{13}	6×10^{10} to 1×10^{12}	2×10^{13} to 3×10^{14}	-	1×10^{11} to 3×10^{12}	1×10^{11} to 4×10^{12}
other gas-rich meteorites[7]	$\sim 10^{14}$ to 5×10^{17}	5×10^{12} to 5×10^{15}	5×10^{11} to 2×10^{14}	-	5×10^{9} to 5×10^{11}	3×10^{9} to 3×10^{11}
ordinary chondrites[8]	$\leq 5\times10^{14}$	$\leq 3\times10^{12}$	$\leq 2\times10^{13}$	$\leq 1.6\times10^{15}$	$\leq 3\times10^{11}$	$\leq 5\times10^{11}$
INTERPLANETARY DUST[9]	$\sim 2.7\times10^{18}$	p	p	-	n.d.	n.d.
COSMIC[10]						
a) Total	4.5×10^{22}	4.9×10^{19}	1.2×10^{18}	-	7.2×10^{14}	9.5×10^{13}
b) Ice and Rock	2.5×10^{24}	2.7×10^{21}	6.8×10^{19}		4.0×10^{16}	5.2×10^{15}

Table 2-2. (continued)

n.d. = not detected p = present

(1)The number of atoms of each gas in the terrestrial atmosphere has been divided by a) 5.98×10^{27}g, b) 4.1×10^{27}g. The mass of the atmosphere is 5.29×10^{21}g, with a mean molecular weight of 28.97. Atmospheric He and ^{40}Ar are radiogenic gases outgassed by the planet (same for Mars and Venus). The atmospheric composition is taken from the CRC Handbook of Chemistry and Physics, 54th edition.

(2)Owen et al. (1977). Ne abundance from observed ^{22}Ne concentration, 0.25 ppm volume, and assumed ^{20}Ne/^{22}Ne ratio of 10±3. Atmospheric mass taken as 3.0×10^{19}g, mean molecular weight 43.4.

(3)Preliminary Pioneer-Venus data. MS data from Hoffman et al. (1979) and McElroy (priv. comm.). GC data from Oyama et al. (1979). Atmospheric mass 4.7×10^{23}g, mean molecular weight 43.4. Differences are unexplained at present.

(4)Eberhardt et al. (1972). Soil data are averages of several size fractions. Ilmenite data are for a 10 micron grain-size fraction. Lunar samples typically contain excess ^{40}Ar implanted from the lunar atmosphere with ^{40}Ar/^{36}Ar varying from about 0.1 to 10.

(5)Mazor et al. (1970), Black (1972b), Smith et al. (1978).

(6)Göbel et al. (1978), Mazor et al. (1970).

(7)Black (1972a), Pepin and Signer (1965).

(8)Heymann (1971). He is predominantly radiogenic, as is ^{40}Ar. Neon is predominantly cosmogenic.

(9)He measured by Rajan et al. (1977). Merrihue (1964) and Tilles (1966) detected He, Ne, and Ar in magnetic concentrates from pelagic sediments.

Table 2-2. (continued)

(10) Noble gas abundances from Table 1-3. Abundances for other elements used for mass normalization taken as solar, from Ross and Aller (1976) and Cameron (1973).

Table 2-3. Elemental ratios for trapped noble gases in solar system materials

	$^{4}He/^{20}Ne$	$^{20}Ne/^{36}Ar$	$^{36}Ar/^{84}Kr$	$^{84}Kr/^{132}Xe$
TERRESTRIAL ATMOSPHERE(1)	(0.319)	0.523	48.6	27.6
MARS ATMOSPHERE(2)	n.d.	~ 0.5	~ 31	~ 11
VENUS ATMOSPHERE(4)	(~ 2)	(~ 0.5-1)	$\geqslant 40$	n.d.
LUNAR SAMPLES(4)				
12001 (soil)	49-87	5.1±0.7	1370±90	6.2±0.3
12001 (Ilmenite)	253±10	27±5	1590±150	7.9±0.7
METEORITES(4)				
Carbonaceous chondrites (bulk)	200 to 400	0.3 to 15	50 to 200	1.3±0.4
Ureilites	$\leqslant 50$	0.01 to 0.002	100 to 300	0.9 to 3
Other gas-rich meteorites	80 to 500	10 to 25	200 to 2300	2 to 8
Ordinary chondrites	n.d.	$\leqslant 1$	~ 80	~ 1.3
SOLAR WIND(3)	570±70	28±9	n.d.	n.d.
COSMIC(5)	800	29	3700	17

(1) ^{20}Ne = 0.905 Ne; ^{84}Kr = 0.57 Kr; ^{132}Xe = 0.27 Xe. ^{4}He in the atmosphere is largely radiogenic.

(2) $^{132}Xe \simeq 0.19$ Xe based on $^{129}Xe/^{132}Xe = 2.5$ and otherwise normal xenon similar to Earth atmosphere.

(3) Geiss (1973).

(4) For references, see notes to Table 2-2.

(5) Isotopic compositions of Ne, Kr, Xe presumed similar to solar wind or Earth atmosphere values.

Table 2-4. Planetary, solar, and atmospheric noble gas components.

	^{3}He	^{20}Ne	^{36}Ar	^{84}Kr	^{132}Xe
"Planetary"					
CII[1]	7×10^{-3}	0.28	$\equiv 1$	1.25×10^{-2}	1.04×10^{-2}
carbon[2]	7×10^{-3}	0.21	$\equiv 1$	$.93\times10^{-2}$	1.09×10^{-2}
"Solar"					
solar wind[3]	6.8	28	$\equiv 1$	-	-
cosmic[4]	1.9	40	$\equiv 1$	4.0×10^{-4}	4.0×10^{-5}
"Atmospheric"	2.33×10^{-7}	0.523	$\equiv 1$	2.06×10^{-2}	7.47×10^{-4}

[1]Mazor *et al.* (1970), p. 811. CII chondrites.

[2]Phinney *et al.* (1976). "Carbon" residues from carbonaceous chondrites.

[3]Geiss (1973).

[4]Marti *et al.* (1972). $^{3}He/^{4}He$ assumed 1.2×10^{-4}.

Table 2-5. Isotopic compositions of noble gases in solar system materials. Data are predominantly for trapped noble gases.

	$^{3}He/^{4}He$	$^{20}Ne/^{22}Ne$	$^{21}Ne/^{22}Ne$	$^{36}Ar/^{38}Ar$	$^{40}Ar/^{36}Ar$ (8)
Terrestrial (1)					
Atmosphere	1.4×10^{-6}	9.80	0.0290	5.32	296.0
Mars Atmosphere (4)	-	-	-	5.2	3000
Venus Atmosphere (4)	-	-	-	5.2	(~ 1)
Lunar Samples (4)					
12001 (soil)	4.1×10^{-4}	12.5	0.032	5.29	0.4
12001 (Ilmenite)	3.7×10^{-4}	12.9	0.031	5.33	0.4
Meteorites					
Carbonaceous (4) Chondrites (Bulk)	1.2×10^{-4} to 4.2×10^{-4}	8 to 13	0.02 to 0.04	5.2 to 5.5	(variable)
Carbonaceous (2) Chondrites (Separates)	1.2×10^{-4} to 4.2×10^{-4}	0.4 to 13.7	0.005 to 0.04	4.8 to 5.4	(variable)
Ureilites (4)	n.d.	10 to 12	~ 0.03	5.2 to 5.5	$< 5\times10^{-4}$
Other Gas-rich (4) Meteorites	~ 3.3×10^{-4}	11 to 13	0.03 to 0.04	5.2±0.4	(variable)
Solar Wind (4)	4.3×10^{-4}	13.7	0.033	n.d.	n.d.

Table 2-5. (continued)

	Krypton (normalized to mass 82)				
	78	80	83	84	86
Terrestrial[1] Atmosphere	0.0302	0.1959	0.9974	4.946	1.511
(Mars Atmosphere: normal)[4]					
Lunar Samples					
BEOC 12001[4]	0.0296	0.1938	1.0020	4.989	1.521
SUCOR[3]	-	0.1933	1.0047	5.024	1.556
"SOLAR"[5]	0.0302	0.1961	0.9984	4.946	1.519
Meteorites					
AVCC[6]	0.0296	0.1945	1.0011	4.963	1.538
"CARBON"[2]	0.0302	0.1941	1.0060	4.960	1.556
"1C1"[2]	0.0301	0.1982	0.9975	4.960	1.543
Ureilites[4]	-	0.1961	0.9945	4.910	1.518

Table 2-5. (continued)

	Xenon (normalized to mass 130)							
	124	126	128	129	131	132	134	136
Terrestrial[1] Atmosphere	0.0234	0.0218	0.471	6.505	5.224	6.614	2.567	2.182
(Mars atmosphere: $^{129}Xe/^{132}Xe = 2.5\pm^{2}_{1}$)[4]								
Lunar Samples								
BEOC 12001[4]	0.0290	0.0259	0.504	6.354	4.988	6.062	2.239	1.818
SUCOR[3]	0.0289	0.0263	0.509	6.371	4.990	6.066	2.252	1.827
"SOLAR"[5]	0.0295	0.0254	0.508	6.361	4.973	6.080	2.238	1.818
Meteorites								
AVCC[6]	0.0285	0.0255	0.510	(variable)	5.081	6.219	2.376	1.996
"CARBON"[2]	0.0290	0.0254	0.507	6.378	5.043	6.147	2.360	1.998
"1C1"[2]	0.0287	0.0252	0.508	(6.40)	5.053	6.162	2.357	1.982
"IT-AVCC"[7]	0.0287	0.0253	0.508	(variable)	5.048	6.158	2.373	2.009
Ureilites[4]	0.0285	0.0256	0.508	6.361	5.037	6.146	2.321	1.937

Table 2-5. (continued)

(1) Mamyrin et al. (1970) (He); Eberhardt et al. (1965) (Ne); Nier (1950a) (Ar); Nier (1950b) (Kr, Xe); Podosek et al. (1971) (Xe).

(2) Phinney et al. (1976); Reynolds et al. (1978) ("Carbon," average for 3 meteorites); Srinivasan et al. (1977) ("1Cl," average for 4 meteorites); Eberhardt et al. (1979); Niederer and Eberhardt (1977).

(3) Podosek et al. (1971).

(4) References as in Tables 2-2, 2-3.

(5) Frick and Moniot (1977).

(6) Krummenacher et al. (1961); Eugster et al. (1967).

(7) Pepin and Phinney (1979).

(8) ^{40}Ar in planetary atmospheres and lunar soils is almost entirely radiogenic argon outgassed from the planets. The primordial abundance of ^{40}Ar is very low, as can be seen from the ureilite data.

Table 2-6. Isotopic signatures of planetary and solar noble gases.[1]

	$^{3}He/^{4}He$	$^{20}Ne/^{22}Ne$	$^{36}Ar/^{38}Ar$
planetary	1.2×10^{-4}	8	5.3
solar	4×10^{-4}	12.5 to 13.7	5.3

[1]For references, see Table 2-4.

CHAPTER 3. ORIGIN AND DISTRIBUTION OF NEON IN THE SOLAR SYSTEM

3.1 INTRODUCTION

In this chapter we examine the problem of the origin and distribution of neon in the solar system. The composition of neon is marked by large isotopic variations that cannot be readily explained by isotopic mass fractionation, or by in situ nuclear processes. We assume here that these variations reflect isotopic inhomogeneities in the primordial matter that formed the solar system. We take as a starting point a simple model of the formation of the solar system from a mixture of interstellar dust and gas. These two phases are presumed to have been independent reservoirs of neon with distinct isotopic compositions. Neon isotopic variations observed today are taken to be the end result of mixing processes that combined different amounts of neon from the gas and dust. Neon in the gas is assumed to have been a single, homogeneous isotopic component. We will also assume that the dust contained only one primordial neon component. In this case, the model for primordial neon is a simple, two-component mixing model. We use the terms "gas-phase neon" and "dust-phase neon" to distinguish between the two primordial neon components. Our purpose in this chapter is to determine the compositions of the primordial neon components, and to try to deduce the nature of some of the mixing processes responsible for the observed isotopic variability. During our investigation, we will also attempt to determine if the simplest two-component model for primordial neon can successfully explain the observed data. To accomplish these aims, we will compare measured neon concentrations and isotopic compositions to values predicted from simple mixtures of gas and dust formed in various ways.

Evidence of the composition of primordial gas-phase neon may be

found today in the sun. The sun is generally believed to be a representative sample of the primordial gas and dust. The composition of neon in the sun is thought not to have been changed by nuclear reactions during or after the sun's formation. Based on the cosmic abundances of condensable heavy elements in the sun, the average dust to gas ratio in the starting material can have been no higher than about 0.02 by mass. Unless the primordial neon content of the dust was remarkably high, the isotopic composition of neon in the sun will have been determined almost entirely by the composition of neon in the gas alone. Most of the neon in the sun is ^{20}Ne; about 10% is ^{22}Ne. These proportions represent the average primordial composition of the solar mixture of dust and gas. The most economical way that addition of neon from the dust to the gas could have changed the bulk $^{20}Ne/^{22}Ne$ ratio of the mixture is for the added neon to have been pure ^{22}Ne. If half the ^{22}Ne now in the sun came originally from dust grains, then the average initial ^{22}Ne content of the dust must have been roughly 10^{20} atoms per gram. This is several tenths of a percent by number of all the atoms in the grains. We regard this high initial neon content as extremely unlikely. For comparison, such a value is some 10^5 to 10^6 times higher than the highest ^{22}Ne content found in gas-rich minerals from primitive meteorites (Srinivasan et al., 1977). We therefore presume that the present solar neon isotopic composition directly reflects the composition of neon in the primordial gas. There is some uncertainty about the actual isotopic composition of solar neon. We will discuss this question in more detail later. For now we simply state that the composition of neon in the solar wind appears to be the best estimate for solar neon and hence for the primordial gas-phase.

This isotopic composition is $^{20}Ne/^{22}Ne = 13.7\pm0.3$ and $^{21}Ne/^{22}Ne = 0.033\pm0.004$ (Geiss, 1973).

Evidence of primordial dust-phase neon is most likely to be found today in solid objects. In order for dust-phase neon to have maintained its isotopic identity throughout the formation of the solar system, it almost certainly must have remained trapped in the original dust grains. Dust-phase neon outgassed into the primitive solar nebula very likely will have been diluted beyond recognition by the abundant gas-phase neon. Neon outgassed after dispersal of the bulk of the original nebula would not be as severely diluted. The density of neon atoms in the residual nebula will be very much lower, however, and it seems unlikely that noble gases could be retrapped at this late stage. The most favorable scenario for survival of dust-phase neon is for undegassed grains to be incorporated directly into primitive solids, such as meteorite parent bodies, cometary nuclei, or protoplanets. Subsequent metamorphism may modify the gas contents of these objects. Dust-phase neon may be mobilized and retrapped in phases other than the original carrier grains. If gas-phase neon were also trapped during formation of the body, it could mix with the dust-phase neon. Outgassing of neon into an atmosphere may occur, or even complete gas loss to space. We expect that primitive, unaltered meteorites are the most likely materials presently available in which to find traces of relatively pristine dust-phase neon, perhaps still trapped in original interstellar grains.

Neon in meteorites is a mixture of trapped and cosmogenic components. As we will show later, the cosmogenic component usually can be subtracted from the data. The remaining trapped component

exhibits a wide range of neon isotopic compositions. Trapped neon compositions extend from near solar to much heavier compositions characterized by very low $^{20}Ne/^{22}Ne$ ratios less than one. In line with the simple two-component model, we attribute this variation to the presence of both gas-phase and dust-phase neon in meteorites. The isotopically heavy component must correspond to dust-phase neon. This heavy component was discovered and named neon-E by Black (1972b), who was the first to suggest that it might represent primordial neon in undegassed interstellar grains. We will review in section 3.4 data that require the dust-phase component E to be nearly pure ^{22}Ne, with $^{20}Ne/^{22}Ne$ and $^{21}Ne/^{22}Ne$ close to zero.

Unraveling the neon components in meteorites and the mixing processes that combined them will be the focus of much of the discussion in following sections of this chapter. We first outline the graphical tools used to display and interpret neon data. Some simple models for mixing gas-phase and dust-phase neon will then be examined. This will be followed by a review of observed neon composition and concentration data for the sun, planets, and meteorites. We will summarize the results of neon measurements made as a part of this thesis to investigate the isotopic end-members of meteoritic neon mixtures. Comparison of the neon observations with the characteristics of the mixing models will be used to infer the nature of some of the processes responsible for the distribution of neon in the solar system.

3.2 GRAPHICAL TOOLS FOR NEON ANALYSIS

The characteristics of two graphs are described in this section. The first is the neon three-isotope diagram, where $^{20}Ne/^{22}Ne$

is plotted versus $^{21}Ne/^{22}Ne$. The second is a composition-concentration diagram, where $^{20}Ne/^{22}Ne$ is plotted versus $1/^{22}Ne$.

3.2.1 The neon three-isotope diagram

Neon isotopic data are most conveniently represented on the three-isotope correlation diagram (Reynolds and Turner, 1964). In Figure 3-1, we plot the observed isotopic compositions of neon in the modern solar wind and the Earth's atmosphere. These compositions are characterized by high amounts of ^{20}Ne (> 90% of total neon) and very low ^{21}Ne ($\leq$ 0.3% of total neon). In the lower right part of the figure, with $^{20}Ne/^{22}Ne < 1$, are shown compositions of galactic cosmic ray spallation neon produced in the most common rock-forming target elements (Bochsler et al., 1969; Smith and Huneke, 1975). In chondritic meteorites the most important target is Mg, so bulk meteorite spallation $^{21}Ne/^{22}Ne$ ratios tend to be close to 0.9. Bulk meteorite spallation $^{21}Ne/^{22}Ne$ ratios can vary by about $\pm$10% due to differences in target composition and target thickness (shielding).

The three-isotope graph has the property that any simple mixture M of two distinct endpoint isotopic compositions X and Y will plot on the straight line segment joining X to Y (Fig. 3-1). The proportions of the two endpoint compositions in the mixture can be obtained from the graph by an inverse-lever rule; the fraction f_X^{22} of the ^{22}Ne contributed from X is the length of segment $\overline{YM}$ divided by the length $\overline{XY}$. If all possible mixtures of two distinct endpoints exist in nature, then we would expect a random sample of neon compositions to populate uniformly the line segment joining the two endpoints. If a third component Z is introduced, then all possible mixtures of X, Y,

Figure 3-1. Neon three-isotope diagram. The isotopic compositions of solar wind and the atmosphere are shown in the upper left. The compositions of galactic cosmic ray spallation neon produced in different targets are indicated near the abscissa. A mixture M of two components X and Y lies on the straight line joining the endpoints. All mixtures N of three or more components lie within the largest polygon constructed by joining all the endpoints. Shifts caused by addition of mono-isotopic components are indicated. Pure ^{22}Ne plots at the origin in this figure. The contribution of component Z to mixture N can be removed graphically by projecting the dashed mixing line to Z^* which contains only X and Y. The fraction of ^{22}Ne in N contributed by Z is given by the inverse lever rule and is $\overline{NZ}^*/\overline{ZZ}^*$.

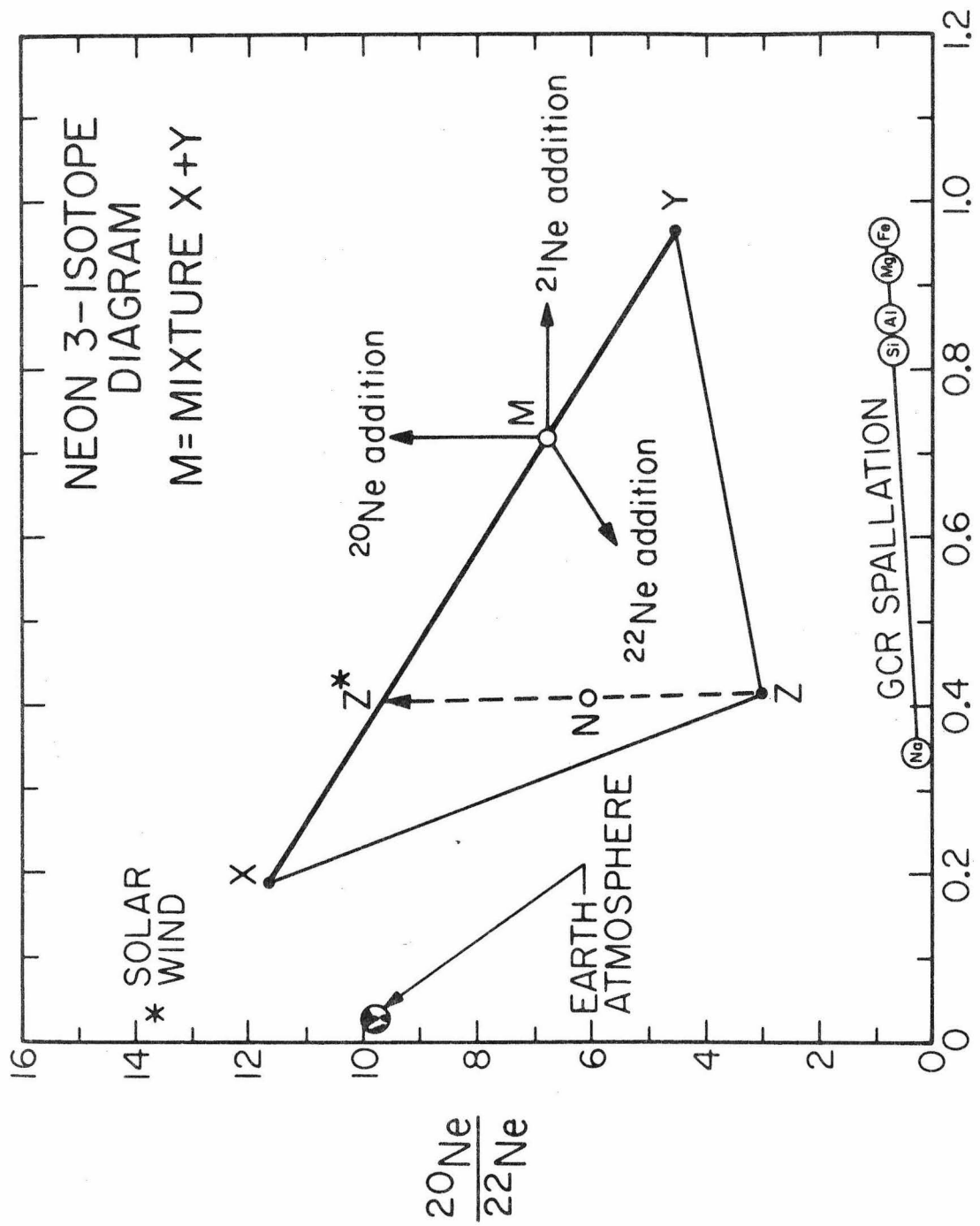
NEON 3-ISOTOPE DIAGRAM
M= MIXTURE X+Y
SOLAR WIND
EARTH ATMOSPHERE
X
Y
Z
Z*
N°
M
20Ne addition
21Ne addition
22Ne addition
GCR SPALLATION
Ne
Si
Al
Mg
Fe
20Ne/22Ne
21Ne/22Ne
0
2
4
6
8
10
12
14
16
0.2
0.4
0.6
0.8
1.0
1.2

Figure 3-1

and Z will lie in the triangle outlined by the three endpoints. For any number of components, all mixtures will lie within the largest polygon that can be constructed by connecting the individual component compositions with straight mixing lines. Given a neon composition M, addition of mono-isotopic components will produce shifts in the directions indicated by the arrows in Fig. 3-1. In particular, since pure ^{22}Ne plots at the origin of Fig. 3-1, addition of ^{22}Ne to any isotopic composition will displace it toward the origin.

Consider a mixture N of components X, Y, and Z. We can subtract the Z-component from the mixture using the following graphical projection technique. On Fig. 3-1, construct a mixing line (dashed line) from the endpoint Z, through N, to the opposite X-Y tie line. The intersection of the projected segment and the tie line defines a point Z^*. Subtraction of the Z-component from the mixture is equivalent to moving N along the dashed line directly away from Z. At the endpoint Z^*, all the Z-component has been subtracted from the original mixture, and only X and Y remain. The inverse lever rule applied to the segment $\overline{ZNZ^*}$ gives f_Z^{22}, the fraction of the total ^{22}Ne in the mixture from Z. The remaining ^{22}Ne from Z^* can be partitioned between X and Y by a second application of the inverse lever rule to segment $\overline{XZ^*Y}$. For neon in meteorites, which typically consists of a mixture of spallation neon and trapped neon, this projection technique is commonly used to subtract the contribution of the spallation component from the mixture.

If the actual concentration of Z in a mixture N is independently known, it can be compared to the formal concentration deduced by the projection technique. This comparison provides a test of the validity

of the X,Y,Z three-component model for the mixture N. If the actual and formal concentrations of Z are not the same, X and Y cannot be the proper end-members to describe the mixture N. In Fig. 3-1, this disagreement corresponds graphically to Z^* plotting off the $\overline{XY}$ tie line, either inside or outside the XYZ triangle. For this example we have redefined Z^* as the projection of N when the known concentration of Z is subtracted from the mixture, not as the point of intersection of the dashed line and $\overline{XY}$ as was done before. If X, Y, and Z are independently known to be valid components in the neon system, then a mismatch of the sort described may provide evidence of an additional component. If X, Y, and Z are the only components present, complete subtraction of Z from various mixtures N must result in an array of points falling along the X-Y mixing line. If a non-linear field of points results, an additional component must be present.

Any field of measured neon isotopic compositions limits the possible compositions of neon end-members. One of the tasks of the experimenter is to test the compositions of proposed end-members to see if new limits for their compositions can be obtained. This can be done by random measurement of new samples, searching for compositions falling outside the field outlined by the end-members. A more directed technique is to select samples with known compositions close to the end-member being tested. Mineral separation or step-wise heating techniques are then used to look for extreme isotopic compositions. Since one is not guaranteed of finding new compositions more extreme than the old, it is necessary to ask what criteria could be used to identify a given preferred composition as a true end-member. We suggest the following criterion. A candidate for an endpoint should

lie at the intersection of the extrapolated trends of two or more independent correlation lines. A single composition lying at the intersection of several lines is an allowed end-member for all the samples. Additional strong support for interpreting an intersection as an endpoint is provided if the point of intersection coincides with the composition of a known component or reservoir of solar-system neon.

3.2.2 The neon composition-concentration diagram

A second useful diagram is a plot of $^{20}Ne/^{22}Ne$ vs. $1/^{22}Ne$, isotopic composition against inverse concentration (Fig. 3-2). This diagram supplements the three-isotope diagram which contains no information about the neon concentrations of samples. Since we plot $1/^{22}Ne$ on the abscissa, concentration increases toward the left. Shown in Fig. 3-2 are points representing neon in the sun and the Earth's atmosphere, and limits on points for neon in the atmospheres of Mars and Venus. For the sun and solar wind, the high cosmic abundance of neon ensures that this point plots essentially on the y-axis. Solar $1/^{22}Ne$ is about 3×10^{-19} $(\text{atoms/gram})^{-1}$.

Consider creating mixtures by combining different masses of two materials, each characterized by a constant neon isotopic composition and concentration. These mixtures will fall on a straight line if no neon or host material is lost from the system during mixing. If matter is lost during the mixing process, the mixing curves need not be straight. The fraction of ^{22}Ne contributed to a particular mixture by one of the end-members can be obtained graphically using the inverse

Figure 3-2. Neon concentration-composition diagram. Data shown are for the solar wind and the atmospheres of the terrestrial planets. Isotopic compositions are not yet known for neon in the Venus or Mars atmospheres. A mixture M of end-members S and E will plot on the straight line joining S and E if no material is lost during the mixing process. Dilution of a reservoir with matter containing no neon will shift the point representing the reservoir to the right. With the scale shown for the abscissa, pure ^{22}Ne plots at the origin.

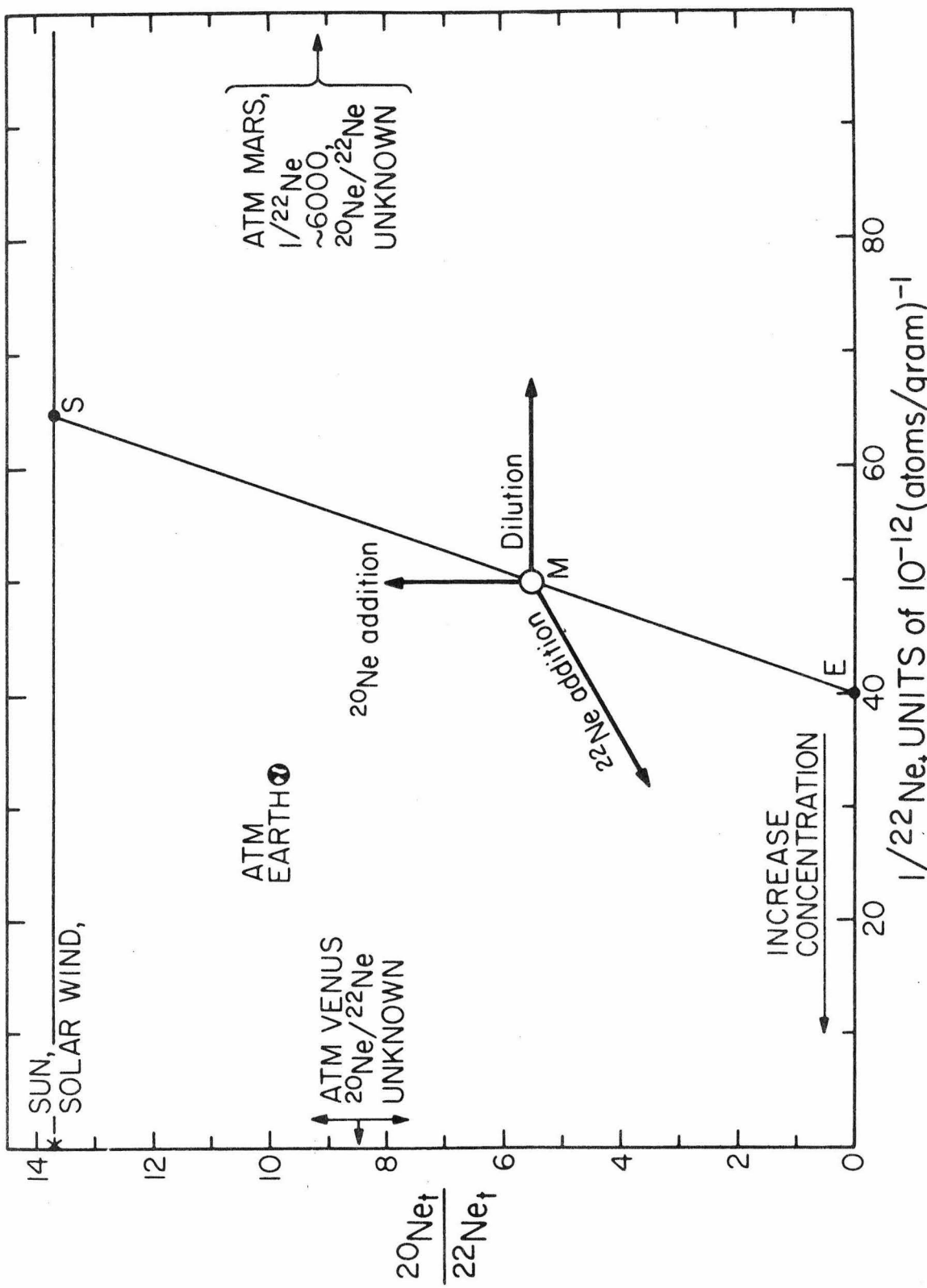
ATM MARS,
1/22Ne
~6000,
20Ne/22Ne
UNKNOWN
S
SUN,
SOLAR WIND,
ATM
EARTH
ATM VENUS
20Ne/22Ne
UNKNOWN
20Ne addition
Dilution
M
22Ne addition
E
INCREASE
CONCENTRATION
20Net / 22Net
1/22Net UNITS of 10-12(atoms/gram)-1
0
2
4
6
8
10
12
14
20
40
60
80

Figure 3-2

lever rule as for the three-isotope plot. In Fig. 3-2, we show a mixing line drawn arbitrarily between a reservoir S with $^{20}Ne/^{22}Ne_S$ = 13.7 and a reservoir E with $^{20}Ne/^{22}Ne_E$ assumed to be 0. If we take a given mixture M and add material containing no neon, $^{20}Ne/^{22}Ne$ will be unchanged, but $1/^{22}Ne$ will increase. In Fig. 3-2 this dilution corresponds to generation of a horizontal mixing line extending to the right of point M, toward infinite $1/^{22}Ne$ at infinite dilution. Mixing lines are also shown for the addition of pure ^{20}Ne or pure ^{22}Ne to mixture M, for example by nuclear processes. The ^{22}Ne concentration in pure ^{22}Ne is about $3x10^{22}$ atoms/gram, about $4x10^{-11}$ in the units of Fig. 3-2, so pure ^{22}Ne plots virtually at the origin.

3.3 MODELS FOR MIXING GAS-PHASE AND DUST-PHASE NEON

3.3.1 Models with no gas-loss during mixing

The simplest mixing model is a box in which we put a known mass of gas and a known mass of dust. We can imagine this as a simple model of the accretion of a planet with a primordial atmosphere. On the concentration-composition diagram, $1/^{22}Ne$ vs. $^{20}Ne/^{22}Ne$, the average composition of the mixture in the box will plot on the straight mixing line joining the pure gas and pure dust endpoints. Different boxes (planets) with different proportions of dust and gas will all fall at various points on the same mixing line.

We can complicate the model slightly by making the plausible assumption that the dust consists of two types of grains, one of which is the carrier of dust-phase neon, while the second contains no neon at all. All mixtures of gas with average dust samples will again fall on a single mixing line. In Fig. 3-3, we have labeled the pure

Figure 3-3. Dust-gas mixing with no gas loss. The dust is assumed to consist of neon carriers plotting at E_0 and gas-free grains plotting to the right at infinity. The average composition of the dust is $\overline{E}$. Mixtures of different amounts of gas with average dust samples plot on the heavy line between $\overline{E}$ and S. Mixtures where the proportion of neon carrier grains to gas-free grains is different than average will plot in the shaded area outlined by the light mixing lines.

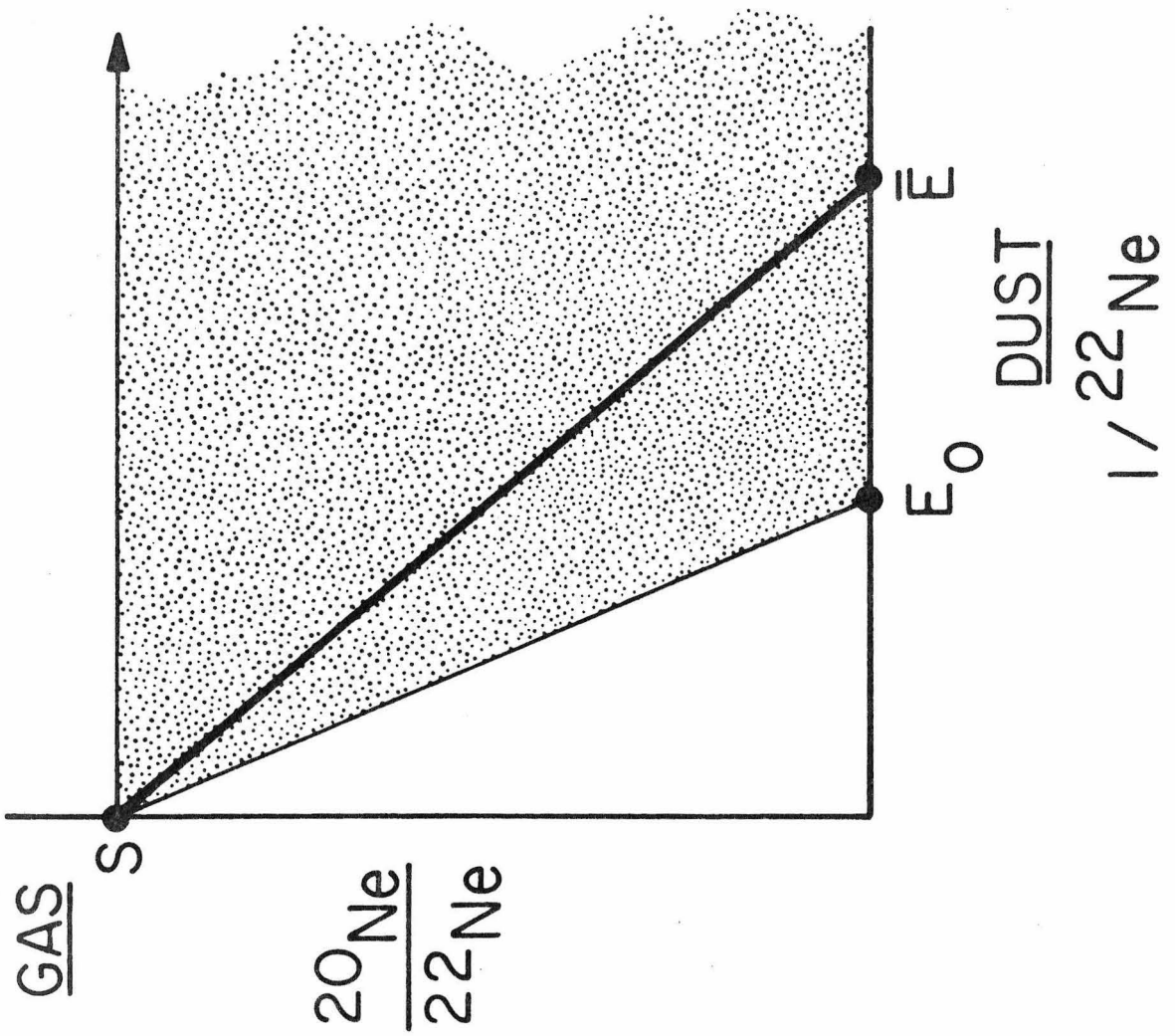

Figure 3-3

gas-phase as reservoir S and the average dust-phase as $\overline{E}$. E_0 represents the concentration of dust-phase neon in the pure carrier grains. It may be possible to separate the two types of dust grains before mixing with the gas phase. If so, limiting cases are (1) gas plus carrier grains giving the mixing line S-E_0, and (2) gas plus neon-free grains, giving the horizontal dilution line extending to the right of S. All other intermediate mixtures would lie in the shaded area in Fig. 3-3.

The presence of both dust-phase neon and gas-phase neon in meteorites is required by the variability of trapped neon compositions. This implies that neon from the gas has been somehow implanted into the solid grains. The specific implantation mechanism might be adsorption and occlusion of gas by a growing grain, diffusion, injection of accelerated ions from a solar wind or solar flares, etc. Here we consider some general features of mixing by implantation without designating a specific mechanism. For now we assume that the implantation of gas-phase neon into a grain does not cause loss of any dust-phase neon from the grain. In Fig. 3-4 we summarize the graphical behavior of mixtures due to this general implantation. In panel (a) at the upper left are given the starting materials; gas S, and dust containing neon carriers plotting at E_0. We also show a point E for a hypothetical reservoir of pure dust-phase neon isolated from its carrier. We now take dust grains and implant gas into them. If we allow all possible degrees of implantation, then neon compositions in individual carrier grains will populate the entire line segment between S and E_0 as shown in panel (b). Note that this line can also be viewed as the trajectory followed by a single grain starting at E_0, and experiencing continued implantation of gas-phase neon. Eventually

Figure 3-4. Mixing caused by implantation of gas-phase neon into dust grains. (a) Starting reservoirs, including gas (S), neon carriers in the dust (E_0) and a hypothetical reservoir of pure dust-phase neon (E). Grains containing no neon plot to the right at infinity. (b) Implantation of S in carrier grains populates the segment between S and E_0. No limit is placed on the amount of S that can be added to a grain. (c) The concentration of gas-phase neon implanted in a grain is limited to a maximum saturation value n_{sat}. Carrier grains originally containing dust-phase neon plot at M when saturated with gas-phase neon. Initially gas-free grains plot at N after saturation. (d) Grains with different initial neon concentrations, or different mixtures of neon carriers and gas-free grains will plot on the heavy arrow to the right of the maximum concentration at E_0. $\overline{E}$ represents an average parcel of dust. Saturation of all grains or mixtures will result in points plotting on the segment between M and N. Unsaturated samples of dust may plot anywhere to the right of $\overline{MN}$ and $\overline{ME}$. (e) Outgassing after implantation. Equal fractional loss of gas-phase neon (S) and dust-phase neon (E) moves points horizontally to the right. In the limit where only gas-phase or dust-phase neon is lost, points move along straight lines to E_0 or S, respectively. Intermediate cases sketched may give rise to curved paths if the relative rates of loss of the two components change with time. (f) The field accessible to gas-dust mixtures by implantation or outgassing as described in previous panels is shaded.

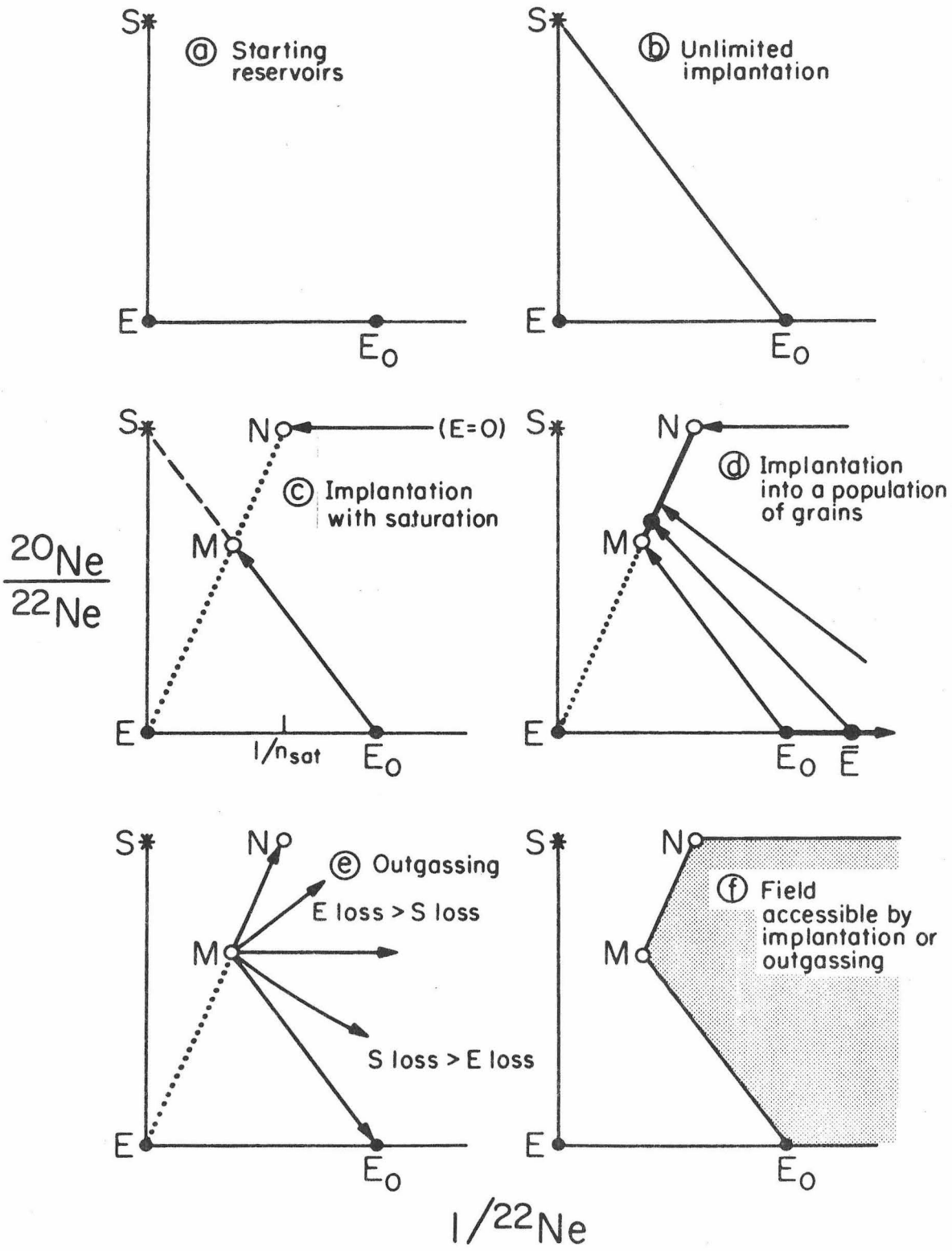
S
E
E0
ⓐ Starting reservoirs
ⓑ Unlimited implantation
N
(E=0)
M
ⓒ Implantation with saturation
1/nsat
ⓓ Implantation into a population of grains
Ē
ⓔ Outgassing
E loss > S loss
S loss > E loss
ⓕ Field accessible by implantation or outgassing
20Ne/22Ne
1/22Ne

Figure 3-4

the implanted neon dominates the original neon, and the grain composition becomes the composition of the gas-phase at S.

We would not normally expect implantation of gas-phase neon to continue without limit. Instead, the implanted ^{22}Ne in the grain will saturate at a value n_{sat}. A grain initially containing no neon, then saturated with gas-phase neon will plot at point N in panel (c). If we were to add dust-phase neon (E) to this grain, the resulting mixture must lie on the dotted mixing line $\overline{EN}$. Therefore, a grain at E_0 which is subsequently saturated with gas-phase neon will plot at point M, the intersection of mixing lines $\overline{SE}_0$ and $\overline{EN}$. This assumes that the saturation concentration of gas-phase neon is the same in both grains.

Implantation into populations of grains is summarized in panel (d). The starting population is signified by the heavy arrow extending to the right of E_0. The initial points may represent different mixtures of carriers (E_0) and inert diluting grains, or alternatively, individual grains containing different initial concentrations of dust-phase neon. As before, we take $\overline{E}$ to represent the average dust-phase. Saturation of all grains to the same concentration n_{sat} of gas-phase neon will populate the segment between M and N. The effects of averaging may be important if samples studied consist of large numbers of grains. The neon compositions of unsaturated average samples of grains will plot along the mixing line extending upward from the point $\overline{E}$. For saturated dust, measurements on large samples will tend to cluster around the single solid point shown on $\overline{MN}$, although compositions of individual grains within the sample can cover the entire range from M to N.

Another process that can lead to dispersion of points on the concentration-composition diagram is outgassing. In panel (e) of Fig. 3-4 we sketch some of the possible results of gas loss from grains that have undergone prior implantation of gas-phase neon. We start with a grain plotting at point M. If gas-phase neon (S) and dust-phase neon (E) are not fractionated during outgassing, the isotopic composition of neon will stay the same. The decrease in ^{22}Ne will shift outgassed grains horizontally to the right on the diagram. On the other hand, if loss of dust-phase neon proceeds more rapidly than loss of gas-phase neon, points will shift upward away from the original point M. In the limit where only dust-phase neon is lost, outgassed grains will plot along $\overline{MN}$, reaching N when all the dust-phase neon has been outgassed. Analogous paths for preferential loss of gas-phase neon are sketched below point M in the figure.

In the final panel (f) of Fig. 3-4 we show the field of compositions accessible by implantation and outgassing in a simple gas-dust system. Varying degrees of incomplete implantation and outgassing can yield grains whose neon compositions plot anywhere in the shaded region of panel (f). The accessible region extends toward the right to infinity to include completely outgassed grains.

The simple mixtures we have discussed above will all plot on a single trapped neon mixing line in the three-isotope plot. The mixing line will connect the composition of pure gas-phase neon (S) to that of dust-phase neon (E).

3.3.2 Solar wind implantation

To this point it has been assumed that no dust-phase neon is

lost as a result of the implantation of gas-phase neon into the grains. If the dust-phase neon is displaced by the implanted gas, then there is no a priori reason to expect implantation to result in straight mixing lines on the neon composition-concentration diagram. Implantation of solar wind ions in grains is an important mechanism for introducing gas-phase neon into solids in the present solar system, and is likely to have been important in the past. Gas loss by sputtering may occur during solar wind implantation. A simple model of this process will be examined below to investigate the degree of departure from linear mixing that might be expected for this implantation mechanism.

The energies of ions in the present solar wind are fairly low, about 0.5 to 1 KeV per nucleon. As a result, the ions are directly implanted only in a thin layer on the surfaces of grains. This layer varies in thickness from roughly 100 Å (10^{-6} cm) for solar wind protons, to about 500 Å for neon, and somewhat thicker for more massive ions with greater energies. We consider a simplified picture of a grain consisting of two distinct regions, a rim of constant thickness into which the solar wind ions are implanted, and an undisturbed core. The average concentration of solar wind neon in the rim is a function of time depending on the rates of implantation and gas loss. Gas loss can occur either by direct sputtering of individual gas atoms in the rim, or by sputter erosion of the entire surface of the grain. We separate the two loss processes since sputtering of neon atoms may proceed even in the absence of measurable surface erosion from sputtering of the major lattice-forming elements. This is because the gas atoms are less tightly bound in the solid than the major elements, and many

interstitial gas atoms may be sputtered by an implanted ion that is relatively ineffective at removing the lattice atoms (Carter and Colligan, 1968).

The grain is modeled as a plane slab (Fig. 3-5) with a uniform initial neon content $^{i}Ne(o)$ atoms/cm^3, where i = 20, 21, or 22. The slab is of thickness x(t), and is irradiated on one side by a total flux of F solar wind ions/cm^2/second. The surface of the slab is assumed to be removed by sputter erosion at a constant rate λ cm/second. The thickness of the rim is constant at a value L which is determined by the range of the incident solar wind ions. The thickness of the core will necessarily decrease by λ cm/second. For this model we will ignore the effects of diffusion of gas in the grain. The neon concentrations in the core (c) and rim (r) as a function of time are labeled $^{i}Ne_c(t)$ and $^{i}Ne_r(t)$, respectively. Since no implantation takes place in the core, $^{i}Ne_c(t)$ is constant, and equal to the initial concentration in the grain, $^{i}Ne(o)$.

For simplicity we assume $^{i}Ne_r(t)$ is uniform throughout the rim at any given time. There is evidence that collisional cascades associated with the slowing down of the implanted solar wind can cause mixing on the scale of the penetration depth of the ions (Haff et al., 1977). The concentration increase per unit time due to the implanted flux of solar wind neon ions is $a_i F/L$, where a_i is the fractional abundance of ^{i}Ne in the total incoming flux F. Because of the erosion of the grain, the rim continually encroaches upon the core of the slab. Neon is lost from the rim in the material eroded, but is also gained across the moving boundary between the inner edge of rim and the core. The loss at the surface due to erosion is $\lambda\,{}^{i}Ne_r(t)/L$. The gain from

Figure 3-5. Implantation of gas-phase neon into dust grains by the solar wind. The grain is modeled as a semi-infinite slab of thickness x(t). Solar wind ions are implanted in a rim of constant thickness L. Erosion of the surface of the grain occurs by sputtering of the major, lattice-forming elements, and causes the surface to recede at a rate λ cm/sec. Neon is lost from the rim both as it is uncovered by erosion and by direct sputtering of neon atoms out of the rim.

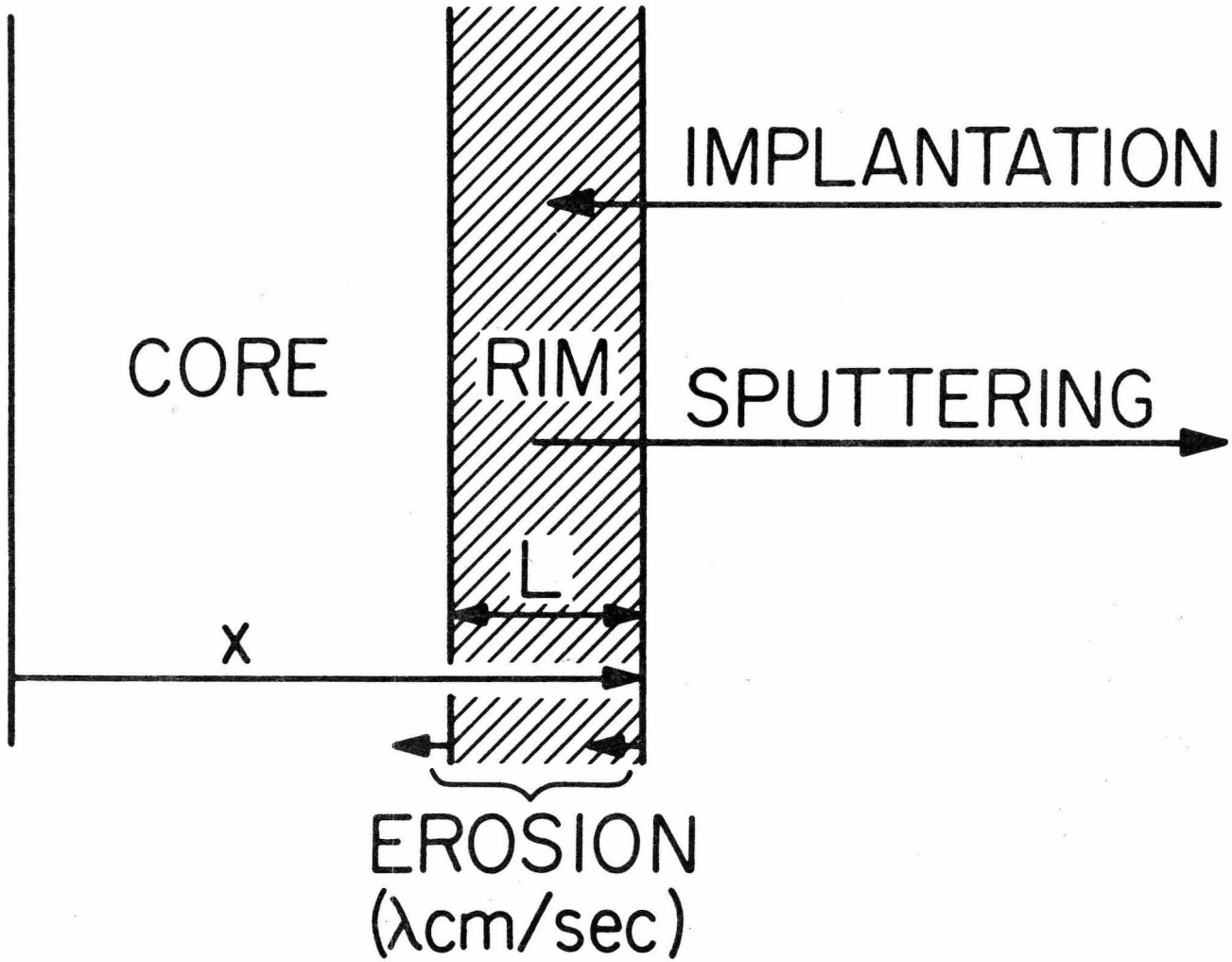
MODEL: PLANE SLAB
IMPLANTATION
CORE
RIM
SPUTTERING
L
x
EROSION
(λcm/sec)

Figure 3-5

the core through the inner edge of the rim is $\lambda {}^{i}Ne(o)/L$. The rate of loss of neon from the rim due to direct sputtering of neon atoms is taken to be $\sigma_i F \, {}^{i}Ne_r(t)$. The rate of sputtering of a single neon atom in the rim volume is assumed to be directly proportional to the total flux F of solar wind ions; σ_i is an empirical sputtering cross-section for a single neon atom in the rim that is exposed to a flux of 1 ion per cm^2. The total rate of change of the neon concentration in the rim is therefore

$$\frac{d\,{}^{i}Ne_r(t)}{dt} = \frac{a_i F}{L} - \sigma_i F \, {}^{i}Ne_r(t) - \frac{\lambda}{L} \, {}^{i}Ne_r(t) + \frac{\lambda}{L} \, {}^{i}Ne(o) \qquad \text{(Eq.3-1)}$$

This equation may be integrated to give

$${}^{i}Ne_r(t) = {}^{i}Ne(o)e^{-(\sigma_i F+\lambda/L)t} + \frac{1}{L}\frac{a_i F+\lambda \, {}^{i}Ne(o)}{\sigma_i F+\lambda/L}\left[1 - e^{-(\sigma_i F+\lambda/L)t}\right] \qquad \text{(Eq.3-2)}$$

By multiplying ${}^{i}Ne_r(t)$ and ${}^{i}Ne_c(t) = {}^{i}Ne(o)$ with the fractional volumes of the rim and core, and adding the two terms, we obtain the average concentration of ${}^{i}Ne$ in the entire slab:

$${}^{i}Ne(t) = \left\{\frac{x_o - L - \lambda t}{x_o - \lambda t}\right\} {}^{i}Ne(o) + \left\{\frac{L}{x_o - \lambda t}\right\}\left\{{}^{i}Ne(o)e^{-(\sigma_i F + \frac{\lambda}{L})t}\right. \qquad \text{(Eq.3-3)}$$

$$\left. + \frac{a_i F + \lambda \, {}^{i}Ne(o)}{L(\sigma_i F + \lambda/L)}\left[1 - e^{-(\sigma_i F + \frac{\lambda}{L})t}\right]\right\}$$

where x_o is the initial thickness of the slab.

Using equation 3-3, ${}^{20}Ne/{}^{22}Ne$ as a function of $1/{}^{22}Ne$ can be calculated for different relative rates of gas implantation and loss. Note that the curves to be discussed can equally well represent the

trajectory of a single grain that undergoes implantation, or the locus of compositions of a population of grains with the same initial dust-phase neon concentration that have been irradiated to different extents. It can be shown that the second derivative of $^{20}Ne/^{22}Ne$ with respect to $1/^{22}Ne$ is equal to zero for all cases where $\sigma_{22} = \sigma_{20}$. With this condition, the mixing lines for solar wind implantation will be straight, even where we allow gas loss by sputtering. For the model under study, any curvature of the mixing lines must therefore originate from differences in the sputtering rates for the different neon isotopes. Haff et al. (1977) suggest the relative sputtering probabilities should be proportional to the fourth root of the inverse mass ratio of the two sputtered species. For neon, this gives $\sigma_{20}/\sigma_{22} = (22/20)^{\frac{1}{4}} = 1.024$. For the sake of illustration, we will generally assume $\sigma_{20}/\sigma_{22} = 1.1$ to magnify the isotopic effects of sputtering on the shapes of the $^{20}Ne/^{22}Ne$ vs. $1/^{22}Ne$ trajectories. We will take the initial dust-phase neon in the grain to consist of neon-E, which we will assume to be pure ^{22}Ne. $1/^{22}Ne(o)$ is arbitrarily set equal to 1. The measured solar wind neon composition (Geiss, 1973) is assumed for the implanted neon.

The three competing rates that determine the general form of each mixing curve are implantation (the first term on the right in Eq. 3-1), sputtering (second term), and erosion (third and fourth terms). We consider first the case where erosion is negligible and $\lambda = 0$. The thickness of the grain is constant. Neon composition-concentration curves calculated for $\lambda = 0$ are shown in Fig. 3-6. In all cases, the initial dust-phase neon concentration in the rim decays exponentially due to sputtering (first term, Eq. 3-2).

Figure 3-6. Solar wind implantation for $\lambda = 0$, no erosion of the grain surface. The dotted reference curve A is a straight mixing line between the solar wind composition and the initial dust-phase neon-E on the x-axis. In all cases, the concentration of neon in the rim builds up to a constant saturation concentration. Curve I is for rapid implantation compared to the rate of sputtering. Since very little dust-phase neon is lost during the early stages of implantation, the lower part of curve I is close to curve A. As saturation is approached, the rate of sputtering becomes significant. Since ^{20}Ne is sputtered more rapidly than ^{22}Ne, the curve turns down away from curve A. The upper endpoint for curve I occurs when saturation of the rim with solar wind neon is complete. Curve II is calculated for a reduced isotopic dependence of σ_i, $\sigma_{20}/\sigma_{22} = 1.024$. The deviation of curve II from curve A is much smaller than for curve I. Curve III is for a slow implantation rate compared to sputtering. Because of the high sputtering rate, the ^{22}Ne concentration in the rim decreases below the initial $^{22}Ne(o)$. The overall ^{22}Ne concentration in the grain also decreases, so the curve III has a positive slope. Curve IV represents an intermediate case.

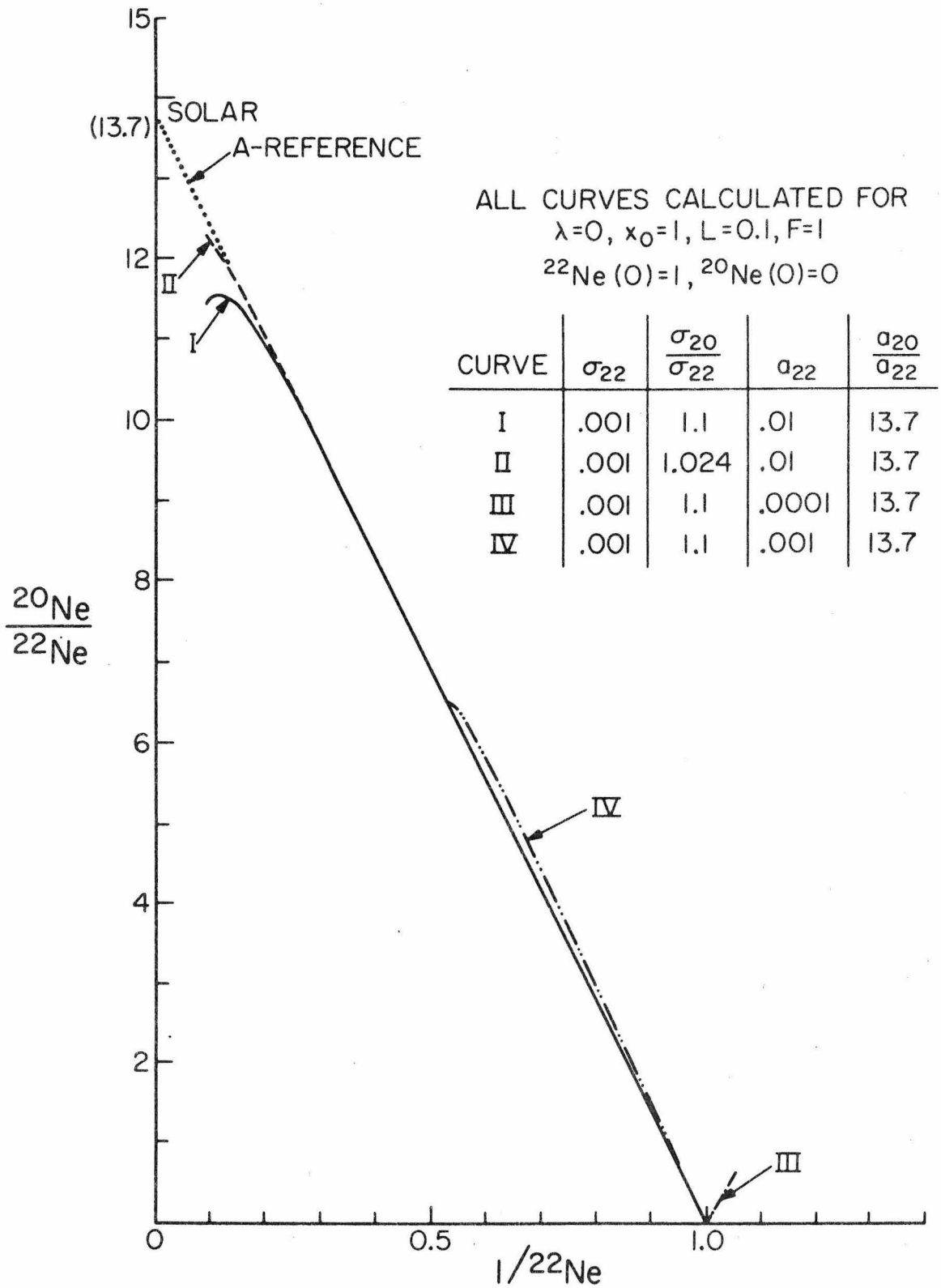

CURVE	σ_{22}	$\frac{\sigma_{20}}{\sigma_{22}}$	a_{22}	$\frac{a_{20}}{a_{22}}$
I	.001	1.1	.01	13.7
II	.001	1.024	.01	13.7
III	.001	1.1	.0001	13.7
IV	.001	1.1	.001	13.7

Figure 3-6

The implanted solar wind neon builds up to a saturation concentration $a_i/L\sigma_i$ (second term, Eq. 3-2). The characteristic time needed to approach saturation is $\sim 1/\sigma_i F$. Curves are computed for the values of the parameters shown in the upper right in Fig. 3-6. The dotted curve labeled A-REFERENCE represents a straight mixing line between the initial dust-phase plotted on the x-axis and the solar wind composition at the upper left.

It is convenient to discuss the results in terms of the ratio a_{22}/σ_{22} which is a measure of the relative importances of the implantation and sputtering rates. Curve I is for a relatively high value of $a_{22}/\sigma_{22} = 10$. The initial implantation rate $a_{22}F/L$ is much greater than the initial sputtering rate $^{22}Ne(o)\sigma_{22}F$. In essence, the grain at first gains only solar-wind neon, so the beginning portion of curve I is close to the straight mixing line given by the reference curve A. ^{20}Ne is lost faster than ^{22}Ne as sputtering becomes important, so curve I drops below the reference curve. The upper endpoint of curve I occurs when the neon concentration reaches the constant saturation value $a_i/\sigma_i L$ in the rim. Since a_{22}/σ_{22} is large for this example, the saturation concentration is relatively high, and the final average concentration and composition of neon in the grain are relatively close to the solar endpoint. Curve II in Fig. 3-6 is calculated for the smaller relative sputtering rate of $\sigma_{20}/\sigma_{22} = 1.024$, with all other parameters the same as for curve I. It can be seen that the deviation of this curve from the straight reference line is much less than for curve I. Curve III is for a low value of $a_{22}/\sigma_{22} = 0.1$. In this case, sputtering is dominant in the rim. Dust-phase ^{22}Ne is lost more rapidly than it is replaced by solar-wind

^{22}Ne. The average ^{22}Ne concentration in the grain decreases, so curve III in Fig. 3-6 has a positive slope. Because of the intense sputtering, the saturation concentration of solar wind neon in the rim is very small. The final overall $^{20}Ne/^{22}Ne$ ratio in the grain is very low because it is dominated by the dust-phase neon remaining in the core of the grain. The final curve IV illustrates an intermediate case with $a_{22}/\sigma_{22} = 1$. The lower portion of the curve is nearly straight, but with a slightly more positive slope than curve I, reflecting the increased importance of gas-loss by sputtering. The final $^{20}Ne/^{22}Ne$ ratio of a saturated grain in this particular example is half the solar-wind value.

We now turn to examples where erosion is significant, $\lambda \neq 0$. The thickness of the grain continually decreases and a point is reached when the core containing only dust-phase neon disappears. We terminate the model calculations at this point when only the rim remains. If further erosion takes place, some solar wind ions and sputtered atoms may be lost through both faces of the grain, a situation which we have not modeled.

In the case where $\sigma_i = 0$, the only mechanism of gas-loss is erosion. This is an example where $\sigma_{20} = \sigma_{22}$, so all curves for different a_i and λ will be straight lines. Furthermore, all curves will lie along the reference curve A. This is because the concentration of dust-phase neon averaged over the entire grain remains constant at $1/^{22}Ne(o)$. Addition of solar-wind neon to such a grain is equivalent to the simple models discussed earlier of mixing dust with gas, each with constant concentrations. Each curve for different a_i and λ will extend from the initial point at $1/^{22}Ne(o)$ on the x-axis, to an end-point determined by the saturation concentration in the rim,

$(a_i F/\lambda) + {}^{i}Ne(o)$.

In the more general case, neither λ nor σ_i is zero. In Fig. 3-7 we plot three curves for increasingly rapid erosion rates. In addition we include the usual reference curve A. Only the upper portions of the curves with $^{20}Ne/^{22}Ne \gtrsim 8$ are shown. Curve I is for no erosion, and is the same as curve I in the previous Fig. 3-6. Curves II and III in Fig. 3-7 are calculated for the same parameters as curve I, with the exception of λ. For curve II, λ is relatively small. The characteristic erosion time is L/λ, the time required to erode the original rim of thickness L. For curve II, this time is much greater than the characteristic sputtering time, $1/\sigma_i F$. Neon implanted in the rim will saturate due to sputtering gas loss before significant erosion takes place. This behavior is close to that expected for the case of no erosion, given by curve I in Fig. 3-7. Thus, the dashed curve II is coincident with curve I for values of $^{20}Ne/^{22}Ne$ less than about 11.5. As saturation of the rim occurs at $1/^{22}Ne \approx 0.1$, the dashed curve II bends sharply down away from the reference curve and is still very similar to curve I. Now, however, erosion comes into play, and curve II turns up again, $^{20}Ne/^{22}Ne$ increasing to a final value of about 12.5. The final portion of curve II is essentially a straight line. This is because after saturation, the rim contains only implanted solar-wind neon, and the core only dust-phase neon. The relative proportions of rim and core change as erosion proceeds, but the concentrations in the two regions are constant. We have previously shown that for reservoirs with constant concentrations, mixtures lie on straight lines. Curve III is an example for relatively rapid erosion. The grain is eroded before significant sputtering and isotopic fractionation of the neon in the

Figure 3-7. Solar wind implantation into dust grains. Curves computed for varying erosion rates λ. The values of other parameters are the same as for curve I in Fig. 3-6, which is repeated in this figure, also as curve I (no erosion). For curve II, the erosion rate is slow compared to sputtering, and the beginning portion of the curve is quite similar to curve I. The sharp downturn in curve II signifies the development of a saturated rim. The subsequent linear trend upward occurs as erosion gradually causes the core containing neon-E to shrink. The result of rapid erosion rate is shown in curve III. The grain erodes and the curve terminates before significant isotopic fractionation due to sputtering takes place. Therefore, curve III does not deviate markedly from the reference mixing line A.

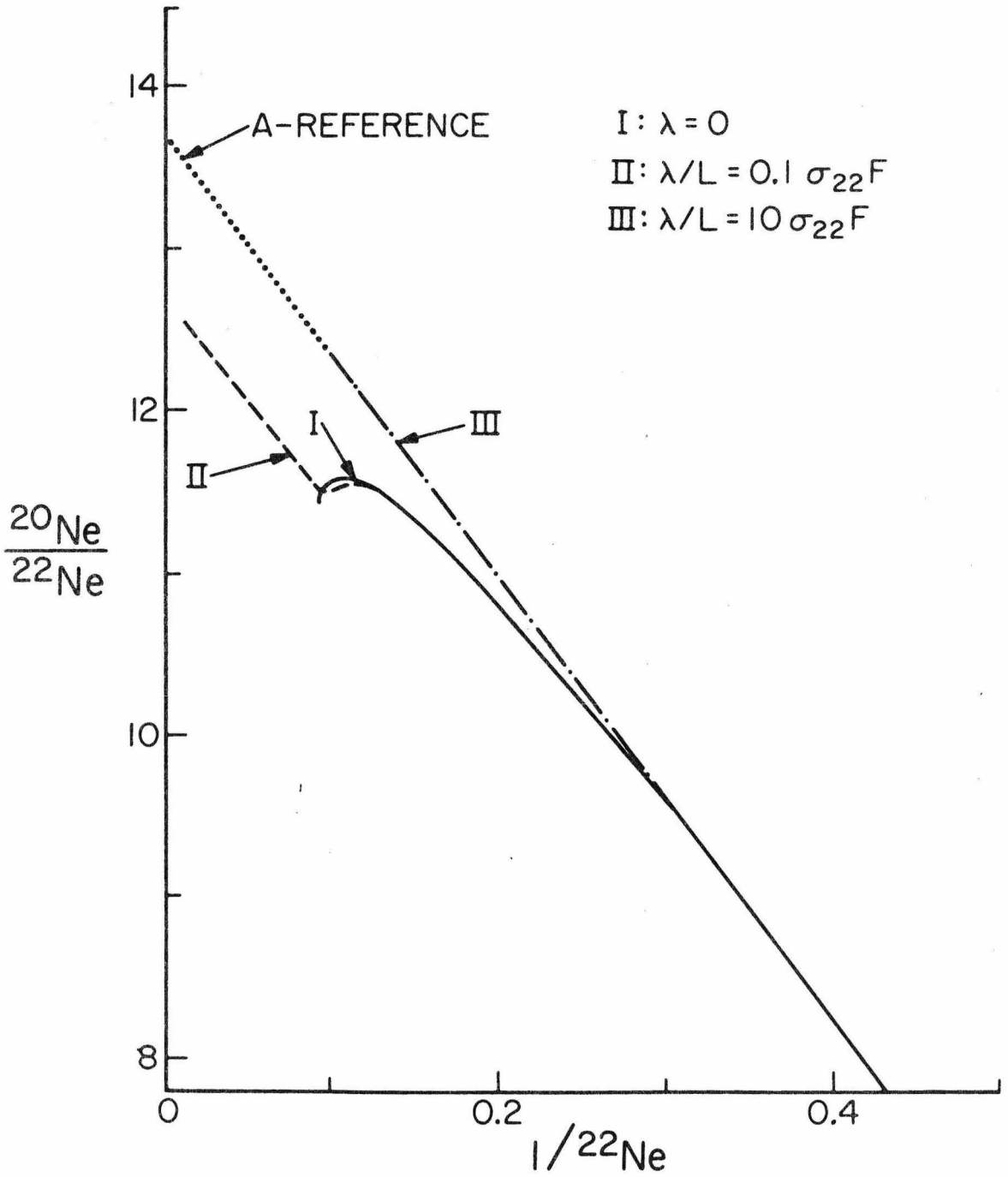
14
12
10
8
0
0.2
0.4
A-REFERENCE
I: λ = 0
II: λ/L = 0.1 σ22F
III: λ/L = 10 σ22F
I
II
III
20Ne/22Ne
1/22Ne

Figure 3-7

rim can occur. The curve is essentially linear, and coincident with curve A. The deviations from the reference curve A shown by curves I and II occur because of the isotopic dependence of the sputtering rate. Since sputtering is of minimal importance for curve III, it does not deviate noticeably from the reference curve.

The parameters used above to construct the curves in Figs. 3-6 to 3-7 have been rather arbitrary. In Fig. 3-8 are shown several curves calculated with the plane-slab model, but using estimated values of the parameters in Eq. 3-3 that are appropriate for solar wind implantation in grains at about 1 A.U. distance from the sun. These include a total flux F of about $10^8/cm^2$-sec (Taylor, 1975; p. 93) with solar abundances of neon, $a_{22} = 10^{-5}$ and $a_{20}/a_{22} = 13.7$. An erosion rate of about 0.1 Å per year (Haff et al., 1977) is used, with a rim thickness of 500 Å corresponding to the approximate range of solar-wind neon in silicates. Initial ^{22}Ne concentrations are taken to be similar to those in meteorites. The most difficult parameter to estimate is the effective sputtering cross section σ_{22}. A value of about $10^{-16} cm^2$ is gotten from experimental data on ion implantation rates and saturation concentrations in various substances (Carter and Colligan, 1968). It is assumed that in those experiments saturation occurs when the known rate of implantation is balanced by the rate of sputtering. Target erosion is presumed to be minimal. If gas loss by target erosion was in fact important in these experiments, then the estimate of $10^{-16} cm^2$ could be too high.

Curve I in Fig. 3-8 is for a 1 micron thick grain with an initial ^{22}Ne content of 10^{13} atoms/cm^3. The sputtering saturation time $1/\sigma_{22}F$ is rapid, $\sim 10^8$ seconds, compared to the erosion time, $L/\lambda \sim 10^{11}$

Figure 3-8. Solar wind implantation into dust grains. Curves are computed for realistic irradiation parameters at about the Earth's orbital radius from the sun. All curves are calculated for $\sigma_{20}/\sigma_{22} = 1.1$ for clarity. Use of the preferred value 1.024 will reduce by about 3/4 the magnitude of deviations from the neon-E to solar neon mixing line. Curve I is for a 1 μ thick grain with initial $^{22}Ne(o) = 10^{13}$ atoms/cm^3. Curve II is for a 10 μ grain, otherwise the same as curve I. In curve III, the initial neon content of a 1 μ thick grain is 10^{15}/cm^3. Finally, in curve IV, σ_{22} is reduced to 10^{-20}cm^2 to allow for possible overestimation of the value derived from experiments described in Carter and Colligan (1968). Under all conditions, the saturation concentration of neon in the rim is much higher than the initial neon content of the core, and the average compositions of the grains are rapidly dominated by the implanted solar wind. None of the curves show large deviations from a straight mixing line, particularly since the isotopic dependence of the sputtering cross sections is probably overestimated.

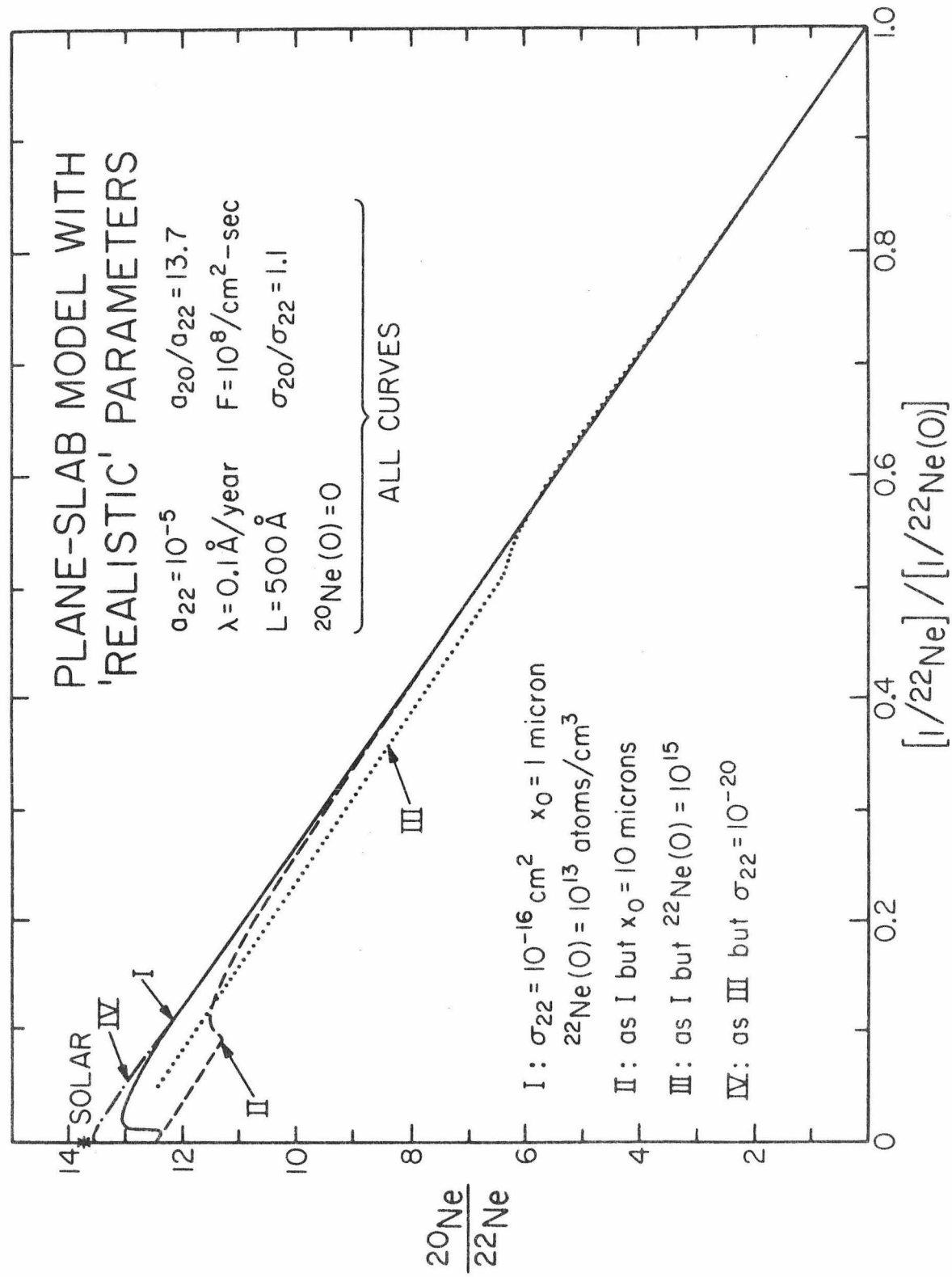
PLANE-SLAB MODEL WITH
'REALISTIC' PARAMETERS
$\sigma_{22} = 10^{-5}$
$\lambda = 0.1$ Å/year
L = 500 Å
$^{20}Ne(0) = 0$
$a_{20}/a_{22} = 13.7$
$F = 10^8/cm^2$-sec
$\sigma_{20}/\sigma_{22} = 1.1$
ALL CURVES
SOLAR
I
II
III
IV
I: $\sigma_{22} = 10^{-16}$ cm^2 $x_0 = 1$ micron
$^{22}Ne(0) = 10^{13}$ atoms/cm^3
II: as I but $x_0 = 10$ microns
III: as I but $^{22}Ne(0) = 10^{15}$
IV: as III but $\sigma_{22} = 10^{-20}$
$\frac{^{20}Ne}{^{22}Ne}$
$[1/^{22}Ne] / [1/^{22}Ne(0)]$
0
0.2
0.4
0.6
0.8
1.0
2
4
6
8
10
12
14

Figure 3-8

seconds. The saturation concentration of ^{22}Ne is high, about $10^{18}/cm^3$. As the saturated rim develops on the grain, curve I shows the resultant abrupt downturn from the straight reference line.

Curve II (dashed) is similar to curve I except that it is for a 10 micron thick grain. Saturation due to sputtering in the rim is again rapid, so curve II also hooks down away from the straight mixing line. Because of the larger core of the grain in case II, the overall concentration of ^{22}Ne in the grain is lower at the time the rim becomes saturated. Curve III is calculated using the curve I parameters, but with an increased initial neon content in the core. This larger proportion of dust-phase neon again causes the downturn due to rim saturation to occur at a lower overall $^{20}Ne/^{22}Ne$. The downturn is followed in curve III by a long, linear portion corresponding to a slowly eroding grain with a constantly saturated rim. For curve IV the value of σ_{22} was reduced to $10^{-20}cm^2$ in case the curve I estimate is too high. As expected, the reduced importance of sputtering and its attendant isotopic fractionation causes curve IV to be closer to a straight mixing line than curve I.

For clarity, all curves in Fig. 3-8 have been calculated using $\sigma_{20}/\sigma_{22} = 1.1$. The more plausible value of 1.024 (Haff et al., 1977) results in much smaller isotopic shifts from the straight mixing line between the solar point and the initial neon concentration on the abscissa. We conclude that for the model of solar wind implantation developed here, deviations from a linear mixing relationship on the neon concentration-composition diagram will be small. It also seems unlikely that this conclusion would be significantly changed by constructing a more detailed model including more realistic irradiation

geometries, depth dependences of implanted species, diffusion, etc. For example, Huneke (1973) modeled the effects of gas loss by diffusion during implantation, and showed that the isotopic composition of neon in a saturated grain might be expected to be fractionated from $^{20}Ne/^{22}Ne$ of 13.7 to about 12.5. The effects of this fractionation on the $^{20}Ne/^{22}Ne$ vs $1/^{22}Ne$ trajectories discussed above should be similar to the effects caused by preferential sputtering of the lighter neon isotopes. No major differences in the form of the trajectories would be expected.

The implantation of solar-wind neon is restricted to surfaces of grains. Measured data from lunar samples and the models calculated above suggest grains typically develop a rim of thickness L saturated with solar-wind neon before substantial erosion occurs. This suggests we construct the following simple model. A spherical grain of total radius R is composed of a core of radius R-L surrounded by a rim of constant thickness L (Fig. 3-9). The rim is saturated with solar-wind neon, $^{22}Ne_r = n_{sat}$, and all dust-phase neon in the rim has been sputtered away during implantation. The core contains only dust-phase neon, $^{22}Ne_c = {}^{22}Ne(o)$. The average neon isotopic composition in the grain will depend on the grain radius. The grain can be regarded as a mixture of two neon reservoirs, the rim and core, with constant concentrations in both. For different proportions of rim to core--i.e., for varying radius--a straight mixing line is generated, curve A in Fig. 3-9. For infinite radius the neon in the rim is unimportant, and the endpoint is ($^{20}Ne/^{22}Ne = 0$, $1/^{22}Ne = 1/^{22}Ne(o)$). For a very small radius $\leq L$, no core exists and the endpoint is at N, ($^{20}Ne/^{22}Ne = 0$, $1/^{22}Ne = 1/n_{sat}$). For a given grain radius R, increase or decrease

Figure 3-9. Implantation of gas-phase neon into the rims of dust grains. A spherical grain is modeled as a core containing neon-E and a rim of thickness L containing a constant concentration of only dust-phase neon. This is appropriate for example for solar-wind implantation that has reached saturation, where all neon-E has been lost from the rim by sputtering. Variations in the initial radii and/or initial neon-E contents result in variations in the average composition/concentration of neon in the composite grains. Variations in the radius are equivalent to mixing different proportions of two reservoirs with constant neon concentrations. This results in grains plotting on a straight mixing line such as curve A. Grains of the same radius, but different initial neon-E contents plot on a mixing line like B which corresponds to the addition of pure neon-E (near the origin). All grains of a population with radii between R_{min} and R_{max} and initial neon-E contents between $^{22}Ne^{E}_{min}$ and $^{22}Ne^{E}_{max}$ will plot in the shaded region. If curves A and B represent the average neon-E content and grain size, then representative samples of large numbers of grains will all fall near the intersection of the two curves, despite the wide variation of individual grain compositions.

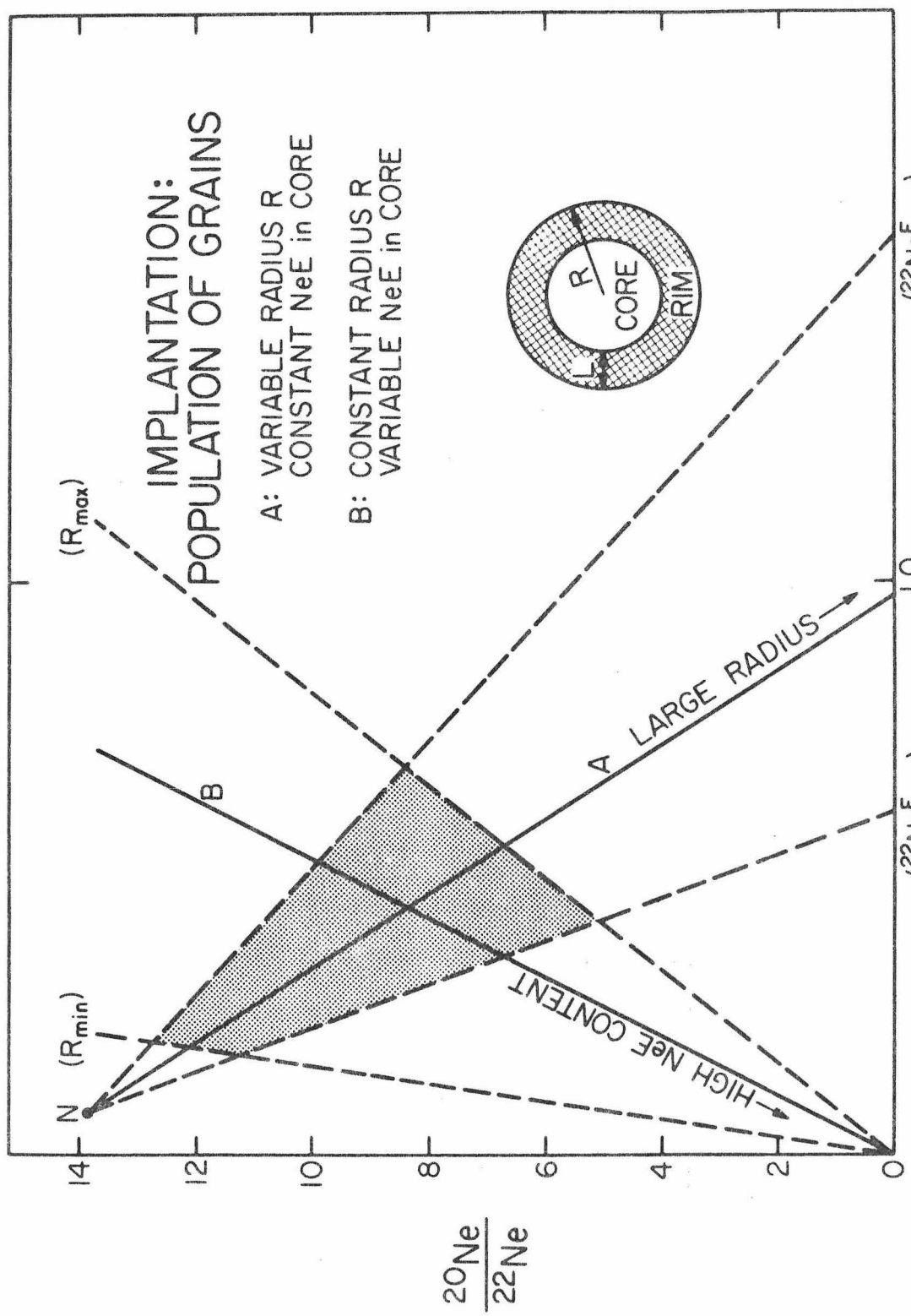
IMPLANTATION:
POPULATION OF GRAINS
A: VARIABLE RADIUS R
CONSTANT NeE in CORE
B: CONSTANT RADIUS R
VARIABLE NeE in CORE
R
CORE
RIM
L
(R_{max})
(R_{min})
N
B
A LARGE RADIUS
HIGH NeE CONTENT
$(^{22}Ne^{E}_{max})$
$(^{22}Ne^{E}_{min})$
1.0
$1/^{22}Ne$
$\frac{^{20}Ne}{^{22}Ne}$
0
2
4
6
8
10
12
14

Figure 3-9

of the dust-phase neon-E content of the core will cause points to move along a mixing line emanating from the origin (curve B, Fig. 3-9). The lower endpoint corresponds to very high neon-E content in the core, $^{22}Ne(o) \gg n_{sat}$. The upper endpoint corresponds to no neon-E in the core. The concentration of ^{22}Ne in the grain at this upper endpoint is $n_{sat}-n_{sat}(1 - \frac{L}{R})^3$. For this model, all possible neon concentrations and isotopic compositions of individual grains from a population characterized by a range of sizes R_{min} to R_{max} and of neon-E contents $^{22}Ne^{E}_{min}$ to $^{22}Ne^{E}_{max}$ will lie in the shaded region in Fig. 3-9. All samples consisting of a number of grains from the population will also fall within this region. Large samples of many grains that comprise representative averages over the distribution of sizes and neon-E contents will all tend to plot near a single point, although the compositions of individual grains may vary widely.

A different mechanism for adding gas-phase neon to pre-existing grains is condensation or overgrowth of new material. The added matter traps neon adsorbed on the growing surface from a surrounding atmosphere. If the concentration of gas-phase neon trapped in the overgrowth is constant, the mixing systematics describing populations of these composite grains will be similar to those described in Fig. 3-9.

3.4 OBSERVED NEON ISOTOPIC COMPOSITIONS IN THE SOLAR SYSTEM

In this section we review known neon isotopic compositions in various solar system objects. These data provide the foundation on which we can construct plausible mixing models for solar system neon. Since with a few exceptions, noble gases are typically determined in solid samples, we first outline some of the techniques used to measure

neon in meteorites and other solids. We next summarize the measurements of solar neon which allow us to infer the composition of primordial gas-phase neon. We then discuss neon in the Earth's atmosphere and in meteorites from which the composition of dust-phase neon is inferred.

3.4.1 Measurement techniques

Almost all individual procedures used for measuring neon in meteorites or other solids are based on extracting the gas from the solid by heating the sample in a vacuum. The gas driven off is purified of chemically-reactive species, generally by exposing it to a reactive metal surface. Isotopic compositions are measured mass-spectrometrically, with concentrations determined by isotope dilution, or peak-height comparison to a standard of known pressure. Differences among individual experiments arise from differences either in the sample preparation or in the heating procedure used to extract the gas. The simplest procedure used is to heat a bulk sample of the meteorite until it melts or evaporates, typically at about 1500°C. All the neon in the sample is extracted in a single step. A technique pioneered by Zähringer (1962) and Reynolds and Turner (1964) that has proven especially fruitful is to heat a meteorite sample in stages to successively higher temperatures. This procedure is commonly called stepwise-release or stepwise-heating. The sample is maintained at a constant temperature for typically one half to one hour for each step. At the end of the step, the gas driven off is removed from the extraction vessel and analyzed. The temperature is then increased for the next step. The rationale behind the use of this technique is that neon and other gases

held in chemically or physically different sites within the sample may be driven off preferentially at different temperatures depending on the nature of the sites. This may therefore provide a method for partial separation of different components of neon within the sample. A complementary technique to aid in the resolution of different gas components is chemically or mechanically to separate the bulk sample into various fractions before analysis. Single-step or multi-step thermal degassing can then be used to measure the neon in each separated fraction of the original material. A variety of different properties have been used to prepare separates, including mineralogy, grain size, magnetic susceptibility, density, and resistance to chemical attack (etching) by a variety of chemical agents. In addition, well-defined sub-regions of a sample--inclusions such as chondrules, crystal fragments, xenoliths, etc.--can be mechanically separated and analyzed.

3.4.2 The isotopic composition of neon in the sun

At present two different neon isotopic compositions have been measured in particle fluxes from the sun. In the solar wind, average values of $^{20}Ne/^{22}Ne$ and $^{21}Ne/^{22}Ne$ are 13.7±0.3 and 0.033±0.004, as measured in Al foils exposed to the wind during the Apollo missions (Geiss, 1973). Very recently, Simpson (private communication) has measured an average $^{20}Ne/^{22}Ne$ ratio of $7.7\pm^{2.3}_{1.5}$ in seven solar flares. The difference between these two compositions can not be ascribed to mass fractionation, since both determinations are made on material with essentially unfractionated elemental abundances similar to the solar photospheric values. The discrepancy is probably due to nuclear reactions taking place in the solar atmosphere. It seems more plausible that such

reactions would be associated with the comparatively high-energy (~ MeV per nucleon) flare particles, than with the much slower (~ KeV per nucleon) solar wind. For example, spallation reactions are known to take place in the solar flare region. These reactions appear to produce Na and Al atoms in abundances comparable to that needed for ^{22}Ne production to convert solar wind composition neon into the heavier composition measured for the flare particles (Dietrich and Simpson, 1978). At present we suggest that the solar wind neon isotopic composition is more likely to represent the photospheric neon composition. As discussed in the Introduction to this chapter, we take the photospheric composition to equal the composition of the primordial gas phase.

3.4.3 The isotopic composition of neon in the Earth's atmosphere

The isotopic composition of neon in the Earth's atmosphere is at present the only measured neon isotopic composition for a planetary-size object in the solar system. The measured atmospheric composition is $^{20}Ne/^{22}Ne = 9.80\pm0.08$ and $^{21}Ne/^{22}Ne = 0.0290\pm0.0003$ (Eberhardt et al., 1965). The possible change with time of this composition due to outgassing of nucleogenic ^{21}Ne and ^{22}Ne formed from (α,n) reactions in the Earth is thought to be small. Estimates are that less than about 5% of the ^{21}Ne in the present atmosphere could be from this source (Wetherill, 1954; Shukolyukov et al., 1973; Heymann et al., 1976), and less than about 4% of the ^{22}Ne (Shukolyukov et al., 1973). Heymann et al. (1976) suggested that up to 20% of the atmospheric ^{21}Ne could be spallation neon inherited from planetesimals out of which the Earth formed. This amount of spallation neon would contribute less than 0.6%

of the ^{22}Ne and less than 0.06% of the ^{20}Ne, so would have negligible effect on the total $^{20}Ne/^{22}Ne$ ratio of the atmosphere. There is presently no evidence of a significant flux of isotopically distinctive primordial neon into the Earth's atmosphere.

The present $^{20}Ne/^{22}Ne$ ratio in the atmosphere should therefore accurately reflect the average composition of terrestrial neon following planetary formation. The atmospheric $^{20}Ne/^{22}Ne$ of 9.8 is lower than the solar wind value of 13.7, which we have taken to be the primordial gas-phase composition. If we presume the difference in composition is caused by the presence of dust-phase neon on the Earth, then we infer that primordial neon in the dust phase was substantially heavier than gas-phase neon. We can obtain further limits on the composition of dust-phase neon from meteorite noble gas data.

3.4.4 The isotopic composition of neon in meteorites

In Figure 3-10, literature data for total neon isotopic compositions are plotted for bulk meteorite samples. Measurements made as a part of this thesis research and reported in the papers in Appendix A are included in the figure. Each point is the result of a single step extraction of neon from a sample, or represents an integrated total neon composition from a stepwise-release experiment. The data cover a very wide range of compositions. The approximately triangular field of data requires the presence of at least three components of neon to explain the observed compositions by mixing.

The component in the lower right with near-equal abundances of the three neon isotopes is galactic cosmic ray spallation neon. The spread in $^{21}Ne/^{22}Ne$ values from about 0.8 to 1 for this end-member can

Figure 3-10. Neon isotopic compositions in bulk meteorite samples. The data are consistent with mixtures of spallation neon in the lower right and trapped neon having $^{21}Ne/^{22}Ne \leqslant 0.03$. Spallation neon can be subtracted approximately by projection of points onto a mixing line drawn through the solar and Earth atmosphere points. The resulting trapped neon compositions are variable and require the presence of two components. The isotopically-light component must have $^{20}Ne/^{22}Ne \geqslant 13$ and is called neon-S. This component is most easily interpreted as gas-phase neon with the same composition as the solar wind. The second, dust-phase component is considerably heavier, with $^{20}Ne/^{22}Ne \leqslant 8$. On the basis of data similar to those plotted here, Pepin (1967) defined a component neon-A with $^{20}Ne/^{22}Ne = 8.2$ and $^{21}Ne/^{22}Ne = 0.025$. (For references see Figure 3-11.)

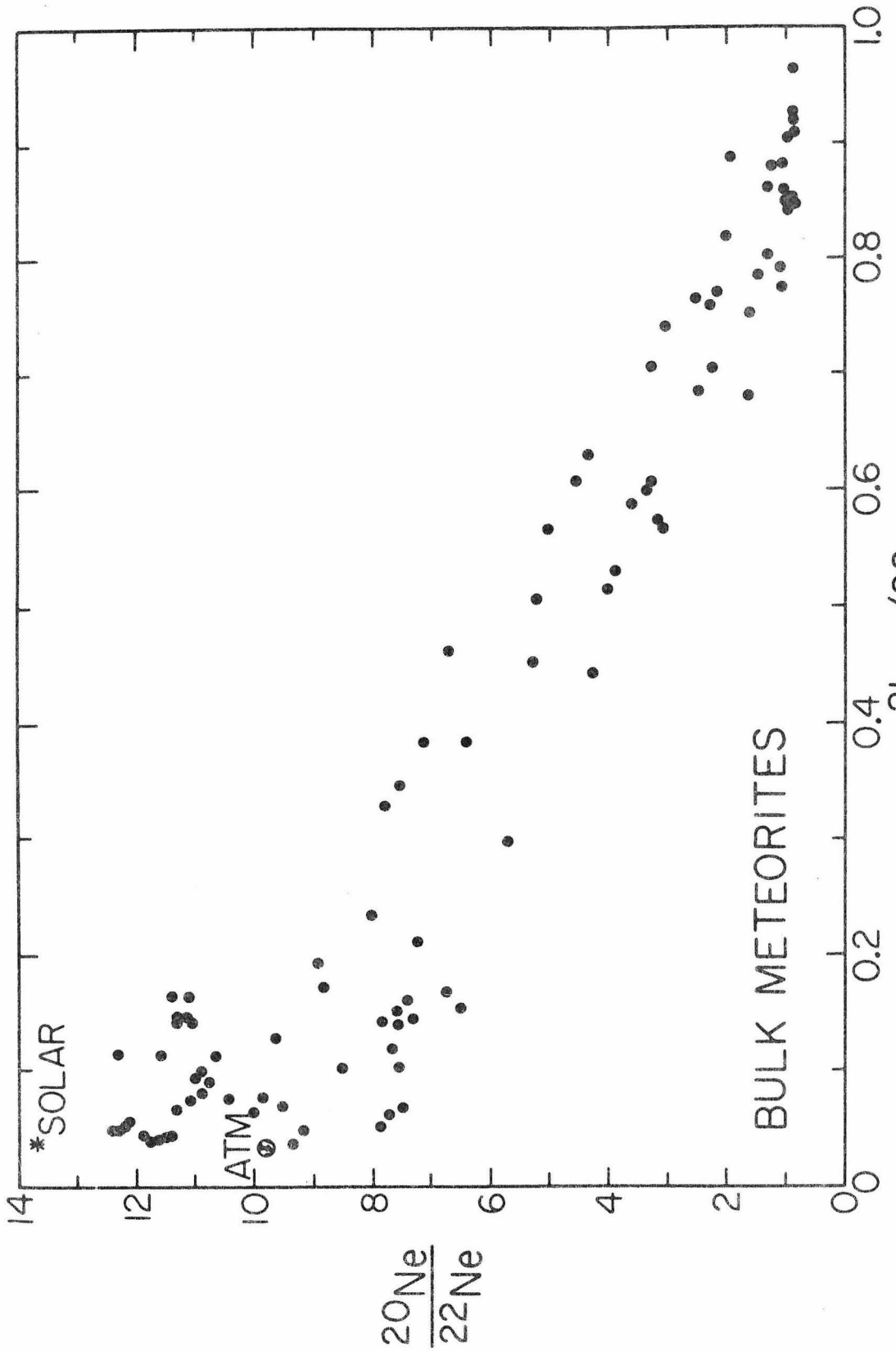
*SOLAR
ATM
BULK METEORITES
$\frac{20Ne}{22Ne}$
$21Ne/22Ne$
0
2
4
6
8
10
12
14
0.2
0.4
0.6
0.8
1.0

Figure 3-10

be explained by variations in target chemistry and shielding conditions. The cosmogenic neon content of a meteorite or meteorite mineral separate is proportional to the length of time the meteorite was exposed to galactic cosmic rays in space. This time is known as the cosmic ray exposure age of the sample. The exposure age properly refers only to the time the meteorite spent as a small, meter-sized body, since the effective penetration depth of primary and secondary cosmic radiation is only one or two meters in rocky material. For stony meteorites containing little or no trapped gases, cosmic ray exposure ages are generally less than about 40 million years, with most ages less than 20 m.y. (cf. Wasson, 1974, p. 128). Such ages are roughly in agreement with the dynamical lifetimes against capture of meteorites in Earth-crossing orbits (Öpik, 1951; Arnold, 1965). The agreement is consistent with the general picture that most meteorites are stored at depths greater than a few meters in parent objects during most of their ~ 4.5 AE history. Recent disruptive events caused break-up of the parent body, and injection of the small meteorite fragments into Earth-crossing orbit, at the same time starting the cosmic-ray exposure clock.

In Fig. 3-10 the trend of the data toward the lower right is consistent with addition of cosmogenic neon to trapped neon which plots on the left of the diagram with $^{21}Ne/^{22}Ne \leq 0.03$. The trapped neon cannot have a single isotopic composition. Projection of points in the middle of the field away from the spallation endpoint and onto a line extending through the solar and atmospheric points defines a range of trapped $^{20}Ne/^{22}Ne$ values from about 7 to 13. We recall from previous discussion that this graphical projection corresponds numerically to

subtraction of a certain amount of spallation neon from the measured composition. If we calculate these spallation contributions for all the data in Fig. 3-10, we obtain a range of values from which model cosmic ray exposure ages can be calculated. Average spallation neon production rates are used for different classes of meteorites (e.g., Bogard and Cressy, 1973). A range of model exposure ages from roughly 0.5 to 50 million years is found for the meteorites represented in Fig. 3-10. The distribution of ages is similar to that obtained for meteorites containing no trapped neon. This agreement means that in a general sense all the excess ^{21}Ne in meteorites implied by the trend of data toward the right in Fig. 3-10 can be attributed to galactic cosmic ray spallation reactions. There is no evidence of any additional ^{21}Ne-rich trapped neon component. For the remaining discussion of neon in this thesis, we will therefore assume that neon compositions lying to the right of the SOLAR-ATM line can be projected back to that line by subtraction of spallation neon. To check the validity of this assumption in detail would require accurate independent determinations of the spallation neon contents of meteorites containing trapped neon. These data do not exist in sufficient quantity.

The range of trapped neon compositions obtained after subtraction of spallation neon implies that meteorites contain at least two components of trapped neon. From the data in Fig. 3-10, the isotopically light component must have $^{20}Ne/^{22}Ne > 13$. We call this component neon-S. Solar wind neon or primordial gas-phase neon with $^{20}Ne/^{22}Ne = 13.7$ are likely candidates for the composition of the neon-S end-member. Pepin (1967) suggested that the cutoff of observed trapped $^{20}Ne/^{22}Ne_t$

ratios at about 8 corresponded to a distinct neon component in meteorites. He labeled this component neon-A, and assigned it a composition $^{20}Ne/^{22}Ne_A = 8.2\pm0.4$ and $^{21}Ne/^{22}Ne_A = 0.025\pm0.003$. We attribute the isotopic difference between neon-S and neon-A to the relative enrichment of dust-phase neon in the meteorites. Therefore, the bulk meteorite data imply that the dust-phase component must have $^{20}Ne/^{22}Ne \leqslant 8$.

In Figure 3-11, the data base is expanded to include neon compositions measured for various chemical and mechanical separates using both single-step extraction and stepwise-heating techniques. Data for lunar soil samples are included in the figure. It should be remembered that the density of points at any point on the graph may be largely an artifact of sampling. For example, the dense cluster of points at $^{20}Ne/^{22}Ne \sim 12.5$, $^{21}Ne/^{22}Ne \sim 0.04$ is a reflection of the large number of analyzed lunar soil samples, whose neon contents are dominated by solar-wind neon.

Compared with the bulk meteorite data, the field in Fig. 3-11 is significantly enlarged. The most striking difference is the addition of points in the lower left of the graph, with $^{21}Ne/^{22}Ne \leqslant 0.15$, and $^{20}Ne/^{22}Ne$ between about 0.5 and 8. This requires a much heavier isotopic composition for the trapped component attributed to dust-phase neon. The dust-phase component must be extremely enriched in ^{22}Ne, lying nearly or exactly at the origin in Fig. 3-11. This is the isotopically-heavy component named neon-E by Black (1972b). Other smaller portions of the graph have also become populated by data. One is a region from $^{21}Ne/^{22}Ne = 0.6$ to 0.8 in the lower right near the

Figure 3-11. Measured neon isotopic compositions in solar system materials. Samples include meteorites, lunar samples, the solar wind, and Earth's atmosphere. Data include compositions obtained by stepwise-heating of both bulk samples and various mineral separates. The major difference from Fig. 3-10 is in the substantial number of points with $^{20}Ne/^{22}Ne < 8$ and $^{21}Ne/^{22}Ne < 0.15$. These imply the existence of an isotopically-heavy trapped neon component that is nearly pure ^{22}Ne. This is the neon-E component described by Black (1972b) and first attributed by him to the presence of undegassed interstellar dust in meteorites. Isotopically-light compositions plotted in this figure imply that $^{20}Ne/^{22}Ne$ of the trapped neon-S component is ≥ 13.7, the solar wind value. Some additional points near the spallation endpoint with $^{21}Ne/^{22}Ne \geq 0.6$ reflect measurements of cosmogenic noble gases in sodium-rich mineral separates (Smith et al., 1977). References for data plotted in Figs. 3-10 and 3-11 are preceded by an asterisk in the list at the end of this chapter.

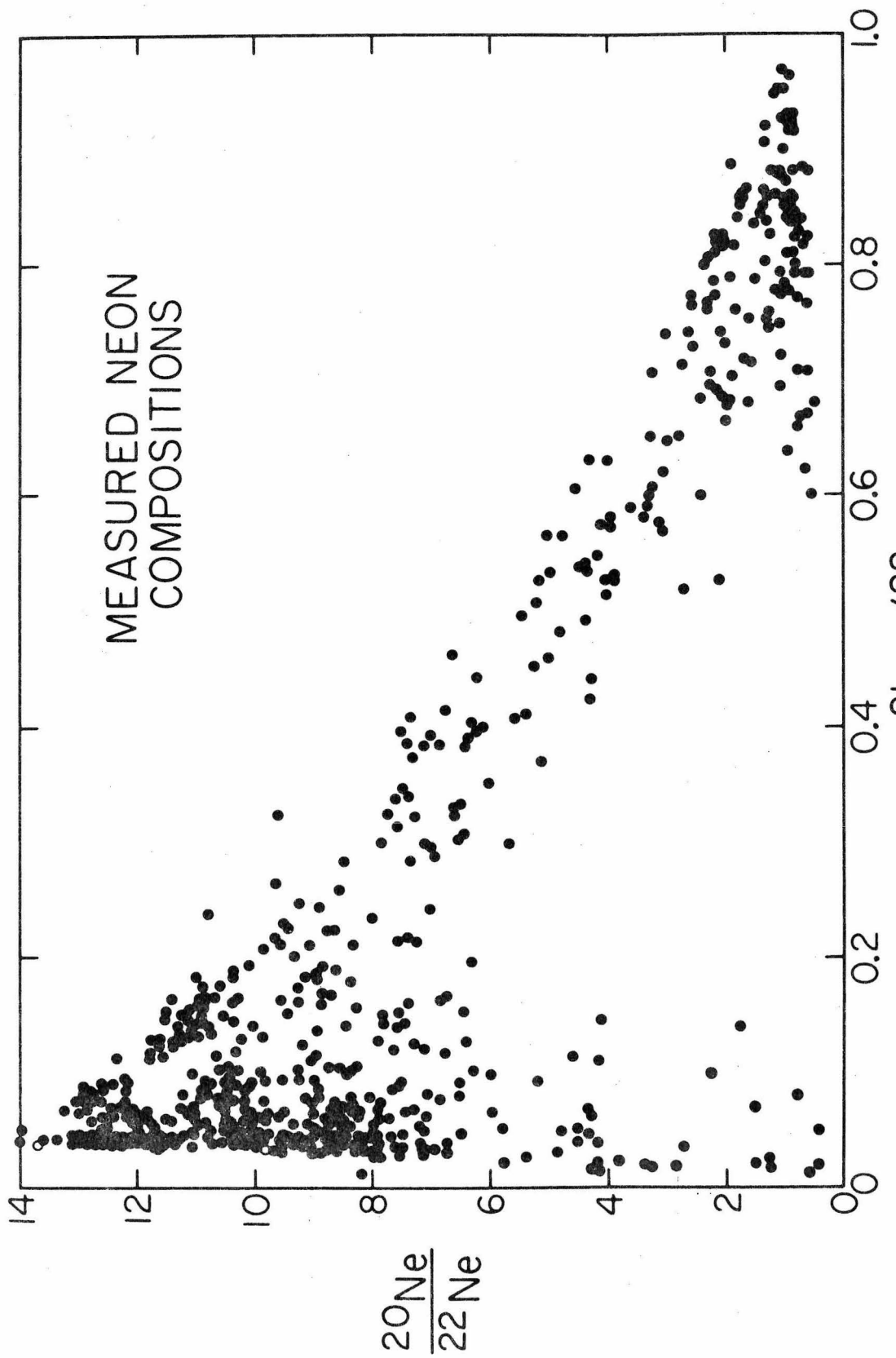
MEASURED NEON
COMPOSITIONS
$\frac{20Ne}{22Ne}$
$^{21}Ne/^{22}Ne$
0
2
4
6
8
10
12
14
0.2
0.4
0.6
0.8
1.0

Figure 3-11

bulk meteorite spallation neon compositions. These points represent spallation neon measured in targets of unusual chemical composition, and in particular, enriched in sodium (Smith et al., 1977). Another newly populated region is the small apex of the triangle extending to the solar wind composition at $^{20}Ne/^{22}Ne = 13.7$. The data imply that $^{20}Ne/^{22}Ne$ of the neon-S component in meteorites and other samples must be greater than or equal to the solar wind value.

At the left side of Fig. 3-11, the data show a well-defined limit. There is a small but finite concentration of ^{21}Ne in all samples, meteorites as well as the solar wind and the Earth's atmosphere. This limit is consistent with a mixing line passing through the solar wind composition at $^{20}Ne/^{22}Ne = 13.7$, $^{21}Ne/^{22}Ne = 0.033$, and the neon-E composition at or near the origin. For future reference we call this line the trapped neon mixing line. The single point lying to the left of this line at about $^{20}Ne/^{22}Ne = 8$ represents a very small neon fraction extracted during stepwise heating of a meteoritic sample (Herzog and Anders, 1975). If this composition could be reproduced in future experiments it would require recognition of a neon component other than the three identified from the bulk of the data.

Striking isotopic variations can occur for neon within a single meteorite. This is illustrated in Figure 3-12 (after Niederer and Eberhardt, 1977). The points on this graph represent successive fractions of neon extracted by stepwise-heating from two acid-resistant graphite-rich residues from the ordinary (H3,4) chondrite Dimmitt. Extraction temperatures run from 500°C or 600°C to 1850°C. The stepwise heating technique has resulted in a nearly complete separation between

Figure 3-12. Isotopic variations in neon from the ordinary chondrite meteorite Dimmitt (after Niederer and Eberhardt, 1977). Stepwise heating of graphite-rich separates from this meteorite reveal spectacular isotopic variations. Observed compositions range systematically from nearly pure solar neon to nearly pure neon-E. The numbers next to certain points represent the beginning and ending temperatures (in °C) of the extraction sequences. Both patterns show evidence of two neon-E-bearing phases. At lower temperatures, the points trend toward the origin. A reversal occurs at intermediate temperatures, with $^{20}Ne/^{22}Ne$ increasing significantly. This is followed at higher temperatures by another reversal toward neon-E. Finally, the compositions trend toward nearly pure solar-like trapped neon.

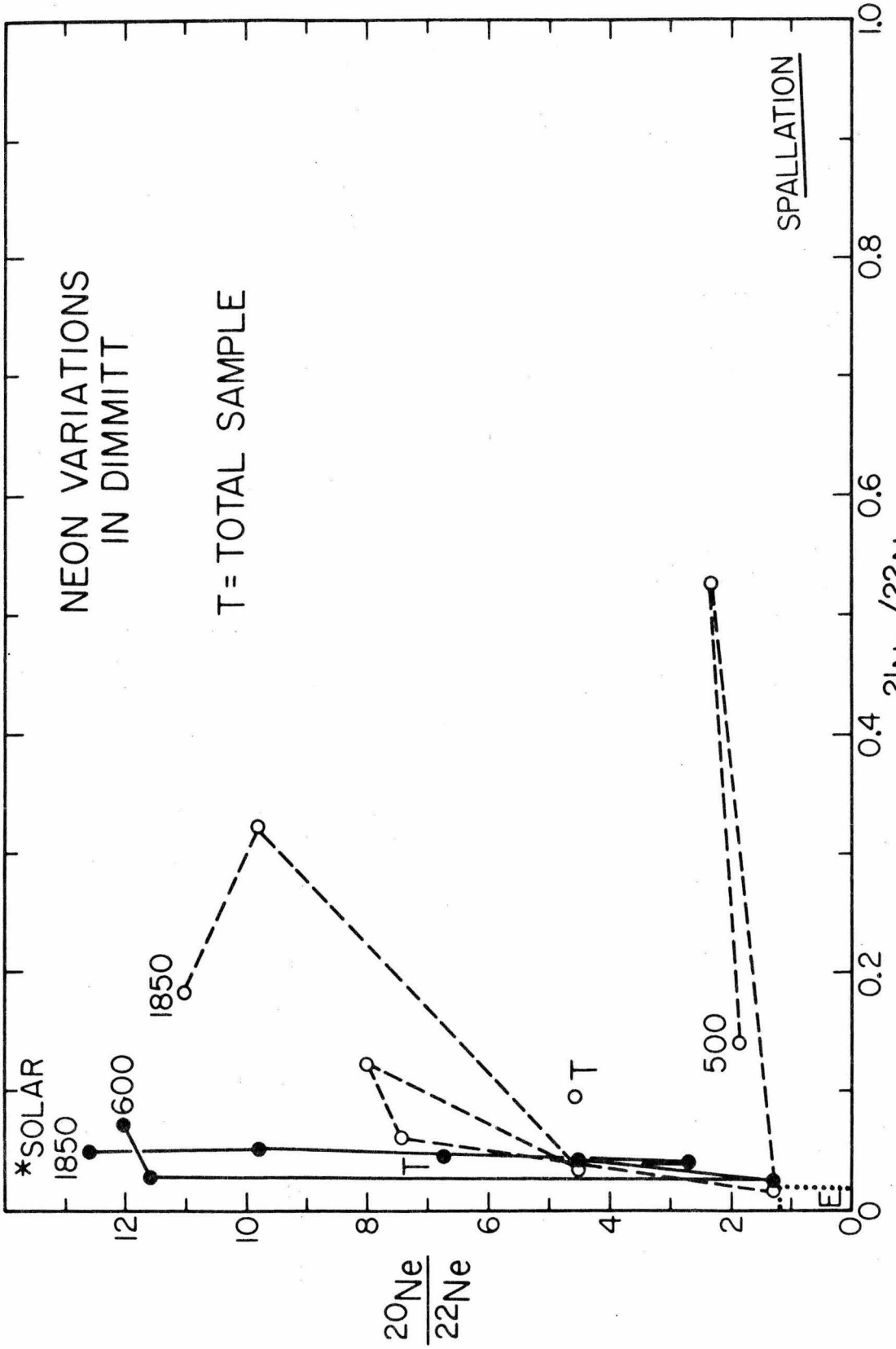
NEON VARIATIONS
IN DIMMITT
T= TOTAL SAMPLE
SPALLATION
*SOLAR
1850
600
1850
500
T
T
E
$\frac{^{20}Ne}{^{22}Ne}$
$^{21}Ne/^{22}Ne$
0
2
4
6
8
10
12
0.2
0.4
0.6
0.8
1.0

Figure 3-12

neon-E and neon-S. For the sample represented by the solid points, neon released initially was close to solar in composition. With increasing temperatures the $^{20}Ne/^{22}Ne$ ratio in the gas extracted dropped by a factor of 10 to about 1.2. With further increasing temperature, the $^{20}Ne/^{22}Ne$ ratio increases for one step to about 4.5, then decreases again to about 2.7 before increasing once again to nearly the solar value at the highest temperatures. A similar complex pattern is seen for the second sample, except that the low-temperature $^{20}Ne/^{22}Ne$ ratios are much smaller, and cosmogenic neon is enriched compared with the first sample. From these data the composition of neon-E is restricted to the outlined region near the origin. More recent experiments have provided even more stringent 1σ limits on the composition of neon-E, $^{20}Ne/^{22}Ne_E \leqslant 0.6$ and $^{21}Ne/^{22}Ne_E \leqslant 0.005$ (Eberhardt et al., 1979).

The complex release patterns in Fig.3-12 suggest the material analyzed is releasing neon from at least three separate phases containing trapped neon of different compositions. Stepwise thermal extraction of neon from bulk meteorite samples yields similar complex release patterns (Black and Pepin, 1969; Black, 1972b; Smith et al., 1978). Lewis et al. (1975) have discovered that a large portion of the meteoritic trapped noble gases--in particular, most of the planetary-type gases--reside in gas-rich trace phases that comprise roughly a percent or less of the mass of the meteorite. The gas-rich phases are initially separated from bulk meteorite samples by dissolving most of the material in concentrated, non-oxidizing acids. The resulting residues from carbonaceous chondrites are characterized by $^{20}Ne/^{22}Ne_t$

between about 8 and 9, with ^{22}Ne contents of about 3×10^{13} atoms/gram. The noble gas elemental abundances show typically planetary patterns with the lighter noble gases preferentially depleted compared to the cosmic abundances. $^{20}Ne/^{36}Ar$ ratios are roughly equal or less than 0.3, compared to the solar value of about 30. Further study of the residues by etching with various reagents, density separation, colloid extraction, stepwise thermal heating, etc., reveals that they consist of several different gas-bearing phases. These phases can tentatively be divided into three loose groups, labeled chromite/carbon, "Q," and E-carrier. In general, these phases do not have the same isotopic and elemental noble gas signatures, so that the characteristic planetary pattern of the total gas-rich separate is a composite pattern. A discussion of the possible origins of the gases in these phases is complicated by the general lack of specific mineral identification, and also by incomplete separation of the different phases in most of the experiments carried out to date.

Chromite/carbon is probably mineralogically complex, comprising one or more forms of carbon, plus chromite (Lewis et al., 1975; Lewis et al., 1979a). It seems to be characterized by a fairly constant $^{20}Ne/^{22}Ne$ ratio of about 8.5 (Lewis et al., 1975; Srinivasan et al., 1977; Frick and Moniot, 1977; Lewis et al., 1979a; Alaerts et al., 1979). In the Allende and Murchison carbonaceous chondrites this material contains roughly 2/3 or more of the neon in the residues. The typical $^{20}Ne/^{22}Ne$ ratio of $\sim$ 8 to 9 in the bulk separates from carbonaceous chondrites is probably controlled largely by chromite/carbon. The $^{20}Ne/^{36}Ar$ ratio of this reservoir in Allende ($\sim$ 5) and

Murchison (~ 0.3-0.7) is somewhat higher than the typical planetary ratio 0.3 and apparently varies from meteorite to meteorite (Srinivasan et al., 1977).

"Q" is operationally defined as a phase that is destroyed when a bulk gas-rich separate is exposed to a strongly oxidizing reagent such as HNO_3 or H_2O_2. In Allende and some unequilibrated ordinary chondrites of petrologic class 3 or 4, Q appears to be characterized by $^{20}Ne/^{22}Ne$ about 10 to 11 (Lewis et al., 1975; Smith et al., 1977; Alaerts et al., 1977; Moniot, 1978). Q in Murchison has neon with a lower $^{20}Ne/^{22}Ne$ ratio of about 6.8, but it is not clear if this might not be due to the addition of a nitric-acid-soluble neon-E phase. Q is a major carrier of the heavy noble gases Ar, Kr, and Xe in the meteorites studied. $^{20}Ne/^{36}Ar$ ratios associated with Q in carbonaceous chondrites and unequilibrated ordinary chondrites are low, about 0.01 to 0.1, and therefore complement the higher ratios seen in chromite/carbon. In ordinary chondrites, Q seems to be the major neon carrier (Alaerts et al., 1977; Moniot, 1978). Chromite/carbon neon in these meteorites is much less abundant than in the carbonaceous chondrites. As a result, bulk gas-rich separates from these chondrites tend to have lower Ne/Ar ratios and higher $^{20}Ne/^{22}Ne$ ratios than the separates from carbonaceous chondrites.

Neon-E-rich phases have been separated from the carbonaceous chondrites Orgueil (Eberhardt, 1974; Eberhardt et al., 1979; Lewis et al., 1979b) and Murchison (Alaerts et al., 1979) and the H3,4 chondrite Dimmitt (Niederer and Eberhardt, 1977). Recent investigation of neon-E-rich material from Orgueil by Eberhardt et al. (1979) using

density separation and stepwise heating provides convincing evidence of the existence of at least two distinct neon-E carriers. Stepwise heating experiments suggest both phases are present also in Murchison and Dimmitt. One, called E(ℓ) has a density < 2.3 g/cm^3, outgasses at relatively low temperatures ($\lesssim$ 700°C), and has tentatively been identified as carbon (Alaerts et al., 1979). The second, E(h), has a density $\sim$ 3.5 g/cm^3, outgasses between 1000-1400°C, and is possibly spinel (Eberhardt et al., 1979). The most stringent 1σ limits on the composition of neon-E are $^{20}Ne/^{22}Ne \lesssim 0.62$ and $^{21}Ne/^{22}Ne \lesssim 0.0047$. The highest neon-E concentration measured is $\sim 1.3 \times 10^{13}$ atoms/g in a mineral separate from Orgueil (Lewis et al., 1979b). Since we have identified neon-E as primordial dust-phase neon, the two carriers discovered by Eberhardt et al. may represent original interstellar grains.

3.4.5 Helium

At this point we digress momentarily to discuss the isotopic composition of helium, which can provide an important tool for understanding the neon isotopic data. It was argued that solar neon is dominated by neon from the interstellar gas. The same arguments apply to helium. However, while the isotopic composition of solar neon should be the same as the original interstellar neon, the $^3He/^4He$ ratio in the sun has been modified by nuclear reactions. Primordial deuterium was converted to ^3He during the early, pre-main-sequence evolution of the sun. The D/H ratio has recently been measured to be $2.3 \pm 1.1 \times 10^{-5}$ in the atmosphere of Jupiter (Combes et al., 1978). Assuming this as the primordial solar-system value and a He/H abundance

ratio of ~ 0.1 (by number), we calculate a $^3He/^4He$ contribution of about 2.3×10^{-4} which must be subtracted from solar helium to obtain an estimate of the interstellar gas-phase helium composition. Geiss (1972) has estimated a solar photospheric $^3He/^4He$ ratio of 3.9×10^{-4}. Correcting for the deuterium contribution leaves a value $1.6 \pm 1.1 \times 10^{-4}$ for an estimated $^3He/^4He$ composition of primordial gas-phase helium. For the simple two-component model of trapped noble gases being considered, we would expect gas-phase neon-S with $^{20}Ne/^{22}Ne = 13.7$ to be associated with helium having $^3He/^4He \simeq 4 \times 10^{-4}$ if derived from post-deuterium-burning solar wind, and with helium having $^3He/^4He \simeq 1.6 \times 10^{-4}$ if derived from a very early solar wind or directly from the interstellar gas.

3.5 EXPERIMENTAL RESULTS ON THE ISOTOPIC COMPOSITION OF NEON IN METEORITES

Neon was measured in six meteorites for this thesis. A combination of mineral separation and stepwise heating techniques was used. Individual experiments were designed to examine aspects of the isotopic compositions of the three neon end-members, cosmogenic neon, neon-S, and neon-E.

Cosmogenic neon in sodium-rich minerals was investigated using stepwise heating to extract neon from plagioclase mineral separates and whole-rock samples from two ordinary chondrites, Guareña and St. Severin (Paper 1, Appendix A). A new, high-resolution stepwise-heating technique was employed to examine the trapped neon-S and E end-members in bulk samples of three carbonaceous chondrites, Mokoia, Cold Bokkeveld, and Murchison (Paper 2, Appendix A). Neon was extracted using 30 to 50

temperature steps for each sample, in contrast to the conventional 5 to 10. Complex variations in the isotopic composition of neon emitted from the samples were followed in great detail. Trapped and cosmogenic neon were studied in a variety of inclusions and matrix samples from the Allende carbonaceous chondrite (Paper 3, Appendix A). Inclusions examined included pyroxene and olivine chondrules, and coarse-grained and fine-grained Ca, Al-rich inclusions. Neon was extracted using both single-step and multiple-step heating cycles.

3.5.1 Compositional variation of the cosmogenic neon end-member

An important source of isotopic variation in spallation neon is differences in the chemical composition of the target materials bombarded by cosmic rays. These variations are large enough in some cases so that they must be taken into account when trapped neon compositions are deduced by subtraction of a cosmogenic component from a measured neon composition.

The compositionsof spallation neon produced the target elements Mg, Si, Al, S, and Fe have been studied previously in some detail (cf. Bieri and Rutsch, 1962; Stauffer, 1962; Bochsler et al., 1969; Signer and Nier, 1962). For this thesis a measurement was made of the production rate and isotopic composition of spallation neon in sodium. Spallation neon was measured in high-purity mineral separates of Na-rich meteoritic plagioclase (oligoclase). Plagioclase was obtained from two ordinary chondrites, Guareña and St. Severin, which are free of trapped neon. The details of this experiment are reported by Smith and Huneke (1975), Paper 1 in Appendix A. It was found by comparing the compositions of spallation neon in the feldspar separates and in the bulk samples

that galactic cosmic ray irradiation of sodium under meteoritic conditions yields spallation neon with $^{21}Ne/^{22}Ne = 0.34 \pm 0.04$. It was also determined that the spallation ^{21}Ne production rate per gram of sodium is about one quarter the production rate for magnesium. Spallation $^{21}Ne/^{22}Ne$ ratios produced in magnesium, aluminum, silicon, sulfur, calcium, and iron range from about 0.8 to 1.

The variation of $^{21}Ne/^{22}Ne$ in spallation neon produced because of chemical variations in the compositions of meteoritic silicate minerals is represented in Fig. 3-13. This figure is a ternary diagram of weight percent sodium, aluminum, and magnesium abundance in the target silicate. The sum Mg + Na + Al is taken as 100%. The silicon abundance is fairly uniform in common silicates, and has been assumed constant at Si/(Si+Mg+Na+Al) = 0.4. Variation in $^{21}Ne/^{22}Ne$ due to differences in this value are not large, since the production cross section for neon from silicon is relatively low. The graph is contoured with isopleths representing the spallation $^{21}Ne/^{22}Ne$ ratios calculated from the relative elemental abundances and literature values of the relative production cross sections. In bulk samples of stony meteorites, magnesium in olivine and pyroxene is the dominant target element, leading to typical spallation neon compositions with $^{21}Ne/^{22}Ne$ about 0.9. The important role of sodium in determining the spallation neon composition for the minerals sodalite, nepheline, albite, and oligoclase is clear from Fig. 3-13. Calculated $^{21}Ne/^{22}Ne$ ratios for these phases range from about 0.55 to 0.65, much below typical bulk meteorite values. The calculated spallation neon compositions for the various minerals are represented on a three-isotope diagram in Fig. 3-14.

Figure 3-13. Ternary diagram of relative Al, Na, and Mg contents showing the composition of galactic cosmic ray spallation neon produced in various meteoritic minerals. The sum Al+Na+Mg = 100%. Silicon contents of the minerals are approximated by Si/(Si+Al+Na+Mg) = 0.4. The contours shown are isopleths of the calculated spallation $^{21}Ne/^{22}Ne$ ratios for variable target composition. Values range from $^{21}Ne/^{22}Ne \sim 0.35$ in pure Na to about 0.92 in pure Mg. The sodium-rich minerals sodalite, albite, nepheline, and oligoclase have calculated $^{21}Ne/^{22}Ne_c$ ratios of 0.55 to 0.65, much lower than the common meteoritic Mg-rich minerals olivine and enstatite. Fassaite, melilite, and anorthite are Ca, Al-rich minerals typical of the light-colored inclusions found in the Allende meteorite.

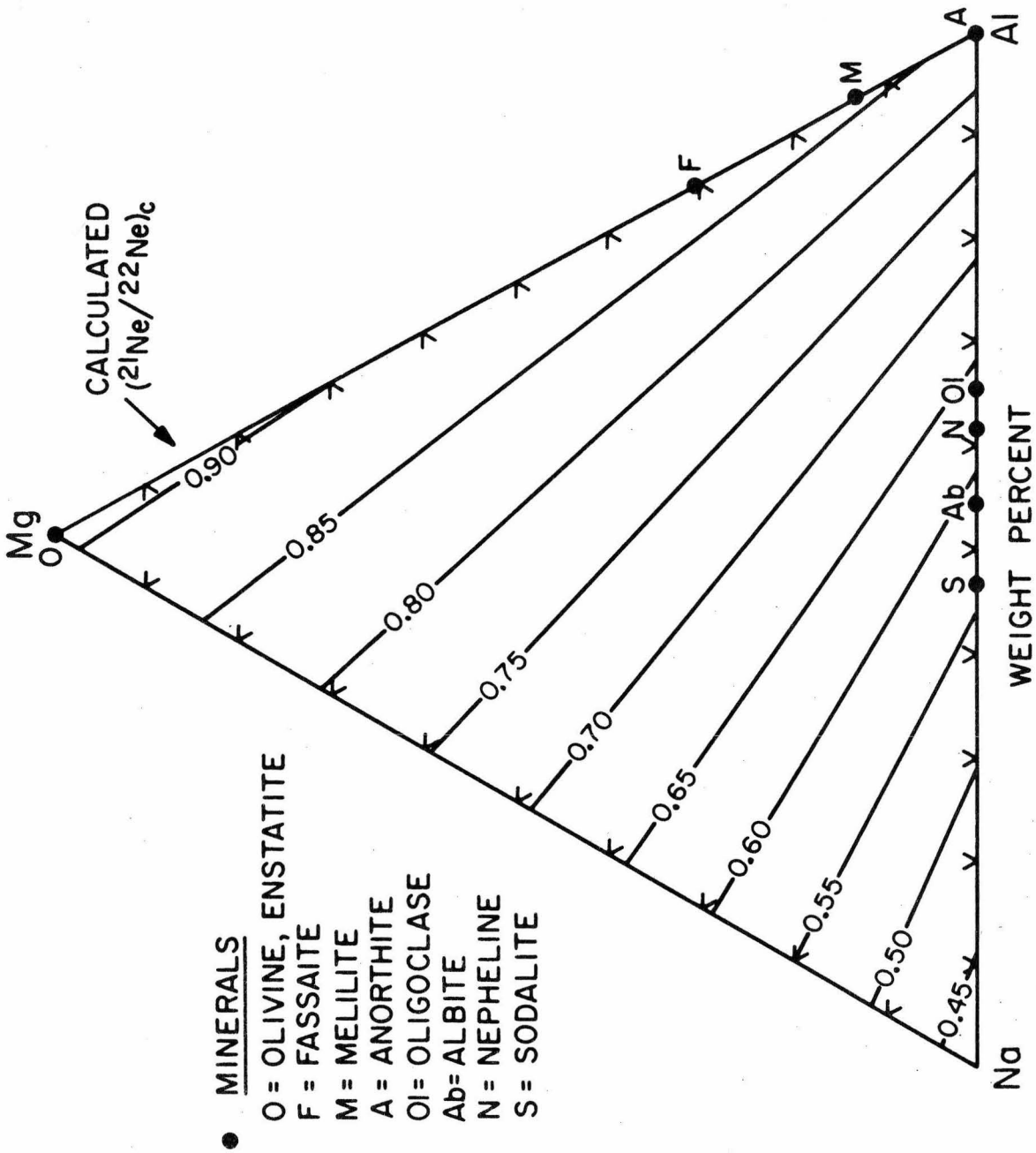
Mg
O
CALCULATED
$(^{21}Ne/^{22}Ne)_c$
0.90
0.85
0.80
0.75
0.70
0.65
0.60
0.55
0.50
0.45
F
M
A
Al
Na
O
N
Ol
Ab
S
WEIGHT PERCENT
MINERALS
O = OLIVINE, ENSTATITE
F = FASSAITE
M = MELILITE
A = ANORTHITE
Ol = OLIGOCLASE
Ab = ALBITE
N = NEPHELINE
S = SODALITE

Figure 3-13

Figure 3-14. Neon three-isotope diagram showing the composition of galactic cosmic ray spallation neon produced in different minerals. The approximate field occupied by bulk meteorite data is outlined. The spallation neon compositions in pure sodium and in sodium-rich minerals are much richer in ^{22}Ne than those from the other Ca, Al-rich and Mg-rich minerals. Addition of Na-spallation neon to meteorites containing relatively little trapped neon results in isotopic shifts that are difficult to distinguish from those arising from the addition of neon-E.

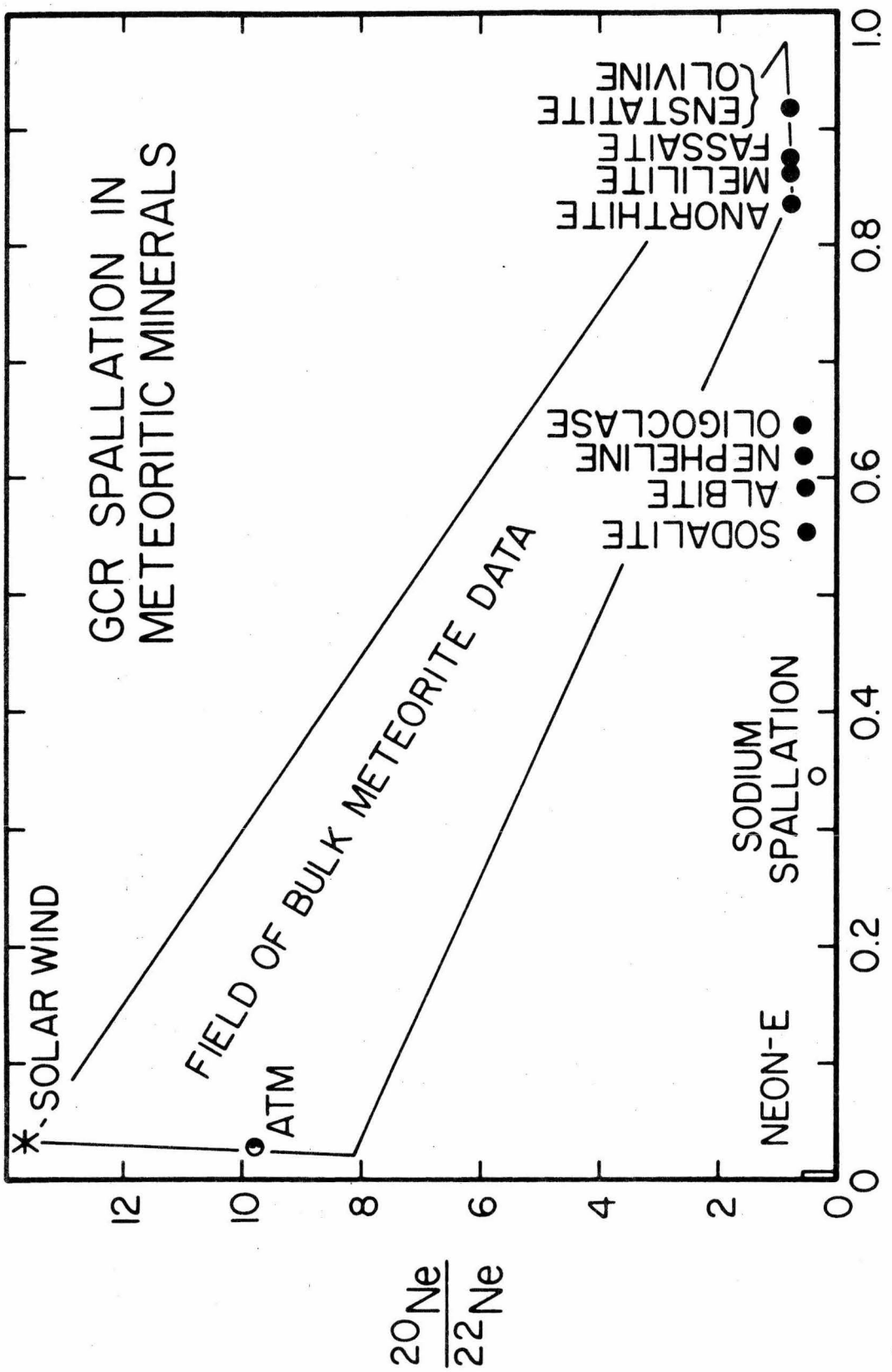
GCR SPALLATION IN METEORITIC MINERALS
SOLAR WIND
ATM
FIELD OF BULK METEORITE DATA
NEON-E
SODIUM SPALLATION
SODALITE
ALBITE
NEPHELINE
OLIGOCLASE
ANORTHITE
MELILITE
FASSAITE
ENSTATITE
OLIVINE
$^{20}Ne/^{22}Ne$
$^{21}Ne/^{22}Ne$
0
2
4
6
8
10
12
0.2
0.4
0.6
0.8
1.0

Figure 3-14

Here the $^{20}Ne/^{21}Ne$ ratio in spallation neon has been taken to be about 0.9 for all elements, a value consistent with all experimental data available to date. The composition of sodium spallation neon is also shown. It is evident that spallation neon compositions can cover quite a wide range. It is also apparent that the effects of increased Na and Na-spallation neon in some samples can mimic the addition of neon-E. Therefore, the interpretation of unusual neon isotopic compositions in material of unusual chemistry as due to addition of anomalous neon components such as neon-E must be made with caution, and with a complete understanding of the possible effects of chemistry on the spallation neon composition in the sample.

3.5.2 The neon-S end-member

From the bulk meteorite data it could be concluded that the $^{20}Ne/^{22}Ne$ ratio of the isotopically-light component of meteoritic trapped neon, neon-S, must be greater than 13. Evidence was sought whether the neon-S end-member in meteorites could be identified with the solar-wind/gas-phase neon composition, $^{20}Ne/^{22}Ne = 13.7$. For this purpose, a sample of the gas-rich carbonaceous chondrite Mokoia was investigated using the high-resolution stepwise release technique. Bulk samples of Mokoia were known to yield trapped $^{20}Ne/^{22}Ne$ ratios as high as 13.1, the highest value found in bulk meteorite samples. The results of this experiment are described in detail by Smith et al. (1978), Paper 2 in Appendix A. The major finding was that at temperatures less than about 1100°C, 35 temperature fractions out of a total of 45 plot within 2σ experimental uncertainty on a single correlation line. The extrapolation of this trend intersects the trapped neon mixing line at $^{20}Ne/^{22}Ne = 13.7$,

precisely the composition of the present solar wind. The 35 points defining the correlation line comprise about 70% of the neon in the sample. This data from Mokoia strongly support a model where the isotopically light neon-S end-member is assigned a composition $^{20}Ne/^{22}Ne = 13.7$, $^{21}Ne/^{22}Ne = 0.03$, the same as the measured solar wind composition. This is the first meteorite for which such agreement has been demonstrated.

Previous measurements (Mazor et al., 1970) showed that the $^{3}He/^{4}He$ and $^{20}Ne/^{36}Ar$ ratios in Mokoia are also close to the solar wind values. Together with the neon data, these results suggest that the source of the neon-S in Mokoia is implanted solar wind ions. If we accept solar wind as the source of neon-S, then the Mokoia results imply that the $^{20}Ne/^{22}Ne$ ratio of the solar wind has not changed substantially since the time of compaction of this primitive carbonaceous chondrite.

3.5.3 The neon-E end-member

Two experiments were done to investigate the nature of the neon-E component in meteorites. In the first, neon was extracted from bulk samples of two carbonaceous chondrites, Cold Bokkeveld and Murchison, using the high-resolution stepwise release technique. Black and Pepin (1969) and Black (1972b) had shown that during conventional stepwise release experiments on carbonaceous chondrites, the two or three neon fractions in the 900°C to 1100°C interval were typically greatly enriched in neon-E. The detailed high-resolution experiments were undertaken to confirm this release pattern, and to attempt to set more stringent limits on the composition of neon-E. The results of this

experiment are given at length in Paper 2 in Appendix A. Neon-E was identified in Murchison. In eight temperature fractions from about 850°C to 1050°C, the trapped $^{20}Ne/^{22}Ne$ ratio dropped from about 10 to 6.9 and then returned to about 10. The minimum ratio is well below the lowest values observed in bulk meteorite samples, implying the presence of neon-E. Over the same temperature interval, a trapped $^{20}Ne/^{22}Ne$ decrease was observed for Cold Bokkeveld as well, from 10.7 to 9.7 and then back to 10.7. The higher values overall in Cold Bokkeveld are due to an unexpectedly high concentration of neon-S in the particular sample analyzed. The pattern of the neon isotopic variations in Cold Bokkeveld suggests that the decrease noted was also due to the release of neon-E, although the ratios observed are not lower than bulk meteorite values, which would be conclusive. Because of the relatively high neon-S concentrations in both meteorites, new limits on the isotopic composition of neon-E were not obtained.

In the second experiment, neon and argon were measured in a variety of inclusions and in bulk samples from the Allende carbonaceous chondrite. Allende in particular was chosen for detailed study, since anomalous isotopic variations in oxygen (Clayton et al., 1973) and magnesium (Lee and Papanastassiou, 1974; Gray and Compston, 1974) had been recently found in Ca, Al-rich inclusions within this meteorite. Allende thus presented an opportunity to investigate the possible relationship between the highly unusual neon-E component found in other carbonaceous chondrites with the newly-discovered oxygen and magnesium anomalies. The findings from this study are discussed fully by Smith et al. (1977), Paper 3 in Appendix A. In summary, large enrichments of ^{22}Ne and ^{36}Ar were found in noble gases extracted at low temperatures

($\leqslant$ 700°C) from several of the inclusions. The most pronounced effects were found in fine-grained inclusions rich in Na and Cl contained in the minerals sodalite and nepheline. As discussed in an earlier section, cosmogenic neon produced in Na-rich material would be expected to be greatly enriched in ^{22}Ne compared to bulk meteorite values. Agreement is good between the observed neon concentrations and compositions, and the expected spallation neon component calculated taking into account the unusual target chemistry of the inclusions studied. The ^{36}Ar enrichments can also be understood as due to capture on ^{35}Cl of secondary neutrons generated by the cosmic-ray bombardment of the meteorite. It was concluded that the low-temperature ^{22}Ne and ^{36}Ar enrichments observed in the Ca, Al-rich inclusions should be attributed to cosmic-ray-induced nuclear reactions during the recent exposure history of the meteorite, and not to the presence of exotic trapped gas such as neon-E. It was not possible to identify neon-E in Allende, neither in inclusions with known oxygen and magnesium anomalies nor from stepwise-release experiments on bulk samples. Therefore no correlation between neon-E and the isotopic anomalies in the other elements could be established.

3.6 COMPARISON OF OBSERVED NEON DATA WITH THE CHARACTERISTICS OF SIMPLE MIXING MODELS

3.6.1 Neon in meteorites

In Figure 3-15 we plot neon concentration and composition data for trapped neon in samples from carbonaceous chondrites. The solid dots represent measurements on bulk samples of C1 and C2 meteorites.

Figure 3-15. Neon composition vs. concentration diagram for trapped (t) neon in C1 and C2 carbonaceous chondrites and bulk gas-rich separates from carbonaceous chondrites. Solid dots represent whole-rock meteorite samples; the uncertainty in $^{20}Ne/^{22}Ne_t$ is roughly ±10%. The crosses are bulk gas-rich separates that have not been treated to remove or isolate individual phases. Because of the high neon-contents of the separates, $^{20}Ne/^{22}Ne_t$ ratios for these samples are accurate to within 1 or 2%. The whole-rock data do not lie on a single straight mixing line, so are not compatible with the simplest gas-dust mixing model. Data used to construct this figure were drawn from the references indicated by an asterisk in the list at the end of this chapter.

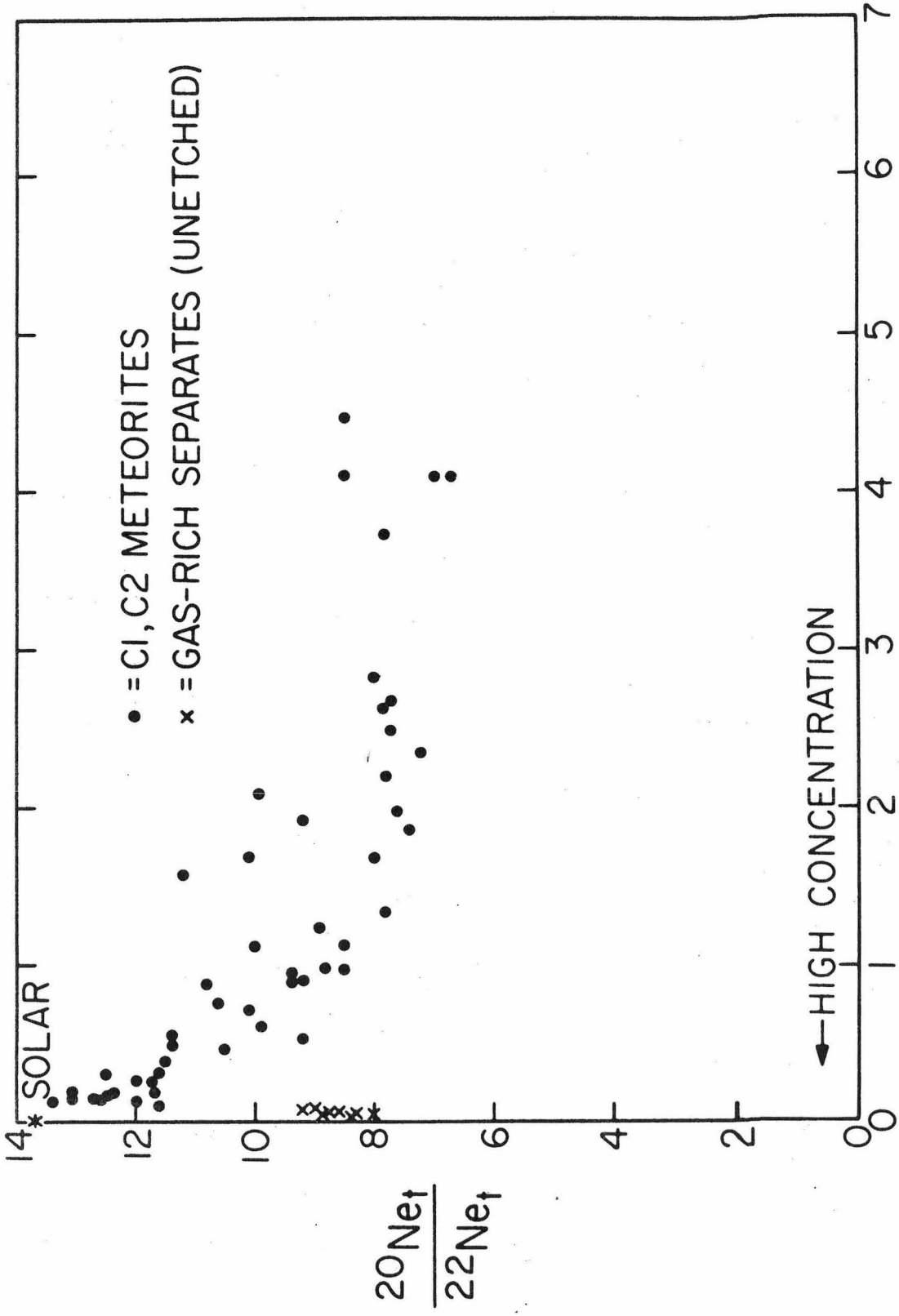
SOLAR
• = CI, C2 METEORITES
× = GAS-RICH SEPARATES (UNETCHED)
HIGH CONCENTRATION
$^{20}Ne_t / ^{22}Ne_t$
$1/^{22}Ne_t$ (unit = 10^{-12} g/atom)
0
2
4
6
8
10
12
14
1
3
5
7

Figure 3-15

Spallation neon contributions have been subtracted from the data using projection onto the trapped neon mixing-line as described earlier. Shown as crosses are neon compositions for bulk gas-rich separates from carbonaceous chondrites. These have not been etched in oxidizing reagents to remove Q.

The gas-rich separates occupy a quite restricted range in Fig. 3-15. The bulk meteorite points define a general concave-upward trend which emanates from the solar point. For samples with $1/^{22}Ne_t$ less than about 1.5×10^{-12}, the data show increasing $^{20}Ne/^{22}Ne_t$ with decreasing $1/^{22}Ne_t$, from about 8 to nearly the solar composition. For higher values of $1/^{22}Ne_t$, the $^{20}Ne/^{22}Ne_t$ ratio is roughly constant at about 8, with a few exceptions tending toward higher ratios. This constant value of ~ 8 corresponds to the neon-A composition defined from the meteorite data plotted on the three-isotope diagram.

Can we explain the distribution of points in Fig. 3-15 in terms of the models described earlier for mixing gas-phase neon (S) with dust-phase neon (E)? For simple random mixtures we would expect to see samples with $^{20}Ne/^{22}Ne$ ranging all the way from ~ 13.7 to ~ 0. Instead, we never find meteorites containing only neon-E as the trapped neon component. In no case can more than about half the ^{22}Ne in any given sample be attributed to neon-E. Most of the bulk meteorite data fall to the right of a line joining the solar composition to the point ($^{20}Ne/^{22}Ne = 0$, $1/^{22}Ne_t \sim 2 \times 10^{-12}$) in Fig. 3-15. For simple mixing or implantation this sets an approximate upper limit of about 5×10^{11} atoms ^{22}Ne/gram for the average initial neon-E content of the dust.

Certain simple models are incompatible with the bulk meteorite

data. The simplest model of a homogeneous initial dust reservoir into which a uniform amount of neon-S was implanted can be ruled out, since it would result in all samples falling near a single point in Fig. 3-15. Also generally unsatisfactory are models in which varying amounts of neon-S were implanted in dust with a uniform initial neon-E concentration. Mixing curves calculated for implantation, both general and solar-wind irradiation, typically are straight, or nearly so. The concave-upward trend for bulk sample data in Fig. 3-15 is unlike the curves generated by these simple models.

An important clue to the interpretation of the bulk meteorite trend is provided by helium isotope data. Anders et al. (1970) have shown that as $^{20}Ne/^{22}Ne_t$ increases from 8 to 13 in carbonaceous meteorite samples, $^{3}He/^{4}He$ increases from about 1.3×10^{-4} to about 4.5×10^{-4}. As discussed previously, the high $^{3}He/^{4}He$ ratios are good evidence that the addition of neon-S giving the high $^{20}Ne/^{22}Ne$ ratios was due to solar wind irradiation of the samples. This is supported by the elemental abundances of the noble gases. In meteorites of high $^{20}Ne/^{22}Ne_t$ ratio, abundances typically are much closer to solar (cosmic) values than those in samples of lower $^{20}Ne/^{22}Ne_t$, in which abundances are typically planetary. Thus in Fig. 3-15, the trend toward higher $^{20}Ne/^{22}Ne$ ratios is explained by the addition of solar wind neon-S to preexisting material.

Solar wind implantation in dust should generate nearly straight mixing lines. Random implantation and sampling of parcels of dust should provide points all along the mixing line. The rather uniform run of points above $^{20}Ne/^{22}Ne_t \sim 8$ strongly suggests that the dust into

which the solar wind was implanted was characterized by $^{20}Ne/^{22}Ne_t$ of 8, and not ~ 0 as would be expected for dust containing pure neon-E. This requires at least two distinct episodes of mixing. One produced a rather uniform neon-A composition in the dust. Another added variable amounts of solar wind neon to different parcels of the dust.

This general picture can be clarified by considering the gas-rich separates extracted from meteorites. The separates are the primary reservoir of planetary noble gases and neon-A in meteorites. The mixing episode that resulted in a uniform distribution of neon-A in the dust can therefore be identified as a process or series of processes that generated the planetary noble gas contents of the bulk gas-rich separates. In meteorites, this gas-rich material has been diluted by a factor of about fifty or more by initially gas-free silicate minerals. The dilution factor corresponds to the gap in Fig. 3-15 between the crosses representing the gas-rich separates, and the bulk-meteorite points with the same $^{20}Ne/^{22}Ne_t$ ratio of 8 to 9. The minimum degree of dilution is probably controlled by the maximum chemical abundance of the gas-rich host phases--particularly carbon--normally available to be incorporated into meteoritic material. The factor of roughly fifty is consistent with the abundance of carbon in C1 and C2 meteorites, typically 2-3 wt % (Vdovykin and Moore, 1971).

In Figure 3-16 we sketch a possible model for the whole-rock carbonaceous chondrite neon abundances. Gas-rich carbonaceous material is diluted yielding a reservoir of material with $^{20}Ne/^{22}Ne_t \sim 8$ to 9 labeled "primitive" meteorite material in Fig. 3-16. Following the dilution, parcels of the primitive material are irradiated to varying

Figure 3-16. A model for neon in bulk carbonaceous chondrite samples. All planetary neon (neon-A) is held in the gas-rich phases. In bulk samples the gas-rich phases are diluted by a factor of about fifty or more by silicate minerals containing no neon-E. The minimum degree of dilution is determined by the maximum chemical abundance of the host phases of the gases. Carbon in particular appears to be the controlling element, with an abundance of 2-3 wt.% in C1 and C2 meteorites. The mixture of carbonaceous gas-rich material and inert silicate is labeled "primitive" meteorite material. Variable amounts of solar wind are implanted in different parcels of the "primitive" meteorite material, resulting in compositions plotting on the large open arrow pointing to the upper left. Larger degrees of dilution and/or gas-loss are responsible for points lying to the right of the "primitive" reservoir. Solar-wind implantation will move these points along the solid arrows toward the solar endpoint.

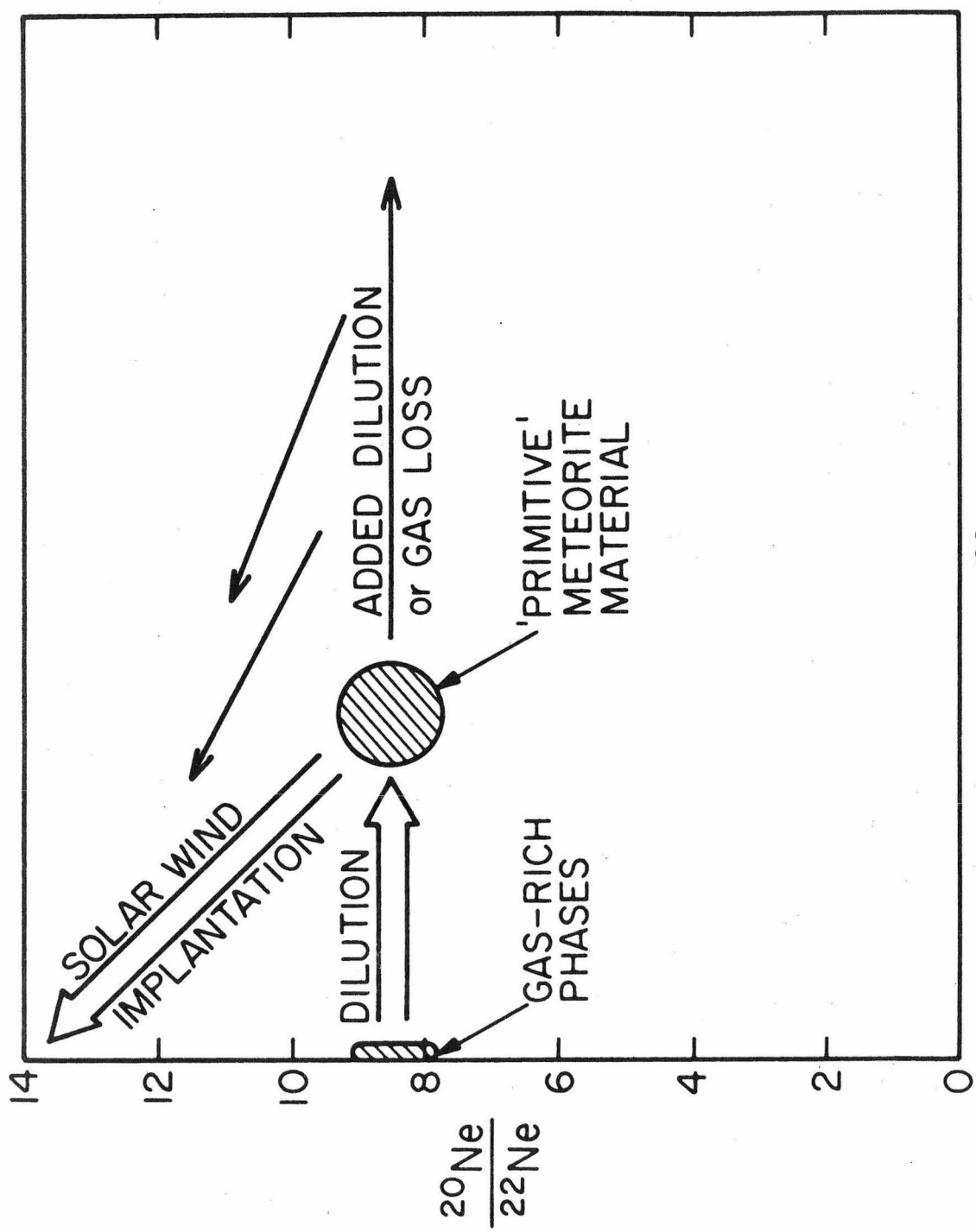
ADDED DILUTION
or GAS LOSS
'PRIMITIVE'
METEORITE
MATERIAL
SOLAR WIND
IMPLANTATION
DILUTION
GAS-RICH
PHASES
14
12
10
8
6
4
2
0
$^{20}Ne/^{22}Ne$
$1/^{22}Ne$

Figure 3-16

degrees by the solar wind. Some parcels may experience additional dilution or possibly gas-loss before or after irradiation, resulting in points falling to the right of the primitive material.

The sequence of events suggested in Fig. 3-16 is not the only one that can lead to the observed bulk meteorite trend. For example, solar-wind implantation need not follow dilution of the gas-rich phases. Portions of a parent-body regolith could be irradiated first to varying degrees by the solar wind. Subsequently, gas-rich phases are added to the regolith. The addition of neon-A-rich material must be widespread on a scale larger than the inhomogeneity of the solar-wind irradiation. This requirement is to ensure formation of mixtures with all possible proportions of neon from the two reservoirs.

Bulk meteorite samples can be understood simply as mechanical mixtures of gas-rich phases and inert diluting material which have been irradiated by the solar wind. The origins of the neon mixtures in the gas-rich phases are less clear. At least four chemically or physically distinct noble-gas carriers have been extracted from bulk gas-rich separates. The carriers are E(h), E(ℓ), chromite/carbon, and Q. All contain trapped neon with $^{20}Ne/^{22}Ne$ substantially lower than the solar/gas-phase value. All must therefore contain dust-phase neon which we have identified as neon-E. In the simplest case, this implies that there were four or more diverse phases in the primordial dust, all of which initially contained some neon-E. Subsequent implantation of neon-S raised initial $^{20}Ne/^{22}Ne_t$ ratios of some of the phases from about zero to various intermediate values depending on the degree of irradiation. This model is outlined in Figure 3-17. Since

Figure 3-17. A model for neon in the various gas-rich phases in meteorites. A variety of physically and chemically distinct neon carriers E_1, E_2, etc., exist in the interstellar dust; initially all contain neon-E with $^{20}Ne/^{22}Ne \sim 0$. Gas-phase neon-S is added to some of the phases giving rise to higher $^{20}Ne/^{22}Ne$ ratios as observed in some of the phases. One initial carrier such as E_2 might serve as a precursor for two or more gas-rich phases, e.g., E(ℓ) and C, if neon-S is added to only part of the E_2 reservoir.

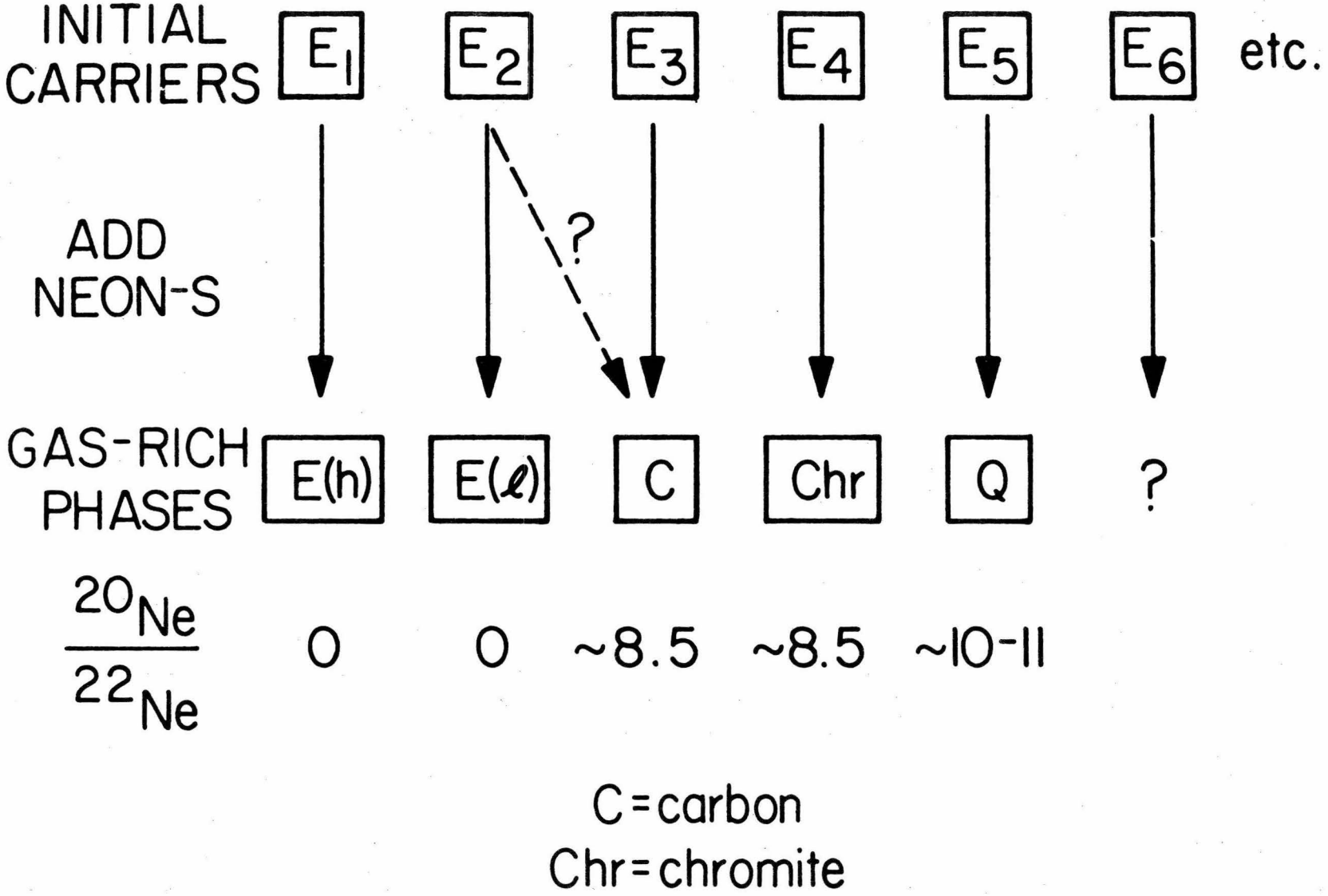
INITIAL CARRIERS
E1
E2
E3
E4
E5
E6
etc.
ADD NEON-S
?
GAS-RICH PHASES
E(h)
E(ℓ)
C
Chr
Q
?
20Ne/22Ne
0
0
~8.5
~8.5
~10-11
C=carbon
Chr=chromite

Figure 3-17

two distinct carriers, E(h) and E(ℓ), containing essentially pure neon-E are known to exist, there is no a priori reason not to believe that several more could have initially been present. The requirement of one E-bearing phase per presently-observed gas-rich phase could be relaxed if neon-S were implanted in only a part of any given reservoir of carrier grains. For example, E_2 in Fig. 3-17 could give rise to both E(ℓ) and C, with E(ℓ) representing original carrier grains that escaped implantation, and C the grains containing both neon-E and neon-S. For this particular example, a genetic relationship may in fact exist. Alaerts et al. (1979) have tentatively identified E(ℓ) as carbon, so E(ℓ) and the carbon in chromite/carbon might share a common ancestral neon-E carrier. More information on the mineralogy and on the isotopic composition of neon associated with each gas-rich phase is needed to investigate this simple model further.

A potential problem with the simple mixing model is the observation that two separate phases, carbon and chromite, seem to contain neon with the same composition (Lewis et al., 1975; Lewis et al., 1979a). This would tend to imply that the neon was obtained from an external reservoir of the intermediate neon-A composition. It is not clear where such a reservoir could exist in a solar system dominated by neon-S in the gas and neon-E in the dust. It is perhaps possible that the neon in chromite is actually trapped in carbon inclusions, in which case carbon might be the only phase containing neon with $^{20}Ne/^{22}Ne \simeq 8.5$.

The high abundances of the heavy noble gases in both chromite/carbon and Q are incompatible with simple solar-wind implantation as

their source (Lewis et al., 1975). The planetary noble gas abundance patterns associated with these phases are most likely the result of adsorption or differential solubility. The $^{3}He/^{4}He$ ratio of $\sim 1.2 \times 10^{-4}$ in these planetary gases in chromite/carbon (Frick and Moniot, 1977; Mazor et al., 1970) is consistent also with gas sorbed from the main interstellar gas reservoir. This evidence suggests that the gas-phase neon-S in these minerals was implanted by similar processes, and not by the solar wind.

3.6.2 Xenon data

Xenon, with nine stable isotopes, should allow unambiguous recognition of many more components than neon. Thus xenon data can provide additional information on the number of primordial noble gas components in the solar system. Pepin and Phinney (1979) have presented a detailed analysis of the isotopic variations in xenon from bulk meteorite samples, meteoritic mineral separates, and lunar soils. These authors define five components, U', DME(L), DME(H), Sp, and Pu, which can be used to describe most of the data. Of the five components described by Pepin and Phinney, U' is the most abundant, and corresponds to a primitive form of ordinary trapped meteoritic xenon (AVCC). DME(L) comprises the light proton-rich isotopes of xenon (124, 126, 128, 129?, 131), while DME(H) comprises the heavy neutron-rich isotopes (129?, 131, 132, 134, 136). The remaining two components, Sp and Pu, correspond to galactic cosmic ray spallation xenon and ^{244}Pu fission xenon. Radiogenic ^{129}Xe is also a common constituent of meteoritic xenon. In addition, an extraordinary xenon component has been discovered in gas-rich separates from Murchison (Srinivasan and Anders, 1978) and

Orgueil (Lewis et al., 1979b). This component, provisionally labeled EX (Smith, 1979; Paper 4 in Appendix A), is apparently strongly enriched in s-process xenon isotopes compared to ordinary trapped xenon (Srinivasan and Anders, 1978; Smith, 1979). The heavy isotopes comprising DME(H) xenon have been suggested to be the products of a fissioning superheavy nucleus (Lewis et al., 1975 and references therein) or to be a primordial nucleosynthetic component (Manuel et al., 1972). DME(L) is probably a primordial nucleosynthetic component (Pepin and Phinney, 1979). Thus solar system xenon appears to contain at least three independent primordial components, U', EX, and DME(L), and possibly four, including DME(H). One of these probably represents xenon from the gas-phase, and the rest are from dust grains.

Arguing from the xenon results, it is conceivable that at least three and perhaps four primordial neon components should exist as well. It is possible to make some tentative associations between the xenon and neon components. Anders and coworkers (Srinivasan and Anders, 1978; Lewis et al., 1979b; Alaerts et al., 1979) have shown that dust-phase neon-E and the s-process-enriched xenon-EX occur together in meteorite mineral separates. U' xenon appears to be a principal constituent of solar wind xenon (Pepin and Phinney, 1979). Therefore, we tentatively identify U' xenon with the neon-S from the interstellar gas. So-called CCFX xenon, consisting largely of a mixture of DME(L) and DME(H) xenon, is enriched in the chromite/carbon separates where it is associated with neon having $^{20}Ne/^{22}Ne \sim 8.5$. This might suggest that the neon-A in chromite/carbon is a primary component associated with one of the

two xenon components. Since the CCFX xenon is however a mixture, it is not unlikely that the neon in chromite/carbon is also. Future detailed study of neon-xenon correlations and of the interrelationships of the xenon components should provide much information about the origins and evolution of various noble gas components in the solar system.

3.6.3 The question of the isotopic composition of solar (and nebular) neon

The agreement between the isotopic composition of solar flare neon (Simpson, priv. comm.) and neon-A in chromite/carbon separates from carbonaceous meteorites suggests an alternative model of solar system neon. It is conceivable that neon in the interstellar gas was neon-A, not neon-S as has been assumed up to this point. This would alleviate the problem of two phases, carbon and chromite, containing the same neon composition, since in this model they both have just sampled the ambient nebular gas. Neon in the original dust grains is still represented by neon-E occurring in two or more different carriers. Now, however, the neon-S composition must be a special attribute of the solar wind acceleration mechanism.

Observed $^{20}Ne/^{22}Ne$ ratios greater than about 8.5 (neon-A) in this model signal the presence of implanted solar wind neon. This is the case for Q, with an observed $^{20}Ne/^{22}Ne$ ratio of 10-11. Because of the very low $^{20}Ne/^{36}Ar$ ratio associated with this phase (< 0.1), the neon composition is very sensitive to addition of small amounts of solar wind neon. Therefore, it is possible that Q derives from material initially like chromite/carbon with $^{20}Ne/^{22}Ne_t \sim 8.5$ to which a

comparatively small amount of solar wind ($\leq$ 50% of the total neon) was added.

3.6.4 Noble gases in the planets

The two-component neon mixing model embodies specific predictions for the isotopic compositions of neon associated with the planets. Cameron and coworkers (e.g., Cameron and Pollack, 1976; Cameron, 1975) have suggested that the formation of the gas-giant planets Jupiter, Saturn, Uranus, and Neptune occurs by accretion of an atmosphere of volatiles, mainly H and the noble gases, to a core of ices and rocky material, i.e., dust. Within the two reservoirs, atmosphere and core, the elements occur in roughly their solar proprotions, but the mass ratio of the two reservoirs can be different among the various planets. This model for gaseous protoplanet formation is the same as the simplest two-component dust/gas mixing model considered earlier. On the neon composition-inverse concentration diagram, such a series of objects accreted with varying proportions of dust and gas will plot along a straight line between the solar point and the point representing the primordial neon in dust, here taken as neon-E.

Podolak and Cameron (Cameron, 1975) have inferred that the gas-phase (principally hydrogen and helium) comprises about 80%, 67%, 15%, and 25% of the masses Jupiter, Saturn, Uranus, and Neptune respectively. With remainder assumed to have been dust, then dust to gas ratios for the four planets are about 0.25, 0.5, 6, and 3, compared to a ratio of about 0.02 for ices and rocky material in the solar composition. In Figure 3-18 several curves of $^{20}Ne/^{22}Ne$ vs. dust/gas ratio are plotted for simple mixtures. The neon in the dust will

Figure 3-18. The isotopic composition of simple mixtures of dust and gas plotted as a function of dust/gas ratio. The different curves correspond to different relative neon concentrations in the gas(S) and dust(E). Dust/gas ratios for the giant planets are indicated by the vertical bars. Measurable differences would be expected in the atmospheres of the four giant planets for $^{22}Ne_E/^{22}Ne_S \geq 0.01$. No shifts would be detected for dust-phase neon concentrations of about 10^{13} $^{22}Ne/g$, similar to the concentrations in meteoritic gas-rich minerals.

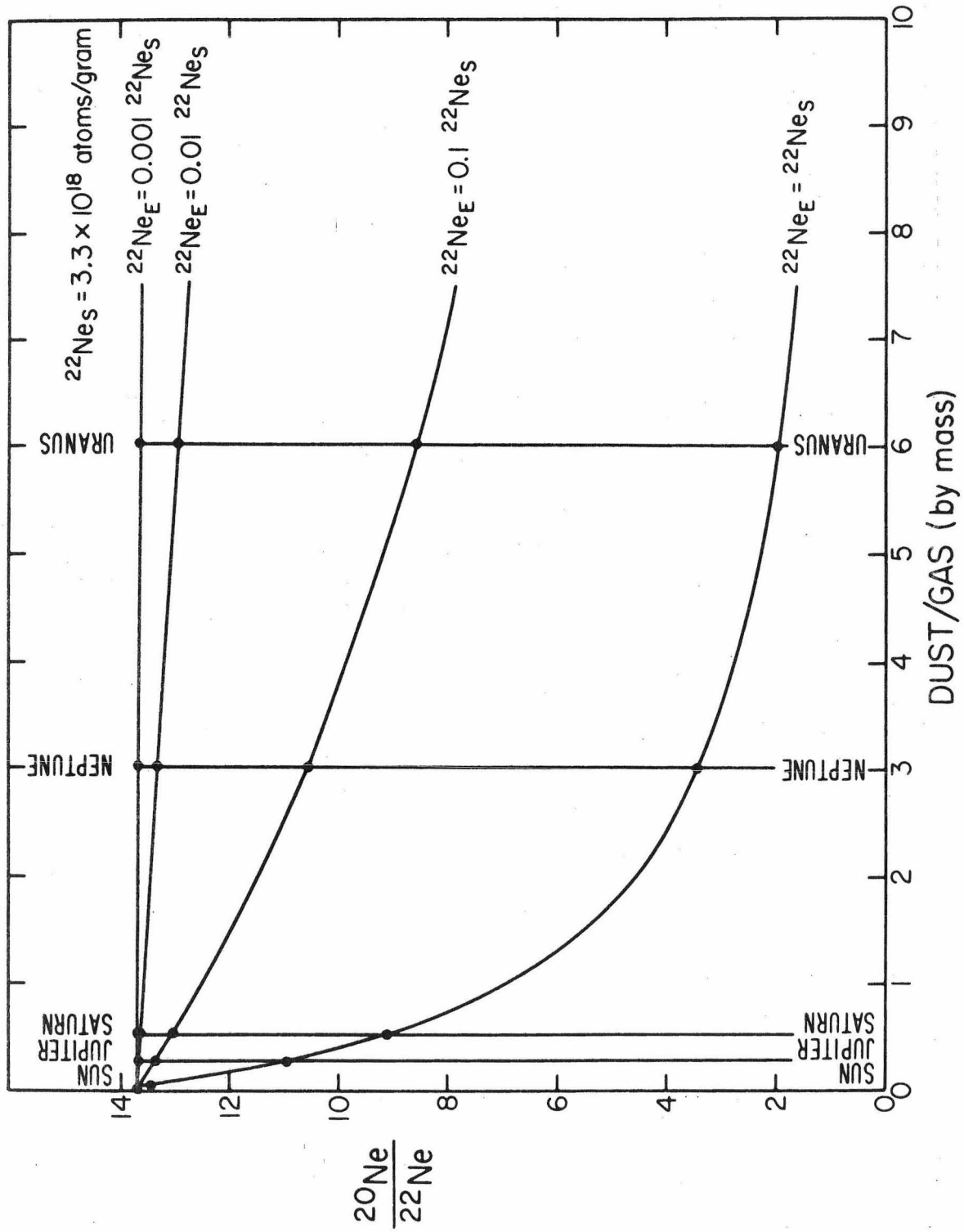
$^{22}Ne_S = 3.3 \times 10^{18}$ atoms/gram
$^{22}Ne_E = 0.001\ ^{22}Ne_S$
$^{22}Ne_E = 0.01\ ^{22}Ne_S$
$^{22}Ne_E = 0.1\ ^{22}Ne_S$
$^{22}Ne_E = {}^{22}Ne_S$
URANUS
NEPTUNE
SATURN
JUPITER
SUN
$\frac{^{20}Ne}{^{22}Ne}$
DUST/GAS (by mass)

Figure 3-18

cause significant isotopic variations in the atmospheres of the giant planets if $^{22}Ne_E/^{22}Ne_S \geq 0.01$, i.e., for $^{22}Ne_E \geq 3.3 \times 10^{16}$ atoms/gram in the dust. On the other hand, if the ^{22}Ne content of the dust were as low as $\sim 10^{13}$ atoms/gram, the highest neon-E concentration measured in gas-rich separates from meteorites, then $^{20}Ne/^{22}Ne$ in the atmospheres of all the giant planets should be equal to the solar ratio. If the $^{20}Ne/^{22}Ne$ ratio in the gas was 8.5 instead of 13.7, then the curves would originate at the lower value. Next to the sun, the composition of Jupiter's atmosphere should be least changed from the gas-phase value by the addition of its complement of dust. Therefore, measurement of the isotopic composition of neon and the other noble gases in Jupiter's atmosphere should provide an invaluable check on the validity of the gas-phase compositions estimated from the solar wind.

In Figure 3-19, available neon data for the atmospheres of the terrestrial planets are represented. The ^{22}Ne concentrations are obtained by dividing the amount of neon in each planet's atmosphere by the planet's mass. Isotopic compositions are not known for the atmospheres of Mars and Venus. Assuming $^{20}Ne/^{22}Ne$ to lie between 0 and 13.7 for each, a vertical dashed line is drawn at the appropriate concentration. Regardless of the isotopic composition of the Martian atmosphere, it cannot lie on a single mixing line with the solar and terrestrial points. Therefore, assuming all the planets' neon to be in their atmospheres, the atmospheres of the terrestrial planets cannot fit into a simple two-component gas-dust mixing model. In other words, it would be impossible to start with Mars-like material, add neon-S, and obtain the terrestrial atmosphere. The same conclusion may be

Figure 3-19. Neon in the atmospheres of the terrestrial planets. Concentrations are obtained by dividing the atmospheric ^{22}Ne content by the total mass of each planet. Isotopic compositions are not known for Mars and Venus but are assumed to lie between 13.7 and 0. It is not possible for all three planets to plot on a single straight mixing line. Assuming degassing of the planetary interiors is reasonably complete, their noble gases cannot have been derived by simple mixing of dust and gas in different proportions.

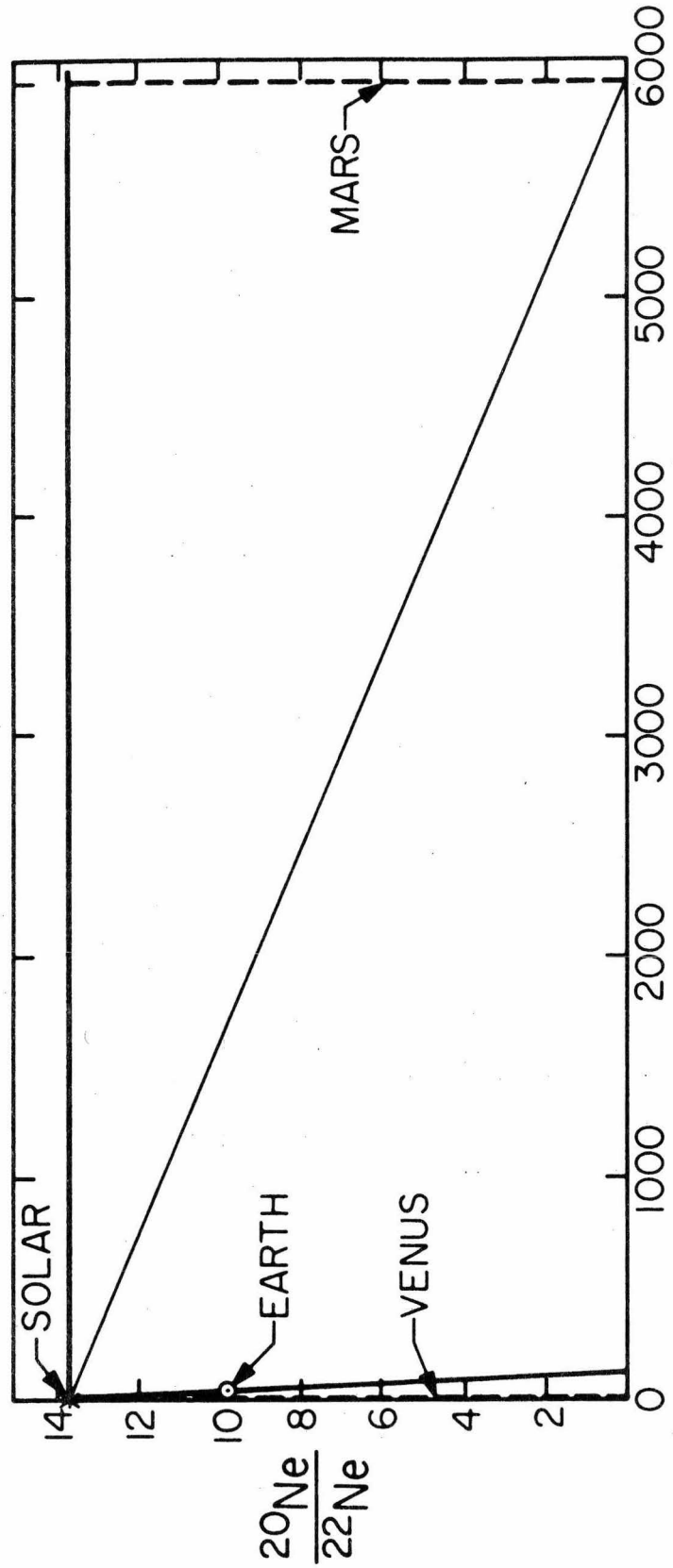
SOLAR
EARTH
VENUS
MARS
14
12
10
8
6
4
2
0
1000
2000
3000
4000
5000
6000
$\frac{^{20}Ne}{^{22}Ne}$
$1/^{22}Ne_{atmosphere}$ (unit = 10^{-12} g/atom)

Figure 3-19

obtained from the $^{20}Ne/^{36}Ar$ ratios for the three planets which are the same within experimental uncertainties (Chap. 2). It is impossible to explain the apparent increase in neon and argon concentration from Mars to the Earth to Venus by the addition of solar wind which has a much higher $^{20}Ne/^{36}Ar$ ratio.

Within the limits of present knowledge, the elemental abundance patterns for the noble gases (^{22}Ne, ^{36}Ar, ^{84}Kr, ^{132}Xe) are very similar on the Earth and Mars, and the $^{20}Ne/^{36}Ar$ ratio very similar between Earth and Venus. All patterns are planetary, in the sense that $Ne/^{36}Ar$ ratios are a factor of 30 to 60 lower than the cosmic or solar ratio, and $Kr/^{36}Ar$ about 50 to 100 times higher. The similarities among the three atmospheres, despite some 3 to 4 decades of difference in concentration, appear to argue conclusively against the rare gases in the atmospheres being residues of the independent loss from each planet of a massive primordial atmosphere starting with essentially cosmic abundances. Instead, the rare gases are probably of secondary origin arising from outgassing of the planets, as was concluded for the major atmospheric constituents water, nitrogen, oxygen, and carbon dioxide by Brown (1952). The similar elemental abundance patterns for all three planets suggest that their atmospheric noble gases could have been obtained from the same source. Isotopic compositions, particularly of neon and xenon, are needed to confirm or deny such a possibility. Since meteorites also contain planetary noble gases, it has been argued that the source of the noble gases (and also the other volatiles) in the terrestrial planets was meteoritic, in particular, material similar to carbonaceous chondrites (Turekian and Clark, 1975;

Anders and Owen, 1977). Cometary material is also a possible source.

The concentrations of the atmospheric noble gases on the terrestrial planets decrease systematically with increasing distance from the sun (Chap. 2). This could be due to real initial differences in volatile contents of the planets (Hoffman et al., 1979). On the other hand, the trend seems to run counter to our preconceived notions. Venus, the most noble-gas-rich, is the closest to the sun, and presumably formed at the highest temperature. Since the atmospheres probably result from outgassing, some of the differences might be due to different degrees of outgassing. Venus would have to have outgassed primordial neon some ten to one hundred times more effectively than the Earth, and Mars some hundred times less thoroughly. The ^{40}Ar contents of the planets' atmospheres can be used to make some inferences about planetary degassing. We presume all three planets had the same initial K content and $^{36}Ar/K$ ratio. For the sake of argument we assume the K content is approximately chondritic, about 800 ppm. The ^{40}Ar presently in the atmospheres of Mars, Earth, and Venus corresponds to about 0.5%, 10%, and 6% of the total planetary ^{40}Ar generated over 4.6 billion years. It is generally assumed that ^{36}Ar should be degassed as thoroughly or more so than ^{40}Ar, since ^{40}Ar is continually replenished by decay. With this assumption, at least 0.5%, 10%, and 6% of the primordial planetary noble gases should be in the atmospheres of Mars, Earth, and Venus. If Venus experienced a complete catastrophic outgassing before significant decay of ^{40}K to ^{40}Ar took place, then as much as 100% of its primordial noble gases could reside in its atmosphere. We assume little or no early release of primordial

gas on Mars and the Earth. With such a scenario, ^{22}Ne and ^{36}Ar concentration differences of a factor of 20 between Mars and Earth, and 10 between Earth and Venus could be explained solely on the basis of different outgassing histories. This is marginally compatible with the data for Venus, but the Mars atmosphere contains 200 times less ^{22}Ne and ^{36}Ar than the terrestrial, rather than 20 times. This difference is not compatible with outgassing alone, unless ^{36}Ar is for some reason lost from the interior of the planet much less easily than ^{40}Ar. The simplest explanation is that the initial $^{36}Ar/K$ ratio on Mars was roughly 10 times or more lower than on the Earth. The limited xenon data available for the Martian atmosphere can be used to support the idea that initial noble gas contents on Mars were low compared with the Earth. On Mars, $^{129}Xe/^{132}Xe$ is about 2.5, but on the Earth it is close to 1. The difference is due to radiogenic ^{129}Xe from the decay of ^{129}I. Compared to primitive trapped xenon in meteorites, the ratios of primordial ^{132}Xe to excess radiogenic ^{129}Xe in the Mars atmosphere and the terrestrial can be inferred to be roughly 0.7 and 10 respectively. Assuming both planets had the same initial $^{129}I/^{127}I$ ratio at formation, then this could be interpreted as evidence that the initial $^{132}Xe/I$ ratio on Mars was 10 to 20 times lower than the Earth, in good agreement with the $\geq$ 10 times lower $^{36}Ar/K$ ratio inferred above. Thus the variations in atmospheric noble gas contents of the terrestrial planets may have been determined by a combination of differences in initial noble gas abundance and differences in subsequent degassing history.

REFERENCES, CHAPTER 3

*Alaerts L., Lewis R. S., and Anders E. (1977) Primordial noble gases in chondrites: the abundance pattern was established in the solar nebula. Science 198, 927-930.

*Alaerts L., Lewis R. S., and Anders E. (1979) Host phases of neon-E and s-process xenon in the Murchison C2 chondrite. In Lunar and Planetary Science X, pp. 12-14. Lunar and Planetary Institute.

Anders E., Heymann D., and Mazor E. (1970) Isotopic composition of primordial helium in carbonaceous chondrites. Geochim. Cosmochim. Acta 34, 127-132.

Anders E. and Owen T. (1977) Mars and Earth: Origin and abundance of volatiles. Science 198, 453-465.

Arnold J. R. (1965) The origin of meteorites as small bodies III. General considerations. Astrophys. J. 141, 1548-1556.

Bieri von R. H. and Rutsch W. (1962) Erzeugungsquerschnitte für Edelgase aus Mg, Al, Fe, Ni, Cu and Ag bei Bestrahlung mit 540 MeV Protonen. Compte Rendu, Soc. Suisse Phys. 35, 553-554.

*Black D. C. (1972a) On the origins of trapped helium, neon, and argon isotopic variations in meteorites - I. Gas-rich meteorites, lunar soil and breccia. Geochim. Cosmochim. Acta 36, 347-375.

*Black D. C. (1972b) On the origins of trapped helium, neon, and argon isotopic variations in meteorites - II. Carbonaceous meteorites. Geochim. Cosmochim. Acta 36, 377-394.

Black D. C. and Pepin R. O. (1969) Trapped neon in meteorites - II. Earth Planet. Sci. Lett 6, 395-405.

Bochsler P., Eberhardt P., Geiss J., and Grögler N. (1969) Rare-gas measurements in separate mineral phases of the Otis and Elenovka chondrites. In Meteorite Research (ed. P. Millman), pp. 857-874. D. Reidel.

Bogard D. D. and Cressy P. J., Jr. (1973) Spallation production of ^{3}He, ^{21}Ne, and ^{38}Ar from target elements in the Bruderheim chondrite. Geochim. Cosmochim. Acta 37, 527-546.

*Bogard D. D. and Nyquist L. E. (1972) Noble gas studies on regolith materials from Apollo 14 and 15. Proc. 3rd Lunar Sci. Conf. Geochim. Cosmochim. Acta, Suppl. 3, pp. 1797-1819.

Brown H. (1952) Rare gases and the formation of the Earth's atmosphere. In The Atmospheres of the Earth and Planets, 2nd ed. (ed. G. P. Kuiper), pp. 258-266. U. of Chicago.

Cameron A. G. W. (1975) The origin and evolution of the solar system. In The Solar System, (A Scientific American Book), pp. 15-23. W. H. Freeman.

Cameron A. G. W. and Pollack J. B. (1976) On the origin of the solar system and of Jupiter and its satellites. In Jupiter (ed. T. Gehrels), pp. 61-84. U. of Arizona.

Carter G. and Colligan J. S. (1968) Ion Bombardment of Solids. American Elsevier.

Clayton R. N., Grossman L., and Mayeda T. K. (1973) A component of primitive nuclear composition in carbonaceous meteorites. Science 182, 485-488.

Combes M., Encrenaz T., and Owen T. (1978) On the abundance of deuterium in Jupiter's atmosphere. Astrophys. J. 221, 378-381.

Dietrich W. F. and Simpson J. A. (1978) Preferential enhancements of the solar flare accelerated nuclei carbon to zinc from ∿ 20-30 MeV - nucleon^{-1}. Preprint.

*Eberhardt P. (1974) A neon-E-rich phase in the Orgueil carbonaceous chondrite. Earth Planet. Sci. Lett. 24, 182-187.

*Eberhardt P., Eugster O., Geiss J., and Marti K. (1966) Rare gas measurements in 30 stone meteorites. Z. Naturforsch. 21a, 414-426.

Eberhardt P., Eugster O., and Marti K. (1965) A redetermination of the isotopic composition of atmospheric neon. Z. Naturforsch. 20a, 623-624.

*Eberhardt P., Geiss J., Graf H., Grögler N, Krähenbühl U., Schwaller H., Schwarzmuller J., and Stettler A. (1970) Trapped solar wind noble gases, exposure age and K/Ar-age in Apollo 11 lunar fine material. Proc. Apollo 11 Lunar Sci. Conf., Geochim. Cosmochim. Acta, Suppl. 1, 1037-1070.

*Eberhardt P., Jungck M. H. A., Meier F. O., and Niederer F. (1979) Neon-E: new limits for isotopic composition. Two host phases? In Lunar and Planetary Science X, pp. 341-343. Lunar and Planetary Institute.

*Frick U. and Moniot R. K. (1977) Planetary noble gas components in Orgueil, Proc. Lunar Sci. Conf. 8th, 229-261.

Geiss J. (1972) Noble gas isotopes and deuterium in the solar system. In Symposium on the Origin of the Solar System, Nice. (ed. M. Reeves) pp. 217-234.

Geiss J. (1973) Solar wind composition and implications about the history of the solar system; Invited paper, 13th Int. Cosmic Ray Conf., Denver.

Gray C. M. and Compston W. (1974) Excess ^{26}Mg in the Allende meteorite. Nature 251, 495-497.

Haff P. K., Switkowski Z. E., Burnett D. S., and Tombrello T. A. (1977) Gravitational and recoil contributions to surface mass fractionation by solar-wind sputtering. Proc. Lunar Sci. Conf. 8th, 3807-3815.

*Herzog G. F. and Anders E. (1975) Primordial noble gases in separated meteoritic minerals. II. Earth Planet. Sci. Lett. 24, 173-181.

Heymann D., Dziczkaniec M., and Palma R. (1976) Limits for the accretion time of the earth from cosmogenic ^{21}Ne produced in planetesimals. Proc. Lunar Sci. Conf. 7th, 3411-3419.

Hoffman J. H., Hodges R. R., Jr., McElroy M. B., Donahue T. M., and Kolpin M. (1979) Venus lower atmospheric composition: preliminary results from Pioneer Venus. Science 203, 800-802.

Huneke J. C. (1973) Diffusive fractionation of surface implanted gases. Earth Planet. Sci. Lett. 21, 35-44.

*Jeffery P. M. and Anders E. (1970) Primordial noble gases in separated meteoritic minerals - I. Geochim. Cosmochim. Acta 34, 1175-1198.

Lee T. and Papanastassiou D. A. (1974) Mg isotopic anomalies in the Allende meteorite and correlation with O and Sr effects. Geophys. Res. Lett. 1, 225-228.

Lewis R. S., Alaerts L., and Anders E. (1979a) Ferrichromite: a major host phase of isotopically anomalous noble gases in primitive meteorites. In Lunar and Planetary Science X, pp. 725-727.

Lunar and Planetary Institute.

*Lewis R. S., Alaerts L., and Anders E. (1979b) Isotopic anomalies in the Orgueil meteorite: neon-E, s-process Xe, and CCFXe. In Lunar and Planetary Science X, pp. 728-730. Lunar and Planetary Institute.

*Lewis R. S., Gros J., and Anders E. (1977) Isotopic Anomalies of noble gases in meteorites and their origins 2. Separated Minerals from Allende. J. Geophys. Res. 82, 779-792.

*Lewis R. S., Srinivasan B., and Anders E. (1975) Host phase of a strange xenon component in Allende. Science 190, 1251-1262.

Manuel O. K., Hennecke E. W., and Sabu D. D. (1972) Xenon in carbonaceous chondrites. Nature 240, 99-101.

*Mazor E., Heymann D., and Anders E. (1970) Noble gases in carbonaceous chondrites. Geochim. Cosmochim. Acta 34, 781-824.

*Moniot R. K. (1978) Noble-gas-rich separates from H-chondrites. In Lunar and Planetary Science IX, pp. 747-749. Lunar and Planetary Institute.

*Niederer F. and Eberhardt P. (1977) A neon-E-rich phase in Dimmitt. Meteoritics 12, 327-331.

Öpik E. J. (1951) Collision probabilities with the planets and distribution of interplanetary matter. Proc. Roy. Irish Acad. 54A, 165-199.

Pepin R. O. (1967) Trapped neon in meteorites. Earth Planet. Sci. Lett. 2, 13-18.

Pepin R. O. and Phinney D. (1979) Components of xenon in the solar system. Submitted to Geochim. Cosmochim. Acta.

*Phinney D., Frick U., and Reynolds J. H. (1976) Rare-gas-rich separates from carbonaceous chondrites. In Lunar Science VII, pp. 691-693, Lunar Science Institute.

*Reynolds J. H., Frick U., Neil J. M., and Phinney D. L. (1978) Rare-gas-rich separates from carbonaceous chondrites. Geochim. Cosmochim. Acta 42, 1775-1797.

Reynolds J. H. and Turner G. (1964) Rare gases in the chondrite Renazzo. J. Geophys. Res. 69, 3263-3281.

Shukolyukov Yu. A., Sharif-Zade V. B., and Ashkinadze G. Sh. (1973) Neon isotopes in natural gases. Geochemistry Int. 10, 346-354.

Signer P. and Nier A. O. (1962) The measurement and interpretation of rare gas concentrations in iron meteorites. In Researches on Meteorites (ed. C. B. Moore), pp. 7-35. Wiley.

Simpson J. A. (private communication). Present address: Enrico Fermi Institute and Dept. of Physics, U. of Chicago, Chicago 60637.

Smith S. P. (1979) Isotopic composition of the anomalous xenon in the Murchison meteorite. Geophys. Res. Lett. 6, 55-58.

*Smith S. P. and Fireman E. L. (1973) Ages of eight recently fallen meteorites. J. Geophys. Res. 78, 3240-3259.

*Smith S. P. and Huneke J. C. (1975) Cosmogenic neon produced from sodium in meteoritic minerals. Earth Planet. Sci. Lett. 27, 191-199.

*Smith S. P., Huneke J. C., Rajan R. S., and Wasserburg G. J. (1977) Neon and argon in the Allende meteorite. Geochim. Cosmochim. Acta 41, 627-647.

*Smith S. P., Huneke J. C., and Wasserburg G. J. (1978) Neon in gas-rich samples of the carbonaceous chondrites Mokoia, Murchison and Cold Bokkeveld. Earth Planet. Sci. Lett. 39, 1-13.

Srinivasan B. and Anders E. (1978) Noble gases in the Murchison meteorite: possible relics of s-process nucleosynthesis. Science 201, 51-56.

*Srinivasan B., Gros J., and Anders E. (1977) Noble gases in separated meteoritic minerals: Murchison (C2), Ornans (C3), Karoonda (C5), and Abee (E4). J. Geophys. Res. 82, 762-778.

Stauffer H. (1962) On the production ratios of rare gas isotopes in stone meteorites. J. Geophys. Res. 67, 2023-2028.

Taylor S. R. (1975) Lunar Science: A Post-Apollo View. Pergamon.

Turekian K. K. and Clark S. P., Jr. (1975) The non-homogeneous accumulation model for terrestrial planet formation and the consequences for the atmosphere of Venus. J. Atmos. Sci. 32, 1257-1261.

Vdovykin G. P. and Moore C. B. (1971) Carbon. In Handbook of Elemental Abundances in Meteorites (ed. B. Mason), pp. 81-91. Gordon and Breach.

Wasson J. T. (1974) Meteorites. Springer-Verlag.

Wetherill G. W. (1954) Variations in the isotopic abundances of neon and argon extracted from radioactive minerals. Phys. Rev. 96, 679-683.

Zähringer J. (1962) Ueber die Uredelgase in den Achondriten Kapoeta und Staroe Pesjanoe. Geochim. Cosmochim. Acta 26, 665-680.

CHAPTER 4. STUDIES OF TERRESTRIAL NOBLE GASES

4.1 INTRODUCTION

The principal topic of this chapter is the present-day distribution of noble gases on the Earth. We divide the Earth into two main noble gas reservoirs, the atmosphere and the solid body of the planet. The research of this chapter addresses two broad questions about these reservoirs. First, what is the present noble gas content of the solid Earth, and second, is there significant cycling of noble gases from one reservoir to the other?

The general approach taken here to study these questions has been to make mass-spectrometric measurements of the concentrations and isotopic compositions of noble gases in rocks from a variety of geological settings. Direct comparison of the amounts of gas in these rocks with the amounts in the atmosphere is used as one way to assess the relative importance of the solid Earth as a reservoir of noble gases. To test the possibility that atmospheric gases are cycled into the crust, we have examined deep-seated plutonic rocks for evidence of an atmospheric noble gas component. Juvenile noble gas components have been sought in all samples using isotopic composition measurements.

Most of the measurements of noble gases reported in this chapter were made on whole-rock samples or large, single crystals. The gases in the samples usually were extracted by fusing the material in vacuum in a single step at high-temperature. This procedure was adopted because in almost all cases there was no prior information available about the total amount of gas in the sample, or about the phases in which gases might possibly be concentrated.

The noble gas contents of most terrestrial rocks are generally

quite low and difficult to measure. It is useful therefore to identify classes of terrestrial material where the concentrations of dissolved gases can be expected to be higher than average. Since the noble gas solubilities should obey Henry's law, rocks that crystallize or are metamorphosed at high fluid pressures should generally contain larger concentrations of trapped ambient gases than rocks formed at the Earth's surface. For example, it is not unusual to find excess radiogenic ^{40}Ar trapped in high-grade metamorphic rocks (e.g., Kaneoka, 1975). Among magmas erupted at the surface, dissolved juvenile gases should be retained best in those cooling most rapidly. A noteworthy example of unusually rapid cooling is the quenched glassy rim commonly found on submarine pillow-basalt flows. Certain classes of minerals with open crystal structures may have comparatively high solubilities for noble gases. Such phases would show much higher noble gas contents than other minerals formed under the same conditions. Examples are ring-silicates such as beryl (Damon and Kulp, 1958) and amphiboles (Saito et al., 1978). Among the samples studied in this work are examples of all these types of material, including plutonic rocks from the upper mantle and crust, basalt glass from mid-ocean ridge lavas, and a suite of beryl crystals.

It is essential for proper sample selection and interpretation of noble gas measurements to place terrestrial noble gas reservoirs and transport cycles into a geologic framework. Fig. 4-1 is a cartoon cross-section of the Earth representing the atmospheric and solid-Earth noble gas reservoirs, and some of the major structural elements of the planet. The body of the planet has been subdivided into several smaller reservoirs, including the continental crust, oceanic

Figure 4-1. Terrestrial noble gas reservoirs, sources, and fluxes. The Earth comprises two main reservoirs, the atmosphere and the body of the planet. The latter is conveniently subdivided into continental crust, oceanic crust, mantle, and core. The arrows loosely represent the cycling of noble gases between reservoirs. Helium is continually lost from the atmosphere to space. Infalling interplanetary dust may provide a small flux of noble gases to the atmosphere or the Earth's surface. Some ^{3}He is generated by cosmic-ray spallation in the atmosphere. Juvenile noble gases from the crust and mantle may be outgassed into the atmosphere by volcanoes on the continents or at oceanic spreading ridges. Sources of juvenile gases include a variety of nuclear reactions taking place in the Earth. Primordial gases from undegassed regions of the mantle may also be emitted. Atmospheric gases are dissolved in surface water. The water can carry the gases into the crust where they may become trapped in rocks. Subduction of altered oceanic crust may provide a mechanism for injecting atmospheric noble gases into the upper mantle.

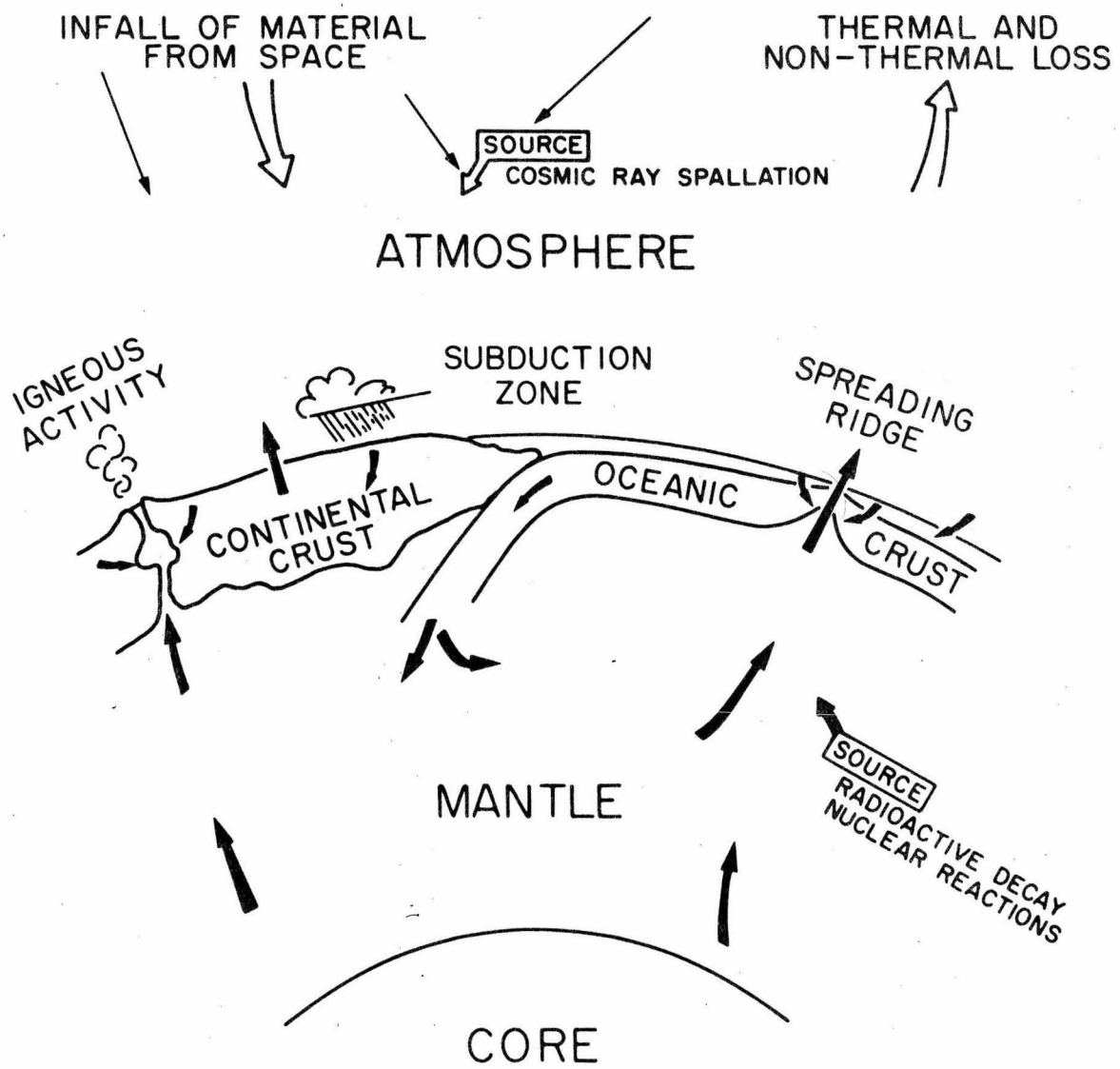
INFALL OF MATERIAL
FROM SPACE
THERMAL AND
NON-THERMAL LOSS
SOURCE
COSMIC RAY SPALLATION
ATMOSPHERE
IGNEOUS
ACTIVITY
SUBDUCTION
ZONE
SPREADING
RIDGE
CONTINENTAL
CRUST
OCEANIC
CRUST
MANTLE
SOURCE
RADIOACTIVE DECAY
NUCLEAR REACTIONS
CORE

Figure 4-1

crust, mantle, and core. The arrows suggest possible noble gas flows to and from different reservoirs. One of the important reasons for undertaking the present measurements of noble gases in rocks is to decipher the actual patterns of these fluxes in the Earth. The boxes labeled "source" indicate generation of noble gases by nuclear reactions in the atmosphere and solid Earth.

Transport of noble gases from the atmosphere into the crust is probably accomplished most effectively by water. Water carrying dissolved atmospheric gases seeps into the crust. Within the crust, the gases may become fixed in the rock during alteration, or may eventually return to the surface in natural gases, hot springs, etc. Exchange of noble gases between the atmosphere and deeper portions of the Earth probably involves the tectonic elements sketched in Fig. 4-1. On the right is pictured an oceanic spreading ridge, where material upwells from the mantle. In the center is a subduction zone, where crustal material sinks back into the mantle. On the left is shown a region of continental igneous activity, where deep-seated material may be intruded into the crust, and possibly erupted at the surface. In each case, the mass-transfer of solid or molten rock may be accompanied by the transport of noble gases into or out of the crust and mantle. Although not indicated explicitly in Fig. 4-1, erosion and metamorphism of the continental crust may also lead to outgassing of noble gases into the atmosphere.

The simple picture presented in Fig. 4-1 raises important questions concerning the cycling of atmospheric noble gases into the solid Earth. How significant is transport by subduction of noble gases into the mantle? Are the transport loops from the subduction

zones to the spreading ridges and other sites of upwelling closed? Are some gases observed in deep-seated magmas and inclusions atmospheric gases that were subducted during an earlier epoch? In a similar, but more speculative vein, can infalling interplanetary dust that collects the ocean sediments be subducted, and if so, can it provide a significant input of juvenile noble gases to the mantle? Could some of the apparently primary juvenile noble gases such as ^{3}He observed in mantle samples have arisen through this mechanism, rather than by outgassing of primitive mantle material? These questions will be considered in more detail near the end of this chapter.

Before turning to the experimental results, we briefly discuss the atmosphere. The atmosphere provides us with an extremely valuable touchstone, since it is the only terrestrial noble gas reservoir for which we accurately know the total noble gas content and isotopic composition. As discussed at the end of Chapter 3, the atmospheres of the Earth and other terrestrial planets were probably generated by outgassing from the interiors of the planets. Therefore, if we divide the atmospheric content of each gas by the mass of the planet, the resulting concentration is a minimum estimate for the initial gas content of the material out of which the planet formed. This is true only for isotopes not generated by nuclear reactions in the planet after its formation. These minimum concentrations for the Earth are listed in Table 4-1 (see also Chap. 2). Also given in Table 4-1 are the most important sources for the different atmospheric noble gas isotopes. ^{40}Ar from radioactive decay of K is by far the most abundant noble gas isotope in the atmosphere. However, its high concentration reflects continuing production, not an initially high concentration.

Table 4-1. Minimum whole-Earth concentrations of noble gases calculated from their atmospheric abundances.[1]

Isotope	Concentration[1] (10^{-16} mole/gram)	Origin[2]	
^{3}He	0.00224	primordial	(nucleogenic; cosmogenic)
^{4}He	(1600)[3]	radiogenic	(primordial?)
^{20}Ne	5020	primordial	
^{21}Ne	14.9	primordial	(nucleogenic?)
^{22}Ne	513	primordial	(nucleogenic?)
^{36}Ar	9610	primordial	
^{38}Ar	1810	primordial	
^{40}Ar	(2.84×10^{6})[3]	radiogenic	(primordial?)
^{78}Kr	1.21	primordial	
^{80}Kr	7.86	primordial	
^{82}Kr	40.1	primordial	
^{83}Kr	40.0	primordial	(fissiogenic?)
^{84}Kr	198	primordial	(fissiogenic?)
^{86}Kr	60.6	primordial	(fissiogenic?)
^{124}Xe	0.0254	primordial	
^{126}Xe	0.0237	primordial	
^{128}Xe	0.511	primordial	
^{129}Xe	(7.06)[3]	primordial	(radiogenic)
^{130}Xe	1.08	primordial	
^{131}Xe	(5.67)[3]	primordial	(fissiogenic)
^{132}Xe	(7.18)[3]	primordial	(fissiogenic)
^{134}Xe	(2.79)[3]	primordial	(fissiogenic)
^{136}Xe	(2.37)[3]	primordial	(fissiogenic)

Table 4-1. (continued)

[1]Concentrations obtained by dividing the atmospheric abundance of each isotope by the mass of the Earth, 5.98×10^{27} grams.

[2]First column gives the principal source of each isotope in the atmosphere. Minor sources are enclosed in parentheses. Queried contributions are probable, but not positively identified.

[3]Values in parentheses are too high because of generation by nuclear reactions subsequent to the Earth's formation. This is a dominant effect for ^{4}He and ^{40}Ar, but only a few percent for the xenon isotopes.

^{36}Ar is the most abundant primordial isotope, followed by ^{20}Ne. At the other end of the scale, ^{3}He is the least abundant. The helium content of the atmosphere represents a balance between its loss to space and its replenishment, primarily by outgassing of juvenile helium from the solid Earth. Loss of the heavier noble gases is not thought to have been significant.

The minimum whole-Earth concentrations in Table 4-1 also provide a convenient reference against which to compare concentrations measured in rocks. For example, in order for 50% of the overall terrestrial noble gas budget to still reside in the solid portions of the planet, the Earth on the average must consist of rocks with the same gas contents as the values in Table 4-1. If we were to find that all measured concentrations in rocks are far lower, then we would have reason to argue that the Earth was thoroughly degassed.

The content of the noble gases in the atmosphere can also provide a measure of the average net flux of each gas (except helium) into the atmosphere. We define this average flux $\overline{J}_a$ as the present atmospheric abundance of a gas divided by 4.5 billion years. In Table 4-2 we list $\overline{J}_a$ for representative isotopes for each noble gas. For helium, the values listed are estimated values of the present fluxes, not average values, since helium is continuously lost to space. The value for ^{3}He is a calculated flux (Johnson and Axford, 1969), which primarily reflects thermal escape from the exosphere. For ^{4}He, the escape mechanism is non-thermal. The value given is a typical estimate based on the current production rate of ^{4}He by U and Th decay (cf. Naughton et al., 1973). Also shown in Table 4-2 are values for a spontaneous fission xenon component, $^{136}Xe_{SF}$, and an

Table 4-2. Atmospheric Average Fluxes $\overline{J}_a$

(Atmospheric content ÷ 4.5 billion years; in moles/year)

^{3}He	(1900)[1]
^{4}He	($8x10^{8}$)[2]
^{20}Ne	$6.7x10^{5}$
^{36}Ar	$1.3x10^{6}$
^{40}Ar	$3.8x10^{8}$
^{84}Kr	$2.6x10^{4}$
^{132}Xe	$9.5x10^{2}$
$^{136}Xe_{SF}$	15
$^{129}Xe_{rad}$	64

[1]Present flux escaping from atmosphere, ~ 7 atoms/cm^2 sec (Johnson and Axford, 1969).

[2]Present flux escaping from atmosphere, ~ $3x10^{6}$ atoms/cm^2 sec (Naughton et al., 1973).

excess radiogenic $^{129}Xe_{rad}$ component in the atmosphere. These are based on the difference between the present atmospheric composition and estimates of the initial primordial xenon composition of the Earth (Pepin and Phinney, 1979). The excess $^{129}Xe_{rad}$ is estimated to be 6.8% of the total ^{129}Xe in the atmosphere. Ideally, comparison of the present fluxes of the noble gases from the solid Earth with the average $\overline{J}_a$ values could be used to obtain information about the degassing history of the Earth. This is not easy in practice because of the difficulty of obtaining reliable estimates of the present fluxes. This problem will be discussed briefly in section 4.3.3.

4.2 EXPERIMENTAL RESULTS

Within the broad framework established in Fig. 4-1, the analyzed samples come mainly from two geologic settings. The first is centers of intrusive and extrusive igneous activity on the continents. The second is the regions of magma upwelling at oceanic ridges. Fig. 4-2 is a summary of some of the noble gas sources and generalized transport processes that may be associated with igneous activity. During magma generation by partial melting, we expect noble gases in the source region to be incorporated by the magma. Some sources of magmatic gases are listed in the boxes in Fig. 4-2. The two upper boxes on the left represent secondary juvenile gases generated by radioactive decay of U, Th, and K and by other ongoing nuclear reactions. At the bottom of the figure are shown two potential sources of primary juvenile gases, xenon isotopes from the decay of short-lived ^{129}I and ^{244}Pu, and primordial noble gases. In addition to dissolved gases, the ascending magma may carry gas-bearing xenoliths from the

Figure 4-2. Noble gases in igneous rocks and magmas. Noble gases in the source region will be incorporated into the magma during partial melting. These magmatic gases may include primordial gases, radiogenic Xe isotopes from the decay of shortlived ^{129}I or ^{244}Pu, radiogenic He, Ar, and Xe from the ongoing decay of U, Th, and K, and the products of a variety of other nuclear reactions. As the magma ascends toward the surface from the source region it may incorporate other noble gases. Atmospheric gases may be added through interaction with meteoric ground water. Crustal gases may be added by assimilation of xenoliths and host rock.

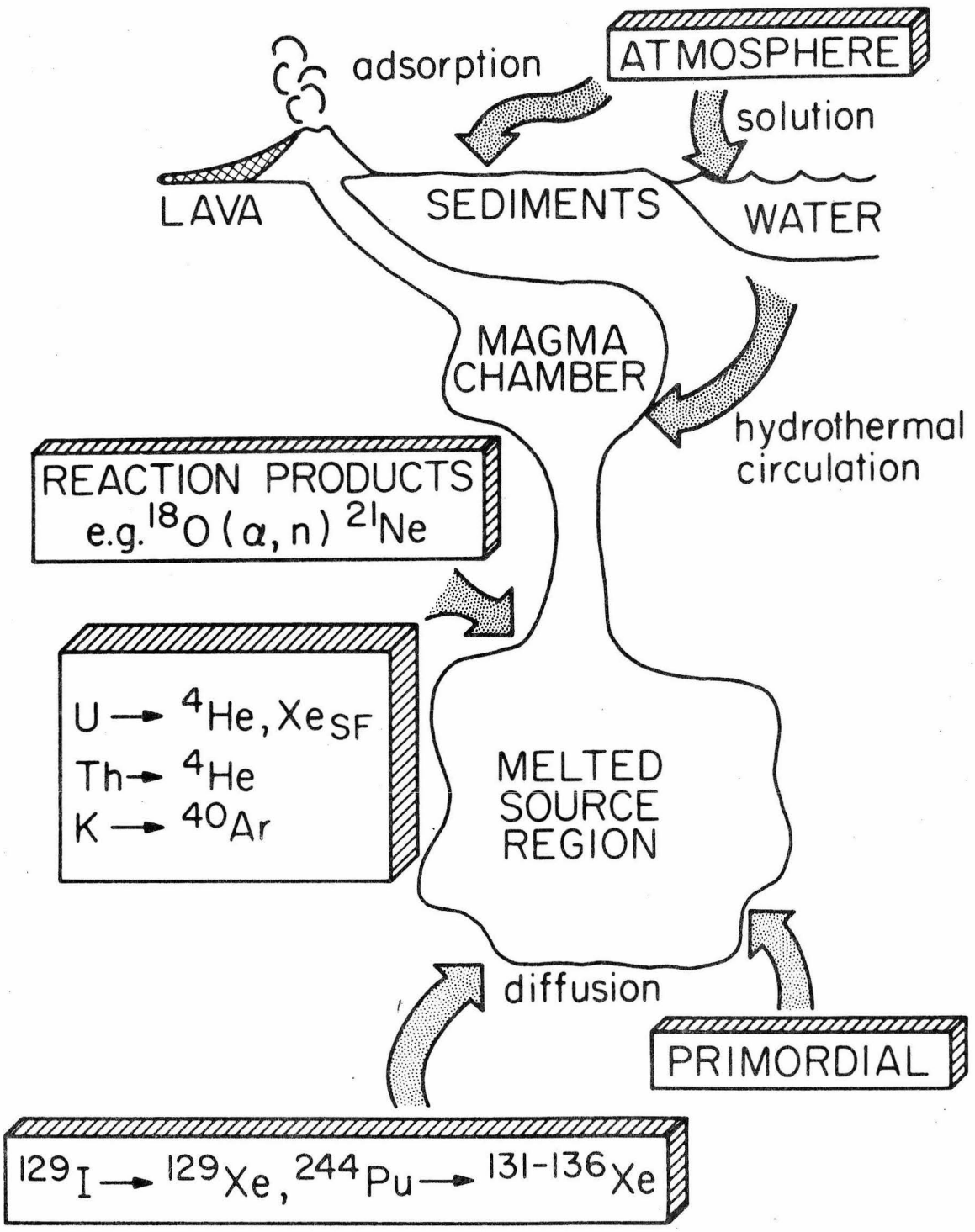
adsorption
ATMOSPHERE
solution
LAVA
SEDIMENTS
WATER
MAGMA CHAMBER
hydrothermal circulation
REACTION PRODUCTS
e.g. $^{18}O(\alpha, n)\ ^{21}Ne$
$U \rightarrow {}^{4}He, Xe_{SF}$
$Th \rightarrow {}^{4}He$
$K \rightarrow {}^{40}Ar$
MELTED SOURCE REGION
diffusion
PRIMORDIAL
$^{129}I \rightarrow {}^{129}Xe, {}^{244}Pu \rightarrow {}^{131\text{-}136}Xe$

Figure 4-2

source region. As the magma rises, the confining pressure will drop, and the magma and any xenoliths it carries may outgas. Absolute concentration levels in xenoliths and quenched magmas sampled near the Earth's surface will therefore not necessarily be representative of the concentrations in the source region.

As the magma migrates out of its source region, it may incorporate additional noble gases by assimilation of host rock or interaction with ground water carrying dissolved atmospheric gases. Lava erupted on the continents may incorporate atmospheric gases directly by diffusion from the air. By the time the magma cools and ceases to exchange noble gases with its environment, it may therefore contain a complex mixture of original magmatic gases and contaminant gases. In general we might expect the original magmatic gases from the source region to be more homogeneously distributed throughout the magma than later contaminants.

4.2.1 Samples from igneous intrusions in continental crust

In Fig. 4-3, we examine the environment of a shallow igneous intrusion in more detail. A magma body injected into the upper crust provides a heat source which can initiate a wide-scale meteoric hydrothermal circulation system. Meteoric ground water circulating through fractures and permeable country rock may introduce atmospheric gases into the cooling intrusion. Taylor and coworkers (Taylor, 1968; Taylor and Forester, 1971; Taylor, 1974; Taylor and Forester, 1979) have documented fossil examples of these circulation systems around intrusions presently exposed by erosion. In a young intrusion, juvenile magmatic gases may be trapped in minerals during

Figure 4-3. Cycling of noble gases near a crustal igneous intrusion. Injection of magma into the crust provides a localized heat source that can initiate a hydrothermal circulation system. At the level of the intrusion, convecting meteoric water may interact directly with the magma or cooling rock. Additional geothermal circulation may take place in aquifers and fractures above the intrusion. Juvenile magmatic gases may be concentrated in fluid-rich pegmatites during the late stages of crystallization, or may be lost to the surrounding hydrothermal circulation system. The meteoric ground water may carry atmospheric gases into the intrusion. Dissolved gases originally present in a geothermal reservoir may be lost by steam separation. Recharge of the geothermal aquifer by cold ground water will introduce atmospheric gases into the system.

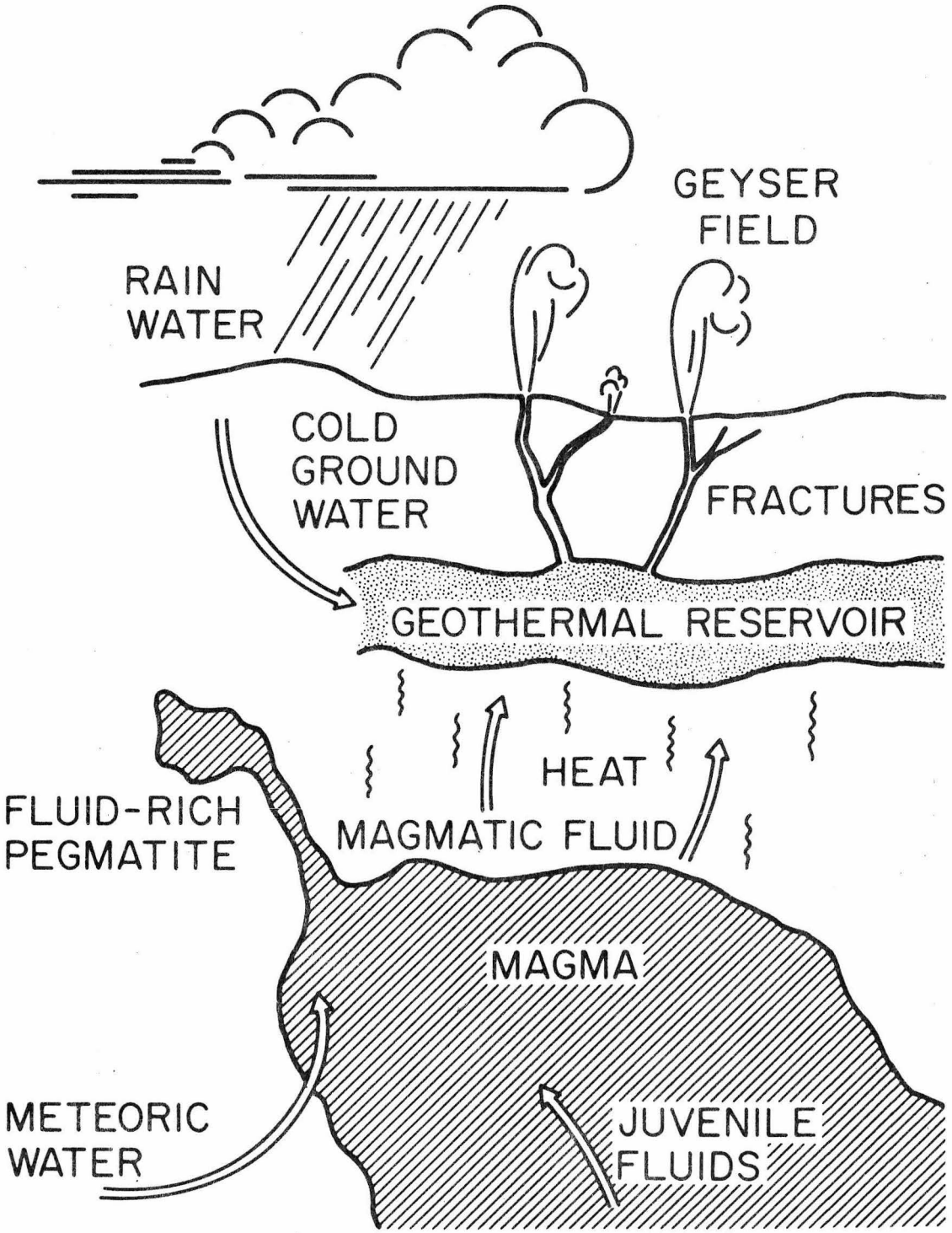
GEYSER
FIELD
RAIN
WATER
COLD
GROUND
WATER
FRACTURES
GEOTHERMAL RESERVOIR
HEAT
MAGMATIC FLUID
FLUID-RICH
PEGMATITE
MAGMA
METEORIC
WATER
JUVENILE
FLUIDS

Figure 4-3

crystallization or may escape into the surrounding hydrothermal circulation system. In the late stages of solidification, magmatic volatiles and incompatible elements often concentrate in pegmatite segregations. Minerals crystallizing in these fluid-rich bodies might incorporate high concentrations of magmatic noble gases in their lattices or perhaps in fluid inclusions.

Above the intrusion, the rising heat may establish geothermal circulation systems in fractures and sufficiently porous reservoir rocks. Recharge of the reservoir by cold ground water will introduce atmospheric noble gases into the system. Juvenile magmatic gases such as ^{3}He may also escape into the geothermal system. The noble gases will tend to remain dissolved in the ground water during transport unless a steam phase is formed. In the presence of vapor bubbles, the noble gases will partition very efficiently into the gas-phase, leaving a depleted water behind (e.g., Zartman et al., 1961). Measurements of the isotopic and elemental compositions of noble gases in thermal waters and steam at the surface can be used to probe a geothermal system (cf. Mazor, 1977).

Two suites of samples have been measured to investigate the noble gases associated with plutonic igneous intrusions. The first is a group of beryl crystals from pegmatites. In these samples we study gases trapped during the latest stages of solidification of a granitic magma. The second is a suite of samples from different levels within the Skaergaard layered igneous intrusion. Here we measure gases trapped at different horizons and times in the main body of a basaltic pluton. The results of these studies are summarized below. Detailed discussions of the individual experiments are found in the

manuscripts included as Appendix B.

Beryls. Beryl is a mineral with an unusually large capacity for noble gases. Previous work has shown that beryls characteristically contain large excesses of radiogenic ^{4}He and ^{40}Ar (Strutt, 1908; Damon and Kulp, 1958). The gases are thought to be trapped in the 4 to 5 Å diameter channels which pierce the beryl crystal lattice.

In the present study, neon, argon, krypton, and xenon were measured in beryls from eleven world-wide localities. The samples all derive from continental crust and range in age from < 70 m.y. to about 2500 m.y. old. The results extend the previous work in two ways. First, beryls are shown typically to contain excess nucleogenic ^{21}Ne and ^{22}Ne from (α,n) reactions, and xenon from ^{238}U spontaneous fission. The amounts of these nucleogenic isotopes correlate with the excess radiogenic ^{40}Ar contents. Second, beryl may also contain significant amounts of non-nucleogenic noble gases. The concentrations of the non-nucleogenic gases do not correlate with excess radiogenic ^{40}Ar. The non-nucleogenic gases are probably of atmospheric origin. No isotopic evidence for a primary juvenile component in beryls is found from the present data.

The isotopic composition of nucleogenic neon in the beryls is seen to be variable. The most extreme compositions measured were in two samples where $^{21}Ne/^{22}Ne$ ratios were respectively twenty and thirty-nine times greater than the atmospheric value. Virtually all the ^{21}Ne is these beryls in nucleogenic. In both samples, $^{20}Ne/^{22}Ne$ was less than one-sixth the atmospheric ratio, indicating that at most about 15% of the ^{22}Ne in these samples is atmospheric. The factor of two difference in $^{21}Ne/^{22}Ne$ probably reflects local

variations in the source region abundances of oxygen and fluorine targets for the (α,n) reactions producing neon.

The observed concentration of nucleogenic neon to radiogenic argon are found to agree with the expected production ratio in ordinary crustal rock with K/U $\cong 10^4$ by weight. However, the fission xenon typically appears to be a factor of ten underabundant compared with the nucleogenic neon or argon. Comparison of the abundance patterns for the non-radiogenic noble gases trapped in the beryls with gases found in other plutonic igneous rocks suggests that the non-radiogenic xenon is also depleted. The most likely explanation of this elemental fractionation is thought to be discrimination against the xenon atoms by the beryl crystals as they grew and trapped magmatic noble gases. The lattice channels in beryl consist of alternating sites of about 1.9 Å and 2.8 Å radius. The Van de Waals radius of xenon is about 2.2 Å. The periodic constriction of the channel to 1.9 Å radius may effectively prevent diffusion of xenon atoms into the trapping sites of a growing crystal. Diffusion of the smaller He, Ne, and Ar atoms with radii $\leq$ 1.9 Å should not be similarly restricted. Typically a large fraction of the 2.8 Å sites may be filled with water molecules (e.g., Hawthorne and Černý, 1977). This preferential occupancy of the larger sites by the abundant water molecules may also reduce the relative xenon content of the crystal, since the xenon atoms can be trapped only in the larger sites.

The dominant suite of noble gases trapped in beryl are the nucleogenic noble gases, including ^{4}He, ^{21}Ne, ^{22}Ne, ^{40}Ar, and fission xenon. Mixed with these isotopes are smaller amounts of non-nucelogenic gases, probably of atmospheric origin. Wasserburg and coworkers

(Wasserburg et al., 1957, 1963; Zartman et al., 1961; Wasserburg and Mazor, 1965) have shown that the noble gases in crustal natural gas pools also consist of radiogenic He, Ar, and Xe mixed with atmospheric noble gases probably carried into the crust by meteoric water. This suite of gases appears to be characteristic of the continental crustal environment, where high abundances of the radioactive elements U, Th, and K produce abundant noble gas daughters that can be trapped at depth in minerals like beryl, or accumulated in natural gas deposits.

Samples from the Skaergaard igneous intrusion. The Skaergaard is a layered igneous intrusion that was emplaced several kilometers deep in the crust in Greenland during lower Eocene time (Wager and Brown, 1967). A simplified, reconstructed cross-section of the intrusion is shown in Fig. 4-4. The intrusion is roughly funnel-shaped, and has been divided by previous workers into several zones, as shown schematically in the figure. Samples from the lower, middle, and upper zones of the layered series, and from the sandwich horizon were studied here. The sandwich horizon is the region of final crystallization lying between the downward solidifying upper border group, and the upward solidifying layered series. Taylor (1974) and Taylor and Forester (1979) have shown with oxygen isotope data that the upper part of the Skaergaard underwent extensive subsolidus exchange with meteoric water in a hydrothermal circulation system established around the cooling intrusion. If the meteoric water carried dissolved atmospheric noble gases into the upper part of the intrusion, then we might expect to find some relationship between the noble gas content of a sample and its degree of oxygen isotope exchange.

Figure 4-4. Noble gases in the Skaergaard igneous intrusion. The Skaergaard is a layered igneous intrusion that was emplaced into the upper crust in East Greenland about 60 m.y. ago (Wager and Brown, 1967). Taylor (1974) and Taylor and Forester (1979) have shown using oxygen isotopes that meteoric water circulating in the porous basalt interacted with parts of the intrusion. Noble gas measurements show that atmospheric gases were introduced into the rocks during the processes leading to oxygen isotope exchange. Samples with low (exchanged) $\delta^{18}O_{plagioclase}$ contain trapped argon with $^{40}Ar/^{36}Ar$ close to atmospheric. Samples with high (magmatic) $\delta^{18}O_{plag}$ contain trapped juvenile argon with $^{40}Ar/^{36}Ar \geq 6000$.

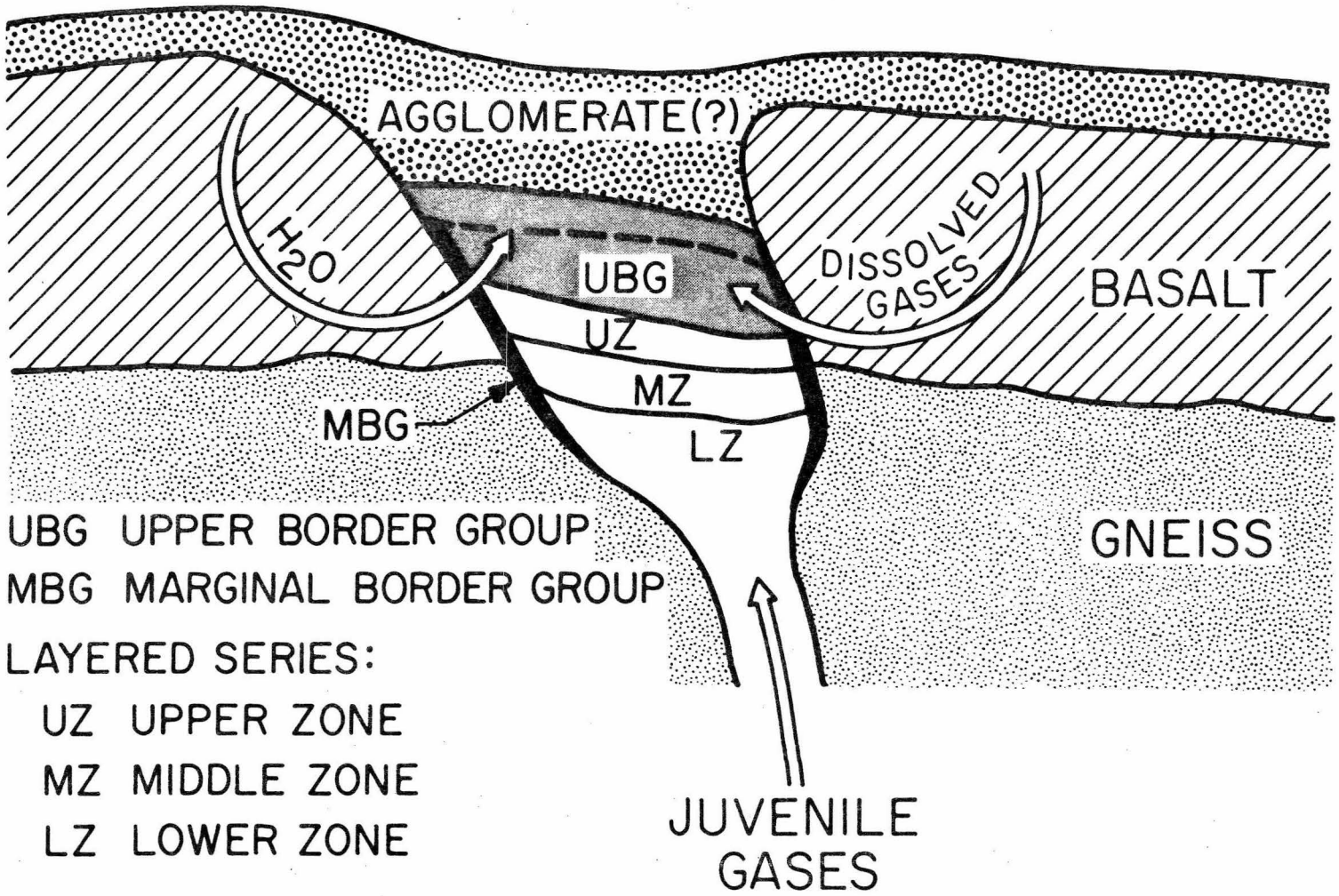
SKAERGAARD (60 m.y.)
AGGLOMERATE(?)
H2O
UBG
UZ
MZ
LZ
MBG
DISSOLVED GASES
BASALT
GNEISS
UBG UPPER BORDER GROUP
MBG MARGINAL BORDER GROUP
LAYERED SERIES:
UZ UPPER ZONE
MZ MIDDLE ZONE
LZ LOWER ZONE
JUVENILE GASES

Figure 4-4

The most striking result of the measurements is the great variability of the argon isotopic composition. After correction for *in situ* decay of K during the last 60 m.y., $^{40}Ar/^{36}Ar$ ratios of argon in the samples range from about 700 to greater than 5000. This variation requires the presence of at least two trapped noble gas components in the samples. The first component is most likely atmospheric argon, with $^{40}Ar/^{36}Ar = 296$. The second component is juvenile argon characterized by a large excess of radiogenic ^{40}Ar. Small amounts of juvenile fission xenon accompany the excess ^{40}Ar. The ratio of fission xenon to radiogenic argon is comparable to the expected production ratio in crustal rocks. The relative elemental abundances of the non-radiogenic noble gases associated with the two argon components appear to differ. Gases accompanying the argon of atmospheric isotopic composition show a strongly fractionated pattern relative to atmospheric abundances. The $^{20}Ne/^{36}Ar$ ratio is several times lower than atmospheric, while $^{132}Xe/^{36}Ar$ is an order of magnitude higher. The noble gases accompanying the juvenile argon more nearly resemble atmospheric abundances. The $^{20}Ne/^{36}Ar$ ratio is equal or slightly greater than atmospheric, while $^{132}Xe/^{36}Ar$ is only a factor of two or three above the air ratio.

Comparison of oxygen isotope data with the noble gas results shows that the occurrence of the two noble gas components can be related to the degree of oxygen isotope exchange. In Fig. 4-5, $^{40}Ar/^{36}Ar$ (corrected for *in situ* decay) is plotted against $\delta^{18}O_{plagioclase}$ (data from Taylor and Forester, 1979). Rocks with $\delta^{18}O_{plag} \geq 6‰$ have undergone little or no exchange with meteoric water, while rocks with lower values have experienced alteration. The argon isotope data

Figure 4-5. Correlation of $^{40}Ar_{excess}/^{36}Ar$ with $\delta^{18}O_{plagioclase}$ in Skaergaard samples. LZ = lower zone, MZ = middle zone, UZ = upper zone, SH = sandwich horizon. $^{40}Ar_{excess}$ is the total ^{40}Ar content less a contribution for *in situ* decay of K over 60 m.y. Unaltered plagioclase contains magmatic oxygen with $\delta^{10}O_{plag} \geq 6‰$. Decreasing $\delta^{18}O_{plag}$ indicates increasing degree of exchange with meteoric water. The variations in argon isotopic composition are reasonably well-correlated with the oxygen isotope shifts. The freshest samples contain juvenile argon characterized by large amounts of excess radiogenic ^{40}Ar, regardless of the original stratigraphic position of the sample in the intrusion. With increasing exchange, $^{40}Ar_{excess}/^{36}Ar$ drops rapidly, approaching the atmospheric composition. It is concluded that atmospheric gases from the meteoric water have been incorporated into the altered rocks of the Skaergaard intrusion.

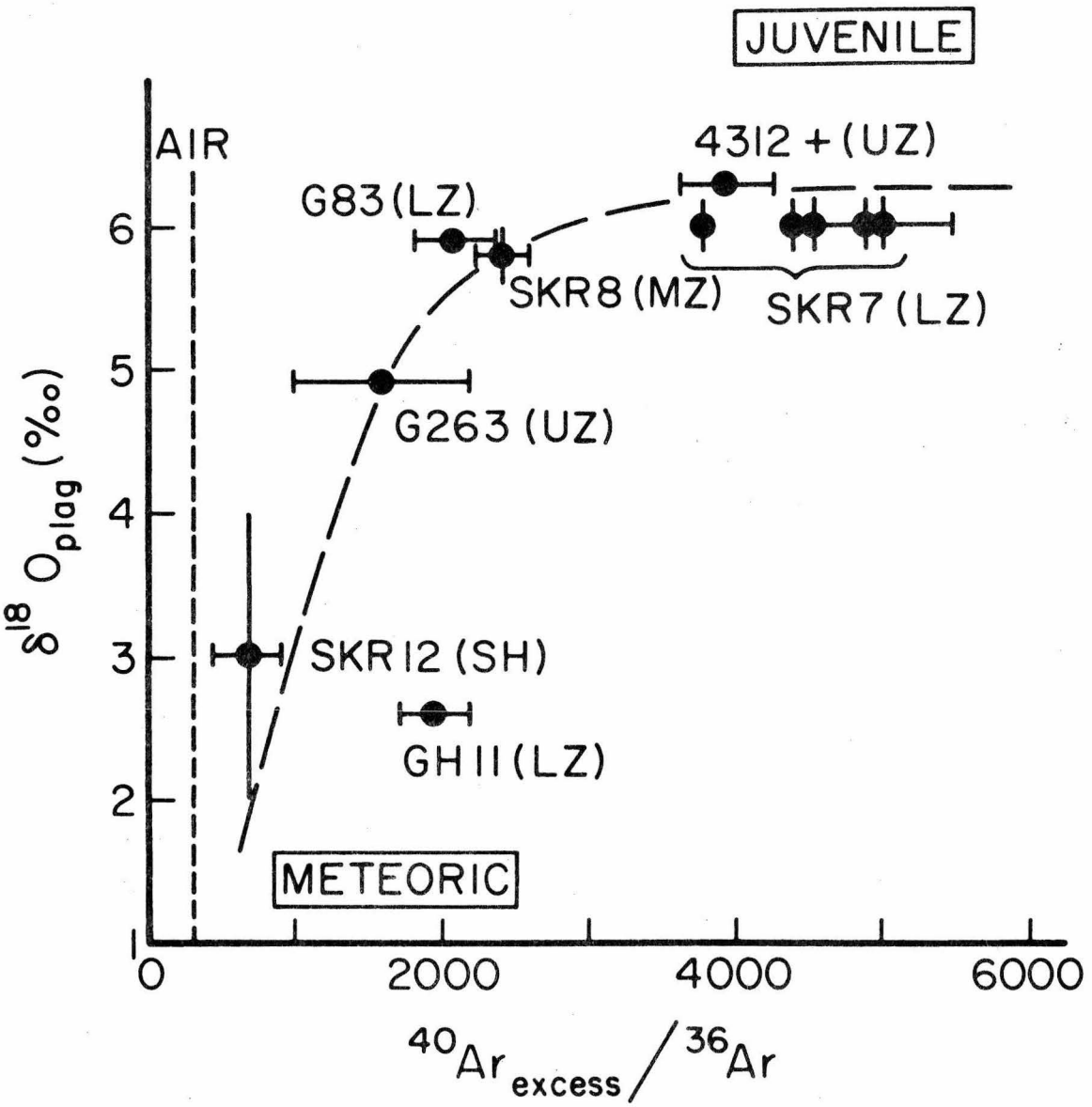
JUVENILE
AIR
4312 + (UZ)
G83 (LZ)
SKR8 (MZ)
SKR7 (LZ)
G263 (UZ)
SKR12 (SH)
GH11 (LZ)
METEORIC
δ18 Oplag (‰)
1
2
3
4
5
6
0
2000
4000
6000
40Ar excess / 36Ar

Figure 4-5

show a good correlation with the oxygen data. Juvenile argon with $^{40}Ar/^{36}Ar \geq 6000$ is dominant in unexchanged samples that have high $\delta^{18}O_{plag}$ values. With increasing meteoric water exchange, as indicated by the lower $\delta^{18}O$ values, the $^{40}Ar/^{36}Ar$ ratios drop rapidly toward the atmospheric value. Samples containing fresh magmatic oxygen contain juvenile argon regardless of the zone of their origin. The decrease in $^{40}Ar/^{36}Ar$ is not related to the vertical stratigraphic position of the sample in the intrusion. For example, we point out rocks 4312+ from the upper zone and SKR-7 from the lower zone that both contain dominantly juvenile argon and unexchanged oxygen. Interaction with meteoric water has occurred in several different zones. Samples SKR-12 (sandwich horizon) and GH11 (lower zone) have both experienced oxygen isotope exchange, and both contain substantial atmospheric argon contributions.

These results indicate that the Skaergaard intrusion was originally emplaced containing a dissolved magmatic component of noble gases characterized by a large excess of radiogenic ^{40}Ar. During solidification, some of the magmatic gases were trapped in the rocks. The exact site of these trapped magmatic gases is not known at present. Meteoric water containing dissolved atmospheric noble gases then interacted with part of the cooling intrusion. Oxygen isotopes were exchanged, and a second noble gas component with atmospheric isotopic composition added to some rocks.

The source of the magmatic noble gas component injected with the magma is not known. It could be either the source region of the basaltic melt, probably the upper mantle, or possibly the ancient crust through which the magma ascended. No convincing evidence of

primary juvenile gases indicative of a mantle source was found in the Skaergaard samples. All measured neon isotopic compositions were atmospheric within errors. Xenon isotopic compositions were also atmospheric, with the exception of very small ^{134}Xe and ^{136}Xe enrichments attributed to secondary juvenile ^{238}U spontaneous fission xenon. The first sample of SKR-7 measured showed a noticeable anomaly at ^{129}Xe, possibly due to primary juvenile radiogenic ^{129}Xe (Smith, 1978). However, subsequent measurements on four additional samples from the same rock failed to confirm the initial result. The first measurement is here withdrawn as a probable experimental artifact. The presence of secondary juvenile ^{40}Ar and fission xenon in the rocks does not distinguish between possible mantle or crustal sources for the magmatic noble gas component.

4.2.2 Samples of igneous rock from the oceanic crust and upper mantle

Another example of a hydrothermal circulation system that may involve transport of noble gases is found at an active mid-ocean spreading ridge (Fig. 4-6). The heat of freshly-intruded magma drives a hydrothermal circulation system that is recharged by percolation of seawater down through fractures along the flank of the ridge. The heated water in the center of the ridge rises, and is emitted along the axis of the ridge in hydrothermal plumes (Weiss et al., 1977). The seawater will carry dissolved atmospheric noble gases into the oceanic crust. A portion of the dissolved gas may become fixed in the crust during hydrothermal alteration of the rock. During crystallization of the magma, juvenile gas components may be lost into the circulating water and injected into the ocean in the heated

Figure 4-6. Noble gases in the oceanic crust and mantle. Hydrothermal circulation of seawater into the oceanic crust occurs at an active spreading ridge. Juvenile gases from the magma may be emitted into the heated water of a rising hydrothermal plume. Dissolved atmospheric gases in the circulating seawater may become fixed in the crust. These gases will be carried away from the ridge by seafloor spreading, and eventually subducted. Gases trapped in sediments may also be subducted. An unknown fraction of the subducted gases may be outgassed during shallow metamorphism of the down-going slab. If this fraction is not large, significant contamination of the upper mantle by atmospheric noble gases can be expected. Mantle convection may eventually bring these gases to the ridge axis, where they may be returned to the atmosphere.

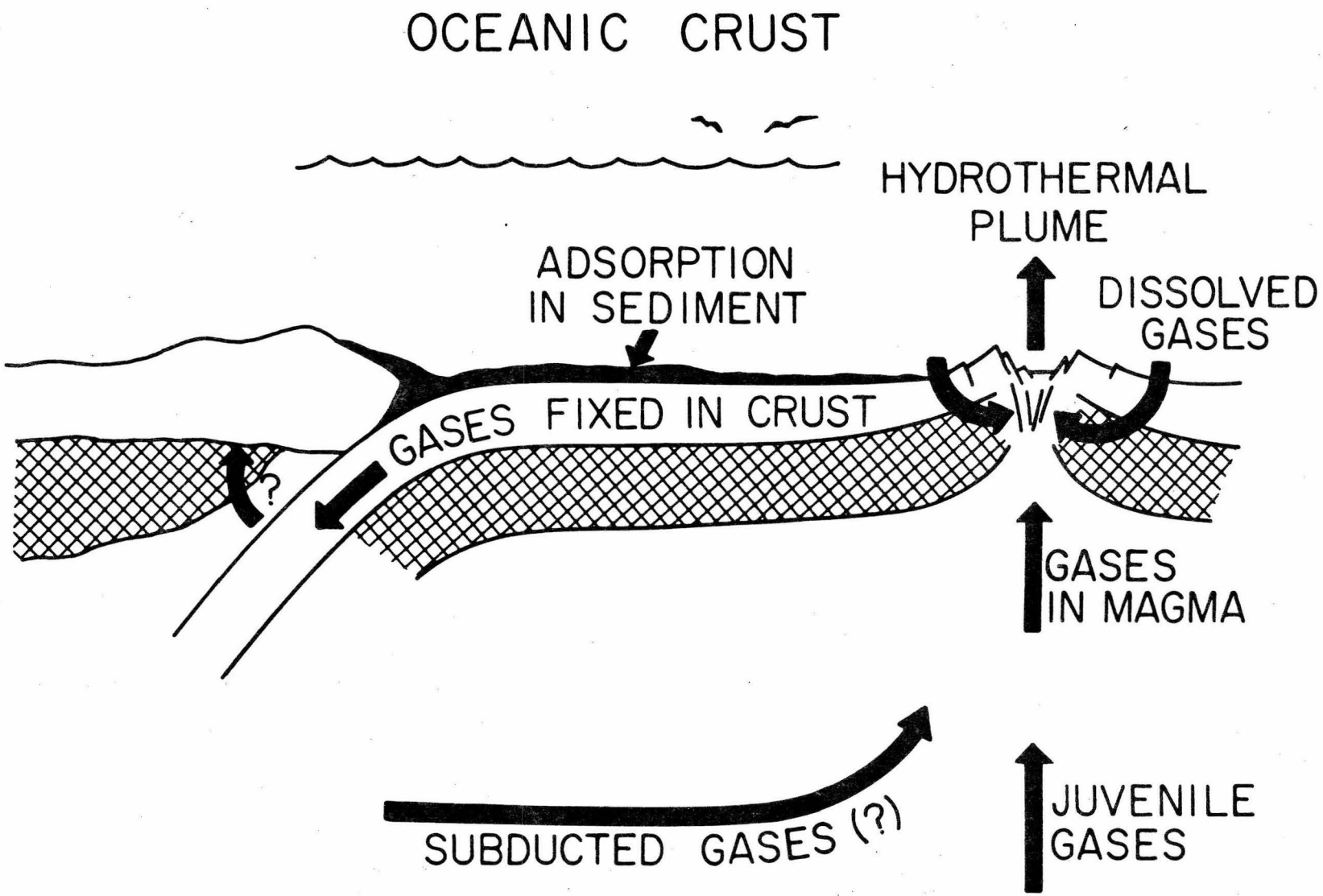
OCEANIC CRUST
HYDROTHERMAL PLUME
ADSORPTION IN SEDIMENT
DISSOLVED GASES
GASES FIXED IN CRUST
?
GASES IN MAGMA
SUBDUCTED GASES (?)
JUVENILE GASES

Figure 4-6

discharge plumes.

Atmospheric gases trapped in the crust will be carried away from the ridge by seafloor spreading, and eventually will be subducted. If the gases are not lost from the slab by heating at shallow depths (arrow with question mark), then subduction of altered oceanic crust could provide a means for transporting atmospheric noble gases into the upper few hundred kilometers of the mantle. Subduction of gases trapped in sediments might provide additional input to the mantle, although these gases would seem more likely to be lost by shallow-level metamorphism. The subducted atmospheric gas could eventually be returned to the spreading axis by mantle convection. Here it could be cycled back into the atmosphere along with juvenile magmatic gases.

The samples studied here include several very fresh, young basalt glasses dredged from mid-ocean ridges (MOR). These glasses were measured particularly to search for juvenile magmatic noble gases from the mantle. Two samples of gabbro from oceanic crust were measured to obtain additional information about the general noble gas content of the oceanic crust. We also studied two upper mantle peridotite nodules erupted as xenoliths in magmas from Hawaii and from Baja, California. Neon, argon, krypton, and xenon concentrations and isotopic compositions were determined.

In agreement with previous work (Funkhouser et al., 1968; Funkhouser and Naughton, 1968), the MOR basalts glass and peridotite samples were found typically to contain excess radiogenic ^{40}Ar indicating the presence of juvenile gases from the upper mantle. We report here the probable first detection of juvenile ^{129}Xe and fission

xenon in MOR basalt glass. A glass sample dredged from the Juan de Fuca ridge in the northeastern Pacific contains xenon with $^{129}Xe/^{132}Xe = 1.016\pm0.027$ (2σ; air = 0.9835) and $^{136}Xe/^{132}Xe = 0.350\pm0.007$ (2σ; air = 0.3299). These isotopic enrichments correspond to concentrations of $2.4\pm1.4 \times 10^{-18}$ moles $^{129}Xe_{rad}$/gram and $1.6\pm0.7 \times 10^{-18}$ moles $^{136}Xe_{SF}$/g. Smaller contributions of these juvenile xenon components appear to be present in two other basalt samples at about the 95% confidence level. In Paper 3 of Appendix B we discuss the problems involved in measuring these slight isotopic effects in samples containing relatively little xenon. We did not obtain sufficiently precise measurements of the xenon isotopic composition in the two peridotites to allow juvenile xenon components to be identified. Upper limits obtained for these samples are several times 10^{-18} moles radiogenic ^{129}Xe and fissiogenic ^{136}Xe. These limits are consistent with the concentrations of juvenile xenon observed in Hawaiian dunite by Hennecke and Manuel (1975) and Kaneoka et al. (1978).

Neither juvenile radiogenic argon nor juvenile xenon was found in a rhyodacite glass from the Galapagos ridge. However, this sample was remarkably enriched in neon with a distinctly non-atmospheric $^{20}Ne/^{22}Ne$ ratio of 10.1 ± 0.1 (2σ). Measured $^{20}Ne/^{36}Ar$ ratios greater than 100 in this sample are higher than in any primordial noble gas component known in the solar system. This fact coupled with the lack of any significant juvenile ^{40}Ar in the rhyodacite lead to the conclusion that the neon enrichment is not due to addition of primary juvenile neon. Rather, it is thought to reflect a fractionation process such as diffusion that strongly enriched originally atmospheric

neon relative to argon and also fractionated ^{20}Ne from ^{22}Ne by about 3%.

No evidence of juvenile noble gas was found in the two oceanic crust gabbros studied. The xenon content of the samples was several times higher than typical of the basalt glass samples, and the xenon was of atmospheric composition. Dymond and Hogan (1973) attributed increased atmospheric noble gas contents in holocrystaline MOR diabase samples to subsolidus interaction with seawater. Gregory and Taylor (1979) have shown from oxygen isotope data on the Oman ophiolite that at least three-quarters of the oceanic crust may have undergone exchange with circulating seawater. From the limited data on crystalline oceanic rocks, and by analogy to the Skaergaard noble gas data discussed earlier, we infer that significant amounts of atmospheric noble gases have probably been added to the oceanic crust by hydrothermal circulation of seawater.

Additional evidence for the addition of atmospheric noble gases to oceanic crustal rock comes from several repeat analyses of fragments from a single basalt glass from the Sheba ridge in the Gulf of Aden. The concentration of juvenile excess ^{40}Ar remained constant to better than ±10% in four samples studied, as would be expected for a dissolved magmatic component. In contrast, the non-radiogenic ^{36}Ar, ^{84}Kr, and ^{132}Xe concentrations in these samples varied by a factor of about seven. A very similar situation was found in two samples of a basalt from the Galapagos ridge. If the non-radiogenic noble gases were juvenile magmatic gases, their concentrations should be homogeneous, just as is the observed concentration of juvenile radiogenic argon. The remarkable variations must be due to relatively late

addition of atmospheric gases to the magma. The distribution of these gases appears to be very uneven on a very small scale ($\leqslant$ 1 cm). The MOR glasses typically are slightly vesicular. Possibly the added atmospheric noble gases reside in occasional unbroached vesicles in the samples studied. The vesicles might have formed from steam injected into the lava as it was erupted onto the ocean bottom. Regardless of the details of the injection, these results imply that most of the non-radiogenic gases in the basalt glasses are atmospheric. The lowest concentrations of non-radiogenic noble gases in MOR basalt glasses should therefore be closest to the immediate pre-eruption gas contents of the magma. These values are approximate upper limits for the primordial noble gas contents of the MOR lavas if we assume that degassing of the magma before its eruption was negligible. The numerical values for the limits are about $^{20}Ne \leqslant 100$, $^{36}Ar \leqslant 40$, $^{84}Kr \leqslant 1$, and $^{132}Xe \leqslant 0.2$, all in 10^{-16} moles/gram. In addition, the $^{40}Ar/^{36}Ar$ ratio of the mantle source of the MOR basalts must be greater than or equal to the largest measured values, about 10^4 for the present samples, and 1.5×10^4 for samples reported in the literature (Fisher, 1975; Dymond and Hogan, 1978). This conclusion should not be sensitive to the degassing history of the magma.

4.2.3 Noble gases in additional crustal samples

Data given in this section are for samples not included among the groups discussed above or in Appendix B. The material studied consists of six whole-rock samples of igneous and metamorphic crustal rock, six samples from carbonatites, two samples of serpentinized kimberlite, and three samples of biotite separates from lamprophyre

dikes. The carbonatites and kimberlite are CO_2-rich samples, probably of upper mantle origin. The biotites were known beforehand to contain excess radiogenic ^{40}Ar (Zartman, private communication). The results of neon, argon, krypton, and xenon concentration measurements are listed in Table 4-3, in units of 10^{-16} moles/g. The concentrations of radiogenic ^{40}Ar in the first six whole-rock samples are generally consistent with production from in situ decay of ^{40}K, based on approximately known geological ages and reasonable estimates of K contents. The range of concentrations of non-radiogenic noble gases are similar to the values measured for the rocks from the Skaergaard intrusion. $^{20}Ne/^{36}Ar$ ratios range from a factor of about four lower than the atmospheric ratio up to the atmospheric value. $^{132}Xe/^{36}Ar$ ratios are about three to thirty times higher than atmospheric. These fractionated abundance patterns are similar to the ones seen for the Skaergaard samples, particularly those showing evidence of addition of atmospheric noble gases and oxygen isotope exchange due to interaction with meteoric water.

The ^{36}Ar and Kr contents of the carbonatite samples tend to be somewhat higher than the typical crustal igneous or metamorphic rocks studied here. Xenon concentrations are roughly similar. Again $^{132}Xe/^{36}Ar$ ratios tend to be higher than atmospheric. The results tabulated for the carbonatites are probably accurate only to a factor of about two. To avoid contamination of the extraction system with CO_2, only very small samples were analyzed, about 0.01 gram instead of the more typical $\sim$ 1 gram. As a result, the absolute amounts of gas measured were generally small, close to the average system blank levels. The estimated uncertainty in the blanks is taken to be about $\pm$ 50%.

Table 4-3. Noble gases in terrestrial igneous and metamorphic samples

Sample	Identification	^{20}Ne	^{36}Ar	^{40}Ar	^{84}Kr	^{132}Xe
			(10^{-16} mole/gram)			
Whole-Rock Samples						
SCB4	Southern California Batholith: San Marcos Gabbro	85	190	5.0×10^5	7.7	1.3
SCB13	Southern California Batholith: Bonsall Tonalite	100	320	1.03×10^6	19.5	6.1
SGAN-2	San Gabriel Anorthosite;California: Ilmenite, Pyroxene, Plagioclase Cumulate	100	830	4.14×10^6	89	10.8
OG33A[1]	Langø Isl., W. Greenland: Scapolite-Bearing Gneiss	470	610	2.07×10^7	15.1	2.4
STW2x	Stillwater Complex, Montana: Gabbro	120	450	1.32×10^7	∿ 30	2.9
PEA-3	Karoo Basalt	670	3800	3.0×10^6	80	7.6
Carbonatite						
OKA-26	Oka, Quebec; Monticellite Sövite	-	400	4.7×10^6	17	3
AL-6	Alnö, Sweden; Carbonatite Dike	-	1600	2.4×10^7	110	13
FEN-6	FEN, Norway; Domkjernite Breccia	(2000)	1200	1.7×10^7	450	5
P7-721	Chilwa Isl., Malawi; Sövite	(1000)	4400	2.0×10^6	130	6
PG158	Kaiserstuhl: Forsterite-Carbonatite	-	2800	8.0×10^5	90	5
MC-17	Magnet Cove,Arkansas; Massive Carbonate	-	1400	6.7×10^5	50	1

Table 4-3. (continued)

Sample Identification		^{20}Ne	^{36}Ar	^{40}Ar	^{84}Kr	^{132}Xe
			(10^{-16} mole/gram)			
Kimberlite						
A	Mule Ear Diatreme, Utah; (Highly Serpentinized)	-	96000	3.9×10^7	5200	260
B	(same)	(360)	105000	5.4×10^7	2800	320
Biotite[2] from Lamprophyre Dikes						
190	Ithaca, N.Y.	-	6900	7.3×10^7	180	7.7
193	Manheim, N.Y.	-	3900	4.8×10^7	91	8.4
H67-28F-1	Phillips Co.,Montana; Williams Dike	-	5800	6.5×10^7	120	7.6
Atmosphere		5020	9610	-	198	7.2

[1]Sample from R. F. Dymek.

[2]Samples from R. E. Zartman.

The ^{36}Ar, Kr, and Xe concentrations in the two serpentinized kimberlite samples from the Mule Ear diatreme are the highest measured in all the samples studied for this thesis. The observed $^{40}Ar/^{36}Ar$ ratios are 400±40 and 510±20. These values suggest that a substantial portion of the argon in the samples is atmospheric. If we assume all the ^{36}Ar to be atmospheric, the inferred radiogenic ^{40}Ar contents of the two samples are 1.0×10^{-9} moles $^{40}Ar/g$ and 2.3×10^{-9} moles $^{40}Ar/g$. The diatreme contains blocks of upper Cretaceous Mancos shale, so must be less than 100 million years old. Unreasonably high K contents of at least ~ 6% and 13% would be required to explain the radiogenic ^{40}Ar by in situ decay. For comparison, the K contents of similar kimberlite from the Moses Rock diatreme located 10 km south of the Mule Ear diatreme is less than or about 0.1% (McGetchin, 1968). This implies that most of the radiogenic argon in the two samples studied is excess. Interpretation of the data is complicated by the presence of abundant xenoliths in the diatremes, including fragments from the Precambrian basement. It is possible that the excess argon in the samples reflects the presence of old xenolith material, and therefore may not be derived from the kimberlite source region.

The three biotite samples had been found previously to contain excess radiogenic argon. From the data in Table 4-3, it can be seen that they also contain relatively high concentrations of ^{36}Ar, Kr, and Xe, similar to the range of values found for carbonatite samples, and higher than in most of the crustal whole-rock samples analyzed. $^{132}Xe/^{36}Ar$ ratios in the biotites are roughly twice the atmospheric value.

Xenon isotopic data obtained for the samples are given in

Table 4-4. For the crustal whole-rock samples, all compositions are essentially atmospheric, with the exception of OG33A. This ancient gneiss from West Greenland contains a measurable amount of fission xenon, probably from in situ spontaneous fission of ^{238}U. Of the carbonatite samples, only P7-721 (Chilwa) contained xenon of demonstrably non-atmospheric composition. The data for the remaining carbonatites are not included because of the large uncertainties ($\sim$ 10%) in the measured ratios. The Chilwa carbonatite sample contains ^{238}U spontaneous fission xenon. The observed concentration of $^{136}Xe_{SF}$ is about 1.8×10^{-16} moles/g. The age of the Chilwa Islands complex is about 130 m.y. (Tuttle and Gittins, 1966, p. 51). If from in situ decay, the measured fission xenon content corresponds to a uranium concentration of about 75 ppm, which is not unreasonable (cf. Tuttle and Gittins, p. 406).

The xenon composition of the Mule Ear kimberlite samples is predominantly atmospheric. Marginal enrichments of ^{134}Xe and ^{136}Xe may indicate a slight component of fission xenon in sample A. The overall atmospheric composition supports the suggestion from the argon data that the large amounts of non-radiogenic noble gases in this material are from the atmosphere. It is plausible that the gases were introduced during the serpentinization of the kimberlite.

Atmospheric composition xenon is also found in the three lamprophyre biotites. No significant excess radiogenic ^{129}Xe is present. Upper limits on the fission ^{136}Xe contents are $\sim 0.1 \times 10^{-16}$ mole/gram, corresponding to $^{136}Xe_{SF}/^{40}Ar_{rad} \leq 2 \times 10^{-9}$. This is a factor of 2 to 4 below the expected production ratio in crustal rocks with K/U of 10^4 by weight. The source of the gases could be slightly

Table 4-4. Xenon isotopes in terrestrial samples

Sample	^{124}Xe	^{126}Xe	^{128}Xe	^{129}Xe	^{130}Xe	^{131}Xe	^{134}Xe	^{136}Xe
	($^{132}Xe \equiv 1000$)							
SCB4	3.3	3.3	70	985	151	790	397	336
	± 1.0	.8	3	13	4	10	7	6
SCB13	4.5	4.0	72	1002	151	790	389	326
	± .4	1.3	4	13	3	6	8	5
SGAN2	4.0	3.6	71.1	989	152	792	390	333
	± .3	.3	.7	5	2	5	3	3
OG33A	3.9	4.3	71	968	148	775	415	365
	± .5	.5	2	23	4	17	8	7
STW2x	3.9	4.1	71	984	153	789	391	331
	± .7	.8	3	6	5	10	5	5
PEA3	-	-	60	1000	155	790	400	351
	±		12	69	11	50	43	26
P7-721	-	-	46	815	103	664	605	604
(Carbonatite)	±		38	74	38	56	48	48
A (Kimberlite)	3.9	3.4	71.9	988	152	791	391	333
	± .3	.3	.8	4	2	3	2	2
B(Kimberlite)	3.6	3.3	70.9	988	150	787	392	332
	± .3	.3	1.1	10	3	5	3	4
190(Biotite)	4.4	3.1	76	976	155	812	380	327
	± .2	.2	5	31	7	25	20	14
193(Biotite)	4.7	3.3	73	995	157	802	392	331
	± 1.0	.9	2	12	4	10	10	10
H67-28F-1(Biotite)	-	3.5	70	994	148	774	392	335
	±	5.3	12	26	10	22	7	7
Atmosphere	3.5	3.3	71.2	984	151	790	388	330

enriched in K, but the difference could have also originated during transport of the gases.

Neon and krypton isotopic compositions were found to be atmospheric when measured; the data have not been included in the tables. Errors on the neon compositions obtained were generally quite large because of the small gas amounts analyzed.

In sum, most or all of the non-radiogenic noble gases reported in this section for crustal samples appear to be atmospheric in isotopic composition. There is a general tendency for $^{20}Ne/^{36}Ar$ ratios to be less than, and $^{132}Xe/^{36}Ar$ ratios to be greater than, the atmospheric values. Varying amounts of radiogenic argon, and occasionally fissiogenic xenon, are present in the samples. In some cases, such as the kimberlite and biotites, the radiogenic argon is in excess over expected in situ production from K.

4.3 DISCUSSION OF RESULTS

In this section we examine three topics. First is the question of the overall noble gas content of the solid Earth. Second is the evidence for the transport of atmospheric noble gases into the crust. Finally, we will estimate the magnitudes of the noble gas fluxes associated with MOR volcanism and with subduction.

4.3.1 Average noble gas concentrations in the solid Earth

In Fig. 4-7, we summarize measured non-radiogenic noble gas contents for whole-rock samples from the continental crust, oceanic crust, and upper mantle. Only new data measured for this thesis are plotted, with the exception of a point for ^{20}Ne (triangle) that represents the average neon concentration in rocks measured by Lord

Figure 4-7. Concentrations of non-radiogenic noble gases in terrestrial rocks. The atmospheric reference concentration (large encircled cross) represents the minimum initial noble gas concentration of the solid Earth. Except for xenon, measured noble gas concentrations are generally much lower than the reference value. This suggests that in general at least the outer portions of the Earth are substantially outgassed of their primordial noble gases.

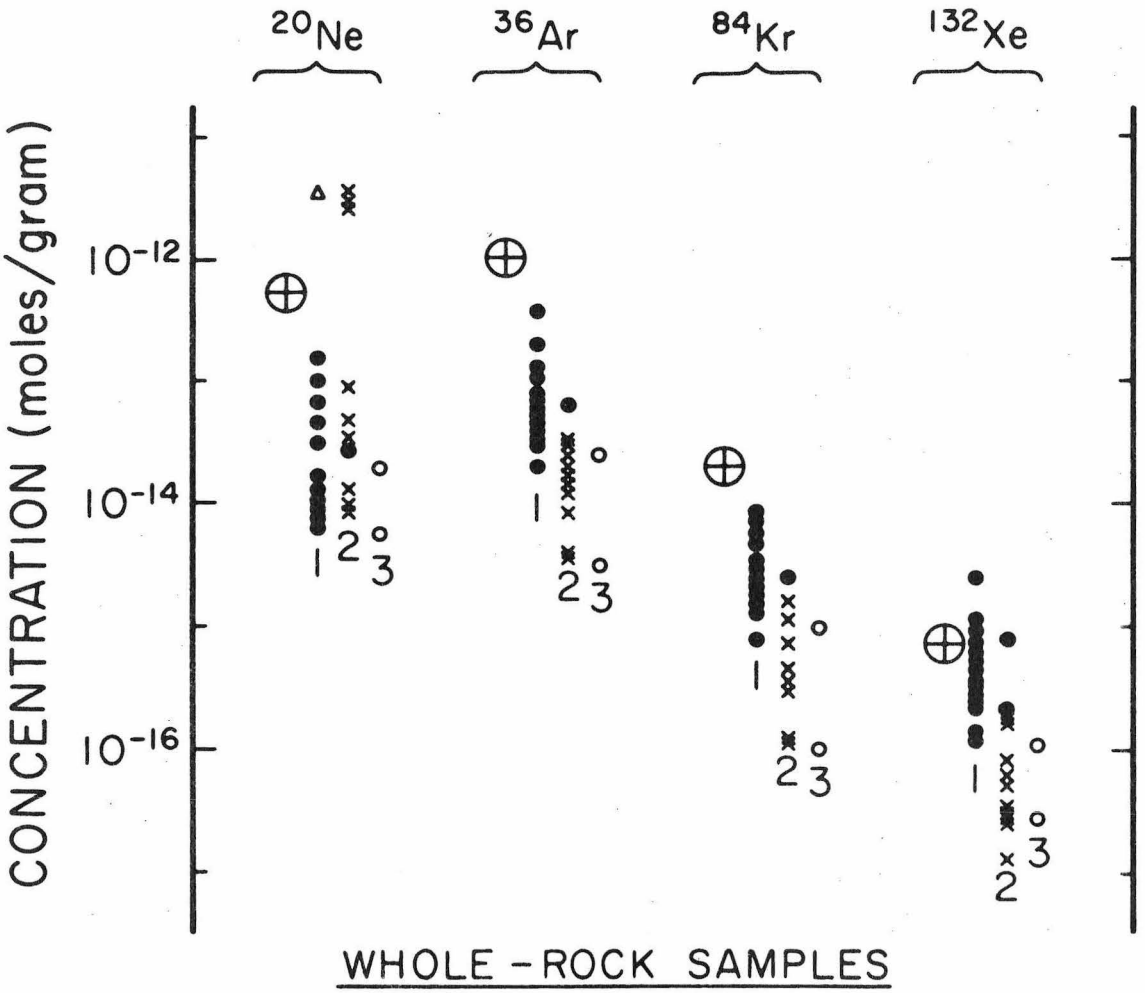

1 = CONTINENTAL CRUST

2 = OCEANIC CRUST; MOR GLASS (×), GABBRO (•)

3 = UPPER MANTLE PERIDOTITE

⊕ = ATMOSPHERE/MASS EARTH

△ = RAYLEIGH (1939)

Figure 4-7

Rayleigh (1939). Compared with the more recent results, Lord Rayleigh's measurements appear to have been systematically too high by a factor of about ten to one hundred. The three very high ^{20}Ne points shown for MOR glasses are the data from the unusual rhyodacite glass from the Galapagos ridge. As discussed above, this neon enrichment is thought to be the result of a near-surface fractionation. The Ar, Kr, and Xe concentrations in most of the other oceanic glasses and upper mantle samples are lower than in the continental crust samples. Neon concentrations are about the same. The concentrations of the heavier noble gases in oceanic gabbros appear from the limited data to be higher than in the MOR glasses, and similar to the values in continental rocks.

The noble gas contents of the rocks should be compared to the atmospheric reference concentrations indicated in Fig. 4-7 by the large encircled crosses. For the solid Earth currently to be an important reservoir of non-radiogenic noble gases, it must consist of rock with average noble gas contents close to or greater than the reference value. With the exception of a few points for neon, and some of the xenon data, the noble gas contents measured in a wide variety of rocks tend to fall substantially below the atmospheric reference. Therefore, if the rocks studied are representative of the entire Earth, then essentially all the non-radiogenic noble gases on the planet are in the atmosphere. A possible exception is xenon. A number of crustal rocks have concentrations equal to the reference atmospheric value. Also, previous investigations have shown that a large fraction, up to about 90%, of the Earth's atmospheric xenon inventory could be trapped in fine-grained sedimentary rocks (Canalas et al., 1968; Phinney, 1972; Fanale and Cannon, 1971).

The assumption that the rocks sampled are representative of the whole Earth cannot, however, be justified. The samples from the crust represent only about 0.5% of the Earth's mass. The mantle peridotites may have sampled gases from the upper few hundred kilometers of the mantle (cf. Kaneoka et al., 1978). However, only about 10% of the Earth's mass lies above a depth of 400 km. If we instead assume that the rocks measured are representative of the outer few hundred kilometers, then the consistently low noble gas contents of the rocks suggest that the outer portions of the Earth, including the portions of the upper mantle sampled by the MOR lavas and peridotite nodules, are thoroughly outgassed. However, we must reiterate an earlier caveat. Gas loss from samples during their transport to the surface may be important. For example, Gramlich and Naughton (1972) suggest that initial concentrations of radiogenic ^{4}He and ^{40}Ar in some Hawaiian ultramafic nodules could have been roughly 100 and 5 times greater respectively than their measured concentrations. It has also been pointed out that about 90% of the juvenile ^{3}He in MOR basalts may have been lost before quenching (Lupton and Craig, 1975). More convincing evidence that the non-radiogenic gases have been thoroughly outgassed from the upper mantle is the high $^{40}Ar/^{36}Ar$ ratio of $\geq 10^{4}$ inferred for the MOR basalt source region (§4.2.2). As discussed by Bernatowicz and Podosek (1978) or Hamano and Ozima (1978), such a high value compared to the low atmospheric ratio of 296 strongly implies nearly complete loss of primordial ^{36}Ar from the upper part of the mantle.

To the best of present knowledge, the remaining ~ 90% of the Earth below a few hundred kilometers in depth could be completely

undegassed. Observations of primary juvenile ^{3}He and $^{129}Xe_{rad}$ in some mantle-derived samples certainly appear to imply that the mantle as a whole has not completely lost its primordial gases (Butler et al., 1963; Mamyrin et al., 1969; Clarke et al., 1969; Tolstikhin et al., 1974; Krylov et al., 1974; Lupton and Craig, 1975; Hennecke and Manuel, 1975). It is instructive to consider briefly a simple two box model for noble gases in the interior of the Earth. We assume that the Earth was initially homogeneous. One box (~ the upper mantle) is taken to be now nearly completely degassed of both radiogenic and non-radiogenic gases, while the second (~ the lower mantle) is assumed to be largely undegassed. Let the mass fraction of the Earth represented by the first box be X.

This two box model has the following simple characteristics. First, essentially all the atmospheric noble gases derive from the outgassed box. Therefore the initial non-radiogenic noble gas contents of the planet and the current contents of the undegassed second box must be greater than the atmospheric reference concentrations (Table 4-1) by a factor of 1/X. However, gas loss during transport to the surface may render unrecognizable such concentration enrichment in deep-seated samples from the undegassed reservoir. Second, the $^{40}Ar/^{36}Ar$ and $^{129}Xe/^{132}Xe$ ratios in the undegassed lower mantle must be nearly the same as the atmospheric values. Unfortunately, this makes samples carrying gases from the undegassed reservoir difficult to distinguish from samples contaminated at shallow levels by atmospheric gases. Third, $^{40}Ar/^{36}Ar$ and possibly $^{129}Xe/^{132}Xe$ in any residual gases in the upper mantle will be greater than the atmospheric values. This is assuming that the non-radiogenic isotopes are more thoroughly

outgassed than the radiogenic isotopes, which may in part be replaced by decay. Fourth, the average K contents of the outgassed reservoir must be about 85/X ppm. The limit of 85 ppm for X = 1 corresponds to the minimum K contents needed for the whole Earth to generate the present ^{40}Ar content of the atmosphere over 4.5 billion years. If we assume that the total K content of the Earth is not likely to be significantly greater than the chondritic value of about 850 ppm, then X must be greater than or equal to 0.1. In other words, at least 10% of the mass of the Earth must be degassed.

The two box model predicts that pristine samples from the mantle could show widely different $^{40}Ar/^{36}Ar$ and possibly also $^{129}Xe/^{132}Xe$ ratios, depending on the degree of outgassing of their source regions. Furthermore, we would expect variations in the ratios to be correlated. High $^{40}Ar/^{36}Ar$ ratios should accompany enhanced $^{129}Xe/^{132}Xe$ ratios, and vice versa. Similar correlations should extend to the helium isotopes. Observed $^{40}Ar/^{36}Ar$ ratios in samples presumed to be from the mantle indeed vary from near atmospheric in amphibole xenocrysts and josephinite (Saito et al., 1978; Bochsler et al., 1978) to $\geq 10^4$ in MOR basalts (Fisher, 1975; this work). However, it is not clear that atmospheric contamination of the sources of some of these samples can be ruled out. Excesses of $^{129}Xe_{rad}$ of up to about 5% over atmospheric have been observed in some samples (Hennecke and Manuel, 1975; Kaneoka et al., 1978; Rison and Kyser, 1977; Downing et al., 1977). The data available at present are too sparse to define reliable correlations--or lack of correlations--among the different isotopic effects. In particular, the number of samples in which the compositions are known for all the noble gases from helium to xenon is

still very small.

4.3.2 Transport of atmospheric noble gases into the outer crust

The identification of atmospheric gases in natural gas samples from deep wells (Zartman et al., 1961) showed that ground water could carry dissolved noble gases several kilometers into the crust. The new results presented here for the Skaergaard intrusion show convincingly that it is possible to transfer the dissolved gases from the water into the rocks. The detailed mechanism by which the transfer takes place cannot be properly addressed from the present whole-rock measurements. Some possibilities include diffusion into major or minor phases in the rocks, or trapping during growth of secondary alteration phases. Trapping might take place by occlusion of an adsorbed layer of gases, or perhaps by the incorporation of fluid inclusions.

The processes involved in transport of the noble gases into the crust can lead to elemental fractionations among the different gases. Both the solution of gases in ground water and the unknown trapping processes may contribute to fractionation. Without knowing the exact processes involved, we can take the relative elemental abundance patterns observed for the altered Skaergaard samples as an indication of the elemental fractionations that may be associated with the incorporation of atmospheric noble gases into the crust.

Elemental abundance patterns for different samples are conveniently compared using a fractionation factor F^m,

$$F^m = \frac{(^mX/^{36}Ar)_{sample}}{(^mX/^{36}Ar)_{air}} \qquad (4\text{-}1)$$

where ^{m}X is any one of the noble gas isotopes. F^{m} for ^{36}Ar is 1 for all samples, and for a sample of air, F^{m} is 1 for all isotopes. In Fig. 4-8, we plot $\log_{10}(F^{m})$ versus m for ^{20}Ne, ^{36}Ar, ^{84}Kr, and ^{132}Xe in samples from the Skaergaard (solid dots), continental crust (open dots), and oceanic crust (crosses). Shown as the light solid and dotted lines are the patterns for air dissolved in fresh water at 28°C ("W") and in molten enstatite silicate ("E") (Kirsten, 1968). Both represent equilibrium solution from an infinite reservoir of air composition. For the Skaergaard data, the lowest $^{20}Ne/^{36}Ar$ ratios, i.e., points furthest below the horizontal "AIR" line in Fig. 4-8, correlate with the highest $^{132}Xe/^{36}Ar$ ratios, and vice versa. The steeply fractionated pattern is characteristic of the samples showing evidence of oxygen-isotope exchange and gas-trapping from ground water. The flatter patterns are associated with high juvenile $^{40}Ar/^{36}Ar$ ratios, and appear to represent the magmatic noble gas component in the Skaergaard samples. We assume that the meteoric water was initially saturated with dissolved atmospheric noble gases with abundances on curve "W" in Fig. 4-8. The abundance patterns in the altered Skaergaard samples are steeper than the "W" curve. The combined transport and alteration processes that led to the trapping of atmospheric gases in these rocks have enhanced the relative abundances of the heavy noble gases. Xenon in particular has been enriched by about an order of magnitude.

The relatively flat pattern of the non-radiogenic gases in the unaltered Skaergaard samples may reflect solution of atmospheric gases in the silicate magma. We consider re-equilibration of noble gases dissolved in water (curve "W" in Fig. 4-8) with molten enstatite. The abundances of the gases absorbed by the melt will be shifted from curve

Figure 4-8. Relative elemental abundances of the noble gases in terrestrial rocks. The fractionation factor is $F^m = (^mX/^{36}Ar)_{sample}/(^mX/^{36}Ar)_{air}$. Curves "W" and "E" show the abundance patterns of air dissolved in water and molten enstatite. The ranges in F^m for the different gases from the Skaergaard and continental crust samples reflect the operation of a variety of elemental fractionation processes. These processes may possibly include solution of gases in ground water, gas loss during percolation of water into the crust, adsorption, trapping, and solution of gases in magma. The characteristic neon enrichments in the MOR basalt glass samples appear to reflect a fractionation process operating commonly in the ocean crust environment.

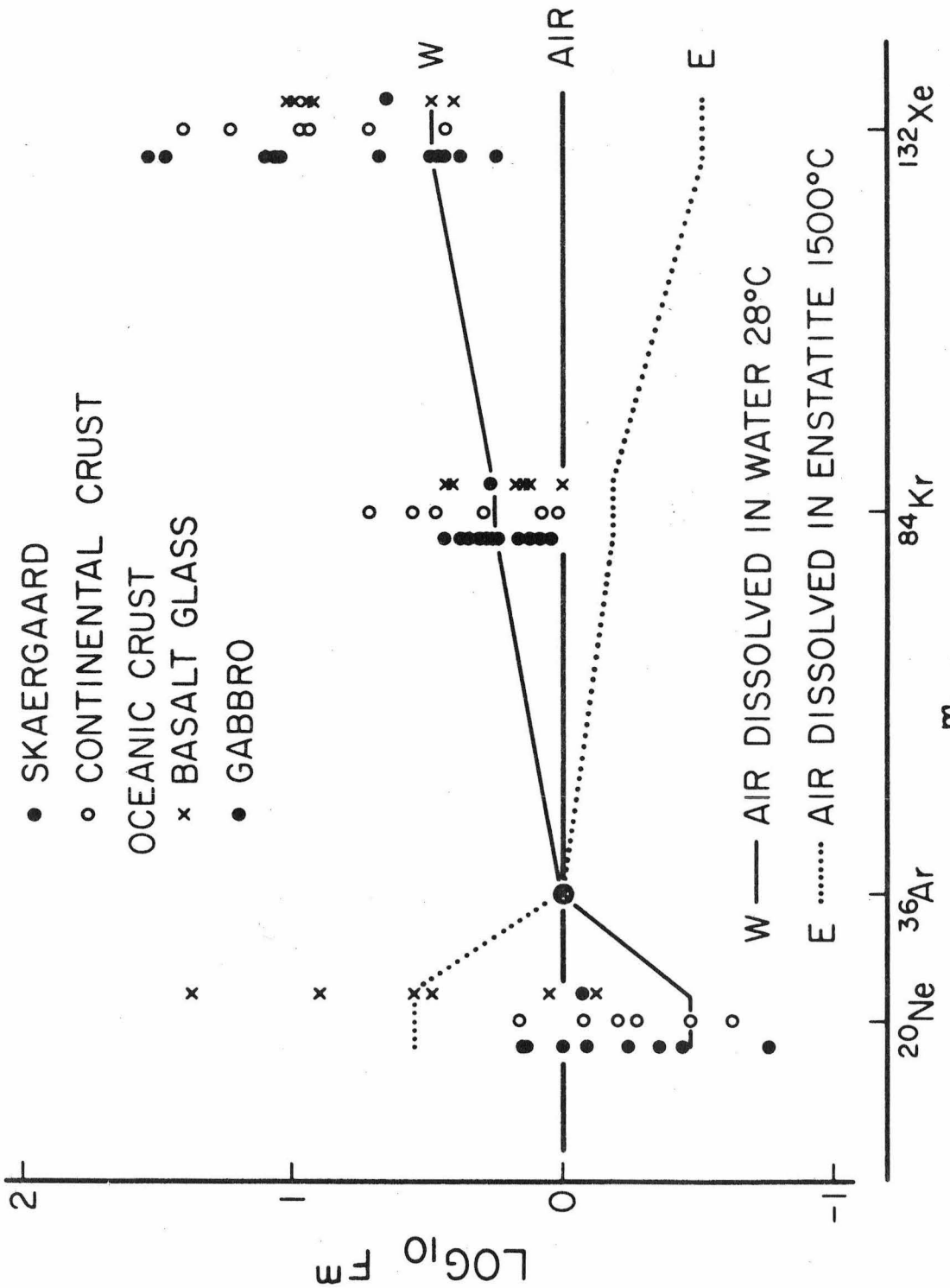
SKAERGAARD
CONTINENTAL CRUST
OCEANIC CRUST
BASALT GLASS
GABBRO
W
AIR
E
W —— AIR DISSOLVED IN WATER 28°C
E ..... AIR DISSOLVED IN ENSTATITE 1500°C
LOG10 F3
2
1
0
-1
20Ne
36Ar
84Kr
132Xe
m

Figure 4-8

"W" toward the enstatite solubility curve "E." The largest shift possible corresponds numerically to the difference between the "AIR" and "E" curves in Fig. 4-8, and occurs for an infinite reservoir of gas. Because of the complementary shapes of the water and enstatite solubility curves, this limit is a nearly flat pattern, very like the unfractionated "AIR" pattern and similar to the flattest abundance patterns among the Skaergaard samples.

We conclude that the different noble gas abundance patterns in the Skaergaard samples probably reflect the action of a spectrum of transport and trapping processes associated with the transfer of atmospheric gases into the crust. Relative abundance patterns in Fig. 4-8 for the other rocks from the continental crust are very similar to the Skaergaard data. Absolute concentration levels and isotopic abundances are also generally similar. We suggest that the non-radiogenic noble gases in these samples are likely to have been incorporated through the same processes involving transport and fixing of atmospheric gases in the crust as documented for the Skaergaard samples.

Gregory and Taylor (1979) present oxygen isotope data for extensive hydrothermal alteration of nearly the whole oceanic crust by circulating seawater. By direct analogy with the Skaergaard results, we would expect that atmospheric noble gases have been added to the oceanic crust during this process. As discussed in section 4.2.2, significant concentrations of atmospheric noble gases were measured in two oceanic gabbros, K9G1 from the Oman ophiolite (circled cross, Fig. 4-8) and 110753/82 from the Romanche fracture zone. Additional measurements on materials of this sort are needed to confirm the

widescale addition of atmospheric gases to the oceanic crust predicted from the oxygen isotope results.

In Fig. 4-8, the argon, krypton, and xenon abundances in the MOR glass samples are generally similar to the pattern for atmospheric gases dissolved in water. This is consistent with the addition to the melt of atmospheric gases originally dissolved in seawater. Such a conclusion was reached earlier from the observed variability of ^{36}Ar concentration and $^{40}Ar/^{36}Ar$ ratio in single glass samples. The neon enrichments of MOR samples are not consistent with simple addition of gases from seawater. An additional, unknown fractionation process is indicated that appears to be characteristic of the oceanic crustal environment, but not the continental.

4.3.3 Evaluation of noble gas fluxes

The average net atmospheric flux $\overline{J}_a$ was defined earlier in this chapter as X_a/T, where X_a is the atmospheric content of a noble gas, and T the age of the Earth. The present net flux J_a can be regarded as the sum of partial fluxes associated with different geologic processes and environments. Partial fluxes into the atmosphere include outgassing accompaning MOR volcanism, sub-aerial eruptions on continents and oceanic islands, or regional and local metamorphism and ground water circulation. Noble gases leave the atmosphere through loss to space, transport and fixing in the crust by ground water, and subduction of gas-bearing material.

The fluxes of noble gases in practice could be used to constrain degassing models of the Earth. We feel that estimates that can be made at present are too uncertain to warrent any further

elaboration of models in this thesis. Discussion of a variety of degassing models is available in the literature (for example, Bernatowicz and Podosek, 1978; Hamano and Ozima, 1978; Hart and Dymond, 1978). Here we will only attempt to estimate the partial fluxes associated with MOR volcanism and with subduction of altered oceanic crust.

We can estimate these noble gas fluxes by multiplying the oceanic crust formation rate times the noble gas concentrations of the MOR magma and the altered oceanic crust respectively. The rate of crust formation used is 5×10^{16} g/yr, estimated from an areal formation rate of 2.5 km^2/yr, an average thickness of about 7 km, and a density of 2.8 g/cm^3. For non-nucleogenic isotopes of neon and heavier gases, the MOR magmatic gas contents were taken as the limits given in section 4.2.2 for MOR basalt glasses least contaminated with atmospheric argon. The ^{40}Ar content of the magma is taken from Dymond and Hogan (1978) to be about 10^{-10} moles/gram. Very approximate upper limits for the outgassing fluxes of radiogenic $^{129}Xe_{rad}$ and fissiogenic ^{136}Xe were calculated from the observed excess $^{129}Xe_{rad}$ and $^{136}Xe_{SF}$ concentrations in MOR glass 111240 (§4.2.2). Helium outgassing fluxes are taken from Craig et al. (1975) and Lupton and Craig (1975). Comparison of the ^3He flux obtained from measurements of excess helium in seawater with the ^3He flux calculated from the helium concentrations in basalts reveals a factor of ten discrepancy. At face value, too little ^3He is injected into the oceans by the magma to explain the observed concentrations in seawater. This situation may be resolved either by assuming the measured ^3He contents of MOR gas samples are only about 10% of the initial magmatic concentrations,

or by assuming that not 7 km but rather 50 to 70 km of the surface is degassed during formation of new crust (Lupton and Craig, 1975). The ^{3}He outgassing flux discrepancy suggests that the nominal calculated values for the other noble gases may be an order of magnitude too low as well.

The calculated subduction fluxes correspond to the range of observed noble gas contents in gabbro K9G1 (this work) and diabase samples TW4-118 and TW10-3 (Dymond and Hogan, 1973). These estimated fluxes are only very tentative values since it is not known how representative these few samples are of the entire oceanic crust. For ^{40}Ar, a contribution due to decay of K in the oceanic crust ($\sim$ 0.26 wt. % K_2O; Melson et al., 1968) has been included. The average age of subducted crust is taken to be 200 million years. This added radiogenic component corresponds to roughly half the ^{40}Ar in the subducted material. A subduction flux for ^{3}He is calculated from the estimated rate of infall of interplanetary dust. Merrihue (1964) and Tilles (1966) showed that oceanic sediments contained a detectable noble gas contribution from interplanetary dust. Recently Rajan et al. (1977) have found average ^{4}He contents of $\sim 4 \times 10^{-6}$ moles/g in several particles collected in the upper atmosphere. The gas is interpreted as implanted solar wind. A $^{3}He/^{4}He$ ratio of about 3×10^{-4} is assumed, along with an infall rate of $\sim 10^{10}$ g/yr (Brownlee, priv. comm.) to calculate the possible ^{3}He flux.

The results of these estimates are summarized in Fig. 4-9. Except for helium, the data are presented as relative fluxes normalized to the average atmospheric fluxes $\bar{J}_a$ from Table 4-2 (filled circles). For helium, the normalizing fluxes (half-filled circles) are the

Figure 4-9. Relative fluxes of noble gases into and out of the oceanic crust and mantle. Fluxes are normalized to the average net atmospheric values (atmospheric gas content ÷ 4.5 AE), except for He which is normalized to present atmospheric loss rates. The higher He outgassing fluxes from Craig et al. (1975) are calculated from excess He concentration profiles observed in ocean water. These values are about ten times the fluxes deduced from the He concentrations in MOR basalt glasses (Lupton and Craig, 1975). The Ne, Ar, Kr, and Xe outgassing fluxes are calculated from the observed noble gas concentrations in MOR basalt glasses. The lower points represent the nominal calculated values. The upper points have been increased by a factor of ten in accord with the apparent discrepancy in the ^{3}He fluxes. The subduction fluxes are based on very limited data for the range of atmospheric noble gas contents of crystalline oceanic crustal rocks. The ^{3}He subduction flux is a speculative value calculated assuming all infalling interplanetary dust trapped in sediments is transported into the upper mantle. From these tentative results, the rate of subduction of noble gases may balance or even surpass the flux outgassed at the mid-ocean spreading ridges.

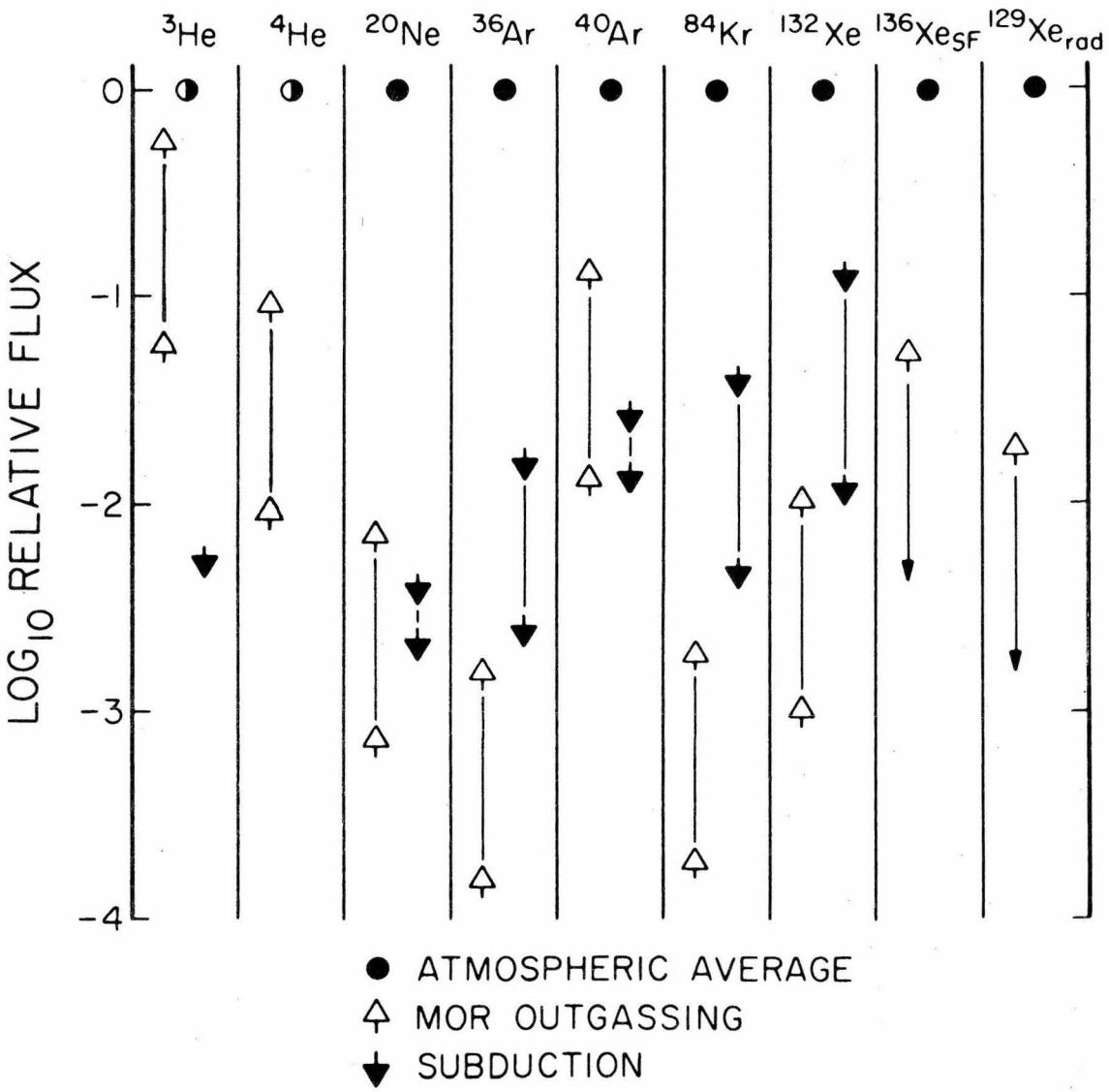
^{3}He
^{4}He
^{20}Ne
^{36}Ar
^{40}Ar
^{84}Kr
^{132}Xe
$^{136}Xe_{SF}$
$^{129}Xe_{rad}$
0
-1
-2
-3
-4
LOG_{10} RELATIVE FLUX
ATMOSPHERIC AVERAGE
MOR OUTGASSING
SUBDUCTION

Figure 4-9

calculated values for the current escape rates of helium from the atmosphere (see Table 4-2). Outgassing fluxes are indicated by the open, upward-pointing arrows, subduction fluxes by the solid, downward-pointing arrows. For helium, the upper open triangles correspond to the outgassing flux deduced from the seawater helium measurements. The lower value represents the ten times smaller fluxes deduced from MOR basalt glass measurements. For the other noble gases the nominal outgassing fluxes calculated from the MOR basalt glass data are the lower open triangles. The upper limits are a factor of ten higher, corresponding to the uncertainty suggested by the helium data. This factor of ten is also incorporated in the upper limits shown for $^{136}Xe_{SF}$ and $^{129}Xe_{rad}$. If $\bar{J}_a$ for xenon is a factor of ten higher than the value in Table 4-2 because of trapping of atmospheric xenon in sediments, then the relative xenon fluxes in Fig. 4-9 will be decreased by the same factor.

The ^{3}He flux from the oceans is within error the same as the calculated total atmospheric loss rate for this gas. The ^{4}He flux is much lower. Most of the ^{4}He in the atmosphere is outgassed from the U,Th-rich continents rather than the oceans. The relative outgassing fluxes for the other noble gases are substantially lower than the atmospheric average values. This is consistent with, but not necessarily indicative of, a source region that is thoroughly outgassed. It should be remembered that the MOR outgassing fluxes are only partial fluxes. For example, we have no way at present of estimating the fluxes of noble gases that may be outgassed through the continents.

A rather unexpected feature of the data shown in Fig. 4-9 is that the potential fluxes of subducted gases are about equal or even

larger than the estimated outgassing fluxes for ^{20}Ne, ^{36}Ar, ^{84}Kr, and ^{132}Xe. Such a situation is not incompatible with some degassing models. In an extreme case, one could imagine an early catastrophic outgassing of noble gases followed by no further release, only gradual subduction of atmospheric gases trapped in the oceanic crust. The comparatively high subduction fluxes suggest that subduction of atmospheric noble gases could be an important source for non-radiogenic gases in the upper mantle. If we simply multiply the present subduction flux by 4×10^9 years, and distribute the gas uniformly over the upper 10% of the Earth (the outer 400 km), we obtain the concentrations given in the first column in Table 4-5. The ^3He concentration reflects the speculative influx from interplanetary dust, while the other data reflect the average noble gas contents of the altered oceanic crustal gabbro and diabase samples. For comparison, the second column includes average measured noble gas contents for minerals from the Hawaiian peridotite nodule studied here, plus average ^3He contents of several nodules given by Tolstikhin et al. (1974). For argon, krypton, and xenon, the potential concentrations due to subduction are four or five times the measured concentrations in the peridotite. For ^3He and neon the concentrations are similar. Thus it is possible that the non-radiogenic noble gases in the peridotite samples could largely have arisen through contamination of the upper mantle by subducted atmospheric noble gases. If the upper mantle does contain significant amounts of subducted gases, then the non-radiogenic noble gases measured in mantle-derived samples cannot necessarily be assumed to be juvenile gases.

Table 4-5. Integrated contribution of atmospheric gases to the upper mantle by subduction[1]

	Subduction over 4 AE[2]	Peridotite[4]
^{3}He	$(6\times10^{-17})^{3}$	$(\sim 5\times10^{-17})^{3}$
^{20}Ne	1.2×10^{-14}	2×10^{-14}
^{36}Ar	1.0×10^{-13}	2×10^{-14}
^{40}Ar	2.9×10^{-11}(atm) 2.7×10^{-11}(rad)	2×10^{-11}
^{84}Kr	5×10^{-15}	10^{-15}
^{132}Xe	4×10^{-16}	10^{-16}

[1]Concentrations in moles/gram.

[2]Gases distributed over the outer 10% of the Earth's mass. Present flux assumed constant over past 4 AE. Values shown are obtained from average fluxes calculated from K9G1 and 110753/82 gabbros (this work) plus TW4 and TW10 diabases (Dymond and Hogan, 1973).

[3]Influx calculated by assuming all ^{3}He carried in interplanetary dust falling into oceanic sediments is subducted. Peridotite datum from Tolstikhin et al. (1974).

[4]Data for Hawaiian peridotite measured in this work. CSQ35-1A peridotite from Baja, California, contains 3 to 10 times less gas.

REFERENCES, CHAPTER 4

Bernatowicz T. J. and Podosek F. A. (1978) Nuclear components in the atmosphere. In Terrestrial Rare Gases (eds. E. C. Alexander, Jr. and M. Ozima) pp. 99-135. Center for Academic Publications Japan.

Bochsler P., Stettler A., Bird J. M., and Weathers M. S. (1978) Excess ^{3}He and ^{21}Ne in Josephinite. Earth Planet. Sci. Lett. 39, 67-74.

Brownlee D. E. (1979) private communication. Present address: U. of Washington, Seattle, Washington 98195.

Butler W. A., Jeffery P. M., Reynolds J. H., and Wasserburg G. J. (1963) Isotopic variations in terrestrial xenon. J. Geophys. Res. 68, 3283-3291.

Canalas R. A., Alexander E. C., Jr., and Manuel O. K. (1968) Terrestrial abundances of noble gases. J. Geophys. Res. 73, 3331-3334.

Clarke W. B., Beg M. A., and Craig H. (1969) Excess ^{3}He in the sea: evidence for terrestrial primordial helium. Earth Planet. Sci. Lett. 6, 213-220.

Craig H., Clarke W. B., and Beg M. A. (1975) Excess ^{3}He in deep water on the East Pacific Rise. Earth Planet. Sci. Lett. 26, 125-132.

Damon P. E. and Kulp J. L. (1958) Excess helium and argon in beryl and other minerals. Amer. Mineral. 43, 433-459.

Downing R. G., Hennecke E. W., and Manuel O. K. (1977) Josephinite: A terrestrial alloy with radiogenic xenon-129 and the noble gas imprint of iron meteorites. Geochem. J. 11, 219-229.

Dymond J. and Hogan L. (1973) Noble gas abundance patterns in deep-sea basalts--primordial gases from the mantle. Earth Planet. Sci. Lett. 20, 131-139.

Dymond J. and Hogan L. (1978) Factors controlling the noble gas abundance patterns of deep-sea basalts. Earth Planet. Sci. Lett. 38, 117-128.

Fanale F. P. and Cannon W. A. (1971) Physical adsorption of rare gas on terrigenous sediments. Earth Planet. Sci. Lett. 11, 362-368.

Fisher D. E. (1975) Trapped helium and argon and the formation of the atmosphere by degassing. Nature 256, 113-114.

Funkhouser J. G., Fisher D. E., and Bonatti E. (1968) Excess argon in deep-sea rocks. Earth Planet. Sci. Lett. 5, 95-100.

Funkhouser J. G. and Naughton J. J. (1968) Radiogenic helium and argon in ultramafic inclusions from Hawaii. J. Geophys. Res. 73, 4601-4607.

Gramlich J. W. and Naughton J. J. (1972) Nature of source material for ultramafic minerals from Salt Lake Crater, Hawaii, from measurement of helium and argon diffusion. J. Geophys. Res. 77, 3032-3042.

Gregory R. T. and Taylor H. P. (1979) $^{18}O/^{16}O$ variations in gabbro, diabase and volcanic sections in Semail ophiolite, southeastern Oman Mountains and the nature of hydrothermal alteration in the oceanic crust. Abstract submitted to International Ophiolite Symposium, Nicosia, Cyprus, 1-8 April 1979.

Hamano Y. and Ozima M. (1978) Earth-atmosphere evolution model based on Ar isotopic data. In Terrestrial Rare Gases (eds. E. C. Alexander, Jr. and M. Ozima) pp. 155-171. Center for Academic Publications Japan.

Hart R. and Dymond J. (1978) The argon isotopic composition of the oceanic crust and a model for formation of the sialic crust--atmosphere from the upper mantle. In Short Papers of the 4th International Conference on Geochemistry, Cosmochemistry, and Isotope Geology (ed. R. E. Zartman) pp. 172-174. U. S. Geol. Surv. Open File Report 78-701.

Hawthorne F. C. and Černý P. (1977) The alkali-metal positions in Cs-Li beryl. Can. Mineral. 15, 414-421.

Hennecke E. W. and Manuel O. K. (1975) Noble gases in an Hawaiian xenolith. Nature 257, 778-780.

Johnson H. E. and Axford W. I. (1969) Production and loss of He^3 in the Earth's atmosphere. J. Geophys. Res. 74, 2433-2438.

Kaneoka I. (1975) Non-radiogenic argon in terrestrial rocks. Geochem. J. 9, 113-124.

Kaneoka I., Takaoka N., and Aoki K. (1978) Rare Gases in mantle-derived rocks and minerals. In Terrestrial Rare Gases (eds. E. C. Alexander, Jr. and M. Ozima) pp. 71-83. Center for Academic Publications Japan.

Kirsten T. (1968) Incorporation of rare gases in solidifying enstatite melts. J. Geophys. Res. 73, 2807-2810.

Krylov A. Ya., Mamyrin B. A., Khabarin L. A., Mazina T. I., and Silin Yu. I. (1974) Helium isotopes in ocean-floor bedrock. Geochemistry Int.11, 839-844.

Lupton J. E. and Craig H. (1975) Excess ^{3}He in oceanic basalts: evidence for terrestrial primordial helium. Earth Planet. Sci. Lett. 26, 133-139.

Mamyrin B. A., Tolstikhin I. N., Anufriev G. S., and Kamenskiy I. L. (1969) Anomalous isotopic composition of helium in volcanic gases. Dokl. Akad. Nauk SSSR 184, 1197-1199.

Mazor E. (1977) Geothermal tracing with atmospheric and radiogenic noble gases. Geothermics 5, 21-36.

McGetchin T. R. (1968) The Moses Rock dike: geology, petrology, and mode of emplacement of a kimberlite-bearing breccia dike, San Juan County, Utah. Doctoral dissertation, California Inst. of Tech.

Melson W. G., Thompson G., and van Andel Tj. H. (1968) Volcanism and metamorphism in the mid-Atlantic Ridge, 22° N. latitude. J. Geophys. Res. 73, 5925-5941.

C. Merrihue (1964) Rare gas evidence for cosmic dust in modern Pacific red clay. Ann. N. Y. Acad. Sci. 119, 351-367.

Naughton J. J., Lee J. H., Keeling D., Finlayson J. B., and Dority G. (1973) Helium flux from the Earth's mantle as estimated from Hawaiian fumarolic degassing. Science 180, 55-57.

Pepin R. O. and Phinney D. (1979) Components of xenon in the solar system. Geochim. Cosmochim. Acta. Submitted for publication.

Phinney D. (1972) ^{36}Ar, Kr, and Xe in terrestrial materials. Earth Planet. Sci. Lett. 16, 413-420.

Rajan R. S., Brownlee D. E., Tomandl D., Hodge P. W., Farrar H. IV, and Britten R. A. (1977) Detection of ^{4}He in stratospheric

particles gives evidence of extraterrestrial origin. Nature 267, 133-134.

Rayleigh (1939) Nitrogen, argon and neon in the earth's crust with applications to cosmology. Proc. Roy. Soc. (London) A 170, 451-464.

Rison W. and Kyser K. (1977) Rare gases, oxygen and hydrogen in Hawaiian xenoliths and basalts (abstract). EOS Trans. Amer. Geophys. Union 58, 537.

Saito K., Alexander E. C., Jr., and Basu A. R. (1978) Rare gases in mantle-derived amphiboles. In Short papers of the 4th International Conference on Geochemistry, Cosmochemistry, and Isotope Geology (ed. R. E. Zartman) pp. 368-370. U. S. Geol. Surv. Open File Report 78-701.

Smith S. P. (1978) Noble gases in plutonic igneous rocks. In Short Papers of the 4th International Conference on Geochemistry, Cosmochemistry, and Isotope Geology (ed. R. E. Zartman) pp. 400-402. U. S. Geol. Surv. Open File Report 78-701.

Strutt R. J. (1908) Helium and radio-activity in rare and common minerals. Proc. Roy. Soc. (London) A 80, 572-594.

Taylor H. P., Jr. (1968) The oxygen isotope geochemistry of igneous rocks. Contrib. Mineral. Petrol. 19, 1-71.

Taylor H. P., Jr. (1974) The application of oxygen and hydrogen isotope studies to problems of hydrothermal alteration and ore deposition. Econ. Geol. 69, 843-883.

Taylor H. P., Jr. and Forester R. W. (1971) Low-^{18}O igneous rocks from the intrusive complexes of Skye, Mull, and Ardnamurchan, western Scotland. J. Petrol. 12, 465-497.

Taylor H. P., Jr. and Forester R. W. (1979) An oxygen and hydrogen isotope study of the Skaergaard intrusion and its country rocks: A description of a 55-m.y. old fossil hydrothermal system. Preprint.

D. Tilles (1966) Implantation in interplanetary dust of rare-gas ions from solar flares, Science 153, 981-984.

Tolstikhin I. N., Mamyrin B. A., Khabarin L. B., and Erlikh E. N. (1974) Isotope composition of helium in ultrabasic xenoliths from volcanic rocks of Kamchatka. Earth Planet. Sci. Lett. 22, 75-84.

Tuttle O. F. and Gittins J. (1966) Carbonatites. Interscience.

Wager L. R. and Brown G. M. (1967) Layered Igneous Rocks. W. H. Freeman.

Wasserburg G. J., Czamanske G., Faul H., and Hayden R. J. (1957) The isotopic composition of argon and carbon in helium wells. In Proceedings of the Conference on Nuclear Geology. Publ. 572, pp. 156-158. Nat. Acad. Sci., Nat. Res. Council.

Wasserburg G. J. and Mazor E. (1965) Spontaneous fission xenon in natural gases. In Fluids in Subsurface Environments - A Symposium. Memoir No. 4, pp. 386-398. Amer. Assoc. of Petroleum Geologists.

Wasserburg G. J., Mazor E., and Zartman R. E. (1963) Isotopic and chemical composition of some terrestrial natural gases. In Earth Science and Meteoritics (eds. J. Geiss and E. D. Goldberg) pp. 219-240. North Holland.

Weiss R. F., Lonsdale P., Lupton J. E., Bainbridge A. E., and Craig H. (1977) Hydrothermal plumes in the Galapagos Rift. Nature 267, 600-603.

Zartman R. E. (1976) private communication. Present address: U. S. Geological Survey, Denver, Colorado 80225.

Zartman R. E., Wasserburg G. J., and Reynolds J. H. (1961) Helium, argon, and carbon in some natural gases. J. Geophys. Res. 66, 277-306.

CHAPTER 5. SUMMARY

The isotopic and elemental abundances of the noble gases in the solar system are highly variable. In the sun and giant planets the noble gases are abundant, and occur in cosmic proportions. In the rocky terrestrial planets and meteorites the noble gases are depleted from the cosmic or solar abundances by many orders of magnitude. The depletions characteristic of the planetary gases are most severe for the lighter gases. Coupled to the abundance variations are major differences in the isotopic compositions of the noble gases. The ratio of ^{3}He to ^{4}He is a factor of three to four lower in the planetary component than in the solar. The average $^{20}Ne/^{22}Ne$ ratio in planetary gases is about 50% lower than in the solar component, and the total range in trapped neon compositions is nearly a factor of thirty. Nuclear reactions occurring in meteorites and the planets can lead to additional isotopic variation in all the noble gases. In this thesis we have investigated the isotopic variability of primordial noble gases using a simple two-component mixing model for primordial neon. Neon was measured in several meteorites to study the composition and occurrence of the cosmogenic and trapped primordial end-members. Measurements of terrestrial noble gases have been used to determine the concentrations and isotopic compositions of gases in rocks and minerals from different geologic settings, and to examine the cycling of noble gases between different parts of the Earth.

To model neon isotopic variations we have assumed that the solar system formed from a mixture of interstellar gas and dust, each with a different neon isotopic composition. The neon content of the dust is unlikely to have been high enough to significantly affect the average composition of a mixture of gas and dust in cosmic proportions. Solar neon can therefore be identified with the composition of neon in the interstellar gas. We have

taken the neon composition of the solar wind, $^{20}Ne/^{22}Ne = 13.7$, $^{21}Ne/^{22}Ne = 0.033$, to represent solar and therefore gas-phase neon. Evidence that dust-phase neon is isotopically heavy compared to solar neon is found from the neon in meteorites and the Earth's atmosphere. The heaviest component of trapped meteoritic neon is neon-E, with $^{20}Ne/^{22}Ne \leq 0.6$ and $^{21}Ne/^{22}Ne \leq 0.005$. This component is taken to be pure dust-phase neon. Intermediate compositions observed in meteorites and planets are presumed to reflect mixing between gas and dust. Simple mixtures of gas and dust involving no neon loss during mixing result in linear correlation lines on the neon three-isotope diagram ($^{20}Ne/^{22}Ne$ vs. $^{21}Ne/^{22}Ne$) and the neon composition-concentration diagram ($^{20}Ne/^{22}Ne$ vs. $1/^{22}Ne$). Some scatter about the correlation lines may arise if the dust consists of a mixture of neon-carrying grains and inert, gas-free grains that can be separated before gas-phase neon is admixed. A simple model was constructed for the solar wind implantation of gas-phase neon into dust grains. Neon is assumed to be implanted into a thin surface layer of constant thickness in which the isotopes are well-mixed. Neon is lost from the layer both by sputtering of individual neon atoms, and as a result of the overall erosion of the grain surface by sputtering and other processes. This model predicts solar wind implantation into neon-E-bearing grains can give rise to non-linear correlations on the neon composition-concentration diagram. The non-linearity arises as a result of preferential sputtering of the lighter neon isotopes. The predicted deviations from linearity are not large, only a few percent in $^{20}Ne/^{22}Ne$, compared to the order of magnitude difference between the compositions of the implanted solar neon and the primordial neon in the solids. We conclude that simple mixing processes that combine dust and gas will yield essentially linear mixing lines on the diagrams used to interpret neon abundance data.

Literature data show that neon in bulk meteorite samples consists of galactic cosmic ray spallation neon and trapped neon. The trapped neon is a mixture of isotopically-light neon with $^{20}Ne/^{22}Ne$ about 13 (neon-S) and planetary gas with $^{20}Ne/^{22}Ne$ about 8 (neon-A). The planetary neon-A composition has been found to reside in gas-rich, carbon-rich separates that make up less than a few percent of the meteorite. The gas-rich separates themselves consist of several distinct phases with different neon compositions, ranging from pure neon-E to values intermediate between neon-A and neon-S.

We have reported the results of several experiments to measure the abundance and isotopic composition of neon end-members in meteorites. Comparison of cosmogenic neon compositions in bulk meteorite samples and plagioclase separates has been used to deduce the composition of cosmic-ray spallation neon produced from sodium. Na-spallation neon with $^{21}Ne/^{22}Ne$ = 0.34 and $^{20}Ne/^{22}Ne \sim 0.3$ is strongly enriched in ^{22}Ne compared to spallation neon produced in other target elements. In samples enriched in sodium, care must be taken not to misinterpret ^{22}Ne enrichments from Na-spallation neon as trapped neon-E.

A new, high-resolution stepwise heating technique was used to examine the neon isotopic variations in great detail in three carbonaceous chondrites. The isotopically-light neon-S end-member of meteoritic neon was shown to have $^{20}Ne/^{22}Ne = 13.7$ in Mokoia. This is the same composition as the modern solar wind. Available literature data on helium, neon, and argon in Mokoia identify this neon-S as implanted solar wind. We therefore infer that the neon composition of the solar wind has been constant since before Mokoia was compacted into its present form. High-resolution neon-release patterns for samples of Murchison and Cold Bokkeveld are very complex. Large isotopic variations and multiple neon release peaks are interpreted as

reflecting the extraction of different mixtures of dust-phase and gas-phase neon from several distinct sites in the meteorites.

A detailed study of neon in inclusions and bulk samples from the Allende meteorite was carried out to search for correlation between neon-E and oxygen or magnesium isotopic anomalies found in the inclusions. ^{22}Ne and ^{36}Ar enrichments were found in several inclusions, but these isotopic effects are explained as cosmogenic noble gases produced by cosmic-ray bombardment of Na, Cl-rich minerals in the inclusions. No evidence of an enhanced neon-E content was found in any of the samples containing oxygen or magnesium isotopic anomalies.

We have compared the observed neon compositions and concentrations in meteorites with the simple mixing models constructed here. The comparison leads to the conclusion that at least two separate episodes of mixing are required to explain the bulk meteorite data. One episode resulted in the addition of neon-S to the gas-rich mineral separates in meteorites. It established the average neon-A composition characteristic of bulk gas-rich separates from carbonaceous chondrites. Several different phases originally containing neon-E are needed to account for the observation today of at least two phases, E(h) and E(ℓ), containing pure neon-E and at least two, chromite/carbon and Q , containing neon of intermediate compositions between neon-E and neon-S. During the mixing process, neon-S was added to some phases, possibly by adsorption or a related process, but not to all. The neon-A composition in bulk carbonaceous meteorite samples is determined largely by the composition of neon in chromite/carbon, $^{20}Ne/^{22}Ne = 8.7$. In ordinary chondrites where chromite/carbon is less abundant, the trapped neon compositions are determined by neon in Q with $^{20}Ne/^{22}Ne$ about 10 to 11. The amounts of neon-E in the pure E-bearing phases apparently are ordinarily

too small to have a major effect of the bulk meteorite neon compositions.

In a different episode, mixtures of the gas-rich phases and other diluting phases containing no dust-phase neon were exposed to the solar wind. During this exposure, possibly in meteorite parent-body regoliths, varying amounts of gas-phase neon-S were implanted. As a result, $^{20}Ne/^{22}Ne$ ratios observed today in bulk samples of carbonaceous chondrites range from about thirteen in meteorites dominated by implanted solar wind, to about eight in samples dominated by neon in the gas-rich phases. In ordinary chondrites, where the principal gas-rich phase appears to be Q with $^{20}Ne/^{22}Ne$ of about ten to eleven, bulk sample ratios are expected to range between the solar composition and this somewhat higher value.

We conclude that a two-component mixing model for primordial neon is adequate, given present knowledge. The alternative is that one or more of the intermediate trapped neon compositions observed in the gas-rich phases such as chromite/carbon or Q represents another primordial component, not a mixture of neon-E and neon-S. Xenon isotopic compositions in meteorites probably require the existence of more than two primordial components. In this case, it may be possible to argue that more primordial neon components should also be present. Future detailed neon measurements and correlation of neon and xenon data from the gas-rich phases will be needed to shed light on this problem.

The relative abundances of the noble gases in the Earth's atmosphere are an example of the planetary pattern, showing a systematic depletion of the lighter gases relative to their cosmic abundances. The average terrestrial concentrations of noble gases determined by dividing their atmospheric abundances by the mass of the Earth are roughly similar to average meteoritic noble gas contents. The noble gases in the present atmosphere have most

likely originated by outgassing of the solid body of the planet. Noble gas contents of volcanic and plutonic igneous rocks reported here are generally substantially lower than the averaged atmospheric abundances. This observation can be interpreted to show that the outer portions of the Earth (roughly 10% of its mass) are substantially outgassed. Insufficient data are available to extend this inference to the entire planet, however.

We have reported the results of measurements on several groups of terrestrial rocks and minerals. Beryl crystals have been found to contain a characteristic suite of noble gases including excess nucleogenic ^{21}Ne and ^{22}Ne from (α,n) reactions, excess radiogenic ^{40}Ar from the decay of ^{40}K, and fission $^{131-136}Xe$ from ^{238}U spontaneous fission. In addition, varying amounts of atmospheric noble gases may be present. Comparisons with expected crustal production ratios and noble gas contents of other plutonic rocks and minerals suggest that xenon in beryls is depleted by an order of magnitude. This fractionation is thought to have occurred during trapping of magmatic gases by growing beryl crystals. The lattice channels where the gases are held in beryl are probably too small to accomodate xenon as easily as the other noble gases. The suite of dominantly radiogenic gases sampled by the beryl crystals is very similar to that found in natural gas deposits, and is characteristic of the U, Th, and K-rich continental crust.

Neon, argon, krypton, and xenon were measured in a group of samples from the tertiary Skaergaard igneous intrusion in East Greenland. Rocks from different stratigraphic levels were studied, and also samples known to have undergone different degrees of oxygen-isotope exchange with meteoric hydrothermal fluids. The samples are found to contain mixtures of atmospheric noble gases and trapped juvenile magmatic gases. $^{40}Ar/^{36}Ar$ ratios corrected

for *in situ* decay of ^{40}K correlate with $\delta^{18}O$ isotope shifts in plagioclase. Samples showing unexchanged magmatic $\delta^{18}O_{plag}$ values of 6‰ or greater contain juvenile excess argon with $^{40}Ar/^{36}Ar$ greater than 6000. Samples with low $\delta^{18}O_{plag}$ values indicating oxygen-isotope exchange are characterized by much lower $^{40}Ar/^{36}Ar$ ratios due to the presence of significant atmospheric argon. These data imply that the circulating meteoric ground water responsible for the oxygen isotope effects has also introduced atmospheric argon into the cooling intrusion.

The Skaergaard results demonstrate that atmospheric gases dissolved in ground water can be transferred into crustal rocks. Active hydrothermal circulation systems are set up in the oceanic crust at mid-ocean ridges where fresh magma is injected. We expect atmospheric gases dissolved in seawater to be fixed in the oceanic crust during this circulation. Subduction of the altered oceanic crust can provide a means of transporting atmospheric gases into the upper mantle. We have estimated the possible amounts transferred, based on the very limited noble gas data available for altered oceanic crustal rock, with the assumption that the subduction rate has been uniform over the past four billion years. The injected atmospheric gas averaged over the upper several hundred kilometers of the mantle is sufficient to explain all the non-radiogenic neon, argon, krypton, and xenon observed in upper-mantle-derived peridotite nodules. Assignment of the heavier noble gases in these samples to a primordial component must be made with caution unless the gases are isotopically distinct from the atmospheric compositions.

To investigate the question of juvenile primordial noble gases outgassing from the Earth, gases were measured in quenched glass rims of MOR basalt flows. The samples contain juvenile gases extracted from their

source regions, as demonstrated by the presence of excess radiogenic ^{40}Ar. Evidence has been presented that several MOR basalt glass samples also contain small excesses of juvenile radiogenic ^{129}Xe and fission xenon. If derived from *in situ* decay of short-lived ^{129}I in the upper mantle, the excess ^{129}Xe in recently-erupted MOR basalts would indicate the source region has not been completely outgassed since the early history of the Earth. Alternatively, the ^{129}Xe could be leaking into an outgassed upper mantle from a deeper portion of the Earth that still retains some primary juvenile gases. However, no isotopic evidence for juvenile primordial neon, argon, krypton, or xenon was found in the MOR samples studied. Large variations in the $^{40}Ar/^{36}Ar$ ratio were measured in different samples of a single MOR glass specimen. These data provide clear evidence of the late-stage addition of atmospheric noble gases to MOR magma, probably by injection of small amounts of seawater. A large fraction or all of the non-radiogenic neon, argon, krypton, and xenon found in MOR glass samples appears to represent atmospheric contamination, not primordial noble gas from the mantle.

APPENDIX A. PAPERS ON THE NOBLE GAS CONTENTS OF METEORITES

PAPER 1. COSMOGENIC NEON PRODUCED FROM SODIUM IN METEORITIC MINERALS

S. P. SMITH AND J. C. HUNEKE

EARTH AND PLANETARY SCIENCE LETTERS
VOL. 27, pp. 191-199, 1975,

Earth and Planetary Science Letters, 27 (1975) 191–199

5

COSMOGENIC NEON PRODUCED FROM SODIUM IN METEORITIC MINERALS*

S.P. SMITH and J.C. HUNEKE

The Lunatic Asylum of the Charles Arms Laboratory of the Geological Sciences, Division of Geological and Planetary Sciences, California Institute of Technology, Pasadena, Calif. (USA)

Received May 12, 1975
Revised version received June 19, 1975

Cosmogenic neon in sodium-rich oligoclase feldspar from the ordinary chondrites St. Severin and Guareña is characterized by an unusually high $^{22}Ne/^{21}Ne = 1.50 \pm 0.02$. This high ratio is due to the cosmogenic $^{22}Ne/^{21}Ne$ production ratio in sodium which is 2.9 ± 0.3, two to three times the production ratio in any other target element. The relative production rate of ^{21}Ne per gram sodium is one quarter the production rate per gram magnesium. The striking enrichment of ^{22}Ne relative to ^{21}Ne in sodium arises from enhanced indirect production from ^{23}Na via ^{22}Na.

The unusual composition of cosmogenic neon in sodium and sodium-rich minerals explains the high $^{22}Ne/^{21}Ne$ ratios observed in inclusions of the Allende carbonaceous chondrite, and observed during low-temperature extraction of neon from ordinary chondrites. The isotopic composition of cosmogenic neon released during the stepwise heating of a trapped gas-rich meteorite containing sodium-rich phases can be expected to vary, and *use of a constant cosmogenic neon composition to derive the composition of the trapped gas may not be justified.* Preferential loss of this ^{22}Ne-enriched cosmogenic neon from meteoritic feldspar can result in a 2–3% drop in the measured cosmogenic $^{22}Ne/^{21}Ne$ ratio in a bulk meteorite sample. This apparent change in composition can lead to overestimation of the minimum pre-atmospheric mass of the meteorite by a factor of two.

1. Introduction

Neon in stony meteorites and lunar samples consists of a mixture of *trapped* neon with *cosmogenic* neon generated by cosmic-ray-induced reactions on various target elements, principally sodium, magnesium, aluminum, and silicon. It is conventional when calculating the isotopic composition of neon in trapped neon-rich samples (meteoritic or lunar) to use an average cosmogenic composition to correct for the sample's galactic cosmic-ray irradiation history. Such a procedure is justified because, for the majority of such samples, 70–80% of the cosmogenic neon is produced from magnesium in olivine and pyroxene, and dominates the isotopic composition of the total cosmogenic neon; therefore cosmogenic $^{22}Ne/^{21}Ne$ in *bulk* samples of most meteorites and lunar samples is reasonably constant ($^{22}Ne/^{21}Ne \approx 1.1$).

There is, however, significant variation in the observed composition of cosmogenic neon. Correlated variation of $^{22}Ne/^{21}Ne$ and $^{3}He/^{21}Ne$ in meteorites has been ascribed to differences in shielding from galactic cosmic rays [1,20]. Reynolds and Turner [2] suggested that some of the variability of the neon isotopic composition obtained during stepwise thermal release experiments on the carbonaceous chondrite Renazzo could be due to variation in the composition of cosmogenic neon in response to variations in target chemistry. Subsequent measurements of cosmogenic neon compositions in mineral separates from the ordinary chondrite Elenovka [3] confirmed that the $^{22}Ne/^{21}Ne$ ratio varied with bulk composition of the various separates. In particular, it was noted that the highest ratio was observed in a feldspar separate ($^{22}Ne/^{21}Ne = 1.25$ compared to 1.1 in mafic minerals). Recently, Huneke et al. [4] observed neon enriched in ^{22}Ne ($^{22}Ne/^{21}Ne$ as high as 1.67) in inclusions from the C3 chondrite Pueblito d'Allende, and suggested that this unusual gas might be attributable to cosmic-ray-induced reactions

* Contribution No. 2606, Division of Geological and Planetary Sciences, California Institute of Technology, Pasadena, California 91125.

on the sodium-rich target minerals. In addition, neon of rather unusual composition ($^{22}Ne/^{21}Ne \gtrsim 1.3$) was observed in a low-temperature extraction of the chondrite San Juan Capistrano [5]. Walton et al. [6,7] have demonstrated that cosmogenic neon produced in aluminum-rich targets by solar cosmic-ray protons ($\lesssim$100 MeV) should exhibit a higher $^{22}Ne/^{21}Ne$ ratio than that produced by the higher energy (~1 GeV) galactic cosmic rays. However, ordinary chondrites (excluding gas-rich objects) have been shielded from solar cosmic rays which produce effects only in about the outer centimeter of the sample. Variation in isotopic composition of cosmogenic neon in mineral separates of ordinary chondrites should thus reflect primarily the variation in target chemistry (with some variation from meteorite to meteorite due to the effect on galactic cosmic-ray-produced neon of variable shielding [1]).

To investigate further the effect of sodium content on cosmogenic neon production, we have measured the neon in bulk samples and in high purity, sodium-rich feldspar separates from two ordinary chondrites, St. Severin and Guareña. Following a description of the samples and experimental procedure, we present the data in subsection 4.1. The data are then used to determine the production of cosmogenic neon in sodium relative to magnesium (subsection 4.2). The isotopic compositions of cosmogenic neon in both sodium-rich plagioclase from ordinary chondrites and sodium-poor plagioclase from achondrites are estimated (subsection 4.3) using the present data and data available in the literature. These results enable a calculation of the isotopic composition of neon produced from sodium alone (subsection 4.4). Finally we discuss some of the implications for rare gas studies of meteorites.

2. Samples

2.1. St. Severin

Neon was measured in 0.0262 g of whole-rock chips and 0.0240 g of a previously prepared 25–125 μm feldspar-rich density separate. The magnesium content of the feldspar separate is 0.62% by weight and implies a contamination of between 3.5 and 4.5 wt.% mafic minerals (pyroxene Fs_{23}, olivine Fa_{29} [8]). The calcium content of the separate (1.69 wt.% [9]) is due almost entirely to the plagioclase, implying no significant contamination from phosphates. SiO_2 is not known to occur in the meteorite [8,10]. Thus the separate is estimated to contain 95 ± 4 wt.% plagioclase. Microprobe analysis indicates the composition of the plagioclase is about An_{12} [11], in reasonable agreement with the composition $Ab_{79}An_{15}Or_6$ calculated from a bulk chemical analysis of the meteorite [12]. From the purity estimate and the feldspar composition we calculate a sodium content of ~6.5 wt.% for the separate.

2.2. Guareña

Neon was measured in 0.0227 g of whole-rock chips and 0.0256 g of a previously prepared 62–125 μm feldspar separate. Microprobe analysis of 243 grains of the feldspar separate indicates ~5% impurities, primarily mafic minerals, again leading to an estimate of 95 ± 4 wt.% plagioclase in the separate. The composition of the feldspar determined by microprobe analysis is $Ab_{76}An_{20}Or_4$. The calculated sodium content of the separate is ~6.2 wt.%.

3. Experimental procedure

Neon was extracted from the samples in a resistance-heated tantalum crucible and analyzed statically in a 6-inch radius all-metal mass spectrometer. Aluminum foil-wrapped samples were heated successively to 500, 700 and 1500°C for an hour at each temperature. Each sample was re-extracted at 1575°C at the end of the heating cycle to verify complete degassing. The rare gases were purified using a hot Ti-Zr getter and a pair of Sorb-Ac Zr-Al chemisorption getters. Neon was admitted to the spectrometer and exposed to charcoal at liquid nitrogen temperature during analysis to minimize Ar^{2+} and CO_2^{2+} contamination. Ne blanks, assumed to have air composition, at 500 and 700°C were (0.34 ± 0.06) × 10^{-10} cm^3 STP ^{20}Ne and at 1500°C, (0.43 ± 0.13) × 10^{-10} cm^3 STP ^{20}Ne. Additional corrections were made at mass 20 for $H_2{}^{18}O^+$ and $^{40}Ar^{2+}$ (generally <10% but up to 40% for steps with little gas), at mass 21 for $^{20}NeH^+$ (<0.1%) and at mass 22 for $CO_2{}^{2+}$ (<4%). Discrimination was (0.2 ± 0.2)%/amu favoring mass 20. The sensitivity was monitored using a standard volumetric pipette. To recalibrate the pipette, we ran a sample of the chondrite Leedy for which the neon content had been previously obtained using isotope dilu-

tion [14]. The sensitivity was (0.376 ± 0.009) × 10^{-10} cm^3 $^{20}Ne/V$, where the error reflects the relative variation of individual determinations. Systematic error in the final calibration is probably less than 10%.

4. Results and discussion

4.1. Results

Our results are presented in Table 1 and Fig. 1. In Fig. 1 the data are plotted on a three-isotope correlation diagram ($^{20}Ne/^{22}Ne$ vs. $^{21}Ne/^{22}Ne$). The full range of trapped and cosmogenic neon compositions are indicated in the inset. Cosmogenic compositions typically observed in bulk meteorites are shown by the near-horizontal line in the lower-right portion of the inset. Errors in the neon isotopic ratios (Table 1) include the 1σ statistical deviation in the zero-time extrapolation of the multiple (generally 15) ratios taken during analysis, and errors due to statistically independent blank corrections ($^{40}Ar^{2+}$, CO_2^{2+}, $^{20}NeH^+$). Correlated uncertainties due to error in the air blank are represented by f^{22}, the fraction of the total ^{22}Ne corresponding to the blank uncertainty. On the three-isotope plot (Fig. 1) this error is represented by a line segment whose length is f^{22} of the total length between the points representing air and the measured composition, and lies along the line joining the two. Combination of this error with the statistically independent errors leads to the error envelopes shown. The errors in the absolute amounts of ^{22}Ne content contain blank errors and the statistical

TABLE 1

Ne content and isotopic composition

	^{22}Ne* ($\times 10^{-8}$ cm^3 STP/g)	$^{20}Ne/^{22}Ne$**	$^{21}Ne/^{22}Ne$**	f^{22}**
St. Severin				
Total rock (0.0262 g)				
500°C	0.342 ± 0.009	0.566 ± 0.004	0.707 ± 0.006	0.006
700°C	0.226 ± 0.006	0.711 ± 0.008	0.839 ± 0.009	0.009
1500°C	5.38 ± 0.13	0.848 ± 0.003	0.917 ± 0.003	0.0008
Sum	5.95 ± 0.13	0.827 ± 0.005	0.902 ± 0.005	0.0009[1]
Plagioclase (0.0240 g)				
500°C	3.43 ± 0.08	0.671 ± 0.002	0.670 ± 0.002	0.0006
700°C	0.581 ± 0.015	0.572 ± 0.005	0.669 ± 0.006	0.004
1500°C	0.322 ± 0.013	1.068 ± 0.052	0.859 ± 0.031	0.014
Sum	4.33 ± 0.09	0.645 ± 0.006	0.684 ± 0.005	0.0013[1]
Guareña				
Total rock (0.0227 g)				
500°C	0.015 ± 0.003	0.034 ± 0.07	0.84 ± 0.07	0.085
700°C	0.056 ± 0.003	0.543 ± 0.030	0.882 ± 0.021	0.035
1500°C	1.81 ± 0.04	0.857 ± 0.003	0.882 ± 0.004	0.003
Sum	1.88 ± 0.04	0.841 ± 0.004	0.882 ± 0.005	0.003[1]
Plagioclase (0.0256 g)				
500°C (lost)	–	–	–	–
700°C	0.080 ± 0.003	0.48 ± 0.07	0.682 ± 0.008	0.024
1500°C	0.164 ± 0.006	0.62 ± 0.03	0.884 ± 0.010	0.025
Sum	–	–	–	–

* Error includes statistical and blank uncertainties. Systematic error $\lesssim$10%.

** Error statistical only; air blank uncertainty represented by f^{22}, the fraction of the ^{22}Ne attributed to blank uncertainty (see text).

[1] Calculated from $(\Sigma_i[22_i f_i^{22}]^2)^{1/2}$ $(22_T)^{-1}$ where 22_T is total ^{22}Ne, $22_i f_i^{22}$ is the uncertainty in 22_i due to blank.

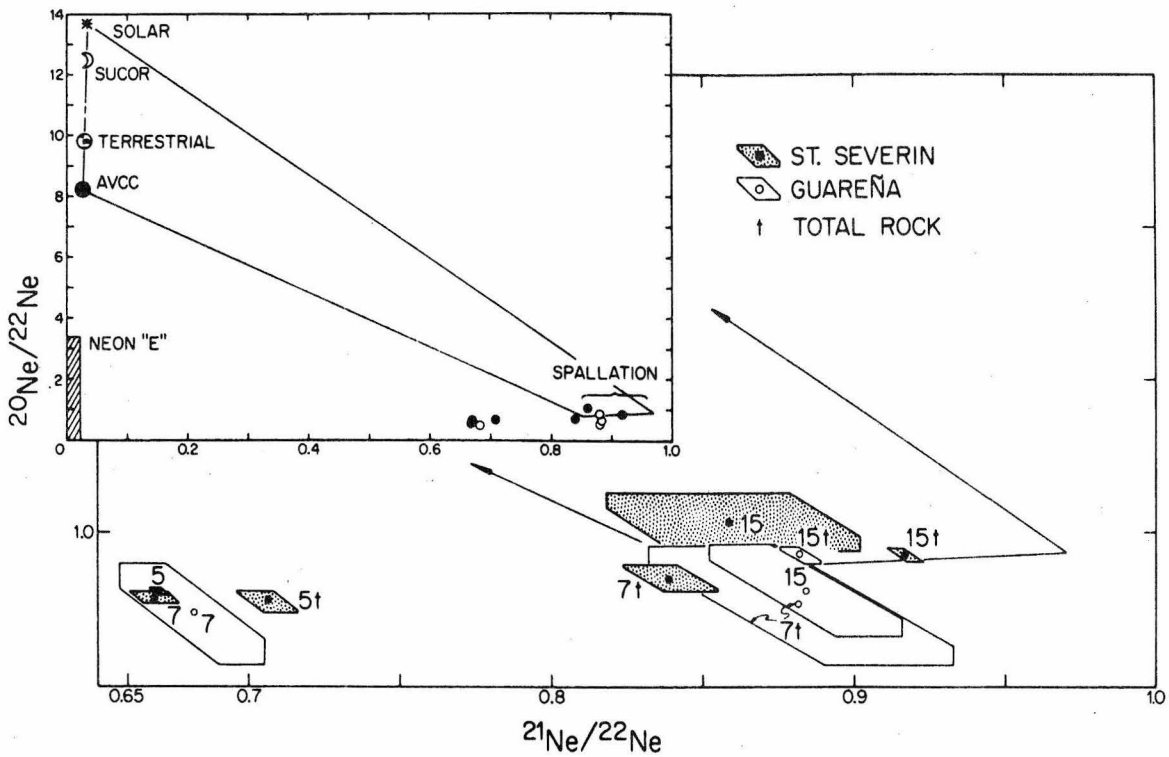

Fig. 1. Correlation of $^{20}Ne/^{22}Ne$ with $^{21}Ne/^{22}Ne$ in the thermal release of neon from feldspar and total-rock samples of the St. Severin and Guareña chondrites. Note that the figure is constructed using $^{21}Ne/^{22}Ne$ in contrast to the discussion in the text where $^{22}Ne/^{21}Ne$ is employed. This results from a tradition of treating cosmogenic neon data in terms of $^{22}Ne/^{21}Ne$ based on ease of computation and the fact that cosmogenic neon production rates are usually given in terms of ^{21}Ne, and a conflicting tradition of plotting neon isotopic data on a correlation plot normalized to ^{22}Ne when discussing trapped Ne. The numbers beside the data points indicate extraction temperature in hundreds of degrees centigrade; "t" indicates total rock samples. Errors are discussed in subsection 4.1. The 500°C point for the Guareña total-rock sample has not been plotted because of its large error. The inset shows the relation of these measured neon compositions to the compositions of neon in different solar system reservoirs (SOLAR = solar wind [21], SUCOR = surface correlated lunar, TERRESTRIAL = terrestrial atmosphere, AVCC = average carbonaceous chondrite), and to the very different neon-"E" component observed by Black in carbonaceous chondrites [19]. The range in cosmic-ray spallation neon observed in bulk meteorite samples is also indicated. Meteoritic neon normally falls within the polygon shown, indicating a mixture of cosmogenic neon with trapped neon intermediate in composition to SOLAR and AVCC. The lowest-temperature releases lie well outside the polygon and show an enhancement in cosmic-ray-produced ^{22}Ne in the sodium-rich oligoclase.

uncertainty in the determination of the sensitivity, but not the 10% systematic uncertainty in the final calibration.

It can be seen from Fig. 1 that there is no evidence for the presence of any significant amount of trapped neon ($^{20}Ne/^{22}Ne \approx 8-14$), but that there are strong systematic variations in the cosmogenic neon composition. Cosmogenic $^{22}Ne/^{21}Ne$ ratios are consistently high in the low-temperature steps. In St. Severin, the great bulk of the neon from the 95% pure feldspar separate is characterized by $(^{22}Ne/^{21}Ne)_c = 1.49-1.50$, suggesting that $^{22}Ne/^{21}Ne$ in the pure St. Severin feldspar is most probably ~1.50. Although the 500°C step for the Guareña feldspar was lost, the 700°C step also is characterized by $(^{22}Ne/^{21}Ne)_c = 1.49$ suggesting that the cosmogenic neon composition in the Guareña plagioclase is identical to that in the St. Severin material. The St. Severin total rock sample was broken from the center of a slab sawn from the upper half of stone H [25]. When compared with depth profiles of cosmogen-

ic rare gases measured in stone A of St. Severin [23], both the ^{21}Ne content and $^{22}Ne/^{21}Ne$ ratio of our sample indicate it came from a depth of ~10 cm within stone H. The feldspar separate was taken from 100 g of the same slab adjacent to and within at most 3–4 cm of the location of the total-rock sample.

4.2. *Production of cosmogenic ^{21}Ne from sodium*

Assuming that the 5% contamination of the feldspar separate from St. Severin is similar in bulk chemical composition to the total rock minus the feldspar, and estimating the plagioclase content of the St. Severin total rock as 10% (from a bulk chemical analysis [12]), we can calculate the concentration of ^{21}Ne in pure feldspar and in total rock minus feldspar. We find $C_f = 2.82 \pm 0.15$ cm^3 STP ^{21}Ne/g pure feldspar(f) and $C_r = 5.68 \pm 0.15$ cm^3 STP ^{21}Ne/g residual (r) material and $C_f/C_r = 0.50 \pm 0.03$.

Sodium, which is substantially enriched in the high-purity feldspar separate is an important target for production of ^{21}Ne for which an observationally based production rate has not previously been available. Using previously determined relative production rates for ^{21}Ne for target elements other than sodium (Mg ≡ 1, Si = 0.19, Al = 0.27, Ca = 0.019, Fe = 0.006, S = 0.14 [3,16]), together with the chemical composition of the feldspar (Ab_{80}) and whole rock [12], we can calculate from C_f/C_r a relative production rate of ^{21}Ne in sodium. The resulting calculated ratio of the production of ^{21}Ne from 1 g of sodium to the production in 1 g of magnesium is 0.22. The calculated value of this ratio is sensitive to the amount of gas loss in the sample. We have assumed no gas loss in deriving the above value; the calculated ratio rises to about 1 if the feldspar has lost ~40% of its neon. ^{40}Ar-^{39}Ar dating of the feldspar fraction yields a good plateau with a plateau age about 4.5 b.y. indicating the mineral has not lost ^{40}Ar [9]. The ^{3}He content of the feldspar is 35–40% lower than that in the whole rock [9], suggesting some loss of helium from feldspar has occurred. The amount of neon loss should be intermediate, less than 40%; hence we can state with confidence that 1 is an upper limit to the ratio of ^{21}Ne production in sodium relative to magnesium. If the neon diffusion coefficient in feldspar is about 100 times less than the helium diffusion coefficient, as is the case in olivine and pyroxene [15], loss of neon would be negligible. Thus it seems probable that the ^{21}Ne production per gram in sodium is about one quarter the production in magnesium.

4.3. *Isotopic composition of cosmogenic neon in feldspar*

We suggested from the thermal release patterns that the ratio $^{22}Ne/^{21}Ne$ in the pure St. Severin feldspar is 1.49–1.50. To confirm this initial conclusion and compare the present data to published data on other meteoritic feldspars we construct a plot of observed $^{22}Ne/^{21}Ne$ versus weight percent feldspar in a sample. We assume that mineral separates from a given meteorite are binary mixtures of pure feldspar (f) and a residual fraction (r) of constant composition. From the relation:

$$\left(\frac{^{22}Ne}{^{21}Ne}\right)_m = \frac{^{21}Ne_f}{^{21}Ne_t}\left(\frac{^{22}Ne}{^{21}Ne}\right)_f + \frac{^{21}Ne_r}{^{21}Ne_t}\left(\frac{^{22}Ne}{^{21}Ne}\right)_r \qquad (1)$$

(m = measured, t = total sample) we obtain:

$$\left(\frac{^{22}Ne}{^{21}Ne}\right)_m = \frac{wP(^{22}Ne/^{21}Ne)_f + (1-w)(^{22}Ne/^{21}Ne)_r}{1 + w(P-1)} \qquad (2)$$

where w is the weight fraction feldspar in a sample and $P = C_f/C_r$, the ratio of *measured* concentration of ^{21}Ne in the pure feldspar to that in the residual material. Variation of P in different meteorites reflects primarily the amount of gas loss from feldspar which may vary for different stones. For the St. Severin feldspar separate $(^{22}Ne/^{21}Ne)_m = 1.463$, $w = 0.95$ and $P = C_f/C_r = 0.50$. Again assuming the composition of the 5% residual is total rock less feldspar, we use $(^{22}Ne/^{21}Ne)_r = 1.1$, the high-temperature total-rock value. The resulting $(^{22}Ne/^{21}Ne)_f$ is 1.50, in exact agreement with the value inferred from the release pattern. In Fig. 2 we plot measured $^{22}Ne/^{21}Ne$ versus weight percent feldspar for the present data and for mineral separates from the ordinary chondrites Elenovka [3] and Bruderheim [16]. The feldspar contents of the various fractions were calculated from the reported chemical analyses, assuming all aluminum, sodium, and potassium is in the feldspar. The solid curve is the fit using eq. 2 to the St. Severin data, where $P = 0.5$, $(^{22}Ne/^{21}Ne)_f = 1.50$ and $(^{22}Ne/^{21}Ne)_r = 1.1$. The data are consistent with this curve, except for the most feldspar-rich Bru-

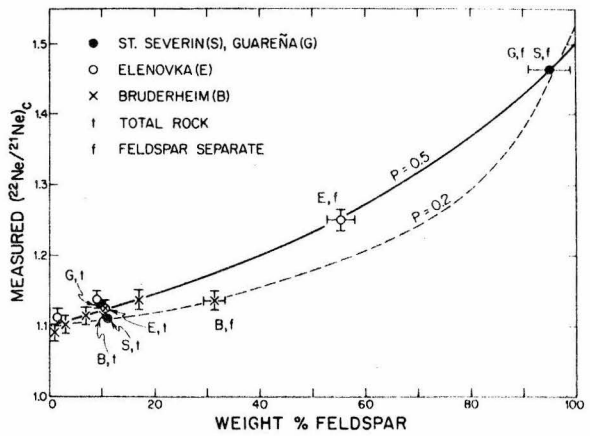

Fig. 2. Variation of $^{22}Ne/^{21}Ne$ with weight percent feldspar for St. Severin and Guareña total-rock and feldspar samples compared to measurements on mineral separates from other ordinary chondrites [3,16]. The neon composition in pure feldspar is determined by fitting the data with eq. 2:

$$\left(\frac{^{22}Ne}{^{21}Ne}\right)_m = \frac{wP(^{22}Ne/^{21}Ne)_f + (1 - w)(^{22}Ne/^{21}Ne)_r}{1 + w(P - 1)}$$

where w is the weight percent feldspar in the sample and P is the measured neon concentration in feldspar (f) relative to the measured neon concentration in the remainder (r). Neon loss from the feldspar will lead to some variation in the inferred P value and thus some scatter about the best fit curve. Moderate neon loss does not affect the $^{22}Ne/^{21}Ne$ of the feldspar. All but one point are fit using a single value of P indicating no, or at least comparable, neon losses from feldspar for these chondrites. A value of $^{22}Ne/^{21}Ne = 1.50 \pm 0.02$ for pure feldspar is indicated (S = St. Severin, G = Guareña, B = Bruderheim, E = Elenovka.)

derheim fraction; however, this meteorite may have suffered loss of neon preferentially from the feldspar. If we reduce P from 0.5 to 0.2 (~60% loss of neon from Bruderheim feldspar), eq. 2 yields the dashed curve (fit to the Bruderheim feldspar-enriched sample datum). Considering the possible effects of gas loss, the previously published data are generally in agreement with the present result, that the cosmogenic $^{22}Ne/^{21}Ne$ ratio is 1.50 ± 0.02 in the oligoclase feldspar (Ab_{75-80}) characteristic of ordinary chondrites.

To calculate the isotopic composition of cosmogenic neon in sodium we need to know the composition of cosmogenic neon in a more calcic plagioclase; the feldspar in calcium-rich achondrites is quite suitable, with compositions about $An_{90 \pm 5}$. Published neon contents and weight percent feldspar in mineral separates from four calcium-rich achondrites [17] were used in eq. (2) to extrapolate $(^{22}Ne/^{21}Ne)_f$ for pure feldspar of composition An_{90+5}. The precision of the data is not high; however, the data are consistent with a cosmogenic ratio $^{22}Ne/^{21}Ne = 1.22 \pm 0.07$ in this calcic plagioclase.

4.4. Isotopic composition of cosmogenic neon in sodium

The principal targets for the production of cosmogenic neon in plagioclase are sodium, aluminum and silicon. With $(^{22}Ne/^{21}Ne)_c$ values for two distinct compositions of feldspar (subsection 4.3), and relative ^{21}Ne production rates in the target elements (subsection 4.2), we are in a position to calculate $(^{22}Ne/^{21}Ne)_c$ in sodium and aluminum from a knowledge of $(^{22}Ne/^{21}Ne)_c$ in silicon. From olivine and pyroxene separates from Elenovka [3] and Bruderheim [16], in which the principal targets are magnesium and silicon, we can calculate $(^{22}Ne/^{21}Ne)_c^{Mg} = 1.09 \pm 0.03$ and $(^{22}Ne/^{21}Ne)_c^{Si} = 1.2 \pm 0.1$. Using the limiting cases of 0.2 and 1.0 for the relative production of ^{21}Ne in sodium (subsection 4.2) we calculate the $(^{22}Ne/^{21}Ne)_c^{Na}$ and $(^{22}Ne/^{21}Ne)_c^{Al}$ values listed in Table 2. The indicated error is due to the uncertainty in the $(^{22}Ne/^{21}Ne)_c$ value in the An_{90} plagioclase. It is evident that despite the uncertainty in the ^{21}Ne production rate in sodium, we can conclude that $(^{22}Ne/^{21}Ne)_c^{Al}$ is about equal to $(^{22}Ne/^{21}Ne)_c^{Si}$ while $(^{22}Ne/^{21}Ne)_c^{Na}$ is *significantly greater*, ranging from values of 1.8 to 3.8. If we use 0.25 as the probable value of the relative ^{21}Ne production rate in sodium, then we find that $(^{22}Ne/^{21}Ne)_c^{Na} = 2.9 \pm 0.3$ and $(^{22}Ne/^{21}Ne)_c^{Al} = 1.17 \pm 0.15$.

Values of $(^{22}Ne/^{21}Ne)_c$ and relative ^{21}Ne production rates for various target elements are summarized in Table 3. The $(^{22}Ne/^{21}Ne)_c$ ratio of ~3 for sodium is distinct from the ratio in other targets. However, we find from thin-target reaction cross sections [18] that at about 1 GeV incident proton energy such a ratio is not unreasonable. The production cross sections of ^{21}Ne and ^{22}Ne from magnesium are about 20 mb at 1 GeV, with about 10 mb of ^{22}Ne production arising from direct production from magnesium and about 10 mb indirectly from the decay of ^{22}Na. Cross sections for direct neon production from sodium are not available; assuming these cross sections are approximately

TABLE 2

$(^{22}Ne/^{21}Ne)_c$ in Al and Na calculated from various values of $(^{22}Ne/^{21}Ne)_c^{Si}$ and the relative production of ^{21}Ne in sodium (PR_{Na}*)

PR_{Na}*	$(^{22}Ne/^{21}Ne)_c^{Si}$	$(^{22}Ne/^{21}Ne)_c^{Al}$	$(^{22}Ne/^{21}Ne)_c^{Na}$
0.2	(1.1–1.3)	(1.25–1.08) ± 0.15	(3.56–3.11) ± 0.30
0.25	1.2 ± 0.1	1.17 ± 0.15	2.9 ± 0.3
1.0	(1.1–1.3)	(1.21–1.05) ± 0.16	(1.92–1.83) ± 0.07

* PR_{Na} = ^{21}Ne produced per gram Na/^{21}Ne produced per gram Mg.

equal or less than those for the direct neon production from magnesium, we adopt 20 mb for the direct production of ^{21}Ne in sodium and 10 mb for ^{22}Ne. The production cross section for ^{22}Na from ^{23}Na is ~40 mb, hence the net production cross section of ^{22}Ne from sodium is 50 mb. Thus the $^{22}Ne/^{21}Ne$ production ratio in sodium at 1 GeV is predicted to be about 2.5. The ^{22}Na production cross section in sodium increases steadily at lower energies to ≳80 mb at 50 MeV. From the data of Walton et al. [6], the direct production cross section of ^{21}Ne from magnesium is about 3 mb at 41 MeV. If the production of ^{21}Ne from sodium is similarly low, then cosmogenic neon produced in sodium by solar cosmic-ray protons may be characterized by extremely high $^{22}Ne/^{21}Ne$ ratios ($^{22}Ne/^{21}Ne$ ≳30 or $^{21}Ne/^{22}Ne$ ≲0.03), similar to, or perhaps more extreme than, those measured in aluminum irradiated with low-energy protons [6]. Should the production cross section for ^{20}Ne also be depressed, then the neon produced by low-energy proton bombardment of sodium would consist in essence of pure ^{22}Ne. Even if the ^{20}Ne production were comparable to the ^{22}Ne production, such low-energy proton-produced neon in sodium might provide an explanation for the composition of neon-E ($^{20}Ne/^{22}Ne$ ≲1.5, $^{21}Ne/^{22}Ne$ ≲0.02 [24]), the unusual ^{22}Ne-rich component observed in carbonaceous chondrites [19]. This speculation can be tested by target irradiation experiments similar to those reported by Walton et al. [6] for magnesium, aluminum, and silicon. We conclude that high cosmogenic $^{22}Ne/^{21}Ne$ ratio derived for meteoritic sodium and sodium-rich minerals can be explained by enhanced indirect production of ^{22}Ne through ^{22}Na compared with the direct production of neon from ^{23}Na.

TABLE 3

Relative ^{21}Ne production rates and $(^{22}Ne/^{21}Ne)_c$ in various target elements in ordinary chondrites

Target	^{21}Ne production rate	$(^{22}Ne/^{21}Ne)_c$
Na	0.25 (0.2–1.0)	2.9 ± 0.3 (3.8–1.8)[3]
Mg	1.0	1.09 ± 0.03
Al	0.27[1]	1.17 ± 0.15
Si	0.19[1]	1.2 ± 0.1
S	0.14[1]	1.21 ± 0.04[1]
Ca	0.019[1]	–
Fe	0.006[1]	1.05 ± 0.15[2]

[1] From Boschler et al. [3].
[2] Nyquist et al. [20].
[3] Calculated using limiting values of ^{21}Ne production in sodium.

4.5. General comments

In the preceding three subsections we have found that the production of ^{21}Ne from sodium is 0.25 relative to magnesium, that the $(^{22}Ne/^{21}Ne)_c$ in sodium-rich feldspar is 1.50 ± 0.02, and most strikingly, that the $(^{22}Ne/^{21}Ne)_c$ in pure sodium is approximately 3. We can now comment on the observations mentioned in the introduction. The high values of $(^{22}Ne/^{21}Ne)_c$ observed in low-temperature release from bulk samples of ordinary chondrites [e.g. $(^{22}Ne/^{21}Ne)_c$ = 1.43 at 500°C in St. Severin whole rock] result from the low-temperature release (<700°C) of the ^{22}Ne-enriched cosmogenic neon from oligoclase. Such an effect has now been observed in bulk samples of St. Severin and Guareña, as well as San Juan Capistrano [5].

In addition, the high $(^{22}Ne/^{21}Ne)_c$ ratio of ~3 in sodium implies that cosmogenic neon of high $^{22}Ne/^{21}Ne$ ratio will also be generated in other sodium-rich min-

erals. In particular, the cosmogenic neon produced in the sodium-rich phases of the Allende inclusions should be enriched in ^{22}Ne relative to ^{21}Ne, as is in fact the case [4,13]. The amounts, composition, and low-temperature release of the unusual cosmogenic neon in the aggregates are completely consonant with the hypothesis of in-situ generation by galactic cosmic ray interactions with sodium-rich targets [4,13].

It must be emphasized that the large variation with temperature of the apparent cosmogenic neon composition during the stepwise thermal release experiments described here can be expected to occur in general in cases where sodium-rich phases are present in a sample. Sodium-rich minerals and glasses generally are much less refractory than other meteoritic minerals and tend to degas at lower temperatures. In particular, corrections made to trapped gas compositions for low-temperature steps of release from trapped neon-enriched samples (e.g., carbonaceous chondrites and gas-rich ordinary chondrites) *cannot be blindly applied assuming a constant galactic cosmic-ray-produced neon composition.* As a rather extreme example, using a $(^{22}Ne/^{21}Ne)_c$ ratio of 0.87, trapped neon in 95 and 200°C release steps from a sample of the C2 chondrite Cold Bokkeveld investigated by Black [19] would be corrected to a trapped $^{20}Ne/^{22}Ne \sim 10$. In contrast, using $(^{22}Ne/^{21}Ne)_c = 0.7$ leads to a trapped composition of $^{20}Ne/^{22}Ne \sim 12$ for the same temperature steps.

Finally, we remark that the effect of the high $(^{22}Ne/^{21}Ne)_c$ ratio in feldspar from ordinary chondrites must be considered in detailed models of the effects of shielding on cosmogenic rare gas composition and in the use of the bulk meteorite $(^{22}Ne/^{21}Ne)_c$ ratio as a monitor of irradiation conditions [1,20]. Preferential gas loss from feldspar can result in a 2–3% drop in the $(^{22}Ne/^{21}Ne)_c$ ratio of a bulk sample containing about 10% feldspar. Such gas loss can lead to overestimation of minimum pre-atmospheric masses calculated from bulk meteorite $^{3}He/^{21}Ne$ and $^{22}Ne/^{21}Ne$ ratios. With the model of Nyquist et al. [20], the degree of overestimation is about 20–40% for bodies with pre-atmospheric masses about 500 kg, and 50–100% or more for bodies with pre-atmospheric masses of 1000 or 2000 kg. In addition, variation in the feldspar content of samples in which rare gases are measured is a possible source of some of the scatter of analyses about the empirical $^{3}He/^{21}Ne$ versus $^{22}Ne/^{21}Ne$ shielding curves derived by various investigators [1,20].

It is clear from the above examples that the isotopic composition of cosmogenic neon produced by galactic cosmic ray irradiation of meteoritic and lunar samples is a strong function of the concentration of sodium in a particular sample or separate. Walton et al. [22] have shown that the isotopic composition of cosmogenic neon produced by solar cosmic-ray protons is strongly dependent on target chemistry, and hence that such cosmogenic neon cannot be represented by a single component.

We have now shown that the same must be said of cosmogenic neon produced by galactic cosmic-ray irradiation. Walton et al. [22] point out that samples (such as unconsolidated lunar soils, or coherent regolith breccias of both lunar and meteoritic origin) which contain abundant implanted solar wind neon will most likely also contain solar cosmic-ray-produced neon, possibly of unusual composition. However, galactic cosmic-ray-produced neon will be independent of solar wind neon and hence large variation in the isotopic composition of cosmogenic neon can occur in gas-poor meteorites as well as gas-rich meteorites.

5. Conclusion

The enhanced production of cosmogenic ^{22}Ne in sodium leads to the high $(^{22}Ne/^{21}Ne)_c$ ratio observed in oligoclase feldspar from ordinary chondrites. The low temperature of release of this cosmogenic neon provides an explanation for the unusual neon isotopic compositions seen at low temperatures during stepwise thermal release experiments on bulk samples of ordinary chondrites. Unusual low-temperature neon compositions observed in Allende inclusions are also due to the release of cosmogenic neon from sodium-rich phases. The temperature-dependent variation of the observed cosmogenic neon composition must be considered in the interpretation of stepwise release experiments on samples containing abundant trapped neon. Neon loss from feldspar and variation in the feldspar content of bulk meteorite samples can affect the formulation and interpretation of detailed models of the effects of shielding on the production of cosmogenic neon in meteorites. Finally, we emphasize that cosmogenic neon in meteorites and lunar samples must be regarded as a complex mixture of compositions produced in phases of differing chemical composition,

both at the low energies of solar cosmic rays [6,7,22] and the higher energies of galactic cosmic rays.

Acknowledgments

We thank G.J. Wasserburg for the mineral separates and for suggestions leading to great simplification in the presentation and discussion of the data. We also thank D.D. Bogard and D. Heymann for review comments aiding in the revision of the manuscript. This work was supported by NSF grant GP-28027.

References

1 P. Eberhardt, O. Eugster, J. Geiss and K. Marti, Rare gas measurements in 30 stone meteorites, Z. Naturforsch. 21 (1966) 414.
2 J.H. Reynolds and G. Turner, Rare gases in the chondrite Renazzo, J. Geophys. Res. 69 (1964) 3263.
3 P. Boschler, P. Eberhardt, J. Geiss and N. Grogler, Rare-gas measurements in separate mineral phases of the Otis and Elenovka chondrites, in: P. Millman, ed., Meteorite Research (D. Reidel, Dordrecht, 1969) 857.
4 J.C. Huneke, S.P. Smith, R.S. Rajan and G.J. Wasserburg, Ne in selected materials from the Allende meteorite (abstract), Meteoritics 9 (1974) 350.
5 K. Marti, Communicated at the Meteoritical Society Meeting, August 1974.
6 J.R. Walton, A. Yaniv, and D. Heymann, He and Ne cross sections in natural Mg, Al, and Si targets and radionuclide cross sections in natural Si, Ca, Ti, and Fe targets bombarded with 14- to 45-MeV protons, J. Geophys. Res. 78 (1973) 6428, with correction in J. Geophys. Res. 79 (1974) 311.
7 J.R. Walton, D. Heymann, A. Yaniv, D. Edgerley and M.W. Rowe, Production of He, Ne, Ar, and ^{236}U in lunar material by solar cosmic-ray protons (abstract), in: Lunar Science V (Lunar Science Institute, Houston, 1974) 817.
8 K. Fredriksson, J. Nelen and B.J. Fredriksson, The LL-group chondrites, in: L.H. Ahrens, ed., Origin and Distribution of the Elements (Pergamon, New York-London, 1968) 457.
9 Unpublished data, Lunatic Asylum, C.I.T.
10 G.J. Wasserburg, Private communication.
11 D.N. Schramm, F. Tera and G.J. Wasserburg, The isotopic abundance of ^{26}Mg and limits on ^{26}Al in the early solar system, Earth Planet. Sci. Lett. 10 (1970) 44.
12 E. Jarosewich and B. Mason, Chemical analyses with notes on one mesosiderite and seven chondrites, Geochim. Cosmochim. Acta 33 (1969) 411.
13 S.P. Smith and J.C. Huneke, Neon and argon in selected materials from the Allende meteorite, and neon in three gas-rich carbonaceous chondrites, (in preparation).
14 J.C. Huneke, F.A. Podosek, D.S. Burnett and G.J. Wasserburg, Rare gas studies of the galactic cosmic ray irradiation history of lunar rocks, Geochim. Cosmochim. Acta 36 (1972) 269.
15 J.C. Huneke, L.E. Nyquist, H. Funk, V. Koppel and P. Signer, The thermal release of rare gases from separated minerals of the Mocs meteorite, in: P. Millman, ed., Meteorite Research (D. Reidel, Dordrecht, 1969) 901.
16 D.D. Bogard and P.J. Cressy, Jr., Spallation production of ^{3}He, ^{21}Ne and ^{38}Ar from target elements in the Bruderheim chondrite, Geochim. Cosmochim. Acta 37 (1973) 527.
17 D. Heymann, E. Mazor and E. Anders, Ages of the Ca-rich achondrites, in: P. Millman, ed., Meteorite Research (D. Reidel, Dordrecht, 1969).
18 T.A. Kirsten and O.A. Schaeffer, High-energy interactions in space, in: L.C.L. Yuan, ed., Elementary Particles; Science, Technology, and Society (Academic Press, New York and London, 1971) 75.
19 D.C. Black, On the origins of trapped helium, neon, and argon isotopic variations in meteorites, II. Carbonaceous meteorites, Geochim. Cosmochim. Acta 36 (1972) 377.
20 L. Nyquist, H. Funk, L. Schultz and P. Signer, He, Ne and Ar in chondritic Ni-Fe as irradiation hardness sensors, Geochim. Cosmochim. Acta 37 (1973) 1655.
21 J. Geiss, Solar wind composition and implications about the history of the solar system; Invited Paper, 13th Int. Cosmic Ray Conf., Denver, August 1973.
22 J.R. Walton, D. Heymann, V.L. Jordon and A. Yaniv, Evidence for solar cosmic-ray proton-produced neon in fines 67701 from the rim of North Ray Crater, Geochim. Cosmochim. Acta, Suppl. 5, 2 (1974) 2045.
23 L. Schultz, D. Phinney and P. Signer, Depth dependence of spallogenic noble gases in the St. Severin chondrite, Meteoritics 8 (1973) 435.
24 P. Eberhardt, Ne-E-rich phase in Orgeuil, EOS, Trans, Am. Geophys. Union, 56 (1975) 392.
25 Y. Cantelaube, P. Pellas, D. Nordemann and J. Tobailem, Reconstitution de la météorite Saint-Séverin dans l'espace, in: P. Millman, ed., Meteorite Research (D. Reidel, Dordrecht, 1969) 705.

PAPER 2. NEON IN GAS-RICH SAMPLES OF THE CARBONACEOUS CHONDRITES MOKOIA, MURCHISON, AND COLD BOKKEVELD

S. P. SMITH, J. C. HUNEKE, AND G. J. WASSERBURG

EARTH AND PLANETARY SCIENCE LETTERS,
VOL. 39, pp. 1-13, 1978,

Earth and Planetary Science Letters, 39 (1978)1–13

[2]

NEON IN GAS-RICH SAMPLES OF THE CARBONACEOUS CHONDRITES MOKOIA, MURCHISON, AND COLD BOKKEVELD

S.P. SMITH, J.C. HUNEKE and G.J. WASSERBURG

The Lunatic Asylum of the Charles Arms Laboratory, Division of Geological and Planetary Sciences, California Institute of Technology, Pasadena, CA 91125 (U.S.A.)

Received April 5, 1977
Revised version received November 10, 1977

High-resolution stepwise-release patterns of neon extracted from gas-rich whole-rock samples of the carbonaceous chondrite meteorites Murchison, Cold Bokkeveld, and Mokoia are characterized by multiple release peaks and complex isotopic variations. Mokoia contains abundant ancient solar wind neon with $^{20}Ne/^{22}Ne = 13.7$, identical in composition to the modern solar wind. For Murchison and Cold Bokkeveld, $^{20}Ne/^{22}Ne$ ratios of low-temperature release fractions are about 11 and 12.4, respectively. In higher-temperature fractions $^{20}Ne/^{22}Ne$ of trapped neon migrates toward neon-E, reaching a minimum of 6.9 for Murchison. Features in the Murchison thermal release and isotopic variation patterns can be associated with the release of neon from the gas-rich trace phases chromite/carbon and "Q". The characteristic high-temperature release of neon-E is closely related to the release of neon from "Q" in Murchison.

For simplicity, in this paper we consider a model in which neon in the early solar system consisted originally of two components, one component in the gas phase and the second trapped in dust grains. Neon present in solar system reservoirs today is then described as a mixture of galactic cosmic ray spallation neon and two primary trapped components, neon with $(^{20}Ne/^{22}Ne)_t = 13.7$ and neon-E. The composition of neon in the gas phase is determined from the composition of neon in the sun. Intermediate neon compositions observed in condensed materials such as the earth and meteorites require mechanisms such as gravitational collection, ion implantation or adsorption to combine gas-phase neon with dust-phase neon. The present detailed release patterns show no clear evidence of preferred intermediate compositions such as neon-A. The apparently uniform composition of neon in gas-rich chromite/carbon residues may represent a special mixture of gas-phase and dust-phase neon, but requires detailed investigation. The composition of neon in "Q" is variable and different from the composition in chromite/carbon. It is suggested that the total neon composition in a solar system object will be determined by the relative proportions of various gas-rich trace phases accreted, plus the amounts incorporated of galactic cosmic ray spallation neon and pure gas-phase neon such as the solar wind.

1. Introduction

The isotopic composition of spallation-free "trapped" neon in carbonaceous chondrites and unmetamorphosed chondrites has been found to be highly variable. Pepin [1,2] and Black [3,4] concluded from the preferred compositions observed during the extraction of neon by stepwise heating from carbonaceous chondrites and gas-rich meteorites that trapped neon consisted of a number of isotopically distinct components which they labeled A through E (Fig. 1). Recently, it has been discovered that a significant portion of the neon and other noble gases in carbonaceous chondrites reside in gas-rich trace phases (cf. [5,6]). The exact nature and origins of the neon components and of the gas-rich phases are presently uncertain. The connection between possible neon components and other isotopic anomalies (e.g., in O, Mg, Kr, and Xe) is still unknown. It has not yet been possible to obtain a clear determina-

Division Contribution No. 2893(239).

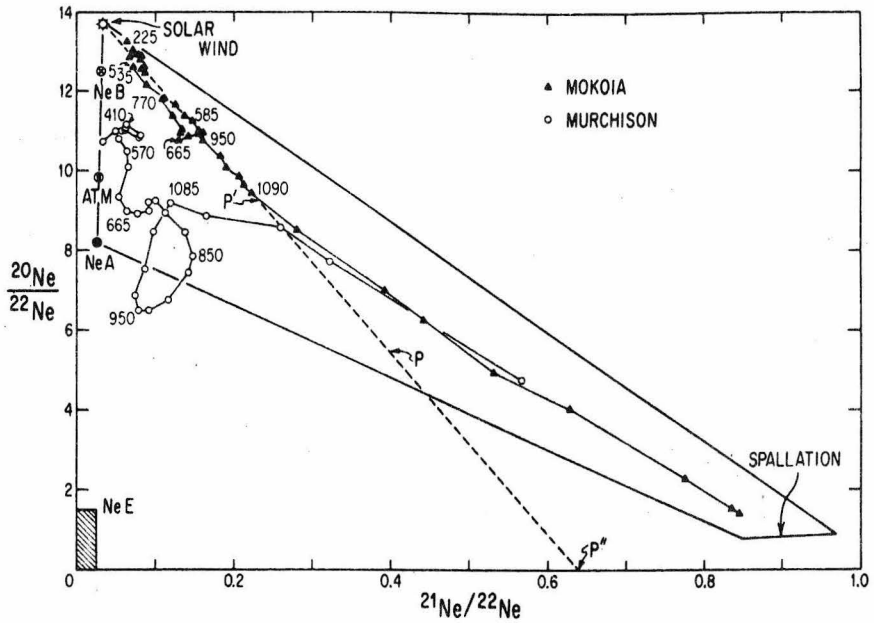

Fig. 1. Correlation of $^{20}Ne/^{22}Ne$ with $^{21}Ne/^{22}Ne$ in stepwise-release fractions from Mokoia and Murchison. Trapped neon compositions plot near the ordinate and include solar wind [17], neon-B (NeB) [4], terrestrial atmosphere (ATM) [32], and neon-A observed predominantly in carbonaceous chondrites (NeA) [1,2]. Neon-C ($(^{20}Ne/^{22}Ne)_t \approx 10.5$) and neon-D ($(^{20}Ne/^{22}Ne)_t \approx 14.5$) are not shown. The limits from Orgueil on the composition of neon-E (NeE) [33] are indicated; also the range of whole-rock meteorite spallation compositions. Whole-rock neon compositions of most carbonaceous chondrites [7] plot within the indicated polygon outlined by neon-A, solar wind, and whole-rock spallation. For Mokoia, neon fractions below 1100°C define a linear trend (dashed line) that can be interpreted as a mixing line between an isotopically light component *identical to the modern solar wind* and an isotopically heavy component P which can range in composition from P' to P''. The complex neon release pattern for Murchison suggests the presence of at least two trapped neon components in addition to spallation neon. The low $(^{20}Ne/^{22}Ne)_t$ in the 950°C fraction indicates the presence of neon rich in neon-E.

tion of the composition of the end-member neon components present in solar system materials and to assess the relative contributions of these components to the major neon reservoirs of the solar system.

In this paper we report measurements by a refined stepwise thermal release procedure of neon in whole-rock samples of the carbonaceous chondrites Mokoia, Murchison and Cold Bokkeveld. The high concentrations of neon found in these samples allowed us to extract the gas in a great number of temperature steps yielding very high-resolution analyses of neon isotopic variations. We used this high-resolution technique to search for extremely light or heavy neon end-members in Mokoia and Cold Bokkeveld which have whole-rock trapped $^{20}Ne/^{22}Ne$ ratios among the highest and lowest previously measured. Total-rock $^{20}Ne/^{22}Ne$ ratios in Mokoia range up to 11.6 [7], yielding a trapped ratio of 13.1, which is the highest bulk value found both in carbonaceous chondrites and in non-carbonaceous, gas-rich meteorites (cf. [8]). Measured $^{20}Ne/^{22}Ne$ ratios of 12.7 and 13.0 in two low-temperature fractions of a seven-step extraction of gases from Mokoia by Manuel et al. [9] suggested the presence of spallation-free neon with $^{20}Ne/^{22}Ne$ greater than 13.1. The small number of temperature steps in that experiment limited the resolution of neon isotopic variations, and prevents precise characterization of this isotopically light neon. Previous analyses of Cold Bokkeveld yielded both bulk and spallation-free $^{20}Ne/^{22}Ne$ ratios close to 8 [4,7], among the lowest known in whole-rock samples of carbonaceous chondrites. Measurements

on two bulk samples of Murchison gave intermediate ratios $^{20}Ne/^{22}Ne = 11.0, 11.1$ and $^{21}Ne/^{22}Ne = 0.090, 0.071$ [10]. The distribution of neon in trace phases of Murchison has been recently studied [5,6], and features in the stepwise-release pattern of our bulk sample will be associated with the release of neon from the gas-rich acid-resistant residues.

We have used sequential gas-release fractions which showed a well-defined linear array on the neon three-isotope correlation diagram to extrapolate spallation-free neon compositions. Arrays were sought indicating possible extreme end-member neon compositions as well as arrays yielding compositions corresponding to identifiable major solar system reservoirs. Data will be presented which demonstrates for the first time that neon is present in a carbonaceous chondrite with an isotopic composition identical to that found in the modern solar wind. We also will re-examine the multi-component model of solar system neon in the light of the data presented here.

2. Samples

Samples were 0.125–0.150 g whole-rock fragments consisting of heterogeneous mixtures of coarse fragments embedded in very fine-grained black matrix. Among the inclusions commonly observed were spherical chondrules, fragments of euhedral olivine crystals, irregular fine-grained white aggregates, and fine-grained greenish aggregates. Murchison and Cold Bokkeveld are type CM2 carbonaceous chondrites (Mighei sub-type, petrologic type 2 [11]) characterized by a fine-grained matrix primarily of hydrous phyllosilicates (cf. [12]). Mokoia has been classified as CV2 (Vigarano sub-type) on the basis of its content of Ni-rich sulfides [11]. The matrix of Mokoia consists of fine-grained olivine, rather than phyllosilicates [13]. Magnetite contents are 4.1 wt.% for Mokoia, $\lesssim$0.75 wt.% for Murchison, and $\lesssim$0.48 wt.% for Cold Bokkeveld [14].

The Mokoia sample, obtained from the University of California, Los Angeles, collection, was labeled "Haripura", but is here identified as Mokoia on the basis of its high spallation ^{21}Ne content and total neon content and isotopic composition (comparison data for Mokoia and Haripura are reported in Mazor et al. [7]).

3. Procedures

Experimental procedures were the same as previously described [15,16]. Neon was extracted from the samples by stepwise heating. Measured total neon contents and isotopic compositions are listed in Table 1. Data for individual release fractions are presented in the figures. Tabulated stepwise-release data may be obtained from the authors. These data have been corrected for extraction oven blanks, mass discrimination, and interfering species including $H_2{}^{18}O^+$, $^{20}NeH^+$, $^{40}Ar^{2+}$, and CO_2^{2+}. Total corrections for each isotope were generally less than 5% for individual temperature fractions. In the table $f^{22} = \Delta/^{22}Ne$ is the fractional error in the ^{22}Ne due to Δ, the estimated error in the air blank; f^{22} has been kept separate from the other errors as this uncertainty introduces correlated errors in $^{20}Ne/^{22}Ne$ and $^{21}Ne/^{22}Ne$ [16]. Extraction oven temperatures, estimated from optical pyrometry and a calibration using a W-Re thermocouple, should be accurate to 50°C.

Bulk neon in the samples (Table 1) was assumed to consist of a two-component mixture of spallation (s) and trapped (t) neon. For spallation neon, $(^{21}Ne/^{22}Ne)_s = 0.89$ was inferred from the high-temperature release fractions from Murchison and Mokoia (Fig. 1) assuming $(^{20}Ne/^{21}Ne)_s = 0.90$ which is consistent with the composition of spallation neon in a variety of samples with very little trapped neon [7,15,16]. Spallation-free "trapped" neon compositions are conventionally defined to lie on or near the tie-line connecting solar wind neon ($^{20}Ne/^{22}Ne = 13.7 \pm 0.3$, $^{21}Ne/^{22}Ne = 0.033 \pm 0.004$) with atmospheric neon ($^{20}Ne/^{22}Ne = 9.80 \pm 0.08$, $^{21}Ne/^{22}Ne = 0.0290 \pm 0.0003$). As recognized by previous workers, no reliably determined neon compositions lie significantly to the left of this line. For a limited number of meteorites where spallation neon contributions can be estimated independently (e.g., obtaining $^{21}Ne_s$ from unsaturated ^{26}Al activities in carbonaceous chondrites [7] or from $^{21}Ne_s$ in trapped-gas-free light-colored portions of gas-rich meteorites [2,8]) the spallation-free neon compositions are consistent with this left-limiting line. In the present case we have approximated this empirical limit by defining trapped neon to have $(^{21}Ne/^{20}Ne)_t = 0.0025$, which corresponds to a straight line in Fig. 1, passing through the origin and between the compositions of solar wind and atmospheric neon.

4. Results

The total neon contents and isotopic compositions for the three meteorites studied are summarized in Table 1. All three samples are very rich in trapped neon. The Mokoia and Cold Bokkeveld samples contain more trapped neon than any other carbonaceous chondrites except Nawapali [7]. The high trapped neon content of the Cold Bokkeveld sample was unexpected; several previous measurements of Cold Bokkeveld had shown less than 20×10^{-8} cm^3 STP ^{20}Ne/g [4,7]. Measured total ^{20}Ne/^{22}Ne ratios for Mokoia, Cold Bokkeveld and Murchison are 11.3, 11.9 and 10.0, respectively. The measured ^{21}Ne/^{22}Ne ratios are greater than the ^{21}Ne/^{22}Ne ratios of trapped neon presumably due to the addition of spallation neon. Therefore the trapped neon compositions are estimated by correcting for spallation using the assumption that $(^{21}Ne/^{20}Ne)_t = 0.0025$. This yields $(^{20}Ne/^{22}Ne)_t$ = 12.8, 12.0 and 10.5 for Mokoia, Cold Bokkeveld and Murchison respectively. Both the uncorrected and the corrected ^{20}Ne/^{22}Ne ratios are greater than ratios in the terrestrial atmosphere and neon-A and point to the presence of isotopically light trapped neon such as solar wind neon.

In Figs. 1 and 2 the measured neon isotopic compositions of the stepwise-release fractions are plotted on a neon three-isotope correlation plot of ^{20}Ne/^{22}Ne vs. ^{21}Ne/^{22}Ne. None of the complete patterns can be interpreted as simple two-component mixing lines; each sample *must* contain three or more different end-member compositions that are released in varying proportions during the stepwise analyses. As well as exhibiting quite variable isotopic compositions, the neon release patterns of the three samples are characterized by multiple peaks in the neon release rate (Fig. 3) which we ascribe to the release of neon from more than one site or mineral. For each sample, the overall trend in the data with increasing temperature is a decrease in ^{20}Ne/^{22}Ne accompanied by an increase in ^{21}Ne/^{22}Ne. The general increase in ^{21}Ne/^{22}Ne reflects an increasing relative contribution from spallation neon, as does in part the decrease in ^{20}Ne/^{22}Ne. With the assumed spallation contribution subtracted, trapped $(^{20}Ne/^{22}Ne)_t$ ratios apparently also decrease in a general way with increasing temperature.

TABLE 1

Total neon content and isotopic composition in gas-rich samples of carbonaceous chondrites (m = measured, t = trapped, s = spallation)

	$^{22}Ne_m$ *	f^{22} **	$^{21}Ne_s$ ***	$^{20}Ne_t$ ***	$(^{21}Ne/^{22}Ne)_m$	$(^{20}Ne/^{22}Ne)_m$	$(^{20}Ne/^{22}Ne)_t$ ***
Murchison	8.69	0.0006	0.39	86.8	0.0717	10.04	10.5
	± 0.10		± 0.03	± 1.1	± 0.0008	± 0.10	± 0.1
Mokoia	31.7	0.0002	3.32	355	0.140	11.30	12.8
	± 1.3 †		± 0.15	± 15	± 0.001	± 0.12	± 0.2
Cold Bokkeveld	33.7	0.0002	0.30	399	0.0395	11.85	11.95
	± 0.7		± 0.05	± 9	± 0.0008	± 0.17	± 0.2
Terrestrial atmosphere [32]					0.0290	9.80	
					± 0.0003	± 0.08	
Modern solar wind [17]					0.033	13.7	
					± 0.004	± 0.3	
Neon-A [2]					0.025	8.2	
					± 0.003	± 0.4	

* Amounts in 10^{-8} cm^3 STP/g are corrected for extraction blank and interferences as indicated in text. Tabulated errors are approximately 1σ. Systematic error due to uncertainty in pipette volume is $\leq$10%.

** f^{22} is the fraction of $^{22}Ne_m$ corresponding to uncertainty in the subtracted air blank [16].

*** Trapped and spallation components calculated assuming $(^{20}Ne/^{21}Ne)_s = 0.90$, $(^{21}Ne/^{22}Ne)_s = 0.89$, and $(^{21}Ne/^{20}Ne)_t = 0.0025$. Literature data for $^{21}Ne_s$ (in 10^{-8} cm^3/g) include: Murchison (0.25, 0.33 [10]), Mokoia (2.1–4.4 [7]) and Cold Bokkeveld (0.1 [7], 0.3 [4]).

† $^{22}Ne_m$ for Mokoia includes $1 \pm 1 \times 10^{-8}$ cm^3 STP/g estimated lost at 290° and 385°C.

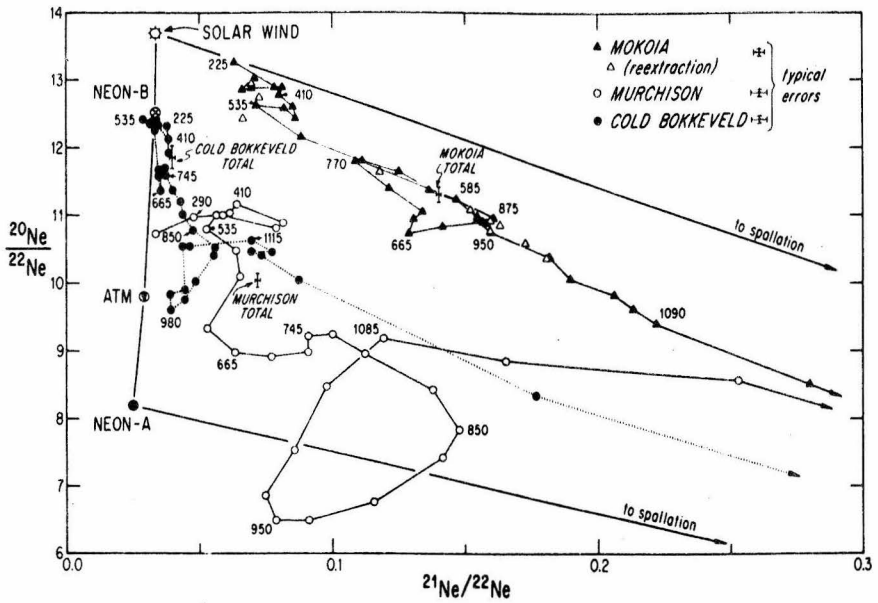

Fig. 2. Correlation of $^{20}Ne/^{22}Ne$ with $^{21}Ne/^{22}Ne$ in stepwise-release fractions from Mokoia, Murchison and Cold Bokkeveld. Total neon compositions obtained by summing over all release steps are also indicated. Release patterns for Murchison and Cold Bokkeveld are very similar, but with the Cold Bokkeveld pattern shifted systematically to higher $^{20}Ne/^{22}Ne$ due to the much higher abundance of isotopically light neon in this sample. For Cold Bokkeveld, 75% of the neon is contained in the first eight release fractions with compositions forming a tight cluster on or near the trapped neon tie-line. The preferred composition indicated by the cluster, $(^{20}Ne/^{22}Ne)_t$ about 12.4, is very close to neon-B which in lunar samples and gas-rich meteorites has been identified as solar wind neon [3], slightly modified during or after implantation.

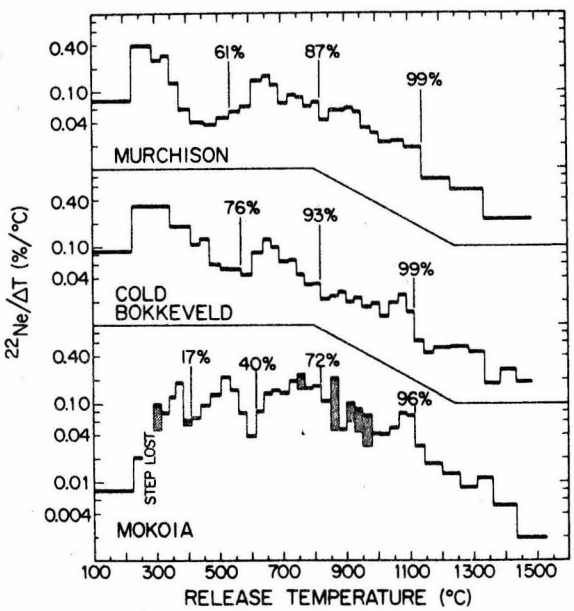

Fig. 3. Neon released from Murchison, Cold Bokkeveld, and Mokoia plotted on a logarithmic scale as a function of temperature. The amount of ^{22}Ne in each release fraction is expressed as a percentage of the total neon extracted from the sample and normalized to ΔT, the number of degrees the temperature was increased from the previous step. Bars representing the gas released in a given step are plotted between the temperatures of that step and the preceding one. The cumulative amounts of neon extracted from each of the samples are indicated at several stages of the stepwise release. For Mokoia, shaded bars represent neon released during isothermal reextractions. The neon in these reextractions has been added to the neon released during the following increase in temperature. The release patterns are characterized by multiple peaks. For Murchison and Cold Bokkeveld a single major release peak occurs at about 300°C and a minor peak at about 650°C. For Mokoia a larger fraction of the neon is released at higher temperatures, with three substantial peaks occurring at about 385°C, 500°C, and 750°C.

Mokoia. Neon is released from Mokoia in a complex series of distinct peaks (Fig. 3). About 17% of the total ^{22}Ne is released in the first peak at ~350°C with an integrated composition $^{20}Ne/^{22}Ne = 12.91$, $^{21}Ne/^{22}Ne = 0.074$ (225°C through 410°C). *It is apparent from Fig. 2 that any reasonable correction of this composite of eleven fractions to the trapped neon line results in a trapped composition which is within error equal to the composition of the present solar wind* [17], confirming previous indications of very light neon in Mokoia [9]. Slightly more than 20% of the neon is released in a second peak at ~535°C. The five fractions 440°C to 560°C encompassing the bulk of this peak plot slightly below and to the right of the ≤410°C fractions (Fig. 2). With increasing temperatures, $^{20}Ne/^{22}Ne$ decreases and $^{21}Ne/^{22}Ne$ increases abruptly to 0.147 in the 585°C fraction and 0.157 in the 615°C fraction, which marks a minimum in the rate of neon release (Fig. 3). In the following two fractions the rate of neon release rises again as $^{20}Ne/^{22}Ne$ continues to fall, but $^{21}Ne/^{22}Ne$ reverses sharply toward lower values. $^{20}Ne/^{22}Ne$ reaches a local minimum at 665°C, and then increases substantially while $^{21}Ne/^{22}Ne$ continues generally to decrease through the 770°C fraction. During this "loop" of isotopic compositions, the neon release rate remains high, forming a broad peak in Fig. 3. Above 770°C about 25% of the neon is released at a generally decreasing rate, and isotopic compositions fall on an essentially straight line leading to the 1090°C fraction (Fig. 2). The proportion of spallation neon increases rapidly in the last 5% of gas release, and the compositions in the final fractions are nearly pure spallation (Fig. 1).

The neon compositions of the low-temperature fractions from Mokoia provide evidence of trapped neon much richer in ^{20}Ne than any proposed planetary neon component (terrestrial or neon-A) and substantially lighter than neon-B observed in gas-rich meteorites and lunar regolith samples. Further definition of preferred trapped neon compositions can be obtained by seeking linear arrays of data that can be reasonably extrapolated to end-point compositions on the trapped neon tie-line, or clusters of points at a single composition on or very near the tie-line. Criteria are needed for recognizing significant linear trends and clusters. We suggest such a trend or cluster should be defined by a large number of points. It is preferable that a trend be uninterrupted by systematic deviations – any deviations present should be minor compared to the total extent of the trend. Also, to avoid experimental artifacts, the trend or cluster should encompass a major portion of the total neon in the sample. For Mokoia, the release fractions through the 1090°C step define a clear linear trend (dashed line in Fig. 1) that we consider satisfies such criteria. Of the 45 fractions ≤1090°C, 35 plot within 2σ of the dashed line in Fig. 1 and comprise about 70% of the neon in the sample. The major systematic deviation from the trend is the small "loop" formed by the 640°C to 745°C fractions which indicates the evolution of an additional component in these steps. The isotopically light end point of the trend is constrained to lie above and to the left of the low-temperature fractions, with $^{20}Ne/^{22}Ne \gtrsim 13.2$ and $^{21}Ne/^{22}Ne \lesssim 0.06$. The dashed line intersects the trapped neon line at $^{20}Ne/^{22}Ne = 13.7$, *the same as the composition of the present solar wind* [17]. The second end point must lie on the dashed line below and to the right of the 1090°C fraction, at a point such as *P*. The possible isotopic compositions of the P end point range from $^{20}Ne/^{22}Ne = 9.4$, $^{21}Ne/^{22}Ne = 0.22$ (P′) to $^{20}Ne/^{22}Ne = 0$, $^{21}Ne/^{22}Ne = 0.64$ (P″).

It is possible to identify preferred neon compositions in meteorites using the systematics of the three-isotope diagram and criteria for significant trends. It is very difficult to decide whether such compositions represent fundamental solar system components, or preferred mixtures of other unidentified components. The only obvious criterion that could be used to argue that a meteoritic composition was also a significant solar system component is agreement with the composition of a previously known major reservoir. Unfortunately, this argument is essentially circular – no new components can be identified – and also restricted at present to compositions matching the solar wind or earth's atmosphere. The fact that any reasonable fit to the trend of the Mokoia data passes through the composition of the modern solar wind, a well-characterized component corresponding to a major solar system reservoir, does suggest that this end point trapped composition represents an actual neon component and not just a preferred mixture that would disappear with more detailed scrutiny.

The "P" composition can not be immediately

identified with a major solar system reservoir. The isotopic composition of the postulated P component in Mokoia is characterized by an unusual, intermediate value of $^{21}Ne/^{22}Ne$ between 0.22 and 0.64. Isotopically, P could represent neon produced by a low-energy proton irradiation; in a Mokoia-composition target, protons of solar flare energies ($\lesssim$200 MeV) will generate neon with $^{21}Ne/^{22}Ne \approx 0.55$ and $^{20}Ne/^{22}Ne \approx 1.5$ [18], near P″ in Fig. 1. In other meteorites for which similar "solar"-P mixing trends can be defined [2,8], the analogous P end-members appear to have varying $^{21}Ne/^{22}Ne$ ratios, which leads to the suggestion [2] that P could instead be a homogeneous mixture of ordinary galactic cosmic ray spallation neon with trapped neon, the proportions of each varying from meteorite to meteorite.

Murchison. Three major features are seen in neon release and isotopic variation patterns from Murchison. First, neon with $^{20}Ne/^{22}Ne$ about 11 is released in the initial fractions (Fig. 2) and corresponds to a large neon release peak comprising about 60% of the total neon (Fig. 3). Second, above ~500°C $^{20}Ne/^{22}Ne$ decreases rapidly to a minimum of about 9 at just above 650°C, the temperature corresponding to a second release peak encompassing ~20% of the neon. Third, another rapid decrease in $^{20}Ne/^{22}Ne$ leads to a second minimum of 6.5 at 950°C, which yields a spallation-free trapped ratio of 6.9. This $(^{20}Ne/^{22}Ne)_t$ ratio is substantially below the value of 8.2 for neon-A, indicating the presence of a component enriched in ^{22}Ne or depleted in ^{20}Ne. On the basis of isotopic composition and temperature of release, this component is probably neon-E which was released at about 1000°C from the carbonaceous chondrites studied by Black and Pepin [8] and Black [4]. In spite of the relatively low total $^{20}Ne/^{22}Ne$ ratio in Murchison and the detailed stepwise release it was not possible to drive the neon composition closer to the neon-E region (Fig. 1). Above 950°C $(^{20}Ne/^{22}Ne)_t$ returns to values >10, and above about 1100°C the proportion of spallation neon increases substantially and the data points plot progressively nearer the position of neon produced solely by spallation on Mg and Si. The complex pattern of isotopic variations for Murchison shows no extensive linear arrays of data points such as was found for Mokoia. No distinctive end point compositions can be recognized; in particular, there is no indication of a well-defined neon-A composition.

It is possible to associate two of the three major stepwise-release features with neon released from gas-rich residues identified in Murchison [5], chromite and carbon with $(^{20}Ne/^{22}Ne)_t = 8.7$ and "Q" with $(^{20}Ne/^{22}Ne)_t = 6.8$. The neon released in the large first release peak is too light to be due to the gas in chromite, carbon or "Q" and reflects a substantial admixture of solar-like neon. Solar wind irradiation as a source for this neon is consistent with the observation of solar flare track-rich grains in Murchison [19]. The second and third features correspond to minima in $(^{20}Ne/^{22}Ne)_t$ at 9.3 and 6.9 which are suggestively close to the ratios 8.7 and 6.8 expected from degassing of pure chromite/carbon and "Q" in Murchison [5]. The minimum at 9.3 corresponds to a distinct trapped neon release peak at ~650°C which we identify with the release of neon from chromite/carbon. We associate the deeper minimum at $(^{20}Ne/^{22}Ne)_t = 6.9$ with the release of neon from "Q". We noted above that this feature is completely analogous to the 1000°C neon-E release feature of Black and Pepin [8]. This result suggests the characteristic high-temperature neon-E release pattern is closely related to the release of neon from "Q".

The composition of "Q" neon defined by dissolution experiments is not a measured value, but is inferred from the differences in neon composition measured for chromite/carbon and chromite/carbon plus "Q" samples [5]. "Q" neon in Murchison is reproducible but is not the same as in Allende [16]. In contrast, the composition of neon in chromite/carbon is the same. The ability to associate features in the neon thermal release and isotopic variation patterns with both gas-rich trace phases attests to the reality of a distinct "Q" neon reservoir in each of the meteorites.

Cold Bokkeveld. About three fourths of the neon in Cold Bokkeveld is released in a low-temperature release peak at ~350°C. The neon is nearly spallation-free with $^{20}Ne/^{22}Ne$ between 12.0 and 12.4, and $^{21}Ne/^{22}Ne$ between 0.03 and 0.04. The 535°C fraction actually plots to the left of the trapped neon line (Fig. 2) but the displacement is not significant. As was the case for Murchison, $^{20}Ne/^{22}Ne$ in the Cold Bokkeveld data reaches a local minimum at 665°C

at the height of a second, smaller release peak. Another local minimum in $^{20}Ne/^{22}Ne$ occurs in the 980°C fraction, corresponding by analogy with the Murchison pattern to the release of neon-E, although in Cold Bokkeveld the minimum trapped $^{20}Ne/^{22}Ne$ is only about 9.7. The pattern of isotopic variations of the Cold Bokkeveld sample is essentially the same as for the Murchison sample, but the pattern is shifted to systematically higher $^{20}Ne/^{22}Ne$ ratios in the more gas-rich Cold Bokkeveld sample. The shift suggests that the overall patterns for Murchison and Cold Bokkeveld reflect the superposition of a release pattern associated with differing amounts of isotopically light neon such as neon-B or solar wind over a second release pattern of trapped neon indigenous to the carbonaceous chondrite material (plus spallation neon). As with Murchison, there are no significant linear arrays of points in the Cold Bokkeveld data, but the eight low-temperature fractions between 225°C and 605°C form a well-defined cluster of points on the trapped neon tie-line representing about 75% of the neon released from the sample. This significant cluster defines a preferred composition with $(^{20}Ne/^{22}Ne)_t$ about 12.4 which does not correspond to the composition of a known solar system reservoir, but does closely resemble neon-B [3] found in gas-rich meteorites and lunar regolith samples. Neon-B in lunar soils has been identified as implanted solar wind, although comparison with the composition of solar wind ions implanted in the Apollo Al-foil experiment shows that the composition in the soils has been modified during or after implantation. Neon-B occurs frequently in chondritic and achondritic meteorites (cf. [3]) and associated evidence of solar particle irradiation has led to the identification of neon-B in these meteorites also as implanted solar wind [3]. Similar evidence of track-rich grains in Cold Bokkeveld [19] suggests the isotopically-light neon in this sample is also predominantly solar wind neon.

Comments on the high-resolution stepwise-release technique. The analyses of neon isotopic variations described above were obtained by extracting the neon in a far greater number of temperature steps than previous studies. A fine-scale stepwise extraction has certain advantages; we have been able to resolve release peaks from different sites (Fig. 3) that would overlap in a coarser-scale experiment (cf. [9]). This resolution allows us to deplete the neon in lower-temperature peaks before extracting neon from the subsequent higher-temperature peaks, possibly yielding a cleaner separation of components with different isotopic compositions. The detailed analyses reported here have revealed complex variations of the neon isotopic composition; in general, precise linear arrays were not obtained. Experiments with a limited number of extraction steps can result in the artificial combination of several distinct compositions which may lead to erroneous extrapolation of end point compositions. Analysis with a large number of extraction steps can also introduce isotopic artifacts into a release pattern, whereby the isotopic composition measured in a release fraction does not correspond to an actual composition of a gas component or mixture of components within the sample [28]. For instance, volume diffusion of 95% of the neon from spherical grains will lead to about a 10% fractionation in $^{20}Ne/^{22}Ne$ for the gas remaining in the grain. In natural samples, the magnitude of such a diffusive artifact will tend to be smaller, because of ranges in grain size, or release of gas by host-phase decomposition rather than diffusion. We do not believe that the major features of the release patterns in the present study can be explained by diffusive fractionation. The observed isotopic shifts are generally too large, or do not occur during final stages of neon release from individual reservoirs; for example, the minima in $(^{20}Ne/^{22}Ne)_t$ observed in 665°C release fractions occur at maxima in the neon release rates.

5. Discussion

The extremely wide range of observed neon compositions in solar system materials has led many workers to suggest that neon in solar system reservoirs consists of mixtures of components with distinctive compositions [1–4,7,20,21,34]. We too will assume that neon in the solar system initially consisted of a restricted number of primary components from various nucleosynthetic sources. We include galactic cosmic ray spallation neon as a primary component. The compositions of all mixtures of these components will plot on the neon three-isotope diagram within the smallest polygon enclosing all the primary components. Solar system processes such as

mixing, mass fractionation or fractionation due to plasma effects [36] may operate on the primary components and yield distinct components we call secondary. The compositions of secondary components could plot outside the polygon defined by the primary components, as well as in the interior or on tie-lines connecting primary components. Neon compositions observed today will plot within the smallest polygon enclosing all primary and secondary components.

At present, three components suffice for a formal explanation of reliably measured neon compositions; galactic cosmic ray spallation neon (with a range of compositions) and two trapped components, a light component with the $^{20}Ne/^{22}Ne = 13.7$, the solar wind composition, and a heavy component with $^{20}Ne/^{22}Ne \leqslant 1.5$, neon-E [21,34]. As recognized by Geiss [21], because of the limited variation observed in $^{21}Ne/^{22}Ne$ of spallation-free neon, all intermediate trapped $^{20}Ne/^{22}Ne$ compositions between solar and neon-E can be explained as special mixtures of these end-members. Similarly, any preferred composition with an intermediate $^{21}Ne/^{22}Ne$ ratio such as the "P" composition in Mokoia can be explained as a special mixture of trapped and spallation neon. Identification of trapped neon with a much lower ^{21}Ne content ($^{21}Ne/^{22}Ne << 0.0025$) could provide evidence of an additional independent trapped neon component.

As a heuristic device, we will describe a simple model of the solar nebula which embodies a minimum number of primary neon components. We recognize that while this minimum model may successfully describe the variations in neon isotopic composition, it may – or may not – require some modification to reconcile isotopic variations in other elements such as xenon, oxygen or magnesium. Since all of the material of the solar system almost certainly initially existed in either a gas-phase or a dust-phase, it is simplest to assume only two primary components of trapped neon existed, one consisting of neon in a well-mixed gas which we will refer to as gas-phase neon, the second consisting of a single neon component in the dust, labeled dust-phase neon. We assume that the light and heavy trapped components required to explain present neon isotopic measurements can be identified with these two primary components, gas-phase neon and dust-phase neon. Other intermediate preferred compositions such as those identified by Black [3,4] will be assumed to be secondary.

Nebular gas-phase neon can be shown to correspond to the isotopically light trapped neon component. The sun represents a largely unfractionated mixture of dust and gas. For typical interstellar dust/gas ratios (1% by mass) and cosmic Ne/H in the gas-phase ($\sim 10^4$ by number), the neon composition of such a mixture of dust and gas is determined solely by the composition of the gas, unless the ^{22}Ne content of the dust is five or more orders of magnitude greater than the ^{22}Ne content of the most gas-rich meteorite residue yet measured (1C59 from Murchison [5]). Thus neon in the sun will be gas-phase neon, assuming the sun has never been hot enough to sustain nuclear reactions modifying neon. The composition of the modern solar wind, although possibly fractionated by a few percent [21], indicates solar neon is light, and therefore that gas-phase neon is the light neon component with $^{20}Ne/^{22}Ne = 13.7$. By our model dust-phase neon must correspond to the heavy component, neon-E. Black [4,34] similarly associated neon-E with dust grains initially present in the solar nebula.

Condensed materials in the present solar system contain neon of intermediate isotopic composition indicating the presence of both gas-phase and dust-phase neon. Therefore mechanisms are required to combine dust-phase and gas-phase neon in the same object. The planets are massive enough to have gravitationally collected gas-phase neon in addition to dust-phase neon, but carbonaceous chondrite parent bodies are unlikely to have been sufficiently massive to do the same. More likely mechanisms for incorporating gas-phase neon into meteorites include ion implantation by a solar wind or similar charged-particle acceleration mechanism, or some process of direct occlusion or adsorption of gas-phase neon. The mechanisms by which the gas-phase neon may have been incorporated into an object can not be distinguished using the neon isotopic composition. However, the $^{3}He/^{4}He$ ratio in helium associated with the gas-phase neon can be used to distinguish relatively recent solar wind implantation from direct occlusion or adsorption from the primitive solar nebula. The ratio $^{3}He/^{4}He$ in the present solar wind, about 4.3×10^{-4} [17], has been augmented by the pre-main-sequence conversion in the sun of primordial deuterium to ^{3}He

(cf. [21,22]). The ^3He produced by deuterium burning yields $^3He/^4He$ about 2×10^{-4} for $D/H \sim 2 \times 10^{-5}$ (from the Jovian atmosphere [22]) and $^4He/H \sim 0.1$. Subtracting this contribution from a photospheric $^3He/^4He$ ratio about 3.9×10^{-4} estimated from the solar wind [21] gives an estimate for the primordial $^3He/^4He$ ratio of $\leq 1.9 \times 10^{-4}$ depending on the degree to which ^3He has been added to the photosphere by mixing from the solar interior. Prior to solar deuterium burning, which probably occurred early in the pre-main-sequence history of the sun (cf. [23]), both the solar wind, if present, and the non-solar gas-phase should have $^3He/^4He$ less than or about 1.9×10^{-4} and $^{20}Ne/^{22}Ne$ about 13.7. Black [24] inferred similar helium and neon compositions for his D component based on unconfirmed literature data and speculated that the D component was a pre-deuterium-burning solar wind [3,34]. However, no convincing evidence of implantation of gas by a pre-deuterium-burning solar wind has yet been presented. After deuterium burning the solar wind should have $^3He/^4He$ about 4×10^{-4} and $^{20}Ne/^{22}Ne = 13.7$, while the unmodified non-solar gas-phase will retain the lower primordial $^3He/^4He$ ratio.

Mokoia contains abundant gas-phase neon with $^{20}Ne/^{22}Ne = 13.7$. The bulk $(^3He/^4He)_t$ ratio in Mokoia is about 4.5×10^{-4} [25], close to the high solar wind value, which is compatible with the gas-phase neon trapped in Mokoia having been implanted by a solar wind after deuterium burning in the sun. That the composition of this neon is indistinguishable from that of the modern solar wind suggests the composition of neon in the solar wind has not changed since prior to the time of final compaction of Mokoia. A possible problem with this interpretation is that the $^{20}Ne/^{22}Ne$ of modern solar wind implanted in bulk lunar soils is about 9% lower than the value measured directly in the solar wind Al-foil experiment (cf. [26,27]). This difference is possibly due to isotopic fractionation accompanying diffusive loss of neon from the predominantly silicate soils during solar wind implantation or laboratory analysis [28]. This explanation is supported by the observation of systematically higher $^{20}Ne/^{22}Ne$ ratios in ilmenite separates from bulk soils. The apparent fidelity of Mokoia to the solar wind ratio might be explained if much of the isotopically light neon is trapped in the abundant magnetite present [14], and if magnetite is less subject to diffusive gas loss and fractionation, as seems to be the case for lunar ilmenite.

We have presented a general model to explain neon isotopic variations by mixtures of two primary trapped neon components, gas-phase neon of solar wind composition and dust-phase neon with the composition of neon-E. As indicated earlier, the systematically higher $^{20}Ne/^{22}Ne$ ratios in the release pattern for the Cold Bokkeveld sample compared with the otherwise similar Murchison pattern (Fig. 2) are compatible with the addition of different amounts of light gas-phase neon to similar distributions of heavy neon.

If variable amounts of gas-phase neon were added to dust with a constant neon-E content, a positive correlation between the amount of neon and $^{20}Ne/^{22}Ne$ in a sample would be expected. For bulk meteorite samples with $^{22}Ne_t$ contents greater than about 3×10^{-8} cm^3 STP/g an approximate correlation between amount and composition exists [7] and is compatible with the addition of gas-phase neon to material with $1-2 \times 10^{-8}$ cm^3 STP/g ^{22}Ne from neon-E. For example, the Cold Bokkeveld and Mokoia samples investigated have both much higher $^{22}Ne_t$ contents and total $(^{20}Ne/^{22}Ne)_t$ ratios than the Murchison sample (Table 1). For meteorites with low neon contents, $^{20}Ne/^{22}Ne$ should approach the composition in the dust-phase, neon-E. However, this is not apparently the case, since in bulk meteorite samples with $^{22}Ne_t$ contents less than about 2×10^{-8} cm^3 STP/g, the $(^{20}Ne/^{22}Ne)_t$ ratio remains roughly constant at about 8, the preferred composition among carbonaceous chondrites defined as neon-A. This composition requires a mechanism for mixing in relatively constant proportion gas-phase neon with grains containing neon-E. As recognized by Black [4] who suggested neon-A might be a mixture, the amount of gas-phase neon received by individual grains could vary widely, but the large number of grains in a bulk sample should ensure a representative sample of the parent population of grains with admixed gas-phase neon. The total neon compositions of bulk samples will be essentially constant, reflecting the mean composition of the parent population of grains. The variation in neon content of bulk samples with $(^{20}Ne/^{22}Ne)_t$ about 8 requires the presence of diluting material containing no trapped neon. This material has lost any neon-E initially present, possibly during heat-

ing of the collapsing solar nebula.

This picture is consistent with the results of stepwise heating experiments ([4]; this work) which generally show no clear evidence of a preferred neon-A composition, but rather a pattern of continuous variation in trapped $^{20}Ne/^{22}Ne$ that, e.g. for Murchison (Fig. 2), starts well above neon-A at low temperatures, and migrates in a complex fashion to well below neon-A at higher temperatures before once again returning to higher values. Such variations are suggestive of mixtures of the two primary components.

The fact that complex variations in the trapped composition *are* seen requires the components to be mixed in various proportions in sites with differing gas-retention characteristics. A large fraction of the trapped neon of intermediate compositions in carbonaceous chondrites is held in a restricted number of trace-mineral phases such as chromite, carbon, and "Q" [5,29]. The composition of neon associated with "Q" is variable, with $^{20}Ne/^{22}Ne = 6.8$ in Murchison [5] and 10.4 in Allende [16]. Thus the composition of neon in "Q" is apparently compatible with varying mixtures of gas-phase and dust-phase neon.

In contrast, neon in chromite/carbon varies little in composition. Chromite and carbon residues from Allende [29,30], Murchison [5], Murray [6], Cold Bokkeveld [6] and Orgueil [31] all contain neon with essentially the same $(^{20}Ne/^{22}Ne)_t$ of about 8.6. This value is close to that of neon-A and we suggest that the neon-A composition deduced from bulk meteorite analyses is due to a major portion of the neon in those meteorites being neon in chromite/carbon with the above composition. The apparently uniform composition of neon in chromite/carbon may again be attributed to the averaging effect of a large number of gas-bearing grains as discussed above. In this case, detailed stepwise-release experiments *on samples containing relatively few grains* might reveal isotopic variations. Alternatively, mixing could have occurred prior to the incorporation of gas into the residues, in which case neon in all the grains might have the same composition. The $^3He/^4He$ ratio in chromite/carbon, about 1.3×10^{-4}, is too low to come from helium implanted by a post-deuterium-burning solar wind, which suggests that the gas-phase neon as well as the helium were incorporated into the chromite/carbon mixture by some other mechanism.

6. Conclusions

Neon in solar system reservoirs can be understood at present as mixtures of galactic cosmic ray spallation neon and two primary components of trapped neon, dust-phase neon-E and gas-phase neon with $^{20}Ne/^{22}Ne = 13.7$. Condensed materials in the solar system, such as the earth and meteorites, contain trapped neon of intermediate composition that requires mechanisms for combining gas-phase and dust-phase neon. Gas-phase neon implanted in grains by the solar wind after deuterium burning in the sun can be distinguished from gas-phase neon incorporated by other mechanisms since associated solar wind helium will have a high $^3He/^4He$ ratio about 4×10^{-4} in contrast to unmodified gas-phase helium with an estimated $^3He/^4He$ ratio $\leq 1.9 \times 10^{-4}$.

The high-resolution stepwise-release technique revealed complex patterns of release peaks and isotopic variations in the neon extracted from Murchison, Cold Bokkeveld, and Mokoia. The isotopic patterns for Murchison and Cold Bokkeveld are compatible with the release of mixtures of gas-phase and dust-phase neon from various sites. Neon in low-temperature fractions is predominantly trapped neon of intermediate isotopic composition with $^{20}Ne/^{22}Ne$ about 11 in Murchison and 12.4 in the more neon-rich Cold Bokkeveld. At higher temperatures, neon compositions migrate toward neon-E along the trapped neon line, with only minor amounts of spallation neon present. Minimum values of $(^{20}Ne/^{22}Ne)_t$ reached at about 950°C are 9.7 for Cold Bokkeveld and 6.9, well below the nominal composition of neon-A, for Murchison.

In Mokoia a preferred neon isotopic composition is apparent. Both the neon compositions of low-temperature release fractions and a significant linear trend extending through high-temperature fractions point to the presence of essentially pure gas-phase neon with $(^{20}Ne/^{22}Ne)_t = 13.7$. The bulk $(^3He/^4He)_t$ of 4.5×10^{-4} in Mokoia identifies this gas-phase neon as implanted solar wind, which allows us to conclude that the $^{20}Ne/^{22}Ne$ ratio in the solar wind has not changed significantly since the time of final compaction of Mokoia.

Some of the details in the neon release patterns of the samples can be associated with neon released from gas-rich trace-mineral phases. The release pat-

terns for all three meteorites show a local minimum in $(^{20}Ne/^{22}Ne)_t$ at 665°C which for Murchison can be identified with the release of neon by chromite/carbon. The Murchison and Cold Bokkeveld patterns also show minima at about 950°C which can be identified with the release of neon from neon-E-rich phases and, again for Murchison, with neon released by "Q". The composition of neon in "Q" is apparently variable and is compatible with mixtures of dust-phase and gas-phase neon. The total composition of neon extracted from chromite/carbon separates from a number of meteorites appears to be constant. Detailed investigations are needed to determine if this is due to averaging over a large number of grains or to the presence of a special mixture of constant composition.

A large fraction of the neon of intermediate isotopic composition in meteorites is found in the gas-rich trace minerals. The composition of neon associated with chromite/carbon, $(^{20}Ne/^{22}Ne)_t \approx 8.6$, is close to the composition assigned to neon-A, suggesting that the neon-A composition determined in bulk meteorite samples is largely controlled by neon in chromite/carbon. In an analogous fashion, we suggest the total isotopic composition of trapped neon in each solar system body is determined by the relative amounts accreted of gas-phase and dust-phase neon. If much of the dust-phase neon is carried by various gas-rich trace phases containing different mixtures of dust-phase and gas-phase neon, the final composition of neon in an object will depend on the relative proportions of the various trace phases accreted, as well as the amounts of galactic cosmic ray neon incorporated and pure gas-phase neon added by processes such as gravitational collection or solar wind implantation. For example, the composition of neon in the sun, which is thought to represent an unfractionated mixture of nebular dust and gas, will be dominated by that of neon in the gas-phase unless the neon content of the dust is exceedingly high. Neon in Jupiter should also be dominated by gas-phase neon even though the planet was probably formed from material with an order of magnitude higher relative dust contribution than the sun (cf. [35]). In contrast, the earth and meteorites have intermediate neon compositions indicating approximately equal contributions from gas-phase and dust-phase neon.

Acknowledgements

The presentation of this work benefited from comments by H. Craig, D. Phinney, and an anonymous reviewer. We acknowledge support of NSF grants GP-28027 and MPS71-02670.

References

1 R.O. Pepin, Neon and xenon in carbonaceous chondrites, in: Origin and Distribution of the Elements, L.H. Ahrens, ed. (Pergamon, Oxford, 1968) 379–386.
2 R.O. Pepin, Trapped neon in meteorites, Earth Planet. Sci. Lett. 2 (1967) 13–18.
3 D.C. Black, On the origins of trapped helium, neon and argon isotopic variations in meteorites, I. Gas-rich meteorites, lunar soil and breccia, Geochim. Cosmochim. Acta 36 (1972) 347–375.
4 D.C. Black, On the origins of trapped helium, neon, and argon isotopic variations in meteorites, II. Carbonaceous meteorites, Geochim. Cosmochim. Acta 36 (1972) 377–394.
5 B. Srinivasan, J. Gros and E. Anders, Noble gases in separated meteoritic minerals: Murchison (C2), Ornans (C3), Karoonda (C5), and Abee (E4), J. Geophys. Res. 82 (1977) 762–778.
6 D. Phinney, U. Frick and J.H. Reynolds, Rare-gas-rich separates from carbonaceous chondrites, in: Lunar Science VII (Lunar Science Institute, Houston, Texas, 1976) 691–693.
7 E. Mazor, D. Heymann and E. Anders, Noble gases in carbonaceous chondrites, Geochim. Cosmochim. Acta 34 (1970) 781–824.
8 D.C. Black and R.O. Pepin, Trapped neon in meteorites, II, Earth Planet. Sci. Lett. 6 (1969) 395–405.
9 O.K. Manuel, R.J. Wright, D.K. Miller and P.K. Kuroda, Isotopic compositions of rare gases in the carbonaceous chondrites Mokoia and Allende, Geochim. Cosmochim. Acta 36 (1972) 961–983.
10 D.D. Bogard, R.S. Clarke, J.E. Keith and M.A. Reynolds, Noble gases and radionuclides in Lost City and other recently fallen meteorites, J. Geophys. Res. 76 (1971) 4076–4083.
11 J.T. Wasson, Meteorites (Springer-Verlag, New York, N.Y., 1974) 16–24, 284.
12 L.H. Fuchs, E. Olsen and K.J. Jensen, Mineralogy, mineral-chemistry, and composition of the Murchison (C2) meteorite, Smithsonian Contrib. Earth Sci. 10 (1973).
13 R.S. Clarke, Jr., E. Jarosewich, B. Mason, J. Nelen, M. Gómez and J.R. Hyde, The Allende, Mexico, meteorite shower, Smithsonian Contrib. Earth Sci. 5 (1970) 47.
14 D.E. Watson, E.E. Larson, J.M. Herndon and M.W. Rowe, Thermomagnetic analysis of meteorites, 2. C2 chondrites, Earth Planet Sci. Lett. 27 (1975) 101–107.

15 S.P. Smith and J.C. Huneke, Cosmogenic neon produced from sodium in meteoritic minerals, Earth Planet. Sci. Lett. 27 (1975) 191–199.
16 S.P. Smith, J.C. Huneke, R.S. Rajan and G.J. Wasserburg, Neon and argon in the Allende meteorite, Geochim. Cosmochim. Acta 41 (1977) 627–647.
17 J. Geiss, F. Bühler, H. Cerutti, P. Eberhardt and Ch. Filleux, Solar wind composition experiment, Apollo 16 Prelim. Sci. Rep., NASA SP-315 (1972) 14-1 to 14-10.
18 J.R. Walton, Production of He, Ne, and Ar isotopes and U-236 by solar cosmic ray protons at various depths in lunar materials, in: Lunar Science VII (Lunar Science Institute, Houston, Texas, 1976) 907–909.
19 J.N. Goswami, I.D. Hutcheon and J.D. Macdougall, Microcraters and solar flare tracks in crystals from carbonaceous chondrites and lunar breccias, Proc. 7th Lunar Sci. Conf., Geochim. Cosmochim. Acta Suppl. 7, 1 (1976) 543–562.
20 P. Signer and H.E. Suess, Rare gases in the sun, in the atmosphere and in meteorites, in: Earth Science and Meteoritics, J. Geiss and E.D. Goldberg, eds. (North-Holland, Amsterdam, 1963) 241–272.
21 J. Geiss, Noble gas isotopes and deuterium in the solar system, in: Symposium on the Origin of the Solar System, Nice, H. Reeves, ed. (1972) 217–234.
22 V. Trimble, The origin and abundances of the chemical elements, Rev. Mod. Phys. 47 (1975) 877–976.
23 D.D. Clayton, Principles of Stellar Evolution and Nucleosynthesis (McGraw-Hill, New York, N.Y., 1968) 364–365.
24 D.C. Black, Trapped helium-neon isotopic correlations in gas-rich meteorites and carbonaceous chondrites, Geochim. Cosmochim. Acta 34 (1970) 132–140.
25 E. Anders, D. Heymann and E. Mazor, Isotopic composition of primordial helium in carbonaceous chondrites, Geochim. Cosmochim. Acta 34 (1970) 127–131.
26 P. Eberhardt, J. Geiss, H. Graf, N. Grögler, U. Krähenbühl, H. Schwaller, J. Schwarzmüller and A. Stettler, Trapped solar wind noble gases, exposure age and K/Ar-age in Apollo 11 lunar fine material, Proc. Apollo 11 Lunar Sci. Conf., Geochim. Cosmochim. Acta Suppl. 1, 2 (1970) 1037–1070.
27 D.D. Bogard and L.E. Nyquist, Noble gas studies on regolith materials from Apollo 14 and 15, Proc. 3rd Lunar Sci. Conf., Geochim. Cosmochim. Acta Suppl. 3, 2 (1972) 1797–1819.
28 J.C. Huneke, Diffusive fractionation of surface implanted gases, Earth Planet. Sci. Lett. 21 (1973) 35–44.
29 R.S. Lewis, J. Gros and E. Anders, Isotopic anomalies of noble gases in meteorites and their origins, 2. Separated minerals from Allende, J. Geophys. Res. 82 (1977) 779–792.
30 U. Frick and J.H. Reynolds. On the host phases for planetary noble gases in Allende, in: Lunar Science VIII (Lunar Science Institute, Houston, Texas, 1977) 319–321.
31 U. Frick and R.K. Moniot, Planetary noble gas components in Orgueil, Proc. 8th Lunar Sci. Conf. (1977) in press.
32 P. Eberhardt, O. Eugster and K. Marti, A redetermination of the isotopic composition of atmospheric neon, Z. Naturforsch. 20a (1965) 623–624.
33 P. Eberhardt, Ne-E-rich phase in Orgueil, Meteoritics 10 (1975) 401.
34 D.C. Black, The A, B, C's of trapped helium, neon and argon in meteorites and lunar samples, in: Symposium on the Origin of the Solar System, Nice, H. Reeves, ed. (1972) 237–244.
35 A.G.W. Cameron and J.B. Pollack, On the origin of the solar system and of Jupiter and its satellites, in: Jupiter, T. Gehrels, ed. (Univ. of Arizona, Tucson, Ariz., 1976) 61–84.
36 G. Arrhenius and H. Alfven, Fractionation and condensation in space, Earth Planet. Sci. Lett. 10 (1971) 353–367.

Table 2: Neon content and isotopic composition in stepwise thermal release fractions from gas-rich samples of carbonaceous chondrites. (r=reextraction)

Temperature	^{22}Ne (10^{-8}cc STP/g)	$^{20}Ne/^{22}Ne$	$^{21}Ne/^{22}Ne$	f^{22}	$(^{20}Ne/^{22}Ne)_t$
MURCHISON					
225°C	0.832 ± 0.023	10.72 ± 0.04	0.0337 ± 0.0009	0.0009	10.80
290°	2.251 ± 0.087	10.97 ± 0.04	0.0480 ± 0.0009	0.0003	11.20
320°	0.657 ± 0.018	11.00 ± 0.05	0.0587 ± 0.0020	0.0011	11.35
345°	0.630 ± 0.017	10.81 ± 0.03	0.0788 ± 0.0014	0.0012	11.55
375°	0.335 ± 0.010	10.89 ± 0.09	0.0814 ± 0.0024	0.0022	11.55
410°	0.182 ± 0.005	11.16 ± 0.09	0.0640 ± 0.0032	0.0041	11.40
455°	0.156 ± 0.004	11.03 ± 0.11	0.0614 ± 0.0068	0.0048	11.40
495°	0.130 ± 0.004	11.00 ± 0.07	0.0565 ± 0.0059	0.0058	11.30
535°	0.159 ± 0.004	10.80 ± 0.05	0.0528 ± 0.0046	0.0047	11.10
570°	0.166 ± 0.005	10.48 ± 0.06	0.0638 ± 0.0032	0.0045	10.90
605°	0.193 ± 0.005	10.09 ± 0.05	0.0652 ± 0.0034	0.0039	10.50
640°	0.417 ± 0.011	9.33 ± 0.04	0.0529 ± 0.0012	0.0018	9.60
665°	0.343 ± 0.009	8.98 ± 0.05	0.0630 ± 0.0017	0.0022	9.35
690°	0.243 ± 0.007	8.91 ± 0.06	0.0767 ± 0.0023	0.0031	9.35
720°	0.182 ± 0.005	8.98 ± 0.05	0.0905 ± 0.0022	0.0041	9.65
745°	0.194 ± 0.005	9.21 ± 0.05	0.0906 ± 0.0016	0.0038	9.90
770°	0.183 ± 0.005	9.24 ± 0.05	0.0996 ± 0.0041	0.0040	10.00
795°	0.138 ± 0.004	8.96 ± 0.07	0.1120 ± 0.0037	0.0054	9.80
820°	0.159 ± 0.004	8.43 ± 0.06	0.1376 ± 0.0038	0.0047	9.50
850°	0.110 ± 0.003	7.84 ± 0.06	0.1474 ± 0.0029	0.0068	9.00
875°	0.127 ± 0.004	7.43 ± 0.05	0.1412 ± 0.0019	0.0059	8.45
900°	0.127 ± 0.004	6.77 ± 0.05	0.1152 ± 0.0036	0.0059	7.50
925°	0.131 ± 0.004	6.50 ± 0.05	0.0907 ± 0.0021	0.0057	7.00
950°	0.116 ± 0.004	6.50 ± 0.05	0.0784 ± 0.0027	0.016	6.90
980°	0.087 ± 0.003	6.87 ± 0.05	0.0744 ± 0.0033	0.0086	7.25
1005°	0.062 ± 0.002	7.53 ± 0.07	0.0853 ± 0.0055	0.012	8.05
1045°	0.076 ± 0.002	8.47 ± 0.06	0.974 ± 0.0047	0.0098	9.15
1085°	0.078 ± 0.002	9.18 ± 0.08	0.1189 ± 0.0058	0.0097	10.15
1140°	0.089 ± 0.003	8.86 ± 0.07	0.1651 ± 0.0052	0.0083	10.40
1230°	0.057 ± 0.002	8.57 ± 0.08	0.2559 ± 0.0075	0.015	11.35
1335°	0.048 ± 0.002	7.71 ± 0.08	0.3225 ± 0.0077	0.019	11.30
1485°	0.029 ± 0.001	4.75 ± 0.07	0.566 ± 0.011	0.034	11.30
Total	8.686 ± 0.097	10.04 ± 0.10	0.0717 ± 0.0008	0.0006	10.5

Table 2: (cont.)

Temperature	^{22}Ne (10^{-8} cc STP/g)	$^{20}Ne/^{22}Ne$	$^{21}Ne/^{22}Ne$	f^{22}	$(^{20}Ne/^{22}Ne)_t$
COLD BOKKEVELD					
225°	3.758 ± 0.145	12.32 ± 0.05	0.0379 ± 0.0006	0.0003	12.40
345°	13.613 ± 0.703	11.91 ± 0.05	0.0385 ± 0.0007	0.0001	12.00
410°	4.045 ± 0.156	12.12 ± 0.05	0.0387 ± 0.0009	0.0002	12.20
440°	1.091 ± 0.042	12.41 ± 0.05	0.0340 ± 0.0012	0.0008	12.45
470°	1.293 ± 0.050	12.39 ± 0.05	0.0327 ± 0.0006	0.0006	12.40
505°	0.713 ± 0.020	12.37 ± 0.05	0.0316 ± 0.0012	0.0011	12.40
535°	0.540 ± 0.015	12.42 ± 0.05	0.0289 ± 0.0025	0.0015	12.40
570°	0.625 ± 0.017	12.33 ± 0.05	0.0349 ± 0.0021	0.0012	12.40
605°	0.521 ± 0.014	12.25 ± 0.05	0.0333 ± 0.0022	0.0016	12.30
640°	1.009 ± 0.039	11.57 ± 0.05	0.0347 ± 0.0009	0.0008	11.60
665°	1.029 ± 0.040	11.36 ± 0.05	0.0356 ± 0.0008	0.0008	11.40
690°	0.827 ± 0.032	11.67 ± 0.05	0.0350 ± 0.0012	0.0009	11.75
720°	0.653 ± 0.018	11.70 ± 0.05	0.0372 ± 0.0020	0.0012	11.80
745°	0.566 ± 0.016	11.58 ± 0.05	0.0376 ± 0.0019	0.0014	11.65
770°	0.370 ± 0.010	11.36 ± 0.05	0.0400 ± 0.0023	0.0022	11.50
795°	0.278 ± 0.008	11.20 ± 0.05	0.0430 ± 0.0022	0.0030	11.40
820°	0.285 ± 0.008	11.01 ± 0.05	0.0437 ± 0.0026	0.0028	11.20
850°	0.217 ± 0.006	10.76 ± 0.06	0.0476 ± 0.0032	0.0037	10.95
875°	0.197 ± 0.006	10.52 ± 0.07	0.0559 ± 0.0031	0.0041	10.80
900°	0.222 ± 0.006	10.41 ± 0.06	0.0554 ± 0.0030	0.0037	10.70
925°	0.162 ± 0.005	10.02 ± 0.06	0.0486 ± 0.0022	0.0050	10.25
950°	0.186 ± 0.005	9.75 ± 0.07	0.0445 ± 0.0030	0.0044	9.90
980°	0.170 ± 0.005	9.61 ± 0.06	0.0392 ± 0.0030	0.0047	9.70
1005°	0.157 ± 0.004	9.83 ± 0.06	0.0390 ± 0.0033	0.0051	9.90
1035°	0.129 ± 0.004	9.90 ± 0.07	0.0446 ± 0.0067	0.0062	10.05
1065°	0.194 ± 0.005	10.53 ± 0.06	0.0437 ± 0.0030	0.0042	10.70
1090°	0.203 ± 0.006	10.53 ± 0.06	0.0464 ± 0.0027	0.0040	10.70
1115°	0.123 ± 0.003	10.63 ± 0.06	0.0696 ± 0.0043	0.0066	11.10
1145°	0.063 ± 0.002	10.45 ± 0.09	0.0772 ± 0.0072	0.013	11.05
1175°	0.044 ± 0.002	10.46 ± 0.11	0.0695 ± 0.0128	0.019	10.95
1230°	0.094 ± 0.003	10.41 ± 0.08	0.0731 ± 0.0053	0.0086	10.95
1285°	0.099 ± 0.003	10.04 ± 0.06	0.0875 ± 0.0051	0.0091	10.70
1335°	0.076 ± 0.002	8.35 ± 0.06	0.1766 ± 0.0054	0.012	9.90
1385°	0.031 ± 0.001	6.61 ± 0.09	0.320 ± 0.011	0.031	9.60
1435°	0.046 ± 0.002	6.54 ± 0.07	0.300 ± 0.010	0.022	9.3
1485°	0.032 ± 0.002	7.08 ± 0.11	0.295 ± 0.012	0.033	9.9
Total	33.66 ± 0.74	11.85 ± 0.17	0.0395 ± 0.0008	0.0002	11.95

Table 2: (cont.)

Temperature	^{22}Ne (10^{-8}cc STP/g)	$^{22}Ne/^{22}Ne$	$^{21}Ne/^{22}Ne$	f^{22}	$(^{20}Ne/^{22}Ne)_t$
MOKOIA					
225°C	0.311 ± 0.009	13.26 ± 0.05	0.0631 ± 0.0017	0.0023	13.69
255°	0.202 ± 0.006	12.89 ± 0.06	0.0783 ± 0.0029	0.0034	13.55
290° (lost)*	---	---	---	---	---
225° (r)	0.005 ± 0.001	13.1 ± 2.8	0.04 ± 0.12	0.026	---
255° (r)	0.112 ± 0.008	12.42 ± 0.15	0.0665 ± 0.0057	0.0044	12.90
290° (r)	0.298 ± 0.021	12.74 ± 0.07	0.0727 ± 0.0025	0.0017	13.32
315°	0.370 ± 0.027	12.88 ± 0.07	0.0699 ± 0.0020	0.0013	13.42
340°	0.621 ± 0.046	12.86 ± 0.05	0.0662 ± 0.0012	0.0008	13.34
360°	0.784 ± 0.058	13.02 ± 0.05	0.0708 ± 0.0011	0.0007	13.57
385°	1.494 ± 0.111	12.89 ± 0.05	0.0815 ± 0.0026	0.0009	13.60
385° (r)	0.072 ± 0.005	12.96 ± 0.16	0.0698 ± 0.0095	0.0068	13.49
410°	0.228 ± 0.017	12.77 ± 0.07	0.0801 ± 0.0031	0.0021	13.46
440°	0.636 ± 0.047	12.60 ± 0.05	0.0852 ± 0.0024	0.0008	13.36
470°	0.917 ± 0.068	12.43 ± 0.05	0.0861 ± 0.0010	0.0005	13.20
505°	1.449 ± 0.108	12.57 ± 0.05	0.0819 ± 0.0005	0.0004	13.28
535°	2.093 ± 0.156	12.61 ± 0.05	0.0715 ± 0.0004	0.0003	13.17
560°	1.187 ± 0.088	12.15 ± 0.05	0.0882 ± 0.0008	0.0004	12.94
585°	0.616 ± 0.046	11.23 ± 0.05	0.1467 ± 0.0013	0.0008	12.84
615°	0.369 ± 0.027	10.89 ± 0.05	0.1565 ± 0.0018	0.0013	12.61
640°	0.638 ± 0.028	10.83 ± 0.05	0.1415 ± 0.0012	0.0008	12.31
665°	1.075 ± 0.047	10.72 ± 0.05	0.1286 ± 0.0006	0.0004	12.00
690°	1.173 ± 0.051	10.94 ± 0.05	0.1307 ± 0.0007	0.0004	12.28
720°	1.289 ± 0.056	11.05 ± 0.05	0.1340 ± 0.0006	0.0003	12.44
745°	1.535 ± 0.067	11.38 ± 0.05	0.1213 ± 0.0006	0.0003	12.62
745° (r)	0.639 ± 0.028	11.64 ± 0.05	0.1177 ± 0.0013	0.0007	12.84
770°	1.184 ± 0.052	11.78 ± 0.05	0.1086 ± 0.0008	0.0004	12.85
795°	1.239 ± 0.054	11.79 ± 0.05	0.1112 ± 0.0010	0.0004	12.90
820°	1.317 ± 0.058	11.64 ± 0.05	0.1251 ± 0.0010	0.0004	12.95
850°	1.041 ± 0.046	11.37 ± 0.05	0.1364 ± 0.0009	0.0005	12.83
850° (r)	0.616 ± 0.027	11.07 ± 0.05	0.1519 ± 0.0015	0.0008	12.74
850° (r)	0.370 ± 0.016	10.92 ± 0.06	0.1597 ± 0.0021	0.0013	12.69
850° (r)	0.305 ± 0.013	10.85 ± 0.06	0.1631 ± 0.0028	0.0015	12.67
875°	0.367 ± 0.016	10.95 ± 0.06	0.1607 ± 0.0023	0.0013	12.74
900°	0.371 ± 0.016	10.97 ± 0.06	0.1544 ± 0.0020	0.0013	12.67
900° (r)	0.319 ± 0.014	10.88 ± 0.06	0.1579 ± 0.0024	0.0015	12.62
925°	0.476 ± 0.021	10.92 ± 0.06	0.1545 ± 0.0017	0.0010	12.61

Table 2: (cont.)

Temperature		^{22}Ne (10^{-8}cc STP/g)	$^{22}Ne/^{22}Ne$	$^{21}Ne/^{22}Ne$	f^{22}	$(^{20}Ne/^{22}Ne)_t$
925°	(r)	0.332 ± 0.015	10.76 ± 0.06	0.1595 ± 0.0018	0.0032	12.51
950°		0.345 ± 0.015	10.74 ± 0.06	0.1598 ± 0.0021	0.0014	12.49
950°	(r)	0.231 ± 0.010	10.58 ± 0.07	0.1729 ± 0.0029	0.0021	12.51
950°	(r)	0.175 ± 0.008	10.36 ± 0.08	0.1809 ± 0.0036	0.0028	12.38
980°		0.269 ± 0.012	10.36 ± 0.06	0.1819 ± 0.0028	0.0018	12.40
1005°		0.331 ± 0.014	10.07 ± 0.06	0.1899 ± 0.0025	0.0014	12.18
1035°		0.386 ± 0.017	9.84 ± 0.05	0.2062 ± 0.0020	0.0013	12.16
1065°		0.468 ± 0.020	9.63 ± 0.05	0.2132 ± 0.0016	0.0011	12.02
1090°		0.600 ± 0.026	9.41 ± 0.04	0.2220 ± 0.0013	0.0009	11.89
1115°		0.557 ± 0.024	8.51 ± 0.04	0.2800 ± 0.0015	0.0009	11.68
1145°		0.275 ± 0.012	7.01 ± 0.05	0.3915 ± 0.0027	0.0018	11.53
1200°		0.302 ± 0.013	6.23 ± 0.04	0.4409 ± 0.0027	0.0016	11.22
1255°		0.226 ± 0.010	4.94 ± 0.04	0.5318 ± 0.0039	0.0022	10.78
1310°		0.152 ± 0.007	4.02 ± 0.03	0.6284 ± 0.0052	0.0033	11.4
1360°		0.178 ± 0.008	2.28 ± 0.02	0.766 ± 0.006	0.0030	11.1
1435°		0.105 ± 0.005	1.38 ± 0.02	0.845 ± 0.010	0.0059	11.9
1530°		0.60 ± 0.003	1.51 ± 0.03	0.835 ± 0.016	0.012	11.9
Total*		30.71 ± .32	11.30 ± 0.12	0.140 ± 0.001	0.0002	12.8

*An additional estimated 1±1 was lost. Entire fraction estimated at 0.8 ± 0.8 was lost at 290° C. After normal extraction and gas transfer at 385°C$_\delta$ the oven was accidentally exposed to pump while still hot. From the reextract at 385° we estimate the gas lost to be 0.2 ± 0.2 x 10^{-8}cc STP/g.

PAPER 3. NEON AND ARGON IN THE ALLENDE METEORITE

S. P. SMITH, J. C. HUNEKE, R. S. RAJAN,

AND G. J. WASSERBURG

GEOCHIMICA ET COSMOCHIMICA ACTA,

VOL. 41, NO. 5, pp. 627-647, 1977,

Geochimica et Cosmochimica Acta, 1977, Vol. 41, pp. 627 to 647. Pergamon Press. Printed in Great Britain

Neon and argon in the Allende meteorite

S. P. SMITH, J. C. HUNEKE, R. S. RAJAN* and G. J. WASSERBURG

The Lunatic Asylum of the Charles Arms Laboratory, Division of Geological and Planetary Sciences,† California Institute of Technology, Pasadena, California 91125, U.S.A.

(*Received* 18 *May* 1976; *accepted in revised form* 1 *December* 1976)

Abstract—Trapped and cosmogenic Ne and Ar were measured in Ca,Al-rich aggregates and chondrules, mafic chondrules, and bulk and matrix samples from the Allende C3V chondritic meteorite to investigate the possible occurrence of anomalous isotopic compositions of noble gases that would correlate with oxygen or magnesium isotopic anomalies previously found in this meteorite.

Large enrichments of both ^{22}Ne and ^{36}Ar were observed in low-temperature release fractions from several Ca,Al-rich inclusions, but the enrichments are consistent with galactic cosmic-ray production of ^{22}Ne by spallation from sodium and ^{36}Ar by neutron capture on chlorine. Trapped neon in matrix samples is comprised of two distinctive compositions, with $(^{20}Ne/^{22}Ne)_t$ equal to 8.7 ± 0.1 and 10.4 ± 1.0, that appear to correlate with the two gas-rich trace phases chromite/carbon and 'Q' described by LEWIS *et al.* (1975). Several Ca,Al-rich aggregates which have high contents of the volatile elements Na, Cl, K, and Rb also contain trapped neon. However, no neon-E has been identified in any of the samples studied, including samples of several inclusions known to contain isotopically anomalous oxygen and magnesium.

1. INTRODUCTION

DISCOVERY of anomalies in the isotopic compositions of oxygen (CLAYTON *et al.*, 1973) and magnesium (LEE and PAPANASTASSIOU, 1974; GRAY and COMPSTON, 1974) in materials from carbonaceous chondrites has spurred the search for isotopic anomalies in other elements in these meteorites. Prior to the observations of enrichments at ^{16}O and ^{26}Mg, BLACK and PEPIN (1969) had measured anomalous enrichments of ^{22}Ne in neon extracted from total-rock samples of C1 and C2 carbonaceous chondrites during stepwise heating. However, neon measurements were not made on meteorites in which oxygen and magnesium anomalies were later observed. An investigation of the correlation between the neon anomaly, labeled neon-E by BLACK (1972), and the oxygen and magnesium anomalies was needed. An obvious candidate for such a study was the C3 chondrite Allende, since Ca,Al-rich inclusions from this object had been shown to carry both oxygen and magnesium isotopic anomalies. The pattern of neon isotopic compositions obtained by MANUEL *et al.* (1972) during a stepwise thermal extraction of rare gases from a total-rock sample of Allende suggested neon-E was released at ~800°C. Preliminary investigations of separates from Allende by HUNEKE *et al.* (1974) showed that certain Ca,Al-rich aggregates did indeed contain neon enriched in ^{22}Ne, possibly neon-E. However, the amounts of ^{22}Ne involved were not large compared to the amounts of spallation neon present, and the possibility that the excess ^{22}Ne was spallogenic, arising from variations in target element concentrations, particularly sodium, could not be eliminated.

The present work is an extensive investigation of the effects first reported by HUNEKE *et al.* (1974). In addition to measuring the isotopic compositions of total neon, we have also used the stepwise thermal extraction technique in attempting to separate the various components of trapped and cosmogenic neon in selected materials from Allende. In order to investigate possible correlations between noble gases and oxygen and magnesium anomalies, we measured noble gases in samples from several inclusions known to contain anomalous oxygen and magnesium.

2. SAMPLES

A number of the samples analyzed for noble gases were fragments of inclusions originally selected and analyzed for Rb/Sr by GRAY *et al.* (1973), who present chemical and mineralogical characteristics of these samples. The isotopic compositions of magnesium and oxygen have been measured in a number of the inclusions investigated here, and anomalous isotopic components are present in several of the inclusions (Table 7). Samples weighed between 13 and 230 mg.

Ca,Al-*rich aggregates*

Ca,Al-rich aggregates are highly irregular in shape and are typically fine grained. In addition to refractory Ca,Al-silicates, these inclusions in some cases also contain abundant alkali-rich minerals such as sodalite and nepheline. Ca,Al-rich aggregates are often visibly zoned parallel to irregular matrix/aggregate contacts.

B29, C5, and B32 are high-Rb aggregates (GRAY *et al.*, 1973; LEE and PAPANASTASSIOU, 1974) with Rb contents ranging from about 8 to 12 ppm (GRAY *et al.*, 1973). Na and K have been measured in B32 and B29 and are enriched relative to the matrix, but quite inhomogeneously distributed. In B32, Na ranges from about 0.5 to 3% by weight and K from <0.1 to 0.25%. In B29 measured Na

* Present address: Department of Terrestrial Magnetism, Washington, D.C. 20015, U.S.A.

† Division Contribution No. 2728.

Table 1. Total neon content and isotopic composition in samples of the C3V chondrite Allende. Neon contents in 10^{-8} cm^3 STP/g

Sample	Description	Weight	^{22}Ne‡	$^{20}Ne/^{22}Ne$‡	$^{21}Ne/^{22}Ne$‡	f^{22}‡
NWT	bulk meteorite	(.0584 g)	2.86 ± 0.15	2.270 ± 0.013	0.761 ± 0.005	0.0003
SWB	bulk meteorite	(.0846 g)	2.89 ± 0.15	2.168 ± 0.013	0.773 ± 0.004	0.0003
B29	aggregate: high alkali	(.0329 g)	2.73 ± 0.15	1.977 ± 0.011	0.664 ± 0.004	0.0005
B29†	matrix	(.2311 g)	2.48 ± 0.04	2.438 ± 0.029	0.764 ± 0.008	0.0003
C5†	aggregate: high alkali	(.0837 g)	2.40 ± 0.05	2.086 ± 0.027	0.700 ± 0.009	0.0012
C5†	matrix	(.1339 g)	2.41 ± 0.09	2.463 ± 0.059	0.760 ± 0.017	0.0008
B6HS†	aggregate: grey rim	(.1204 g)	2.43 ± 0.02	0.858 ± 0.008	0.800 ± 0.006	0.0009
B6HS†	aggregate: pink core	(.0328 g)	1.93 ± 0.02	0.777 ± 0.011	0.757 ± 0.008	0.0036
B6HS†	matrix	(.1664 g)	2.81 ± 0.03	2.609 ± 0.020	0.743 ± 0.005	0.0005
B32	aggregate: high alkali	(.0254 g)	2.53 ± 0.25	1.049 ± 0.011	0.695 ± 0.007	0.0014
B32†	" " "	(.0580 g)	2.62 ± 0.03	1.021 ± 0.015	0.683 ± 0.006	0.0021
D7	Ca,Al chondrule	(.0131 g)	1.41 ± 0.15*	0.816 ± 0.013	0.790 ± 0.013	0.0050
B28	Ca,Al chondrule	(.0216 g)	1.52 ± 0.16*	0.869 ± 0.011	0.860 ± 0.011	0.0028
B12	barred olivine chondrule	(.0336 g)	2.29 ± 0.23	0.899 ± 0.010	0.927 ± 0.007	0.0018
A5†	pyroxene chondrule	(.0779 g)	2.56 ± 0.11	0.898 ± 0.021	0.916 ± 0.022	0.0018
#1	chondrule	(.0278 g)	2.58 ± 0.26	1.055 ± 0.009	0.877 ± 0.007	0.0019
#2	chondrule	(.0195 g)	2.39 ± 0.24*	0.988 ± 0.013	0.872 ± 0.009	0.0020
Reextract*	(D7, B28, #2)		0.17	0.92 ± 0.02	0.967 ± 0.021	0.020

* After individual 1500°C extractions of Ne from samples D7, B28, and No. 2, the combined residues (total 0.0542 g) were heated to 1550°C and an additional 0.92×10^{-10} cm^3 ^{22}Ne extracted. This additional neon if assumed to be evenly derived from the three samples corresponds to 0.17×10^{-8} cm^3 STP^{22} Ne/g which when added to the tabulated (1500°C) data yields approximate corrected ^{22}Ne contents for these samples of 1.58 (D7), 1.70 (B28), and 2.56 (No. 2) $\times 10^{-8}$ cm^3 STP^{22}Ne/g.

† Integrated thermal release (individual data are in the Appendix). B6HS samples and the second B32 sample were run in a second series of analyses.

‡ Error in ^{22}Ne includes statistical and blank uncertainties; systematic error is $\lesssim 10\%$. Tabulated error in ratios is statistical only; the air blank uncertainty is represented by f^{22}, the fraction of ^{22}Ne attributed to blank uncertainty. For integrated thermal release data, f^{22} is

$$(\sum_i [22_i f_i^{22}]^2)^{1/2}/22_T,$$

where the subscript i refers to individual temperature steps, and 22_T is the total ^{22}Ne.

and K contents are as high as 5.4 and 0.7%, respectively. Higher alkali contents tend to occur near the rims of the high-Rb aggregates (GRAY *et al.*, 1973). The samples studied here were taken from the rims of the aggregates.

The B6HS aggregate was sampled for the present work and was located about 2 cm below fusion crust. The ~ 1 cm dia. aggregate was highly irregular in shape (amoeboid) and consisted of a grey rim surrounding a ~ 1 × 3 mm pink core. The pink core was fine-grained and much more friable than the coarser-grained rim which exhibited marginal banding parallel to the irregular aggregate–matrix contact. A cluster of free-standing, acicular crystals was observed in the rim with a low-power binocular microscope. Oxygen isotopes in a split of the rim material were analysed by S. Epstein.

Ca,Al-*rich chondrules*

Ca,Al-rich chondrules are rounded or subrounded and tend to be coarser grained than the aggregates. D7 and B28 are Ca,Al-rich chondrules consisting of melilite, fassaite, anorthite, and spinel, and contain relatively little Rb (0.01–0.04 ppm in D7; 0.2–0.4 ppm in B28). D7 contains large, well-developed crystals, and has a lower Mg content than B28 which has a texture suggestive of quench crystallization from a melt (GRAY *et al.*, 1973).

Mafic chondrules

These samples are fragments of individual chondrules composed primarily of olivine or pyroxene. B12 is a barred olivine chondrule with olivine of composition Fo_{67} (GRAY *et al.*, 1973). A5 is a poorly-crystallized pyroxene chondrule with ill-defined, radiating crystals (GRAY *et al.*, 1973). Numbers 1 and 2 are uncharacterized chondrules picked at random from the Allende matrix. The high $^{21}Ne_c$ contents in these two chondrules (Table 2) indicates they have high Mg contents similar to chondrules B12 and A5.

Bulk and matrix samples

Bulk and matrix samples are essentially equivalent. Bulk samples were selected at random, with no attempt at separation or exclusion of any chondrules, white inclusions, etc. Matrix samples were selected from the volume immediately adjacent to a specific large inclusion. Material from the large inclusion was avoided during selection of the matrix material. No other inclusions or chondrules were excluded.

Matrix samples were taken adjacent to the B29, C5, and B6HS aggregates. SWB and NWT are bulk samples from a single stone, NMNH3512, and were originally separated from each other by about 5 cm. The latter two samples were kindly provided by D. S. Burnett.

3. EXPERIMENTAL TECHNIQUES AND DATA REDUCTION

Samples were wrapped in aluminum foil and degassed overnight in vacuum at about 100°C. Noble gases were extracted from the samples in a resistance-heated tantalum crucible and analyzed statically in a 6 in. radius all-metal

Table 2. Total cosmogenic (c) and trapped (t) neon in Allende.‡ Neon contents in 10^{-8} cm^3 STP/g

Sample		$^{21}Ne_c$	$(^{21}Ne/^{22}Ne)_c$	$^{20}Ne_t$
NWT	bulk meteorite	2.16 ± 0.11	0.928 ± 0.009	4.55 ± 0.20
SWB	bulk meteorite	2.22 ± 0.11	0.928 ± 0.008	4.27 ± 0.20
B29	aggregate: high alkali	1.80 ± 0.10	0.786 ± 0.008	3.78 ± 0.20
B29†	matrix	1.88 ± 0.04	0.953 ± 0.012	4.35 ± 0.06
C5†	aggregate: high alkali	1.67 ± 0.04	0.838 ± 0.013	3.51 ± 0.09
C5†	matrix	1.82 ± 0.07	0.952 ± 0.021	4.29 ± 0.15
B6HS†	aggregate: grey rim	1.94 ± 0.03	0.813 ± 0.007	0.35 ± 0.05
B6HS†	aggregate: pink core	1.46 ± 0.03	0.765 ± 0.009	0.2 ± 0.1
B6HS†	matrix	2.07 ± 0.03	0.953 ± 0.009	5.49 ± 0.07
B32	aggregate: high alkali	1.75 ± 0.18	0.730 ± 0.008	1.09 ± 0.15
B32†	" " "	1.78 ± 0.03	0.716 ± 0.007	1.07 ± 0.05
D7	Ca,Al chondrule	1.11(1.27)* ± 0.12	0.799 ± 0.014	0.1(0.1)* ± 0.1
B28	Ca,Al chondrule	1.31(1.47)* ± 0.14	0.869 ± 0.012	0.1(0.1)* ± 0.1
B12	barred olivine chondrule	2.12 ± 0.21	0.934 ± 0.008	0.15 ± 0.05
A5†	pyroxene chondrule	2.34 ± 0.12	0.924 ± 0.025	0.20 ± 0.05
#1	chondrule	2.26 ± 0.23	0.904 ± 0.008	0.69 ± 0.05
#2	chondrule	2.08(2.24)* ± 0.21	0.893 ± 0.010	0.49(.50)* ± 0.05
Reextract	(D7, B28, #2)	0.16	0.97	0.01

* Values in parentheses are corrected for the re-extract (see notes, Table 1.)

† Integrated thermal release.

‡ Separation of trapped and cosmogenic gases was achieved by assuming ratios $(^{20}Ne/^{22}Ne)_t = 8.6 \pm 0.2$, $(^{21}Ne/^{22}Ne)_t = 0.026$, and assuming that for cosmogenic neon $(^{20}Ne/^{21}Ne)_c = 0.90$.

mass spectrometer using an automated data acquistion system with an on-line PDP-11 computer. Extraction times were ½ hr at 1500°C for single step extractions and ½ hr at each temperature during stepwise extraction. The extraction temperature was increased in steps of about 100–150°C. Oven power was monitored continuously and kept constant to within ~1%. Crucible temperatures ≥850°C were measured using an optical pyrometer; measurements were extrapolated to lower temperatures. A more recent temperature calibration done with a W–Re thermocouple placed in the crucible indicated that the temperatures used in this report are systematically high. The error is about 90°C at 500°C (i.e. corrected temperature is 410°C) and decreases roughly linearly to about 15°C at 1500°C. None of the discussion or conclusions drawn in the text are materially affected. Gases were cleaned using a Ti–Zr getter cooled from ~850°C to room temperature and a pair of SORB-AC Zr–Al chemisorption getters. Neon was separated from argon using activated charcoal at liquid nitrogen temperature. In those runs where both neon and argon were measured, neon was admitted to the mass spectrometer first, and exposed to charcoal at liquid nitrogen temperature during analysis to minimize $^{40}Ar^{2+}$ and CO_2^{2+} contamination. ^{40}Ar was measured with a Faraday cup detector, while all other argon and neon isotopes were measured using an electron multiplier. Samples were run in two series separated by several months. A source magnet was used during the second series. Samples in the second series were the B32 stepwise release, and all B6HS samples.

Procedural blanks have been subtracted from the data in the tables. Neon blanks, assumed to have air composition, were less than 5×10^{-11} cm^3 STP ^{20}Ne at 1500°C and about 2×10^{-11} cm^3 STP ^{20}Ne at low temperatures for both series of runs. Additional corrections were made at mass 20 for interferences from $H_2{}^{18}O^+$ and $^{40}Ar^{2+}$, at mass 21 for $^{20}NeH^+$, and at mass 22 for CO_2^{2+}. Total blanks at masses 20, 21, and 22 were generally ≲10, ≲0.1, and ≲5%, respectively, of the total signal. Mass discrimination at neon was determined using pipettes of atmospheric composition, and for the first series of runs was 0.5 ± 0.2% per mass unit favoring mass 20. During the second series discrimination was 0.2 ± 0.2% per mass unit favoring mass 20.

Ar was measured only in the second series of Allende analyses. Argon blanks for the second series of Allende samples were ≲2×10^{-11} cm^3 STP ^{36}Ar, ≲5×10^{-12} cm^3 STP ^{38}Ar, and ≲6×10^{-9} cm^3 STP ^{40}Ar at high temperatures, and were a factor of six (^{36}Ar, ^{40}Ar) or three (^{38}Ar) lower at low temperatures. Mass discrimination could not be measured accurately for argon because of rapid scrubbing of memory ^{38}Ar by the large amount of gas in the standard pipette. Comparison of our uncorrected value of $^{36}Ar/^{38}Ar$ in the B6HS matrix sample with a number of literature analyses (MANUEL *et al.*, 1972; BOGARD *et al.*, 1971; FIREMAN *et al.*, 1970) indicates discrimination is probably less than 1% per mass unit.

The sensitivities were monitored using a standard volumetric pipette. The neon sensitivity during the first series of runs decreased systematically by a factor of two, introducing a 5–10% relative uncertainty in the absolute amounts of neon measured from sample to sample in addition to the usual 1σ error of ~5%. This additional error has been included in the tabulated errors. During the second series of runs systematic drift in the neon sensitivity was minor, and the 1σ relative variation of individual determinations was ~5%. Argon sensitivities were constant to within about 8%. Comparisons with a second independent argon pipette and with a standard sample of the Leedey chondrite previously calibrated by isotope dilution suggest that systematic error in the final calibration is less than 10%.

Data were obtained by repeated scanning of the mass spectrum by automatic stepping of the magnetic field. Ten to fifteen complete scans were taken of the gas in each temperature fraction. Isotopic ratios and the concentration

of a reference isotope (e.g. ^{20}Ne or ^{36}Ar) were extrapolated to the time when the gas was admitted to the mass spectrometer. Errors in the neon and argon isotopic ratios of the tabulated data for each temperature fraction include the 1σ standard deviation in the extrapolation of the ratios to the time of gas admittance, as well as estimated errors due to statistically independent background corrections ($^{40}Ar^{2+}$, CO_2^{2+}, $H_2{}^{18}O^+$, $^{20}NeH^+$). For neon, errors in $^{20}Ne/^{22}Ne$ and $^{21}Ne/^{22}Ne$ ratios due to the atmospheric blank correction are not independent, and have not been included in tabulated errors. Instead, these correlated uncertainties are represented by f^{22}, the fraction of the blank-corrected ^{22}Ne corresponding to the blank uncertainty: e.g. for a sample containing 10^{-9} cm^3 STP ^{22}Ne and with a blank uncertainty of $\pm 2 \times 10^{-12}$ cm^3 STP ^{22}Ne, $f^{22} = 0.002$. On the three isotope diagram ($^{20}Ne/^{22}Ne$ vs $^{21}Ne/^{22}Ne$) the correlated uncertainties in the air blank result in a diagonal error bar aligned with the composition of atmospheric neon. The dimensions of the diagonal error bar are asymmetric. Let D be the distance on the three isotope diagram from the point ATM representing air neon to the point P for the measured, blank-corrected neon composition in the sample. The error bar at P will extend $[f^{22}/(1+f^{22}) \times D]$ toward ATM and $[f^{22}/(1-f^{22}) \times D]$ away from ATM. For small $f^{22}(\lesssim 0.05)$ the error bar is essentially symmetric with dimensions $\pm(f^{22} \times D)$. To construct the error boxes in the figures, the rectangular error box representing statistically independent errors in the isotopic ratios was translated along the full extent of the diagonal error bar of the blank uncertainty.

The tabulated errors in the absolute amounts of neon and argon include blank uncertainties and the statistical uncertainty in the determination of the sensitivity, but not the systematic uncertainty in the final calibration ($\lesssim 10\%$).

4. NEON AND ARGON ISOTOPIC SYSTEMATICS

To provide a setting for later discussions of the noble gas results from Allende, we will provide a general, but not exhaustive review of the systematics of neon and argon isotopic compositions observed in the solar system. Neon and argon in carbonaceous chondrites consist of a mixture of *trapped* gases with *cosmogenic* gases generated by cosmic-ray induced reactions on a variety of target elements. Major sources of the trapped components are thought to include solar-wind implantation of low-energy ions, and adsorption or occlusion of gases from the residual primordial solar nebula. An additional source, minor in terms of volume of associated gas, but major in terms of cosmochemical implications, has been postulated to be interstellar grains. It has been suggested (BLACK, 1972; CLAYTON *et al.*, 1973) that interstellar grains that survived unvaporized during the formation of the solar system could have acted as carriers of anomalous isotopic compositions such as have been observed for neon, oxygen, and magnesium in Allende and other carbonaceous chondrites.

In the text to follow we will use the following subscripts to identify noble gases from various sources; c = cosmogenic, t = trapped, m = measured.

The isotopic composition of trapped neon varies substantially in the several reservoirs that have been studied. A tool that has proven very useful in the presentation and discussion of the large isotopic variations in neon is the three-isotope diagram, $^{20}Ne/^{22}Ne$ vs $^{21}Ne/^{22}Ne$ (REYNOLDS and TURNER, 1964; PEPIN, 1967). On the three-isotope diagram, the composition of neon composed of a mixture of two distinct components will lie on the straight line linking the two endpoint components. If the mixture is composed of more than two components, its composition will lie within the largest polygon that can be formed by connecting all endpoints with straight lines. In Fig. 1 we have plotted the isotopic compositions of neon from various reservoirs and spallation reactions. Compositions of trapped neon from the solar wind, lunar soil (SUCOR), and terrestrial atmosphere (ATM) fall on a nearly vertical line segment in the upper left portion of the figure. $^{20}Ne/^{22}Ne$ ranges from 13.7 in the solar wind as measured by the Apollo Al-foil experiment (GEISS, 1973), ~ 12.6 in the surface-correlated (SUCOR) gases derived from implanted solar wind Ne in lunar soil (cf. BOGARD and NYQUIST, 1972), to 9.8 in the terrestrial atmosphere (EBERHARDT *et al.*, 1965). The range of $(^{20}Ne/^{22}Ne)_t$ is even larger in carbonaceous chondrites; ratios in whole-rock samples extend from about 13 or 14 to about 8 (PEPIN, 1968; MAZOR *et al.*, 1970). The composition labeled neon-A in Fig. 1 (PEPIN, 1968) essentially represents the lower limit of $(^{20}Ne/^{22}Ne)_t$ observed in whole-rock carbonaceous chondrites. On the basis of detailed stepwise release experiments on carbonaceous chondrites, BLACK (1972) has identified in these meteorites a number of additional preferred compositions not plotted in the figure with $8 < {}^{20}Ne/^{22}Ne \lesssim 14$ (neon B, C, D). Trapped $^{21}Ne/^{22}Ne$ ratios for the various above reservoirs vary from about 0.033 to 0.025. Much lower $^{20}Ne/^{22}Ne$ ratios ≤ 1.5 characterize the anomalous neon-E composition which will be discussed further below.

The isotopic composition of cosmogenic neon in meteorites is distinctly different from that of trapped neon. Compositions of spallation neon in whole-rock meteorite samples plot on the near-horizontal line segment at the lower right. $^{20}Ne/^{22}Ne$ and $^{21}Ne/^{22}Ne$ ratios of about 0.8 and 0.9 characterize spallation neon produced from magnesium, the principal target in most whole-rock meteorite samples, and the spread in whole-rock ratios is due primarily to variations in shielding. Spallation neon with $^{21}Ne/^{22}Ne = 0.34$ is produced from sodium and is an important contribution in certain meteoritic minerals including feldspar (SMITH and HUNEKE, 1975).

Virtually all measured compositions of total-rock neon in carbonaceous chondrites plot within the polygon constructed by joining the compositions of solar, neon-A and spallation neon (MAZOR *et al.*, 1970), which we have labeled the 'reference polygon' in Fig. 1. This observation suggests that neon in these meteorites is composed primarily of mixtures of variable proportions of spallation and trapped neon, including both solar and neon-A (SIGNER and SUESS, 1963; PEPIN and SIGNER, 1965; PEPIN, 1967).

Neon compositions that plot outside the field

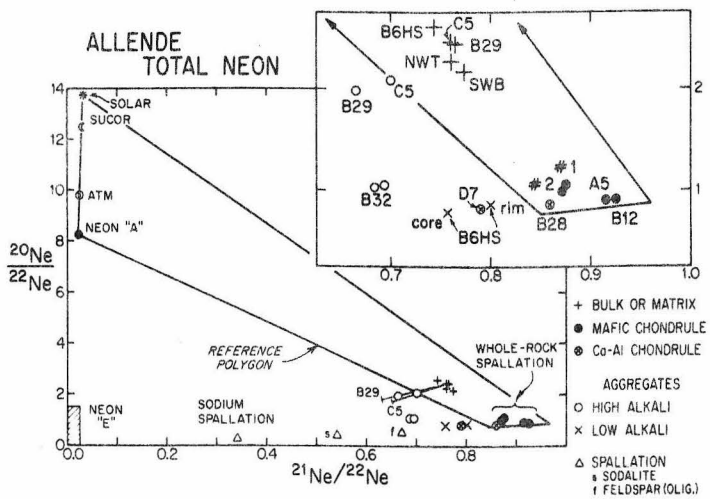

Fig. 1. Correlation of $^{20}Ne/^{22}Ne$ with $^{21}Ne/^{22}Ne$ for total neon in Allende samples. Trapped neon compositions plot near the ordinate and include solar wind (SOLAR) (GEISS, 1973), surface-correlated lunar neon (SUCOR) (cf. BOGARD and NYQUIST, 1972), terrestrial atmosphere (ATM) (EBERARDT *et al.*, 1965), and NEON-A (PEPIN, 1968) observed predominantly in carbonaceous chondrites. Also shown are the limits on the composition of NEON-E (EBERHARDT, 1975), the range of whole-rock spallation compositions, and the composition of sodium spallation neon (SMITH and HUNEKE, 1975). Whole-rock neon compositions of carbonaceous chondrites plot within the indicated 'reference polygon' outlined by NEON-A, SOLAR, and whole-rock spallation (MAZOR *et al.*, 1970). For Allende, neon compositions from bulk and matrix samples and mafic chondrules fall within the reference polygon, but neon compositions from Ca,Al-rich samples, including Ca,Al-rich chondrules and aggregates, tend to plot below and to the left of the polygon. These ^{22}Ne-rich compositions are consistent with the addition of either neon-E or sodium spallation neon. In the lower part of the figure, the ticks on the ends of the short lines extending from the B29 and C5 matrix points through the respective aggregate compositions indicate the isotopic compositions of neon in these aggregates when a correction for adhering matrix is subtracted. The inset shows an enlargement of part of the three-isotope diagram.

enclosed by the reference polygon can be defined as anomalous with respect to the observed total-rock compositions. Due to enhanced production of ^{22}Ne, the composition of neon produced by galactic cosmic-ray induced spallation from sodium (SMITH and HUNEKE, 1975) plots well below the reference polygon and to the left of whole-rock spallation. The unusual composition of sodium spallation neon is not reflected in whole-rock compositions because of the low sodium content compared to the content of magnesium in meteorites. A more remarkable neon isotopic composition is that of the anomaly known as neon-E. First recognized by BLACK and PEPIN (1969) in 1000°C fractions of stepwise thermal release experiments on C1 and C2 carbonaceous chondrites, neon-E has been shown by the most recent work on mineral separates from Orgueil to have $^{20}Ne/^{22}Ne \leq 1.5$ and $^{21}Ne/^{22}Ne \leq 0.02$ (EBERHARDT, 1975). BLACK (1972) suggested that ^{22}Ne-enriched neon-E might represent a nucleosynthetic remnant of hydrostatic He-burning introduced into carbonaceous chondrites on unvaporized interstellar dust grains. Black also suggested that neon-A in carbonaceous chondrites might represent a mixture of neon-E and a primitive solar-wind component, similar in neon isotopic composition to the present solar wind.

We conclude this summary of neon isotopic systematics by pointing out that while neon-E represents a substantial lower limit to $^{20}Ne/^{22}Ne$ in trapped noble gases, a firm upper limit to this ratio has not been established. The major reservoir of neon in the solar system is the Sun. The isotopic composition of solar wind neon is undoubtedly related in some fashion to the bulk solar neon composition, but we know little concerning fractionations that may occur during acceleration of gas from the solar photosphere, through the corona, and into the solar wind. $^{20}Ne/^{22}Ne$ in the Sun may be higher (or lower) than the ratio of 13.7 measured in the present solar wind.

Unlike the variation in trapped neon compositions, the variation in the isotopic composition of trapped argon is limited. The $^{36}Ar/^{38}Ar$ ratios of both argon from the terrestrial atmosphere and solar-wind argon from lunar soil are close to 5.35. A slightly lower ratio of 5.20 ± 0.06 has been measured for trapped argon in carbon-rich material from the ureilite Haverö (WEBER *et al.*, 1976). In Fig. 2 we have plotted measured $^{36}Ar/^{38}Ar$ ratios for a large number of chondritic meteorites as a function of the amount of cosmogenic gas present, using the ratio of cosmic-ray produced $^{21}Ne_c$ to total measured $^{38}Ar_m$ as a measure of the cosmogenic component. All meteorites from the references listed in the figure caption have been plotted in Fig. 2 except those showing evidence of $^{3}He_c$ loss and which therefore may have lost $^{21}Ne_c$ relative to $^{38}Ar_m$. Gas loss was assumed for samples with $^{3}He_c/^{21}Ne_c \leq 3$ or ^{3}He exposure ages more than a factor of two less than ^{21}Ne ages. For pure trapped

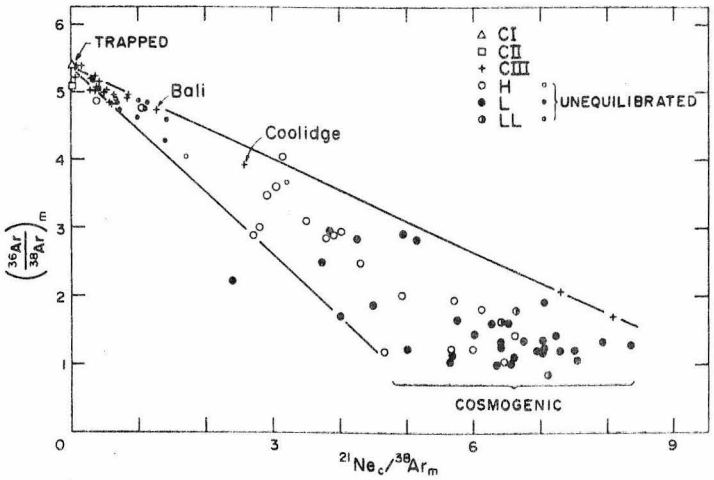

Fig. 2. Correlation of measured (m) $^{36}Ar/^{38}Ar$ with the ratio of cosmogenic (c) ^{21}Ne to measured ^{38}Ar for chondritic meteorites (MAZOR *et al.*, 1970; NYQUIST *et al.*, 1973; BOGARD *et al.*, 1971; SMITH and FIREMAN, 1973; BOGARD *et al.*, 1973; EBERHARDT *et al.*, 1966). Only meteorites showing no evidence of $^{3}He_c$ loss are included. In the absence of cosmogenic gas, $^{21}Ne_c = 0$ and the measured $^{36}Ar/^{38}Ar$ ratio plots on the *y*-axis and is the composition of trapped argon. If no trapped argon is present, $^{21}Ne_c/^{38}Ar_m$ reduces to the cosmogenic production ratio $(^{21}Ne/^{38}Ar)_c$ which ranges from about 5 to 9. $(^{36}Ar/^{38}Ar)_c$ should be about 0.6 if the only source of cosmogenic gas is spallation on Fe and Ca. Mixtures of trapped and cosmogenic gas will plot between the two endmembers. The diagonal lines are drawn from $(^{36}Ar/^{38}Ar)_t = 5.3$ to enclose the majority of the data points. There is no evidence of $(^{36}Ar/^{38}Ar)_t > 5.5$. The sharp cutoff of the measured $^{36}Ar/^{38}Ar$ ratio at 1.0 is attributed to the production of $^{36}Ar_{Cl}$ from neutron capture on the 100 ppm Cl in ordinary chondrites. The production rate inferred from the observed cutoff at 1.0 is about 2×10^{-6} cm^3 STP $^{36}Ar_{Cl}$/gCl/million yr.

gas, $^{21}Ne_c = {}^{38}Ar_c = 0$, so the composition of trapped argon plots on the *y*-axis. The principal targets for the production of spallation argon in most meteorites are calcium and iron; $(^{36}Ar/^{38}Ar)_c$ ratios produced from both these targets are about 0.6. An additional source of cosmogenic argon is neutron capture on chlorine. This reaction produces nearly pure ^{36}Ar, and as we shall discuss later, can lead to cosmogenic $^{36}Ar/^{38}Ar$ ratios greater than 0.6 in Cl-bearing samples. For $(^{36}Ar/^{38}Ar)_m \lesssim 1$, the amount of trapped argon is small, and the ratio $^{21}Ne_c/^{38}Ar_m$ reduces to the cosmogenic production ratio $(^{21}Ne/^{38}Ar)_c$ which ranges from about 5 to 9. Thus pure cosmogenic gas plots in the lower right in Fig. 2. The range in $(^{21}Ne/^{38}Ar)_c$ is due in part to the effects of variable shielding; less-shielded meteorites have lower $(^{21}Ne/^{38}Ar)_c$ (NYQUIST *et al.*, 1973). Mixtures of trapped and cosmogenic gas will plot between the two endmembers. It is evident from Fig. 2 that the data for virtually all meteorites in the figure can be represented by mixing cosmogenic gas of somewhat variable $(^{21}Ne/^{38}Ar)_c$ and $(^{36}Ar/^{38}Ar)_c$ with a single trapped argon component characterized by a trapped $^{36}Ar/^{38}Ar$ ratio that is essentially constant at about 5.3, or varies at most from about 5.2 to 5.5.

5. RESULTS FROM ALLENDE

5.1 *Total neon and argon data*

Total neon contents and isotopic compositions measured in Allende samples are summarized in Table 1 and Fig. 1. In Fig. 1, isotopic compositions of all materials, including bulk or matrix samples, mafic and Ca,Al-rich chondrules, and Ca,Al-rich aggregates, plot in the lower-right, spallation-dominated portion of the figure. However, the spread of the data off any single mixing line indicates the presence of at least three components of neon in the samples.

Two important observations may be made from the data in Fig. 1. First, several of the Ca,Al-rich inclusions contain neon of compositions plotting outside and below the reference polygon. These samples must contain a ^{22}Ne-rich component different from the components outlining the reference polygon, i.e. whole-rock spallation, neon-A, or solar neon. The identity of this additional component can not be determined from the total neon compositions alone. From Fig. 1 it can be seen that an admixture of either neon-E or sodium spallation neon can move compositions such as bulk sample or mafic chondrule neon below the reference polygon.

The second observation concerns the distribution of trapped neon among the various types of material analyzed. The isotopic compositions of neon in mafic chondrules and several of the Ca,Al-rich samples (e.g. chondrules D7, B28 and aggregates B6HS, B32) lie on or near mixing lines between whole-rock spallation and sodium spallation or neon-E. These data are compatible with the absence of trapped neon-A or solar neon, since the points do not have $^{20}Ne/^{22}Ne$ ratios >1 that would signal the presence of such trapped neon. However, $^{20}Ne/^{22}Ne$ ratios substantially >1 in bulk and matrix samples and some of

Table 3. Neon in high-alkali aggregates after correction for adhering matrix. Neon contents in 10^{-8} cm^3 STP/g

Sample	Percent * aggregate	^{22}Ne	$\frac{^{20}Ne}{^{22}Ne}$	$\frac{^{21}Ne}{^{22}Ne}$	$^{21}Ne_c$	$\frac{^{21}Ne_c}{^{22}Ne_c}$	$^{20}Ne_t$
B29	70	2.83	1.81	0.63	1.77	0.73	3.46
C5†	55	2.39	1.78	0.65	1.55	0.75	2.84
B32†	100	2.58	1.04	0.69	1.77	0.72	1.08

* Estimated visually.

† C5 data is from integrated thermal release. B32 is the average of two samples, one a single-step extraction and the second an integrated thermal release.

the aggregates (B29 and C5) provide evidence of trapped neon in these samples. From Table 2 we see the amounts of trapped neon in the bulk and matrix samples range from 4.3 to 5.5×10^{-8} cm^3 STP ^{20}Ne/g, characteristic of the contents found in C3 meteorites (MAZOR *et al.*, 1970), and in agreement with previous measurements on Allende samples (MANUEL *et al.*, 1972; BOGARD *et al.*, 1971; FIREMAN *et al.*, 1970).

The presence of substantial amounts of trapped noble gases in samples of Ca,Al-rich aggregates is somewhat surprising. In general, a high-temperature origin has been inferred for the Ca,Al-rich minerals of these aggregates (e.g. MARVIN *et al.*, 1970), and such a high temperature environment seems inappropriate for trapping volatile noble gases. However, it has been shown that many of the Ca,Al-rich aggregates contain abundant volatiles such as Rb, Na, K, and Cl (GRAY *et al.*, 1973; GROSSMAN and GANAPATHY, 1975) indicative of a complex history that allowed for the accumulation of volatile elements. The C5 and B29 aggregates that contain trapped gases are of the latter, volatile-bearing type (GRAY *et al.*, 1973). The samples of the C5 and B29 aggregates were contaminated by adhering matrix (Table 3) which could contribute some trapped neon. From Table 2 we find that the trapped neon content of the five bulk and matrix samples is reasonably uniform, allowing us to estimate the trapped gas contribution of a given amount of contaminating matrix. To explain all the trapped neon as contamination would require the C5 and B29 samples to have consisted of about 80 and 85% matrix, respectively. We regard such amounts of contamination as unrealistic, and conclude that these aggregates contain trapped-neon bearing phases other than those associated with matrix contamination. The trapped neon contents of C5 and B29 are 2.8 and 3.5×10^{-8} cm^3 STP ^{20}Ne/g after correction for the amounts of adhering matrix estimated visually using a low-power binocular microscope (Table 3).

We measured argon in a matrix sample, and samples from two Ca,Al-rich aggregates. The total argon amounts and compositions for these samples are listed in Table 4. The trapped $^{20}Ne/^{36}Ar$ ratio for the B6HS matrix sample is 0.29, typical of 'planetary'-type rare gas (MAZOR *et al.*, 1970), and in contrast to the $^{20}Ne/^{36}Ar$ ratio of solar gas which is about 30 (GEISS, 1973). $^{36}Ar/^{38}Ar$ ratios in mixtures of trapped argon and Ca,Fe-spallation argon will lie between 5.3 and 0.6. The observed ratios of 7.87 and 6.85 in two samples of the Ca,Al-rich aggregates B32 and B6HS are much higher, and indicate the presence of large excesses of ^{36}Ar.

5.2 *Stepwise thermal release data*

The results of the stepwise heating experiments are presented graphically in Figs. 3–6, and the numerical data for individual temperature fractions are tabulated in the Data Appendix. We will describe the results with emphasis placed on the problems suggested in Section 5.1 by the total neon and total argon data: (1) the nature of the ^{22}Ne- and ^{36}Ar-enrichments found in Ca,Al-rich aggregates, and (2) the distribution and composition of trapped neon in the materials studied.

The stepwise thermal release data for argon are summarized in Fig. 3. Observed $^{36}Ar/^{38}Ar$ ratios are plotted as a function of temperature in the upper portion of the figure. Temperature fractions with clearly-defined ^{36}Ar excesses plot above the heavy line designated 'trapped' at $^{36}Ar/^{38}Ar = 5.3$. Anomalous ratios occur only in argon release fractions at temperatures ≤ 1000°C. Extreme values, as high as $^{36}Ar/^{38}Ar = 48$, were measured in the 700°C release fractions of all three Ca,Al-rich aggregate samples. Amounts of ^{36}Ar released are plotted in the lower part of Fig. 3. Dis-

Table 4. Argon content and isotopic composition in samples from Allende.* Argon contents in 10^{-8} cm^3 STP/g

Sample	^{36}Ar	^{40}Ar	$^{36}Ar/^{38}Ar$	$^{40}Ar/^{36}Ar$	$^{36}Ar_t$	$^{38}Ar_c$
B32** aggregate	9.84 ± 0.32	17100 ± 600	7.87 ± 0.36	1740 ± 80	3.84 ± 0.40†	0.52 ± 0.06
B6HS** matrix	19.40 ± 0.68	2061 ± 47	5.03 ± 0.25	106 ± 4	18.8 ± 0.2+	0.30 ± 0.05+
B6HS** aggregate						
grey rim	2.86 ± 0.07	1930 ± 40	3.01 ± 0.12	668 ± 22	1.21 ± 0.25†	0.73 ± 0.07
pink core	2.75 ± 0.08	2320 ± 80	6.85 ± 0.37	840 ± 40	0.62 ± 0.25†	≥0.36 ± 0.06‡

* Data are uncorrected for mass discrimination, which is estimated to be less than 1% per mass unit.

** Integrated thermal release.

† Calculated from $^{20}Ne_t$ using $(^{20}Ne/^{36}Ar)_t = 0.29$ as determined for the B6HS matrix.

‡ Thermal release pattern suggests argon in this sample may not have been completely extracted.

+ $^{38}Ar_c$ estimated from stepwise thermal release data which are unaffected by $^{36}Ar_{Cl}$. $^{36}Ar_c = 0.65\ ^{38}Ar_c + {}^{36}Ar_{Cl}$, and is thus about 0.6×10^{-8} cm^3 STP/g for the matrix sample (see Section 6.1).

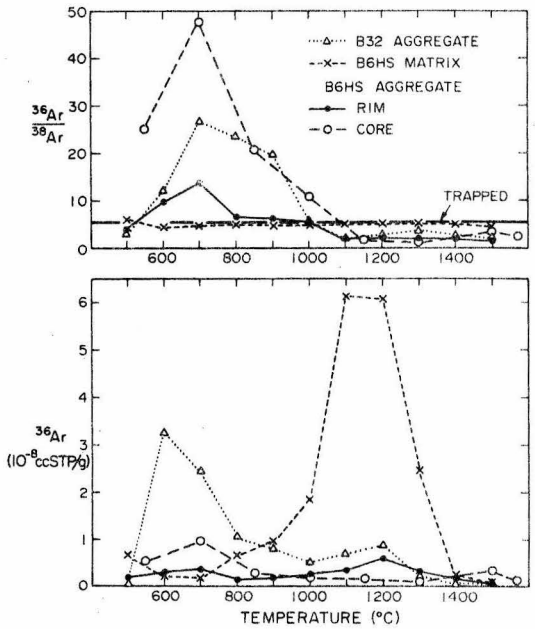

Fig. 3. Measured $^{36}Ar/^{38}Ar$ ratios and ^{36}Ar contents as a function of temperature for stepwise thermal release fractions from Allende samples. In the upper panel, mixtures of trapped argon ($^{36}Ar/^{38}Ar = 5.3$) and spallation argon from Ca and Fe ($^{36}Ar/^{38}Ar = 0.6$) will plot below the heavy reference line labeled TRAPPED. In the aggregate samples, $^{36}Ar/^{38}Ar$ ratios as high as 48 are observed in temperature fractions ≤ 1000°C due to the addition of ^{36}Ar from neutron capture on chlorine. The $^{36}Ar/^{38}Ar$ ratio in the B6HS matrix sample is nearly constant at about 5.0 in all fractions except 500°C where a small excess of $^{36}Ar_{Cl}$ is observed. In the lower panel, the release of argon from the B6HS matrix sample is strongly peaked in the 1100 and 1200°C fractions, in contrast to the release from aggregate samples where distinct maxima occur at 600 or 700°C. These low-temperature release peaks from the aggregates correlate with the extreme $^{36}Ar/^{38}Ar$ ratios in the upper panel indicating that most of the low-temperature ^{36}Ar is $^{36}Ar_{Cl}$ from neutron capture.

tinct maxima in the release of ^{36}Ar occur at 600–700°C, correlating with the anomalous $^{36}Ar/^{38}Ar$ ratios. *Thus the* ^{36}Ar*-enriched gas is released primarily in temperature fractions well below* 1000°C. Release of argon from the matrix sample is much different than that from the aggregates. $^{36}Ar/^{38}Ar$ ratios are nearly constant at about 5.0, and a marked maximum in the release of ^{36}Ar occurs in the 1100 and 1200°C fractions.

The stepwise thermal release data for neon extracted from Ca,Al-rich aggregates are presented in Fig. 4. The patterns are quite similar for each of the four samples analyzed. At the lowest temperatures (500–600°C) neon is released with remarkably low $^{21}Ne/^{22}Ne$ ratios considering that $^{20}Ne/^{22}Ne$ is $\lesssim 1.0$, indicating little or no trapped neon-A or solar neon is present in these fractions. As temperature is increased from 700 to 900°C, $^{20}Ne/^{22}Ne$ ratios increase substantially above 1.0 due to the release of trapped neon with a high $^{20}Ne/^{22}Ne$ ratio. The release of this trapped component decreases with further temperature increase, and the neon released at temperatures $\gtrsim 1100$°C is primarily spallation neon with $^{20}Ne/^{22}Ne \lesssim 1.0$ and $^{21}Ne/^{22}Ne$ ratios between about 0.80 and 0.85. These $^{21}Ne/^{22}Ne$ ratios are slightly lower than typical whole-rock spallation values due to the effect of target chemistry on the isotopic composition of cosmogenic neon. The compositions of galactic cosmic ray spallation neon produced from pure Mg, Si, and Al (BOCHSLER *et al.*, 1969) are indicated on the C5 plot in the upper part of Fig. 4. Cosmogenic $^{21}Ne/^{22}Ne$ ratios in magnesium-poor material such as the Ca,Al-rich aggregates will be about 0.83 to 0.85. *Most important, the release patterns in Fig.* 4 *reveal that the unusual* ^{22}Ne*-rich component of neon in the* Ca,Al*-rich inclusions is released in the lowest temperature fractions as was the case for the argon enriched in* ^{36}Ar. In Fig. 4, the isotopic composition of the ^{22}Ne-rich gas must plot to the left of the 500°C fraction from B32, the temperature fraction with the smallest $^{21}Ne/^{22}Ne$ ratio, which limits the $^{21}Ne/^{22}Ne$ ratio in the unknown gas to $\lesssim 0.60$.

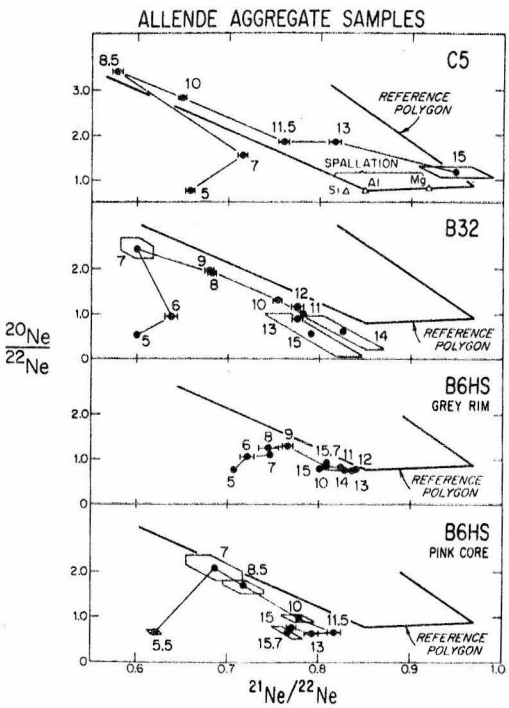

Fig. 4. Correlation of $^{20}Ne/^{22}Ne$ with $^{21}Ne/^{22}Ne$ for stepwise thermal release fractions from Allende aggregate samples. Extraction temperatures are indicated in hundreds of degrees centigrade. The reference polygon is the same as in Fig. 1. ^{22}Ne-rich gas ($^{20}Ne/^{22}Ne$ and $^{21}Ne/^{22}Ne$ as low as 0.5 and 0.6) is released preferentially in the lowest temperature fractions (500–600°C). At intermediate temperatures (~700–1000°C), $^{20}Ne/^{22}Ne$ rises above 1, indicating the release of trapped neon. Except for C5, at higher temperatures $^{20}Ne/^{22}Ne$ returns to values below 1 and $^{21}Ne/^{22}Ne$ ranges from about 0.80 to 0.85, values similar to the compositions of spallation neon from pure Si and Al as indicated in the uppermost box in the figure. For the C5 sample, high-temperature $^{21}Ne/^{22}Ne$ ratios are $\gtrsim 0.9$ reflecting the presence of Mg-rich olivine from adhering matrix. For a discussion of error envelopes, see Section 3 of the text.

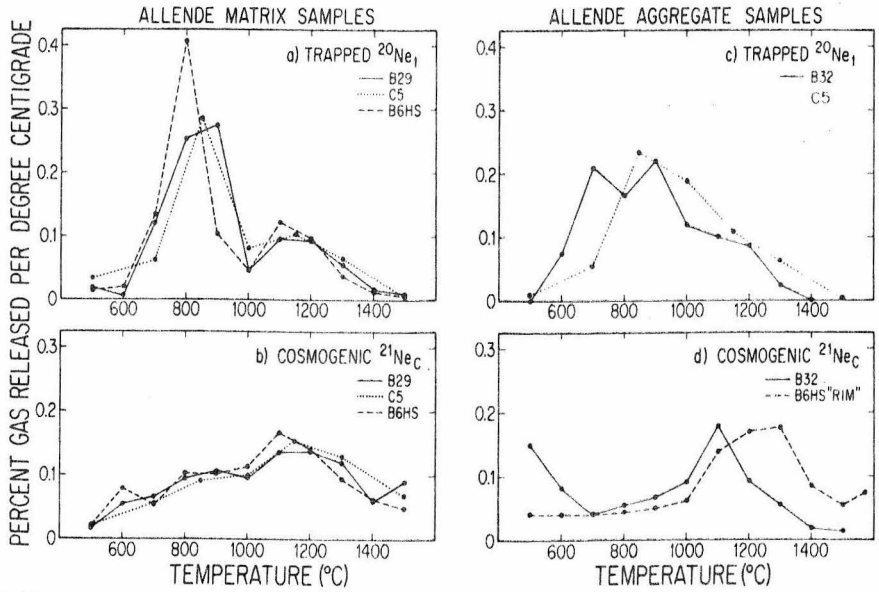

Fig. 5. The percentage of total trapped and cosmogenic neon released per degree centigrade as a function of temperature for stepwise release fractions from Allende samples. Trapped neon (upper panels) and cosmogenic neon (lower panels) are separated by assuming $(^{20}Ne/^{21}Ne)_c = 0.90$, and assuming $(^{20}Ne/^{22}Ne)_t = 8.6$ for aggregates and 500–900°C release fractions of matrix samples, and 10.4 for ≥1000°C matrix fractions (see Appendix). Trapped neon is released from matrix samples in two peaks at about 850 and 1150°C which are separated by minima at 1000°C. In contrast, trapped neon is released from aggregate samples in a single, broad peak with no minimum at 1000°C. The broad release of cosmogenic neon from matrix samples is probably due to the wide range of grain size of olivine in this material. In the B32 aggregate, a 500–600°C peak in cosmogenic $^{21}Ne_c$ release correlates with the release of ^{22}Ne-rich cosmogenic neon from sodium-rich phases.

Having shown that the ^{22}Ne and ^{36}Ar enrichments are enhanced in the low-temperature release fractions of Ca,Al-rich aggregates, we turn to the problem of the distribution of trapped neon in the samples.

From the total neon data (Section 5.1) we argued that trapped neon was present in aggregates B29 and C5; the trapped neon contents of the samples from the aggregates were too high to be due to matrix

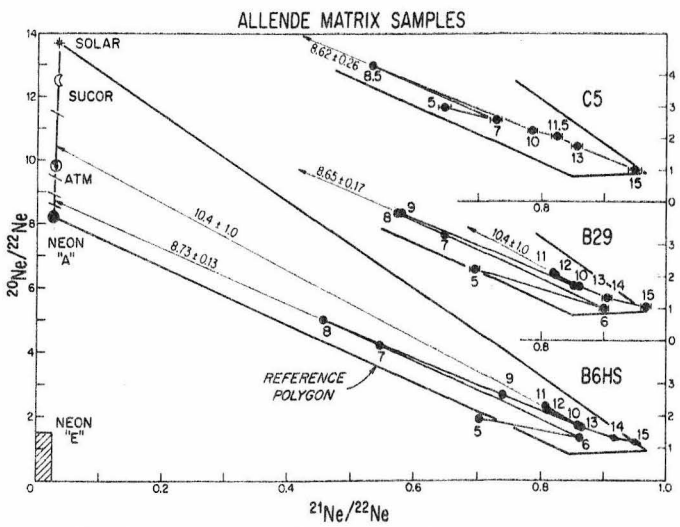

Fig. 6. Correlations of $^{20}Ne/^{22}Ne$ with $^{21}Ne/^{22}Ne$ for stepwise thermal release fractions from Allende matrix samples. The reference polygon and trapped neon compositions are as in Fig. 1. Extraction temperatures are in hundreds of degrees centigrade. 600–1000°C release fractions correspond to the first trapped neon release peak (Fig. 5), and the isotopic compositions plot on a linear trend between trapped and spallation neon. Trapped neon compositions inferred from projection of the trends to the upper left are indicated, and range from about 8.6 to 8.7. For B29 and B6HS, temperature fractions >1000°C correspond to the second release peak of trapped neon (Fig. 5), and fall on a trend line indicating the presence of a second trapped neon composition with $(^{20}Ne/^{22}Ne)_t \approx 10.4$. The errors indicated correspond to extreme positions of the mixing lines drawn through the 600–1000° and 1000–1300°C data points.

contamination. Total neon data from aggregates B32 and B6HS (Section 5.1) gave no strong suggestion of the presence of trapped neon-A or solar neon. From the presence of Ne release fractions with $^{20}Ne/^{22}Ne > 1$ in the isotopic release patterns in Fig. 4, it is clear that these aggregate samples did contain such trapped neon. The amounts contained in the two samples from B6HS are small, $<0.4 \times 10^{-8}$ cm^3 STP ^{20}Ne/g, corresponding to 5 or 10% contamination with matrix material which may be present despite efforts to avoid contamination during sampling. The amount in B32, 1.1×10^{-8} cm^3 STP ^{20}Ne/g is substantially larger, and the same concentration of $^{20}Ne_t$ was measured in two separate samples, both of which were carefully selected to be as free from contamination as possible. We infer that the B32 aggregate contains trapped neon as well as the aggregates B29 and C5. While the presence of trapped neon is revealed by the release patterns of isotopic compositions from the Ca,Al-rich aggregates, the trends are not sharply-enough defined to allow us to determine precisely the isotopic composition of the trapped neon.

The neon release patterns for matrix samples are complex. In Figs. 5a and 5b we have graphed the percentage of trapped and cosmogenic neon released from three matrix samples as a function of temperature. Cosmogenic $^{21}Ne_c$ is released at a rate that increases slowly until about 1100 or 1200°C, and decreases thereafter. The broad release pattern of this cosmogenic gas is attributable to the fact that nearly all the cosmogenic neon is produced from the single mineral olivine which has a wide range of grain sizes. The release of trapped neon is quite different, showing two well-defined release peaks at about 850 and 1150°C separated by a minimum in the release rate at 1000°C. About two-thirds of the trapped neon is released in the 850°C peak, and the remaining third is released in the 1150°C peak.

The bimodality of the trapped neon release rate is also found in the isotopic compositions measured during the stepwise extraction of neon from the three matrix samples (Fig. 6). As was also the case for the Ca,Al-rich aggregates, isotopic patterns for the different matrix samples are quite similar to one another. 500°C points are shifted toward low $^{21}Ne/^{22}Ne$ ratios reflecting the low-temperature degassing of a few per cent of Ca,Al-rich aggregate material bearing the ^{22}Ne-rich component. Ne from the 600–1000°C fractions constitutes the first release peak of trapped neon. From 600 to 800 or 900°C, $^{20}Ne/^{22}Ne$ ratios increase and points plot successively nearer to the trapped neon compositions as the rate of release of trapped neon from the first peak reaches a maximum. Above the temperature of maximum release, the trend reverses, and isotopic compositions become more spallogenic. The 600–1000°C points constituting the first release peak appear to define a good linear trend, with apparent end members being spallation neon, and a trapped neon of an isotopic composition similar to neon-A. Inferred isotopic compositions of the trapped component may be obtained by projection of the mixing lines to intersection with the line of trapped neon compositions in the upper left of Fig. 6. The inferred $^{20}Ne/^{22}Ne$ ratios for this trapped component are 8.73 ± 0.13, 8.65 ± 0.17, and 8.62 ± 0.26 for the matrix samples B6HS, B29, and C5. The average value of 8.7 ± 0.1 is close to, but slightly higher than, the value of 8.2 ± 0.4 attributed to neon-A by PEPIN (1968).

Above 1000°C, in the patterns from the B29 and B6HS samples, the trend reverses again. The reversal corresponds to the second peak in the release of trapped neon, and the isotopic compositions in the 1100 and 1200°C fractions again plot closer to the trapped neon axis. However, the isotopic composition of the trapped neon released in this 1150°C peak is not the same as that of the gas extracted below 1000°C. Projection of the mixing lines defined by the 1000–1300°C fractions yields a trapped $^{20}Ne/^{22}Ne$ ratio of 10.4 ± 1.0 for both the B29 and B6HS samples.

6. DISCUSSION

6.1 *Low-temperature* ^{22}Ne *and* ^{36}Ar *enrichments and cosmogenic rare gases*

We have found that several of the Ca,Al-rich aggregates from Allende contain neon and argon unusually rich in ^{22}Ne and ^{36}Ar that are both released at low temperatures ($\lesssim$700°C) during stepwise-heating experiments. The magnitudes of the ^{22}Ne- and ^{36}Ar-enrichments are correlated. In B32, B6HS rim, and B6HS core, the three aggregate samples for which both neon and argon data are available, the ratio of excess ^{36}Ar (defined as the ^{36}Ar remaining after subtraction of trapped and spallation ^{36}Ar from total ^{36}Ar) to the ^{22}Ne in the 500°C temperature fraction (where the ^{22}Ne-enrichment is most pronounced) is constant within errors at 6 ± 1, despite variation by a factor of five in the excess argon content. Any explanation of the neon and argon isotopic effects must explain this association.

The total neon isotopic compositions (Fig. 1) and the neon isotopic compositions of the low-temperature release fractions (Fig. 4) from Ca,Al-rich samples are consistent with the addition of either neon-E or sodium spallation neon as the ^{22}Ne-rich component. Sodium spallation should be important; microprobe analyses of Ca,Al-rich aggregates (including B29 and B32) show these samples may contain between 4 and 6 wt % sodium, ten to twenty times the sodium content of the bulk meteorite (CLARKE *et al.*, 1970). Meteoritic oligoclase feldspar which contains just over 6% by weight sodium has been shown to contain spallation neon with a measured $(^{21}Ne/^{22}Ne)_c$ ratio of 0.67 (SMITH and HUNEKE, 1975). The likely explanation of the ^{36}Ar-enrichments is neutron capture on chlorine. MANUEL *et al.* (1972) attributed anomalously high $^{36}Ar/^{38}Ar$ ratios (up to 6.05) observed in tem-

perature fractions from a bulk sample of Allende to excess ^{36}Ar produced by neutron capture on ^{35}Cl. Alkali-rich Ca,Al-inclusions may contain up to about 1.5% Cl, 70 times the bulk meteorite Cl content (CLARKE *et al.*, 1970; GROSSMAN and GANAPATHY, 1975), and thus would be expected to show large ^{36}Ar-enrichments relative to the bulk sample results of MANUEL *et al.* (1972).

In the following discussion, we will first show that the variations in cosmogenic ^{21}Ne content are consistent with the varying chemical compositions of the Allende samples. We will then compare calculated cosmogenic $^{21}Ne/^{22}Ne$ ratios to measured values to see if the ^{22}Ne is also consistent with purely cosmogenic neon. We will also show that the large excesses of ^{36}Ar in the Ca,Al-rich aggregates can indeed be explained by neutron capture on chlorine. We will arrive at an explanation of the nature and correlation of the ^{22}Ne- and ^{36}Ar-enrichments in terms of the chemistry and mineralogy of the Allende samples.

The content and composition of cosmogenic neon generated in a sample of a given target chemistry can be calculated from the following equations:

$$^{21}Ne_c(\text{cm}^3\ \text{STP/g}) = \sum_i P_i^{21} \cdot C_i \cdot t_{exp} \qquad (1)$$

$$(^{21}Ne/^{22}Ne)_c = \sum_i F_i^{22} \cdot (21/22)_i, \qquad (2)$$

where

$$F_i^{22} = P_i^{22} \cdot C_i \Big/ \sum_i P_i^{22} \cdot C_i$$

$$i = \text{Na, Mg, Al, Si, } \ldots .$$

P_i^{21} and P_i^{22} are the production rates of $^{21,22}Ne$ in cm^3 STP/g/10^6 yr from the target element i whose concentration in g/g is C_i. t_{exp} is the exposure age, in millions of years, $(21/22)_i$ is the ratio of $^{21}Ne_c$ to $^{22}Ne_c$ produced in the pure target element i, and F_i^{22} is the fraction of the total cosmogenic ^{22}Ne produced from i.

In Table 5, measured $^{21}Ne_c$ contents are compared to cosmogenic $^{21}Ne_c$ contents calculated using equation (1) and $^{21}Ne_c$ production rates available in the literature (BOCHSLER *et al.*, 1969; SMITH and HUNEKE, 1975). Measured values range from 1.3×10^{-8} cm^3 STP $^{21}Ne_c$/g in Ca,Al-rich chondrules to $2.0 \pm 0.2 \times 10^{-8}$ cm^3 STP/g in bulk and matrix samples. The agreement between the measured and calculated contents of $^{21}Ne_c$ in the aggregates and chondrules is good. *We conclude the observed variation in the concentration of* $^{21}Ne_c$ *can adequately be explained as an effect of variation in target chemistry*, and that all materials studied, including bulk meteorite samples and Ca,Al-rich chondrules and aggregates, have experienced substantially the same exposure to galactic cosmic rays.

We will now compare calculated and measured $(^{21}Ne/^{22}Ne)_c$ ratios to determine if the measured ^{22}Ne can also be explained as purely cosmogenic neon. The four major target elements for the production of cosmogenic neon in chondritic meteorites are Na, Mg, Al, and Si. In Allende samples, the variation in $(^{21}Ne/^{22}Ne)_c$ due to target chemistry can be expressed in terms of the relative proportions of Mg, Na, and Al. This is because the proportion of silicon is constant within 25% in the major minerals in the Allende materials, so the variation in $(^{21}Ne/^{22}Ne)_c$ due to variation in silicon content is no more than a few per cent. In Fig. 7 we have constructed a ternary diagram of Mg vs Na vs Al (expressed as percentages of Mg + Na + Al). On the figure we have superimposed isopleths of constant $(^{21}Ne/^{22}Ne)_c$ calculated using equation (2) and a fixed value of 0.4 for the ratio Si/Si + Mg + Na + Al. For a given chemical composition, the calculated $(^{21}Ne/^{22}Ne)_c$ ratio is read off the isopleth that passes through the point representing that composition. For example, the point labeled 'c' represents a composition where Na/Na + Mg + Al = 0.3, Mg/Na + Mg + Al = 0.35, and Al/Na + Mg + Al = 0.35. This point lies on the isopleth labeled 0.75, which is the calculated $(^{21}Ne/^{22}Ne)_c$ ratio for this example. No attempt has been made to include the effects of shielding on calculated $(^{21}Ne/^{22}Ne)_c$ ratios. Errors in calculated $(^{21}Ne/^{22}Ne)_c$ due to shielding and uncertainties in the production rates in equation (2) are probably less than 10%.

The points plotted on Fig. 7 represent chemical compositions for a variety of materials from Allende, including the bulk meteorite (MARTIN and MASON, 1974), average high- and low-Rb aggregates (GRAY *et al.*, 1973), traverses across individual aggregates (unpublished microprobe analyses, Lunatic Asylum, CIT), and individual mineral phases (GRAY *et al.*, 1973), including the Na-rich feldspathoid minerals sodalite and nepheline.

Table 5. Comparison of measured and calculated cosmogenic $^{21}Ne_c$ in Allende materials

	$^{21}Ne_c$ (10^{-8} ccSTP/g)	
	Measured	Calculated*
Bulk meteorite	2.0 ± 0.2	≡ 2.0
Ca,Al aggregates (high-Rb)		1.5 - 1.8†
B32	1.77	
B29	1.77	
C5	1.55	
Ca,Al chondrules (low-Rb)		1.35†
D7	1.27	
B28	1.47	

* Calculated as production rates relative to the bulk meteorite composition (MARTIN and MASON, 1974) and then normalised to the bulk meteorite $^{21}Ne_c$ contents of 2.0×10^{-8} cm^3 STP/g.

† Chemical analyses of the specific aggregates and chondrules studied here are not generally available. The average composition of low-Rb agregates (GRAY *et al.*, 1973) was used to calculate $^{21}Ne_c$ for the chemically-similar Ca,Al chondrules D7 and B28. Samples of the Ca,Al agregates B32, C5, and B29 came from the rims of the aggregates. Calculated $^{21}Ne_c$ is for microprobe analyses of rims of several alkali-rich aggregates (including B32 and B29).

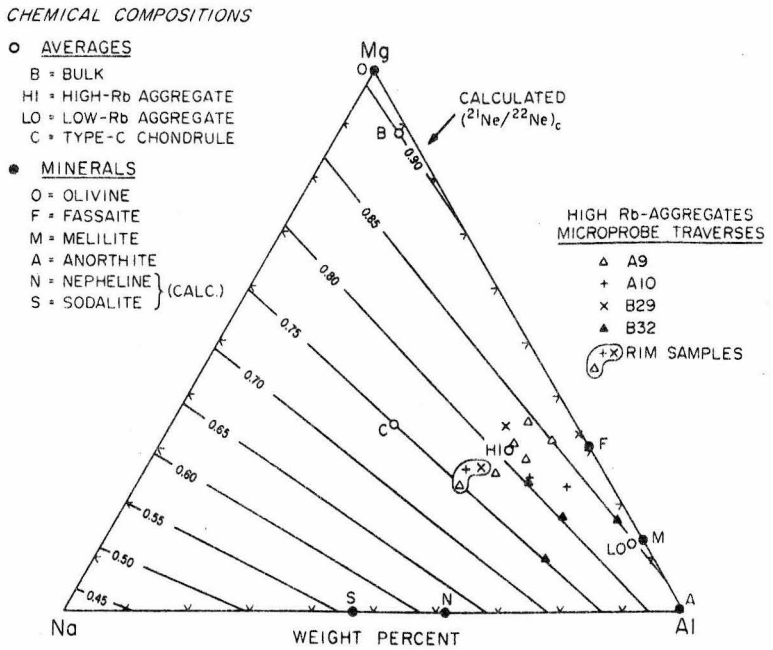

Fig. 7. Ternary diagram of weight percent Na vs Al vs Mg (normalized to 100%) in materials from Allende. Literature references for chemical compositions are: B (MARTIN and MASON, 1974); HI, LO, O, F, M, A (GRAY *et al.*, 1973); C (CLARKE *et al.*, 1970); N, S calculated from ideal chemical formula. Data for the microprobe traverses are unpublished. A9 and A10 are Ca,Al-rich aggregates similar to B32 and B29. Superimposed on the figure are isopleths of constant cosmogenic $(^{21}Ne/^{22}Ne)_c$ calculated from equation (2) using production rates from BOCHSLER *et al.* (1969) and SMITH and HUNEKE (1975) and assuming Si/Si + Mg + Na + Al = 0.4. Measured chemical compositions of Allende materials lie on isopleths from 0.91 (olivine, bulk) to 0.75 (rim samples of high-Rb aggregates) corresponding to calculated $(^{21}Ne/^{22}Ne)_c$ ratios of 0.91 to 0.75. Sodalite and nepheline fall on isopleths of 0.55 and 0.62. These low calculated $(^{221}Ne/^{22}Ne)_c$ ratios are due to the high abundance of sodium in these minerals.

The sodium content is obviously very important in determining $(^{21}Ne/^{22}Ne)_c$, due to the low production ratio in pure sodium, $(21/22)_{Na} = 0.34$ (SMITH and HUNEKE, 1975). For materials containing little sodium, such as low-Rb aggregates and the minerals olivine, fassaite, melilite, and anorthite, points fall on isopleths between 0.91 and 0.83, corresponding to variation in calculated $(^{21}Ne/^{22}Ne)_c$ ratios by only about 10%, depending on the ratio of Mg to Al. For sodium-bearing materials such as rim samples from high-Rb aggregates and the type-C chondrule of CLARKE *et al.* (1970), points plot on isopleths as low as 0.75. The most dramatic shift in calculated $(^{21}Ne/^{22}Ne)_c$ is for the Na-rich minerals sodalite and nepheline (S, N in Fig. 7) which plot on isopleths of 0.55 and 0.62. These minerals should contribute cosmogenic neon significantly enriched in ^{22}Ne compared with that from other minerals in Allende.

Comparison of calculated and measured $(^{21}Ne/^{22}Ne)_c$ values is made in Table 6. The high $(^{21}Ne/^{22}Ne)_c$ ratios of bulk and matrix samples reflect the high Mg and low Al and Na contents of these materials (B in Fig. 7). High Al content, but still low Na, is characteristic of the Ca,Al chondrules and low-Rb aggregates which consist largely of melilite and fassaite (M, F in Fig. 7). These Ca,Al chondrules are known to contain very little Rb (GRAY *et al.*, 1973), and show a reasonable but not precise correlation with the $(^{21}Ne/^{22}Ne)_c$ ratio calculated for low-Rb aggregates (LO in Fig. 7).

The three aggregates B32, B29, and C5 are high-Rb aggregates (GRAY *et al.*, 1973) and microprobe analyses have shown that B32 and B29 contain as much as several percent sodium. The low measured $(^{21}Ne/^{22}Ne)_c$ ratios of 0.72 to 0.75 reflect the relatively high sodium contents, and are in reasonable agreement with values calculated for a number of high-Rb aggregates. In addition, for two of these high-alkali aggregates, B32 and C5, the 500°C release fractions have very low measured $^{21}Ne/^{22}Ne$ ratios similar to those expected from sodalite or nepheline (S, N in Fig. 7). These minerals have been identified in high-alkali aggregates by X-ray methods (CLARKE *et al.*, 1970; GROSSMAN and GANAPATHY, 1975). *From the agreement outlined in Table 6 between the calculated cosmogenic* $^{21}Ne/^{22}Ne$ *ratios and the measured values we conclude that* ^{22}Ne *as well as* ^{21}Ne *concentrations can be explained by galactic cosmic-ray spallation reactions.* The variations in both ^{22}Ne and ^{21}Ne content are consistent with the variations in target chemistry, in particular the variation in sodium content.

The ^{36}Ar-enrichments observed in the aggregates B32 and B6HS can also be explained as the result

Table 6. Comparison of measured and calculated $(^{21}Ne/^{22}Ne)_c$ ratios in Allende materials

Measured* $(^{21}Ne/^{22}Ne)_c$		Calculated** $(^{21}Ne/^{22}Ne)_c$	
Bulk and matrix samples		Bulk meteorite (MARTIN and MASON, 1974)	0.90
NWT	0.93		
SWB	0.93		
B29	0.95		
C5	0.95		
B6HS	0.93		
Ca,Al chondrules		Ca,Al aggregates (low-Rb) (GRAY et al., 1973)	0.85
D7	0.80		
B28	0.87		
High-temperature fractions from Ca,Al aggregates†	0.80 - 0.85		
Ca,Al aggregates (high-Rb)		Ca,Al aggregates (high-Rb) Alkali-rich rim samples	0.75 - 0.78
B32	0.72		
B29	0.75		
C5	0.75		
500°C fractions from Ca,Al aggregates		Nepheline $Na_3(Na,K)Al_4Si_4O_{16}$	0.62
		Sodalite $Na_8Al_6Si_6O_{24}Cl_2$	0.55
B32	0.60		
C5	0.66		

* Tables 2 and 3.

** Calculated using equation (2) with production rates and ratios from BOCHSLER *et al.* (1969) and SMITH and HUNEKE (1975).

† These temperature fractions contain only cosmogenic neon, and probably represent the neon released from Ca,Al-rich minerals such as melilite or fassaite, etc., similar to the phases comprising the Ca,Al chondrules.

of cosmic-ray induced reactions. ^{36}Ar is produced from chlorine by the capture of neutrons from the cascade of secondary particles generated by the irradiation of meteoritic material with galactic cosmic rays. We will use the subscript 'Cl' to denote ^{36}Ar so produced. MABUCHI *et al.* (1975) have measured a ^{36}Cl activity for a total sample of Allende of 54 dpm/kg. From an assumed whole-rock Cl content of 225 ppm (CLARKE *et al.*, 1970) and making a $\sim 10\%$ correction for ^{36}Cl produced by spallation, we infer a production rate of ^{36}Ar from Cl of $\sim 4.2 \times 10^{-6}$ cm^3 STP $^{36}Ar_{Cl}/g$ Cl/10^6 yr in Allende. The B32 aggregate contains 0.3 ± 0.2 wt % Cl; therefore, in B32 the amount of $^{36}Ar_{Cl}$ produced over the 5 million yr exposure age should be $6 \pm 4 \times 10^{-8}$ cm^3 STP/g. This estimate of $^{36}Ar_{Cl}$ is in good agreement with the measured content of excess ^{36}Ar, $5.6 \pm 1 \times 10^{-8}$ cm^3 STP/g. *We conclude that the observed* ^{36}Ar *excesses in the* Ca,Al*-rich samples are produced by neutron capture on chlorine.*

The low-temperature release characteristics of the gas enriched in ^{22}Ne and ^{36}Ar and the good correlation between these isotopic effects can be shown to be due to the chemical and mineralogical nature of the Ca,Al-rich aggregates. We concluded that the ^{22}Ne-enrichment in Ca,Al-rich aggregates was consistent with galactic cosmic-ray spallation on Na-rich target material. In these aggregates, the sodium is concentrated in very fine-grained material which is often interstitial or encrusts slightly larger grains of refractory Ca,Al-rich minerals. The Na-rich feldspathoid minerals sodalite, $Na_8Al_6Si_6O_{24}Cl_2$, and nepheline, $Na_3(Na,K)Al_4Si_4O_{16}$, have been identified in high-alkali Ca,Al-aggregates similar to those examined here (CLARKE *et al.*, 1970; GROSSMAN and GANAPATHY, 1975). In Table 6, the isotopic composition of the neon in 500°C temperature fractions is shown to be close to that expected of spallation neon from sodalite and nepheline. The low degassing temperatures for this neon is consistent with the very fine grain size of the Na-rich phases. Also for comparison, spallation neon is degassed at ≤ 500°C from meteoritic oligoclase, a Na-rich feldspar mineral similar to the feldspathoids (SMITH and HUNEKE, 1975). We therefore attribute the low-temperature ^{22}Ne-enrichments to cosmic-ray spallation from the Na-rich feldspathoid minerals. Sodalite is also probably the major source of chlorine and hence excess ^{36}Ar in the alkali-rich aggregates. The occurrence of major amounts of both the Cl and Na in sodalite provides a natural explanation for the observed correlation between the ^{22}Ne- and ^{36}Ar-enrichments in the aggregates. *We conclude that the dominant isotopic effects seen in the neon and argon from the* Ca,Al*-rich samples are the result of cosmic-ray induced reactions on sodium and chlorine, and not due to admixture of an exotic trapped gas component such as neon-E.* We note that MANUEL *et al.* (1972) inferred an unusually-low trapped $^{20}Ne/^{22}Ne$ ratio ≈ 4 from the neon in an 800°C release fraction from a sample of Allende, and attributed this low value to the addition of neon-E. However, the authors also report a high $^{36}Ar/^{38}Ar$ ratio of 6.05 in the same release fraction. We suggest on the basis of the above discussion that the correlated ^{22}Ne and ^{36}Ar enhancements arise from the release of cosmogenic gas from sodium- and chlorine-rich

material such as sodalite, rather than from the release of neon-E.

6.2 *Implications of* ^{36}Ar *produced by neutron capture on chlorine*

Before continuing with discussion of the trapped neon in Allende, we would like to pursue the implications of the production of $^{36}Ar_{Cl}$ in meteoritic samples other than the extreme case of the Cl-rich Allende Ca,Al-rich inclusions. For a bulk sample of Allende, with 225 ppm Cl (CLARK *et al.*, 1970), the production of $^{36}Ar_{Cl}$ will be about 0.45×10^{-8} cm^3 STP/g over the 5 million yr exposure. The spallation $^{36}Ar_c$ from Ca and Fe is about 0.2×10^{-8} cm^3 STP/g, so the net cosmogenic $^{36}Ar_c$ is about 0.65×10^{-8} cm^3 STP/g. Since $^{38}Ar_c = 0.3 \times 10^{-8}$ cm^3 STP/g, the effective cosmogenic production ratio $(^{36}Ar/^{38}Ar)_c$ is 0.65/0.3, or about 2, and thus is much higher than the value of 0.6 obtained from spallation on Fe and Ca alone. Chlorine contents of other carbonaceous chondrites are similar to the Cl abundance in Allende, leading us to suggest that the cosmogenic $^{36}Ar/^{38}Ar$ ratio in these meteorites may well be closer to 2 than to 0.6 depending on the size of the meteorite. This has the consequence that trapped $^{36}Ar/^{38}Ar$ ratios >5.5 inferred for samples of carbonaceous chondrites by MAZOR *et al.* (1970) cannot be strictly supported. The authors used $(^{36}Ar/^{38}Ar)_c = 0.65$ and $(^{21}Ne/^{38}Ar)_c \approx 5.5$ to infer trapped $^{36}Ar/^{38}Ar$ ratios as high as 5.8 in Mokoia, and their data for the C3 chondrites Bali and Coolidge would give ratios as high as 6.0 and 6.7 if treated in the same fashion (cf. Fig. 2). If we instead use a $(^{36}Ar/^{38}Ar)_c$ ratio of about 2 as calculated for Allende, we obtain $(^{36}Ar/^{38}Ar)_t \approx 5.5$ for Bali and Coolidge. As we discussed in the systematics section, $(^{36}Ar/^{38}Ar)_t$ appears to lie between about 5.2 and 5.5 for almost all the meteorite samples in Fig. 2. The total range of $(^{36}Ar/^{38}Ar)_t$ in various solar system reservoirs, including the Earth's atmosphere, the solar wind, and meteorites, is also evidently about 5.2 to 5.5. The observation by SIGNER and SUESS (1963) that there are no large variations in Ar_t isotopic compositions remains valid. There is no unequivocal evidence of a 40% variation in $(^{36}Ar/^{38}Ar)_t$ implied by the mass fractionation theory of SRINIVASAN and MANUEL (1971). The high $(^{36}Ar/^{38}Ar)_t$ ratios inferred by MAZOR *et al.* (1970) cannot be substantiated, and therefore cannot be used as evidence of mass-fractionated trapped argon.

EBERHARDT *et al.* (1963) suggested that the production of $^{36}Ar_{Cl}$ is important in ordinary chondrites. The chlorine content of ordinary chondrites is about 100 ppm (REED, 1971). If the production rate of $^{36}Ar_{Cl}$ found in Allende were valid for ordinary chondrites, we would expect the total cosmogenic $(^{36}Ar/^{38}Ar)_c$ ratio in ordinary chondrites to be about 1.3. Reexamining Fig. 2 we find a sharp lower limit of 1.0 for measured $^{36}Ar/^{38}Ar$, which we suggest reflects the production of $^{36}Ar_{Cl}$ in ordinary chondrites. A $(^{36}Ar/^{38}Ar)_c$ ratio of 1.0 for material with 100 ppm Cl implies a $^{36}Ar_{Cl}$ production rate of about 2×10^{-6} cm^3 STP/g Cl/10^6 yr compared with 4×10^{-6} cm^3 STP/g Cl/10^6 yr for Allende. The slightly higher rate inferred for Allende is consistent with a somewhat higher degree of shielding for Allende. In ordinary chondrites, measured $^{36}Ar/^{38}Ar$ ratios of about 1 are typically taken to indicate the presence of small amounts of trapped argon (cf. ZAHRINGER, 1968). Such is not the case if $(^{36}Ar/^{38}Ar)_c = 1$. In addition, $^{38}Ar_c$ contents are usually calculated by partitioning total ^{38}Ar using measured $^{36}Ar/^{38}Ar$ ratios and assumed end-member compositions $(^{36}Ar/^{38}Ar)_t = 5.35$ and $(^{36}Ar/^{38}Ar)_c = 0.65$. If $(^{36}Ar/^{38}Ar)_c$ is in fact >0.65, then the $^{38}Ar_c$ inferred using 0.65 will be too low—by as much as 40% if $(^{36}Ar/^{38}Ar)_c$ is actually 2.0.

6.3 *The overall distribution of trapped rare gases in Allende*

Recent work (LEWIS *et al.*, 1975; PHINNEY *et al.*, 1976; WEBER *et al.*, 1976) has shown that the distribution of the trapped gases in meteorites may be very heterogeneous, and the gas concentrated in trace phases of the meteorites. LEWIS *et al.* (1975) found that a large portion, if not all, of the trapped noble gas in bulk samples of Allende appears to reside in two minor phases, a complex mixture of chromite and carbon and an incompletely characterized phase 'Q'. Together these two phases comprise about 0.5% of the meteorite, but have noble gas contents about 200 times the bulk meteorite values. By selective chemical etching, Lewis *et al.* were able to estimate the relative amounts of chromite/carbon and 'Q', and to estimate the trapped gas contents and compositions in the two phases. Their results suggest that roughly 2/3 of the trapped neon is incorporated in the chromite/carbon and 1/3 in 'Q'. The isotopic compositions of the trapped neon in three etched chromite/carbon samples were $(^{20}Ne/^{22}Ne)_t = 8.7 \pm 0.2$, 8.6 ± 0.3, and 8.7 ± 0.4. Comparison of etched and unetched samples indicated that the third of the neon located in 'Q' has a higher $(^{20}Ne/^{22}Ne)_t$ ratio ~ 11.

From the results obtained by stepwise extraction of neon from matrix samples (Section 5.2), we inferred the presence of two trapped neon compositions. The first, with a peak release rate at about 850°C, has $(^{20}Ne/^{22}Ne)_t = 8.7 \pm 0.1$, and the second, with a peak release rate at about 1150°C, has $(^{20}Ne/^{22}Ne)_t = 10.4 \pm 1$. The good agreement of the isotopic compositions inferred from our results and those of LEWIS *et al.* (1975) suggests we identify the 850°C trapped-neon release peak in matrix samples with the release of neon from chromite/carbon, and the 1150°C peak with 'Q'. We also found that about 2/3 of the trapped neon was present in the 850°C peak and the remaining 1/3 in the second, 1150°C peak. These proportions agree well with the apportionment of neon between chromite/carbon and 'Q' derived from the data of LEWIS *et al.* (1975), providing further support for the identification of the two stepwise release peaks with

the two trace phases identified by Lewis *et al.* We caution that since the chromite/carbon and 'Q' phases are trace phases of uncertain physical association or distribution within the Allende matrix, the relative proportion of the phases and the associated trapped neon could be sensitive to inhomogeneities in the matrix which might lead in further experiments to trapped neon proportions other than the 2/3 and 1/3 observed in the present samples.

The relatively high noble gas retentivity of 'Q' indicated by the 1150°C temperature of neon release is supported by data for argon and xenon. Lewis *et al.* found that $\gtrsim 90\%$ of the argon and xenon in Allende are contained in 'Q'. From the stepwise thermal release data for argon in the B6HS matrix sample (Fig. 3) we find that trapped argon in this matrix sample was indeed released in a single peak, with 2/3 of the ^{36}Ar released in the 1100 and 1200°C fractions. MANUEL *et al.* (1972) found that most of the xenon is also released from a bulk sample of the meteorite in a single peak, at about 1200°C.

We note that essentially all the trapped neon in our matrix samples resides in the two release peaks identifiable with the chromite/carbon and 'Q' of LEWIS *et al.* (1975). The procedures of Lewis *et al.* involved acid dissolution of nearly the entire mass of their samples, with the attendant possibility that important trapped-gas-bearing phases could have been lost. Since no separation of phases was done for our matrix samples other than the exclusion of unrepresentatively large pieces of Ca,Al-rich aggregate, the agreement between results confirms that the bulk of the trapped neon in Allende resides in the trace phases described by Lewis *et al.*

If we examine inclusions in Allende, we find evidence that other trapped components exist which in bulk samples of Allende are masked by the gases in the matrix chromite/carbon and 'Q'. In Section 5.2 we concluded that trapped neon is present in the Ca,Al-rich aggregates C5, B29, and B32. In addition, D. Phinney has kindly shown us results of a stepwise release experiment on a dark inclusion from Allende where a large fraction of the trapped neon was released at temperatures ≤ 600°C, distinctly lower than the release from chromite/carbon which occurred at about 800°C. However, the neon from this low-temperature site was characterized by $(^{20}Ne/^{22}Ne)_t \approx 8.8$, indistinguishable from the composition associated here with chromite/carbon. Two distinctive sites of gas with the same isotopic composition suggest that this neon may represent samples from a fundamental reservoir associated with the early history of Allende.

6.4 *Is there neon-E in Allende?*

Although the presence of neon-E has been discounted as an explanation for the dominant neon isotopic effects in the Ca,Al-rich aggregates, the question of whether any neon-E at all can be observed in the Allende samples is still important, since both oxygen and magnesium isotopic anomalies are found in Allende materials.

Neon in the bulk and matrix samples studied can be formally regarded as a three-component mixture of cosmogenic neon, neon-E, and an average trapped component consisting of the combination of any other trapped neon compositions present. If we have independent measurements of the isotopic compositions of the cosmogenic and average trapped components, then the displacement of a sample from the mixing line defined by these two components will give the amount of neon-E present in the sample.

Over 90% of the cosmogenic ^{22}Ne in Allende is generated from the Mg and Si in mafic silicates such as olivine and pyroxene. The $(^{21}Ne/^{22}Ne)_c$ ratio of ~ 0.93 in the B12 olivine chondrule is a measure of the average composition of Mg + Si spallation neon in Allende that is independent of the measurements from the bulk samples. This spallation composition is confirmed by the stepwise release from the A5 pyroxene chondrule which was found to contain no significant neon-E or sodium spallation neon. In the three-isotope diagram in Fig. 8, if the average trapped neon composition in Allende were that of solar wind neon and the samples contained no neon-E, then the measured total neon isotopic compositions would lie on the mixing line labeled SOLAR–COSMOGENIC. The displacement of the actual data points would then be due to neon-E comprising about 6% of the total ^{22}Ne, or $\sim 0.17 \times 10^{-8}$ cm^3 STP $^{22}Ne_E$/g. This amount of neon-E is an upper limit for the neon-E in Allende, since $(^{20}Ne/^{22}Ne)_t = 13.7$ in the solar wind is the highest well-established trapped neon ratio. The work of BLACK (1972) indicates that the amount of neon-E in C1 and C2 carbonaceous chondrites which is released in a recognizable peak around 900–1000°C is characteristically ~ 0.1 to 0.2×10^{-8} cm^3 STP $^{22}Ne_E$/g. Neon-E is certainly not enriched in Allende. We can refine our estimate of the neon-E in Allende further, since an independent estimate of the average composition of trapped neon in Allende is available from the work of LEWIS *et al.* (1975) and PHINNEY *et al.* (1976). As discussed in Section 6.3, LEWIS *et al.* (1975) demonstrated that the bulk of the trapped neon in Allende is found in a mixture of the trace phases labeled chromite/carbon and 'Q' with an average trapped $^{20}Ne/^{22}Ne$ ratio (taken from unetched separates) of about 8.9 to 9.6. Similar results were obtained by PHINNEY *et al.* (1976). Using these results for the average trapped neon component, then neon in Allende samples with no neon-E should plot on the shaded mixing trend labeled ALLENDE TRAPPED–COSMOGENIC in Fig. 8. Addition of a separate neon-E component would shift the measured compositions toward the origin. Note that this treatment does not rule out the possibility of neon-E in the chromite/carbon or 'Q' separates. The matrix samples B29, C5, and B6HS (see Fig. 1 for identification of points) plot squarely on the mixing trend, and therefore can contain negligible amounts

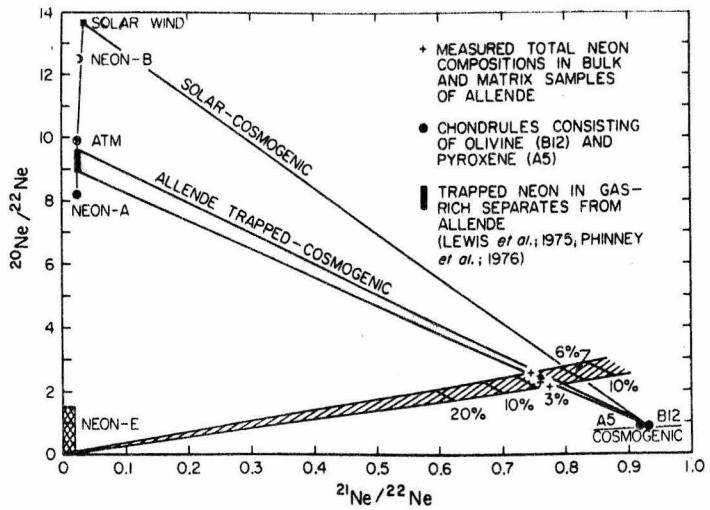

Fig. 8. Neon three-isotope plot showing the relationship of measured neon compositions in bulk and matrix samples to compositions expected by simple two-component mixing of trapped neon from gas-rich separates from Allende and cosmogenic neon (shaded trend labeled ALLENDE TRAPPED–COSMOGENIC). The agreement between the 2-component mixing trend and the bulk neon compositions implies that less than 2% of the ^{22}Ne in these samples is from neon-E, or $^{22}Ne_E < 0.06 \times 10^{-8}$ cm^3 STP/g.

of a distinct neon-E component. An upper limit for these samples is about 1% of the total ^{22}Ne or $<0.03 \times 10^{-8}$ cm^3 STP $^{22}Ne_E$/g, three to six times less neon-E than in the C1 and C2 meteorites studied. An upper limit for samples SWB and NWT is somewhat higher, 2% or $\lesssim 0.06 \times 10^{-8}$ cm^3 STP $^{22}Ne_E$/g, since these latter samples are shifted slightly relative to the former three. However, the shift is small enough to be accommodated in a more mundane way, by a change in $(^{21}Ne/^{22}Ne)_c$ caused by a slightly lower degree of shielding in SWB and NWT, or by a slightly higher content of Ca,Al-rich aggregates which have lower $(^{21}Ne/^{22}Ne)_c$ ratios. There is no clear indication of neon-E in Allende from any of the total neon compositions of the bulk and matrix samples studied.

Nor is there any evidence for neon-E in the stepwise release data for matrix samples (Fig. 6). The work of Black (Black and Pepin, 1969; Black, 1972) showed that in C1 and C2 chondrites the release of neon-E occurred over an interval of about 200°C at around 900–1000°C and resulted in marked deviations of the isotopic compositions of the affected temperature steps toward the origin on the three-isotope plot. As discussed in Section 6.3, the present data are consistent with linear mixing trends between cosmogenic neon and the two trapped neon compositions associated with chromite/carbon and 'Q' measured by Lewis *et al.* (1975). There are no distinctive deviations that would signal the release of neon-E. If neon-E is present at all it would seem that it could only be as a well-homogenized constituent in the neon trapped in the chromite/carbon or 'Q' reservoirs, and not as a separately observable component.

We cannot do the exactly analogous calculations for the total neon data from Ca,Al-rich aggregates because no independent estimates of the compositions of trapped or spallation neon are available. However, if there were a significant enrichment of neon-E in the aggregates, the measured cosmogenic $^{21}Ne/^{22}Ne$ ratios (corrected only for trapped neon-A or the average Allende trapped neon in the matrix) would be significantly lower than the calculated values in Table 6. In fact, the substantial agreement between these two sets of numbers was used in Section 6.1 to conclude that observed ^{22}Ne-enrichments could adequately be explained by addition of sodium spallation neon alone. Taking differences between measured and calculated $(^{21}Ne/^{22}Ne)_c$ values in Table 6 at face value allows us to set an upper limit for neon-E in the aggregates of $<10\%$ of the total ^{22}Ne, corresponding to less than about 0.25×10^{-8} cm^3 STP ^{22}Ne/g. There is no evidence of neon-E in the stepwise release data from the aggregates (Fig. 4) either; all measured compositions and patterns are consistent with the degassing of spallation neon from sodalite and nepheline, of spallation neon from Ca,Al-rich silicates, and of a small amount of trapped neon-A.

What are the implications of the apparent lack of observable neon-E in Allende? The Ca,Al-rich aggregates in Allende have been shown to contain isotopic anomalies in oxygen (Clayton *et al.*, 1973) and magnesium (Lee and Papanastassiou, 1974; Gray and Compston, 1974). As listed in Table 7, samples of Ca,Al-rich aggregates and chondrules studied here (including B29, B32, B6HS, and D7) contained substantial oxygen anomalies (1–2% excess ^{16}O) and magnesium anomalies ($\delta^{26}Mg = 1.35$–2.63‰). The B6HS (rim) sample studied here was a split of the sample in which the oxygen isotopes were measured. The other samples were fragments from the same aggregates, and not specifically splits, but the nearly identical noble gas results obtained for the two com-

Table 7. Magnesium and oxygen anomalies in Allende samples. None of the samples contain observable amounts of neon-E

	$\delta^{26}Mg$†	excess ^{16}O
	per mil	percent
Ca,Al aggregates		
B29	2.6 ± 0.2	~2*
B32	1.4 ± 0.4	~2*
C5	-0.5 ± 0.3	--
B6HS (rim)	--	~1**
Ca,Al chondrules		
D7	1.9 ± 0.3	--
Mafic chondrules		
B12 (olivine)	-0.3 ± 0.3	--
A5 (pyroxene)	-0.1 ± 0.2	--

† LEE and PAPANASTASSIOU (1974).
* R. N. Clayton, private communication.
** S. Epstein, private communication.

pletely separate samples of B32 aggregate suggests the distribution of noble gases in the aggregates is fairly uniform. Two of these Ca,Al-rich samples (B32, B29) contain trapped neon, and therefore should have been capable of retaining neon-E, yet we have found no evidence of neon-E in either these two aggregates or any other Allende samples. It follows that there is no straightforward correlation between the neon-E anomaly and either the magnesium or oxygen anomalies.

EBERHARDT (1974) has shown that neon-E in the C1 chondrite Orgueil resides in a trace mineral phase identified as a refractory clay mineral or phyllosilicate. If this carrier is universal in other meteorites with neon-E, the lack of observable neon-E in Allende may be due to absence of this mineral. We note that the principal matrix phase in Allende is olivine, and not the low-temperature, hydrous phyllosilicate characteristic of all carbonaceous chondrites in which neon-E has been identified. Alternatively, if the carrier is present in Allende, then it has evidently lost whatever neon-E it once contained.

CONCLUSIONS

We draw the following four conclusions from our study of the neon and argon in Allende:

(1) the low-temperature ^{22}Ne and ^{36}Ar enrichments observed in Ca.Al-rich aggregates arise from cosmic-ray-induced nuclear reactions—spallation from sodium and neutron capture by chlorine.

(2) Neon-E cannot be identified in any of the samples studied.

(3) Trapped neon in matrix samples can be described in terms of two distinctive Ne isotopic compositions.

(4) Trapped neon is contained in several Ca.Al-rich aggregates which also have high contents of volatile elements such as Na, Cl, K, and Rb.

The observation of large isotopic effects in neon from Ca,Al-rich aggregates due to the addition of ^{22}Ne from sodium spallation has important implications for the identification of the neon-E anomaly in other samples. ^{22}Ne-rich isotopic compositions which cannot be explained by mixing whole-rock spallation neon with solar neon or neon-A cannot be indiscriminately attributed to the presence of neon-E. The possibility of sodium spallation neon must be kept in mind. However, we note that the observations of neon-E in C1 and C2 carbonaceous chondrites made by BLACK (1972) *cannot* be explained by galactic cosmic-ray spallation from sodium.

Neutron capture on chlorine in meteorites may generate substantial cosmogenic ^{36}Ar. $(^{36}Ar/^{38}Ar)_c$ ratios are probably ≈ 1 in ordinary chondrites and ≈ 2 in carbonaceouus chondrites. As a result, high calculated values of trapped $^{36}Ar/^{38}Ar$ ratios in carbonaceous chondrites (MAZOR *et al.* 1970) must be revised downward to $\lesssim 5.5$. There is no evidence of $(^{36}Ar/^{38}Ar)_t$ ratios outside the range 5.2–5.5 in carbonaceous chondrites.

The lack of observable neon-E in the samples studied precludes the establishment of any direct correlation between neon-E and the magnesium or oxygen anomalies in Allende. If any neon-E is present, it is presently in too low amounts to be identified or has apparently been homogenized with the other trapped neon in Allende. A separate neon-E bearing phase such as observed in C1 and C2 chondrites is either of much lower abundance in Allende, or the E-bearing phase or phases were degassed prior to their incorporation into the meteorite.

The two trapped neon compositions observed in matrix samples can be identified with the two components observed by LEWIS *et al.* (1975). Neon with $(^{20}Ne/^{22}Ne)_t = 8.7 \pm 0.1$ is located in chromite/carbon and released at about 850°C. Neon with $(^{20}Ne/^{22}Ne)_t = 10.4 \pm 1.0$ is located in 'Q' and released at about 1150°C. Almost all the trapped neon in Allende is found in these two sites. Additional reservoirs of gas in Allende do exist, however, and include the high-Rb Ca,Al-aggregates and dark inclusions (Phinney, private communication).

The presence of trapped neon in the high-alkali Ca,Al aggregates adds an additional dimension to the complexity of these samples. The present results do not allow a characterization of the isotopic composition of this gas.

Acknowledgements—We gratefully acknowledge constructive criticism provided in a review of this manuscript by D. PHINNEY.

This work was supported by NSF grants GP-28027 and MPS71-02670 A05.

REFERENCES

BLACK D. C. (1972) On the origins of trapped helium, neon, and argon isotopic variations in meteorites—II. Carbonaceous meteorites. *Geochim. Cosmochim. Acta* **36**, 377–394.

BLACK D. C. and PEPIN R. O. (1969) Trapped neon in meteorites—II. *Earth Planet. Sci. Lett.* **6**, 395–405.

BOCHSLER P., EBERHARDT P., GEISS J. and GROGLER N. (1969) Rare-gas measurements in separate mineral phases of the Otis and Elenovka chondrites. In *Meteorite Reesearch*, (editor P. Millman), pp. 857–874. D. Reidel.

BOGARD D. D., CLARK R. S., KEITH J. E. and REYNOLDS M. A. (1971) Noble gases and radionuclides in Lost City and other recently fallen meteorites. *J. Geophys. Res.* **76**, 4076–4083.

BOGARD D. D. and NYQUIST L. E. (1972) Noble gas studies on regolith materials from Apollo 14 and 15. *Proc. 3rd Lunar Sci. Conf. Geochim. Cosmochim. Acta, Suppl.* **3**, Vol. 2, pp. 1797–1819. M.I.T. Press.

BOGARD D. D., REYNOLDS M. A. and SIMMS L. A. (1973) Noble gas concentrations and cosmic ray exposure ages of eight recently fallen chondrites. *Geochim. Cosmochim. Acta* **37**, 2417–2433.

CLARKE R. S., JR., JAROSEWICH E., MASON B., NELEN J., GÓMEZ M. and HYDE J. R. (1970) The Allende, Mexico, meteorite shower. *Smithsonian Contrib. Earth Sci.* **5**.

CLAYTON R. N., GROSSMAN L. and MAYEDA T. K. (1973) A component of primitive nuclear composition in carbonaceous meteorites. *Science* **182**, 485–488.

EBERHARDT P. (1974) A neon-E-rich phase in the Orgueil carbonaceous chondrite. *Earth Planet. Sci. Lett.* **24**, 182–187.

EBERHARDT P. (1975) Ne–E rich phase in Orgueil. *Meteoritics* **10**, 401 (abstract).

EBERHARDT P., EUGSTER O., GEISS J. and MARTI K. (1966) Rare gas measurements in 30 stone meteorites. *Z. Naturforsch*, **21a**, 414–426.

EBERHARDT P., EUGSTER O. and MARTI K. (1965) A redetermination of the isotopic composition of atmospheric neon. *Z. Naturforsch.* **20a**, 623–624.

EBERHARDT P., GEISS J. and LUTZ H. (1963) Neutrons in meteorites. In *Earth Science and Meteoritics*, (editors J. Geiss and E. D. Goldberg), pp. 143–168, North-Holland.

FIREMAN E. L., DE FELICE J. and NORTON E. (1970) Ages of the Allende meteorite. *Geochim. Cosmochim. Acta* **34**, 873–881.

GEISS J. (1973) Solar wind composition and implications about the history of the solar system. Invited paper, 13th Int. Cosmic Ray Conf., Denver.

GRAY C. M. and COMPSTON W. (1974) Excess ^{26}Mg in the Allende meteorite. *Nature* **251**, 495–497.

GRAY C. M., PAPANASTASSIOU D. A. and WASSERBURG G. J. (1973) The identification of early condensates from the solar nebula. *Icarus* **20**, 213–239.

GROSSMAN L. and GANAPATHY R. (1975) Volatile elements in Allende inclusions. *Proc. 6th Lunar Sci. Conf. Geochim. Cosmochim. Acta, Suppl.* **6**, Vol. 2, pp. 1729–1736. Pergamon Press.

HUNEKE J. C., SMITH S. P., RAJAN R. S. and WASSERBURG G. J. (1974) Ne in selected materials from the Allende meteorite. *Meteoritics* **9**, 350–351 (abstract).

LEE T. and PAPANASTASSIOU D. A. (1974) Mg isotopic anomalies in the Allende meteorite and correlation with O and Sr effects. *Geophys. Res. Lett.* **1**, 225–228.

LEWIS R. S., SRINIVASAN B. and ANDERS E. (1975) Host phase of a strange xenon component in Allende. *Science* **190**, 1251–1262.

MABUCHI H., NAKAMURA Y., TAKAHASHI H., IMAMURA M., YOKOYAMA Y. and REYSS J. L. (1975) Cosmogenic radionuclides in the Allende meteorite. *Meteoritics* **10**, 449 (abstract).

MANUEL O. K., WRIGHT R. J., MILLER D. K. and KURODA P. K. (1972) Isotopic compositions of rare gases in the carbonaceous chondrites Mokoia and Allende. *Geochim. Cosmochim. Acta* **36**, 961–983.

MARTIN P. M. and MASON B. (1974) Major and trace elements in the Allende meteorite. *Nature* **249**, 333–334.

MARVIN U. B., WOOD J. A. and DICKEY J. S., JR. (1970) Ca–Al rich phases in the Allende meteorite. *Earth Planet. Sci. Lett.* **7**, 346–350.

MAZOR E., HEYMANN D. and ANDERS E. (1970) Noble gases in carbonaceous chondrites. *Geochim. Cosmochim. Acta* **34**, 781–824.

NYQUIST L., FUNK H., SCHULTZ L. and SIGNER P. (1973) He, Ne and Ar in chondritic Ni–Fe as irradiation hardness sensors. *Geochim. Cosmochim. Acta* **37**, 1655–1685.

PEPIN R. O. (1967) Trapped neon in meteorites. *Earth Planet. Sci. Lett.* **2**, 13–18.

PEPIN R. O. (1968) Neon and xenon in carbonaceous chondrites. In *Origin and Distribution of the Elements*, (editor L. H. Ahrens), pp. 379–386. Pergamon Press.

PEPIN R. O. and SIGNER P. (1965) Primordial rare gases in meteorites. *Science* **149**, 253–265.

PHINNEY D., FRICK U. and REYNOLDS J. H. (1976) Rare-gas-rich separates from carbonaceous chondrites. In *Lunar Science* VII, pp. 691–693. Lunar Science Institute, Houston.

REED G. W., JR. (1971) Chlorine (17). In *Handbook of Elemental Abundances in Meteorites*, (editor B. Mason), pp. 143–148. Gordon & Breach.

REYNOLDS J. H. and TURNER G. (1964) Rare gases in the chondrite Renazzo. *J. Geophys. Res.* **69**, 3263–3281.

SIGNER P. and SUESS H. E. (1963) Rare gases in the sun, in the atmosphere and in meteorites. In *Earth Science and Meteoritics*, (editors J. Geiss and E. D. Goldberg), pp. 241–272. North-Holland.

SMITH S. and FIREMAN E. L. (1973) Ages of eight recently fallen meteorites. *J. Geophys. Res.* **78**, 3249–3259.

SMITH S. P. and HUNEKE J. C. (1975) Cosmogenic neon produced from sodium in meteoritic minerals. *Earth Planet. Sci. Lett.* **27**, 191–199.

SRINIVASAN B. and MANUEL O. K. (1971) On the isotopic composition of trapped helium and neon in carbonaceous chondrites. *Earth Planet. Sci. Lett.* **12**, 282–286.

WEBER H. W., BEGEMAN F. and HINTENBERGER H. (1976) Primordial gases in graphite–diamond–kamacite inclusions from the Haverö ureilite. *Earth. Planet. Sci. Lett.* **29**, 81–90.

ZAHRINGER J. (1968) Rare gases in stony meteorites. *Geochim. Cosmochim. Acta* **32**, 209–237.

DATA APPENDIX: STEPWISE THERMAL RELEASE DATA (TABLES A1 AND A2)

As in Table 1, errors in the absolute amounts of gases reported in Tables A1 and A2 do not include the systematic error due to uncertainty in the sensitivity ($\geq 10\%$). Only statistically independent errors are included in the errors in ratios for neon; the air blank uncertainty is given by f^{22}, the fraction of the ^{22}Ne represented by the blank error. Separation of trapped and cosmogenic components of neon for stepwise thermal release data was accomplished by assuming $(^{20}Ne/^{21}Ne)_c = 0.90$ and that $(^{20}Ne/^{22}Ne)_t = 8.6$ and $(^{21}Ne/^{22}Ne)_t = 0.026$ for all except matrix samples. For matrix samples, $(^{20}Ne/^{22}Ne)_t = 8.6$ was used for 500–900°C release fractions, and $(^{20}Ne/^{22}Ne)_t = 10.4$ for fractions ≥ 1000°C. In Table 2, the separation was done using 8.6 throughout, but comparison of integrated $^{21}Ne_c$, $^{20}Ne_t$, and $(^{21}Ne/^{22}Ne)_c$ values in Tables 2 and A1 shows no substantial differences. However, the use of two trapped neon compositions results in a smoother distribution of $(^{21}Ne/^{22}Ne)_c$ as a function of temperature for the stepwise release fractions.

Table A1. Neon in stepwise thermal release fractions from Allende samples. (Neon contents in 10^{-8} cm^3 STP/g)

	^{22}Ne	$^{20}Ne/^{22}Ne$	$^{21}Ne/^{22}Ne$	f^{22}	$^{21}Ne_c$	$\frac{^{21}Ne_c}{^{22}Ne_c}$	$^{20}Ne_t$
B29 Matrix (0.2311 g)							
500° C	0.094 ± 0.004	2.222 ± 0.027	0.695 ± 0.008	0.0021	0.065	0.848	0.150
600°	0.115 ± 0.005	1.008 ± 0.011	0.901 ± 0.008	0.0017	0.104	0.922	0.023
700°	0.195 ± 0.008	3.257 ± 0.023	0.648 ± 0.005	0.0010	0.125	0.930	0.523
800°	0.318 ± 0.013	3.938 ± 0.024	0.573 ± 0.004	0.0006	0.179	0.936	1.091
900°	0.346 ± 0.014	3.944 ± 0.028	0.580 ± 0.004	0.0006	0.197	0.948	1.187
1000°	0.210 ± 0.008	1.716 ± 0.015	0.852 ± 0.007	0.0010	0.178	0.935	0.201
1100°	0.314 ± 0.013	2.103 ± 0.016	0.819 ± 0.006	0.0006	0.256	0.939	0.416
1200°	0.316 ± 0.013	2.053 ± 0.014	0.822 ± 0.006	0.0006	0.259	0.937	0.403
1300°	0.266 ± 0.011	1.680 ± 0.013	0.861 ± 0.006	0.0008	0.228	0.941	0.243
1400°	0.122 ± 0.005	1.325 ± 0.011	0.906 ± 0.008	0.0016	0.110	0.951	0.062
1500°	0.178 ± 0.007	1.046 ± 0.009	0.968 ± 0.008	0.0011	0.172	0.984	0.031
1500° (r)	0.009 ± 0.001	1.09 ± 0.10	1.32 ± 0.12	0.023	0.009	1.31	0.0
Total	2.48 ± 0.04	2.438 ± 0.029	0.764 ± 0.008	0.003	1.88	0.940	4.33
C5 Matrix (0.1339 g)							
500° C	0.123 ± 0.010	2.974 ± 0.045	0.647 ± 0.010	0.0056	0.079	0.887	0.295
700°	0.277 ± 0.023	2.568 ± 0.032	0.728 ± 0.009	0.0025	0.200	0.930	0.532
850°	0.477 ± 0.038	4.322 ± 0.038	0.533 ± 0.006	0.0014	0.249	0.944	1.837
1000°	0.346 ± 0.028	2.216 ± 0.022	0.785 ± 0.008	0.0020	0.270	0.938	0.522
1150°	0.513 ± 0.042	2.035 ± 0.022	0.825 ± 0.009	0.0013	0.421	0.938	0.663
1300°	0.411 ± 0.034	1.752 ± 0.017	0.856 ± 0.009	0.0017	0.351	0.943	0.406
1500°	0.260 ± 0.021	0.997 ± 0.011	0.952 ± 0.011	0.0027	0.247	0.965	0.038
Total	2.41 ± 0.09	2.463 ± 0.059	0.760 ± 0.017	0.0008	1.82	0.940	4.29
C5 Aggregate (0.0837 g)							
500° C	0.333 ± 0.014	0.769 ± 0.008	0.658 ± 0.006	0.0033	0.219	0.671	0.058
700°	0.324 ± 0.014	1.543 ± 0.016	0.716 ± 0.006	0.0034	0.231	0.797	0.293
850°	0.424 ± 0.017	3.396 ± 0.028	0.578 ± 0.006	0.0026	0.241	0.856	1.221
1000°	0.441 ± 0.018	2.812 ± 0.022	0.649 ± 0.005	0.0025	0.283	0.868	0.986
1150°	0.500 ± 0.021	1.837 ± 0.018	0.760 ± 0.006	0.0022	0.378	0.874	0.578
1300°	0.305 ± 0.013	1.835 ± 0.020	0.816 ± 0.008	0.0036	0.248	0.932	0.336
1500°	0.072 ± 0.005	1.17 ± 0.03	0.948 ± 0.030	0.015	0.068	0.983	0.023
Total	2.40 ± 0.05	2.086 ± 0.027	0.700 ± 0.009	0.0012	1.67	0.841	3.50
B6HS Matrix (0.1664 g)							
500° C	0.114 ± 0.003	1.865 ± 0.007	0.703 ± 0.003	0.0029	0.080	0.817	0.141
600°	0.190 ± 0.005	1.298 ± 0.014	0.863 ± 0.005	0.0017	0.164	0.917	0.099
700°	0.199 ± 0.005	4.183 ± 0.019	0.547 ± 0.003	0.0017	0.107	0.941	0.737
800°	0.479 ± 0.012	4.983 ± 0.010	0.457 ± 0.002	0.0007	0.212	0.949	2.196
900°	0.288 ± 0.007	2.613 ± 0.007	0.738 ± 0.003	0.0012	0.211	0.947	0.562
1000°	0.275 ± 0.006	1.695 ± 0.004	0.859 ± 0.002	0.0013	0.236	0.940	0.254
1100°	0.431 ± 0.011	2.264 ± 0.006	0.807 ± 0.003	0.0010	0.346	0.943	0.666
1200°	0.362 ± 0.009	2.188 ± 0.008	0.809 ± 0.004	0.0011	0.291	0.937	0.530
1300°	0.231 ± 0.005	1.627 ± 0.006	0.864 ± 0.004	0.0019	0.199	0.939	0.198
1400°	0.138 ± 0.004	1.291 ± 0.004	0.918 ± 0.004	0.0040	0.127	0.960	0.065
1500°	0.107 ± 0.003	1.161 ± 0.008	0.949 ± 0.007	0.0064	0.101	0.977	0.033
Total	2.814 ± 0.025	2.609 ± 0.020	0.743 ± 0.005	0.0005	2.07	0.938	5.48
B6HS Aggregate - grey rim (0.1204 g)							
500° C	0.232 ± 0.005	0.744 ± 0.007	0.707 ± 0.004	0.0020	0.164	0.716	0.026
600°	0.110 ± 0.003	1.045 ± 0.030	0.721 ± 0.008	0.0041	0.079	0.755	0.044
700°	0.106 ± 0.003	1.072 ± 0.031	0.747 ± 0.005	0.0042	0.079	0.782	0.042
800°	0.114 ± 0.003	1.261 ± 0.055	0.744 ± 0.011	0.0039	0.085	0.797	0.068
900°	0.130 ± 0.004	1.267 ± 0.028	0.758 ± 0.007	0.0035	0.098	0.812	0.077
1000°	0.148 ± 0.004	0.830 ± 0.005	0.808 ± 0.004	0.0033	0.120	0.817	0.014
1100°	0.327 ± 0.008	0.808 ± 0.004	0.824 ± 0.003	0.0017	0.269	0.830	0.021
1200°	0.395 ± 0.010	0.776 ± 0.003	0.841 ± 0.003	0.0015	0.332	0.843	0.008
1300°	0.410 ± 0.010	0.754 ± 0.003	0.836 ± 0.003	0.0015	0.343	0.836	0.0
1400°	0.201 ± 0.005	0.758 ± 0.007	0.828 ± 0.006	0.0038	0.167	0.829	0.0
1500°	0.127 ± 0.004	0.802 ± 0.009	0.800 ± 0.005	0.0074	0.102	0.807	0.010
1570°	0.126 ± 0.004	0.916 ± 0.020	0.808 ± 0.005	0.0089	0.102	0.826	0.024
Total	2.426 ± 0.020	0.858 ± 0.008	0.800 ± 0.006	0.0009	1.94	0.812	0.33

Table A1 (*cont.*)

	^{22}Ne	$^{20}Ne/^{22}Ne$	$^{21}Ne/^{22}Ne$	f^{22}	$^{21}Ne_c$	$\frac{^{21}Ne_c}{^{22}Ne_c}$	$^{20}Ne_t$
B6HS Aggregate - pink core (0.0328 g)							
550° C	0.257 ± 0.007	0.635 ± 0.010	0.621 ± 0.006	0.0064	0.160	0.626	0.018
700°	0.053 ± 0.003	2.07 ± 0.10	0.686 ± 0.014	0.027	0.036	0.821	0.077
850°	0.098 ± 0.004	1.64 ± 0.06	0.717 ± 0.012	0.016	0.070	0.808	0.098
1000°	0.118 ± 0.004	0.955 ± 0.034	0.779 ± 0.011	0.014	0.092	0.802	0.030
1150°	0.304 ± 0.008	0.654 ± 0.005	0.817 ± 0.007	0.0068	0.246	0.810	0.0
1300°	0.366 ± 0.010	0.627 ± 0.005	0.792 ± 0.008	0.0060	0.287	0.784	0.0
1500°	0.469 ± 0.013	0.757 ± 0.004	0.771 ± 0.005	0.0073	0.362	0.777	0.03
1570°	0.266 ± 0.008	0.647 ± 0.005	0.767 ± 0.007	0.015	0.203	0.763	0.0
Total	1.931 ± 0.022	0.777 ± 0.011	0.757 ± 0.008	0.0036	1.46	0.766	0.25
B32 Aggregate (0.058 g)							
500° C	0.899 ± 0.024	0.521 ± 0.002	0.599 ± 0.002	0.0018	0.538	0.598	0.0
600°	0.229 ± 0.006	0.919 ± 0.062	0.637 ± 0.007	0.0068	0.146	0.663	0.081
700°	0.122 ± 0.005	2.42 ± 0.14	0.599 ± 0.011	0.013	0.072	0.760	0.230
800°	0.141 ± 0.005	1.89 ± 0.01	0.682 ± 0.005	0.011	0.096	0.797	0.181
900°	0.178 ± 0.005	1.96 ± 0.02	0.679 ± 0.005	0.0088	0.120	0.801	0.240
1000°	0.216 ± 0.006	1.28 ± 0.03	0.754 ± 0.005	0.0073	0.162	0.809	0.130
1100°	0.410 ± 0.012	0.979 ± 0.009	0.782 ± 0.004	0.0039	0.321	0.807	0.109
1200°	0.213 ± 0.006	1.146 ± 0.009	0.776 ± 0.007	0.0074	0.165	0.817	0.095
1300°	0.131 ± 0.004	0.879 ± 0.011	0.776 ± 0.006	0.013	0.102	0.792	0.024
1400°	0.042 ± 0.003	0.587 ± 0.029	0.826 ± 0.011	0.041	0.034	0.812	0.0
1500°	0.034 ± 0.003	0.528 ± 0.033	0.791 ± 0.014	0.054	0.026	0.775	0.0
Total	2.615 ± 0.032	1.021 ± 0.015	0.683 ± 0.006	0.0021	1.78	0.719	1.09
A5 Chondrule - pyroxene (0.0779 g)							
500° C	0.039 ± 0.005	1.98 ± 0.11	0.73 ± 0.04	0.046	0.028	0.86	0.052
700°	0.109 ± 0.010	1.34 ± 0.03	0.849 ± 0.020	0.016	0.092	0.908	0.063
850°	0.554 ± 0.044	0.898 ± 0.010	0.916 ± 0.007	0.0032	0.507	0.924	0.042
1000°	1.048 ± 0.084	0.846 ± 0.006	0.924 ± 0.007	0.0017	0.969	0.926	0.015
1150°	0.354 ± 0.029	0.823 ± 0.012	0.930 ± 0.012	0.0051	0.329	0.930	0.0
1300°	0.348 ± 0.029	0.832 ± 0.012	0.919 ± 0.012	0.0051	0.320	0.919	0.0
1500°	0.105 ± 0.009	1.04 ± 0.03	0.925 ± 0.021	0.017	0.097	0.947	0.02
Total	2.56 ± 0.11	0.898 ± 0.021	0.916 ± 0.022	0.0018	2.34	0.923	0.19

Table A2. Argon in stepwise thermal release fractions from Allende samples. (Argon contents in 10^{-8} cm^3 STP/g)

	^{36}Ar	^{40}Ar	$^{36}Ar/^{38}Ar$	$^{40}Ar/^{36}Ar$
B6HS Matrix				
500° C	0.67 ± 0.05	371 ± 22	5.82 ± 0.04	550 ± 50
600°	0.21 ± 0.01	577 ± 34	4.20 ± 0.21	2800 ± 250
700°	0.17 ± 0.01	188 ± 11	4.82 ± 0.18	1130 ± 100
800°	0.64 ± 0.05	121 ± 7	4.98 ± 0.27	189 ± 18
900°	0.93 ± 0.07	142 ± 8	4.87 ± 0.12	153 ± 14
1000°	1.86 ± 0.14	190 ± 11	5.05 ± 0.05	102 ± 10
1100°	6.11 ± 0.45	211 ± 12	5.00 ± 0.03	35 ± 3
1200°	6.06 ± 0.44	121 ± 7	5.05 ± 0.02	20 ± 2
1300°	2.46 ± 0.18	92 ± 5	5.07 ± 0.02	37 ± 4
1400°	0.23 ± 0.02	29 ± 2	4.86 ± 0.07	124 ± 11
1500°	0.08 ± 0.01	19 ± 1	4.43 ± 0.22	253 ± 23
Total	19.40 ± 0.68	2061 ± 47	5.03 ± 0.25	106 ± 4

Table A2 (*cont.*)

	^{36}Ar	^{40}Ar	$^{36}Ar/^{38}Ar$	$^{40}Ar/^{36}Ar$
B6HS Aggregate - grey rim				
500° C	0.184 ± 0.012	284 ± 17	3.95 ± 0.08	1540 ± 140
600°	0.314 ± 0.021	471 ± 28	9.7 ± 0.8	1500 ± 130
700°	0.357 ± 0.024	330 ± 19	13.7 ± 0.5	920 ± 80
800°	0.161 ± 0.011	149 ± 9	6.52 ± 0.21	930 ± 80
900°	0.185 ± 0.012	131 ± 8	6.31 ± 0.17	710 ± 60
1000°	0.243 ± 0.016	141 ± 8	5.17 ± 0.09	580 ± 50
1100°	0.334 ± 0.025	88 ± 5	1.98 ± 0.03	260 ± 25
1200°	0.587 ± 0.043	95 ± 6	1.94 ± 0.01	160 ± 15
1300°	0.309 ± 0.021	135 ± 8	1.91 ± 0.01	440 ± 40
1400°	0.165 ± 0.011	86 ± 5	1.86 ± 0.02	520 ± 50
1500°	0.046 ± 0.004	17 ± 1	1.54 ± 0.11	370 ± 40
Total	2.86 ± 0.07	1930 ± 40	3.01 ± 0.12	668 ± 22
B6HS Aggregate - pink core				
550° C	0.555 ± 0.037	928 ± 55	25.1 ± 2.8	1670 ± 150
700°	0.971 ± 0.065	874 ± 52	47.7 ± 7.1	900 ± 80
850°	0.279 ± 0.019	200 ± 12	20.7 ± 4.5	720 ± 70
1000°	0.204 ± 0.014	72 ± 4	11.0 ± 1.8	350 ± 30
1150°	0.161 ± 0.012	47 ± 3	1.67 ± 0.07	290 ± 30
1300°	0.113 ± 0.009	31 ± 2	1.45 ± 0.08	270 ± 30
1500°	0.338 ± 0.025	123 ± 7	3.38 ± 0.16	360 ± 30
1570°	0.132 ± 0.030	41 ± 2	2.5 ± 0.7	310 ± 70
Total	2.75 ± 0.08	2320 ± 80	6.85 ± 0.37	840 ± 40
B32R Aggregate				
500° C	0.022 ± 0.002	2340 ± 140	2.8 ± 0.5	106000 ±11000
600°	3.25 ± 0.24	9370 ± 550	12.1 ± 0.9	2880 ± 270
700°	2.42 ± 0.18	2990 ± 180	26.8 ± 3.8	1240 ± 120
800°	1.05 ± 0.08	900 ± 50	23.7 ± 2.5	860 ± 80
900°	0.70 ± 0.05	630 ± 40	19.8 ± 0.9	900 ± 80
1000°	0.51 ± 0.03	440 ± 30	5.69 ± 0.11	870 ± 70
1100°	0.68 ± 0.05	270 ± 20	2.05 ± 0.01	400 ± 40
1200°	0.87 ± 0.06	120 ± 10	3.10 ± 0.02	140 ± 10
1300°	0.22 ± 0.02	20 ± 1	3.76 ± 0.11	100 ± 10
1400°	0.083 ± 0.006	10 ± 5	2.77 ± 0.18	110 ± 60
1500°	0.031 ± 0.006	10 ± 5	2.1 ± 0.5	290 ± 150
Total	9.84 ± 0.32	17100 ± 600	7.87 ± 0.36	1740 ± 80

PAPER 4. ISOTOPIC COMPOSITION OF THE ANOMALOUS XENON IN THE MURCHISON METEORITE

STEPHEN P. SMITH

GEOPHYSICAL RESEARCH LETTERS,
VOL. 6, NO. 1, pp. 55-58, 1979,

VOL. 6, NO. 1 GEOPHYSICAL RESEARCH LETTERS JANUARY 1979

ISOTOPIC COMPOSITION OF THE ANOMALOUS XENON IN THE MURCHISON METEORITE

Stephen P. Smith

The Lunatic Asylum, Div. of Geological and Planetary Sciences, California Institute of Technology, Pasadena, California 91125

Abstract. The calculated isotopic composition of the anomalous new xenon component enriched in ^{128}Xe, ^{130}Xe, and ^{132}Xe discovered by *Srinivasan and Anders* [1978] in Murchison depends strongly on the technique used to partition the measured spectra among the different components present in the sample. With little *a priori* justification, Srinivasan and Anders initially assume ^{134}Xe and ^{136}Xe are absent from the new component to derive a composition that matches calculated spectra of xenon produced by s-process nucleosynthesis. The reported data when plotted on xenon three isotope diagrams fall on mixing lines that may be extrapolated to define an allowed range of end point compositions for the new component. This approach to the data yields a well-defined family of unusual xenon spectra, none of which is the same as the composition obtained by Srinivasan and Anders, and none of which is directly compatible with a component of pure s-process nucleosynthesis.

Srinivasan and Anders [1978] have reported the discovery in a gas-rich separate (1C10) from the Murchison carbonaceous chondrite meteorite of an isotopic composition of xenon enriched in ^{128}Xe, ^{130}Xe, and ^{132}Xe, and unlike any component previously described. This important discovery is given especial significance by the close association of the unusual xenon with a very high concentration of neon-E, the remarkable ^{22}Ne-rich component attributed by *Black* [1972] to unvaporised interstellar grains. A clear link between neon-E and a particular xenon composition should provide a valuable constraint on the origin of these and other associated unusual noble gases.

The stepwise heating data presented by *Srinivasan and Anders* [1978; Fig. 1] clearly show that the 1C10 sample contains a minimum of three xenon components, first an ordinary trapped component similar to AVCC (average carbonaceous chondrite), second a fission-like component CCFX, and third a new component enriched in ^{128}Xe, ^{130}Xe, and ^{132}Xe. Srinivasan and Anders argued from qualitative trends in their xenon data that the most probable origin of the unusual new xenon component is s-process nucleosynthesis, and therefore that ^{134}Xe and ^{136}Xe cannot be present in the new component. This assumption allows the two heavy isotopes ^{134}Xe and ^{136}Xe to be used to obtain the relative contributions of the other two components, trapped and CCFX, which are then subtracted from the total measured composition to obtain a xenon spectrum for the new component. The resulting composition derived by Srinivasan and Anders for the new component is a good fit to theoretical s-process xenon spectra, but this result is strongly dependent on the initial assumption that the new component contains no ^{134}Xe or ^{136}Xe. This restrictive assumption ruled out with little *a priori* justification any candidate anomalous composition that might contain ^{134}Xe and ^{136}Xe and be otherwise consistent with the measured data. The purpose of this letter is to describe a more conservative treatment of the data that leads to a well-defined range of possible compositions for the new xenon component, all of which do contain ^{134}Xe and all but one end-member of which do contain ^{136}Xe. The procedure detailed below is based on first using the systematics of three-isotope diagrams to restrict the range of anomalous xenon compositions compatible with the measured data. Linear correlations indicating mixing of distinct end-members are sought. In this approach, the possible end-members must lie on the extension of the correlation line segments. Possible compositions of components that fit the allowed range can then be suggested. The pure s-process xenon composition obtained by Srinivasan and Anders is not a possible end-member of the correlation lines found. Therefore, none of the restricted range of compositions for the new component defined here from the correlations is directly compatible with an origin solely by s-process nucleosynthesis. The uncertainties arising from these differences suggest that some of the detailed discussion of the astrophysical source of this component presented by Srinivasan and Anders is perhaps premature.

Paper number 8L1037.
0094-8276/79/018L-1037$01.00

Measured xenon data obtained by *Srinivasan and Anders* [1978] during stepwise heating of the gas-rich residue 1C10 from Murchison are plotted in Figs. 1a-d, diagrams of δ^{M}_{130} versus δ^{136}_{130}, where

$$\delta^{M}_{130} = \left\{ \frac{(^{M}Xe/^{130}Xe)_{sample}}{(^{M}Xe/^{130}Xe)_{air}} - 1 \right\} \times 1000.$$

The data have been normalized to ^{130}Xe to yield the maximum range of deviations, and because ^{130}Xe is shielded from fission or r-process nucleosynthesis. Errors shown are 1σ, compounded quadratically from the data presented by Srinivasan and Anders which is normalized to ^{132}Xe. The δ plots in Fig. 1 are a modified form of the usual three isotope plot, $^{i}Xe/^{j}Xe$ versus $^{k}Xe/^{j}Xe$, and share with it the important characteristic that mixtures of any two distinct compositions will plot on a straight line joining the two end points. More important to the present discussion, the observation of a collinear set of consecutive data points is usually taken as strong evidence that the xenon involved is a binary mixture of two well-defined components whose compositions lie on the opposite extensions of the line segment defined by the data. The hatched bands extending from the composition of AVCC xenon [*Eugster et al.*, 1967] toward high δ^{136}_{130} represent correlation lines defined by data from the Allende and Orgueil meteorites [*Frick and Moniot*, 1977] due to the admixing of CCFX xenon. CCFX xenon is the highly anomalous component simultaneously enriched in the light (^{124}Xe, ^{126}Xe) and heavy (^{134}Xe, ^{136}Xe) isotopes first noted by *Manuel et al.* [1972], and recently found to be enriched in mineral separates from carbonaceous chondrites by *Lewis et al.* [1975]. Note that for $^{M}Xe/^{130}Xe = 0$, $\delta^{M}_{130} = -1000$, so in Figs. 1a-d a component consisting of pure ^{130}Xe will plot at the lower left corner of each diagram.

The xenon in the 800°C fraction from 1C10 is dominated by ordinary trapped xenon similar to AVCC xenon. The 1000°C fraction plots on the mixing line between trapped and CCFX xenon, with a substantial admixture of the CCFX component. The subsequent high-temperature fractions plot well away from any possible mixtures of ordinary trapped with CCFX xenon. The 1100°C-1600°C fractions trend progressively toward the lower left in Fig. 1, reflecting the qualitative enrichment of ^{130}Xe in the new component as pointed out by Srinivasan and Anders. Similar correlations for the light xenon isotopes (not plotted) show this ^{130}Xe is unaccompanied by significant amounts of ^{124}Xe or ^{126}Xe, ruling out typical galactic cosmic ray spallation xenon [*Marti et al.*, 1966; *Hunecke et al.*, 1972] as a source for the variation. For convenience the anomalous xenon is provisionally referred to as xenon-EX (see ex').

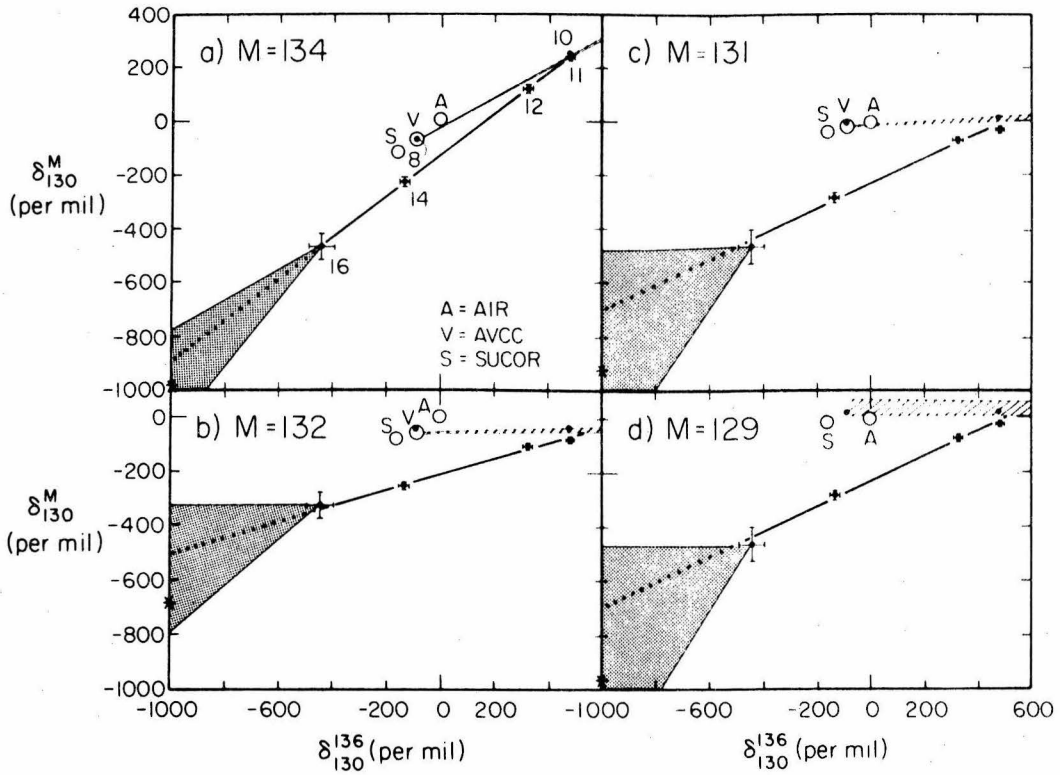

Fig. 1a-d. Isotopic compositions of xenon (solid dots) extracted by stepwise heating from Murchison 1C10 gas-rich residue [*Srinivasan and Anders*, 1978] are plotted as δ^{M}_{130} versus δ^{136}_{130} deviations in parts per thousand from the atmospheric composition. In Fig. 1a (upper left) M = 134; in 1b (lower left) M = 132; in 1c (upper right) M = 131; and in 1d (lower right) M = 130. In Fig. 1a, numbers next to data points are extraction temperatures in hundreds of degrees Celsius. In 1a-d, errors are 1σ, compounded quadratically from data normalized to ^{132}Xe by Srinivasan and Anders. Compositions of ordinary trapped xenon shown as open circles are atmospheric, AVCC (average carbonaceous chondrite) and SUCOR (surface-correlated from lunar samples [*Podosek et al.*, 1971]). The hatched bands extending to the right of AVCC reflect the admixture of CCFX xenon to ordinary trapped xenon. The 1100°C through 1600°C xenon fractions from 1C10 trend systematically toward the lower left, away from the trapped-CCFX mixing line. The collinearity of the high-temperature release fractions is interpreted as evidence of mixing two well-defined end point compositions. The upper end point appears as a uniform mixture of ordinary trapped xenon with CCFX xenon. The lower anomalous xenon-EX end point must lie on the dotted extensions of the mixing lines, with δ^{136}_{130} between −1000‰ and −450‰ ($0 \leqslant {}^{136}\mathrm{Xe}/{}^{130}\mathrm{Xe} \leqslant 1.2$).

signifying its EXtraordinary composition, as well as its possible link to neon-E. The total range of possible compositions of xenon-EX is indicated by the shaded regions to the left of the 1600°C points in Fig. 1. These areas are constructed assuming the 1600°C fraction could be a mixture of xenon-EX with any other known xenon component likely to contribute to the high-temperature data, including ordinary trapped xenon (SUCOR, AVCC, atmospheric), CCFX xenon, and actinide spontaneous-fission xenon. Low ^{124}Xe and ^{126}Xe contents rule out appreciable contributions of spallation to the heavier isotopes at high temperatures. Possible neutron-capture contributions to ^{131}Xe or ^{129}Xe and excess radiogenic ^{129}Xe have been ignored, but would only shift the lower boundary of the shaded areas in Figs. 1c and 1d to vertical lines leading from the 1600°C point to the abscissa. The shaded regions thus represent the most generous estimate for the range of possible compositions of xenon-EX. Three-isotope mixing systematics provide criteria to further restrict this range. It can be seen in Fig. 1 that the final four of the six xenon fractions from 1C10 lie on straight lines well within 2σ errors. These lines are here interpreted in the usual way as representing mixing lines between two distinct end point compositions. The upper end point is consistent with a uniform mixture of ordinary trapped and CCFX xenon with a δ^{136}_{130} of about 550‰. The second end point corresponding to xenon-EX must lie on the dotted extensions of the mixing lines to the lower left of the 1600°C points. Xenon-EX compositions consistent with the mixing lines in Fig. 1 are represented in Fig. 2 by a family of xenon spectra, normalized to $^{130}\mathrm{Xe} \equiv 1$. Unlike the spectrum obtained by Srinivasan and Anders, shown as a dashed line in Fig. 2, the compositions for xenon-EX obtained here are characterized by $^{129}\mathrm{Xe}/^{130}\mathrm{Xe}$ and $^{131}\mathrm{Xe}/^{130}\mathrm{Xe}$ ratios significantly greater than one, and by a range of possible non-zero ^{134}Xe and ^{136}Xe contents.

The differences arise from the initial assumption made by Srinivasan and Anders that the anomalous xenon was a product purely of s-process nucleosynthesis and hence that $^{134}\mathrm{Xe}/^{130}\mathrm{Xe}$ and $^{136}\mathrm{Xe}/^{130}\mathrm{Xe}$ equalled zero in the new component. This corresponds in Fig. 1a to assuming xenon-EX plots at $\delta^{134}_{130} = \delta^{136}_{130} = -1000$, a single composition which falls off the

excellent correlation line defined by the high-temperature data. In Figs. 1b, 1c and 1d, this assumption restricts xenon-EX to lie on the ordinate. The resulting composition obtained by Srinivasan and Anders is indicated by the asterisks, and is clearly not a possible end-member of the high-temperature correlation. In this way all suitable candidate compositions for xenon-EX that lie in the shaded areas in the interiors of Figs. 1a-d were arbitrarily excluded from further consideration. There would seem to be little *a priori* justification for selecting the (−1000, 1000) point in Fig. 1a as an initial restriction on the xenon-EX composition over points on the mixing line described above, or indeed any arbitrary point within the shaded region. Since in Fig. 1a the initial assumed composition lies off the correlation line through the high-temperature data, the relative proportions of ordinary trapped and CCFX xenon inferred by Srinivasan and Anders are different in each temperature fraction. The proportion of xenon-EX in each temperature fraction varies as well, and as a consequence it must be assumed under the interpretation given by Srinivasan and Anders that the collinearity of the four data points is coincidental. This contrasts with the interpretation followed here where the alignment is taken to be significant. The present treatment requires no *a priori* assumption concerning the origin of the anomalous xenon.

Since the data in Fig. 1a do not extend to the left of mixing lines joining ordinary trapped xenon to the point (−1000, 1000), the xenon-EX end point inferred here to lie on the dotted line could formally consist of a homogeneous mixture of ordinary trapped xenon, such as AVCC or SUCOR, with an s-process component plotting at (−1000, 1000) having $^{134}Xe/^{130}Xe$ and $^{136}Xe/^{130}Xe$ equal zero, as assumed by Srinivasan and Anders. In the case of admixed AVCC, for example, the xenon-EX end point is restricted to lie at $\delta^{136}_{130} \cong 600‰$ at the intersection of the line connecting (−1000, −1000) to AVCC and the dotted xenon-EX mixing line in Fig. 1a. Under such an hypothesis, about 60% of the ^{130}Xe in xenon-EX arises from the s-process component. The corresponding calculated composition of s-process xenon with $^{134}Xe/^{130}Xe$ and $^{136}Xe/^{130}Xe$ defined to be zero is 128/129/130/131/132 ≅ 0.42/0.72/≡ 1/0.55/2.40, which is analogous to the compositions derived by Srinivasan and Anders, and compatible with the suggested pure s-process addition. If the xenon-EX end point does consist of ordinary trapped xenon mixed with an s-process component, then the existence of the high-temperature correlation implies the two were inseparable in the reported stepwise heating experiment. Either they were admixed prior to incorporation in the mineral phase now carrying them, or the thermal release did not discriminate between the differently sited xenon components, or possibly the mixing is an experimental artifact. Note that finding points lying on the xenon-EX mixing line with $\delta^{136}_{130} < 650‰$, would rule out homogenization with ordinary trapped xenon and rule out an s-process xenon component containing no ^{134}Xe and ^{136}Xe.

It is important not to lose sight of the fact that the xenon component in 1C10 found by Srinivasan and Anders is highly unusual, regardless of the exact spectrum-stripping technique used to define its composition. The range of end point compositions derived using the mixing lines in Fig. 1 is not consistent with a component similar to a pure s-process nucleosynthesis product as described by Srinivasan and Anders. However, as pointed out by these authors, the important s-process isotopes ^{128}Xe, ^{130}Xe, and ^{132}Xe are enriched relative to the other isotopes of mass ≥129. The composition obtained by Srinivasan and Anders agrees with theoretical s-process xenon spectra. There is no *a priori* reason to expect that the initial subtraction of all ^{134}Xe and ^{136}Xe from the measured compositions should cause the remaining isotopes to resemble an s-process spectrum. That they do lends weight to the assumption that xenon-EX contains s-process xenon, but the agreement cannot be used to argue or imply that the new component contains only s-process xenon. The unmixing

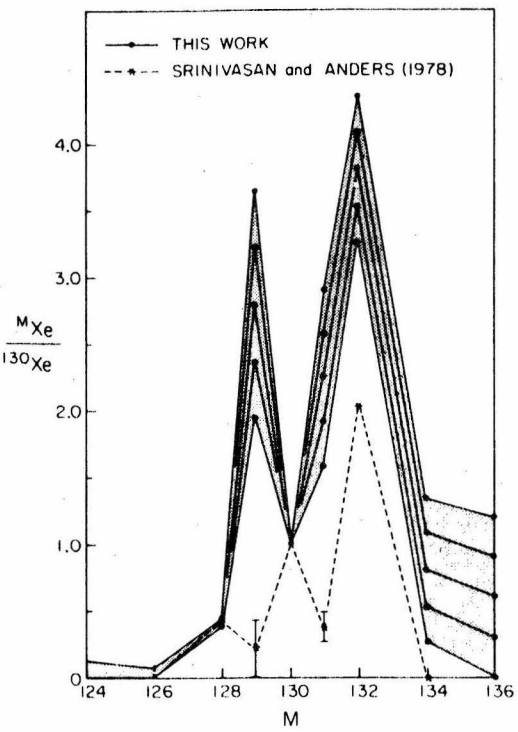

Fig. 2. The shaded region represents the complete family of candidate xenon spectra for xenon-EX derived from the range of end point compositions given by the dotted lines in Fig. 1. The solid lines give specific examples of spectra for $^{136}Xe/^{130}Xe$ = 0,0.3,0.6,0.9, and 1.2. The substantially different spectrum obtained by *Srinivasan and Anders* [1978] is indicated by the dashed line, and is not an end-member of the range of spectra obtained here. The dissimilarities arise primarily from the assumption by Srinivasan and Anders that $^{134}Xe = {}^{136}Xe \equiv 0$ in the anomalous xenon-EX component. Theoretical spectra of a pure s-process nucleosynthetic component of xenon are essentially the same as the dashed-line spectrum [*Srinivasan and Anders*, 1978].

procedure adopted by Srinivasan and Anders to separate the high-temperature xenon components in effect corresponds to subtracting all CCFX xenon and all solar system-like r-process xenon (i.e. all ^{134}Xe and ^{136}Xe) as well as s-process xenon in ordinary solar system trapped xenon proportions. However, an indeterminate fraction of the subtracted r-process contribution could in fact belong to the new xenon-EX component. Thus the source of the anomalous component appears to be characterized by a ratio of s-process to r-process nuclei which is higher than in ordinary solar system matter, but r-process nuclei need not be absent. Note that neither the s-process nor any r-process xenon contributions contained in xenon-EX need *a priori* match the isotopic compositions of ordinary solar system s-process and r-process xenon. The fact that subtraction of significant amounts of both standard s-process and r-process xenon from the high-temperature data results in a normal s-process pattern leads one to conclude that, at present levels of precision, the s-process and any r-process xenon associated with xenon-EX are isotopically similar to solar system values, occurring only in different relative proportions. Whether or not the p-process isotopes ^{124}Xe and ^{126}Xe are associated with the anomalous heavier isotopes cannot be determined. The

high-temperature trend is not well-defined for these two isotopes because of the presence of a small contribution from galactic cosmic ray spallation xenon. The abundances indicated in Fig. 2 are approximate upper limits for ^{124}Xe and ^{126}Xe.

In conclusion, it has been demonstrated that the xenon isotopic compositions derived for the new anomalous component discovered by *Srinivasan and Anders* [1978] in Murchison are dependent on the computational technique used to separate the contributions of the various components present in the sample. The s-process xenon isotopes are enriched in the new component compared to ordinary solar system abundances. The conclusion that the observed isotopic variations are due to the addition of a component derived solely from s-process nucleosynthesis cannot be rigorously defended, although such a component remains one of a broad family of components that can be used to explain the data obtained by Srinivasan and Anders.

Acknowledgments. I thank J. C. Huneke, G. J. Wasserburg, U. Frick, R. O. Pepin and an anonymous reviewer for helpful suggestions. This work supported by NSF grant PHY 76-02724. This is Contribution No. 3122 (279) of the Division of Geological and Planetary Sciences.

References

Black, D. C., On the origins of trapped helium, neon, and argon isotopic variations in meteorites-II. Carbonaceous meteorites, *Geochim. Cosmochim. Acta, 36,* 377-394, 1972.

Eugster, O., P. Eberhardt and J. Geiss, Krypton and xenon isotopic composition in three carbonaceous chondrites, *Earth Planet. Sci. Lett., 3,* 249-257, 1967.

Frick, U. and R. K. Moniot, Planetary noble gas components in Orgueil, *Proc. Lunar Sci. Conf. 8th,* 229-261, 1977.

Huneke, J. C., F. A. Podosek, D. S. Burnett, and G. J. Wasserburg, Rare gas studies of the galactic cosmic ray irradiation history of lunar rocks, *Geochim. Cosmochim. Acta, 36,* 269-301, 1972.

Lewis, R. S., B. Srinivasan and E. Anders, Host phase of a strange xenon component in Allende, *Science, 190,* 1251-1262, 1975.

Manuel, O. K., E. W. Hennecke and D. D. Sabu, Xenon in carbonaceous chondrites, *Nature, 240,* 99-101, 1972.

Marti, K., P. Eberhardt, and J. Geiss, Spallation, fission and neutron capture anomalies in meteoritic krypton and xenon, *Z. Naturforsch., 21a,* 398-413, 1966.

Podosek, F. A., J. C. Huneke, D. S. Burnett, and G. J. Wasserburg, Isotopic composition of xenon and krypton in the lunar soil and in the solar wind, *Earth Planet. Sci. Lett., 10,* 199-216, 1971.

Srinivasan, B. and Edward Anders, Noble gases in the Murchison meteorite: possible relics of s-process nucleosynthesis, *Science, 201,* 51-56, 1978.

(Received September 1, 1978;
accepted September 29, 1978.)

APPENDIX B. PAPERS ON THE ABUNDANCES OF ATMOSPHERIC AND JUVENILE NOBLE GASES IN TERRESTRIAL ROCKS AND MINERALS

PAPER 1. NOBLE GASES IN BERYL

NOBLE GASES IN BERYL

S. P. Smith and G. J. Wasserburg

The Lunatic Asylum of the Charles Arms Laboratory
Division of Geological and Planetary Sciences
California Institute of Technology
Pasadena, California 91125

ABSTRACT

Ne, Ar, Kr, and Xe concentrations and isotopic abundances were measured in terrestrial samples of eleven beryls and one tourmaline. Measured neon isotopic compositions range from near atmospheric to extreme values of $^{20}Ne/^{22}Ne = 1.14$ and $^{21}Ne/^{22}Ne = 1.12$. The excess ^{21}Ne and ^{22}Ne reflect contributions from (α,n) reactions in the crust (Wetherill, 1954). Excess radiogenic ^{40}Ar is present in the beryls, in accord with earlier results by Damon and Kulp (1958). Radiogenic Xe from ^{238}U spontaneous fission is found in beryl for the first time, in amounts correlated with the other excess radiogenic gases. $^{21}Ne_{nuc}$ and $^{40}Ar_{rad}$ are present in relative proportions consistent with expected production ratios in ordinary crustal rocks. $^{136}Xe_{SF}$ is depleted by a factor of about ten. Non-radiogenic gases are found in the beryls and also appear to be strongly depleted in Xe relative to abundance patterns seen in plutonic igneous rocks. We suggest the depletions are most likely due to preferential exclusion of the large xenon gas atoms from the beryl lattice channels during crystallization.

In contrast with the beryls, nucleogenic neon, radiogenic ^{40}Ar and fission xenon in tourmaline from Pala, California, appear to arise from *in situ* decay.

INTRODUCTION

Noble gases in the atmosphere and body of the earth arise from a variety of sources. Gases present since the formation of the planet are termed primordial. Primordial noble gases may include gases incorporated directly from the solar nebula into the primitive terrestrial atmosphere. They will also include gases trapped in the solid material accreted to form the earth. Gases held initially in the body of the earth may eventually be degassed into the atmosphere. Subsequent to the formation of the earth, noble gases have been added to the primordial component by the radioactive decay of various parent nuclei, and by other nuclear reactions. In this paper we will present and discuss results on the noble gas contents of minerals formed several kilometers deep within the earth's crust. Our general aim is to discover the nature of the gases in the minerals and by extension in certain regions of the crust. We will investigate whether the gases are in part primordial, or instead dominated by atmospheric gases and/or the products of radioactive decay and nuclear reactions in the crust. The particular minerals we have chosen to study are the silicates beryl and tourmaline, which are known for their ability to trap relatively large amounts of gases (e.g., Damon and Kulp, 1958). In beryl, this capacity is the result of comparatively large channels piercing the crystal lattices of this mineral. The noble gases--and other impurities including water, CO_2, and alkali metal atoms--are held in these channels.

The daughter products of radioactive decay are known as radiogenic isotopes; the most important radiogenic noble gases are ^{4}He from the decay of U and Th, ^{40}Ar from K, ^{129}Xe from ^{129}I, and $^{131-136}Xe$ from spontaneous fission of ^{238}U and ^{244}Pu. Gases produced in other

nuclear reactions will here be called nucleogenic. The several MeV α-particles and neutrons emitted during the decay of U and Th can cause nuclear transformations among the atoms surrounding the radioactive nuclei, producing nucleogenic species. A particular case of concern here is the production of nucleogenic neon isotopes, ^{20}Ne and ^{21}Ne by (α,n) reactions on ^{17}O and ^{18}O and ^{22}Ne by either α reactions on fluorine or possibly neutron reactions on magnesium (Wetherill, 1954; Sharif-Zade et al., 1972).

Noble gases which have never resided in the earth's atmosphere are known as juvenile gases. We find it convenient to distinguish between primary and secondary juvenile gases. Primary juvenile gases include primordial noble gases, plus ^{129}Xe and $^{131-136}Xe$ from the decay of the short-lived radioactivities ^{129}I ($t_{1/2}$ = 17 x 10^6 y) and ^{244}Pu ($t_{1/2}$ = 82 x 10^6 y) present in the material from which the earth formed. These gases are called primary because they have not been produced in significant quantities since early in the earth's history. The observation today of primary juvenile noble gases such as ^{3}He (Clarke et al., 1969; Krylov et al., 1974) and ^{129}Xe (Butler et al., 1963; Hennecke and Manuel, 1975) in terrestrial samples indicates that portions of the earth have remained incompletely degassed over the age of the planet. In contrast, secondary juvenile gases comprise those radiogenic and nucleogenic gases including ^{4}He, ^{40}Ar, Ne, and ^{238}U spontaneous fission xenon that have been produced over the entire history of the earth by the on-going decay of long-lived U, Th, and K parent nuclei.

Noble gases on the earth are found in a variety of reservoirs; the atmosphere, natural gas pools, dissolved in seawater or meteoric groundwater, adsorbed in sediments, trapped in rocks and minerals,

dissolved in magmas. Gases may be exchanged among the different reservoirs by various transport processes. Radiogenic and nucleogenic gases formed *in situ* in the crust and mantle may be outgassed during metamorphism or partial melting, incorporated into metamorphic fluids or magmas, and subsequently injected into natural gas reservoirs, groundwater, or into the atmosphere. Thus, for example, essentially all ^{4}He and ^{40}Ar in the atmosphere is radiogenic, derived from the decay of U, Th, and K, through continuous outgassing of the earth. Minerals crystallizing or equilibrating at depth under elevated pressures of formation or metamorphism may incorporate measurable amounts of noble gases. Radiogenic and nucleogenic gases trapped in this way are not formed by subsequent *in situ* decay in the rock or mineral, so are termed 'excess' radiogenic or nucleogenic gases. In addition to the movement of gases out of the solid earth, atmospheric gases dissolved in groundwater can be transported into the crust. There they may accumulate in natural gas pools, return to the surface in thermal springs, or possibly be incorporated directly into rocks, minerals, or magmas by diffusion or during alteration. Transport of atmospheric noble gases into the crust or mantle may possibly also take place by burial of sediments containing gases, or by subduction of altered oceanic crust.

The elemental and isotopic compositions of noble gases in terrestrial samples provide clues to the origin of the gases and the transport processes affecting them. Noble gases entering the crust dissolved in groundwater will be systematically enriched in the heavier species because of their relatively greater solubility. Partial degassing may further enrich the relative amount of heavy noble gases in the water. In contrast, heavy noble gases are relatively less soluble in silicate

magma than the light gases. Adsorption of gases by fine-grained sediments or alteration phases can lead to enrichment of heavy noble gases in the adsorbed gas, and depletion of heavy gases in the unadsorbed material. Diffusive transport of noble gases in the crust can also lead to fractionations. In such processes, changes in isotopic composition will be much smaller than the changes in elemental abundance patterns.

Because the radiogenic and nucleogenic gases are an important component in the samples studied, we review the production of these gases in more detail. The various radiogenic and nucleogenic isotopes are generated from different parent or target nuclei. Therefore, observed variations in their relative abundances can reflect variations in chemical compositions of the source regions from which the gases derive. On the other hand, for cases where relative production rates should be nearly constant--for example, for ^{4}He, ^{21}Ne, and fission xenon produced by the decay of U--drastic deviations from the expected production ratios may reflect operation of transport processes such as diffusion or differential solubility or trapping in minerals, magmas, or water. Equations summarizing production rates for the secondary juvenile gases are listed in Table 2. For the radiogenic gases we give instantaneous production rates today, and average production rates over the past one, two, and three billion years. The production rate for nucleogenic $^{21}Ne_{nuc}$ by $^{18}O(\alpha,n)$ is taken to be 2.8×10^{-8} times the production of ^{4}He, based on data in Wetherill (1954) and assuming the radioactive U and Th to be

surrounded by silicate containing 45% by weight oxygen (Craig and Lupton, 1976). The thick target yield for $^{20}Ne_{nuc}$ from ^{17}O is similar or somewhat less than that for $^{21}Ne_{nuc}$ (Wetherill, 1954; Gurfinkel, 1963). Since ^{17}O is only 1/5 as abundant as ^{18}O in natural materials, the production ratio of nucleogenic $^{20}Ne/^{21}Ne$ should be ≤ 0.2. The relative production rate of nucleogenic $^{22}Ne_{nuc}$ depends on the abundance of a different target, probably fluorine, surrounding the U and Th. We will see below that the ratio of $^{22}Ne_{nuc}$ to $^{21}Ne_{nuc}$ varies from about 0 to roughly 30 in natural materials, probably due at least in part to variation in the target abundances.

In Figure 1 we show ratios of the instantaneous production rates for $^{21}Ne_{nuc}$, $^{40}Ar_{rad}$, and $^{136}Xe_{SF}$ as a function of time for a source characterized by Th/U = 3.5 and K/U = 10^4 today. The ratio of $^{40}Ar_{rad}/^{4}He_{rad}$ is not shown but can be easily obtained by multiplying $^{40}Ar_{rad}/^{21}Ne_{nuc}$ by $^{21}Ne_{nuc}/^{4}He_{rad} = 2.8 \times 10^{-8}$. The ratios are not constant because of the different half-lives of the parent nuclei. Note that, all other things equal, a mineral crystallizing several billion years ago will most likely trap radiogenic and nucleogenic gases of a different chemical composition than the same mineral formed within the last 500 million years. We might expect that $^{136}Xe_{SF}/^{40}Ar_{rad}$ ratios in excess radiogenic gases trapped in samples should decrease with increasing age of the sample. Unfortunately there are a number of factors that can combine to blur this trend by causing additional variation in the observed ratios. These include variations in parent element abundances, differences in transport of gases from their source, variations in trapping efficiency, etc.

In 1908, R. J. Strutt (Lord Rayleigh) discovered that beryl

crystals commonly contain ^{4}He far in excess of that which could be due to *in situ* decay of uranium. Aldrich and Nier (1948) found that the excess ^{4}He was in some cases accompanied by excess radiogenic ^{40}Ar. Damon and Kulp (1958) in a thorough study of He and Ar in a large number of beryls showed that excess ^{4}He and ^{40}Ar were present in all samples in proportions consistent with the expected production ratio in ordinary crustal rock with $K/U \approx 10^{4}$ by mass. Damon and Kulp concluded that the excess noble gases represented samples of magmatic gases derived from mantle or crustal rock and incorporated during crystallization into the large lattice channels characteristic of beryl crystals. Damon and Kulp as well found ^{4}He and ^{40}Ar excesses in other ring-silicates, tourmaline, and cordierite. More recently, Verkhovskiy *et al.* (1976) and Smith (1977) have reported the presence of excess nucleogenic ^{21}Ne and ^{22}Ne in beryls.

In this paper we present results on the Ne, Ar, Kr, and Xe concentrations and isotopic abundances in beryls from diverse localities and for a sample of tourmaline. The samples exhibit a wide range of concentrations of nucleogenic neon, radiogenic argon, and substantial amounts of xenon from spontaneous fission of ^{238}U. All the excess nucleogenic and radiogenic gases are found to correlate with each other. In addition to the excess radiogenic noble gases, beryls are also found to contain measurable and, in some cases, large concentrations of non-radiogenic noble gases which are inferred to represent trapped magmatic gases.

EXPERIMENTAL PROCEDURES

The specimens studied are described briefly in Table 1. Estimated geological ages for most of the samples are given. Where not directly

available, ages are estimated from known ages of similar, nearby pegmatites, or more generally from the age of the igneous or metamorphic province in which the sample is found. For beryls, the sample numbers (1) through (11) will be used for identification in later tables, figures, and discussion.

Samples were crushed in a stainless steel mortar to roughly millimeter-sized grains and rinsed thoroughly with acetone to remove fine-grained particles, and so minimize contamination by adsorbed atmospheric gases. When necessary, material for analysis was hand-picked to eliminate macroscopic impurities such as muscovite. Samples analyzed weighed between 0.11 and 0.36 grams. Noble gases were extracted in a tungsten crucible by radio-frequency induction heating. Chemically reactive gases were removed using Ti-Zr and Zr-Al getters. The noble gases were analyzed statically in a 6-inch radius, all-metal mass spectrometer, using both Faraday cup and electron multiplier detectors. Signals from two Cary 401 vibrating reed electrometers were integrated for two or four seconds with a digital voltmeter and then transmitted to an on-line PDP-11 computer. Data were obtained by automatically stepping the magnetic field through ten to fifteen complete scans of the appropriate mass region for each gas. Isotope ratios and the concentrations of one or more reference isotopes were extrapolated to the time the gas was admitted to the spectrometer, or for argon, the time when the accellerating voltage was turned on (see below).

Most of the samples were analyzed in two separate groups, labeled (1) and (A) in T ɔle 3. After the completion of group (1) it was found that the sequence of steps used to transfer the gases from the

extraction oven into the spectrometer allowed the Kr and Xe from the samples to be contaminated with Kr and Xe scrubbed from the mass spectrometer by the large amounts of ^{40}Ar present. Therefore, only Ne and Ar data are reported for group (1) analyses. Samples in group (A) were measured later using a revised procedure to eliminate this contamination.

For group (1), argon was adsorbed and isolated on an activated charcoal cold-finger at liquid nitrogen temperature prior to analysis of neon. During neon measurement, interference at mass 20 due to $^{40}Ar^{++}$ was minimized by reducing the ionizing electron potential in the spectrometer source, and by exposing the spectrometer volume to a second charcoal trap kept at liquid nitrogen temperature. Previous studies of beryls (Damon and Kulp, 1958) showed that variable and, in some cases, very large amounts of ^{40}Ar could be expected. The following procedure was adopted to ensure measurements were made on an amount of argon less than or comparable to the amount of air argon in the standard pipette used to moniter the sensitivity and mass discrimination. The total amount of argon extracted from the sample was equilibrated with both the mass spectrometer and a portion of the sample handling manifold equivalent to one-sixteenth the spectrometer volume. During this initial equilibration the accelerating high voltage was shut off to avoid scrubbing argon from previous samples out of the walls of the spectrometer. The inlet valve to the spectrometer was then closed to isolate the 1/16th fraction in the sample manifold, and the accelerating voltage turned on to determine the size of the total argon sample. If this first signal was too large for reliable measurement (because of uncalibrated non-linearity in the voltages generated at high pressures) the spectrometer was pumped out. The 1/16th

fraction retained in the sample manifold could then be admitted for analysis. Only ^{36}Ar and ^{40}Ar data are reported in Table 3. Precise measurement of ^{38}Ar was impossible. Tailing of the ^{40}Ar peak under mass 38 was significant due to the very high $^{40}Ar/^{38}Ar$ ratios of many samples. This resulted in very unequal background levels on either side of the very small ^{38}Ar peak. The background could not be measured with adequate precision to correct the argon peak. Rapid scrubbing in the spectrometer of ^{38}Ar from previous meteorite and lunar samples made the zero-time extrapolation of ^{38}Ar very difficult. Within the large resulting uncertainties, $^{38}Ar/^{36}Ar$ ratios seen were atmospheric.

For samples in group (A), Kr and Xe were adsorbed on charcoal at dry-ice temperature, and the unadsorbed He, Ne, and Ar pumped off. About 45% of the Kr was also pumped off at this stage. From the preliminary results on group (1) and because of the low fission yield for Kr from ^{238}U spontaneous fission, no significant Kr isotopic effects were expected, so only ^{84}Kr was measured.

The tabulated data have been corrected for mass discrimination, extraction oven blanks and interfering species including $H_2{}^{18}O$, $^{40}Ar^{++}$, HF, $CO_2{}^{++}$, $(\text{mass } 42)^{++}$, and neon and xenon hydrides. Despite the precautions taken to reduce the importance of $^{40}Ar^{++}$, it was still a major interference at mass 20 because of the tremendous amounts of argon often present. Correction for $^{40}Ar^{++}$ was complicated by a dependence of the $^{40}Ar^{++}/^{40}Ar^{+}$ ratio on pressure. The large amounts of He accompanying neon in some samples caused $^{40}Ar^{++}/^{40}Ar^{+}$ to be at least a factor of ten lower than its nominal value at low pressures. The $^{40}Ar^{++}/^{40}Ar^{+}$ ratio used to correct the neon in each sample was estimated from the strength of the ^{4}He signal measured during the neon analyses.

The relatively large errors in the $^{20}Ne/^{22}Ne$ ratios reported in Table 3 reflect the estimated uncertainty ($\sim 1\sigma$) in this correction. Fortunately, in beryl samples from Keystone and Pointe du Bois which contained large amounts of nucleogenic neon, $^{20}Ne/^{22}Ne$ ratios uncorrected for $^{40}Ar^{++}$ were as low as two, providing well-defined limits on the nucleogenic neon composition, regardless of any uncertainty in the $^{40}Ar^{++}$ correction. The extraction oven blanks were of atmospheric isotopic composition, in amounts corresponding to 5×10^{-15} mole ^{20}Ne, 3×10^{-15} mole ^{36}Ar, 3×10^{-17} mole ^{84}Kr, and 5×10^{-18} mole ^{132}Xe. The spectrometer sensitivity and mass discrimination were monitored by repeated measurements of a pipette of standard volume and atmospheric isotopic composition. The pipette was calibrated using a split of the Berkeley Bruderheim meteorite standard of well-known gas contents. Estimated error in the reported gas amounts due to uncertainty in the calibration is approximately ± 20%.

To calculate the concentrations of nucleogenic ^{21}Ne and ^{22}Ne, radiogenic ^{40}Ar, and fissiogenic ^{136}Xe, the gases in the samples were treated as mixtures of two components; one, the nucleogenic and radiogenic gases, and two, a component of atmospheric isotopic composition. The isotopes ^{20}Ne, ^{36}Ar, ^{84}Kr, and ^{130}Xe are taken to be entirely atmospheric. From these isotopes, atmospheric contributions at ^{21}Ne, ^{22}Ne, ^{40}Ar, and $^{131-136}Xe$ were calculated, and subtracted from the measured concentrations to obtain the nucleogenic and radiogenic components in each sample. It is possible that in the Keystone and Pointe du Bois beryls a portion of the ^{20}Ne could actually be nucleogenic. For an (α,n) production ratio $^{20}Ne_{nuc}/^{21}Ne_{nuc} \leqslant 0.2$, the maximum nucleogenic ^{20}Ne contents are 7% and 20%

of the total ^{20}Ne in the Keystone and Pointe du Bois samples respectively. Nucleogenic ^{20}Ne contributions in the remaining samples will be unimportant.

RESULTS

The concentrations of ^{22}Ne, ^{36}Ar, ^{84}Kr, and ^{130}Xe measured in eleven beryls and a rubellite tourmaline are given in Table 3, in units of 10^{-14} mole/gram. The ^{22}Ne consists of a mixture of nucleogenic and non-nucleogenic components; the other three are essentially free of radiogenic or nucleogenic contributions. The concentrations of the noble gases vary greatly from sample to sample. Tabulated ^{22}Ne, ^{36}Ar, and ^{84}Kr concentrations vary by roughly a factor of fifty, and ^{130}Xe by a factor of about seven. In the beryls, concentrations of ^{40}Ar differing by a factor of nearly 1000 were measured, from 4.5×10^{-10} mole/g in specimens (10) and (11) to 3.7×10^{-7} in (1). Beryls (3) and (6) from Gravelotte and Lac Pied du Monte are particularly noteworthy in containing markedly larger concentrations of the non-radiogenic gases ^{36}Ar, ^{84}Kr, and ^{130}Xe than the remaining samples. The non-radiogenic noble gas contents of these samples are similar to values calculated for the whole earth by dividing the atmospheric content of each gas by the mass of the earth (bottom of Table 3). The beryl concentrations are as much as one to two orders of magnitude greater than is typical of most other plutonic igneous rocks studied (Smith, 1978, 1979 a,b; Kaneoka et al., 1978).

The variations in the measured isotopic compositions are also very large. Neon isotopic compositions and $^{40}Ar/^{36}Ar$ ratios are given in Table 3, with 1σ errors. Xenon isotopic data are listed separately in Table 4, with 2σ errors. Beryl specimens (1) and (2) from Keystone and

Pointe du Bois contain neon highly enriched in nucleogenic ^{21}Ne and ^{22}Ne. In Pointe du Bois, $^{21}Ne/^{22}Ne$ is nearly 40 times the atmospheric ratio. In these two beryls, the three neon isotopes are of approximately equal abundance, in contrast to atmospheric neon which consists of 90% ^{20}Ne with only 0.3% ^{21}Ne. Argon in these two samples is extremely radiogenic, as shown by the measured $^{40}Ar/^{36}Ar$ ratios which are more than 1000 times the atmospheric value. These two specimens also show large enrichments in $^{131-136}Xe$ (Table 4). $^{136}Xe/^{130}Xe$ is about four times the atmospheric ratio, indicating a dominant contribution from fission xenon. The remaining samples show smaller but still significant isotopic effects from the addition of nucleogenic and radiogenic gases. In Table 3, $^{21}Ne/^{22}Ne$ ratios are greater than the atmospheric value for all specimens, except (11) White Mtn. This demonstrates the widespread occurrence of nucleogenic neon isotopes in these crystals. Similarly, argon in all the beryls is dominantly radiogenic, with $^{40}Ar/^{36}Ar$ ratios at least thirty times atmospheric. Fission xenon is present in beryl specimens (3), (4), (5), and (6) and the tourmaline. Xenon in the Minas Gerais beryl seems to be atmospheric only.

The concentrations of nucleogenic and radiogenic gases in each sample calculated by the procedures given in the previous section are listed in Table 5. The concentrations are quite variable, but also are correlated in a general way. Beryl typically contains roughly 10^{-3} g/g potassium and $\leqslant 10^{-6}$ g/g uranium (Deer *et al.*, 1962; Damon and Kulp, 1958). The amounts of nucleogenic and radiogenic gases expected in the crystals from *in situ* decay of U and K can be estimated using these values, and the ages and average production rates in Tables 1 and 2.

Essentially all the ^{40}Ar in the samples is excess radiogenic argon. This observation is in agreement with previous work (Damon and Kulp, 1958). It can similarly be shown that the concentration of nucleogenic neon in all the beryls except (11) White Mtn. is at least several times in excess of the amount produced by the decay of 1 ppm U. The fission ^{136}Xe contents of the beryls are not so clearly in excess of possible in situ contributions. In situ decay of 1 ppm U would produce only about 20% of the observed amount of $^{136}Xe_{SF}$ in the Keystone beryl, but about 40% for beryls (2) Pointe due Bois and (6) Lac Pied du Monte. In the remaining beryls studied, the observed fission xenon could be entirely due to in situ decay. For purposes of discussion we will treat the observed $^{136}Xe_{SF}$ as excess radiogenic xenon, but remembering that the actual excess xenon contents could be lower.

The results on the neon isotopic compositions are presented in more detail in Figure 2, a three isotope diagram of $^{20}Ne/^{22}Ne$ vs. $^{21}Ne/^{22}Ne$. The compositions of neon in the atmosphere and in the solar wind are plotted in the upper left. On this diagram, mixtures of two components of distinct isotopic compositions will plot on a straight line joining the two endpoints. Addition of pure ^{21}Ne to a given initial composition will shift that point horizontally to the right, and addition of pure ^{22}Ne will shift a point toward the origin. Radiogenic neon with $^{20}Ne_{nuc}/^{21}Ne_{nuc} \leq 0.2$ will plot on a nearly horizontal line close to the x-axis. It is evident from the data plotted in Figure 2 that the radiogenic neon in beryl and tourmaline is characterized by excesses of

both $^{21}Ne_{nuc}$ and $^{22}Ne_{nuc}$, since points plot well below the horizontal line extending from the atmospheric composition that would signify addition of $^{21}Ne_{nuc}$ only. Furthermore, since the data are not collinear, the ratio of excess ^{21}Ne to excess ^{22}Ne must vary, as is most clearly shown by the neon in the Keystone (1) and Pointe de Bois (2) samples. Assuming the neon in these samples to be mixtures of atmospheric neon and radiogenic neon with $^{20}Ne_{nuc}/^{21}Ne_{nuc} = 0.2$, the $^{21}Ne_{nuc}/^{22}Ne_{nuc}$ ratio varies by nearly a factor of two from about 0.68 (Keystone) to 1.22 (Pointe de Bois). The radiogenic neon in the Pala tourmaline appears to be somewhat more enriched in $^{22}Ne_{nuc}$, with $^{21}Ne_{nuc}/^{22}Ne_{nuc} \approx 0.3$, while neon in beryl samples from Ampangabe (5) and Beryl Mtn. (9) suggests relatively high $^{21}Ne_{nuc}/^{22}Ne_{nuc}$ ratios. A wide range of inferred radiogenic $^{21}Ne/^{22}Ne$ ratios from about 0.03 to essentially infinity is found for radiogenic neon produced in situ in radioactive minerals (Wetherill, 1954; Sharif-Zade et al., 1972; Shukolyukov et al., 1973), and in natural gases (Emerson et al., 1966, 1968; Shukolyukov et al., 1973). Such a range is not unexpected because of the different target elements for the production of the two radiogenic neon isotopes. Careful study of the systematic variation of radiogenic neon compositions in samples from different geological provinces potentially could provide information about variations in the relative abundances of these targets. However, utilization of such a technique probably requires a better understanding of the nuclear reactions leading to the neon isotopes, particularly ^{22}Ne, as well as of fractionations that can occur during release by heating of the gases from their sites of production (Shukolyukov et al., 1973).

DISCUSSION

Several main topics will be covered in this section. First, the specific question whether any of the samples contain primary juvenile gases will be examined. Next the nature of the dominant secondary juvenile gases will be investigated by comparing the relative proportions of the radiogenic and nucleogenic gases trapped in the beryls to the crustal production rates summarized in the Introduction. The origin of the non-radiogenic, non-nucleogenic noble gas component will then be discussed. The abundances of both the radiogenic and non-radiogenic gases will lead to the conclusion that xenon is depleted in the beryls. The possible effects on the noble gas elemental abundances of transport processes or preferential trapping will be considered in light of the beryl data.

The most sensitive tests for the presence of a primary juvenile component in measurements of Ne, Ar, Kr, and Xe are the isotopic compositions of Ne and Xe. This is first because the isotopic compositions of primordial neon and xenon found in meteorites and the solar wind typically show large differences from the atmospheric isotopic compositions. A second reason is the potential presence of the two distinctive xenon components at masses 129 and 131-136 from the decay of short-lived ^{129}I and ^{244}Pu. Recognition of a primary juvenile component in the present neon results is hampered by the relatively large amounts of variable-composition nucleogenic neon in the samples. In Fig. 2 primordial neon components plot close to the y-axis, with $^{21}Ne/^{22}Ne \leq 0.03$, and with $^{20}Ne/^{22}Ne$ ranging from about 13.7 in the solar wind, to about 8 in bulk meteorite samples, and even lower, to about 0.6 in meteorite

mineral separates. None of the measured neon isotopic compositions plot with $^{20}Ne/^{22}Ne$ significantly greater than the atmospheric value. This is consistent with the data representing different mixtures of nucleogenic neon of variable composition with atmospheric neon only. The known range of nucleogenic neon compositions in radioactive minerals is sufficient to explain the range of compositions observed in the beryls. While there is thus no evidence of a primordial neon component in the beryls, neither can its presence be completely ruled out. For example, samples (5B), (7), (3), and (4) in Fig. 2 could be interpreted as lying on a mixing line between a primordial component with the solar wind composition and a nucleogenic component with $^{21}Ne/^{22}Ne \sim 0.42$.

Turning to the xenon data in Table 4, we find no evidence of excess radiogenic ^{129}Xe. None of the $^{129}Xe/^{130}Xe$ ratios measured are significantly different from the atmospheric value. Excess ^{129}Xe is absent from samples with both high and low fission xenon contents, and also from samples with high and low contents of non-radiogenic xenon. Nor is there any evidence of primary juvenile fission xenon from the decay of ^{244}Pu. The observed spectra of the fission xenon excesses at masses 131 to 136 are given in Table 5, and are in good agreement with the relative yields from ^{238}U spontaneous fission. Finally, the non-radiogenic xenon in the beryls is consistent with the atmospheric isotopic composition. This is true for the lighter, fission-shielded isotopes, although not with sufficient precision to preclude a meteoritic AVCC-like component. It is also true for the heavier isotopes, as may be inferred from the agreement with the ^{238}U spontaneous fission yields of the fission yields obtained using the assumption of mixing with

atmospheric xenon. We conclude that there is no evidence in the present results that requires the presence of primary juvenile noble gases in the beryls.

The noble gas content of the beryls is dominated by the large concentrations of secondary juvenile radiogenic and nucleogenic gases trapped in the crystals. Remarkable excesses of radiogenic ^{4}He and ^{40}Ar were demonstrated by earlier workers (Damon and Kulp, 1958, and references therein). Verkhovskiy et al. (1976) found distinct contributions of nucleogenic neon in three beryls. We confirm that excess nucleogenic neon is of common occurrence in this mineral. We have also found that ^{238}U fission xenon occurs along with the radiogenic and nucleogenic He, Ne, and Ar. These gases make up a characteristic suite much as one would qualitatively expect from a source in differentiated continental crust of high U, Th, and K contents. For a more quantitative comparison, the ratios $^{40}Ar_{rad}/^{21}Ne_{nuc}$, $^{136}Xe_{SF}/^{21}Ne_{nuc}$, and $^{136}Xe_{SF}/^{40}Ar_{rad}$ are listed in Table 6. At the bottom of the table are instantaneous production ratios taken from Fig. 1 for times of 500 and 2500 million years ago. These production rates are for average crustal rocks with Th/U = 3.5 and $K/U = 10^{4}$ by mass. The observed ratios in the beryls show some scatter about mean values. In part this may reflect chemical differences in the source regions where the gases were generated. For example, for (2) Pointe du Bois the comparatively low $^{40}Ar_{rad}/^{21}Ne_{nuc}$ and high $^{136}Xe_{SF}/^{40}Ar_{rad}$ ratios may signal a source enriched in U. Also, both beryls from New Hampshire, (9) Beryl Mtn. and (10) Palermo Quarry, have $^{40}Ar_{rad}/^{21}Ne_{nuc}$ ratios roughly a factor of ten lower than the other beryl values. This difference could also be the result of regional

chemical differences in the crust.

The data in Table 6 are represented graphically in Fig. 3. The observed ratios of radiogenic gases in beryls are displayed as the filled histograms, with the calculated production ratios indicated by the arrows. Additional data from Verkhovskiy et al. (1976) for $^{40}Ar_{rad}/^{21}Ne_{nuc}$ in natural gases and various minerals is also shown. For $^{40}Ar_{rad}/^{21}Ne_{nuc}$ in beryls, the measured values show a definite spread, but the center of the histogram agrees in general with the calculated production ratio. Excess radiogenic Ne and Ar measured by Verkhovskiy et al. (1976) in similar minerals also shows a range of ratios, but with a definite peak again close to the expected ratios. Ratios of $^{4}He_{rad}/^{40}Ar_{rad}$ and $^{21}Ne_{rad}/^{4}He_{rad}$ obtained by Verkhovskiy et al. also agree very well with the average crustal production ratios, and clearly imply the radiogenic noble gases trapped in the beryls and other minerals are on the average samples of the gases generated by radioactive decay of U, Th, and K in ordinary crustal rocks. The $^{40}Ar_{rad}/^{21}Ne_{rad}$ ratios found in natural gases (Verkhovskiy et al., 1976) show somewhat wider variations, which probably reflect additional fractionation occurring during transport of the gases from sources to present reservoirs.

A range of values is also found for $^{136}Xe_{SF}$ normalized to either $^{21}Ne_{rad}$ or $^{40}Ar_{rad}$, but now the centers of the histograms in Fig. 3 no longer agree with the expected production ratios. Radiogenic Xe in the beryls is depleted by a factor of about ten. Since $^{4}He_{rad}$, $^{21}Ne_{rad}$, and $^{40}Ar_{rad}$ are quite generally present in the expected proportions, this depletion clearly cannot be due to a consistently low U/K ratio in the source region of the gases. We will defer discussion of the origin of

this xenon depletion until after discussing the non-radiogenic and non-nucleogenic noble gas abundances, which will provide an additional constraint on the problem.

In the absence of any evidence for primordial noble gases in the samples, we presume the non-radiogenic gases are atmospheric in origin. Elemental abundance patterns for the non-radiogenic gases in the samples are shown in Figure 4, a graph of a fractionation factor, $\log_{10}F^m$, versus atomic weight. The factor F^m is defined as

$$F^m = \frac{(^mX/^{36}Ar)_{sample}}{(^mX/^{36}Ar)_{air}}$$

and permits comparison of sample patterns with the abundance pattern of the unfractionated atmosphere, which plots as a horizontal line at 0 in this representation. Also shown are the elemental abundance patterns for gases dissolved in water at 28°C and in molten enstatite silicate (Kirsten, 1968) in equilibrium with an infinite reservoir of atmospheric composition. The majority of the beryl patterns resemble neither of these two solubility curves. The beryl patterns are unusual in that both $^{20}Ne/^{36}Ar$ and $^{130}Xe/^{36}Ar$ are characteristically depressed relative to atmospheric values. This is unlike patterns typically seen in plutonic igneous rocks where Xe depletions are rarely if ever found, and samples showing Ne depletions generally show large enrichments of Xe, with $\log_{10}F^{130}$ ranging from about 0.4 to 1.6 (Smith, 1978; Kaneoka et al., 1978). The abundance patterns in the tourmaline and Minas Gerais beryl (8) are more like the usual patterns of igneous rocks. These data strongly suggest that the atmospheric xenon trapped in the beryls is depleted

relative to its original source abundance, just as is the radiogenic xenon.

The gases in the beryls are trapped from a reservoir of ambient gases during crystallization. The unusual abundance patterns may reflect either of two possibilities. First, fractionation occurs during the trapping process. Second, fractionation during trapping is unimportant, and the gases in the ambient reservoir are fractionated to start with. At present neither possibility can be conclusively ruled out. A clue to the nature of the ambient reservoir is obtained from the light noble gas abundances. The observation that radiogenic and nucleogenic He, Ne, and Ar are found in beryls in their expected production ratios implies that no major fractionation occurs for these gases during crystallization. Therefore the observed depletion of atmospheric neon relative to argon must be characteristic of the ambient reservoir. This suggests the source of the atmospheric component was either air dissolved in meteoric water (Fig. 4), or atmospheric gases in crustal rocks, which generally show Ne depletions (Smith, 1978, 1979 a,b) Both of these sources ordinarily are characterized by substantial xenon enrichments, not depletions. Therefore, in order for the ambient gases sampled by the beryls to be xenon deficient, xenon loss must occur during transport of the gases from their original source regions. This is not impossible; for example, incomplete extraction of xenon by diffusion during partial melting of a gas-bearing source rock could explain the depletion in both radiogenic and atmospheric xenon. However, we question whether xenon loss during transport would be a sufficiently uniform process to explain the apparently typical depletion we observe in at least six of the seven beryls from

world-wide localities for which xenon was studied. It would be much easier to understand this effect if it were due to an inherent feature of beryl, namely, discrimination against xenon during gas trapping.

We suggest that xenon fractionation during beryl crystallization is a plausible result of this mineral's crystal structure. The hexagonal beryl lattice may be thought of approximately as of rings of six silica tetrahedrons aligned vertically along the crystallographic c-axis to form long cylindrical channels parallel this axis. Individual columns of rings are joined laterally by tetrahedrally and octahedrally coordinated Be and Al cations. The channels formed by the rings comprise two alternating sites that can be occupied by water molecules, alkali metal ions, noble gases, and other species. One site labeled C2 (or 2b) lies in the plane of the rings and is 2.55 Å in radius. The second labeled C1 (or 2a) lies sandwiched between two adjacent rings and is 3.44 Å in radius. If we subtract about 0.65 Å for the radius of the oxygen atoms surrounding the sites, then the vacant C2 and C1 sites are about 1.9 Å and 2.8 Å in radius respectively. For comparison, the Van der Waals radii of the noble gases He, Ne, Ar, Kr, and Xe are about 1.5, 1.6, 1.9, 2.0, and 2.2 Å respectively. Several factors may act to reduce the amount of xenon trapped in a growing crystal. The relatively large Xe atom (and probably also Kr) can be held only in the larger C1 site, while the three lighter gas atoms may fit in either site. An additional factor that may affect site availability for noble gas trapping is site-occupancy competition from other species, most importantly water and the alkali metals. For example, in a beryl studied by Hawthorne and Černý (1977) nearly 85% of the large C1 sites were filled by H_2O or Cs, and about 35% of the C2 sites by Na.

Occupancy of a Cl site by H_2O will certainly prevent incorporation of xenon into the same site, although possibly not He, Ne, or Ar, depending on the exact location of the H_2O molecule. Thus the common incorporation of H_2O into beryl may disproportionately reduce the sites available for xenon trapping. Finally, it seems likely that the 1.9 Å radius of the Si_6O_{18} ring would hamper diffusion of xenon atoms from the ambient gas reservoir to vacant sites below the surface of the growing crystal. The lattice in essence may act like a sieve and prevent xenon from entering the crystallizing beryl. This suggestion of discrimination against xenon during crystal growth could be tested by hydrothermal synthesis of beryl in noble gas atmospheres. Also, the composition of the ambient reservoir could be investigated by measurement of gases trapped in fluid inclusions in other minerals co-existing with beryls.

In contrast to the gases in the beryls, the $^{136}Xe_{SF}/^{21}Ne_{rad}$ ratio (Table 6) in the Pala tourmaline is not significantly different from the expected production ratio, while the $^{40}Ar_{rad}$ appears to be depleted by two orders of magnitude relative to radiogenic Ne or Xe. The explanation for this difference is straightforward; the radiogenic gases in the tourmaline are most likely due to <u>in situ</u> decay in a sample characterized by a very low K/U ratio. The observed $^{40}Ar_{rad}$ content can be generated by decay of 0.1 wt.% K over the 92 m. y. age of the mineral. Electron microprobe measurements of typical grains from the material analyzed showed $\lesssim$ 0.01% K in the tourmaline itself, but revealed the presence of lepidolite inclusions containing slightly more than 5% K. The required 0.1% K corresponds to ~ 2% contamination of the sample by lepidolite. The observed $^{136}Xe_{SF}$ calls for a U concentration of about

10 ppm in the tourmaline which does not seem unreasonable. Since trapping gas from an external source is not involved, the $^{136}Xe_{SF}/^{21}Ne_{rad}$ ratio is not noticeably affected.

Wasserburg and co-workers have concluded from extensive studies of noble gases in natural gases that the radiogenic He, Ar, and Xe characteristic of these gases are consistent with production in ordinary crustal materials (Wasserburg et al., 1957, 1963: Zartman et al., 1961; Wasserburg and Mazor, 1965). These workers also demonstrated that the natural gases contain atmospheric noble gases probably carried into the crust dissolved in ground water. The juvenile noble gases trapped in beryls appear to represent the same suite of highly radiogenic noble gases, a suite of gases characteristic of the continental crustal environment where high abundances of radioactive U, Th, and K generate large amounts radiogenic daughters that can be trapped at depth in crystallizing minerals like the beryls, or accumulated in natural gas deposits.

CONCLUSIONS

Beryls have long been known to contain varying concentrations of excess radiogenic ^{4}He and ^{40}Ar (Strutt, 1908; Aldrich and Nier, 1948; Damon and Kulp, 1958). We have extended this earlier work to show that beryls also contain excess radiogenic ^{21}Ne and ^{22}Ne, and spontaneous fission Xe. We find that beryls may also contain substantial concentrations of non-radiogenic noble gases.

The composition of nucleogenic neon trapped in beryls is quite variable. The ratio $^{21}Ne_{nuc}/^{22}Ne_{nuc}$ varies at least from about 0.68 to 1.12, probably reflecting variation in the relative target abundances for ^{21}Ne and ^{22}Ne production from (α,n) or (n,α) reactions in the crust.

Ratios of $^{40}Ar_{rad}/^{21}Ne_{rad}$ observed in beryls vary, but cluster about the expected production ratio for radiogenic gases generated in ordinary crustal rock with $K/U \simeq 10^4$. Studies by Verkhovskiy et al. (1976) show that $^{40}Ar_{rad}/^{4}He_{rad}$ and $^{21}Ne_{rad}/^{4}He_{rad}$ of gases trapped in beryls and similar minerals are also similar to expected ratios. In contrast, $^{136}Xe_{SF}$ from ^{238}U spontaneous fission is depleted in beryls relative to radiogenic Ne or Ar by a factor of about 10. This depletion is also reflected in the abundance of non-radiogenic Xe in the beryls which appears to be too low with respect to abundances typical of plutonic igneous rocks. We feel that this fractionation is most likely due to discrimination against Xe atoms by the beryl crystals as they grew and trapped gas from their surroundings. The complete suite of noble gases trapped in the beryls is very similar to the noble gases found in natural gas. Both types of occurrence probably reflect sampling of abundant radiogenic gases generated in typical continental crustal rocks plus atmospheric gases transported into the crust by ground water.

ACKNOWLEDGMENTS

This work was supported by grant EY-76-G-03-1305 from the U. S. Department of Energy, and an institutional grant for energy research by the Ford Motor Company to the California Institute of Technology.

REFERENCES

Aldrich L. T. and Nier A. O. (1948) The occurrence of ^{3}He in natural sources of helium. Phys. Rev. 74, 1590-1594.

Besairie H. (1956) Madagascar. (Lexique Stratigraphique International, Vol. IV Afrique) Centre National de la Recherche Scientifique, Paris.

Besairie H. (1971) Madagascar. In Tectonique de l'Afrique (Tectonics of Africa), pp. 549-558. Unesco.

Bishopp D. W. and Van Eeden O. R. (1971) Southern Africa. In Tectonique de l'Afrique (Tectonics of Africa), pp. 559-585. Unesco.

Butler W. A., Jeffery P. M., Reynolds J. H., and Wasserburg, G. J. (1963) Isotopic variations in terrestrial xenon. J. Geophys. Res. 68, 3283-3291.

Clarke W. B., Beg M. A., and Craig H. (1969) Excess ^{3}He in the sea: evidence for terrestrial primordial helium. Earth Planet. Sci. Lett. 6, 213-220.

Craig H. and Lupton J. E. (1976) Primordial neon, helium and hydrogen in oceanic basalts. Earth Planet. Sci. Lett. 31, 369-385.

Damon P. E. and Kulp J. L. (1958) Excess helium and argon in beryl and other minerals. Amer. Mineral. 43, 433-459.

Deer W. A., Howie R. A., and Zussman J. (1962) Rock-Forming Minerals, Volume 1 (Ortho and Ring Silicates), pp. 256-267. Wiley.

Dings M. G. and Robinson C. S. (1957) Geology and ore deposits of the Garfield Quadrangle, Colorado. U. S. Geol. Surv. Prof. Paper 289.

Emerson D. E., Stroud L., and Meyer T. O. (1966) The isotopic abundance of neon from helium-bearing natural gases. Geochim. Cosmochim. Acta 30, 847-854.

Emerson D. E., Suttle E. T., and Hoffman C. A. (1968) The separation of neon from high-helium-content natural gases and the atmosphere for isotopic analyses. Int. J. Mass. Spect. Ion Phys. 1, 105-110.

Gurfinkel Y. (1963) (α,n) reactions on heavy isotopes of oxygen. Masters Thesis, Hebrew U.

Hawthorne F. C. and Černý P. (1977) The alkali-metal positions in Cs-Li beryl. Can. Mineral. 15, 414-421.

Hennecke E. W. and Manuel O. K. (1975) Noble gases in an Hawaiian xenolith. Nature 257, 778-780.

Kaneoka I., Takaoka N., and Aoki K. (1978) Rare gases in mantle-derived rocks and minerals. In Terrestrial Rare Gases (eds. E. C. Alexander, Jr. and M. Ozima), pp. 71-83. Center for Academic Publications Japan.

Kirsten T. (1968) Incorporation of rare gases in solidifying enstatite melts. J. Geophys. Res. 73, 2807-2810.

Krylov A. Ya., Mamyrin B. A., Khabarin L. A., Mazina T. I., and Silin Yu. I. (1974) Helium isotopes in ocean-floor bedrock. Geochemistry Int. 11, 839-844.

Laughlin A. W. (1969) Excess radiogenic argon in pegmatite minerals. Doctoral dissertation, U. of Arizona.

Sharif-Zade V. B., Shukolyukov Yu. A., Gerling E. K., and Ashkinadze G. Sh. (1972) The neon isotopes in radioactive minerals. Geochemistry Int. 9, 199-207.

Shukolyukov Yu. A., Sharif-Zade V. B., and Ashkinadze G. Sh. (1973) Neon isotopes in natural gases. Geochemistry Int. 10, 346-354.

Smith S. P. (1977) Noble gases in igneous rocks and minerals (abstract). EOS Trans. Amer. Geophys. Union 58, 536.

Smith S. P. (1978) Noble gases in plutonic igneous rocks. In Short Papers of the 4th International Conference on Geochemistry, Cosmochemistry, and Isotope Geology (ed. R. E. Zartman), pp. 400-402. U. S. Geol. Surv. Open File Report 78-701.

Smith S. P. (1979a) Atmospheric and juvenile noble gases in the Skaergaard layered igneous intrusion. In preparation.

Smith S. P. (1979b) Studies of noble gases in meteorites and in the Earth. Doctoral dissertation, California Inst. of Tech.

Strutt R. J. (1908) Helium and radio-activity in rare and common minerals. Proc. Roy. Soc. (London) A80, 572-594.

Verkhovskiy A. B., Shukolyukov Yu. A., and Ashkinadze G. Sh. (1976) Neon isotopes in minerals containing excess helium and argon. Geokhimiya, 315-322 (in Russian).

Wanless R. K. (1969) Isotopic Age Map of Canada. Map 1256A, Geol. Surv. of Canada.

Wasserburg G. J., Czamanske G., Faul H., and Hayden R. J. (1957) The isotopic composition of argon and carbon in helium wells. In Proceedings of the Conference on Nuclear Geology, Publ. 572, pp. 156-158. Nat. Acad. Sci., Nat. Res. Council.

Wasserburg G. J. and Mazor E. (1965) Spontaneous fission xenon in natural gases. In Fluids in Subsurface Environments - A Symposium, Memoir No. 4, pp. 386-398. Amer. Assoc. of Petroleum Geologists.

Wasserburg G. J., Mazor E., and Zartman R. E. (1963) Isotopic and chemical composition of some terrestrial natural gases. In Earth Science and Meteoritics (eds. J. Geiss and E. D. Goldberg), pp. 219-240. North Holland.

Wetherill G. W. (1954) Variations in the isotopic abundances of Ne and Ar extracted from radioactive minerals. Phys. Rev. 96, 679-683.

Zartman R. E., Wasserburg G. J., and Reynolds J. H. (1961) Helium, argon, and carbon in some natural gases. J. Geophys. Res. 66, 277-306.

Table 1. Sample descriptions.

		Estimated geological age (m.y.)
BERYL		
(1) Keystone, South Dakota	translucent, white	1630[1]
(2) Pointe du Bois, Manitoba (103507)	translucent, creamy white	2500[2]
(3) Gravelotte, S. Africa Brady collection, collected 1963	translucent, pale emerald green	2500[3]
(4) Klein Spitzskopje, S. Africa (90750)	transparent, pale blue	
(5) Ampangabe, Madagascar (85206)	transparent, pale green	500?(< 2000)[4]
(6) Lac Pied du Monte, Charlevoix Co., Quebec (102551)	translucent, pale yellow-white	900[2]
(7) Erajarvi, Viitaniemi, Finland (106876)	translucent, white	1800[1]
(8) Minas Gerais, Brazil	transparent, colorless	
(9) Beryl Mountain, S. Acworth, New Hampshire (103330)	translucent, pale blue-white	320[1]
(10) Palermo Quarry, North Groton, New Hampshire (103490)	transparent, colorless	320[1]
(11) White Mountain, Colorado (92155) (near summit, west of Mt. Antero)	transparent, colorless	< 70[5]
TOURMALINE		
Stewart mine, Pala, California	transparent, pink (var. rubellite)	92[6]

[1]Damon and Kulp, 1958. [2]Wanless, 1969. [3]Bishopp and Van Eaden, 1971.

[4]Besairie 1956, 1971. [5]Dings and Robinson, 1957. [6]Laughlin, 1969.

Table 2. Production rates for nucleogenic and radiogenic noble gases

	Average Production Rates			
	Today (instantaneous)	1000 m.y.	2000 m.y.	3000 m.y.
$\frac{^4He_{rad}}{U} = 8\{e^{\lambda 238 t}-1\} + \frac{7}{137.9}\{e^{\lambda 235 t}-1\} + 6\frac{Th}{U}\{e^{\lambda 232 t}-1\}$	0.67	0.73	0.81	0.93 (Th/U=1)
	0.98	1.05	1.14	1.26 (Th/U=3.5)
	1.79	1.88	1.98	2.14 (Th/U=10)
	(10^{-11} moles $^4He/10^{-6}$gU-m.y.)			
$\frac{^{21}Ne_{nuc}}{U} = (2.8\times10^{-8})\ \frac{^4He_{rad}}{U}\ \frac{\%\ Oxygen}{45}$	1.87	2.04	2.26	2.60 (Th/U=1)
	2.74	2.93	3.18	3.54 (Th/U=3.5)
	5.02	5.27	5.56	5.99 (Th/U=10)
	(10^{-19} moles $^{21}Ne/10^{-6}$gU-m.y.)			
$\frac{^{40}Ar_{rad}}{K} = (1.167\times10^{-4})(0.1048)\{e^{\lambda 40 t}-1\}$	1.73	2.32	3.18	4.46
	(10^{-13} moles $^{40}Ar/10^{-3}$gK-m.y.)			
$\frac{^{136}Xe_{SF}}{U} = (0.06)(4.6\times10^{-7})\{e^{\lambda 238 t}-1\}$	1.79	1.94	2.10	2.28
	(10^{-20} moles $^{136}Xe/10^{-6}$gU-m.y.)			

Table 3. Noble gas concentrations and isotopic compositions[†]

Sample	^{22}Ne	$\frac{^{20}Ne}{^{22}Ne}$	$\frac{^{21}Ne}{^{22}Ne}$	^{36}Ar	$\frac{^{40}Ar}{^{36}Ar}$ (unit=1000)	^{84}Kr	^{130}Xe
BERYL							
(1) Keystone (1)	6.7	1.56±0.33	0.58±0.01	80	463±23	-	-
(A)	-	-	-	-	-	0.49	0.0025
(2) Pointe du Bois (1)	6.7	$1.14^{+0.31}_{-0.16}$	1.12±0.03	35	332±17	-	-
(A)	-	-	-	-	-	0.41	0.0020
(3) Gravelotte (1)	8.5	$6.7^{+1.6}_{-2.2}$	0.23±0.02	190	55±3		
(A)	-	-	-	-	-	3.3	0.0110
(4) Klein Spitzskopje (1)	0.76*	5.3±1.4*	0.27±0.04*	67	78±4	-	-
(A)	-	-	-	-	-	0.58	0.0014
(5) Ampangabe (1)	0.28	11.2±4.6	0.30±0.06	18	158±8	-	-
(A)	-	-	-	-	-	0.45	0.0018
(B)	0.76	9.3±0.4	0.15±0.02	-	-	-	-
(6) Lac Pied du Monte (1)	4.9	$9.4^{+0.6}_{-1.9}$	0.10±0.01	290	9.4±7	-	-
(A)	-	-	-	-	-	4.5	0.0097

Table 3. (continued)†

Sample	^{22}Ne	$\frac{^{20}Ne}{^{22}Ne}$	$\frac{^{21}Ne}{^{22}Ne}$	^{36}Ar	$\frac{^{40}Ar}{^{36}Ar}$ (unit=1000)	^{84}Kr	^{130}Xe
BERYL (continued)							
(7) Erajarvii (1)	9.4	$8.5^{+1.2}_{-0.8}$	0.18±0.02	62	38±3	-	-
(8) Minas Gerais	-	-	-	5.4	27±2	0.21	0.0026
(9) Beryl Mtn. (1)	1.2	9.7±1.7	0.30±0.02	17	8.7±0.4	-	-
(10) Palermo Quarry (1)	0.15	5.4±8.0	0.53±0.22	0.67	68±12	-	-
(11) White Mtn. (1)	0.23	0.2±14	0.05±0.03	1.8	25±1	-	-
TOURMALINE							
Pala	0.26	5.6±0.8	0.15±0.03	3.6	0.79±.04	0.14	0.0027
"Whole Earth"	5.13	9.80	0.029	96	0.2955	1.99	0.0109

†Concentrations in 10^{-14} moles/g. Estimated systematic error ±20%. Error in ratios is 1σ.

*^{22}Ne is sum of high and low temperature steps. Isotopic composition measured only for high temperature.

Table 4. Xenon isotopic compositions ($^{130}Xe \equiv 1.0$)[†]

	^{124}Xe	^{126}Xe	^{128}Xe	^{129}Xe	^{131}Xe	^{132}Xe	^{134}Xe	^{136}Xe
BERYL								
(1) Keystone (A)	0.053	0.028	0.63	6.48	5.53	9.73	8.12	8.88
	± .016	.019	.17	.92	.83	1.42	1.14	1.24
(2) Pointe du Bois (A)	0.032	0.023	0.42	6.33	5.60	9.91	7.17	7.86
	± .011	.010	.07	.52	.49	.97	.83	.93
(3) Gravelotte (A)	0.022	0.029	0.49	6.76	5.32	6.87	2.86	2.55
	± .007	.006	.04	.27	.20	.26	.13	.09
(4) Klein Spitzskopje (A)	0.024	0.027	0.52	6.35	5.53	8.37	5.19	5.48
	± .010	.007	.06	.34	.29	.51	.47	.46
(5) Ampangabe (A)	0.023	0.022	0.49	6.61	5.30	6.72	2.88	2.49
	± .008	.008	.04	.45	.33	.41	.21	.15
(6) Lac Pied du Monte (A)	0.025	0.022	0.48	6.57	5.29	6.89	2.94	2.64
	± .004	.002	.02	.20	.17	.21	.11	.07
(8) Minas Gerais	-	-	0.50	6.49	5.29	6.85	2.64	2.22
	±		.03	.31	.30	.28	.12	.12
TOURMALINE								
Pala	-	-	0.49	6.80	5.39	7.35	3.31	3.00
	±		.15	.49	.38	.49	.24	.22
ATMOSPHERE	0.023	0.022	0.471	6.51	5.22	6.61	2.57	2.18
AVCC (Meteorites)	0.029	0.026	0.510	(varies)	5.08	6.22	2.38	2.00

[†]Error is 2σ.

Table 5. Radiogenic and nucleogenic noble gases

Sample	$^{21}Ne_{nuc}$ (10^{-14}mole/g)	$^{22}Ne_{nuc}$ (10^{-14}mole/g)	$^{40}Ar_{rad}$ (10^{-9}mole/g)	$^{136}Xe_{SF}$ (10^{-16}mole/g)	Calculated Fission Xe Spectra $\frac{134}{136}$	$\frac{132}{136}$	$\frac{131}{136}$
BERYL							
(1) Keystone*	3.8±0.5	5.6±0.3	366	1.7	0.83±0.04	0.47±0.12	0.05±0.10
(2) Pointe du Bois*	7.45±0.09	$5.9^{+0.2}_{-0.3}$	116	1.2	0.81±0.04	0.59±0.06	0.08±0.06
(3) Gravelotte*	1.79±0.09	$3^{+2}_{-1.5}$	103	0.38	-	-	-
(4) Klein Spitzskopje*	≥ 0.11† (0.2)	≥ 0.20† (0.4)	53	0.49	0.80±0.04	0.55±0.10	0.11±0.08
(5) Ampangabe*	0.071±0.009	0±0.2	29	0.049	-	-	-
Ampangabe (B)	0.094±0.018	0.04±0.03	-	-	-	-	-
(6) Lac Pied du Monte*	0.3±0.05	0.2±0.9	26	0.45	0.81±0.04	0.53±0.12	0.08±0.12
(7) Erajarvii	1.43±0.09	$1.3^{+0.9}_{-1.3}$	23	-	-	-	-
(8) Minas Gerais	-	-	1.5	< 0.01	-	-	-
(9) Beryl Mtn.	0.3±0.05	0±0.3	1.4	-	-	-	-
(10) Palermo Quarry	0.076±0.005	0.1±0.1	0.45	-	-	-	-
(11) White Mtn.	0.01±0.01	0.2±0.4	0.45	-	-	-	-
TOURMALINE							
Pala	0.04±0.01	0.11±0.03	0.017	0.17	0.87±0.17	0.61±0.25	-
$^{238}U_{SF}$	-	-	-	-	0.82	0.58	0.08
$^{244}Pu_{SF}$	-	-	-	-	0.92	0.88	0.25

Table 5. (continued)

*Combined data from groups (1) and (A).

†Limits from measured high-temperature fraction. Values in parentheses calculated from total ^{22}Ne and high-temperature isotopic composition.

Table 6. Radiogenic noble gases; ratios

	$^{40}Ar_{rad}/^{21}Ne_{nuc}$ (unit=10^{7})	$^{136}Xe_{SF}/^{21}Ne_{nuc}$ (unit=10^{-2})	$^{136}Xe_{SF}/^{40}Ar_{rad}$ (unit=10^{-9})
BERYL			
(1) Keystone	0.97	0.44	0.46
(2) Pointe du Bois	0.15	0.16	1.02
(3) Gravelotte	0.58	0.21	0.36
(4) Klein Spitzskopje	∿ 2.9	∿ 2.9	0.97
(5) Ampangabe	3.4	0.58	0.17
(6) Lac Pied du Monte	0.80	1.4	0.17
(7) Erajarvii	0.16	-	-
(9) Beryl Mtn.	0.044	-	-
(10) Palermo Quarry	0.059	-	-
TOURMALINE			
Pala	0.005	4.9	970
Calculated ratio of instantaneous production rates at			
500 m.y.	0.78	6.6	8.5
2500 m.y.	1.64	6.2	3.8

Figure 1. Instantaneous production rates for radiogenic and nucleogenic noble gases. Ratios are plotted as a function of time. The curves shown are calculated for present-day Th/U = 3.5 and K/U = 10^4 by weight. $^{21}Ne_{nuc}$ is produced by (α,n) on ^{18}O from the α particles emitted by the decay of uranium and thorium. The decrease in $^{136}Xe_{SF}/^{40}Ar_{rad}$ in the past reflects the increased relative production of ^{40}Ar because of the shorter half-life of ^{40}K compared to ^{238}U. $^{136}Xe_{SF}/^{21}Ne_{nuc}$ is relatively constant, since both are produced from uranium. The slight decrease in the past represents increased ^{21}Ne generation from α particles produced during ^{235}U decay. The shape of the curve for $^{40}Ar_{rad}/^{21}Ne_{nuc}$ is determined by the half-lives of all four parent nuclides, ^{40}K, ^{232}Th, ^{235}U, and ^{238}U.

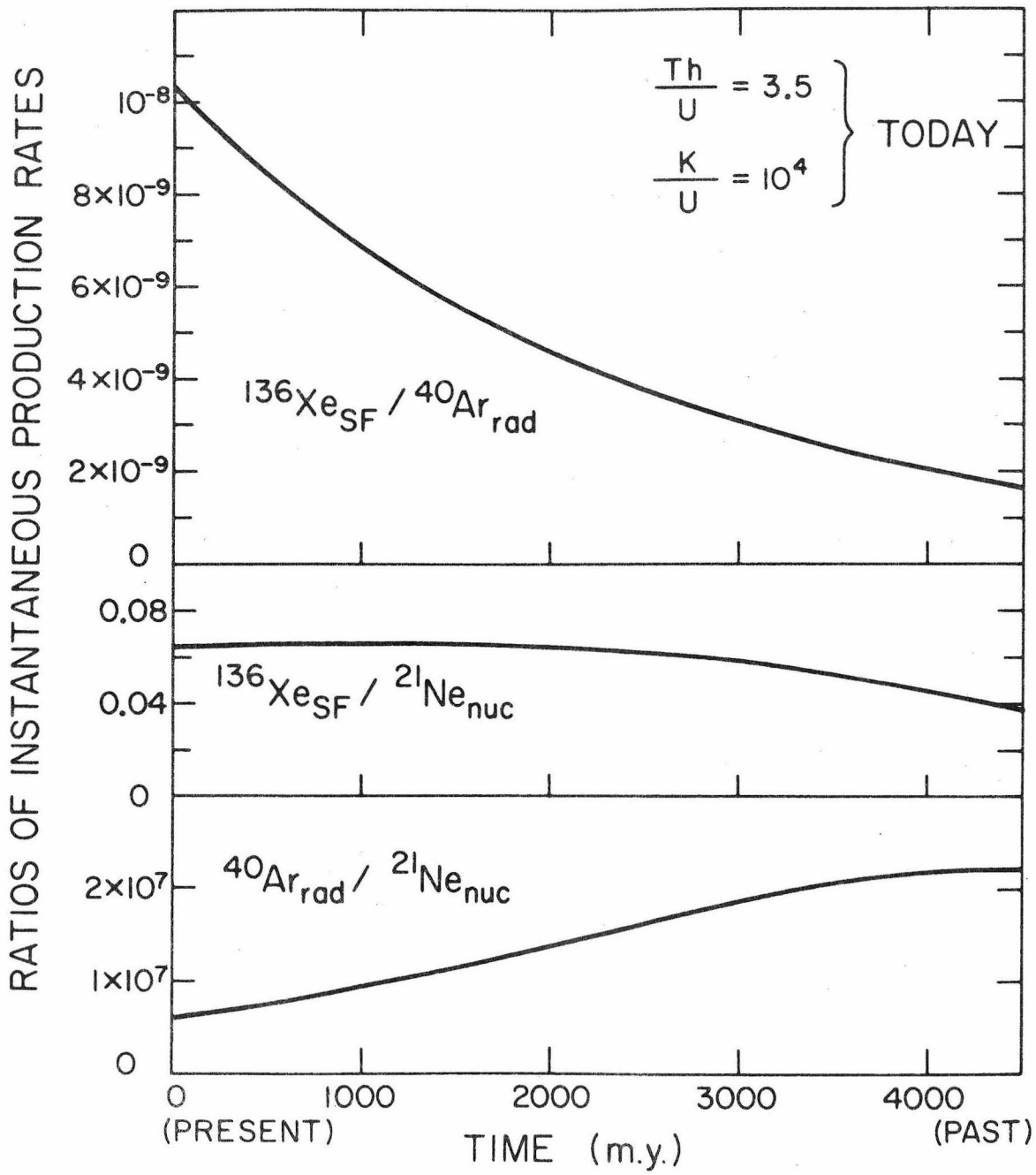

Figure 1

(Beryl)

Figure 2. Three-isotope correlation diagram for neon in beryl and tourmaline. Mixtures of two distinct isotopic components plot on a straight line between the two endpoints. The numbered points represent beryl samples measured in this work, and are identified in Table 3. Crosses are neon compositions in minerals with high U or Th content (Wetherill, 1954; Shukolyukov et al., 1973; Sharif-Zade et al., 1972). Shaded regions are neon compositions measured in natural gases (Emerson et al., 1966, 1968; Shukolyukov et al., 1973). Neon in all the samples is characterized by excesses of ^{21}Ne and ^{22}Ne produced by (α,n) reactions on ^{18}O and ^{19}F (Wetherill, 1954). Addition of pure ^{21}Ne shifts points horizontally to the right. Addition of pure ^{22}Ne shifts points toward the origin. The beryl samples do not fall on a single mixing line, so the relative composition of the nucleogenic end-member must be variable. This is clearly demonstrated by samples (1) and (2) which contain nearly pure nucleogenic neon. $^{21}Ne/^{22}Ne$ varies by nearly a factor of two, probably due to differences in the O and F target abundances in the source regions of the neon. Neon from the radioactive minerals and natural gases exhibits nearly the entire range of $^{21}Ne/^{22}Ne$ ratios possible for the nucleogenic component. Nucleogenic ^{21}Ne and ^{22}Ne are evidently not well correlated in different terrestrial samples.

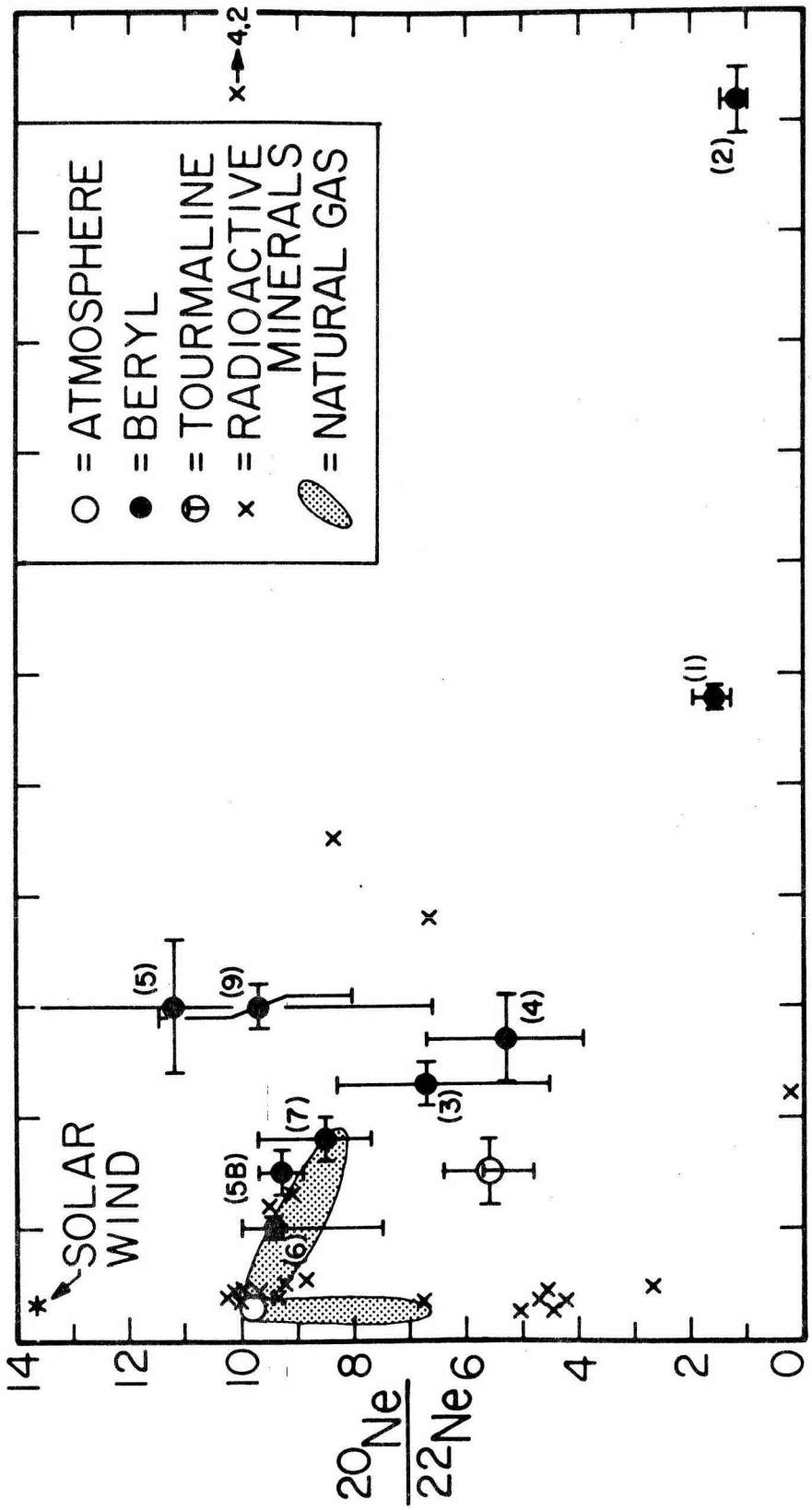

Figure 2
(Beryl)

Figure 3. Histograms of the observed ratios of the different radiogenic and nucleogenic noble gases in beryls. Each square block represents one sample. The vertical arrows below each histogram are calculated instantaneous production ratios at 500 m. y. and 2500 m. y. in the past (see Fig. 1 and Table 2). Medians (M) refer only to beryl samples measured in this work (filled squares). The topmost histogram is constructed from data given by Verkhovskiy et al. (1976). The dashed line represents the envelope of a large number of $^{40}Ar_{rad}/^{21}Ne_{nuc}$ measurements in natural gases. The observed ratios in all samples typically show a range of values, probably due to differences in source region chemistry and fractionation during transport. For $^{40}Ar/^{21}Ne$, the values observed in beryls (this work) agree with the data for similar minerals and natural gases presented by Verkhovskiy et al. (1976). The median value of $^{40}Ar_{rad}/^{21}Ne_{nuc}$ is not substantially different from the calculated production ratio (which is for $K/U = 10^4$). For both $^{136}Xe_{SF}/^{21}Ne_{nuc}$ and $^{136}Xe_{SF}/^{40}Ar_{rad}$, the median values are a factor of ten below the calculated production rates. Radiogenic xenon is strongly depleted in the beryls.

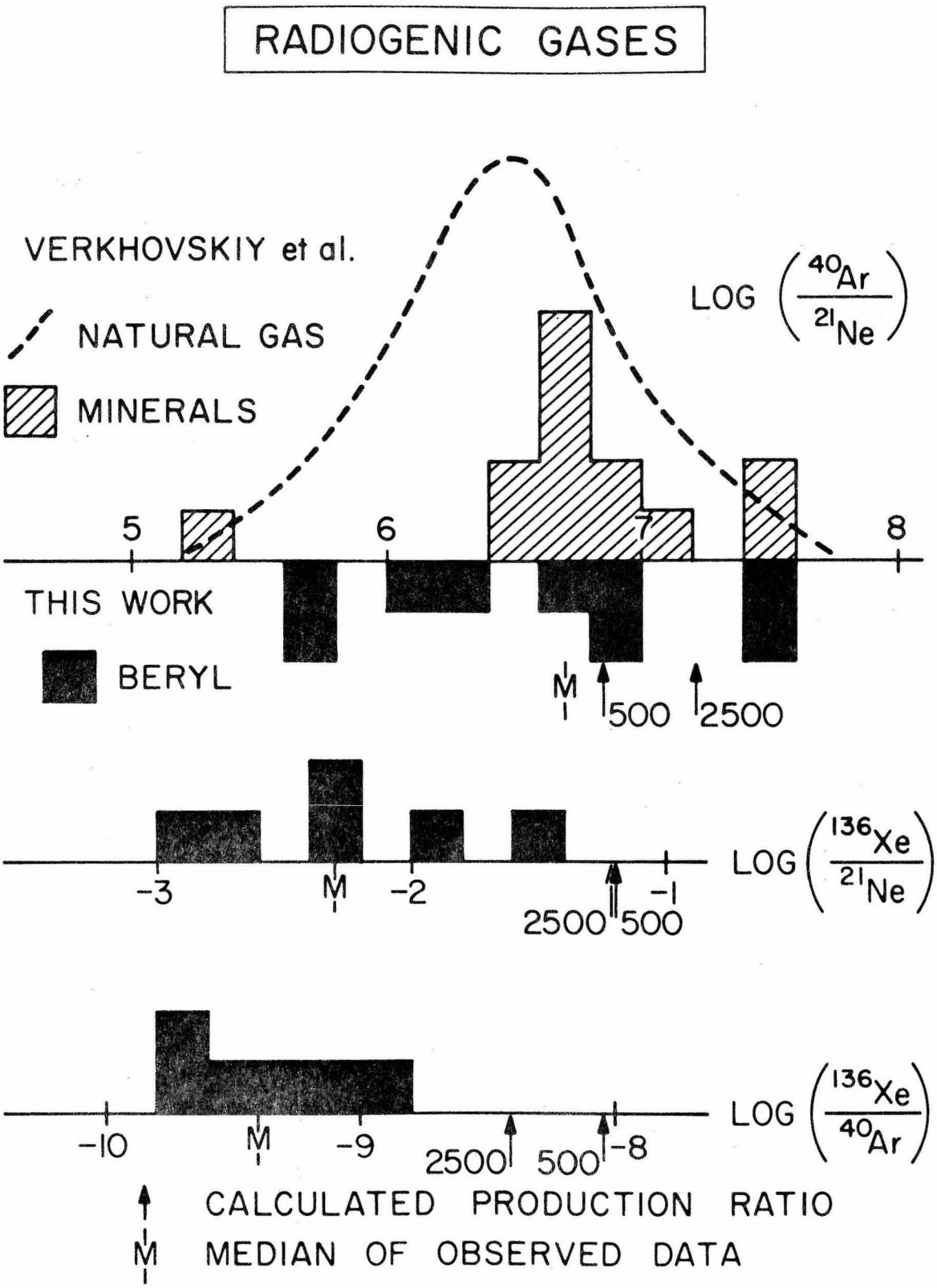

Figure 3

(Beryl)

Figure 4. Elemental abundance patterns of the non-radiogenic noble gases in beryl and tourmaline. The fractionation factor $F^m = (^mX/^{36}Ar)_{sample}/(^mX/^{36}Ar)_{air}$. The pattern for air is a horizontal line at 0. The points 'W' and 'E' represent air dissolved from an infinite reservoir in water at 28°C and in molten enstatite at 1500°C (Kirsten, 1968). Water shows a pattern of increasing differential solubility for the heavier noble gases. Enstatite shows the opposite pattern of decreasing solubility for the heavier species. The patterns for most of the beryl samples are unlike either the water or enstatite solubility curves. The patterns are unusual, in that neon, krypton, and xenon are depleted relative to the atmospheric pattern. This characteristic pattern is unlike abundance patterns in most plutonic igneous rocks (e.g. Smith 1978, 1979 a,b). Rocks with Kr and Xe depletions are very rare. Those with Ne depletions similar to the beryl values typically show strong Kr and Xe enrichments, similar or more extreme than the values shown here for beryl sample 8 (Minas Gerais) or the tourmaline.

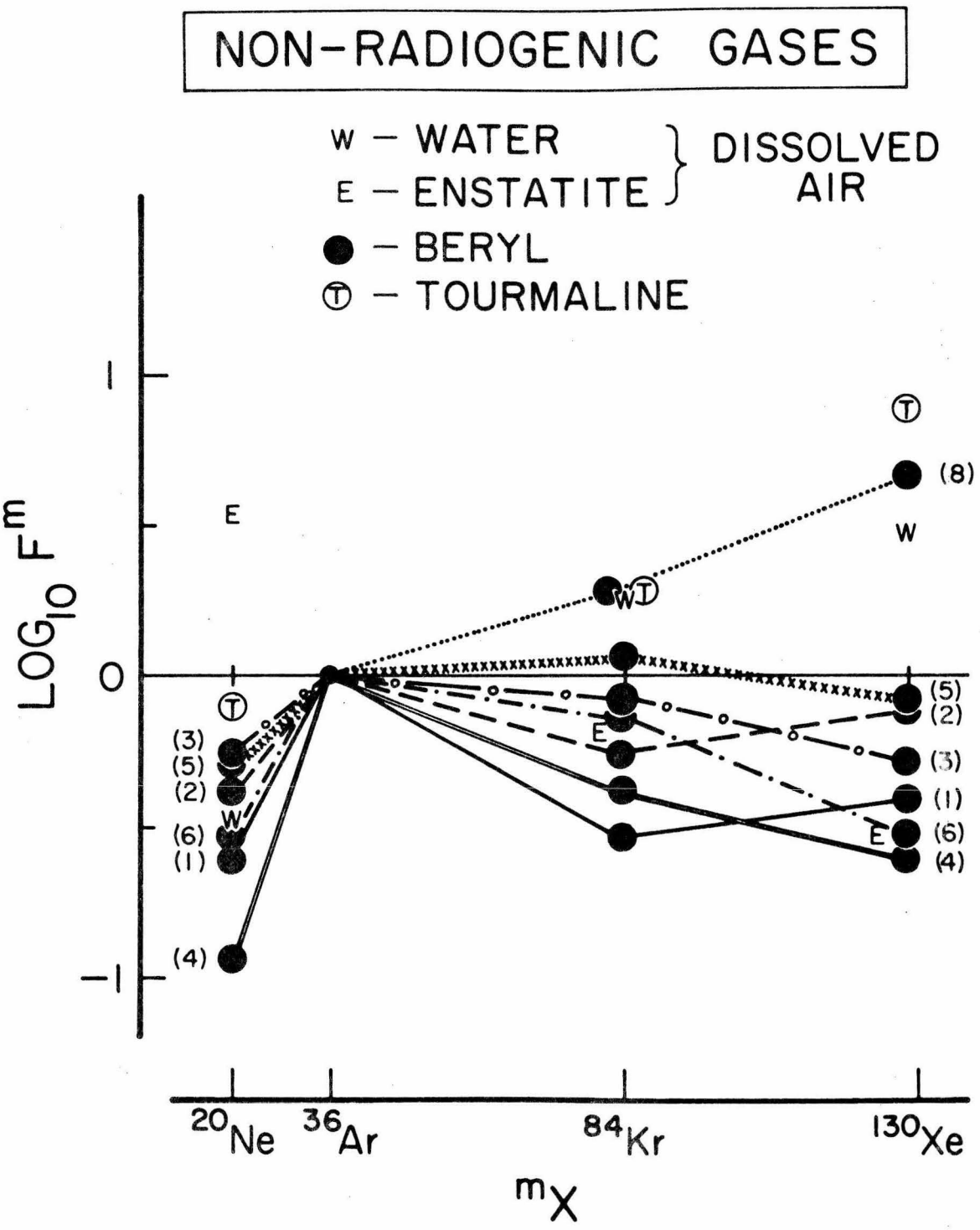

Figure 4

(Beryl)

PAPER 2. ATMOSPHERIC AND JUVENILE NOBLE GASES IN THE SKAERGAARD LAYERED IGNEOUS INTRUSION

ATMOSPHERIC AND JUVENILE NOBLE GASES IN THE SKAERGAARD LAYERED IGNEOUS INTRUSION

Stephen P. Smith

The Lunatic Asylum of the Charles Arms Laboratory
Division of Geological and Planetary Sciences
California Institute of Technology
Pasadena, California 91125

Abstract

Gabbro and diorite from the Skaergaard layered igneous intrusion contain noble gases which are mixtures of atmospheric and juvenile components. Atmospheric noble gases predominate in samples known to have undergone extensive oxygen isotope exchange with meteoric-hydrothermal water. The source of the atmospheric noble gas component is inferred to be the hydrothermal circulation system. A juvenile magmatic component with $^{40}Ar/^{36}Ar \geq 6000$ and containing fission xenon is also present. This component predominates in samples showing unaltered magmatic oxygen isotope compositions. Neon of atmospheric isotopic composition is associated with the juvenile radiogenic ^{40}Ar and fission xenon. The source of the magmatic noble gas component may be either the Precambrian basement or the upper mantle. If the neon is juvenile primordial neon from a mantle source region, terrestrial primordial $^{20}Ne/^{22}Ne$ is the same as atmospheric to within 3%. However, subduction of atmospheric noble gases into the upper mantle may provide an alternate source of neon and other noble gases in the mantle.

INTRODUCTION

Noble gases in terrestrial samples can be classified as either atmospheric or juvenile. Atmospheric gases in a sample were at one time contained in the Earth's atmosphere. Juvenile gases have never been a part of the atmosphere. We also distinguish between nucleogenic and non-nucleogenic gases. Nucleogenic noble gases arise through nuclear reactions in the Earth or its atmosphere. An important group of nucleogenic species are the radiogenic isotopes. Radiogenic noble gases are daughter products of radioactive decay, for example ^{4}He from α-decay of U and Th, ^{40}Ar from β-decay of ^{40}K, $^{83-86}Kr$ and $^{131-136}Xe$ from spontaneous fission (SF) of ^{238}U, or short-lived ^{244}Pu, and ^{129}Xe from the decay of short-lived ^{129}I. Other nucleogenic gases may be produced in secondary nuclear reactions involving the α-particles and neutrons emitted during primary decays, and include most notably ^{21}Ne, ^{22}Ne, and ^{38}Ar (Wetherill, 1954). Non-nucleogenic gases consist of primordial noble gases accumulated during the formation of the Earth, and presently residing either in the atmosphere, or in incompletely degassed portions of the Earth. The atmosphere contains both nucleogenic and non-nucleogenic components. The most abundant nucleogenic isotopes in air are ^{4}He and ^{40}Ar, which are virtually purely radiogenic. The typical well-identified juvenile nucleogenic noble gases found in terrestrial rock or natural gas samples are the radiogenic daughters ^{4}He, ^{40}Ar, and Xe_{SF}, and nucleogenic ^{21}Ne from (α,n) reactions on ^{18}O. The most prominent and best-studied non-nucleogenic juvenile gas in terrestrial samples is helium enriched in ^{3}He relative to the atmosphere (see Tolstikhin [1978] for a review of He observations). Juvenile gases may be classed as primary or

secondary. Primary components are defined as those which have never been or are not now being generated within the Earth. Primary juvenile gases include ^{244}Pu fission xenon, ^{129}Xe from decay of ^{129}I, and primordial noble gases. Secondary juvenile gases are those nucleogenic components presently being produced on the Earth.

In terrestrial samples, the amounts of noble gases other than those produced in situ are often very small because of the generally low solubilities of noble gases in magmas and igneous rocks and minerals. It is useful to identify classes of samples where the concentrations of dissolved gases can be expected to be highest. Since the noble gas solubilities are likely to obey Henry's law, rocks crystallizing and cooling under elevated (plutonic) fluid pressures should generally contain larger concentrations of trapped ambient gases than rocks emplaced at the Earth's surface. For example, it is not unusual to find excess radiogenic ^{40}Ar trapped in high-grade metamorphic rocks (e.g., Kaneoka, 1975). Among magmas erupted at the surface, dissolved juvenile gases should be retained best in those cooling most rapidly; a noteworthy example where this is the case is the glassy quenched rims of submarine basalt flows. For this study we have chosen to examine the noble gases in a suite of plutonic rocks from the Skaergaard igneous intrusion located in East Greenland.

In general it is not to be expected that plutonic rocks will contain only juvenile gases. The presence of an atmospheric component in deep well gases (Wasserburg et al., 1963) provides evidence of the

transport by meteoric water of atmospheric gases several kilometers. into the crust, where they could be trapped during alteration of solid phases. Extensive oxygen isotope studies by Taylor (1974) have shown that there are large hydrothermal circulation systems set up around many igneous plutons which have caused major exchange between the silicates and the circulating ground water. Taylor (1974) and Taylor and Forester (1979) have shown that the upper portions of the Skaergaard intrusion have interacted with meteoric water of a hydrothermal circulation system established in the permeable basalts overlying the cooling intrusion. A schematic cross section of the Skaergaard intrusion after Wager and Brown (1967) and Taylor (1974) is shown in Fig. 1. The intrusion is divided into three main parts, the layered series, marginal border group, and upper border group. The layered series is further divided into lower, middle, and upper zones, based on systematic mineralogical characteristics. The layered series crystallized from the bottom up, and shows many textural features related to crystal settling. The upper border group crystallized from the top down. The region where these two solidifying units met is called the sandwich horizon. The alteration of the upper part of the intrusion by meteoric ground water is indicated schematically by the arrows in the upper part of Fig. 1. The ground water may carry dissolved atmospheric noble gases into the cooling intrusion. The possibility that the magma may have been emplaced while carrying juvenile noble gases is suggested by the arrow in the lower part of the figure.

Neon, argon, krypton, and xenon contents of several gabbro and

diorite samples from the layered series and sandwich horizon of the Skaergaard intrusion are reported here. Noble gases were measured in samples of known oxygen isotopic composition from several stratigraphic horizons in the intrusion, first to establish their noble gas contents, and second to investigate the effects of the hydrothermal circulation on the gas contents of the rocks. The samples have been found to contain both juvenile radiogenic gases and a component of gases of apparent atmospheric origin. The elemental and isotopic abundances of the noble gases in individual samples are related systematically to the degree of exchange of the rocks with meteoric water as determined from oxygen isotope measurements.

The first measurements of noble gases in igneous rocks were made by R. J. Strutt (later Lord Rayleigh) in 1907. He found helium, argon, and traces of neon in granite and syenite. In 1939 Lord Rayleigh published a more extensive series of measurements of argon and neon in igneous rocks including granites, dunites, eclogite, obsidian, and pumice. The samples were found to contain typically about 2×10^{-5} cc of argon (including radiogenic ^{40}Ar) and 8×10^{-8} cc of neon per gram. Subsequent studies of igneous rocks until about the past decade have emphasized the radiogenic component of noble gases. Radiogenic ^{4}He and ^{40}Ar produced *in situ* have been widely measured for use in radiometric age dating. Damon and Kulp (1958) concluded that large excesses of ^{4}He and ^{40}Ar trapped in beryls and other ring-silicates represent samples of magmatic noble gases derived from outgassing of the lower crust and mantle. Butler *et al.* (1963) measured xenon in granite and eclogite, finding ^{238}U spontaneous fission xenon in the granites, as well as non-radiogenic xenon of

atmospheric composition in the eclogite. In related work, the presence of the radiogenic component (including ^{4}He, ^{40}Ar, Xe_{SF}) in natural gases has been extensively documented by Wasserburg and coworkers (Wasserburg et al., 1957; Zartman et al., 1961; Wasserburg et al., 1963; Wasserburg and Mazor, 1965). The ratios of radiogenic He/Ar in these gases are essentially equal to the expected production ratios from U, Th, and K in average igneous rocks, and consistent with derivation from average crustal material. The natural gases were also found typically to contain a significant atmospheric noble gas component in amounts consistent with transport of atmospheric gases by meteoric water several kilometers into the crust. Butler et al. (1963) discovered evidence in CO_2 well gas from New Mexico of excess ^{129}Xe from the decay of short-lived ^{129}I ($t_{1/2}$ = 17 million years). The authors pointed out that this observation implied that the outgassing of the Earth's interior is incomplete. The presence of this primary juvenile xenon in the well gas was confirmed by Boulos and Manuel (1971), and excess ^{129}Xe has also been found in a peridotite nodule from Hawaii (Hennecke and Manuel, 1975).

A revival of interest in the non-radiogenic noble gas contents of igneous rocks was sparked by the discovery of helium enriched in ^{3}He by a factor of about ten over atmospheric $^{3}He/^{4}He$ in natural gases, seawater, ultrabasic xenoliths, and glassy rims of mid-ocean ridge basalt flows (Mamyrin et al., 1969; Clarke et al., 1969; Tolstikhin et al., 1974; Krylov et al., 1974; Lupton and Craig, 1975). This ^{3}He enrichment is thought to be due to outgassing of primordial ^{3}He. Most recent research has concentrated on gases in submarine basalts, or plutonic xenoliths of presumed upper-mantle origin (Dymond and Hogan,

1973; Fisher, 1970, 1971, 1973, 1974; Craig and Lupton, 1976; Rison and Kyser, 1977; Smith, 1977; Kaneoka et al., 1978). Limited results on the non-radiogenic gases in ordinary plutonic igneous rocks from continental crust have been given by Smith (1977, 1978), and by Kuroda and Sherrill (1978) who report noble gas contents substantially lower than those estimated on the basis of Lord Rayleigh's pioneering work.

EXPERIMENTAL PROCEDURES AND SAMPLE DESCRIPTION

Noble gases were extracted from samples and analyzed mass-spectrometrically using conventional techniques (e.g., Smith et al., 1977; Smith and Wasserburg, 1979a). In brief, samples weighing about 0.5 to 1 gram were crushed in a stainless steel mortar to roughly 0.5 mm radius, and rinsed thoroughly in acetone or ethanol to remove the finest particles so to minimize adsorbed atmospheric gases. Samples were degassed in a tungsten crucible by RF induction, and active gases removed using Ti-Zr and Zr-Al getters. Neon was separated from argon, krypton, and zenon using a cold finger of activated charcoal at liquid nitrogen temperatures. Neon was analyzed while exposed to a second cold finger and with a reduced ionizing potential of about 30 eV in the spectrometer source to minimize $^{40}Ar^{++}$ interference at mass 20. Argon, krypton, and xenon were analyzed in a single fraction.

The tabulated data have been corrected for mass discrimination, extraction oven blanks, and interfering species including $H_2^{18}O$, $^{40}Ar^{++}$, CO_2^{++}, HF, and neon and xenon hydrides. Extraction oven blanks ranged from about 2 to 6 x 10^{-15} mole ^{20}Ne, 3 to 9 x 10^{-16} mole ^{36}Ar, 2 to 4 x 10^{-13} mole ^{40}Ar, 0.5 to 4 x 10^{-17} mole ^{84}Kr, and 0.2 to 1 x 10^{-17} mole ^{132}Xe. Total corrections amount to about 7% or less for argon,

krypton, or xenon, but as much as about 50% of the measured signal for neon. The spectrometer sensitivity and mass discrimination were monitored using a pipette of standard volume and atmospheric isotopic composition, and calibrated by comparison to a previously measured sample of the Berkeley Bruderheim standard. Systematic uncertainty in the absolute calibration is estimated to be about 15%.

Table 1 includes a brief description of each sample. The samples are listed in order of their original stratigraphic position within the intrusion, with the uppermost sample listed at the top of the table. The stratigraphically highest, SKR-12, is from the sandwich horizon. The remaining samples are from successively deeper levels in the layered series. Chemically and mineralogically the rocks are rather similar to one another, consisting of iron-rich gabbros and diorites. Wager and Brown (1967) discuss the geology and geochemistry of the Skaergaard intrusion in detail.

RESULTS

The measured concentrations of ^{20}Ne, ^{36}Ar, ^{84}Kr, and ^{132}Xe are given in Table 1 in units of 10^{-16} mole per gram. The range in observed concentrations is substantial. ^{20}Ne and ^{132}Xe concentrations vary by factors of about 15 and 20 respectively. ^{36}Ar and ^{84}Kr are less variable. ^{132}Xe contents are greatest in the stratigraphically highest sample SKR-12 from the sandwich horizon, and appear to decrease steadily in samples from lower levels in the intrusion. The concentrations of the other isotopes do not exhibit similar, clear-cut trends. Listed for comparison at the bottom of the table is a whole-Earth "atmospheric" datum calculated by dividing the atmospheric content

of each isotope by the total mass of the Earth. Assuming a secondary origin of the Earth's atmosphere by degassing (Brown, 1952), the whole-Earth "atmospheric" values represent the minimum noble gas contents of the original material comprising the Earth. Except for xenon, the gas contents of the Skaergaard rocks are considerably less than the whole-Earth values; xenon is roughly equal, or in the case of SKR-12, in excess of the "atmospheric" concentration. The neon contents of the samples are also much less than the 36000×10^{-16} mole/gram reported for granites and dunites by Lord Rayleigh (1939). If the gas contents of the Skaergaard samples were representative of the present noble gas contents of the solid Earth, we would conclude that more than three-fourths the terrestrial Ne, Ar, and Kr are in the atmosphere. A more conservative conclusion is that the crust represented by the Skaergaard samples is largely outgassed of primordial species.

Noble gas abundance data for terrestrial samples can be compared to the pattern of noble gas abundances in the atmosphere by a graph of a fractionation factor F^m plotted against mass number, where $F^m = ({}^mX/{}^{36}Ar)_{sample}/({}^mX/{}^{36}Ar)_{air}$ (Fig. 2). The atmospheric pattern is a horizontal line at Log $F^m = 0$. Various physical processes, such as solubility, adsorption, Rayleigh distillation, etc., acting on atmospheric gases can generate reservoirs of noble gases with elemental patterns much different from the atmospheric abundances. For example, differential equilibrium solubility of the various gases in water causes an enhancement compared with air in the ${}^{132}Xe/{}^{36}Ar$ ratio of the dissolved gases, and a relative depletion in ${}^{20}Ne$ (Fig. 2). In contrast, gases dissolved in molten enstatite (Kirsten, 1968) from a reservoir of atmospheric composition are relatively depleted in xenon

and enriched in neon. The relative elemental abundance patterns measured for the Skaergaard samples are plotted in Fig. 3. The abundance patterns are quite variable. The pattern for SKR-7 (Fig. 3d) is comparatively flat, exhibiting small excesses of neon and xenon compared to the atmosphere. This type of pattern with an enhanced $^{20}Ne/^{36}Ar$ ratio has been observed previously for gases in quenched rims of submarine basalts and in peridotite nodules (Dymond and Hogan, 1973); Smith and Wasserburg, 1979b). The other Skaergaard samples are characterized by larger relative excesses of xenon, and variable depletions of neon. Similar steep patterns have been observed for gases trapped in shale (Canalas et al., 1968), in holocrystalline submarine basalts (Dymond and Hogan, 1973), and in other plutonic rocks (Smith 1978, 1979). There is no noteworthy correlation of abundance pattern with stratigraphic position of the sample in the intrusion. We will discuss the relation of these abundance patterns to the oxygen isotope data in the next section.

The isotopic compositions measured for neon, argon, and krypton are given in Table 2. The compositions of neon and krypton in none of the samples are significantly different from atmospheric. The $^{40}Ar/^{36}Ar$ ratios are variable, and are much higher than the air ratio, indicating the presence of radiogenic ^{40}Ar. The ^{40}Ar contributions due to in situ decay of potassium can be calculated from the K contents of the samples, assuming an age of about 60 million years for the Skaergaard intrusion (Carmichael et al., 1974; p. 462). In all cases the measured ^{40}Ar contents of the rocks are too large to be due to in situ decay (Table 3). After subtraction of in situ produced ^{40}Ar, the ratio of

the remaining excess ^{40}Ar to the total ^{36}Ar varies from about 5000 in SKR-7 to about 680 in SKR-12. For samples SKR-7(1) and SKR-7(2), gases were extracted in two fractions, a low-temperature fraction about 700° to 800° C, and a high-temperature fraction at about 1500°C to 1600°C. $^{40}Ar/^{36}Ar$ ratios of 6100 and 5900, somewhat higher than the bulk sample values, were observed in the high-temperature fractions. The overall variation in argon isotopic composition requires two distinct components to be present in varying proportions in the samples. The component with low $^{40}Ar_{excess}/^{36}Ar \leq 680$ is probably atmospheric argon, with $^{40}Ar/^{36}Ar = 296$. The high $^{40}Ar_{excess}/^{36}Ar$ ratios provide clear evidence of juvenile magmatic noble gases with $^{40}Ar/^{36}Ar \geq 6100$ trapped in the rocks of the Skaergaard. This juvenile radiogenic ^{40}Ar originated by the decay of ^{40}K prior to the formation and emplacement of the Skaergaard magma. There are two possible sources of the excess argon. One is the magma source region at depth, where the argon was incorporated during partial melting. A second possibility is that the excess radiogenic argon was added to the ascending magma by assimilation of or diffusion from country rock.

Measured xenon isotopic compositions are listed in Table 4. The large amount of xenon in SKR-12 from the sandwich horizon (Table 1) is seen from this data to be purely atmospheric in composition. This is consistent with the addition of atmospheric noble gases to this sample, as suggested above from its low $^{40}Ar_{excess}/^{36}Ar$ ratio. Xenon of atmospheric composition is also found in sample GH11. In 4312+, $^{136}Xe/^{132}Xe$ and $^{134}Xe/^{132}Xe$ appear to be slightly lower than atmospheric. This perhaps reflects a slight mass fractionation of unknown origin. Similar effects are not seen in any of the other samples. In several

of the samples (G263, SKR-8, SKR-7), $^{136}Xe/^{132}Xe$ ratios are slightly greater than atmospheric. The enrichments are consistent with the presence of small amounts of fission xenon. In SKR-7, a small but apparently uniform ^{136}Xe excess is seen in the five samples analyzed. The inferred concentration of fission ^{136}Xe is about $2.6\pm1 \times 10^{-18}$ mole/gram for SKR-7. This amount of fission xenon implies a uranium concentration of about 2.4 ppm if due to in situ decay over 60 m.y. Measured U contents in lower zone rocks are an order of magnitude lower (Wager and Brown, 1967, p. 197). Therefore, the fission xenon in this sample is largely an excess radiogenic component, just as is the bulk of the ^{40}Ar. The ratio of excess $^{136}Xe_{SF}$ to $^{40}Ar_{rad}$ in SKR-7 is about 5×10^{-9}, which is consistent with production in ordinary crustal rock having K/U of about 10^4 by weight (e.g., Smith and Wasserburg, 1979a). The data for the other samples are generally consistent with this ratio of fission xenon to excess radiogenic argon. The juvenile component marked by high $^{40}Ar/^{36}Ar$ thus appears also to contain fission xenon.

As reported previously (Smith, 1978), xenon in the sample SKR-7(0) was measured to have a $^{129}Xe/^{132}Xe$ ratio about 3 to 4% greater than the atmospheric value. This excess could be interpreted as evidence of primary juvenile $^{129}Xe_{rad}$ in the Skaergaard magma. This observation would then suggest that the juvenile gases were probably derived from a mantle source. Xenon analyses from four additional samples of the same SKR-7 hand specimen however fail to confirm the ^{129}Xe excess observed in SKR-7(0), although they do uniformly indicate a small $^{136}Xe_{SF}$ excess. The average value of $^{129}Xe/^{132}Xe$ measured in SKR-7 samples (1)-(4) is 0.983 ± 0.008 (Table 4), indistinguishable from

the atmospheric ratio of 0.984. These results are illustrated graphically in Fig. 4, where $^{129}Xe/^{132}Xe$ is plotted versus $^{136}Xe/^{132}Xe$. The data for the SKR-7 samples are shown in the lower panel, and for the remaining samples in the upper panel. In this figure, addition of pure ^{129}Xe to a sample will displace its plotted position vertically upward. Addition of fission xenon from either ^{244}Pu or ^{238}U spontaneous fission will cause points to move to the right along the indicated dashed lines. The data for SKR-7 samples (1)-(4) are consistent with the addition of ^{238}U spontaneous fission xenon to atmospheric xenon. Data in the upper panel for the other samples are also consistent with mixtures of these two components. The SKR-7(0) sample appears to be displaced toward higher $^{136}Xe/^{132}Xe$ ratios to the same extent as other SKR-7 samples, but in addition shows an excess of ^{129}Xe. Given the failure of the other four SKR-7 samples to show such an excess, we conclude that the effect seen in SKR-7(0) was most likely an experimental artifact, and that excess ^{129}Xe is not characteristic of the Skaergaard material. The amounts of xenon measured in these samples, and in terrestrial samples in general, are small. For SKR-7, the total number of ^{129}Xe atoms measured is typically 1 to 2 x 10^8 for each sample, and the ^{129}Xe excess in SKR-7(0) corresponds to only about five million atoms. The mass spectrometer system used for these analyses has through the years been used to measure many meteorite samples containing large radiogenic ^{129}Xe excesses. Xenon from these samples has been implanted in the walls of the spectrometer, and can at times be scrubbed out again into the gas being analyzed. In a series of experiments on beryl crystals (Smith and Wasserburg, 1979a), scrubbing of excess ^{129}Xe by the large amounts of radiogenic argon in the samples

was a serious source of xenon contamination, due to an improperly designed gas-handling procedure. While this exact problem was corrected before the analyses of the Skaergaard samples, it demonstrates that the mass-spectrometer can at times provide a virtual leak of excess ^{129}Xe capable of contaminating samples. Considering again the small amounts of xenon typical of terrestrial samples, one should ideally use a mass-spectrometer dedicated solely to the analysis of terrestrial samples. In the absence of such an instrument, caution and repeat analyses must be used to establish the reality of small anomalies such as under consideration here.

DISCUSSION

Taylor (1974) and Taylor and Forester (1979) have shown that the upper portions of the Skaergaard intrusion that were emplaced against permeable Tertiary basalt have undergone extensive oxygen isotope exchange with meteoric-hydrothermal water that probably circulated through fractures in the solidified and cooling intrusion. Oxygen isotope data from Taylor and Forester (1979) for the samples measured here are given in Table 5. The numbers in parenthesis are estimated values, based on known sample locations and $\delta^{18}O_{plag}$ values measured in different samples from the same or nearby locations. The $\delta^{18}O_{plag}$ values for the other samples were determined on the same hand specimens as the noble gas results. Values of $\delta^{18}O_{plag}$ greater than or about equal to six are typical magmatic oxygen compositions, and indicate little or no oxygen exchange with meteoric water. Increasingly lower values reflect progressively greater degrees of exchange. Thus samples 4312+ and SKR-7 from the upper and lower zones

are both relatively unaltered, while samples GH11 and SKR-12 from the lower zone and sandwich horizon show the greatest degree of exchange.

In Fig. 5 we plot $\delta^{18}O_{plag}$ against $^{40}Ar_{excess}/^{36}Ar$ (Table 3) to investigate the relationship between the observed argon isotopic variations and degree of oxygen isotope exchange. The noble gas and oxygen isotopic variations are clearly correlated. Juvenile argon with high $^{40}Ar/^{36}Ar$ is dominant in the two least exchanged samples, 4312+ and SKR-7. As $\delta^{18}O_{plag}$ decreases, indicating increased interaction with meteoric water, the $^{40}Ar/^{36}Ar$ ratios of samples decrease (dashed trend) and approach the atmospheric $^{40}Ar/^{36}Ar$ ratio of 296, as shown on the left side of the figure. This correlation provides convincing evidence that the observed decrease in $^{40}Ar/^{36}Ar$ is due to the addition of atmospheric argon to samples that have undergone interaction with meteoric groundwater. It should be emphasized that the argon isotopic variations are correlated with the oxygen isotope shifts, and not with stratigraphic position or degree of fractional crystallization of the intrusion. Different samples from one stratigraphic level can show widely varying degrees of interaction with the groundwater. For example, 4312+, G263, and SKR-12 from the upper zone and sandwich horizon show a smooth progression from characteristically high juvenile $^{40}Ar/^{36}Ar$ and $\delta^{18}O$ values, to low $\delta^{18}O$ and low $^{40}Ar/^{36}Ar$ in altered samples. The same trend can be seen across the lower zone, in samples SKR-7, G83, and GH11, although the $^{40}Ar/^{36}Ar$ ratio in GH11 is not as low as might be expected from its very low reported $\delta^{18}O_{plag}$ value. Possibly this discrepancy could be due to small-scale sample heterogeneity such as veining, and more intense alteration along fractures, so that the two samples of GH11 studied

for argon and oxygen were not completely equivalent.

The correlation trend between $^{40}Ar_{excess}/^{36}Ar$ and $\delta^{18}O_{plag}$ displayed in Fig. 5 is strongly curved. The positive curvature is such that initial alteration of a sample characterized by juvenile argon and magmatic oxygen appears to lead to a very rapid decrease in $^{40}Ar/^{36}Ar$, but relatively little change in $\delta^{18}O_{plag}$. $^{40}Ar/^{36}Ar$ drops by a factor of about two from samples 4312+ and SKR-7 to samples G83 and SKR-8, but $\delta^{18}O$ only decreases by a few tenths per mil, or about 5%. Subsequently, $^{40}Ar/^{36}Ar$ and $\delta^{18}O_{plag}$ decrease at more nearly equal rates. This apparent sensitivity of the $^{40}Ar/^{36}Ar$ ratio may prove complementary to the oxygen isotope technique. It may allow detection of samples characterized by comparatively low degrees of meteoric water exchange that show relatively little shift in their oxygen isotope composition. The exact nature of the correlation is presumably related to the mechanisms by which argon and oxygen isotopes are exchanged in the samples. For example, it is possible that most of the argon exchange occurs in phases of relatively low abundance that comprise only a small fraction of the oxygen in the rock. Alteration of these phases would produce large effects on the argon composition, but little or none on the oxygen. Further detailed experiments on the distribution of the noble gases within individual samples are needed to elucidate this problem.

The concentrations and relative abundance patterns of the different noble gases appear to show some variation correlated with the oxygen isotope shifts, although the effects appear to be more complex than for the argon isotopic composition. In Fig. 3 the samples represented by the open circles are those showing the lowest degree of

oxygen isotope exchange, and also the highest $^{40}Ar_{excess}/^{36}Ar$ ratios. For pairs of samples from the same stratigraphic horizon, the less altered samples (4312+ in Fig. 3a, and G83 in Fig. 3c) show "flatter" abundance patterns, with abundance ratios closer to the atmospheric values than those in the more highly exchanged rocks. This shift implies that the magmatic noble gas component associated with the juvenile ^{40}Ar is characterized by a relatively flat abundance pattern compared to the very steep pattern that is associated with the atmospheric isotopic component in the exchanged samples. This inference is supported by the observation that SKR-7, which contains the largest concentration of juvenile ^{40}Ar among the samples studied, shows the flattest relative abundance pattern. We noted earlier that two-step extractions of the noble gases from two SKR-7 samples gave $^{40}Ar/^{36}Ar$ ratios of about 6000 in the high-temperature fractions. Since the bulk ratios are about 5000, this implies that even this relatively unaltered sample contains a component of atmospheric noble gases. If this atmospheric component is characterized by the same steeply-fractionated abundance pattern as the atmospheric gases in the more altered samples, then the $^{20}Ne/^{36}Ar$ and $^{132}Xe/^{36}Ar$ ratios of the initial magmatic component could be somewhat higher and lower respectively than the measured values in SKR-7 samples.

The ultimate source of the atmospheric component in the altered samples was of course the air. However, the elemental abundance pattern of the atmospheric component (taken as similar to SKR-12, Fig. 3a) is much steeper than that of gases dissolved in water equilibrated with unfractionated air (Fig. 2). Additional processes have fractionated the noble gases at some stage of their transport from the atmosphere to

the intrusion. One possibility is gas-loss from the meteoric water, perhaps by an episode of boiling or by a gradual Rayleigh distillation process, either of which would result in further enrichment of the relatively more soluble heavy noble gases in the residual dissolved gas (Wasserburg and Mazor, 1965). Another source of gases preferentially enriched in the heavier isotopes could be gases previously adsorbed on fine-grained silicate or organic material in the country rock (Fanale and Cannon, 1971; Frick and Chang, 1977). Groundwater circulating through this host rock might become enriched in these gases. A third possibility is that the fractionation occurred during the immediate trapping process that transferred the gases from the water to the rock in which they are now found.

Regardless of the precise origin and mode of incorporation of the atmospheric component into the Skaergaard, the present results provide clear evidence that atmospheric noble gases transported to substantial depths within the crust can be trapped in the rocks. The layered series of the Skaergaard is estimated to have been emplaced at a depth of about 4 or 5 km. (Wager and Brown, 1967). The possibility of such transfer of noble gases from the atmosphere into the solid body of the Earth has received scant attention to date. Because of the generally low noble gas contents of crustal rocks, incorporation of atmospheric gases into the outer portions of the Earth may have an important influence on the gas contents of materials we sample.

The origin of the magmatic noble gas component in the Skaergaard is less easy to define. The lower portion of the intrusion rests against 1800 million year old Precambrian gneiss (Wager and Brown, 1967,

p. 187). This country rock certainly contains abundant radiogenic argon and fission xenon which could have been released by the heat given off by the magma, and incorporated in the intrusion. The gneiss might also provide non-radiogenic gases; for comparison a gneiss from West Greenland (Langø Island near Godhavn) contains noble gases with an elemental abundance pattern quite similar to that in SKR-7 (Smith, 1979). An alternative origin is gas dissolved in the Skaergaard magma that has been transported from the source region of the tholeiitic magma. This source is generally thought on petrologic grounds including chemical and isotopic primitiveness of the derived basalts to lie within the mantle (e.g., Carmichael et al., 1974; Verhoogen et al., 1970; Yoder, 1976; Wager and Brown, 1967; Leeman and Dasch, 1978). If the juvenile noble gases came from the magma source region, then the region is characterized by a $^{40}Ar/^{36}Ar$ ratio of $\geq$ 6000, which is not incompatible with a mantle source. Glassy mid-ocean ridge basalts contain excess radiogenic argon which is almost certainly from a mantle source. The magmas are emplaced into very young oceanic crust of low K contents yet, have $^{40}Ar/^{36}Ar$ ratios as high as about 15000 (Fisher, 1975; Smith and Wasserburg, 1979b). At present there is, however, no evidence requiring a mantle origin for the magmatic noble gas component in the Skaergaard samples.

The high juvenile ^{40}Ar concentration in SKR-7 is associated with a very high neon concentration. The isotopic composition of this neon is atmospheric within the 2σ uncertainty of the measurement (Table 2). If this neon is juvenile primordial neon, then the inferred limits on the composition of terrestrial primordial neon would be

$9.65 \leq {}^{20}Ne/{}^{22}Ne_p \leq 10.17$, little or no different from the atmospheric composition. On the other hand, the possibility that the source region of the neon was contaminated by atmospheric neon cannot be entirely ruled out. First, if the source was the crustal country rock, then atmospheric neon could have been introduced into the crust during earlier alteration by circulating meteoric water. Second, even if the source was in the mantle, it can be shown that a substantial amount of gas may have been transported into the upper mantle by subduction. Crystalline oceanic crustal rocks contain noble gases of atmospheric isotopic composition probably taken up during interaction of the oceanic crust with seawater (Dymond and Hogan, 1973; Smith and Wasserburg, 1979b). These gases may be injected into the upper mantle by subduction. The entire oceanic crust presently is subducted once about every 200 million years. Average noble gas contents of four oceanic diabase and gabbro samples (Dymond and Hogan, 1973; Smith and Wasserburg, 1979b) are (in units of 10^{-16} mole/gram) ${}^{20}Ne = 370$, ${}^{36}Ar = 2900$, ${}^{84}Kr = 140$, and ${}^{132}Xe = 13$. We assume these concentrations are typical of the upper 7 km of oceanic crust, and that they are subducted with 100% efficiency. We allow subduction to occur at the present rate for the past 4×10^9 years. Averaging over the upper 400 km of the Earth--about 10% of the Earth's mass--we obtain atmospheric gas contents for the upper mantle of ${}^{20}Ne = 120$, ${}^{36}Ar = 1000$, ${}^{84}Kr = 50$, and ${}^{132}Xe = 4$, again in 10^{-16} mole/g. The calculated concentrations of Ar, Kr, and Xe are about a factor of five greater than measured in peridotite xenoliths from the mantle (Hennecke and Manuel, 1975; Smith, 1978; Kaneoka et al., 1978). The calculated Ne content is about equal measured values.

Assuming the peridotites are approximately representative of the gas contents of the upper mantle, this comparison shows that much or all of the noble gases in these samples (except the obviously juvenile components including excess ^{3}He, radiogenic ^{40}Ar, excess ^{129}Xe) could be subducted atmospheric gases, and not primordial gases as is often assumed. This hypothesis is consistent with the fact that non-radiogenic xenon in mantle samples is typically of atmospheric isotopic composition (Saito et al., 1978; Hennecke and Manuel, 1975; Kaneoka and Takeoka, 1978) rather than the substantially different meteoritic or solar compositions. If xenon in samples showing excess $^{129}Xe_{rad}$ is a mixture of juvenile and atmospheric xenon, then the $^{129}Xe/^{132}Xe$ ratio of pure juvenile Xe may be substantially greater than the maximum values of about 1.03 observed to date. Similarly, if mantle argon in mid-ocean ridge basalts is a mixture of atmospheric and juvenile contributions, $^{40}Ar/^{36}Ar$ of the juvenile component could be much higher than the observed values of about 10^{4}, which would imply an even larger degree of degassing of primordial ^{36}Ar from the MORB source regions than inferred from lower ratios (cf. Bernatowicz and Podosek, 1978). The subduction of atmospheric noble gases in amounts varying with location could provide a mechanism for generating noble gas heterogeneity (as appears to characterize $^{40}Ar/^{36}Ar$, e.g., Kaneoka, 1975) in a mantle containing a relatively uniform component of juvenile radiogenic and primordial noble gases.

CONCLUSIONS

The gabbros and diorites of the layered series and sandwich horizon of the Skaergaard igneous intrusion contain mixtures of two components of noble gases. The first, characterized by atmospheric isotopic abundances and a fractionated elemental abundance pattern enriched in the heavy gases, is most abundant samples known from oxygen isotope data (Taylor, 1974) to have undergone extensive exchange with meteoric-hydrothermal water. The most reasonable origin of this noble gas component is atmospheric gas transported into the cooling intrusion several kilometers deep in the crust by the meteoric water. The second component appears to be a dissolved magmatic component. It is most abundant in samples showing unaltered magmatic oxygen isotopic compositions. This component is characterized by juvenile radiogenic ^{40}Ar and fission xenon, along with substantial concentrations of non-radiogenic isotopes. One source of this magmatic component could be the Precambrian metamorphic country rock through which the Skaergaard magma was intruded. Alternatively, these gases may have had a more remote origin in the upper mantle. In this case, the source region of the Skaergaard magma and second component of noble gases was apparently characterized by $^{40}Ar/^{36}Ar \geq 6000$ and neon of isotopic composition indistinguishable from atmospheric. It is possible that the neon as well as some or all of the other non-radiogenic gases in a mantle source region could be subducted atmospheric gases.

ACKNOWLEDGMENTS

I thank Professor H. P. Taylor, Jr., for graciously providing samples G263, 4312+, GH11, and G83. I also thank Professor G. J. Wasserburg for patient guidance and many fruitful discussions. This work was carried out under grant EY-76-G-03-1305 from the U. S. Department of Energy, and an institutional grant for energy research by the Ford Motor Company to the California Institute of Technology.

REFERENCES

Bernatowicz T. J. and Podosek F. A. (1978) Nuclear components in the atmosphere. In Terrestrial Rare Gases (eds. E. C. Alexander, Jr. and M. Ozima), pp. 99-135. Center for Academic Publications Japan.

Boulos M. S. and Manuel O. K. (1971) The xenon record of extinct radioactivities in the Earth. Science 174, 1334-1336.

Brown H. (1952) Rare gases and the formation of the Earth's atmosphere. In The Atmospheres of the Earth and Planets (revised edition, ed. G. P. Kuiper), pp. 258-266. U. of Chicago.

Butler W. A., Jeffery P. M., Reynolds J. H., and Wasserburg G. J. (1963) Isotopic variations in terrestrial xenon. J. Geophys. Res. 68, 3283-3291.

Canalas R. A., Alexander E. C., Jr., and Manuel O. K. (1968) Terrestrial abundance of noble gases. J. Geophys. Res. 73, 3331-3334.

Carmichael I. S. E., Turner F. J., and Verhoogen J. (1974) Igneous Petrology. McGraw-Hill.

Clarke W. B., Beg M. A., and Craig H. (1969) Excess ^{3}He in the sea; evidence for terrestrial primordial helium. Earth Planet. Sci. Lett. 6, 213-220.

Craig H. and Lupton J. E. (1976) Primordial neon, helium, and hydrogen in oceanic basalts. Earth Planet. Sci. Lett. 31, 369-385.

Damon P. E. and Kulp J. L. (1958) Excess helium and argon in beryl and other minerals. Amer. Mineral. 43, 433-459.

Dymond J. and Hogan L. (1973) Noble gas abundance patterns in deep-sea basalts - primordial gases from the mantle. Earth Planet. Sci. Lett. 20, 131-139.

Fanale F. P. and Cannon W. A. (1971) Physical adsorption of rare gas on terrigenous sediments. Earth Planet. Sci. Lett. 11, 362-368.

Fisher D. E. (1970) Heavy rare gases in a Pacific seamount. Earth Planet. Sci. Lett 9, 331-335.

Fisher D. E. (1971) Incorporation of Ar in East Pacific basalts. Earth Planet. Sci. Lett. 12, 321-324.

Fisher D. E. (1973) Primordial rare gases in the deep Earth. Nature 244, 344-345.

Fisher D. E. (1974) The planetary primordial component of rare gases in the deep Earth. Geophys. Res. Lett. 1, 161-164.

Fisher D. E. (1975) Trapped helium and argon and the formation of the atmosphere by degassing. Nature 256, 113-114.

Frick U. and Chang S. (1977) Ancient carbon and noble gas fractionation. Proc. Lunar Sci. Conf. 8th, 263-272.

Hennecke E. W. and Manuel O. K. (1975) Noble gases in an Hawaiian xenolith. Nature 257, 778-780.

Kaneoka I. (1975) Non-radiogenic argon in terrestrial rocks. Geochem J. 9, 113-124.

Kaneoka I., Takaoka N., and Aoki K. (1978) Rare gases in mantle-derived rocks and minerals. In Terrestrial Rare Gases (eds. E. C. Alexander, Jr. and M. Ozima), pp. 71-83. Center for Academic Publications Japan.

Kirsten T. (1968) Incorporation of rare gases in solidifying enstatite melts. J. Geophys. Res. 73, 2807-2810.

Krylov A. Ya., Mamyrin B. A., Khabarin L. A., Mazina T. I., and Silin Yu. I. (1974) Helium isotopes in ocean-floor bedrock. Geochemistry Int. 11, 839-844.

Kuroda P. K. and Sherrill R. D. (1978) Abundances and isotopic compositions of rare gases in granites and thucolites. In Terrestrial Rare Gases (eds. E. C. Alexander, Jr. and M. Ozima), pp. 63-64. Center for Academic Publications Japan.

Leeman W. P. and Dasch E. J. (1978) Strontium, lead and oxygen isotopic investigation of the Skaergard intrusion, East Greenland. Earth Planet. Sci. Lett. 41, 47-59.

Lupton J. E. and Craig H. (1975) Excess ^{3}He in oceanic basalts: evidence for terrestrial primordial helium. Earth Planet. Sci. Lett. 26, 133-139.

Mamyrin B. A., Tolstikhin I. N., Anufriev G. S., and Kamenskiy I. L. (1969) Anomalous isotopic composition of helium in volcanic gases. Dokl. Akad. Nauk SSSR 184, 1197-1199 (in Russian).

Rayleigh (1939) Nitrogen, argon and neon in the earth's crust with applications to cosmology. Proc. Roy. Soc. (London) A170, 451-464.

Rison W. and Kyser K. (1977) Rare gases, oxygen and hydrogen in Hawaiian xenoliths and basalts (abstract). EOS Trans. Amer. Geophys. Union 58, 537.

Saito K., Alexander E. C., Jr., and Basu A. R. (1978) Rare gases in mantle-derived amphiboles. In Short Papers of the 4th International Conference on Geochemistry, Cosmochemistry, and Isotope Geology (ed. R. E. Zartman), pp. 368-370. U. S. Geol. Surv. Open File Report 78-701.

Smith S. P. (1977) Noble gases in igneous rocks and minerals (abstract). EOS Trans. Amer. Geophys. Union 58, 536.

Smith S. P. (1978) Noble gases in plutonic igneous rocks. In Short Papers of the 4th International Conference on Geochemistry, Cosmochemistry, and Isotope Geology (ed. R. E. Zartman), pp. 400-402. U. S. Geol. Surv. Open File Report 78-701.

Smith S. P. (1979) Studies of noble gases in meteorites and in the Earth. Doctoral dissertation, California Institute of Technology.

Smith S. P., Huneke J. C., Rajan R. S., and Wasserburg G. J. (1977) Neon and argon in the Allende meteorite. Geochim. Cosmochim. Acta 41, 627-647.

Smith S. P. and Wasserburg G. J. (1979a) Noble gases in beryl. In preparation.

Smith S. P. and Wasserburg G. J. (1979b) Atmospheric and juvenile noble gases in MOR volcanic rocks and related samples. In preparation.

Strutt R. J. (1907) On the origin of the gases evolved by mineral springs. Proc. Roy. Soc. (London) A79, 436-439.

Taylor H. P., Jr. (1974) The application of oxygen and hydrogen isotope studies to problems of hydrothermal alteration and ore deposition. Econ. Geol. 69, 843-883.

Taylor H. P. Jr. and Forester R. W. (1979) An oxygen and hydrogen isotope study of the Skaergaard intrusion and its country rocks: A description of a 55-m. y. old fossil hydrothermal system. Preprint.

Tolstikhin I. N., Mamyrin B. A., Khabarin L. B., and Erlikh E. N. (1974) Isotope composition of helium in ultrabasic Xenoliths from volcanic rocks of Kamchatka. Earth Planet. Sci. Lett. 22, 75-84.

Tolstikhin I. N. (1978) A review: some recent advances in isotope geochemistry of light rare gases. In Terrestrial Rare Gases (eds. E. C. Alexander, Jr. and M. Ozima), pp. 33-62. Center for Academic

Publications Japan.

Verhoogen J., Turner F. J., Weiss L. E., Wahrhaftig C., and Fyfe W. S. (1970) The Earth. Holt, Rinehart and Winston.

Wager L. R. and Brown G. M. (1967) Layered Igneous Rocks. W. H. Freeman.

Wasserburg G. J., Czamanske G., Faul H., and Hayden R. J. (1957) The isotopic composition of argon and carbon in helium wells. In Proceedings of the Conference on Nuclear Geology, Publ. 572, pp. 156-158. Nat. Acad. Sci., Nat. Res. Council.

Wasserburg G. J. and Mazor E. (1965) Spontaneous fission xenon in natural gases. In Fluids in Subsurface Environments - A Symposium Memoir No. 4, pp. 386-398. Amer. Assoc. of Petroleum Geologists.

Wasserburg G. J., Mazor E., and Zartman R. E. (1963) Isotopic and chemical composition of some terrestrial natural gases. In Earth Science and Meteoritics (eds. J. Geiss and E. D. Goldberg), pp. 219-240. North Holland.

Wetherill G. W. (1954) Variations in the isotopic abundances of Ne and Ar extracted from radioactive minerals. Phys. Rev. 96, 679-683.

Yoder H. S., Jr. (1976) Generation of Basaltic Magma. Nat. Acad. Sci.

Zartman R. E., Wasserburg G. J., and Reynolds J. H. (1961) Helium, argon, and carbon in some natural gases. J. Geophys. Res. 66, 277-306.

Table 1. Skaergaard intrusion: sample description and noble gas contents*

Sample	Description**	^{20}Ne	^{36}Ar	^{84}Kr	^{132}Xe
SKR-12	Sandwich horizon (SH) Ferrodiorite (q, plag An_{30} †, ol, aug, mag, ap)	96	1060	59	24
G263	Upper zone b (UZb) Ferrodiorite (plag, ol, aug, mag, ap)	67	350	18	8.9
4312+	Upper zone b (UZb) Ferrodiorite	300	580	23	5.4
SKR-8	Middle zone (MZ) Gabbro (plag An_{50}, aug, mag)	160	540	20	4.5
SKR-7(0)	Lower zone c (LZc) Olivine gabbro (plag An_{55}, aug, ol, mag)	1530	2150	48	2.8
SKR-7(1)		-	1030	32	2.2
SKR-7(2)		-	1330	34	3.0
SKR-7(3)		1020	1430	39	2.6
SKR-7(4)		-	1140	43	2.6
GH11	Lower zone b (LZb) Olivine gabbro	94	410	20	3.9
G83	Lower zone b (LZb) Olivine gabbro	140	330	13	1.2
Whole Earth atmospheric††		5020	9610	198	7.18

*All concentrations in 10^{-16} mole/g. Absolute uncertainty ≤ 15%.

**Stratigraphic location, rock type and principal mineralogy. An content of plagioclase determined optically.

q = quartz, plag = plagioclase, ol = olivine, aug = augite, mag = magnetite, ap = apatite.

†Wager and Brown (1967).

††Atmospheric abundance divided by the mass of the Earth.

Table 2. Isotopic composition of neon, argon, and krypton

Sample	$\frac{^{20}Ne}{^{22}Ne}$	$\frac{^{21}Ne}{^{22}Ne}$	$\frac{^{40}Ar}{^{36}Ar}$	$\frac{^{83}Kr}{^{84}Kr}$	$\frac{^{86}Kr}{^{84}Kr}$
SKR-12	10.0 ±1.8	0.033 ±0.014	1530 ±20	0.203 ±0.004	0.304 ±0.005
G263	7.9 ±2.9	0.028 ±0.010	2620 ±100	0.200 ±0.004	0.300 ±0.008
4312+	11.9 ±2.6	0.067 ±0.062	4600 ±80	-	-
SKR-8	9.6 ±1.6	0.095 ±0.060	2750 ±150	0.202 ±0.004	0.307 ±0.005
SKR-7(0)	9.91 ±0.26	0.031 ±0.007	3860 ±80	0.206 ±0.003	0.303 ±0.003
SKR-7(1)	-	-	5040 ±240	-	-
SKR-7(2)	-	-	5120 ±480	-	-
SKR-7(3)	10.1 ±0.8	0.036 ±0.016	4540 ±70	-	-
SKR-7(4)	-	-	4640 ±230	-	-
GH11	14 ±12	<0.24	2400 ±50	-	-
G83	10.8 ±5.4	0.25 ±0.20	2660 ±90	-	-
Atmospheric	9.80	0.029	295.5	0.202	0.306

(errors 2σ)

Table 3. ^{40}Ar in excess of *in situ* production from ^{40}K†

Sample	K_2O (wt.%)	^{40}Ar (measured)	^{40}Ar†† (from *in situ* decay)	$^{40}Ar_{excess}/^{36}Ar$§
SKR-12	1.00*	16.2	9.0	680±220
G263	~0.4±0.2**	9.2	3.6	1600±600
4312+ (UZb)	0.4±0.2**	26.6	3.6	3970±300
SKR-8	0.20*	14.7	1.8	2420±180
SKR-7(0)	0.17*	83.0	1.5	3790±80
SKR-7(1)	0.17*	51.9	1.5	4890±240
SKR-7(2)	0.17*	68.4	1.5	5010±480
SKR-7(3)	0.17*	65.0	1.5	4440±70
SKR-7(4)	0.17*	53.1	1.5	4510±230
GH11(LZb)	0.2±0.1**	9.8	1.8	1960±220
G83 (LZb)	0.2±0.1**	8.7	1.8	2115±290

†All concentrations in 10^{-11} mole/g.

††Calculated assuming an age of 60 m.y. for the Skaergaard (Carmichael *et al.*, 1974, p.462).

§Error in measured $^{40}Ar/^{36}Ar$ compounded with an assumed 25% uncertainty in K_2O contents (SKR-7,8,12). Systematic error in measured Ar concentrations not included.

*Data from Western Minerals, Inc. Skaergaard descriptive sheets.

**Estimated from known sample locality and data in Wager and Brown (1967).

Table 4. Isotopic composition of xenon ($^{132}Xe \equiv 1$)

Sample	^{124}Xe	^{126}Xe	^{128}Xe	^{129}Xe	^{130}Xe	^{131}Xe	^{134}Xe	^{136}Xe
SKR-12	0.0038	0.0036	0.070	0.983	0.149	0.789	0.387	0.329
	± 3	4	2	9	2	6	3	4
G263	0.0035	0.0032	0.070	0.982	0.151	0.784	0.389	0.337
	± 8	10	1	13	2	9	6	6
4312+	0.0040	0.0036	0.071	0.987	0.152	0.783	0.382	0.323
	± 7	7	2	10	3	12	7	5
SKR-8	0.0043	0.0038	0.068	0.981	0.148	0.792	0.390	0.339
	± 22	24	4	17	4	14	7	6
SKR-7 (0)	0.0047	0.0024	0.073	1.020	0.146	0.794	0.392	0.338
	± 4	11	2	10	2	7	4	4
SKR-7 (1)	0.0037	0.0039	0.084	0.990	0.151	0.813	0.396	0.342
	± 11	11	3	9	3	12	8	5
SKR-7 (2)	0.0033	0.0030	0.073	0.976	0.149	0.806	0.401	0.343
	± 26	25	11	21	5	23	9	9
SKR-7 (3)	0.0036	0.0025	0.074	0.988	0.151	0.789	0.395	0.339
	± 21	11	3	15	5	12	9	6
SKR-7 (4)	0.0036	0.0037	0.072	0.979	0.155	0.795	0.390	0.334
	± 13	13	2	10	2	16	5	6
SKR-7 (1)-(4) combined	0.0035	0.0032	0.075	0.983	0.152	0.800	0.395	0.339
	± 10	8	3	8	2	8	4	4
GH11	0.0037	0.0034	0.073	0.975	0.148	0.783	0.387	0.329
	± 7	7	2	8	4	8	7	6
G83	0.0047	0.0026	0.085	0.987	0.154	0.801	0.388	0.340
	± 16	6	5	14	6	20	7	11
Atmospheric	0.0035	0.0033	0.071	0.984	0.151	0.790	0.388	0.330

(error 2σ)

Table 5. Oxygen isotope data for Skaergaard samples (from Taylor and Forester, 1979).

		$\delta^{18}O_{plagioclase}$ (‰)
SKR-12	(SH)	(3±1)†
G263	(UZb)	4.9
4312+	(UZb)	6.3
SKR-8	(MZ)	(5.8)†
SKR-7	(LZc)	(6.0)†
GH11	(LZb)	2.6
G83	(LZb)	5.9

†Values estimated from known sample locations and $\delta^{18}O$ data for nearby samples studied by Taylor and Forester (1979).

Figure 1. Generalized cross section of the Skaergaard layered igneous intrusion (after Wager and Brown, 1967, and Taylor, 1974). This body of basaltic magma was intruded into Precambrian gneiss and Tertiary basalt in East Greenland. During cooling, extensive crystal settling occurred causing the development of pervasive cumulate layering (Wager and Brown, 1967). Juvenile magmatic gases can be trapped during solidification of the magma. Taylor and Forester (1979) have shown from oxygen isotope data that a hydrothermal circulation system was established in the upper part of the cooling intrusion and in the relatively porous basalt country rock. Atmospheric noble gases dissolved in the circulating meteoric groundwater may have been introduced into exchanged portions of the intrusion.

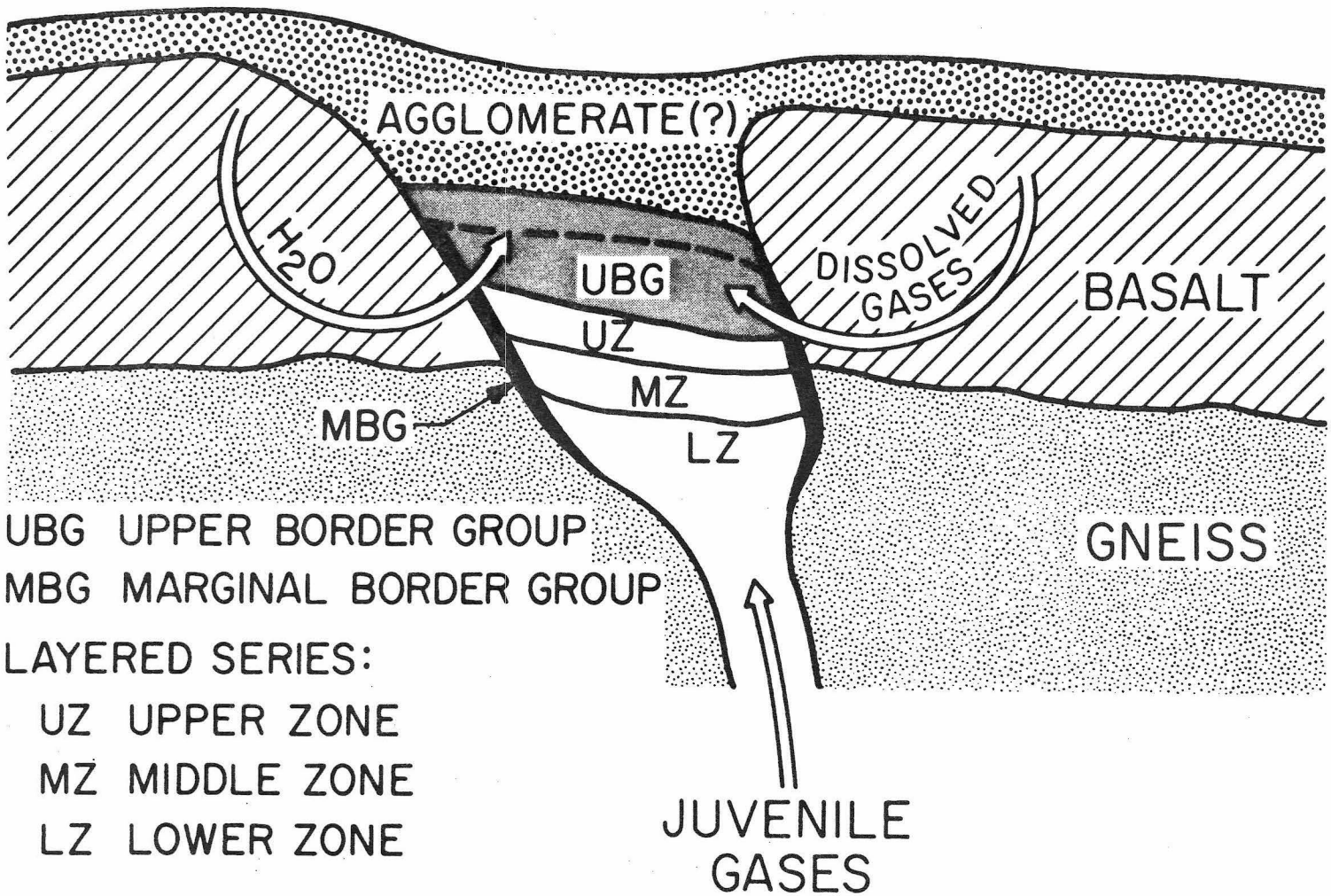

Figure 1

(Skaergaard)

Figure 2. Fractionation factor F^m for comparing elemental abundance patterns of the non-radiogenic noble gases in various samples. For air, $F^m = 1$ for all gases, and the abundance pattern is a horizontal line. Curves for water and molten enstatite (Kirsten, 1968) reflect the differential solubility of the different noble gases from an infinite reservoir of atmospheric composition.

NON-RADIOGENIC GASES

$$F^m = \left(\frac{^mX}{^{36}Ar}\right)_{SAMPLE} \Big/ \left(\frac{^mX}{^{36}Ar}\right)_{AIR}$$

$$^mX = {}^{20}Ne, {}^{36}Ar, {}^{84}Kr, {}^{132}Xe$$

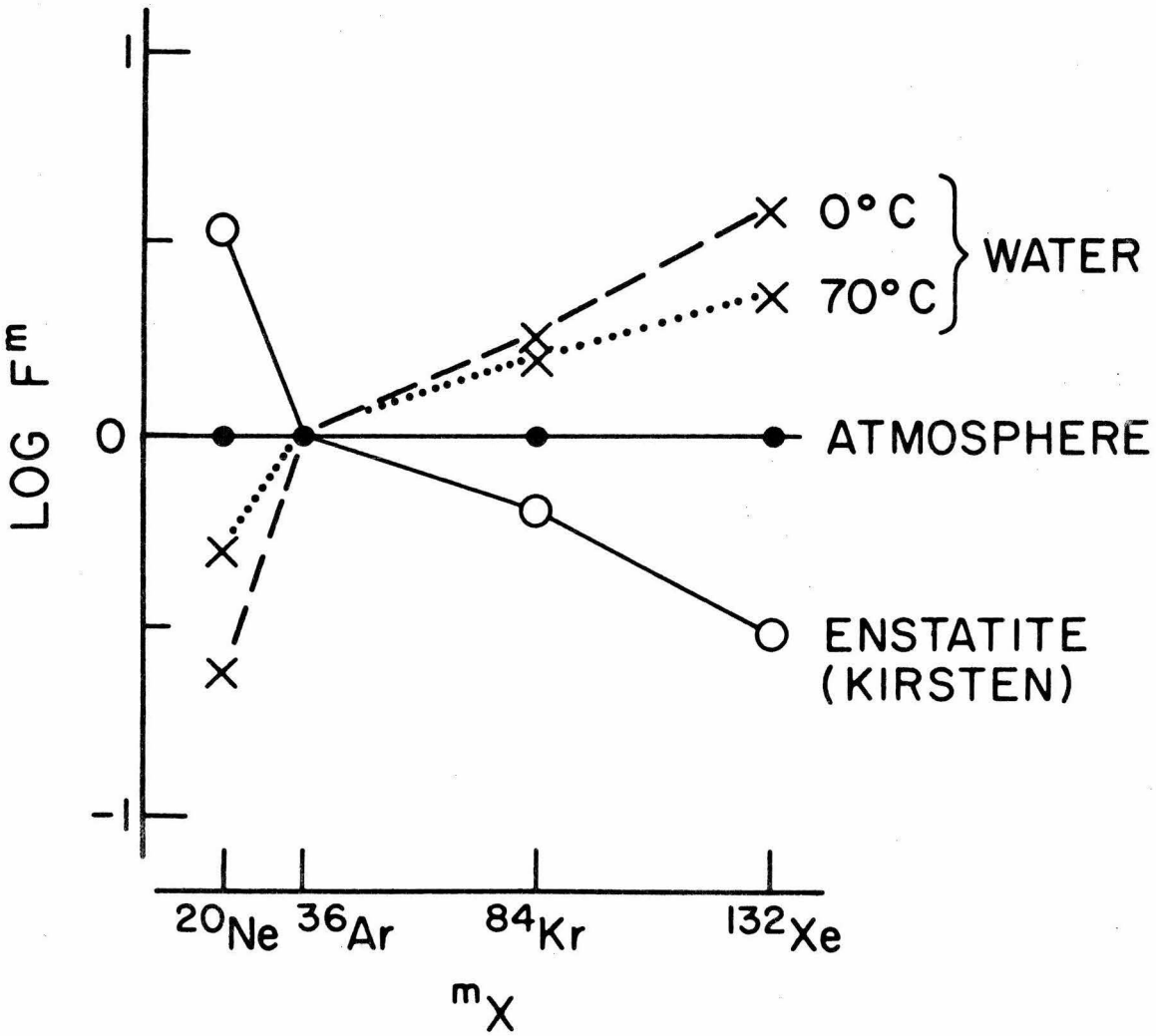

Figure 2
(Skaergaard)

Figure 3. Elemental abundance patterns for non-radiogenic noble gases in Skaergaard samples. A substantial range of patterns is seen. Observed $^{20}Ne/^{36}Ar$ ratios and $^{132}Xe/^{36}Ar$ ratios vary by about a factor of ten. The highest $^{132}Xe/^{36}Ar$ ratios are associated with the lowest $^{20}Ne/^{36}Ar$ ratios, and vice versa. Thus the abundance patterns range from the comparatively flat pattern for SKR 7 from the lower zone, to a very strongly fractionated pattern for SKR 12 from the sandwich horizon. There is little correlation of abundance pattern with original stratigraphic position in the intrusion. Samples from the lower zone (panels c and d) show both comparatively flat and comparatively steep abundance patterns.

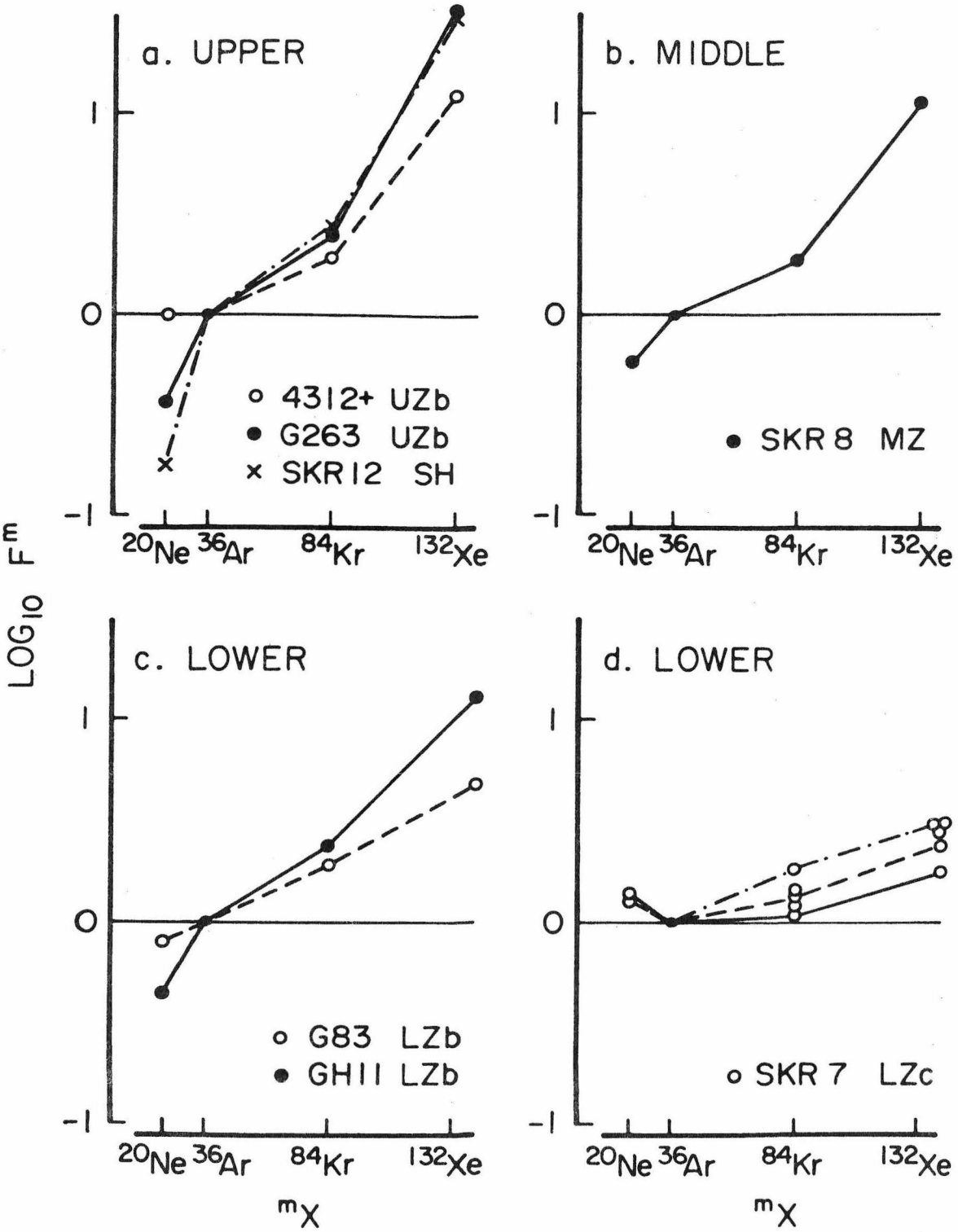

Figure 3

(Skaergaard)

Figure 4. Three-isotope correlation diagram for xenon in the Skaergaard samples. Data for SKR 7 are shown in the lower panel, and for the other samples in the upper. Error bars represent 2σ uncertainties. Mixtures of distinct components will plot on straight lines. Mixing lines for addition of ^{238}U fission xenon and ^{244}Pu fission xenon to atmospheric xenon are shown. Addition of radiogenic ^{129}Xe shifts a point vertically upward. The Skaergaard data are generally consistent with mixtures of air and ^{238}U fission xenon. The first sample of SKR 7 measured showed a ∿4% ^{129}Xe excess (Smith, 1978). Four subsequent samples from the same specimen failed to duplicate this isotopic effect, which is here withdrawn as an experimental artifact. Note that the 3% fission ^{136}Xe excess is reproducible among the SKR 7 samples. Sample 4312+ (upper panel) possibly shows a slight isotopic mass-fractionation not recognizable in any of the other samples.

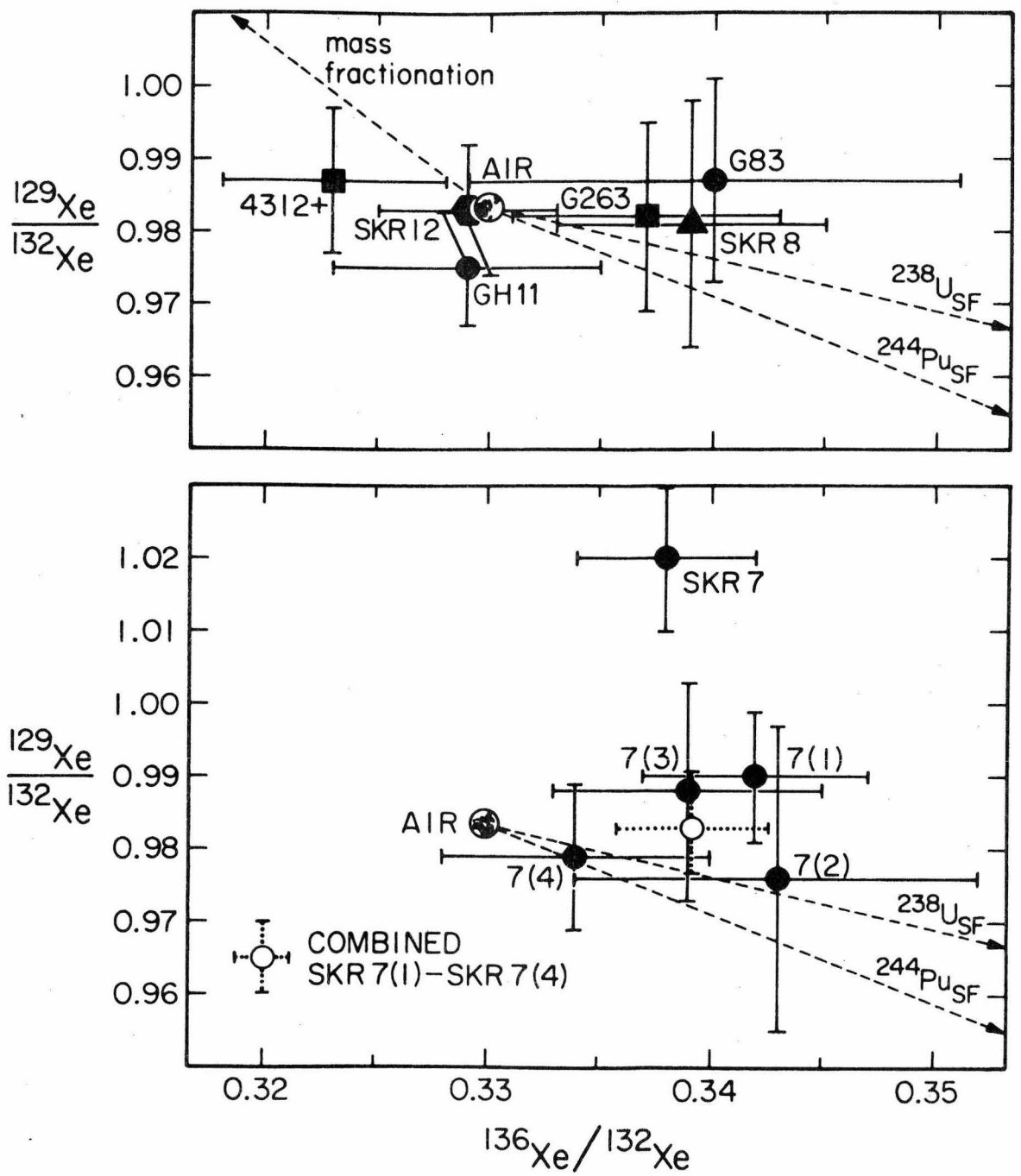

Figure 4

(Skaergaard)

Figure 5. Correlation of argon isotopic composition with oxygen isotope shift in the Skaergaard rocks. ^{40}Ar due to *in situ* decay of potassium has been subtracted from the total to give $^{40}Ar_{excess}$. ^{36}Ar is the total concentration of this isotope. Oxygen isotope data for plagioclase are from Taylor and Forester (1979). The errors shown for the argon compositions are 2σ. For SKR 12, SKR 8, and SKR 7, oxygen isotope shifts are estimated from known sampling localities. The probable uncertainty associated with the estimates is indicated by the vertical error bars.

Both the oxygen and argon isotopes reflect mixing of juvenile and meteoric (atmospheric) components. The heated meteoric water responsible for the oxygen isotope exchange has also introduced atmospheric argon into the rocks. The correlation is not linear. From the initial juvenile composition, $^{40}Ar/^{36}Ar$ drops rapidly by a factor of more than two, while $\delta^{18}O_{plag}$ shifts only by a few tenths ‰. Further exchange affects primarily the oxygen isotopes.

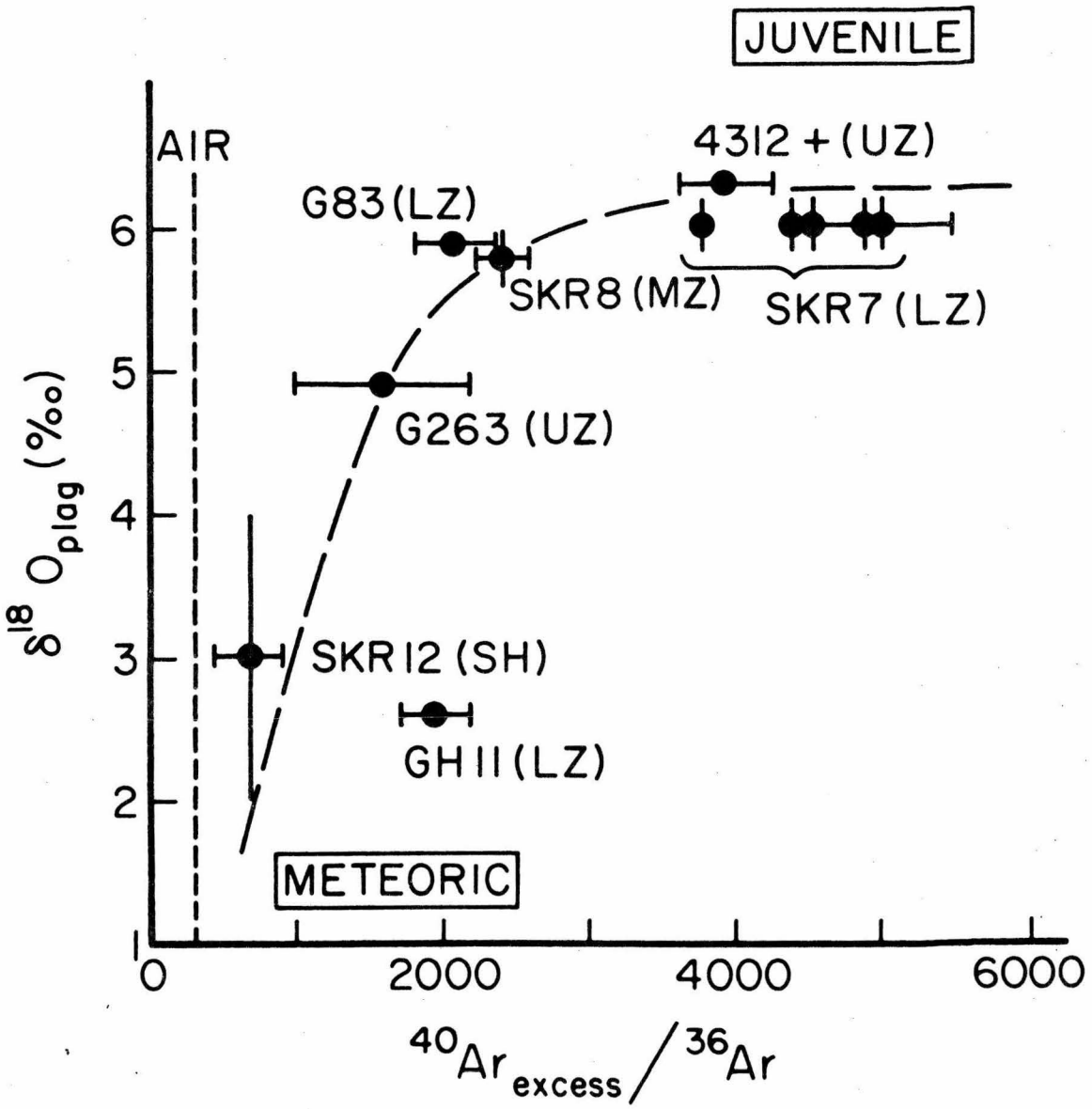

Figure 5

(Skaergaard)

PAPER 3. ATMOSPHERIC AND JUVENILE NOBLE GASES IN MOR VOLCANIC ROCKS AND RELATED SAMPLES

ATMOSPHERIC AND JUVENILE NOBLE GASES IN MOR VOLCANIC ROCKS AND RELATED SAMPLES

Stephen P. Smith and G. J. Wasserburg

The Lunatic Asylum of the Charles Arms Laboratory
Division of Geological and Planetary Sciences
California Institute of Technology
Pasadena, California 91125

Abstract

Ne, Ar, Kr, and Xe were measured in mid-ocean ridge (MOR) basalt and rhyodacite glasses, oceanic gabbro, and upper-mantle peridotite samples. A peridotite from Hawaii and the MOR basalt glasses contain excess radiogenic ^{40}Ar indicating the presence of juvenile noble gases from the upper-mantle. Three MOR basalts contain small excesses ($\sim 10^6$ atoms/gram) of ^{129}Xe presumably from the decay of short-lived ^{129}I, and fissiogenic ^{134}Xe and ^{136}Xe. This is the first evidence for $^{129}Xe_{rad}$ and fission xenon outgassing at oceanic spreading ridges.

No isotopic evidence is found for juvenile primordial Ne, Ar, Kr, or Xe in the samples. High $^{20}Ne/^{36}Ar$ ratios in MOR glasses are unaccompanied by significantly increased $^{20}Ne/^{22}Ne$ ratios, so cannot be due to the presence of solar primordial noble gases as suggested by Dymond and Hogan (1973). A non-atmospheric $^{20}Ne/^{22}Ne$ of 10.1 ± 0.1 observed in rhyodacite glass from the Galapagos is most likely due to mass-fractionation, not addition of primordial neon. Variations in $^{40}Ar/^{36}Ar$ by a factor of 7 coupled with essentially constant ^{40}Ar concentrations in several samples of a single MOR basalt glass from the Gulf of Aden provide clear evidence of the late-stage addition of atmospheric noble gases to the magma. This result suggests that most or all of the non-radiogenic noble gases in MOR basalt glasses (except helium) are due to atmospheric contamination, probably by seawater.

INTRODUCTION

The mid-ocean ridges (MOR) are sites of active transport of material from the upper mantle into the Earth's crust. The magmas erupted at the spreading ridges may contain dissolved noble gases extracted from their source regions. The rapid quenching by seawater of erupted MOR lavas can trap dissolved magmatic noble gases in the resulting glass. The magmatic gases may include a number of juvenile components, gases which have never been in the Earth's atmosphere. Among these are radiogenic ^{4}He, ^{40}Ar, and fission xenon produced by the decay of U, Th, and K in the mantle source region. The magma may contain primordial noble gases leaking out of incompletely degassed regions of the mantle. The decay products of short-lived radioactivities, ^{129}Xe from ^{129}I (17 m.y. half-life) and $^{131-136}Xe$ from fission of ^{244}Pu (82 m.y. half-life), may also arise from undegassed portions of the Earth. By studying fresh basalt glass rims from submarine pillow lava flows, we hope to gain information about the composition of noble gases in the upper mantle.

The transport of noble gases in the oceanic crust and upper mantle is likely to be more complicated than a simple, one-way flow. In Figure 1 we have sketched a possible picture of the cycling of noble gases in the oceanic crust/mantle system. A spreading ridge is illustrated on the right side of the figure, and a subduction zone on the left. At the ridge, the heat of the freshly-intruded magma establishes a hydrothermal circulation system. Cold seawater percolates down through fractures along the flank of the ridge, is heated, and emitted along the axis of the ridge in hydrothermal plumes (Weiss et al.,

1977). The seawater will carry dissolved atmospheric noble gases into the oceanic crust. Some of the dissolved gas may become trapped in the crust during hydrothermal alteration of the rocks. At the center of the ridge, exchange of noble gases between the magma and seawater may take place. Magmatic gases can be outgassed into the seawater, and transported into the oceans by the hydrothermal plumes. Atmospheric gases from seawater may be transferred into the magma.

At the subduction zone, the gases fixed in altered oceanic crust potentially can be drawn down into the upper mantle. The efficiency of such transport will depend on the unknown degree of gas loss at shallow levels from the subducting slab. This possible loss is indicated by the upward arrow with a question mark. Atmospheric gases may be adsorbed in sediments and trapped during diagenesis. If the sediments are subducted, they could provide an additional input of atmospheric noble gases into the upper mantle. If atmospheric gases are subducted into the upper mantle, they eventually may be transported by convection to beneath a spreading ridge. There they could be incorporated into newly-derived magma, and cycled back into the atmosphere along with any juvenile components in the magma.

During its ascent from the source region, the MOR lava may experience gas loss as the ambient pressure drops. Many MOR glass samples are vesicular, suggesting that a gas phase was being evolved prior to quenching. Noble gases will partition very strongly into a gas phase at equilibrium because of their low solubilities in the magma (Kirsten, 1968). Thus a magma that undergoes vesiculation before being erupted may lose a substantial fraction of its initial dissolved

noble gases. Absolute concentrations as a guide to conditions in the source must be interpreted with caution. Isotopic compositions and relative elemental concentrations are less affected by gas loss, so can provide more reliable information about the noble gases in the source.

In this paper we report measurements of the concentrations and isotopic compositions of neon, argon, krypton, and xenon in several MOR basalt glasses, an unusual rhyodacite glass from the Galapagos ridge, two peridotite nodules from Hawaii and Baja California, and two ocean crust gabbros. The MOR glass samples were studied with two main objectives in mind. The first was to discover if juvenile radiogenic ^{129}Xe or fission xenon could be detected in MOR lavas. Previous workers have shown that the glassy rims of MOR pillow basalts contain juvenile magmatic noble gases which include primordial ^{3}He (Krylov et al., 1974; Lupton and Craig, 1975) and excess radiogenic ^{40}Ar (e.g., Funkhouser et al., 1968; Fisher, 1971; Kaneoka, 1975; Dymond and Hogan, 1978). The second aim was to investigate the nature of any non-radiogenic noble gases in the MOR samples, and in particular to search for isotopic evidence of a primordial noble gas component in the magmas. Other investigators have generally found small amounts of non-radiogenic gases in MOR volcanic rocks, but the origin of these gases is unclear. Based on elemental abundance patterns, Dymond and Hogan (1973) and Fisher (1973, 1974) suggested the non-radiogenic isotopes were primordial gases from the mantle. These gases have alternatively been suggested to be due to atmospheric contamination near the ocean floor (Saito, 1978), or possibly from subduction of

atmospheric gases into the upper mantle (Smith, 1978).

Juvenile radiogenic and primordial noble gases were also sought in the peridotite samples. Earlier investigations have shown that some ultramafic nodules and minerals of upper mantle origin may contain juvenile excess ^{129}Xe (Hennecke and Manuel, 1975a; Rison and Kyser, 1977; Kaneoka et al., 1978). These materials often contain juvenile ^{3}He and excess radiogenic ^{4}He and ^{40}Ar (Funkhouser and Naughton, 1968; Tolstikhin et al., 1974; Saito et al., 1978a,b). The measurements on the two gabbro samples represent an initial investigation of the plutonic equivalent of the surface-erupted MOR basalts. While the gabbros cooled much more slowly than the quenched basalt glass samples, their crystallization at greater depth and pressure may enable them to trap ambient noble gases.

EXPERIMENTAL PROCEDURES

Noble gases were extracted from samples by heating to about 1500°C. Active gases were removed using hot Ti-Zr and Zr-Al getters, and the noble gases analyzed mass-spectrometrically using conventional techniques (Smith, 1979a; Smith and Wasserburg, 1979; Smith et al., 1977). Samples are described briefly in Table 1. Except where noted in the text, all glass samples analyzed were of fresh material without palagonite alteration. The material was generally crushed to about 0.1 to 1 mm diameter grains, and rinsed thoroughly in ethanol to remove finer particles. Sample masses ranged from about 0.06 to 1.8 grams. Samples were run in several groups at different times under slightly varying conditions. Sample groups are identified by the numbers in parentheses following the masses listed in Table 2. In

particular, we note that samples of group 2 were extracted in a clean crucible which had not been used previously to extract other samples. Samples in the other groups were generally analyzed during extraction sequences including several grams of various terrestrial rocks (Smith, 1978, 1979a,b; Smith and Wasserburg, 1979). Samples V33-07(0) and VGA11(a) of group 1 were melted in a crucible which had been used to extract two small meteorite samples containing excess ^{129}Xe, followed by several grams of terrestrial igneous rock. The rock samples showed no measurable isotopic anomalies and should have fluxed any meteoritic residues. However, it is not impossible for contamination to occur, since the amounts of xenon released by the MOR samples are quite small.

The tabulated data have been corrected for mass discrimination, extraction oven blanks, and interferences including $H_2{}^{18}O$, $^{40}Ar^{++}$, $CO_2{}^{++}$, HF, and neon and xenon hydrides. Extraction oven blanks varied by about a factor of 5 over the different run sequences, with average values about 0.5×10^{-14} moles ^{20}Ne, 1.3×10^{-15} moles ^{36}Ar, 0.4×10^{-16} moles ^{84}Kr, and 0.7×10^{-17} moles ^{132}Xe. Errors in the concentrations in Table 2 represent about 50% of the total background (extraction blank and interferences) subtracted from the measured signals. The spectrometer sensitivity and mass discrimination were monitored using a pipette of standard volume and atmospheric isotopic composition, and by comparison with meteorite standards from the Leedey and Bruderheim chondrites. Systematic uncertainty in the final calibrations is estimated to be about 15%.

RESULTS

Measured concentrations of ^{20}Ne, ^{36}Ar, ^{40}Ar, ^{84}Kr, and ^{132}Xe are reported in Table 2, in units of 10^{-16} mole/gram. The concentrations observed are with a few exceptions typically quite low. Ar, Kr, and Xe concentrations in MOR basalt glasses and ultramafic nodules average about an order of magnitude or more lower than in typical crustal igneous rocks (Smith, 1978, 1979a,b). Neon concentrations are similar. Noble gas contents of MOR basalt and peridotite samples are also generally much lower than the average whole-earth concentration obtained by dividing the amount of each gas in the atmosphere by the mass of the Earth (Table 2). Thus if the gas contents of these samples were characteristic of the interior of the Earth we could infer that $\geq$ 90% of the Earth's noble gases had been degassed. Since the samples may have lost gases during transport from their source regions, this inference may not be valid.

The Ar, Kr, and Xe concentrations vary by a factor of about twenty among the samples analyzed (excluding the Romanche gabbro, for which only xenon was measured). The ^{20}Ne concentration varies by a factor of 700 in toto, but most of the variation arises from the very high Ne contents of VG997, a rhyodacite glass from the Galapagos ridge. This unusual material contains 30 to 40 times more neon than the next most Ne-rich sample, VGA11, a basalt also from the Galapagos. High neon concentrations similar to that measured in VG997 have also been reported in MOR basalt glasses by Dymond and Hogan (1973), suggesting that the neon concentration in MOR volcanic rocks is more variable than the heavier noble gas contents. The variability of noble gas

concentrations extends to analyses made on several different samples of the same rock. The most remarkable example is the MOR basalt glass V33-07 from the Sheba Ridge, Gulf of Aden. The sample V33-07(2) contains nearly an order of magnitude less ^{36}Ar, Kr, and Xe than V33-07(3+4). Two other samples show intermediate gas contents. A similar variation in ^{36}Ar content is seen in the two samples of VGA11 basalt (Galapagos). Note, however, that the ^{40}Ar concentration in both V33-07 and VGA11 is much less variable than that of ^{36}Ar and the other noble gases. Possible reasons for this difference will be discussed in the next section.

The sample VG997(d) was intentionally selected to include a substantial mass of palagonitic alteration. The amount of alteration material is estimated to be roughly 100 times that in VG997(c1), which to the naked eye was free of palagonite. The factor of two increase for ^{36}Ar, ^{84}Kr, and about three for ^{132}Xe in VG997(d) may be associated with the alteration phases. Neon shows no significant increase. The increases in heavy noble gas content are far too small in relation to the estimated increase in palagonite content to allow a significant portion of the gases in VG997(c1) to be due to superficial alteration. Nor can the unusually high neon content of the rhyodacite reside in palagonite.

The ^{40}Ar contents of the different hand-picked mineral separates from the Hawaiian peridotite nodule fall in the middle or at the low end of the range from about 2×10^{-12} to 80×10^{-12} moles/gram measured by Funkhouser and Naughton (1968) and Gramlich and Naughton (1972) for a variety of similar mineral separates from Hawaiian ultramafic nodules.

The lower ^{40}Ar content of olivine relative to the co-existing phases (Table 2) appears to be characteristic of these samples (Funkhouser and Naughton, 1968; Gramlich and Naughton, 1972). Gramlich and Naughton suggested that the noble gas contents of some of the nodules had been lowered by diffusive gas loss during their transport to the Earth's surface. Such loss might well explain the low gas contents of the San Quintin nodule CSQ35-1A compared with the Hawaiian samples, since the CSQ35-1A nodule was only about 2 cm in diameter.

The relative abundances of ^{20}Ne, ^{36}Ar, ^{84}Kr, and ^{132}Xe are conveniently compared using the fractionation factor F^m,

$$F^m = \frac{(^mX/^{36}Ar)_{sample}}{(^mX/^{36}Ar)_{atmosphere}}$$

Figure 2 is a plot of $\log_{10} F^m$ vs. ^mX. The atmospheric abundance pattern is a horizontal line at log $F^m = 0$. On the left side of the figure we show several reference abundance patterns. These include solar and planetary components of primordial noble gases (Table 3). The solar pattern in Fig. 2 is obtained from the $^{20}Ne/^{36}Ar$ ratio measured in the solar wind (Geiss, 1973), together with values for Kr and Xe interpolated using nuclear abundance systematics (cf. Marti et al., 1972). The planetary pattern is characteristic of the noble gases measured in carbonaceous chondrites and gas-rich separates extracted from primitive meteorites. Also shown are abundance patterns for noble gases dissolved in water at 0°C (Mazor, 1977; crosses) and molten enstatite pyroxene at 1500°C (Kirsten, 1968; open circles) from an infinite reservoir of gas with atmospheric composition. The water

pattern is characterized by systematically increasing solubility for the heavier noble gases. For molten enstatite, the heavier gases are systematically less soluble.

On the right side of Fig. 2 we show the noble gas abundance patterns measured in this work. $^{20}Ne/^{36}Ar$ is substantially greater than the atmospheric ratio in many of the samples. The largest enhancement is a factor of nearly 1000 for the rhyodacite glass. $^{84}Kr/^{36}Ar$ and $^{132}Xe/^{36}Ar$ are also enriched relative to the atmospheric values, by factors of up to 2.6 and about 2.5 to 10 respectively. These concave-upward abundance patterns are similar to those found previously for MOR basalts (Dymond and Hogan, 1973) and ultramafic nodules from Hawaii (Hennecke and Manuel, 1975a; Kaneoka et al., 1978). The observed abundance patterns match none of the individual reference patterns completely. The relative abundances of ^{36}Ar, ^{84}Kr, and ^{132}Xe are generally similar to the pattern of noble gases dissolved in bottom seawater at close to °0C. The ^{20}Ne enrichments found here and by Dymond and Hogan (1973) are completely unlike the pattern expected for air dissolved in seawater. The $^{20}Ne/^{36}Ar$ ratios also show values too extreme to be consistent with solubility in a mafic melt similar to enstatite composition. Nor are the abundance patterns like either the planetary or solar primordial noble gas patterns. The relative concentrations of the noble gases in the MOR and peridotite samples apparently reflect contributions from a variety of sources and processes.

Isotopic data obtained for neon, argon, and krypton are given in Table 4 and for xenon in Table 5. Errors listed are 2σ and include

estimated uncertainties due to interferences and blanks. Atmospheric isotopic compositions are given at the bottom of each table. For neon, the measured isotopic compositions are atmospheric in most cases. The rather large uncertainties are due to the small amounts of gas available for analysis. There is a suggestion of small excesses of ^{21}Ne from (α,n) reactions on ^{18}O (Wetherill, 1954) in the pyroxenes from the Hawaiian peridotite nodule that might correlate with the relatively radiogenic high ^{40}Ar contents of these separates. Neon of clearly non-atmospheric composition is found in the rhyodacite VG997 from the Galapagos ridge. The $^{20}Ne/^{22}Ne$ ratio of 10.1±0.1 in this sample is about 3% higher than the atmospheric ratio 9.80±0.08. The $^{21}Ne/^{22}Ne$ ratio in VG997 is atmospheric within error.

The $^{40}Ar/^{36}Ar$ ratios measured in the samples are typically greater than atmospheric. For the MOR basalt glasses, the excess ^{40}Ar contents are too great to be due to <u>in situ</u> decay of ^{40}K in these very young samples, and must represent radiogenic ^{40}Ar from the source region of the magmas. The bulk of ^{40}Ar in the mineral separates from the Hawaiian peridotite nodule is also unsupported by <u>in situ</u> decay (cf. Funkhouser and Naughton, 1968). The radiogenic ^{40}Ar content of the Galapagos rhyodacite corresponds to an age of about 1/2 million years as calculated from the K_2O content of 1.32 wt.% (Melson, private communication) with the assumption that all ^{36}Ar is atmospheric. This is consistent with the sample's age of < 5 m.y. deduced from sea floor magnetic lineations (W. Melson, private communication) so radiogenic ^{40}Ar in VG997 can be attributed to <u>in situ</u> decay. Similarly, radiogenic argon in gabbro K9G1 from the Oman ophiolite is consistent with

in situ decay over the ~ 100 m.y. age of the ophiolite (R. Gregory, private communication).

Only limited measurements of $^{38}Ar/^{36}Ar$ ratios were made, and values obtained are consistent with the atmospheric composition. Kr isotopic compositions measured are also atmospheric.

Xenon isotopic compositions presented in Table 5 are generally close to atmospheric. In a number of cases, including the rhyodacite and peridotite samples, the small amounts of gas analyzed precluded obtaining precise isotopic compositions. For the Hawaiian peridotite, the xenon amounts measured for the different mineral separates were added to try to improve the precision. The resulting combined value is not significantly different from atmospheric. Xenon in the two gabbro samples was also found to be atmospheric. Small deviations from the air values are seen for $^{129}Xe/^{132}Xe$, $^{134}Xe/^{132}Xe$, and $^{136}Xe/^{132}Xe$ in the MOR basalt glass samples V33-07, TR138, and 111240. Xenon data for the basalt glasses are plotted in Figure 3 on a three-isotope correlation diagram of $^{129}Xe/^{132}Xe$ vs. $^{136}Xe/^{132}Xe$. In this diagram, addition of excess radiogenic ^{129}Xe displaces points vertically upward. Addition of spontaneous fission xenon from the decay of ^{238}U or short-lived ^{244}Pu displaces points downward and toward the right in the directions indicated by the dashed lines in Fig. 3. Excess radiogenic ^{129}Xe contents for a sample represented on the graph can be obtained by measuring its vertical displacement from the dashed mixing lines. E.g., for sample 111240, point (5) in Fig. 3, the displacement is .045 relative to ^{238}U fission and slightly larger for ^{244}Pu. Thus about 5% of the ^{129}Xe in this sample is excess radiogenic

xenon. In this work, we calculate the ^{129}Xe and ^{136}Xe excesses for glass samples V33-07, TR138, and 111240 (points (1), (2), and (5) respectively) by assuming the fission xenon component is from ^{238}U decay. If it is from ^{244}Pu, the calculated ^{129}Xe excesses will be slightly too low. We calculate the xenon excesses in this way rather than using ^{130}Xe as a measure of the fission-free component because of the larger error in the small ^{130}Xe signal. Significant excesses ($\sim 4\sigma$) are measured in the single sample of 111240 glass from the Juan de Fuca Ridge. The calculated excesses are 2.4×10^{-18} moles $^{129}Xe_r/g$ and 1.6×10^{-18} moles $^{136}Xe_{SF}/g$. Repeated measurements on samples from V33-07 appear to be consistent at roughly the 2σ level with average concentrations of about 1×10^{-18} moles/g radiogenic ^{129}Xe and about 2×10^{-18} moles/g fissiogenic ^{136}Xe. The xenon excesses for TR138 are smaller, 0.6×10^{-18} moles $^{129}Xe_r/g$ and 0.3×10^{-18} moles $^{136}Xe_{SF}/g$, and are also significant at about the 2σ level. The sample V33-07(0), which plots as the point labeled (1) directly above the air point in Fig. 3, is somewhat inconsistent with the other V33-07 determinations. It appears to show a concentration of excess $^{129}Xe_r$ similar to those for the other samples, but no $^{136}Xe_{SF}$ excess. The V33-07(0) sample was run in a crucible in which two meteorite samples had previously been run (see Experimental Procedures). It is possible that some contamination of this sample with meteoritic trapped xenon of unusually low $^{136}Xe/^{132}Xe$ could have occurred that would have had the effect of cancelling out the nominal $^{136}Xe_{SF}$ excess in this sample. As discussed by Smith (1979a), the measurement and certain identification of the small xenon anomalies

($\sim 10^6$ atoms per gram) in terrestrial samples are complicated in our case by the limited maximum sample size ($\sim$ 1 gram) and by possible effects of spectrometer memory in a machine which has in the past seen many meteorite samples with abundant anomalous xenon. At present we have no strong reason to doubt the validity of the $^{129}Xe_r$ and $^{136}Xe_{SF}$ excesses reported here, particularly for sample 111240, which was melted in a previously unused crucible. Further careful measurements on larger samples than could be examined here are needed to confirm these small xenon isotopic effects.

DISCUSSION

On the basis of elemental abundance patterns, Dymond and Hogan (1973) and Fisher (1973, 1974) have identified non-radiogenic noble gases in a number of MOR basalt glasses as juvenile primordial gases. We argue here that the elemental abundance patterns do not provide convincing evidence of the general presence of juvenile non-radiogenic gases in MOR basalts. We will examine the available isotopic data for clues to the origin of the non-radiogenic noble gases. Finally, we discuss the significance of the juvenile radiogenic component of argon and xenon found in the MOR samples and in other upper-mantle derived rocks.

Dymond and Hogan (1973) observed $^{36}Ar/^{20}Ne$ ratios in MOR basalts over 100 times lower than the atmospheric ratio, and inferred that the samples contained primordial gases resembling neon-rich solar primordial gases (Table 3). Neon isotopic data from this report can be used to rule out a component of solar primordial neon in MOR samples. In Figure 4 we plot $^{22}Ne/^{20}Ne$ vs. $^{36}Ar/^{20}Ne$ for MOR samples

studied here. Also shown are points representing solar and planetary primordial gases (Table 3) and the atmospheric composition. In this representation, mixtures of two distinct endpoint compositions will fall on the straight line segment joining the two endpoints. If the low $^{36}Ar/^{20}Ne$ ratios in MOR samples were due to admixture of solar primordial gases, data points would lie on the line shown joining the atmospheric and solar compositions. Because of the very low $^{22}Ne/^{20}Ne$ ratio in the solar gas, $^{22}Ne/^{20}Ne$ ratios would decrease noticeably. Clearly this is not the case; $^{22}Ne/^{20}Ne$ remains close to the atmospheric ratio despite observation of very low $^{36}Ar/^{20}Ne$ ratios that nominally imply the presence of essentially pure solar primordial gas. Either the $^{36}Ar/^{20}Ne$ variations are due to the addition of a previously unrecognized primordial component with nearly atmospheric $^{22}Ne/^{20}Ne$ and remarkably low $^{36}Ar/^{20}Ne$, or the source of the neon and argon is atmospheric gas that was highly fractionated during its transport from the atmosphere to the MOR glass samples. We regard the possibility that the neon and argon represent a new primordial component as remote. The unusually high neon content of the rhyodacite VG997 (sample 9) is unaccompanied by any significant amount of juvenile radiogenic ^{40}Ar. This excess argon is almost invariably present in MOR basalt magmas and signals the presence of juvenile noble gases escaping from depth. We conclude it is more likely that the neon has become fractionated relative to argon during transport in the terrestrial environment. We suggest the small $\sim 3\%$ isotopic enrichment of ^{20}Ne relative to ^{22}Ne in VG997 is related to the extreme elemental enrichment of neon over argon in this sample, and is not evidence of a

primordial component of neon. We also suggest the ~ 5% enrichment of ^{20}Ne in a fumarole gas sample from Kilauea (Craig and Lupton, 1976) similarly need not reflect the presence of primordial neon. The magnitudes of the isotopic effects are small, and easily explained by diffusive fractionation in a variety of settings. The mechanism responsible for fractionating neon and argon in MOR samples cannot be specified at present. Processes such as diffusion, Rayleigh distillation (via bubble formation), differential solubility, adsorption, etc., acting singly or in combination are possibilities.

Fisher (1973, 1974) inferred that samples from the Juan de Fuca Ridge and Vema Fracture Zone contained a component of primordial noble gases which he identified as planetary rather than solar on the basis of low $^{36}Ar/Kr$ and Kr/Xe ratios. Xenon is strongly enriched relative to argon in these samples compared with atmospheric abundances. A similar enrichment of Xe has been seen in ultramatic nodules and amphiboles of presumed upper mantle origin (Hennecke and Manuel, 1975a; Saito et al., 1978a,b), and has been interpreted as evidence of planetary primordial noble gases in the mantle. The uncertainties associated with interpreting the abundance patterns are illustrated by the contrasting conclusion of Saito (1978), that the non-radiogenic heavy noble gases in the MOR basalt glasses are fractionated samples of atmospheric gases dissolved in seawater. The question of the origin of these gases in MOR samples is difficult if not impossible to answer satisfactorily from elemental abundance patterns alone. Many processes may have affected the samples that are capable of fractionating the different gases. We therefore will consider further only isotopic

evidence for the nature of the MOR noble gases. We turn first to the well-studied example of argon, where isotopic variations are very large and unambiguous.

Argon isotopic data for MOR basalt samples have been summarized by Dymond and Hogan (1978). They conclude that variations in the argon isotopic composition among the samples are due to mixing air with a highly radiogenic mantle component having $^{40}Ar/^{36}Ar \gtrsim 16000$. Very similar variations are seen in the data reported here. In particular, $^{40}Ar/^{36}Ar$ and ^{36}Ar concentrations in the several samples of V33-07 differ by as much as a factor of about 7, while the ^{40}Ar content is virtually constant. Similar variability is seen in VGA11. The differences in V33-07 occur on a scale of roughly a centimeter or less. These data imply that atmospheric argon has been added very inhomogeneously to a magma containing a uniform Ar content of about 4.3×10^{-11} moles/gram excess radiogenic ^{40}Ar, and with $^{40}Ar/^{36}Ar \gtrsim 12000$. The small scale of the argon isotopic variations is remarkable. Fisher (1971) and Dymond and Hogan (1973, 1978) have documented argon isotopic variations paralleling the degree of crystallization across quenched rims of MOR basalt pillows. The variations are apparently due to incorporation of seawater atmospheric argon into the more crystallized portions of the rock. These variations are accompanied by loss of the initial excess radiogenic ^{40}Ar as the basalt crystallizes. This is possibly the cause of variability for basalt VGA11, where the radiogenic ^{40}Ar content of sample VGA11(0) is only about 40% that of VGA11(a) which has the higher $^{40}Ar/^{36}Ar$ ratio. However, for V33-07 samples, the radiogenic ^{40}Ar content is constant. Also, the degree of

crystallinity of the V33-07 material is low, ~ 5%. These observations strongly suggest the argon isotopic variations are not due to this mechanism of contamination. Vesicles ranging from microscopic size to about 1 millimeter in diameter indicate the presence of a gas phase in the V33-07 magma at the time of quenching. Unbroken vesicles possibly could be the site of the increased air argon contents of some samples. Possibly the vesicles were caused by incorporation of seawater containing dissolved noble gases during the eruption of the magma on the seafloor. Regardless of the exact location of the air argon, the small scale of the isotopic variations requires the contamination to have occurred late enough that diffusive homogenization with the indigenous magmatic argon did not occur.

It can be seen from the data in Table 2 that the increased atmospheric argon content of samples V33-07(1) and V33-07(3+4) is accompanied by increased amounts of krypton and xenon, to which we also ascribe an atmospheric origin. The absolute amounts of non-radiogenic gases in these and the other MOR basalt samples are not large, and can be explained by the addition of less than 0.1 wt.% seawater with its complement of dissolved atmospheric gases. For example, 10^{-4} grams of bottom seawater contains about 7×10^{-16} moles ^{20}Ne, 45×10^{-16} moles ^{36}Ar, 1.9×10^{-16} moles ^{84}Kr, and 0.13×10^{-16} moles ^{132}Xe. Evidence for the introduction of atmospheric argon into MOR magmas by seawater contamination has also been presented by Hart and Dymond (1978). These authors found decreasing $^{40}Ar/^{36}Ar$ with increasing H_2O contents of a suite of basalts from the Juan de Fuca Ridge.

We conclude from the above considerations that much of the

non-radiogenic argon, krypton, and xenon content of MOR basalt glass samples is due to late contamination of the magma with atmospheric noble gases. This does not mean necessarily that all the non-radiogenic noble gases in these samples are atmospheric. The most outstanding example of juvenile non-radiogenic gases in MOR basalts is the widespread ^{3}He excess (Craig and Lupton, 1976 and references therein). The observation of juvenile radiogenic ^{40}Ar and ^{129}Xe in mantle-derived samples demonstrates that juvenile components of the heavier noble gases are being transported to the Earth's surface. There is no a priori reason not to expect them to be accompanied by juvenile non-radiogenic gases. However, the clear evidence for atmospheric contamination leads us to suggest that the concentrations of juvenile non-radiogenic gases in uncontaminated MOR basalt magmas at the time they are quenched are generally lower than or equal to the lowest measured concentrations. Estimating from V33-07(2), VGA11(a), and TR138, we therefore suggest juvenile magmatic noble gas contents of less than or about 38×10^{-16} moles/g ^{36}Ar, 1.1×10^{-16} moles/g ^{84}Kr, and 0.2×10^{-16} moles/g ^{132}Xe. The case for neon is less clear since the mechanism producing the characteristic enrichment of neon in the MOR samples is not understood. We argue for the VG997 rhyodacite that the lack of any excess mantle-derived radiogenic ^{40}Ar in the rock with the largest neon enrichment suggests that the neon fractionation is also a relatively late, high-level effect. If this is so, then we might also take the lowest measured ^{20}Ne contents, about 90×10^{-16} moles/g, as an upper limit on the erupted magmatic neon concentration. These limits must be interpreted with some caution.

We have by no means ruled out the possibility of bulk gas loss from the MOR magma as it ascends from its source region into the oceanic crust. The limits refer only to the gas content of the magma when it was quenched. From various lines of evidence Dymond and Hogan (1978) and Lupton and Craig (1975) have suggested the magmas may have lost ^{40}Ar and ^{3}He prior to eruption on the ocean floor. Thus the concentration of non-radiogenic noble gases in the MOR basalt magma at depth must remain an open question at present.

There is no clear evidence from the isotopic data for juvenile primordial Ne, Ar, Kr, or Xe in mantle-derived samples. The most useful indicators should be the isotopic compositions of neon and xenon for which known solar or planetary primordial components in extraterrestrial samples differ substantially from the atmospheric composition. Because of the low gas concentrations in the MOR samples inferred to be the least affected by late atmospheric contamination, errors on isotopic compositions are large, and little can be concluded from the available data. Isotopic compositions have been determined with better precision for xenon in kaersutite amphibole (Saito et al., 1978a,b) and Hawaiian peridotite (Hennecke and Manuel, 1975a) of presumed mantle origin, and in CO_2 well gas (Phinney et al., 1978). Phinney et al. (1978) have proposed the presence of $\sim$ 6% of primordial xenon similar to meteoritic primordial xenon in the CO_2 well gas. However, the isotopic effects could equally well be explained by a slight mass-fractionation of atmospheric xenon. Both the kaersutite and peridotite have been suggested to contain primordial gases on the basis of elemental abundance patterns, but in both samples the isotopic

composition of non-radiogenic xenon is atmospheric. This raises the possibility that juvenile xenon from the mantle might have essentially the same composition as the atmosphere rather than as extraterrestrial primordial xenon (Saito et al., 1978a). Atmospheric and extraterrestrial primordial xenon differ primarily by a mass-dependent fractionation (e.g., Pepin and Phinney, 1979), but the nature and timing of the processes which resulted in the differentiation of the two compositions are unknown. It is possible that all the material from which the Earth formed was characterized by atmospheric composition xenon, so that juvenile xenon still trapped within the solid Earth is atmospheric. Unfortunately, this hypothesis cannot be easily distinguished from the possibility that the upper mantle has been contaminated by atmospheric xenon from subduction of altered oceanic crust (Smith, 1978, 1979a,b). We feel that at present there is no unambiguous evidence available that would indicate the Earth is actively degassing primordial non-radiogenic noble gases other than ^{3}He.

The juvenile radiogenic components that can be identified in MOR basalts and mantle-derived samples can provide information about the degree of homogeneity in the distribution of noble gases in the Earth. As a consequence of identifying most of the ^{36}Ar in MOR basalt glasses as atmospheric contamination, we can conclude that the mantle source region of the MOR magmas is most likely characterized by $^{40}Ar/^{36}Ar$ greater than about 10^{4}. High values have been reported for widely separated spreading ridges, including the East Pacific and Mid-Atlantic (Fisher, 1975) and the Sheba Ridge in the Gulf of Aden (this work). Similarly high ratios have been measured or inferred for

some ultramafic nodules of presumed upper mantle origin (Funkhouser and Naughton, 1968; Kaneoka et al., 1978). Thus a $^{40}Ar/^{36}Ar$ ratio $\geq 10^4$ may be characteristic of the mantle in some general way. As has been emphasized by many authors, and recently summarized by Bernatowicz and Podosek (1978), knowledge of the $^{40}Ar/^{36}Ar$ ratio of the mantle and its comparison with the atmospheric ratio provide significant constraints on models of the degassing history of the Earth. An important uncertainty in this modelling is the extent to which argon isotopic compositions measured in a limited suite of samples from possibly special locations are representative of the entire mantle, or only of particular zones in the mantle. For example, Hart and Dymond (1978) have suggested that argon in the atmosphere may have been derived from degassing of only the upper several hundred kilometers of the mantle. In this case the high $^{40}Ar/^{36}Ar$ ratios observed in MOR basalts and ultramafic nodules would result from thorough degassing of primordial ^{36}Ar from the upper mantle, coupled with in situ decay of ^{40}K. The $^{40}Ar/^{36}Ar$ ratio in a deeper undegassed portion of the mantle could be much lower.

Differences among argon isotopic compositions measured in ultramafic nodules and xenocrysts from the upper mantle have led to the suggestion of significant heterogeneity in the distribution of argon isotopes in the mantle (Kaneoka et al., 1978; Rison and Kyser, 1977; Saito et al., 1978a; Bernatowicz and Podosek, 1978). For example, in contrast with the high $^{40}Ar/^{36}Ar$ ratios $\geq 10^4$ in some MOR basalts and mantle nodules, $^{40}Ar/^{36}Ar$ ratios measured in kaersutite amphiboles of possible mantle origin are close to the atmospheric ratio

(Saito et al., 1978a,b). In particular, when allowance is made for possible in situ production of ^{40}Ar in a specimen from New Zealand, the $^{40}Ar/^{36}Ar$ ratio of the remaining gas is significantly below atmospheric (Saito et al., 1978a). As discussed by Saito et al., such a low ratio requires a source region of unusually low $K/^{36}Ar$ ratio, possibly due to preferential loss of K over primordial argon from some region of the mantle. Alternatively, some of the differences in $^{40}Ar/^{36}Ar$ in these materials could be due to varying contamination of the upper mantle by atmospheric noble gases. It can be shown (Smith, 1978, 1979a,b) that a significant concentration of atmospheric Ar, Kr, and Xe can be injected into the upper few hundred kilometers of the mantle by subduction of metamorphosed oceanic crust with noble gas contents similar to those reported here for gabbros K9G1 from the Oman ophiolite and 110753/82 from the Romanche trench, and for crystalline MOR diabase samples studied by Dymond and Hogan (1973). The unusually low $^{40}Ar/^{36}Ar$ ratio inferred for the New Zealand kaersutite could possibly reflect contamination by ancient atmospheric argon which should be characterized by lower $^{40}Ar/^{36}Ar$ ratios than the modern value (e.g., Bernatowicz and Podosek, 1978; Kaneoka, 1975).

The present results suggest that MOR basalt glasses from spreading ridges in the Gulf of Aden, Atlantic and Pacific Oceans contain small excesses of radiogenic ^{129}Xe and fissiogenic $^{131-136}Xe$ in addition to excess radiogenic ^{40}Ar. Similar xenon isotopic excesses have been found in ultramafic nodules (Hennecke and Manuel, 1975a; Rison and Kyser, 1977; Kaneoka et al., 1978)
and CO_2-rich natural gas from wells in New Mexico (Butler et al., 1963;

Hennecke and Manuel, 1975b; Phinney et al., 1978). Like the excess radiogenic ^{40}Ar in MOR basalts, these xenon isotopic components can unambiguously be identified as juvenile gases from a deep source. If the excess radiogenic ^{129}Xe was formed by in situ decay of short-lived ^{129}I in the upper-mantle source regions, then they cannot have been completely degassed since about 4.4 billion years ago. On the other hand, it is possible that the radiogenic ^{129}Xe is being transported into a previously degassed upper mantle from an ancient source in the lower mantle. Comparison of $^{129}Xe_r$ excesses and ^{244}Pu fission xenon potentially can be very informative. Since both were produced early in the Earth's history, significant variations in the ratio of these two components in modern juvenile gases would require the maintenance of separate unhomogenized reservoirs of xenon within the Earth over its entire history. More high-precision xenon isotopic data than are presently available are needed to assess the variability of the terrestrial distribution of these xenon components.

CONCLUSIONS

The mantle-derived samples studied here contain mixtures of atmospheric and juvenile noble gas components. The identifiable juvenile components of neon, argon, krypton, and xenon are restricted to radiogenic isotopes. Excess radiogenic ^{40}Ar is found in Hawaiian peridotite, and is very characteristic of MOR basalt glass. We also find small excesses of radiogenic ^{129}Xe and fissiogenic xenon isotopes in several of the MOR basalt glasses studied.

An earlier suggestion by Dymond and Hogan (1973) that the high neon content of MOR volcanic glasses could be due to the addition of

solar primordial gases can be ruled out. Data reported here show that in samples with nominally solar proportions of neon and ^{36}Ar, the neon isotopic compositions are not solar, but instead are close to atmospheric. We conclude that the neon in these samples is atmospheric neon that has been fractionated relative to argon during transport of the gases. In the VG997 rhyodacite, this fractionation has resulted in a 3% isotopic enrichment of ^{20}Ne relative to ^{22}Ne.

Argon concentrations and isotopic compositions in MOR basalt glass provide clear evidence for late-stage addition of atmospheric noble gases to MOR magmas on a very small ($\leq$ cm) scale, probably by contamination with seawater. In many samples the non-radiogenic argon, krypton, and xenon isotopes are dominated by this atmospheric contamination. The ratio of excess radiogenic ^{40}Ar to ^{36}Ar in uncontaminated magmas, and therefore their upper-mantle source, is probably greater than 1.5×10^4. The concentrations of the non-radiogenic, heavy noble gases in uncontaminated magmas just prior to eruption are very low, and could be absent. Some gas-loss from the magma may have occurred during its ascent from the mantle. No isotopic evidence was found for primordial, non-radiogenic neon, argon, krypton, or xenon in the samples examined.

Acknowledgments

We sincerely thank the donors listed in Table 1 who generously provided samples measured for this report. This work was supported by an institutional grant for energy research by the Ford Motor Company to the California Institute of Technology and by grant EY-76-G-03-1305 from the U. S. Department of Energy.

REFERENCES

Bernatowicz T. J. and Podosek F. A. (1978) Nuclear components in the atmosphere. In Terrestrial Rare Gases (eds. E. C. Alexander, Jr. and M. Ozima) pp. 99-135. Center for Academic Publications Japan.

Butler W. A., Jeffery P. M., Reynolds J. H., and Wasserburg G. J. (1963) Isotopic variations in terrestrial xenon. J. Geophys. Res. 68, 3283-3291.

Craig H. and Lupton J. E. (1976) Primordial neon, helium, and hydrogen in oceanic basalts. Earth Planet. Sci. Lett. 31, 369-385.

Dymond J. and Hogan L. (1973) Noble gas abundance patterns in deep-sea basalts--primordial gases from the mantle. Earth Planet. Sci. Lett. 20, 131-139.

Dymond J. and Hogan L. (1978) Factors controlling the noble gas abundance patterns of deep-sea basalts. Earth Planet. Sci. Lett. 38, 117-128.

Fisher D. E. (1971) Incorporation of Ar in East Pacific basalts. Earth Planet. Sci. Lett. 12, 321-324.

Fisher D. E. (1973) Primordial rare gases in the deep Earth. Nature 244, 344-345.

Fisher D. E. (1974) The planetary primordial component of rare gases in the deep Earth. Geophys. Res. Lett. 1, 161-164.

Fisher D. E. (1975) Trapped helium and argon and the formation of the atmosphere by degassing. Nature 256, 113-114.

Funkhouser J. G., Fisher D. E., and Bonatti E. (1968) Excess argon in deep-sea rocks. Earth Planet. Sci. Lett. 5, 95-100.

Funkhouser J. G. and Naughton J. J. (1968) Radiogenic helium and argon in ultramafic inclusions from Hawaii. J. Geophys. Res. 73, 4601-4607.

Geiss J. (1973) Solar wind composition and implications about the history of the solar system. Invited paper, 13th Int. Cosmic Ray Conf., Denver.

Gramlich J. W. and Naughton J. J. (1972) Nature and source material for ultramafic minerals from Salt Lake Crater, Hawaii, from measurement of helium and argon diffusion. J. Geophys. Res. 77, 3032-3042.

Hart R. and Dymond J. (1978) The argon isotopic composition of the oceanic crust and a model for formation of the sialic crust--atmosphere from the upper mantle. In Short Papers of the 4th International Conference on Geochemistry, Cosmochemistry, and Isotope Geology (ed. R. E. Zartman) pp. 172-174. U. S. Geol. Surv. Open File Report 78-701.

Hennecke E. W. and Manuel O. K. (1975a) Noble gases in an Hawaiian xenolith. Nature 257, 778-780.

Hennecke E. W. and Manuel O. K. (1975b) Noble gases in CO_2 well gas, Harding County, New Mexico. Earth Planet. Sci. Lett. 27, 346-355.

Kaneoka I. (1975) Non-radiogenic argon in terrestrial rocks. Geochem. J. 9, 113-124.

Kaneoka I., Takaoka N., and Aoki K. (1978) Rare gases in mantle-derived rocks and minerals. In Terrestrial Rare Gases (eds. E. C. Alexander, Jr. and M. Ozima) pp. 71-83. Center for Academic Publications Japan.

Kirsten T. (1968) Incorporation of rare gases in solidifying enstatite melts. J. Geophys. Res. 73, 2807-2810.

Krylov A. Ya., Mamyrin B. A., Khabarin L. A., Mazina T. I., and Silin Yu. I. (1974) Helium isotopes in ocean-floor bedrock. Geochemistry Int. 11, 839-844.

Lupton J. E. and Craig H. (1975) Excess ^{3}He in oceanic basalts: evidence for terrestrial primordial helium. Earth Planet. Sci. Lett. 26, 133-139.

Marti K., Wilkening L. L., and Suess H. E. (1972) Solar rare gases and the abundances of the elements. Astrophys. J. 173, 445-450.

Mazor E. (1977) Geothermal tracing with atmospheric and radiogenic noble gases. Geothermics 5, 21-36.

Mazor E., Heymann D., and Anders E. (1970) Noble gases in carbonaceous chondrites. Geochim. Cosmochim. Acta 34, 781-824.

Pepin R. O. and Phinney D. (1979) Components of xenon in the solar system. Geochim. Cosmochim. Acta. Submitted for publication.

Phinney D. L., Frick U., and Reynolds J. H. (1976) Rare-gas-rich separates from carbonaceous chondrites (abstract). In Lunar Science VII, pp. 691-693. The Lunar Science Institute.

Phinney D., Tennyson J., and Frick U. (1978) Xenon in CO_2 well gas revisited. J. Geophys. Res. 83, 2313-2319.

Rison W. and Kyser K. (1977) Rare gases, oxygen and hydrogen in Hawaiian xenoliths and basalts (abstract). EOS Trans. Amer. Geophys. Union 58, 537.

Saito K. (1978) Classification and generation of terrestrial rare gases. In Terrestrial Rare Gases (eds. E. C. Alexander, Jr. and M. Ozima) pp. 145-153. Center for Academic Publications Japan.

Saito K., Basu A. R., and Alexander E. C., Jr. (1978a) Planetary type rare gases in an upper mantle-derived amphibole. Earth Planet. Sci. Lett. 39, 274-280.

Saito K., Alexander E. C., Jr.,and Basu A. R. (1978b) Rare gases in mantle-derived amphiboles. In Short Papers of the 4th International Conference on Geochemistry, Cosmochemistry, and Isotope Geology (ed. R. E. Zartman) pp. 368-370. U. S. Geol. Surv. Open File Report 78-701.

Smith S. P. (1978) Noble gases in plutonic igneous rocks. In Short Papers of the 4th International Conference on Geochemistry, Cosmochemistry, and Isotope Geology (ed. R. E. Zartman) pp. 400-402. U. S. Geol. Surv. Open File Report 78-701.

Smith S. P. (1979a) Atmospheric and juvenile noble gases in the Skaergaard layered igneous intrusion. In preparation.

Smith S. P. (1979b) Studies of noble gases in meteorites and in the Earth. Doctoral dissertation, California Inst. of Tech.

Smith S. P., Huneke J.C., Rajan R. S., and Wasserburg G. J. (1977) Neon and argon in the Allende meteorite. Geochim. Cosmochim. Acta 41, 627-647.

Smith S. P. and Wasserburg G. J. (1979) Noble gases in beryl. In preparation.

Tolstikhin I. N., Mamyrin B. A., Khabarin L. B., and Erlikh E. N. (1974) Isotope composition of helium in ultrabasic xenoliths from volcanic rocks of Kamchatka. Earth Planet. Sci. Lett. 22, 75-84.

Weiss R. F., Lonsdale P., Lupton J. E., Bainbridge A. E., and Craig H. (1977) Hydrothermal plumes in the Galapagos Rift. Nature 267, 600-603.

Wetherill G. W. (1954) Variations in the isotopic abundances of neon and argon extracted from radioactive minerals. Phys. Rev. 96, 679-683.

Table 1. Sample Descriptions

(1) V33-07 64D-5g source: J.-G. Schilling U. of Rhode Island	West Sheba Ridge, Gulf of Aden 13°20.2'N 50°41.5'W 3440-3110 meters depth	Fresh basalt glass, slightly vesicular.
(2) TR138 7D-sg source: J.-G. Schilling	Mid Atlantic Ridge (central rift) 50°27.5'N 29°25.4'W 3800-3960 meters	Fresh basalt glass, slightly vesicular.
(3) VG212 USNM 111308/58-27 source: W.G. Melson Smithsonian-USNM	MAR intersection with Vema Fracture Zone 09°36'N 40°39'W 3340-2475 meters	Basalt glass, moderate palagonite. Abundant 1-5 mm equant plagioclase phenocrysts.
(4) USNM 113087 source: W.G. Melson	Juan de Fuca Ridge 44°40'N 130°20'W 2195-2220 meters	Fresh basalt glass, slightly vesicular (5 mm thick rim on pillow).
(5) USNM 111240/195 source: W.G. Melson	Juan de Fuca Ridge (N.E. Pacific) 44°40'N 130°20'W 2195-2220 meters	Fresh basalt glass, slightly vesicular with rare 1 mm plagioclase phenocrysts.
(6) VGA11 USNM 113152.D121 source: W.G. Melson, from donor: P. Vogt U.S. Navy Oceanographic Office	Galapagos Ridge 00°42.3'N 85°30.0'W 1380 fathoms (uncorrected)	Fresh basalt glass, slightly vesicular. High iron, titanium.
(7) USNM 110753/82 source: W.G. Melson	Romanche Trench	Gabbro, coarse grained (~5 mm) enclave in brecciated host gabbro.
(8) K9G1 source: R.T. Gregory Caltech	Samail Ophiolite near Ibra, Sultanate of Oman	Fresh cumulate gabbro.
(9) VG997 USNM 113155.D612 source: W.G. Melson, from P. Vogt	Galapagos Ridge 02°41.9'N 95°14.5'W 1420 fathoms (uncorrected)	"Rhyolite" (Rhyodacite) Vesicular, abundant tabular plagioclase phenocrysts.
(10) CSQ 35-1 source: collected	San Quintin, Baja California, Mexico	Peridotite nodule, 2 cm. dia., unoxidized.
(11) HAW source: R.F. Dymek Harvard U.	Hawaii	Peridotite nodule, ~20 cm. dia.

Table 2. Noble gas concentrations in MOR and related samples.[a]

Sample	Mass[b] (grams)	^{20}Ne	^{36}Ar	^{40}Ar	^{84}Kr	^{132}Xe
BASALT						
V33-07(0) (Sheba, G. of Aden)	1.1225 (1)	89 ± 30	150 20	422000 6000	4.6 .5	0.29 .02
V33-07(a)	1.1378 (2)	- ±	-	-	-	0.73 .02
V33-07(1)	1.0427 (6)	86 ± 30	210 20	500000 5000	11.3 .9	1.59 .09
V33-07(2)	0.9956 (6)	- ±	39 15	455000 5000	1.13 .60	0.29 .09
V33-07(3+4)	1.7935 (6)	120 ± 20	300 10	540000 5000	16.0 .6	1.87 .08
TR138 (Mid-Atlantic)	1.0019 (2)	- ±	-	-	-	0.13 .02
VG212(0) (Vema F.Z.)	0.2089 (3)	270 ± 40	170 20	142000 13000	-	-
VG212(a)	0.0560 (4)	- ±	160 50	234000 15000	3.3 3.1	0.36 .36
VG212(b)	0.9590 (2)	- ±	-	-	-	0.64 .04
113087 (Juan de Fuca)	0.2039 (3)	350 ± 50	190 20	79000 7000	-	-
111240 (Juan de Fuca)	0.9992 (2)	- ±	-	-	-	0.51 .03
VGA11(0) (Galapagos)	0.2098 (3)	890 ± 50	220 20	111000 8000	-	-
VGA11(a)	0.9748 (1)	470 ± 80	37 9	155000 4000	1.1 .2	0.24 .02
GABBRO						
110753/82 (Romanche Trench)	0.9720 (2)	- ±	-	-	-	8.0 .1
K9G1 (Oman Ophiolite)	0.9379 (6)	280 ± 60	630 10	195000 5000	24.3 .5	2.1 .1

Table 2. (continued)

Sample	Mass[b] (grams)	^{20}Ne	^{36}Ar	^{40}Ar	^{84}Kr	^{132}Xe
RHYODACITE						
VG997(0) (Galapagos)	0.1909 (3)	40400 ± 1700	83 15	27000 4000	-	-
VG997(a)	0.1339 (4)	- ±	140 100	53000 27000	3.8 1.5	0.44 .33
VG997(c1)	0.2995 (5)	25700 ± 300	130 20	49000 9000	3.2 .8	0.42 .30
VG997(d)	0.2765 (5)	27400 ± 300	250 20	88000 6000	7.1 .6	1.38 .11
PERIDOTITE						
CSQ35-1A (San Quintin, Baja Ca.)	0.9188 (5)	56 ± 20	31 5	28000 5000	1.0 .3	0.20 .05
HAW (Hawaii)						
Olivine	0.1811 (4)	- ±	180 60	71000 18000	9.5 8.0	1.1 .6
Orthopyroxene	0.8047 (5)	150 ± 20	210 10	220000 7000	5.7 .5	0.46 .04
Orthopyroxene(a)	0.4382 (5)	240 ± 40	320 10	249000 5000	13.1 .5	1.72 .07
Clinopyroxene	0.4817 (5)	170 ± 40	250 10	403000 5000	8.0 .5	0.66 .05
Clinopyroxene(a)	0.4703 (5)	-	incomplete extraction			-
Spinel	0.3092 (5)	270 ± 50	240 20	135000 6000	11.2 .9	1.44 .11
ATMOSPHERE		5020	9610	2840000	198	7.18

[a] Concentrations in 10^{-16} moles/gram. Errors represent 50% of the subtracted blank correction. Systematic calibration error estimated ≤ 15%.

[b] Numbers in parentheses following masses are run groupings (samples run at the same time). Relative calibration errors for samples of one group are estimated to be 5 to 10%.

Table 3. Primordial and atmospheric noble gas components.

	^{3}He	^{20}Ne	^{36}Ar	^{84}Kr	^{132}Xe
"Planetary"					
CII[1]	$7x10^{-3}$	0.28	≡ 1	$1.25x10^{-2}$	$1.04x10^{-2}$
carbon[2]	$7x10^{-3}$	0.21	≡ 1	$.93x10^{-2}$	$1.09x10^{-2}$
"Solar"					
solar wind[3]	6.8	28	≡ 1	-	-
cosmic[4]	1.9	40	≡ 1	$4.0x10^{-4}$	$4.0x10^{-5}$
"Atmospheric"	$2.33x10^{-7}$	0.523	≡ 1	$2.06x10^{-2}$	$7.47x10^{-4}$

[1]Mazor *et al.* (1970) CII chondrites (p.811).
[2]Phinney *et al.* (1976) "carbon" residues from carbonaceous chondrites.
[3]Geiss (1973)
[4]Marti *et al.* (1972) $^{3}He/^{4}He$ assumed $1.2x10^{-4}$.

Table 4. Neon, argon, and krypton isotopic compositions.

Sample	$\frac{^{20}Ne}{^{22}Ne}$	$\frac{^{21}Ne}{^{22}Ne}$	$\frac{^{38}Ar}{^{36}Ar}$	$\frac{^{40}Ar}{^{36}Ar}$	$\frac{^{83}Kr}{^{84}Kr}$	$\frac{^{86}Kr}{^{84}Kr}$
BASALT						
V33-07(0)	-	-	0.186 ±.002	2790 ± 400	-	0.305 ±.003
V33-07(1)	11.1 ± 5.4	0.087 ± .196	-	2380 ± 250	-	
V33-07(2)	-	-	-	11700 ±6700	-	-
V33-07(3+4)	9.9 ± 2.0	-	-	1790 ± 80	-	-
VG212(0)	10.3 ± 1.8	0.038 ± .022	-	846 ± 90	-	-
VG212(a)	-	-	-	1450 ± 150	-	0.313 ±.010
113087	9.97 ± .94	0.039 ± .018	-	421 ± 25	-	-
VGA11(0)	9.90 ± .60	0.037 ± .014	-	516 ± 40	-	-
VGA11(a)	10.00 ± .30	0.031 ± .008	0.191 ±.003	4100 ±2600	-	0.303 ±.009
GABBRO						
K9G1	10.1 ± 2.6	0.070 ± .076	-	310.1 ± 6.3	-	-
RHYODACITE						
VG997(0)	10.00 ± .10	0.031 ± .008	-	324 ± 15	-	-
VG997(a)	-	-	-	365 ± 40	-	0.304 ±.015
VG997(c1)	10.09 ± .14	0.0287 ± .0012	-	384 ± 40	-	-
VG997(d)	10.22 ± .16	0.0298 ± .0012	0.185 ±.010	360 ± 20	0.202 ±.008	0.304 ±.010

Table 4. (continued)

Sample	$\frac{^{20}Ne}{^{22}Ne}$	$\frac{^{21}Ne}{^{22}Ne}$	$\frac{^{38}Ar}{^{36}Ar}$	$\frac{^{40}Ar}{^{36}Ar}$	$\frac{^{83}Kr}{^{84}Kr}$	$\frac{^{86}Kr}{^{84}Kr}$
PERIDOTITE						
CSQ-35-1A	10.7 ± 3.6	0.053 ± .026	-	890 ± 250	-	-
HAW						
Olivine	-	-	-	395 ± 80	-	-
Opx	10.7 ± 1.2	0.060 ± .014	-	1040 ± 100	-	-
Opx(a)	10.3 ± 1.2	0.038 ± .022	0.193 ± .010	770 ± 50	0.203 ± .007	0.308 ± .011
Cpx	10.5 ± 2.4	0.045 ± .018	-	1620 ± 100	-	-
Spinel	9.8 ± 1.4	0.029 ± .020	0.187 ± .019	590 ± 50	0.203 ± .009	0.306 ± .012
ATMOSPHERE	9.80	0.0290	0.187	296	0.202	0.305
SOLAR	13.7	0.033	0.187	< 1		

Table 5. Xenon isotopic compositions in MOR and related samples.

Sample	^{124}Xe	^{126}Xe	^{128}Xe	^{129}Xe	^{130}Xe	^{131}Xe	^{134}Xe	^{136}Xe
	($^{132}Xe \equiv 1000$)							
BASALT								
V33-07(0)	2.2	3.5	74.9	1035	154	778	390	331
	±2.1	1.7	4.4	12	9	14	8	7
V33-07(a)	4.3	4.3	75.5	996	152	809	402	342
	±1.7	1.6	6.5	14	4	12	8	7
V33-07(1)	4.3	2.6	69.4	967	149	792	402	345
	±1.8	1.4	2.7	16	4	21	13	13
V33-07(2)	4.1	≤ 4	66.9	986	150	790	413	374
	±4.9		5.3	30	14	39	23	20
V33-07(3+4)	4.3	3.2	69.8	988	150	790	389	335
	± .9	.6	2.3	9	4	10	6	7
TR138	1	4	72	1029	155	788	401	354
	±12	11	27	44	17	39	26	25
VG212(b)	4.2	4.0	69	981	147	797	386	335
	±2.0	1.8	12	20	5	16	11	12
111240	4.8	4.9	67	1016	150	812	399	350
	±2.4	2.8	10	27	7	11	8	7
VGA11(a)	5.3	2.9	70.4	974	154	784	388	330
	±2.4	2.6	4.0	23	7	15	8	8
GABBRO								
110753/82	3.46	3.56	70.7	981.0	151.5	793.1	387.4	332.4
	± .30	.33	2.2	4.9	1.6	4.0	2.3	2.9
K9G1 (OMAN)	3.4	3.7	71.2	984	151	795	387	327
	±1.8	1.6	2.2	14	4	16	7	8
RHYODACITE								
VG997(d)	-	-	70	940	151	777	394	326
			±10	40	15	27	25	23

Table 5. (continued)

Sample	^{124}Xe	^{126}Xe	^{128}Xe	^{129}Xe	^{130}Xe	^{131}Xe	^{134}Xe	^{136}Xe
				($^{132}Xe \equiv 1000$)				
PERIDOTITE								
CSQ35-1A	-	-	100 ± 30	970 70	160 40	780 50	360 50	290 40
HAW								
Opx	-	-	70 ± 14	995 31	145 16	773 22	383 17	327 14
Opx(a)	-	-	70 ± 8	974 22	144 8	778 28	395 13	330 15
Cpx	-	-	72 ± 28	983 44	156 26	782 34	368 40	314 22
Cpx(a)	-	-	70 ± 15	1011 51	145 16	751 22	386 19	333 13
Spinel	-	-	77 ± 11	986 40	151 9	784 40	375 16	334 15
HAW, combined	-	-	(72) ± 6	(984) 16	(147) 6	(777) 15	(384) 9	(329) 8
ATMOSPHERE	3.53	3.29	71.2	983.5	151.2	789.8	388.1	329.9
AVCC (meteoritic)	4.58	4.10	82.0	(variable)	161	817	376.2	321.5

Figure 1. Noble gases in the oceanic crust and mantle. Hydrothermal circulation of seawater into the oceanic crust occurs at an active spreading ridge. Juvenile gases from the magma may be emitted into the heated water of a rising hydrothermal plume. Dissolved atmospheric gases in the circulating seawater may become fixed in the crust. These gases will be carried away from the ridge by seafloor spreading, and eventually subducted. Gases trapped in sediments may also be subducted. An unknown fraction of the subducted gases may be outgassed during shallow metamorphism of the down-going slab. If this fraction is not large, significant contamination of the upper mantle by atmospheric noble gases can be expected. Mantle convection may eventually bring these gases to the ridge axis, where they may be returned to the atmosphere.

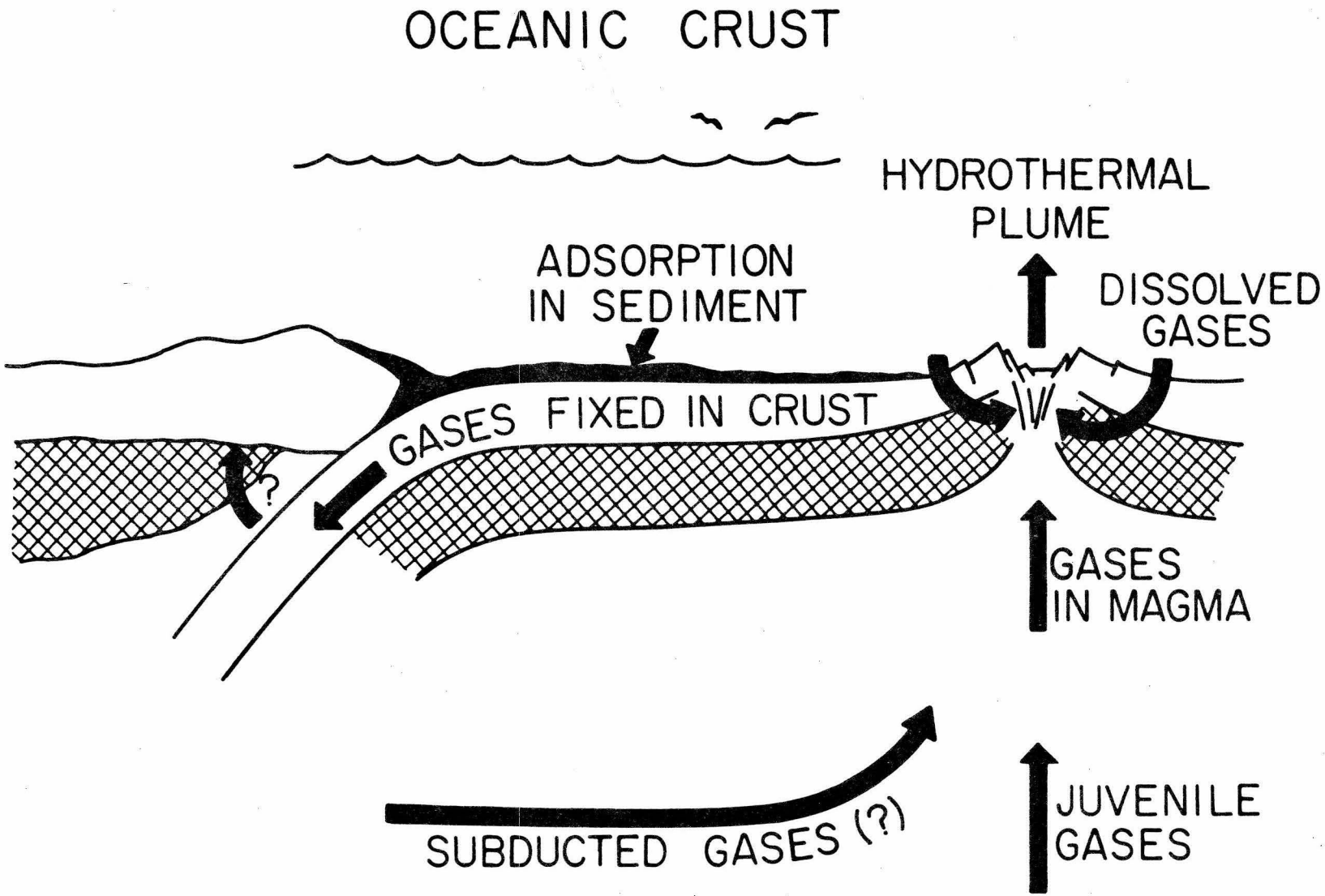
OCEANIC CRUST
HYDROTHERMAL PLUME
ADSORPTION IN SEDIMENT
DISSOLVED GASES
GASES FIXED IN CRUST
?
GASES IN MAGMA
SUBDUCTED GASES (?)
JUVENILE GASES

Figure 1

(MOR)

Figure 2. Elemental abundance patterns for noble gases. $F^m=(^mX/^{36}Ar)_{sample}/(^mX/^{36}Ar)_{air}$. The pattern for a sample of air is a horizontal line. On the left are shown reference patterns including solar and planetary primordial gases (Table 3). Air from an infinite reservoir dissolved in water is enriched in the heavy noble gases and depleted in neon (crosses). Air dissolved in molten enstatite pyroxene (Kirsten, 1968) is depleted in the heavy noble gases and enriched in neon. On the right are shown abundance patterns for the samples studied. Numbered samples may be identified from Table 1. In most of the samples, neon, krypton, and xenon are all enriched relative to the atmospheric normalization. Similar abundance patterns for MOR basalts were observed by Dymond and Hogan (1973). The U-shaped patterns are not consistent with any one reference pattern. Presumably, the observed patterns are the result of a number of processes such as differential solubility, diffusion, gas-loss, etc.

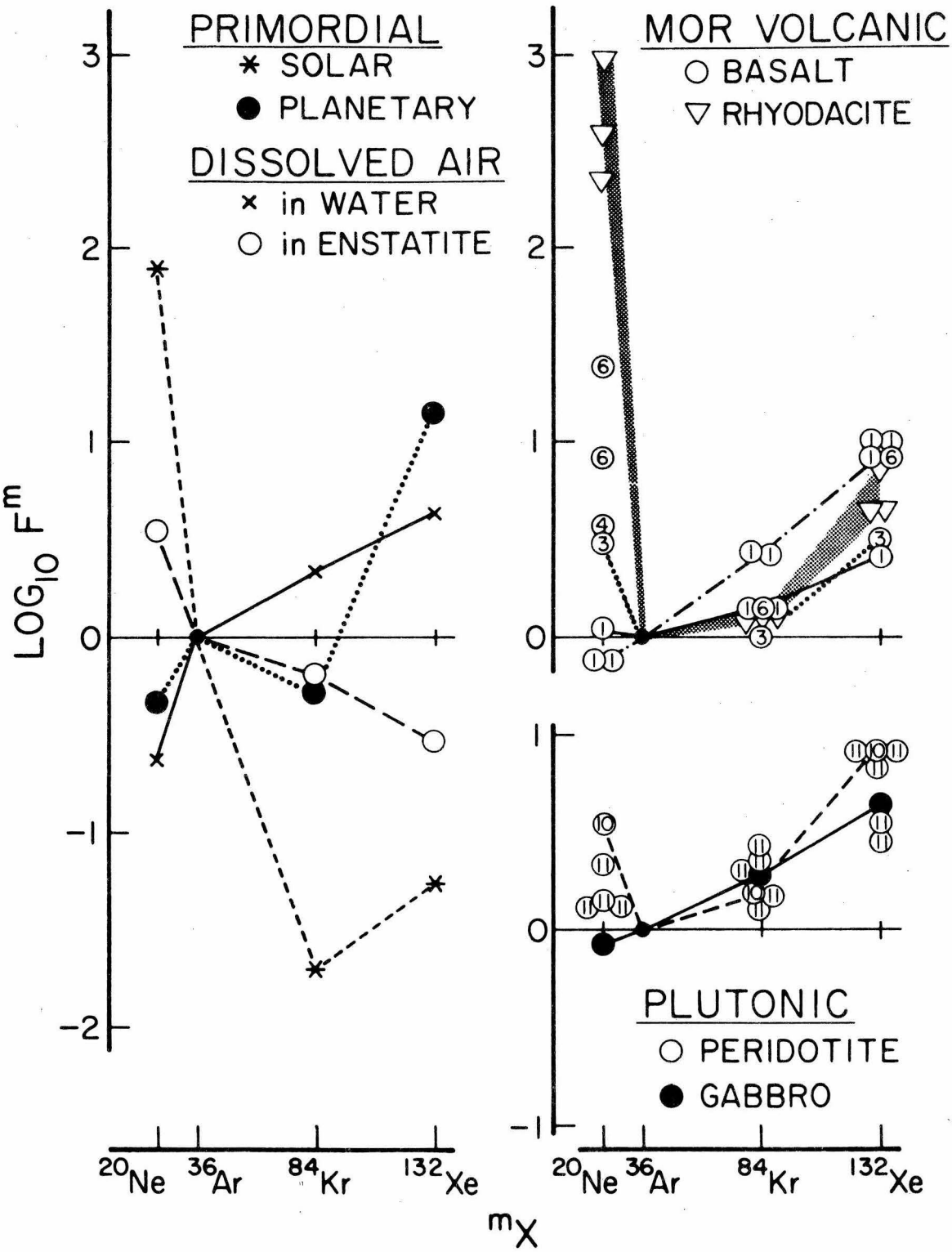
PRIMORDIAL
* SOLAR
● PLANETARY
DISSOLVED AIR
× in WATER
○ in ENSTATITE
MOR VOLCANIC
○ BASALT
▽ RHYODACITE
PLUTONIC
○ PERIDOTITE
● GABBRO
LOG10 Fm
mX
20Ne
36Ar
84Kr
132Xe

Figure 2
(MOR)

Figure 3. Three-isotope correlation diagram for xenon in MOR basalt glass samples. Mixtures of two distinct components will plot on straight mixing lines. Addition of radiogenic ^{129}Xe will displace points vertically upward. Addition of fission xenon from ^{238}U or ^{244}Pu will shift points to the right and down, as indicated by dashed lines. Error bars shown represent 2σ limits. Samples from specimens 3(VG212) and 6(VGA11) show xenon of atmospheric composition, while those from 1(V33-07), 2(TR138), and 5(111240) show small excesses of both ^{129}Xe and ^{136}Xe relative to the atmospheric composition. The isotopic shifts correspond to excesses of about 10^{-18} moles xenon/gram sample or only about 10^{6} atoms/gram.

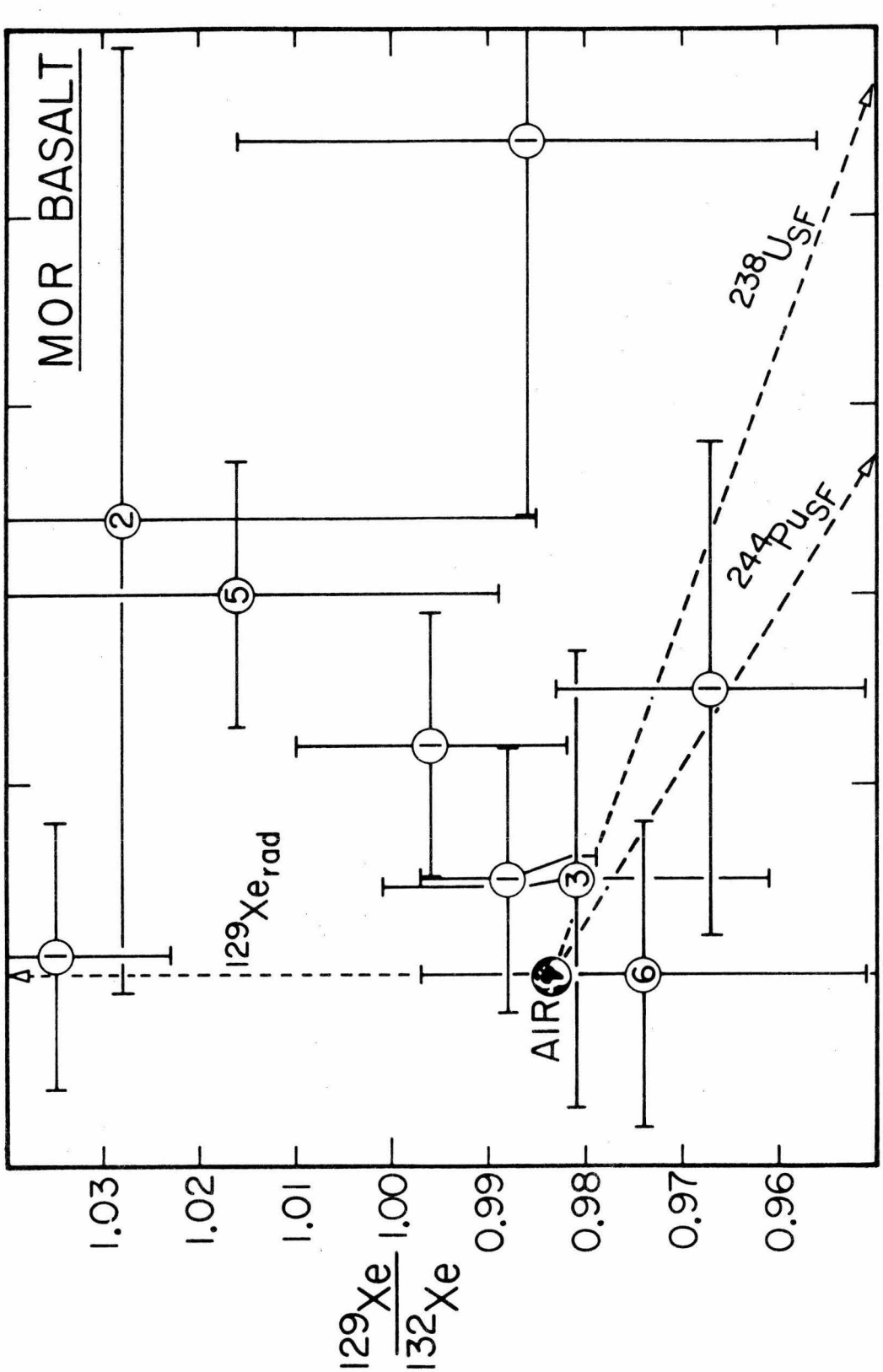
MOR BASALT
AIR
$^{129}Xe_{rad}$
$^{238}U_{SF}$
$^{244}Pu_{SF}$
$\frac{^{129}Xe}{^{132}Xe}$
$^{136}Xe / ^{132}Xe$
1.03
1.02
1.01
1.00
0.99
0.98
0.97
0.96
0.33
0.34
0.35
0.36
0.37
0.38

Figure 3
(MOR)

Figure 4. Non-radiogenic neon and argon in MOR glass samples. If the noble gases were a mixture of atmospheric and solar primordial components, samples should plot along the mixing line shown. They do not, so the neon enrichments observed cannot be due to addition of solar primordial gases as suggested by Dymond and Hogan (1973). The enrichment is probably the product of a fractionation process such as diffusion or Rayleigh distillation operating during transport of the noble gases. We suggest that the 3% isotopic enhancement of ^{20}Ne relative to ^{22}Ne in VG997 (sample 9) arose by the same fractionation process that enriched neon relative to argon by a factor of several hundred in this sample.

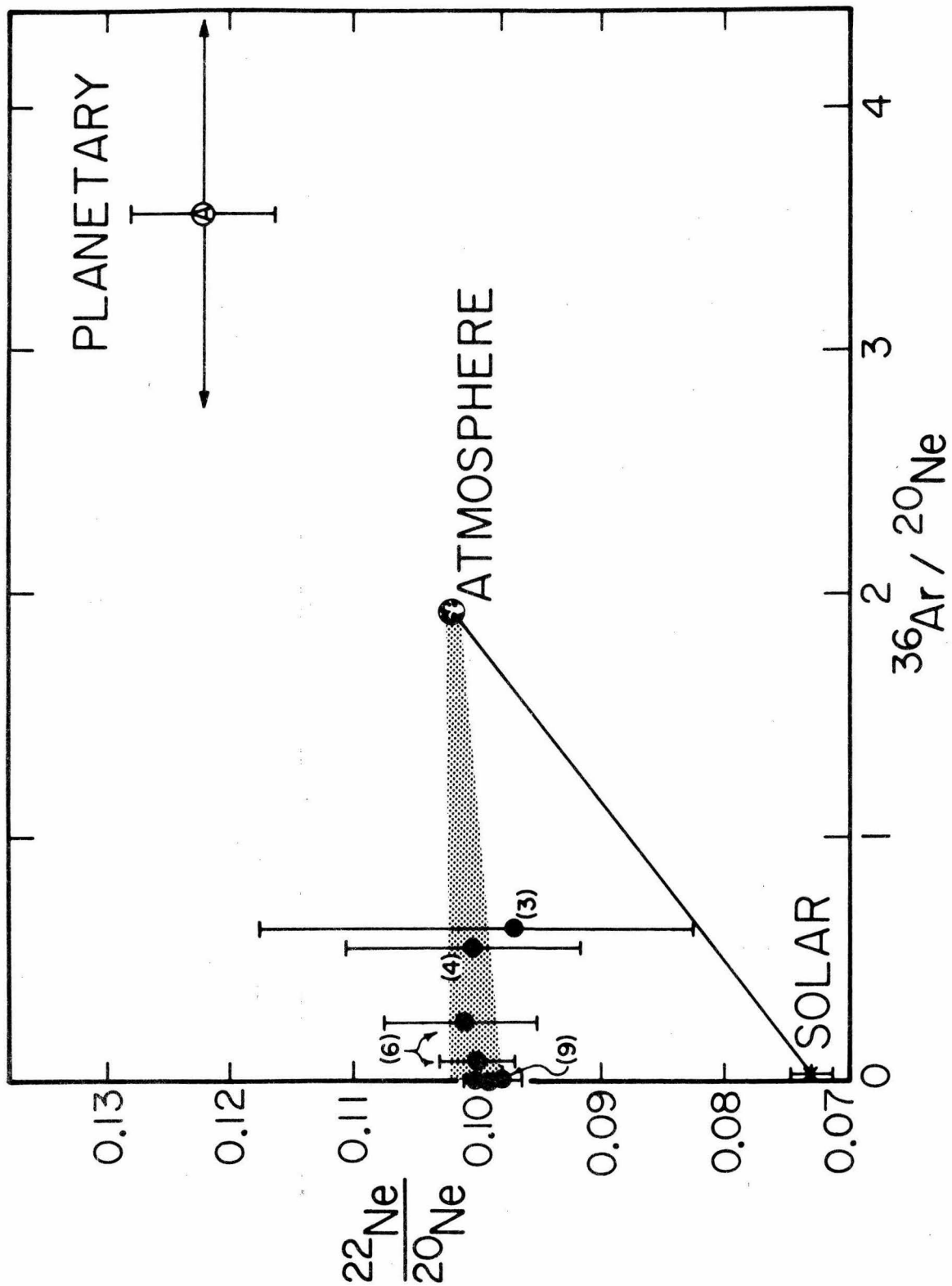
PLANETARY
ATMOSPHERE
SOLAR
(3)
(4)
(6)
(9)
0.13
0.12
0.11
0.10
0.09
0.08
0.07
0
1
2
3
4
$\frac{22Ne}{20Ne}$
$36Ar / 20Ne$

Figure 4
(MOR)